



HAL
open science

Time-resolved serial femtosecond crystallography at X-ray free electron lasers to study light-sensitive proteins on the ultra-fast time scale

Kyprianos Hadjidemetriou

► **To cite this version:**

Kyprianos Hadjidemetriou. Time-resolved serial femtosecond crystallography at X-ray free electron lasers to study light-sensitive proteins on the ultra-fast time scale. *Biological Physics* [physics.bio-ph]. Université Grenoble Alpes [2020-..], 2022. English. NNT : 2022GRALY030 . tel-04009105

HAL Id: tel-04009105

<https://theses.hal.science/tel-04009105v1>

Submitted on 1 Mar 2023

HAL is a multi-disciplinary open access archive for the deposit and dissemination of scientific research documents, whether they are published or not. The documents may come from teaching and research institutions in France or abroad, or from public or private research centers.

L'archive ouverte pluridisciplinaire **HAL**, est destinée au dépôt et à la diffusion de documents scientifiques de niveau recherche, publiés ou non, émanant des établissements d'enseignement et de recherche français ou étrangers, des laboratoires publics ou privés.

THÈSE

Pour obtenir le grade de

DOCTEUR DE L'UNIVERSITÉ GRENOBLE ALPES

Spécialité : Physique pour les Sciences du Vivant

Arrêté ministériel : 25 mai 2016

Présentée par

Kyprianos HADJIDEMETRIOU

Thèse dirigée par **Martin WEIK**, Université Grenoble Alpes

préparée au sein du **Laboratoire Institut de Biologie Structurale**
dans l'**École Doctorale Physique**

**Utilisation des lasers à électrons libre pour
étudier les protéines photosensibles par
cristallographie résolue en temps**

**Time-resolved serial femtosecond
crystallography at X-ray free electron lasers to
study light-sensitive proteins on the ultra-fast
time scale**

Thèse soutenue publiquement le **3 mai 2022**,
devant le jury composé de :

Madame ARWEN R. PEARSON

Professeur, Universität Hamburg, Rapporteur

Monsieur BRUNO ROBERT

Ingénieur HDR, CEA CENTRE DE PARIS-SACLAY, Rapporteur

Monsieur MARC JAMIN

Professeur des Universités, UNIVERSITE GRENOBLE ALPES, Président

Monsieur HIDEAKI MIZUNO

Professeur, Katholieke Universiteit Leuven, Examineur

Monsieur MICHAEL C. THOMPSON

Professeur assistant, University of California, Examineur

Monsieur JACQUES-PHILIPPE COLLETIER

Directeur de Recherche, HDR, Institut de Biologie Structurale, Invité



Table of Contents

<i>I Preface</i>	4
<i>II Acknowledgements</i>	7
<i>III Glossary and abbreviations</i>	9
<i>IV Abstract</i>	12
<i>V Résumé</i>	13
<i>Chapter 1 Introduction</i>	15
<i>1.1 Electromagnetic radiation</i>	16
1.1.1 Introduction.....	16
1.1.2 Visible light	17
1.1.3 X-ray light.....	18
1.1.4 Lasers	18
1.1.5 Figures.....	20
<i>1.2 X-ray diffraction and data collection</i>	21
1.2.1 Interaction of X-rays with matter	21
1.2.2 X-ray diffraction by crystals	23
1.2.3 Synchrotrons.....	24
1.2.4 X-ray free-electron lasers	25
1.2.5 From serial femtosecond crystallography at XFELs to serial crystallography at synchrotrons	26
1.2.6 Time-resolved X-ray crystallography	30
1.2.7 Sample delivery for serial crystallography.....	34
1.2.8 Detectors for XFEL experiments	37
1.2.9 Figures.....	39
<i>1.3 Analysis of serial crystallography data</i>	42
1.3.1 General concepts	42
1.3.2 Hit-finding	42
1.3.3 Indexing and integration	43
1.3.4 Merging.....	44
1.3.5 Phase problem and molecular replacement	45
1.3.6 Model building and refinement.....	46

1.3.7 Difference Fourier map calculation	47
1.3.8 Structure factor extrapolation	48
1.3.9 Figures.....	49
<i>Chapter 2 Fatty acid photodecarboxylase</i>	<i>50</i>
<i>2.1 Introduction</i>	<i>51</i>
2.1.1 Enzymes and their reactions	51
2.1.2 Photoenzymes	53
2.1.3 Fatty acid photodecarboxylase.....	55
2.1.4 Figures.....	57
<i>2.2 Time-resolved SFX studies on fatty acid photodecarboxylase</i>	<i>58</i>
2.2.1 Introduction.....	58
2.2.2 Results and Discussion	59
2.2.3 Ongoing work and perspectives	64
2.2.4 Materials and Methods	65
2.2.5 Figures and Tables	71
<i>2.3 Time-resolved serial femtosecond crystallography on fatty acid photodecarboxylase: lessons learned</i>	<i>84</i>
2.3.1 Synopsis.....	84
2.3.2 Abstract.....	84
2.3.3 Introduction.....	85
2.3.4 Materials and Methods	87
2.3.5 Results and Discussion	91
2.3.6 Conclusion	97
2.3.7 Acknowledgements.....	98
2.3.8 Figures.....	99
2.3.9 Supporting information	108
2.3.10 References	124
<i>Chapter 3 Reversibly photoswitchable fluorescent proteins</i>	<i>128</i>
<i>3.1 Introduction</i>	<i>129</i>
3.1.1 Fluorescent proteins.....	129
3.1.2 Reversibly photoswitchable fluorescent proteins.....	131
3.1.3 Super-resolution microscopy.....	132
3.1.4 rsEGFP2.....	134

3.1.5 Figures.....	138
3.2 Time-resolved SFX studies on rsEGFP2 mutants	143
3.2.1 Introduction.....	143
3.2.2 Results and Discussion.....	145
3.2.3 Conclusions and Perspectives.....	148
3.2.4 Materials and Methods	149
3.2.5 Figures and Tables	158
3.3 Rational control of off-state heterogeneity in a photoswitchable fluorescent protein	176
3.3.1 Introduction.....	176
3.3.2 Results	177
3.3.3 Discussion.....	179
3.3.4 Ongoing work and perspectives	182
3.3.5 Materials and Methods	182
3.3.6 Figure and Tables.....	187
3.4 Comparison of synchrotron and XFEL room-temperature serial crystallography data collected on protein crystals 3 μm in diameter	203
3.4.1 Introduction.....	204
3.4.2 Results and Discussion.....	207
3.4.3 Conclusion and Perspectives	209
3.4.4 Materials and Methods	210
3.4.5 Figures and Tables	214
4 Summary.....	224
5 References.....	226
6 Appendices	277
6.1 Mechanism and dynamics of fatty acid photodecarboxylase.....	278
6.2 Rational control of structural off-state heterogeneity in a photoswitchable fluorescent protein provides switching contrast enhancement	292
6.3 Structural Information on the Trans-to-Cis Isomerisation Mechanism of the Photoswitchable Fluorescent Protein rsEGFP2 Revealed by Multiscale Infrared Transient Absorption.....	304

I Preface

The current manuscript refers to my Ph.D. work, entitled “Time-resolved serial femtosecond crystallography at X-ray free electron lasers to study light-sensitive proteins on the ultra-fast time scale.” My Ph.D. work was conducted under the supervision of Dr. Martin Weik and was prepared at the Institut de Biologie Structurale in Grenoble (France). The awarding body is the Doctorate School of Physics of the Université Grenoble-Alpes, and it was funded by the Université Grenoble-Alpes and the Ministère de l'Enseignement supérieur, de la Recherche et de l'Innovation between September 2017 to April 2021, and the Commissariat à l'énergie atomique et aux énergies alternatives from May 2021 to January 2022. The work focuses on the use of X-ray free electron lasers (XFELs) to study the structure and function of two light-sensitive proteins, fatty acid photodecarboxylase (FAP), and rsEGFP2 and its mutants.

Chapter 1 gives a general introduction to X-ray radiation, time-resolved serial crystallography, and data analysis methods. Chapter 2 focuses on the newly discovered photoenzyme, FAP, using time-resolved serial femtosecond crystallography (TR-SFX) from the pico- to the millisecond time scale. It also describes the problems I have encountered during the data analysis. Chapter 3 presents the work on the reversibly photoswitchable fluorescent proteins, rsEGFP2, and its mutants V151A and V151L. Investigation was carried out on the static structures of the *off*-state rsEGFP2 and its mutants and TR-SFX on the rsEGFP2 mutants in the nanosecond time scale. At the end of Chapter 3, a systematic comparison of rsEGFP2 data from XFEL and synchrotrons is made.

By the end of my Ph.D. work, the following articles were prepared or submitted showing my contribution and work as described in the corresponding sections. The complete articles can be found in the Appendices.

FAP project (Chapter 2):

Described in Section 2.2 and shown in Appendix 6.1

Sorigué D., **Hadjidemetriou K.**, Blangy S., Gotthard G., Bonvalet A., Coquelle N., Samire P., Aleksandrov A., Antonucci L., Benachir A., Boutet S., Byrdin M., Cammarata M., Carbajo S., Cuiné S., Doak R. B., Foucar L., Gorel A., Grünbein M., Hartmann E., Hienerwadel R., Hilpert M., Kloos M., Lane T. J., Légeret B., Legrand P., Li-Beisson Y., Moulin S., Nurizzo D., Peltier

G., Schirò G., Shoeman R. L., Sliwa M., Solinas X., Zhuang B., Barends T. R. M., Colletier J.-P., Joffre M., Royant A., Berthomieu C., Weik M., Domratcheva T., Brettel K., Vos M. H., Schlichting I., Arnoux P., Müller P., Beisson F. (2021)

“Mechanism and dynamics of fatty acid photodecarboxylase”. *Science* 372(6538):eabd5687

Doi: 10.1126/science.abd5687

Described in Section 2.3

Hadjidemetriou K., Coquelle N., Barends T.R. M., De Zitter E., Schlichting I., Colletier J.-P., Weik M. “Time-resolved serial femtosecond crystallography on fatty acid photodecarboxylase: lessons learned”. Accepted in *Acta. Cryst. D*.

Reversibly photoswitchable fluorescent proteins project (Chapter 3):

Described in Section 3.3 and shown in Appendix 6.2

Adam V.*, **Hadjidemetriou K.***, Jensen N.*, Shoeman R. L.*, Woodhouse J.*, Aquila A., Banneville A.-S., Barends T. R. M., Bezchastnov V., Boutet S., Byrdin M., Cammarata M., Carbajo S., Christou N. E., Coquelle N., De la Mora E., El Khatib M., Moreno Chicano T., Doak R. B., Fieschi F., Foucar L., Glushonkov O., Gorel A., Grünbein M.-L., Hilpert M., Hunter M., Kloos., Koglin J. E., Lane T. J., Liang M., Mantovanelli A., Nass K., Nass Kovacs G., Owada S., Roome C. M., Schirò G., Seaberg M., Stricker M., Thépaut M., Tono K., Ueda K., Uriarte L. M., You D., Zala N., Domrarcheva T., Jackobs S., Sliwa M., Schlichting I., Colletier J.-P., Bourgeois D. & Weik M. (2021). Rational control of structural off-state heterogeneity in a photoswitchable fluorescent protein provides switching contrast enhancement.

Preprint in bioRxiv. Doi: 10.1101/2021.11.05.462999

Accepted in *ChemPhysChem*. Doi: 10.1002/cphc.202200192

Shown in Appendix 6.2

Uriarte L. M., Vitale R., Niziski S., **Hadjidemetriou K.**, Zala N., Lukacs A., Greetham G., Sazanovich I., Weik M., Ruckebusch C., Meech S., Sliwa M. “Structural Information on the Trans-to-Cis Isomerisation Mechanism of the Photoswitchable Fluorescent Protein rsEGFP2 Revealed by Multiscale Infrared Transient Absorption”. *J. Phys. Chem. Lett.* 2022, 13, 5, 1194–1202

Doi: 10.1021/acs.jpcclett.1c02920

The articles in preparation are:

Described in Section 3.2

Uriarte* L. M., **Hadjidemetriou K.***, Banneville A.-S., Barends T. R. M., Coquelle N., Doak R. B., Fieschi F., Foucar L., Gorel A., Hilpert M., Kloos M., Roome C. M., Shoeman R. L., Owada S., Schirò G., Stricker M., Thépaut M., Ueda K., You D., Zala N., Lukacs A. Greetham

G., Sazanovich I., Tono K., Meech S. R., Schlichting I., Colletier J.-P., Weik M., Sliwa M. Trans to cis photo-isomerization in fluorescent proteins is independent of the free volume. In preparation.

Described in Section 3.4

Hadjidemetriou K.*, Coquelle N.* , Woodhouse J.* , de la Mora E., Shilova A., Rosenthal M., Barends T. R. M., Schlichting I., Burghammer M., Colletier J.-P., Weik M. Comparison of synchrotron and XFEL room-temperature serial crystallography data collected on protein crystals 3 μm in diameter. In preparation.

II Acknowledgements

This work could not have come to an end without the valuable contribution and help from certain persons.

First of all, I would like to thank my Ph.D. supervisor, Dr. Martin Weik who gave me the opportunity to start a Ph.D. under his supervision. I would like to thank him for his support and guide throughout these years, especially the difficult years of 2020, 2021 and 2022. By the end, of my Ph.D. work I understood literally the meaning of the German word “*Doktorvater*”.

I would like to express my gratitude to the jury of my Ph.D. defense Dr. Jacques-Philippe Colletier, Prof. Marc Jamin, Prof. Hideaki Mizuno, Prof. Arwen Pearson, Dr. Bruno Robert, and Prof. Michael Thompson who kindly accepted to assess my Ph.D. work.

I would like to thank my Comité Suivi de Thèse Prof. Eva Pebay-Peyroula, Dr. Bernhard Brutscher and Dr. Dominique Bourgeois for following my PhD work every year, giving me advises and encouraging me to continue my project.

I would like to express my gratitude and appreciation to Dr. Jacque Philippe Colletier for his support, help and teaching the X-ray crystallography as well as our friendly chats.

I am deeply grateful to Prof. Ilme Schlichting who shared her microcrystallisation protocol and for the fruitful discussions of my results. A special thanks to her team who participated in all the XFEL experiments of my Ph.D. work and who was responsible for sample injection and online monitoring. I am grateful to Dr. Thomas Barends for his help and input on the FAP data processing.

I also would like to say special thanks to Dr. Nicolas Coquelle who assisted me during data processing on FAP and rsEGFP2 projects.

I am thankful to Dr. Michel Sliwa and Lucas M. Uriarte for their support and continues discussions especially on the rsEGFP2 and FAP projects.

I would like to extend my sincere thanks to Dr. Damien Sorigué and Dr. Frederic Beisson for their insightful comments and suggestions on the FAP project.

I would like to offer my special thanks to Dr. Tatiana Domratcheva for our beneficial discussions on the FAP and rsEGFP2 projects.

Nothing would not be possible for my Ph.D. work without the hard work of the scientists of the XFEL facilities of LCLS in the USA, SwissFEL in Switzerland, and SACLA in Japan.

I am also grateful to Dr. Virgile Adam and Dr. Oleksandr Glushonkov for their help and discussions concerning the rsEGFP2 project.

I am indebted to my team colleagues Elena Andreeva, Anne-Sophie Banneville, Martin Byrdin, Elke De Zitter, Sofia Kapetanaki, Julie Lopes, Tadeo Moreno Chicano, Rory Munro, Kevin Pounot, Ronald Rios Santacruz, Giorgio Schirò, Guillaume Tetreau, Joyce Woodhouse, Ninon Zala, for their help, discussions, and the friendly environment in the lab.

Dear friends, Iwanna Demosthenous, Andreas Fouskotos, Yiorgos Kapesides, Johan Montagna, Dorina Papanastasiou, Michael Theodoulides, Nikolas Sapountzoglou, Christina Yiannapi, I would like to thank you for your support and because you were always available to hear me.

Dear Kyriacos Constantinou, my alter-ego. You have been always by my side for the last 19 years. Thank you!

My dearest Sofia Jaho, your encouragement and understanding helped me through the dark times. Without you believing in me, I never would have made it.

Last but not least, my family. You were the first, who believed in me and have always supported me all these years abroad. Nikola, Giorgo, mamma et papa your love is endless.

III Glossary and abbreviations

ADE: Acoustic Droplet Ejection

AGIPD: Adaptive Gain Integrating Pixel
Detector

AM: Ammonium sulfate

ASL: Advanced Light Source

bET: back Electron Transfer

CCD: Charge-Couple Device

CoMESH: Concentric Microfluidic
Electrokinetic Eample Eolder

CPD: Cyclobutane Pyrimidine Dimer

CSPAD: Cornell-SLAC Pixel Array
Detector

CvFAP: FAP from *Chlorella variabilis*

CXI: Coherent X-ray Imaging

DAPHNIS: Diverse Application Platform
for Hard x-ray diffraction In SACLA

DESY: Deutsches Elektronen-SYnchrotron

DLS: Dynamic Light Scattering

DNA: DeoxyriboNucleic Acid

EBS: Extremely Brilliant Source

EGFP: Enhanced Green Fluorescent
Protein

ESRF: European Synchrotron Radiation
Facility

FAD: Flavin Adenine Dinucleotide

FAP: Fatty Acid Photodecarboxylase

FEM: Front-End Module

fET: forward Electron Transfer

FFT: Fast Fourier Transform

FP: Fluorescent Protein

FQY: Fluorescence Quantum Yield

FTIR: Fourier Transform InfraRed
spectroscopy

FWHM: Full Width at Half Maximum

GDVN: Gas Dynamic Virtual Nozzle

GFP: Green Fluorescent Protein

GMC: Glucose-Methanol-Choline

HEPES: acide 4-(2-hydroxyéthyl)-1-
pipérazine éthane sulfonique

HMBA: Hybrid Multi-Bend Achromat

HVE: High-Viscosity Extrusion

IR: InfraRed

IUBMB: International Union of Biochemistry and Molecular Biology

JUNGFRAU: adJUstiNg Gain detector FoR the Aramis User station

LCLS: Linac Coherent Light Source

LPOR: Light-dependent Protochlorophyllide OxidoReductase

MC: Monte Carlo

MESH: Microfluidic Electrokinetic Eample Eolder

MPCCD: Multi-Port Charge-Coupled Device

MX: Macromolecular crystallography

NCS: Non-Crystallographic Symmetry

NL-SIM: Non-Linear Structured Illumination Microscopy

p-HBI: 4-(p-HdroxyBenzylidene)-5-Imidazolinone

PAD: Pixel Array Detector

PAFP: PhotoActivable FP

PAGE: PolyAcrylamide Gel Electrophoresis

PAL-XFEL: Pohang Accelerator Laboratory X-ray Free Electron Laser

PALM: Photo Activated Localization Microscopy

PCET: Proton-Coupled Electron-Transfer

PCFP: PhotoConvertible FP

PCTFE: PolyChloroTriFluoroEthylene

PDB: Protein Data Bank

PEG: PolyEthylene Glycol

PEG: PolyEthylene Glycol

PLM: PaLMitate

PTFP: PhotoTransformable FP

QY: Quantum Yield

r.m.s.: root mean square

RESOLFT: Reversible Saturable Optical Fluorescence Transition

rsEGFP: reversibly switchable EGFP

RSFP: Reversibly photoSwitchable FP

SACLA: SPring-8 Angstrom Compact free electron LAser

SASE: Self-Amplified Spontaneous Emission

SEC: Size Exclusion Chromatography

SFX: Serial Femtosecond Crystallography

SOFI: Super-resolution Optical Fluctuation
Imaging

SSX: Serial Synchrotron Crystallography

TR: time-resolved

Tris: 2-Amino-2-(hydroxymethyl)propane-
1,3-diol

UV: Ultraviolet

WLE: Wirelessly powered Light Emitters

XFEL: X-ray Free-Electron Laser

IV Abstract

X-ray free-electron lasers (XFELs) are large-scale facilities that produce highly brilliant and short X-ray pulses. XFELs, complementing synchrotrons, allow the determination of the structure of fragile proteins to be solved from small microcrystals and their dynamics to be examined with femtosecond time resolution using a suite of techniques known as serial femtosecond crystallography (SFX). The goal of this Ph.D. work was to examine short-lived intermediates ranging from pico- to microseconds in two light-sensitive proteins using time-resolved SFX (TR-SFX) at XFELs. The two systems that have been studied were a photoenzyme, named fatty acid photodecarboxylase (FAP), and a reversible photoswitchable fluorescent protein (RSFP), named rsEGFP2.

FAP is one of the three enzymes discovered so far, whose catalytic activity requires a continuous flux of light. FAP, which harbors a FAD cofactor, is involved in the metabolism of lipids in microalgae and catalyzes the decarboxylation of free fatty acids to alkanes or alkenes in response to blue light. We have been able to solve the radiation damage-free SFX structure of FAP's resting state at 2 Å resolution that confirmed the observation made in a high-resolution cryo-MX structure that unusual bending of the isoalloxazine ring of the FAD is present in the oxidized starting state. Furthermore, our TR-SFX study made it possible to follow light-induced decarboxylation in real-time. A detailed description of data analysis of TR-SFX data on FAP as well as structure factor extrapolation of the intermediate states is presented.

RSFPs and thus rsEGFP2 are essential tools in advanced fluorescence microscopy of live cells. They have the ability to be constantly cycled between two states, a fluorescent (on) and a non-fluorescent (off) state after exposition of RSFPs at proper wavelengths (Bourgeois and Adam 2012). Based on the reaction intermediates determined by TR-SFX on parental rsEGFP2 determined on the pico- to nanosecond time scale, two rationally designed variants of rsEGFP2 have been generated. In this thesis, off-state structures of the variants were solved by SFX. Furthermore, nanosecond TR-SFX experiments on these rsEGFP2 variants were carried out that provide insight into modified energy landscapes. Nanosecond TR-SFX intermediate structures on rsEGFP2 variants were described and a systematic comparison of rsEGFP2 SFX and SSX data to prepare for millisecond TR synchrotron serial crystallography (SSX) experiments on rsEGFP2 in the near future.

V Résumé

Les lasers X à électrons libres (XFELs) sont des installations à grande échelle qui produisent des impulsions de rayons X très brillantes et courtes. Les XFELs, complémentaires des synchrotrons, permettent de déterminer la structure des protéines fragiles à partir de petits microcristaux et d'examiner leur dynamique avec une résolution temporelle femtoseconde à l'aide d'une suite de techniques connues sous le nom de cristallographie sérielle femtoseconde (SFX). Le but de ce doctorat consistait à examiner les intermédiaires de courte durée allant de la pico- à la microseconde dans deux protéines sensibles à la lumière en utilisant la SFX résolu en temps (TR-SFX) aux XFELs. Les deux systèmes qui ont été étudiés étaient une photoenzyme, appelée photodécarboxylase d'acide gras (FAP) et une protéine fluorescente photocommutable réversible (RSFPs), appelée rsEGFP2.

La FAP est l'une des trois enzymes découvertes à ce jour, dont l'activité catalytique nécessite un flux continu de lumière. La FAP, qui abrite un cofacteur FAD, est impliquée dans le métabolisme des lipides dans les microalgues et catalyse la décarboxylation des acides gras libres en alcanes ou alcènes en réponse à la lumière bleue. Nous avons été en mesure de résoudre la structure SFX sans dommage par des rayons X de l'état "off" de la FAP à une résolution de 2 Å qui a confirmé l'observation faite dans une structure cryo-MX à haute résolution selon laquelle une flexion inhabituelle de l'anneau isoalloxazine du FAD est présente dans l'état oxydé. Notre étude TR-SFX a ensuite permis de suivre en temps réel la décarboxylation induite par la lumière. Une description détaillée de l'analyse des données TR-SFX sur FAP ainsi que l'extrapolation du facteur de structure des états intermédiaires est présentée.

Les RSFPs et donc rsEGFP2 sont des outils essentiels dans la nanoscopie de fluorescence avancée des cellules vivantes. Elles peuvent être basculées à plusieurs reprises entre un état fluorescent (on) et un état non fluorescent (off) par irradiation avec de la lumière à deux longueurs d'onde différentes. Basé sur les structures intermédiaires de réaction déterminées par TR-SFX sur rsEGFP2 parental déterminées à l'échelle de temps pico- à nanoseconde, deux variants rationnellement conçus du rsEGFP2 ont été générés. Dans cette thèse, les structures "off" des variants ont été résolues par SFX. De plus, des expériences TR-SFX nanosecondes sur ces variants de rsEGFP2 ont été menées. Des structures intermédiaires nanosecondes TR-

SFX sur des variants de rsEGFP2 ont été décrites et une comparaison systématique de données SFX et SSX a été effectuée, en vue d'expériences résolues en temps au synchrotron (TR-SSX).

Chapter 1

Introduction

1.1 Electromagnetic radiation

1.1.1 Introduction

Light has been at the center of the life of mankind for centuries. It has been a tool for humans to explore and investigate the world around them. It all started with curiosity and the desire to understand it and then the exploitation of its properties to study different phenomena in their lives.

Between the 4th century B.C. and 2nd century A.D., the observations of the Greek natural philosophers, such as Aristotle, Euclid, and Ptolemy, were centered on the study of vision and optics. The observations were then extended to studying the eye anatomy and physiology by Herophilus and Galen and the Arabs, such as Ibn al-Haytham and al-Kindi. By that time the nature of light was ignored but this didn't prevent humanity to continue to observe and study Nature using the light properties. It is worthwhile to mention that the Greeks in those days studied two strange phenomena, according to their understanding. The first one was noted by Thales of Miletus who observed that after rubbing a piece of amber it could lift small pieces of papyrus. The second one was that a mineral from Magnesia (Μαγνησία, a city in Greece) was able to attract iron metals. These phenomena are able to be explained by (static) electricity and magnetism, respectively. Magnetism comes from the Greek word Magnesia and electricity from the Greek word ἤλεκτρον (electron) which is the Greek word for amber. For centuries mankind has ignored the connection between these observations. It would take many centuries to find out what was the link with the properties of light.

In the middle of the 19th century, two British scientists, Michael Faraday and James Clerk Maxwell concentrated their research on electricity and magnetism whose results have determined and changed the everyday life of mankind. In 1865, James Clerk Maxwell published his work on electromagnetic fields (Maxwell 1865) in which, in a very simplistic way, he combined the laws of electricity and magnetism with the laws of light.

Nowadays, we refer to the electromagnetic spectrum in order to define a range of electromagnetic radiation. It is a set of energetic radiation of various frequencies. In other

words, the electromagnetic radiations are of the same nature, but their frequencies (and thus their energy) are different. The photons are the carriers of this energy. It has been defined in this spectrum, which it starts from low energy radiation to high energy radiation, and includes long-wave radio waves, microwaves, infrared radiation, visible light, ultraviolet light, X-rays, and γ -rays (Figure 1.1.1). The relationship between energy and frequency of these radiations is given by:

$$E = h\nu = \frac{hc}{\lambda} \quad (\text{eq. 1.1.1})$$

where E is the energy of a photon in joule (J), $h = \sim 6.626 \times 10^{-34} \text{ J}\cdot\text{s}^\#$ is Planck's constant, ν is the frequency in Hz, $c = \sim 2.9979 \times 10^8 \text{ m}\cdot\text{s}^{-1}^\#$ is the speed of light in a vacuum and λ is the wavelength of light in vacuum in meters. In the present work, as it refers to photon energy, it would be more appropriate to use a modified version of the equation 1.1.1:

$$\lambda = \frac{12.3984}{E} \quad (\text{eq. 1.1.2})$$

where the wavelength λ is given in \AA and the photon energy E in keV.

Two different ranges of the electromagnetic spectrum are important in this study, visible light and X-rays.

1.1.2 Visible light

All electromagnetic radiation is light, but the human eye can only view radiation in a narrow wavelength range. This narrow range is called visible light (Figure 1.1.1). Photoreceptor cells, such as rod-shaped, cone-shaped, and intrinsically photosensitive ganglion cells, are found in the retina of the eye and they are responsible for converting visible light into signals that can stimulate biological processes (*i.e.* vision). Important components of these cells are the

[#] The General Conference on Weights and Measures (CGPM), at its 26th meeting, on the revision of the International System of Units (SI), suggested in Resolution 1 that the Planck constant h is $6.626\ 070\ 15 \times 10^{-34} \text{ J}\cdot\text{s}$ and the speed of light in vacuum c is $299\ 792\ 458 \text{ m}\cdot\text{s}^{-1}$.

membranous photoreceptor proteins, opsins, which contain a pigment molecule called retinal. The opsins found in rod-shaped, cone-shaped, and intrinsically photosensitive ganglion cells are called rhodopsins (Ernst et al. 2014), iodopsins or photopsins (Yoshizawa and Wald 1967), and melanopsins (Berson 2002), respectively. The overall spectral sensitivity range of these photoreceptors in the human eye is between ~400 and ~700 nm which defines the visible light spectrum (Blume, Garbazza, and Spitschan 2019; Christie 2001).

1.1.3 X-ray light

In 1895, Wilhelm C. Röntgen detected a new range of the electromagnetic spectrum, that he called “X-rays” (or “*X-Strahlen*” as it was first reported in his publication written in German) to underline that its nature was unknown (Röntgen 1898). The new type of radiation was able (among others) to penetrate biological tissues and exposed photographic films. Most X-rays have a wavelength ranging from 10 pm (hard X-rays) to 10 nm (soft X-rays). In a laboratory, X-rays may be created by focusing a high-energy electron beam against metal atoms such as copper or gallium.

In 1909, Charles G. Barkla and Charles A. Sadler discovered the characteristic X-ray radiation of the elements (Barkla and Sadler 1909). When a material is bombarded with X-rays, intense secondary X-ray emission lines are observed which are unique for each element. This fingerprint represents discrete energy levels of electronic states in atoms that are related to the atomic number of the element.

In 1914, Henry G. J. Moseley discovered the relationship between atomic number and the specific wavelength of X-rays of the elements (Moseley’s law) and therefore the basis of X-ray fluorescence spectroscopy (Moseley 1914).

The concepts of X-ray diffraction are described in section 1.2.

1.1.4 Lasers

The laser, which stands for "Light Amplification by Stimulated Emission of Radiation," is a device and/or light source that emits spatially and temporally coherent light. A laser may be concentrated on a tiny area while remaining focused across a large distance due to spatial coherence (collimation). A laser can emit light with a certain wavelength (monochromatic) or pulses of light with a large spectrum, but durations can be achieved down to femtosecond time-scale due to temporal coherence.

In this study, two types of lasers were used to study biological macromolecules, a visible-light laser, and an X-ray free-electron laser. The former is used as the radiation which triggers the reaction (pump) and the latter is the radiation that gives the diffraction patterns (probe) in a pump-probe scheme of time-resolved serial femtosecond crystallography (TR-SFX). The characteristics of these two lasers are:

- i) Laser gain medium: it is a medium that can amplify the power of electromagnetic radiation. For example, solid-state lasers use the properties of atomic or molecular states as the laser gain medium. X-ray free-electron lasers (and therefore XFELs as a probe laser) use a relativistic electron beam as the laser gain medium. In the case of the pump laser, a crystal of Ti:sapphire is used as a laser gain medium during a TR-SFX at the LCLS (USA), SACLA (Japan), and SwissFEL (Switzerland) X-ray free-electron lasers (XFELs).

- ii) Laser beam polarization: it defines its state of polarization. It is described as the direction in which the electric field is oscillating. Please be noted that during the TR-SFX experiments, an optical pump laser with circular polarized light was used. This means that the electric field changes its orientation by 360° within one wavelength. A circularly polarized optical pump laser was preferred because the chromophores or light-capturing molecules which crystalline proteins bind have different orientations (*i.e.* different orientation of the electric dipole moment of the chromophore) with respect to the optical pump laser direction. In the case of the XFEL probe, linearly polarized beams are available at the XFEL facilities. Circularly polarized beams at XFELs have been commissioned recently and they will be available for external users soon, allowing studies on chiral dynamics as well as the anisotropic and magnetic properties of the sample (Geloni, Kocharyan, and Saldin 2011; Kubota et al. 2019; Lutman et al. 2016; Roussel et al. 2017).

1.1.5 Figures

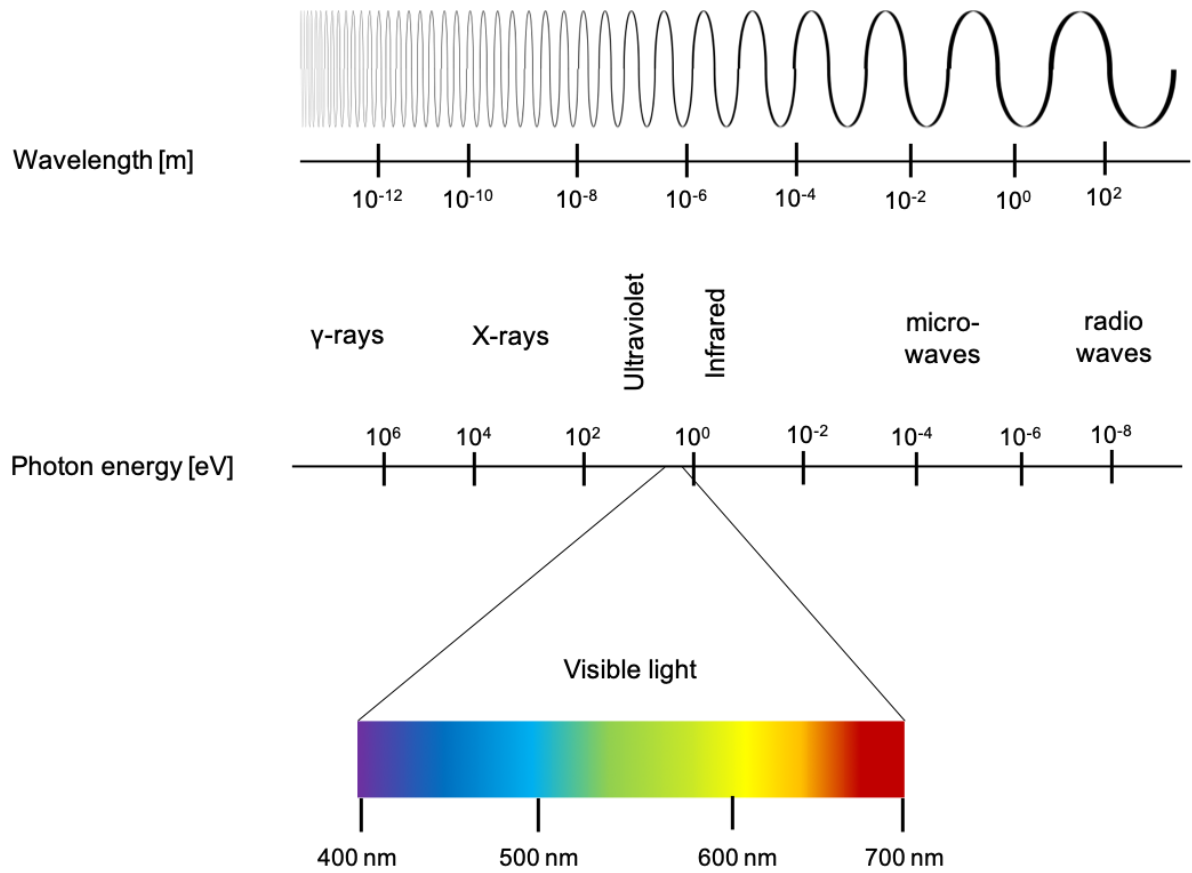


Figure 1.1.1: The electromagnetic spectrum.

Electromagnetic radiation extends from small wavelengths via γ -rays and X-rays to radio waves.

1.2 X-ray diffraction and data collection

1.2.1 Interaction of X-rays with matter

The question raised now is how electromagnetic radiation interacts with matter, and more precisely, how X-ray radiation interacts with crystalline macromolecules. To the extents, we are familiar with everyday phenomena of interactions of visible light with matter like refraction, reflection, and absorption.

Electromagnetic radiation predominantly interacts with matter *via* the electric field vector and the interaction with the magnetic field vector is weak. This is because the interaction of the electric field vector with the dielectric polarizability is several orders of magnitude higher than the diamagnetic susceptibility and as a consequence, we will focus on electronic interactions. The polarizability α is simply the interaction constant relating the induced dipole moment \mathbf{p} to the electric field vector \mathbf{E} .

$$p = \alpha \times E \quad (\text{eq. 1.2.1})$$

Regarding the above equation, once past infrared frequency, only the electrons of an atom can be polarizable enough to interact with the electric field vector. Therefore, from the visible light range up to the hard X-ray energy ranges, only electron polarization remains the basis for interaction with electromagnetic radiation.

Clausius-Mossotti (reviewed in Rysselberghe 1932) and Lorenz-Lorentz (reviewed in Kragh 2018) show the direct correlation of the dielectric polarizability with the refractive index of a material. Optical dispersion is caused when the refractive index changes as a function of frequency. An example of optical dispersion is when the blue light gets refracted more than red light as it is observed in rainbows or glass prisms. Also, electronic polarizability becomes very weak at high frequencies of electromagnetic radiation and asymptotically reaches practically identical values for all matter.

Considering the above remarks, the three following conclusions can be drawn for X-ray radiation. First, there are no refractive lenses for X-rays which would allow direct imaging of an object. This is because lenses depend on the change of refractive index when light transitions from one medium to the other. As the polarizability of materials and also the refractive index in the X-ray range are practically identical for all materials, there is no difference in refractive index between media. Second, the phenomenon of anomalous dispersion is exploited in anomalous diffraction phasing techniques and *ab initio* structure determination with X-ray crystallography. Precisely, dispersion is the phenomenon describing that the rate at which the wave is propagated depends on its frequency. The effects of dispersion and absorption are also observed for X-rays. Anomalous X-ray dispersion or anomalous scattering of X-rays is the energy-dependent change of the scattering factor of X-rays when absorption occurs at the absorption edge of an atom. Finally, X-rays as ionizing radiation interact with organic matter (proteins) causing radiation damage.

When protein crystals are exposed to highly brilliant X-ray beams, atoms absorb X-rays, and an electron escapes from the high-energy inner shell of the atom. These free electrons then can directly react with other atoms, break bonds, or generate free radicals.

The primary X-ray interaction processes with atoms (Garman 2010) (Figure 1.2.1) are:

- i) Elastic (Thompson) or coherent scattering (Figure 1.2.1A). The electron is sinusoidally accelerated by the incident X-ray radiation and emits radiation at the same wavelength. Therefore, there is no energy difference between the incident and the reemitted radiation. This process is at the origin of the diffraction pattern.
- ii) Inelastic (Compton) or incoherent scattering (Figure 1.2.1B). The X-ray radiation transfers part of its energy to the electron and thus the reemitted radiation has lower energy after the interaction.
- iii) Photoelectric effect (Figure 1.2.1C). The X-ray radiation transfers all its energy to an electron (in the inner shell of the atom) that is ejected from the atom (photoelectron). Subsequently, an electron from lower-energy shells takes the place of the ejected electron followed by characteristic X-ray emission, or the energy is transferred to an electron of the outer shell and it is then ejected (Auger electron). It

is estimated that a single absorbed 12 keV photon can cause roughly 500 additional ionization events (O'Neill, Stevens, and Garman 2002). The generated free radicals from these ionization events are directly correlated to secondary and specific radiation damage (O'Neill et al. 2002).

At 12 keV, about 98% of the incident X-ray photons do not interact at all with matter. Only 2% do interact, of which 84% interacts *via* the photoelectric effect, 8% causes inelastic (Compton) scattering, and 8% leads to elastic (Thompson) scattering (Garman and Owen 2006).

1.2.2 X-ray diffraction by crystals

Seventeen years after Wilhelm C. Röntgen's discovery, Max von Laue had the idea to diffract salt crystals with X-ray radiation believing that the interatomic distances were close to the wavelength of the X-ray radiation as it was estimated previously to be in the range of 10 – 0.01 nm (Sommerfeld 1912; Wien 1907). This idea came after discussions with Paul P. Ewald, Arnold Sommerfeld and Wilhelm Wien (von Laue 1915). With the help of the experimentalists, Walter Friedrich and Paul Knipping, the first diffraction pattern using X-rays of a copper sulfate was acquired (Friedrich, Knipping, and Laue 1913). Although the experiment was quite successful, the three diffraction conditions represented by the Laue equations (Friedrich et al. 1913) in each direction in the crystal lattice were not overly convenient and not easy to visualize in practical use. Sir William H. Bragg and Sir William L. Bragg, a father-and-son team, introduced a drastically simplified interpretation of X-ray diffraction by a crystal (Bragg and Bragg 1913). They interpreted the diffraction as a reflection off sets of equidistant discrete lattices planes (hkl), and the equation they introduced (Bragg's law), established a quantitative relation between the lattice spacing and the diffraction angle of discrete reflections (Figure 1.2.2A):

$$n \times \lambda = 2 \times d_{hkl} \times \sin \theta \quad (\text{eq. 1.2.2})$$

where n is the "order" of reflection, λ is the wavelength of the X-ray radiation, d_{hkl} is the spacing of the lattice planes and θ is the angle of the incident X-ray radiation.

Generally, diffraction (Figure 4B) is the interaction of electromagnetic radiation (*e.g.* X-ray radiation) with periodically arranged matter (*e.g.* crystal) into directions other than the original direction of the light, without change of the wavelength. It is necessary to quantify the intensity of this discrete diffraction as a function of the actual atomic or molecular content of the diffracting crystals. This quantification of the intensity is called structure factor amplitude (eq. 1.2.3). The structure factor ($F_{(hkl)}$), as a mathematical function, describes the relationship between the amplitude and the phase of a diffracted wave from crystal lattice planes. These crystal lattice planes are characterized by Miller indices (h, k, l).

$$F_{(hkl)} = \sum_{j=1}^{atoms} f_{(j)} e^{2\pi i[hx+ky+lz]} \quad (\text{eq. 1.2.3})$$

The unavailability of phase angles for experimentally measured structure factor amplitudes implies the phase problem in molecular structure reconstruction.

1.2.3 Synchrotrons

Synchrotrons facilities used for the collection of X-ray diffraction data. It is a type of particle accelerator in which negatively charged particles, in this case, the electrons are generated and accelerated in the linear accelerator, and they are injected into the storage ring, where they circulate at nearly the speed of light. When the electron beam changes direction, the electrons are accelerated towards the center of the storage ring losing energy by emitting X-ray radiation. The resulting X-ray radiation is then provided to the surrounding beamlines where the experiments take place. The electron energy that is lost through X-ray emission is recovered by radio-frequency cavities at each cycle. Originally, synchrotrons have been used as a tool to study particle physics by colliding charged particles, and X-ray emission was considered as being a byproduct. In the early 1970s, a group of chemists, while working at the Deutsches Elektronen-Synchrotron (DESY) synchrotron (Hamburg, Germany), discovered that the non-desirable X-ray emission could be used for X-ray diffraction (Rosenbaum, Holmes, and Witz 1971).

Since then, more than fifty synchrotrons have been constructed worldwide and they have been used among others for structural biology research using X-ray diffraction. But only a few of

them can produce high-energy (“hard”) X-rays. An example of such a source is the European Synchrotron Radiation Facility (ESRF) (Grenoble, France) where part of the experiments described in this study was performed. The ESRF storage ring is a tube of 844 meters in circumference and is maintained at low pressure ($\sim 10^{-9}$ mbar). It consists of 32 straight and 32 curved sections. In each straight section, focusing magnetic structures, such as undulators, ensure the generation of the focused and brilliant beam. In curved sections, the bending magnets bend the electron beam from their straight trajectory and hence X-ray emission occurs. A new era of synchrotron light sources has begun with the upgrade of the ESRF into a fourth-generation synchrotron (ESRF-EBS; (Extremely Brilliant Source)) in 2020. The new magnetic configuration, Hybrid Multi-Bend Achromat (HMBA) lattice (Raimondi 2017), guides and focuses the electron beam to generate X-ray radiation 100 times more brilliant and coherent than a third-generation synchrotron.

1.2.4 X-ray free-electron lasers

The XFEL radiation provides about ten orders of magnitude increase in peak brilliance compared to synchrotron radiation (Emma et al. 2010). In contrast to synchrotron light sources which are cyclic particle accelerators, XFEL facilities are linear particle accelerators (Hwu and Margaritondo 2021).

The electrons are generated by a UV pulse that strikes the surface of a copper cathode plate inside the gun injector. The electrons are then guided to the linear accelerator where the electron bunches are brought to high energies at nearly the speed of light. Then, the electron pulse enters the undulators magnets, a periodic arrangement of north and south magnetic poles spaced only a few millimeters apart, that forces the electrons onto a tight slalom course. These poles cause the electron bunch to move up and down in an undulating motion. The electrons emit X-ray radiation as they gradually organize themselves into a large number of thin discs. Therefore, X-rays and electrons travel together and interact with each other. The X-rays then become tuned or coherent with short and intense flashes with properties of laser light. While passing only once through the XFEL undulator, self-amplified spontaneous emission (SASE) (Bonifacio, Pellegrini, and Narducci 1984; Geloni, Huang, and Pellegrini 2017; Margaritondo and Rebernik Ribic 2011) occurs originating from a stochastic process. This undulator length in the

synchrotron is short (a few meters), whereas XFEL undulators are long (> 100 m). Only long undulators allow SASE to occur. Afterward, electrons are not needed, and they are discarded into an electron dump while the X-ray laser pulses continue in a straight line to the experimental hall. The X-ray pulse duration is estimated between 10 to 500 fs (Emma et al. 2010). A more in-depth description of how XFEL works can be found in (Feldhaus, Arthur, and Hastings 2005).

John Madey introduced the FEL concept in the early 1970s (Madey 1971) based on the work of Hans Motz at Stanford University (Motz 1951; Motz, Thon, and Whitehurst 1953). In the 1980s, Claudio Pellegrini and James Murphy were interested in the possibility to develop XFEL using the SASE amplifier (J. B. Murphy and Pellegrini 1985; J.B. Murphy and Pellegrini 1985). In 2009, the first hard XFEL experiment was performed at the LCLS facility (Stanford, USA) (Emma et al. 2010). As of 2021, there are five fully operational hard XFEL facilities around the globe, LCLS (Stanford, USA), SACLA (Hyogo, Japan), PAL-XFEL (Pohang, Korea), European XFEL (Schenefeld, Germany), and SwissFEL (Villigen, Switzerland). Data collections for the presented study were carried out at LCLS, SACLA, and SwissFEL. They operate at repetition rates of 120 Hz, 60 Hz, 100 Hz, and at 15, 8.5, and 6 GeV of maximum electron energy, respectively.

1.2.5 From serial femtosecond crystallography at XFELs to serial crystallography at synchrotrons

The concept of serial crystallography (SX) has originated from the multi-crystal data collection approaches at synchrotrons which was first introduced in the 1970s (Winkler, Schutt, and Harrison 1979). This concept relied on the X-ray dose distribution over many isomorphous crystals during data collection. The SX concept found application in XFEL facilities as serial femtosecond crystallography (SFX) (Boutet et al. 2012). The SFX data collection strategy allows recording of still images of randomly oriented crystals. This relies on the concept of “diffraction-before-destruction” that was introduced by Richard Neutze and co-workers by simulating XFEL diffraction with single molecules of T4 lysozyme (Neutze et al. 2000). The results showed that diffraction of a single molecule occurs before their destruction when using an XFEL pulse length less than 50 fs. Thus, the sample needs to be replenished constantly in

order to deliver fresh crystals to the interaction point with the X-ray beam which is the basis of the SX concept.

Based on the “diffraction-before-destruction” concept, early proposals of serial crystallography started in the 2000s in the work of John Spence and Bruce Doak in which a jet provided droplets containing biomolecules onto a continuum electron beam in order to obtain electron diffraction patterns (Spence and Doak 2004). The first proof-of-concept experiment in microcrystals of a membrane protein, the photosystem I, took place at ALS (Berkeley, USA) in which powder diffraction data was collected using a continuous microjet as sample delivery method (Shapiro et al. 2008). This experiment was a preparation of the first SX experiment at XFELs at LCLS (Stanford, USA) on the same biological system (Chapman et al. 2011).

The first high-resolution SFX structure was obtained of lysozyme at 1.9 Å resolution at the LCLS (Boutet et al. 2012). A difference electron density map calculated from the SFX data and low-dose synchrotron oscillation data, $F_{\text{obs}}(\text{SFX}) - F_{\text{obs}}(\text{synchrotron})$, showed no significant changes. The authors did not observe any noticeable radiation damage, confirming the “diffraction-before-destruction” concept. Later, however, radiation damage in SFX has been reported especially when using high flux density and/or long pulse durations (Nass 2019; Nass et al. 2015).

Global radiation damage was reported in (Lomb et al. 2011) in which the authors study the diffraction patterns of data collected from 70 to 400 fs of XFEL pulse length. In this study, it was reported that a uniform distribution of radiation damage was not feasible because the ionization processes within the unit cell were nonhomogeneous. Similar conclusions were reported experimentally in (Barty et al. 2012) by combining experimental and simulated data. By increasing the pulse duration, a decay of Bragg intensities at higher resolution was observed along with an increase of r.m.s. atomic displacement of biomolecules in a crystalline lattice. It was predicted that the decay of the diffraction intensity as a function of resolution caused by radiation damage could be scaled as the damage was distributed uniformly in the unit cell (Barty et al. 2012). Using a high beam intensity ($1.8 \times 10^9 \text{ W.cm}^{-2}$), it was to characterize the effects of local damage on ferredoxin crystals (Nass et al. 2015). Ferredoxin proteins contain two [4Fe-4S] clusters and it was found that the electron density of these two clusters was different in the SFX structure but not in the synchrotron structure (Nass et al. 2015). This suggests that local structure composition and geometry influence the ionization in an XFEL experiment and the

effects of radiation damage cannot be corrected with global correction factors (Nass et al. 2015). Changes in the protein backbone, aromatic residues, and disulfide bridges on thaumatin and lysozyme. Gd microcrystals were identified with femtosecond time-resolved X-ray pump / X-ray probe experiment (Nass et al. 2020). The authors in Nass et al. 2020 suggested being more careful when performing an XFEL experiment while using single-pulses of X-ray radiation (which are usually between 10 and 50 fs) and assessing whether the diffraction data is truly free of radiation damage. In SFX experiments, doses had been calculated using RADDOSE-3D (Bury et al. 2018; Oliver B. Zeldin, Gerstel, and Garman 2013). The corresponding structures have been solved at doses in the GGy range (Barty et al. 2012, 2012; Lomb et al. 2011; Nass et al. 2020) which is about two orders of magnitude higher than the experimental dose limit of 30 MGy suggested for synchrotron MX at 100 K (Owen, Rudino-Pinera, and Garman 2006). Moreover, diffraction-weighted dose (DWD) (O. B. Zeldin et al. 2013) is a metric that represents the dose at each volume element of the crystal and the contribution of the latter to the current diffraction image. All the above dose estimations did not take into account photoelectron escape from the diffraction volume, which reduces the absorbed dose (Marman, Darmanin, and Abbey 2018; Nave and Hill 2005). It has been estimated that a dose of 400 MGy was enough to ionize once each atom within a protein crystal after each typical XFEL pulse (Chapman, Caleman, and Timneanu 2014). Simulations on lysozyme microcrystals using an extension of RADDOSE-3D, called RADDOSE-XFEL (Dickerson, McCubbin, and Garman 2020), revealed that the dose for a single ionization event per atom after each XFEL pulse for all atoms and non-hydrogen atoms was ~480 MGy and ~310 MGy, respectively.

Since the early years of XFEL experiments, several static structures of biological macromolecules (whose structures were first determined by synchrotron experiments) have been solved also by SFX, e.g. those of large membrane proteins, such as G protein-coupled receptors (GPCR) (Liu et al. 2013; Weierstall et al. 2014), and highly radiosensitive metal-containing proteins, such as the photosynthetic reaction center (Johansson et al. 2013) and the photosystem II (Kern et al. 2012; Suga et al. 2015). It is worthwhile to mention that it was also possible to determine structures from *in vivo*-grown crystals whose size is down to the nanometer scale (Colletier et al. 2016; Redecke et al. 2013; Sawaya et al. 2014; Tetreau et al. 2020).

As the phase information is lost in a diffraction experiment, several experimental phasing approaches have been applied in SFX data collection to retrieve phase information. In the early

years of XFEL in the 2010s, several attempts were made for *de novo* phasing that were unsuccessful regarding structure determination (Ayyer et al. 2016; Son, Chapman, and Santra 2011; Spence et al. 2011). Since then, SFX experiments and data analysis approaches have evolved and new efforts allowed successful structure determination using *de novo* phasing. They include structure determination using isomorphous replacement (Barends et al. 2013; Nakane et al. 2016; Yamashita et al. 2015) as well as single-wavelength anomalous diffraction (Barends et al. 2014; Batyuk et al. 2016; Colletier et al. 2016; Fukuda et al. 2016; Hunter et al. 2016; Nakane et al. 2015, 2016; Nass et al. 2016; Yamashita et al. 2017).

As there are not many XFEL facilities around the world, the demand for performing serial crystallography cannot be met on XFELs. As an alternative, serial synchrotron crystallography (SSX) has been used. This data collection method is a complementary method to “conventional” X-ray crystallography and SFX. In order to perform SSX experiments, one needs high photon flux of the X-ray beam ($1-2 \times 10^{12}$ photons. s^{-1}), crystals about the size of the X-ray beam, appropriate sample delivery methods for serial crystallography, high-speed readout detectors (exposure time less than 10 ms), and a computational infrastructure capable to process large amounts of data.

First, proof-of-concept SSX experiments have been carried out using *in vivo* grown crystals mounted on a loop at cryo conditions (Gati et al. 2014), native (Stellato et al. 2014) and derivatized lysozyme microcrystals (Botha et al. 2015) delivered using a lipidic cubic phase (LCP) injection at room temperature, bacteriorhodopsin microcrystals injected in LCP (Nogly et al. 2015) and by using fixed-target devices such as a microfluidic chip with predefined microcrystal positions (Heymann et al. 2015) and chips without predefined microcrystal positions using silicon nitride windows (Coquelle et al. 2015) and mylar sheets (Doak et al. 2018). Furthermore, it has been shown that SSX is also suitable for characterization of novel pharmacological targets within protein crystals (Kováčsová et al. 2017; Weinert et al. 2017) and it has been demonstrated to be used for *de novo* phasing approaches (Botha et al. 2018). Several SSX experiments have already been performed so far that are reviewed in (Diederichs and Wang 2017; Martin-Garcia 2021; Nam 2020a)). Finally, half-doses of global damage have been estimated for cryo and room temperature SSX data collection to be 17.8 MGy and 0.38 MGy, respectively (de la Mora et al. 2020).

1.2.6 Time-resolved X-ray crystallography

Time-resolved (TR) X-ray crystallography (Hajdu et al. 1988, 2000; Moffat 2001; Schlichting and Goody 1997) performed at XFELs (TR-SFX) (Brändén and Neutze 2021; Colletier, Schirò, and Weik 2018) and synchrotrons (TR-SSX) (Schulz et al. 2022) is used to visualize reactions in biomolecules in both space and time. This enables the study of transient phenomena (*e.g.* structural and dynamical changes, catalysis, phase transitions, *etc.*) that occur in biomolecules during biological activity. In such approaches, temporal resolution is accomplished by activating the protein in the crystal prior to X-ray exposure and then collecting data at various time delays. The aim is to identify short-lived reaction intermediates, determine their structure and elucidate the complete reaction mechanism. TR crystallography offers the advantage in providing direct and global three-dimensional structural information at the atomic level as a function of time.

TR crystallography could be divided into several categories depending on how the reaction in protein crystals is initiated. The reaction could be triggered by the following methods: visible light (Brändén and Neutze 2021; Colletier et al. 2018), electric fields (Hekstra et al. 2016), X-rays (Nass et al. 2020), infrared (Keedy et al. 2015; Thompson et al. 2019) and small-molecule diffusion (Schmidt 2013; Stagno et al. 2017). As alternative techniques to TR crystallography, various physical or chemical trapping methods have been used. The intermediates with lifetimes longer than the flash-cooling process can be trapped and studied by static crystallography (trigger-freeze). Alternatively, the reaction can be initiated at cryo temperatures and allowed to proceed up to a reaction intermediate that cannot proceed further at cryo temperatures (freeze-trigger). Trapping intermediate states can be done by freezing the sample (Kovalev et al. 2020) or, by solvent or pH modification, and chemical modifications of the biomacromolecule, substrate, or cofactor (Bourgeois and Weik 2009; Schmidt et al. 2005; Stoddard 2001) or inactive caged substrates that can be diffused into crystals and be activated by light (Bourgeois and Weik 2008; Monteiro et al. 2021; Stoddard et al. 1998). By using a polychromatic X-ray beam (Laue diffraction) generated at high photon flux density at a synchrotron, the rate of data collection may be increased so that the exposure times are equivalent to the chemical lifetimes of transient intermediates in the crystal. This allows the structure determination of short-lived chemical species (Stoddard 1996; Stoddard et al. 1998) and the exposure time of a polychromatic X-ray beam can be as short as 100 ps at a synchrotron (Moffat 2019).

Studies on light-sensitive proteins have dominated the field of TR crystallography (Poddar et al. 2021). Even though such systems are not very common in Nature, the relatively easy way to trigger the reaction by light in crystals, it prompts light-sensitive proteins to be the first and most used systems to be studied. Structural intermediates can be captured by a pump-probe scheme (Figure 1.2.3). The pump-probe technique allows monitoring of ultrafast events inside proteins in crystals such as atom movement. To initiate the reaction, an extremely brief and intense optical pulsed laser ("pump") is delivered to the sample. Then, an X-ray pulsed laser ("probe") is used to collect diffraction data from which the structure of the intermediate state can be solved. By varying the interval between the pump and the probe pulses, the structural evolution of the reaction within the microcrystals can be followed from the femtosecond (XFELs) to second (synchrotrons) timescale. Time resolution in the pump-probe scheme is defined by both the pump and the probe pulse lengths. To increase the occupancy of the intermediate states facilitating structural interpretation, structural biologists have been using a much higher pump laser energies than employed for spectroscopic techniques. This pushes the experimental conditions into the multi-photon regime (Grünbein et al. 2020). It has been suggested to use a power density of the pump laser that corresponds to less than the average one-photon absorption per light-capturing molecule in the crystal (Grünbein et al. 2020). As suggested, a way of calculating the absorbed photons per light-capturing molecule by considering the crystal thickness and its refractive index, the concentration and the molar extinction coefficient of the light-capturing molecule in crystal, the photophysical parameters of the pump laser, as well as the sample delivery method (see Section 1.2.7) (Grünbein et al. 2020).

TR crystallography experiments are usually combined with TR spectroscopic techniques including UV/Vis absorption spectroscopy that provide information to directly correlate electronic transitions with structural transitions in the sample. Moreover, three-dimensional structural changes are not directly observed, however, the measured spectral changes are to be interpreted in terms of underlying structural changes. TR spectroscopic experiments are ideally performed on crystals to guide and complement crystallographic experiments. It is worthwhile to mention that, the kinetics of the reaction mechanisms might not be the same in crystals and in solution (Konold et al. 2020). Possible differences, apart from the experimental setup, are the solution conditions, like pH, ionic strength, viscosity, that might not be the same for protein in crystal or in solution, and that the crystal packing might restrict motions or alter the kinetics.

Recent examples of TR-SFX experiments on light-sensitive proteins include those on photosystem I (PS-I) (Aquila et al. 2012) and II (PS-II)(Kern et al. 2018:201; Suga et al. 2019)(Kern et al. 2018:201; Suga et al. 2019), several rhodopsins (Mous et al. 2022; Nango et al. 2016; Nass Kovacs et al. 2019; Oda et al. 2021; Skopintsev et al. 2020; Yun et al. 2021), phytochromes (Claesson et al. 2020), photoactive yellow protein (PYP) (Pande et al. 2016), photosynthetic reaction center (Dods et al. 2021), reversibly photoswitchable enhanced green fluorescent protein 2 (rsEGFP2) (Coquelle et al. 2018a), myoglobin (Barends et al. 2015), P450nor (Nomura et al. 2021; Tosha et al. 2017), cytochrome c oxidase (Shimada et al. 2017) and fatty acid photodecarboxylase (FAP) (Sorigué et al. 2021). PS-I is a complex that is present in all green plants and reduces NADP^+ to NADPH and it was the first attempt to perform a TR-SFX experiment (Aquila et al. 2012). PS-II is a protein complex that is omnipresent in photosynthetic organisms (unicellular and multicellular) and it is implicated in the first steps of oxygenic photosynthesis. Four photons absorbed by the reaction center of PS-II (P680) can energize electrons that are then transferred through different coenzymes and cofactors to reduce plastoquinone to plastoquinol by splitting two molecules of H_2O into molecular O_2 and four protons. Characterization of the S-state intermediates and water network surrounding the oxygen-evolving complex has been carried out by TR-SFX for cyanobacterial PS-II (Ibrahim et al. 2020; Kern et al. 2013, 2014, 2018; Kupitz et al. 2014; Suga et al. 2017, 2019, 2020; Young et al. 2016) and for bacterial photosynthetic reaction center (Dods et al. 2021). Another major family of proteins that has been widely studied by TR-SFX is retinylidene protein (rhodopsin) which uses retinal as a chromophore for light reception. Upon light absorption, retinal undergoes *cis-to-trans* isomerization and, subsequent protein conformational changes are observed that are coupled with an ion channel function. Structural intermediates, water network, and chromophore isomerization as a function of time have been characterized for bacteriorhodopsins from haloarchaea that are proton pumps (Nango et al. 2016; Nass Kovacs et al. 2019; Nogly et al. 2018), for bacterial sodium cation (KR2) (Skopintsev et al. 2020) and chloride anion (Mous et al. 2022; Yun et al. 2021) pumping rhodopsins as well as for a non-specific cation pump, the channelrhodopsin from unicellular algae (Oda et al. 2021). Phytochromes are photoreceptor proteins in plants, bacteria, and fungi that control photosynthesis as well as the growth and reproduction of these organisms. *Z-to-E* isomerization of the light-capturing chromophore, biliverdin, and global structural changes are observed at the intermediate states during the photoconversion (Carrillo et al. 2021; Claesson et al. 2020). PYP is a bacterial photoreceptor involved in negative phototaxis in response to blue light (Sprenger et al. 1993). Its p-coumaric chromophore enters a reversible photocycle after photon

absorption (Pande et al. 2016; Pandey et al. 2020; Tenboer et al. 2014). Rationally designed green fluorescent protein, rsEGFP2 (Grotjohann et al. 2012a), is reversibly photoswitchable between fluorescent and non-fluorescent state upon laser illumination. Structural characterization of intermediate states of the hydroxybenzylidene imidazolinone chromophore was carried out using TR-SFX (Coquelle et al. 2018a; Woodhouse et al. 2020a). Dynamics of ligand dissociation in myoglobin were also performed. It is worthwhile to mention that dissociation of the ligand can be reproduced using light as the heme cofactor absorbs the light and enables the ligand dissociation (Barends et al. 2015). Lastly, the photocycle mechanism of FAP was complemented with TR-SFX results (Sorigué et al. 2021) (see Chapter 2).

Reactions within crystals can also be triggered by diffusing small molecules into the crystal, also known as “mix-and-inject”. This method consists of two solutions containing the microcrystals and the small molecule that are mixed before the interaction with an XFEL beam (Calvey et al. 2016; Schmidt 2013). Some experiments to study ligand-binding were performed for β -lactam, for β -lactamase (Kupitz et al. 2017; Olmos et al. 2018), for adenine to RNA riboswitch (Ramakrishnan et al. 2021; Stagno et al. 2017), and para-nitrophenyl isocyanide (p-NPIC) for isocyanide hydratase (Dasgupta et al. 2019). Time resolution using the mix-and-inject method that is defined by the mixing time between the two solutions, the crystal size, and the diffusion time of the small molecule into the crystal, has been calculated from a few tens of milliseconds to a few seconds (Ishigami et al. 2019; Schmidt 2020). Two main mixing devices have been described so far, the T-junction device (Kupitz et al. 2017) and the microfluidic mixing device (Calvey et al. 2016; Monteiro et al. 2020).

Other ways to trigger a reaction in crystals include temperature jump shifts (Keedy et al. 2015; Thompson et al. 2019), electric field pulses (Hekstra et al. 2016), and photo-caged molecules (Tosha et al. 2017).

Time resolution in time-resolved SSX (TR-SSX) (Pearson and Mehrabi 2020) is achieved by the synchrotron beamline parameters such as the photon flux of the X-ray beam and today it is limited to the millisecond time-scale for monochromatic beam (Pearson and Mehrabi 2020) and to 100 ps for polychromatic beam (pink beam) (Meents et al. 2017). The broadest range of time-scales that has been studied was three orders of magnitude (from 30 ms to 30 s) and concerned fluoroacetate dehalogenase (Mehrabi, Schulz, Dsouza, et al. 2019; Schulz et al. 2018). These studies described an experiment with 18-time points that covered four turnover reactions of the

irreversible mechanism of the enzyme. The authors used a photo-caged substrate that was released within the enzyme by UV photolysis. The data collection was performed at room temperature using a fixed-target device (Mehrabi, Schulz, Dsouza, et al. 2019; Schulz et al. 2018). This proof-of-concept experiment was performed to demonstrate that TR-SSX could be used for mix-and-diffuse studies (Beyerlein et al. 2017a). Using an inline T-shaped mixing device that delivered the mixed solution on a tape, Beyerlein and co-workers (Beyerlein et al. 2017a) showed that the ligand binds the microcrystalline protein in 2 s, which corresponds thus to the time-resolution of a mix-and-diffuse study (Beyerlein et al. 2017a). A modified device that combines a fixed-target SSX approach with a piezo-driven droplet injector has been reported that allows to determine a structure at ~10 ms after ligand-droplet deposition (Mehrabi, Schulz, Agthe, et al. 2019). In order to reduce sample consumption during TR-SSX experiments, it was suggested to use serial oscillation crystallography (SOX) (Aumonier et al. 2020). This method allowed structure determination from less than a hundred crystals to observe photoinduced structural dynamics at room temperature with a time resolution of 63 ms (Aumonier et al. 2020).

Experiments on the membrane protein bacteriorhodopsin demonstrated the synergy between TR-SSX and TR-SFX methods that allowed elucidating structural changes in the protein's photocycle. TR-SFX from fs to ms permitted to elucidate I-, J-, K-, L-, M-intermediates as well as conformational changes on the cytoplasmic side of the protein (Nango et al. 2016; Nogly et al. 2018), whereas TR-SSX experiment from 5 ms to 200 ms allowed to characterize proton release and uptake (N-intermediate) (Weinert et al. 2019). Hence, a complete structural view of the photocycle of bacteriorhodopsin has been given, *i.e.* how the protein transports a proton from the cytoplasmic to the extracellular side *via* the retinal Schiff base.

TR crystallography in both SFX and SSX experiments are usually complemented by quantum chemical and molecular dynamics simulations that provide information about hydrogen-bond networks and energies, description of the excited-state, *etc* (Cheng 2020; Coquelle et al. 2018a; Dasgupta et al. 2019; Mehrabi, Schulz, Dsouza, et al. 2019; Sorigué et al. 2021).

1.2.7 Sample delivery for serial crystallography

Essential hardware for a successful SX data collection, next to the X-ray source and a high-sensitivity detector, is the sample delivery system by which the sample is constantly replenished as required by the diffraction-before-destruction principle. An ideal sample delivery system limits sample consumption, reduces the diffraction background, and minimizes the data collection time. In general, the existing sample delivery devices could be divided into two categories, injection devices (liquid jets, viscous jets) (Grünbein and Nass Kovacs 2019), and solid supports (fixed target devices) (Martiel, Müller-Werkmeister, and Cohen 2019). The first category consists of crystal migration relative to the delivery system (moving target systems) whereas in the latter category the crystals are immobilized during diffraction and the fixed-target support is scanned across the X-ray beam.).

The sample delivery method used during the first SFX experiment on photosystem I (Chapman et al. 2011) was the gas dynamic virtual nozzle (GDVN) (DePonte et al. 2008). It is a liquid microjet that ejects the microcrystal solution into the XFEL beam with a sub-100- μm -diameter capillary and by a coaxial flow of helium, the jet is focused to less than 5- μm -diameter. It is widely used in time-resolved studies such as pump-probe and mix-and-inject schemes. To keep the jet flow focused onto the XFEL interaction point, a relatively high flow rate is required, typically at 30-50 $\mu\text{L}\cdot\text{min}^{-1}$. This results in high sample consumption. This sample delivery system was used to perform the time-resolved SFX experiments described in this thesis. Another liquid jet system that consumes 10-100 times less sample than GDVN is the microfluidic electrokinetic sample holder (MESH) and its upgraded version, the concentric MESH (CoMESH) (Sierra et al. 2012, 2016) that was used to study photosystem II and 30S subunit of the ribosome (Kern et al. 2012; Sierra et al. 2016). Electrospray sample injectors are liquid jet systems that generate atomized droplets and were first used for single-particle imaging at XFELs (Bielecki et al. 2019; Oberthür 2018). Lastly, acoustic droplet ejection (ADE) uses sound pulses to deliver nano- to picolitre droplets to the XFEL beam (Roessler et al. 2016). High-viscosity extrusion (HVE), also referred to as lipidic cubic phase (LCP) injection (Cheng 2020; Grünbein and Nass Kovacs 2019; Kováčsová et al. 2017; Weierstall et al. 2014) is a similar system as GDVN, but with the difference that the medium is very viscous. The high viscosity reduces sample consumption as the flow rate is below 0.05 $\mu\text{L}\cdot\text{min}^{-1}$. This sample delivery method is widely used for membrane proteins, as LCP (or *in meso* crystallization) is frequently used to crystallize membrane proteins (Johansson et al. 2012; Landau and Rosenbusch 1996; Liu et al. 2013; Rosenbaum et al. 2007). LCP is also used as a medium for soluble-protein crystals such as lysozyme and phycobiliprotein (Fromme et al. 2015) as well as

Flpp3, thaumatin, proteinase K (Martin-Garcia et al. 2017) and carbonic anhydrase II (Lomelino et al. 2018). It has been shown that several matrices could be used as an injection medium, such as agarose (Conrad et al. 2015), beef tallow (Nam 2022), grease (Sugahara et al. 2015), hyaluronic acid (Sugahara et al. 2016), hydrogels, lard (pork fat) (Nam 2020b), sodium carboxymethyl cellulose, Pluronic F-127 (Kováčsová et al. 2017; Sugahara et al. 2017), polyacrylamide (Park et al. 2019), poly(ethylene oxide) (Martin-Garcia et al. 2017), vaseline (Botha et al. 2015), *etc.* GDVN, MESH, and ADE have been used during SFX experiments while HVE has been used for both SFX and SSX experiments.

In fixed-target systems, the crystals are fixed in a sample holder and it is the sample holder that is moving so that the immobilized crystals are presented sequentially to the X-ray beam. Using fixed-target systems, sample consumption can be greatly reduced compared to the moving target systems. A pre-scan of the sample holder is often recommended to locate the crystals. For instance, spectroscopic mapping of the sample holder is performed to locate crystals achieving a ~100% hit rate and provide the possibility of performing additional diagnostics such as spectroscopic characterization of the crystals before and after diffraction (Oghbaey et al. 2016). Such systems include goniometer-based instrumentation such as nylon loops, meshes, grids, chips as well as conveyor belts, *etc.*, at both XFEL and synchrotron facilities. Sample delivery using nylon loops, meshes and grids is achieved by suspending single or multiple crystals in it. Data collection strategies include multiple single shoots, raster scanning, or helical (spiral) scan. This sometimes allows multiple exposures on the same crystal. It has been reported that both SFX and SSX data collection methods can be performed at both cryogenic (Gati et al. 2014; Halsted et al. 2018; Hirata et al. 2014) and room temperatures (Cohen et al. 2014). Silicon-based chips have also been used to avoid multiple exposures of microcrystals and reduce sample consumption (Coquelle et al. 2015; Hunter et al. 2014; Mehrabi et al. 2020; Owen et al. 2017; Roedig et al. 2015). To overcome potential dehydration in such devices during data collection, it has been suggested to use humidified air or helium gas (Roedig et al. 2016) or seal the chips with a Kapton film (Murray et al. 2015), graphene (Sui et al. 2016) or a polymer/graphene sandwich (Shelby et al. 2020). Another type of fixed-target device is the Sheet-On-Sheet “chip-less” sandwich which eliminates the challenges of sample loading (Doak et al. 2018). Transferring crystals to fixed-target devices increases the risk of damage and loss of crystals. Microfluidic chips for *in situ* data collection can avoid this problem by providing both a sample delivery and a crystal growth device. Such devices also make it possible to obtain

protein structures in the growth environment of crystals (Gicquel et al. 2018; Huang et al. 2018; Ren et al. 2018, 2020).

Conveyor belt systems are usually sample delivery systems that are connected with other devices such as liquid jets or syringes. Such systems are responsible for depositing crystal suspension on a Kapton foil by ADE (Fuller et al. 2017) or an injector (Beyerlein et al. 2017b).

Recent advances on XFEL devices with MHz repetition rates place high demands on sample delivery speeds and necessitate the growth of large quantities of crystals. The European XFEL, operating since September 2017, is the first superconducting MHz repetition rate hard XFEL (Altarelli 2011, 2015). Its bunch structure is designed to deliver 10 pulse trains per second of which each train carries (eventually) 2,700 pulses spaced by less than 1 μs . Thus, pulse frequency will eventually be 4.5 MHz. Additionally, the upgraded LCLS-II facility (Dunne 2020) is operating at one million pulses per second. Given the short spacing between pulses, the X-ray beam causes a shockwave to travel upstream the liquid jet (Grünbein et al. 2018; Wiedorn, Oberthür, et al. 2018). This results in no crystal diffraction because the shockwave damages the microcrystals on their way to the interaction point. The first experiments (Grünbein et al. 2018; Wiedorn, Oberthür, et al. 2018) at the European XFEL facility show that the sample can be replenished in 886 ns between the X-ray pulses with an X-ray beam diameter of less than 2 μm (Grünbein et al. 2018) or 15 μm at full width at half maximum (FWHM) (Wiedorn, Oberthür, et al. 2018) by using a GDVN liquid injector (DePonte et al. 2008) with a flow rate of 15 $\mu\text{L}\cdot\text{min}^{-1}$ (jet linear speed of 50 $\text{m}\cdot\text{s}^{-1}$) (Gisriel et al. 2019; Grünbein et al. 2018; Wiedorn, Awel, et al. 2018; Wiedorn, Oberthür, et al. 2018).

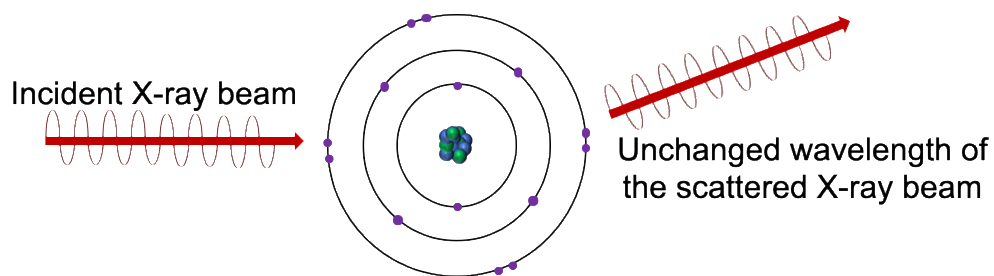
1.2.8 Detectors for XFEL experiments

The short pulse length, the high peak brilliance, and the high repetition rate of the X-ray beam of an XFEL facility make photon-counting by the detector difficult. Hence, detectors for SFX experiments should have a high signal-to-noise ratio, dynamic range, and a repetition rate that matches this of the XFEL beam. Improvement and integration of the technology of the existing synchrotron detectors, such as charge-coupled device (CCD) and pixel array detector (PAD) were made. The first detector that had been designed was Cornell-SLAC Pixel Array Detector

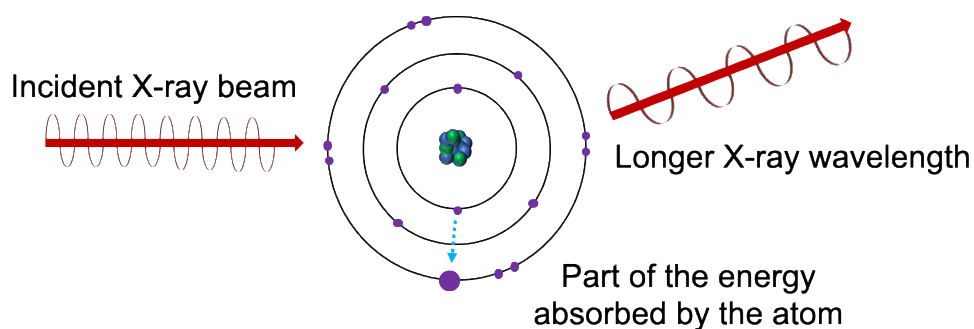
(CSPAD) (Blaj et al. 2015) at the Coherent X-ray Imaging (CXI) instrument (Liang et al. 2015) at the LCLS in the USA. The CSPAD reads out at 120 Hz and it is composed of 32 separate sensors whose positions can change with respect to each other and thus refinement of detector geometry must be carried out (see section 1.3.3 Indexing and integration). This detector can operate in hybrid dual-mode (or dual gain mode) in order to prevent saturating Bragg peaks at low resolution and thus maximizing Bragg peak intensities at high resolution (see section 1.3.4 Merging). An X-ray pixel detector multi-port charge-coupled device (MPCCD) was developed for the DAPHNIS platform of the SACLA facility (Tono et al. 2013). By contrast with the CSPAD, the MPCDD is composed of a single panel and its readout rate is 60 Hz. MPCDD detector is used at the PAL-XFEL (Kang et al. 2017) in Korea. The next generation of detectors for XFEL facilities has been developed. For example, the Adaptive Gain Integrating Pixel Detector (AGIPD) (Henrich et al. 2011) at the European XFEL, incorporating 16 sensors (front-end module – FEM) and having a frame rate of 4.5 MHz and an automatic setting of the gain to the incoming X-ray beam. A new promising detector for XFEL and synchrotron experiments is the adJUsTiNg Gain detector FoR the Aramis User station (JUNGFRAU) (Mozzanica et al. 2018), developed by DECTRIS AG (Baden-Daettwil, Switzerland) and first tested at the SwissFEL (Milne et al. 2017). It can be operated with frame rates from a few Hz up to 1.4 kHz and it is composed of eight sensors whose positions are precisely defined.

1.2.9 Figures

A



B



C

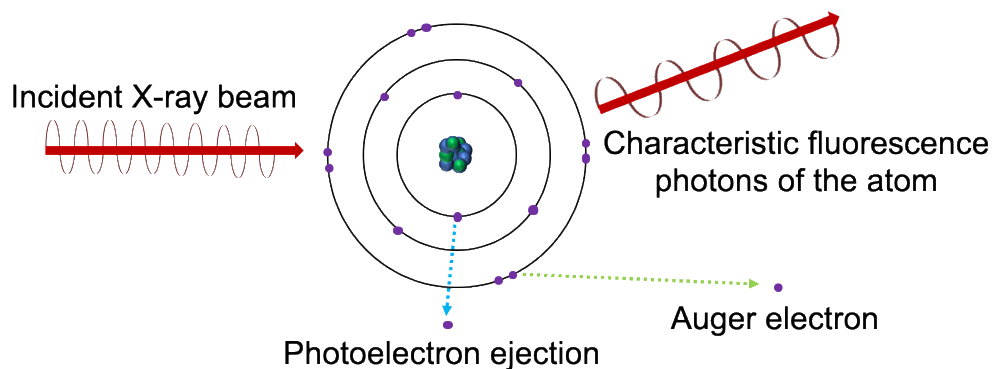


Figure 1.2.1 3: Primary X-ray interaction processes with the atoms within a crystal.

(A) Coherent scattering. It gives the diffraction pattern. (B) Incoherent scattering. A part of the incident X-ray beam energy is transferred to the atom and results in lower X-ray energy. (C) Photoelectric effect. The majority of the energy of the incident X-ray beam is transferred to an electron that is ejected (photoelectron). The excited atom can emit an Auger electron from the outer shell or emit characteristic X-ray radiation in order to return to its ground state.

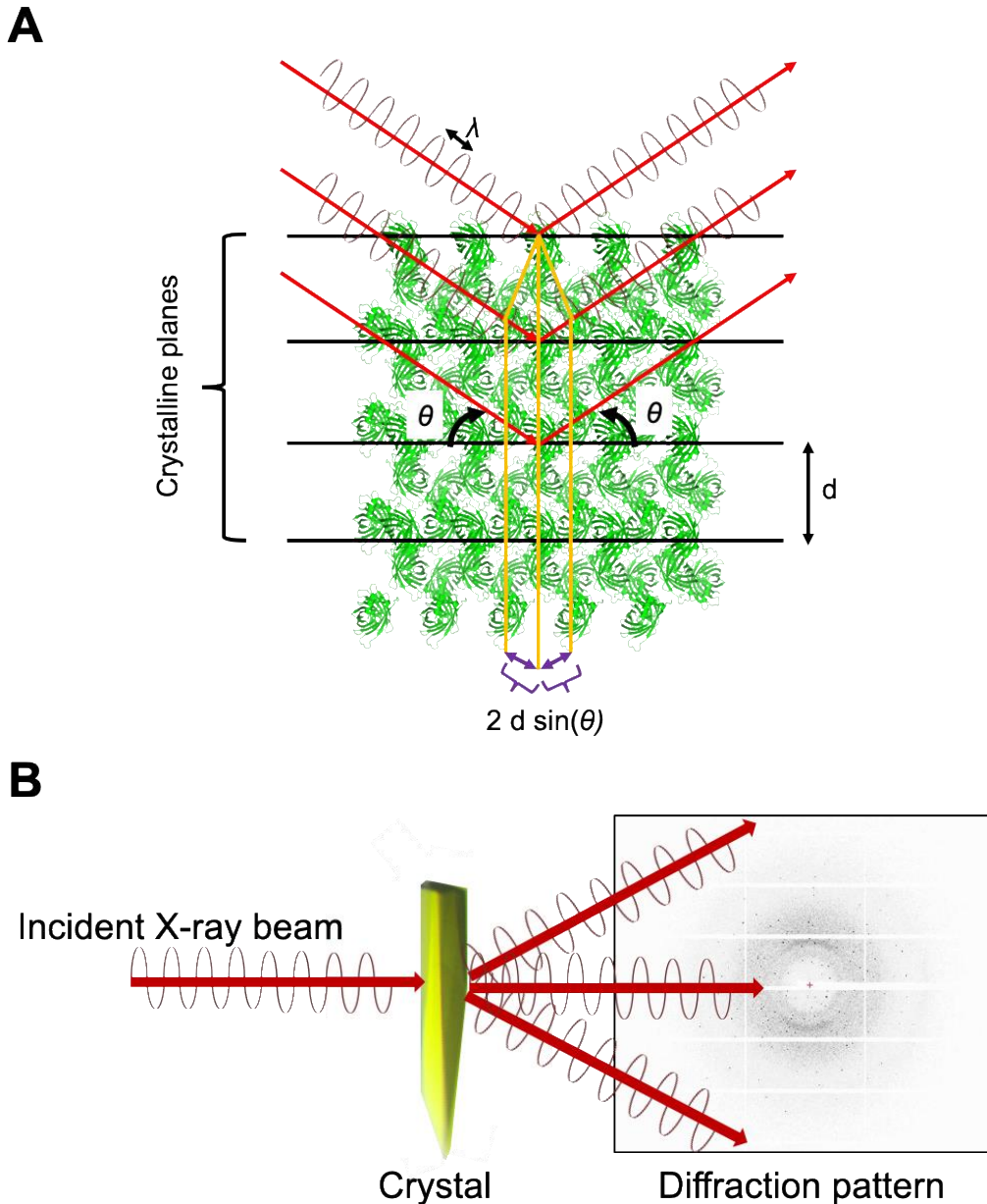


Figure 1.2.2: X-ray diffraction.

(A) Graphical interpretation of Bragg's law, which considers the X-ray diffraction as a reflection off a set of planes in the crystal. The total pathway between two waves is $2 d \sin(\theta)$, which is equal to $n\lambda$ in the case of constructive interference. Reconstruction of ten unit cells of rsEGFP2 (in green) in $P2_12_12_1$ space group using the supercell command in PyMOL (Schrödinger and DeLano 2020). (B) Simplified illustration of X-ray diffraction. The molecules organized in the crystal form a regular network. The intensity of each Bragg spot contains information on the entire structure of the macromolecule (eq. 1.2.3). rsEGFP2 crystal and the corresponding diffraction pattern are shown.

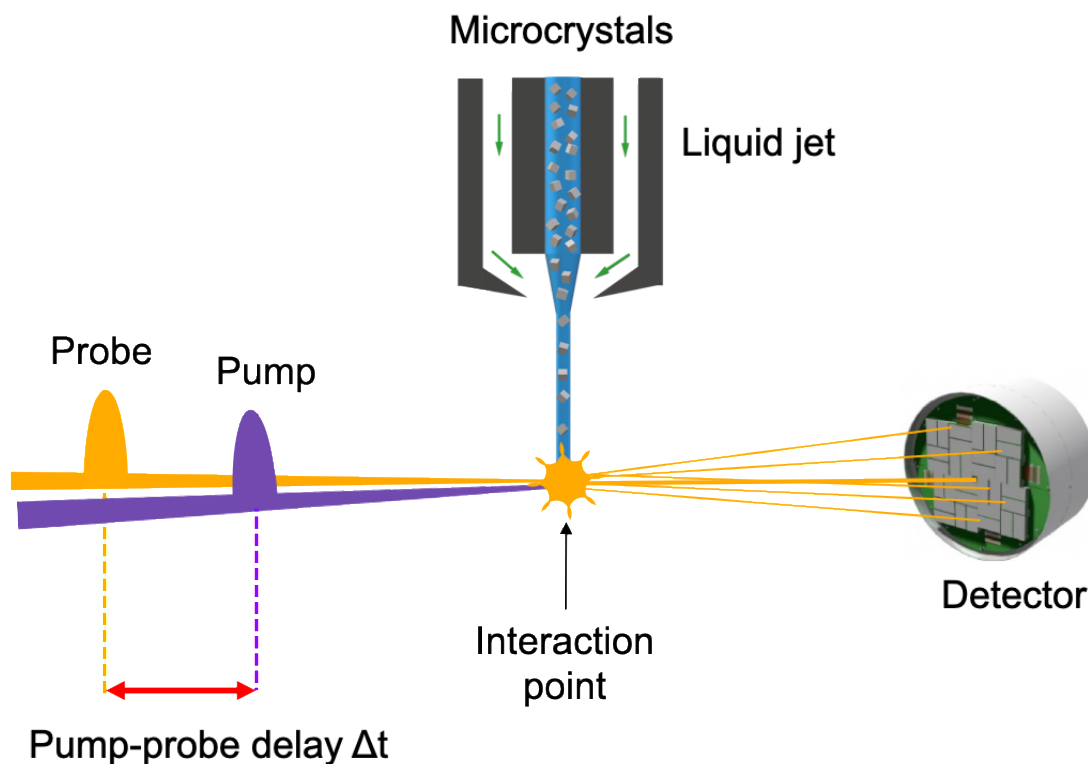


Figure 1.2.3: Principle of pump-probe scheme for TR crystallography.

Microcrystals are delivered to the interaction point via a liquid jet as an example. Intermediate structures can be characterized by introducing an optical pump laser that is synchronized with the X-ray beam (probe). Time $t=0$ is defined by the moment of triggering the reaction in the proteins within the microcrystals by the optical pump laser. By varying the pump-probe time delay (Δt), photo-intermediates can be captured and their structures determined at different stages of a biological process.

1.3 Analysis of serial crystallography data

1.3.1 General concepts

In serial crystallography technique, a large number of X-ray diffraction patterns are acquired, each from single crystals that are presented to the X-ray beam in random orientations. These diffraction images represent “still” images, as the crystal does not rotate during data acquisition, and there is no geometrical relationship of a pattern with the preceding or the following. The major challenges of serial crystallography during the pre-processing step of the structure solution are:

- i) the sorting of the diffraction patterns that contain diffraction spots from the patterns that are empty,
- ii) the indexing and integration of diffraction patterns, and
- iii) the merging and scaling of the intensities.

The data processing workflow described in the manuscript is summarized in Figure 1.3.1. A detailed description of data processing for serial crystallography is presented in this section.

1.3.2 Hit-finding

In SFX, X-ray pulses are generated at 60, 100, and 120 Hz at SACLA, SwissFEL, and LCLS, respectively. As the X-ray pulses are generated constantly, the X-ray beam does not always hit a crystal. Therefore, many of the detector recordings are empty or the diffraction from a crystal may be weak. A need to identify and sort “hits”, *i.e.* images containing useful diffraction information, from empty images is required. This process is called hit-finding. The development of software capable to detect and select the diffraction images have been advanced. Such software packages are *NanoPeakCell* (Coquelle et al. 2015), *Cheetah* (Barty et

al. 2014), *Hummingbird* (Daurer et al. 2016), *CASS* (Foucar 2016; Foucar et al. 2012), *cctbx.xfel* (Sauter et al. 2013) and *OnDA* (Mariani et al. 2016).

In this work, *CASS* and *NanoPeakCell* were used as real-time and on-/off-line monitors, respectively. *CASS* which stands for CFEL-ASG Software Suite, is a tool of pre-processing data analysis and visualization using the live data stream from the XFEL facility data acquisition. Its graphical interface is used during the data acquisition and the experimenter has access to important parameters which allow adjusting and improving the experiment. Such parameters are hit-rate, estimation of diffraction resolution, and the fraction of multiple hits. *NanoPeakCell* is a Python-based software that performs data-sorting (when a time-resolved experiment is carried out), hit- and Bragg-peak-finding, and provides compatible output files for further data processing (see 1.3.3 Indexing and integration).

1.3.3 Indexing and integration

Two pieces of information can be found by exploiting the reflections of the sorted diffraction images, the crystal lattice, symmetry, and the content of the lattice. The former comes from the geometrical arrangement of the reflections and the latter comes from the intensity of the reflections. However, the last information is partial because there is no information about the phases (see 1.3.5 Phase problem and molecular replacement).

During this indexing step, the Bragg spots have to be defined, *i.e.* to identify pixels that contain diffraction information. To identify the Bragg spots the following need to be determined:

- i) the background counts on images,
- ii) the intensity of the Bragg spots above background,
- iii) the distribution, the number, and the shape of the Bragg spots on the images,

- iv) the number of pixels that compose each Bragg spot and
- v) the integration of the reflections and thus an intensity determination for each reflection.

All the above five steps are performed individually for each diffraction image.

Software packages, such as *CrystFEL* (White 2019) or *cctbx.xfel* (Hattne et al. 2014) are used for auto-indexing, integration, and merging of the data. Both programs are used for serial crystallography at XFELs as well as at synchrotrons (*dails.stills_process* adapted program from *cctbx.xfel*). The core tool for indexing and integration of *CrystFEL* is *indexamajig*, in which a variety of indexing and integration methods and algorithms can be used. A complete list of these can be found on the *CrystFEL*'s website (<https://www.desy.de/~twhite/crystfel/manual-indexamajig.html>). The *cctbx.xfel* uses the one-dimensional FFT to identify initial sets of basis vectors that can potentially determine the crystal space group by providing a prior knowledge of the unit-cell length and angles. Another program package is *nXDS* (Kabsch 2014), which is a version of *XDS* (Kabsch 2010) adapted for serial crystallography data processing. However, in this thesis, *CrystFEL* was used.

1.3.4 Merging

Merging is the process during which various measurements of identical or symmetry-related reflections are combined into one dataset. The concept of merging serial or multiple-crystal crystallography data is as old as the first attempts of structure determination using X-ray crystallography. Two main approaches for merging serial crystallography data are available. The first is the “post-refinement” approach that models the diffraction geometry for each pattern (crystal orientation, unit cell parameters, X-ray bandwidth, *etc.*) and attempts to optimize the geometrical parameters using the model agreed as closely as possible between the patterns (Rossmann and van Beek 1999; Winkler et al. 1979). In the second, Monte Carlo, approach an average intensity for each unique reflection is calculated from different patterns (Kirian et al. 2010). The former algorithm is implemented in the program *partialator* (White 2014) and the

latter in the program *process_hkl* (White et al. 2012) of the *CrystFEL* suite. Both approaches were used in the presented work.

1.3.5 Phase problem and molecular replacement

As the detectors measure the intensity I , the information about phases (φ) is lost. As a consequence, crystallographers are not able to complete the Fourier transform relating the experimental data (in reciprocal space) to real-space electron density into which the atomic model is built. The first goal for crystallographers is to obtain an electron density map that is related to diffracted waves as follows:

$$\rho(x, y, z) = \frac{1}{V} \sum_h \sum_k \sum_l |F_{hkl}| e^{(2\pi i)(hx+ky+lz)+i\varphi(hkl)} \quad (\text{eq. 1.3.1})$$

where V is the unit cell volume, F the structure factor amplitudes that are calculated from the intensities using the relation $I = F \cdot F^*$, hkl are the Miller indices, and x , y , and z are coordinates in the unit cell.

The phase problem can be solved using the following approaches:

- i) The isomorphous replacement method requires the placement of heavy atoms in crystalline macromolecules (Baker et al. 1990).
- ii) The single and multiple wavelength anomalous diffraction method. It relies on the presence of sufficiently strong anomalous scattering atoms in the protein structure itself (Hendrickson 2014).
- iii) Direct methods, usually used for small molecules, are based on the principle that phase information is included in the intensities and that it depends on the assumption that the electron density is always positive (Usón and Sheldrick 1999).
- iv) Molecular replacement method, for which the similarity of the unknown structure to an already known structure is a prerequisite, a structure with a sequence identity of at least 30% (Evans and McCoy 2008; Rossmann 1990).

In this study, the molecular replacement method was used to solve the phase problem.

Molecular replacement is a method in which a known structure (*A*) is used to solve the unknown crystal structure (*B*). This concept relies on rigid-body displacements of structure *A* on the data of structure *B*. Displacements are rotations and translations with respect to a reference point defining a system of coordinates. A very straightforward case is when structure *A* has the same crystal symmetry, and the unit cell parameters are nearly the same as structure *B*. This practically means that structure *A* does not undergo any rigid-body displacements and the difference between the two structures can be revealed by calculating electron-density difference maps between the two structures. In the case in which crystal forms of structures *A* and *B* are different and thus the space-group along with the unit cell parameters are also different, a more complex approach is used:

- i) Determine the symmetry and the unit cell parameters of structure *B*.
- ii) Determine the composition of the asymmetric unit of *B*. The unit cell volume and the molecular weight of the structure *B* that composes it, allow the calculation of the Matthews coefficient or V_M (Matthews 1968). In other words, it is expressed as the ratio between the crystal volume and the molecular weight of the structure *B*. A major fraction of the crystal volume is occupied by solvent, typically around 50%. Probabilities from the Matthews coefficient (P_{Matthew}) give the probability of how many molecules the asymmetric unit contains for a particular Matthews coefficient (Kantardjieff and Rupp 2003).

Among the most widely used programs that perform both translational and rotational searches are *MOLREP* (Vagin and Teplyakov 1997) and *AMORE* (Navaza 1994) of the *CCP4* suite (Collaborative Computational Project, Number 4 1994) and *PHASER* (McCoy et al. 2007) of the *PHENIX* suite (Liebschner et al. 2019).

1.3.6 Model building and refinement

After the step of calculating the initial phases (and thus the initial model using molecular replacement), model building and structure refinement need to be carried out. These two steps

are closely related during which model building and fitting of the initial model into electron density in real space is iteratively alternated with reciprocal space refinement of both positional and B-factor parameters of the model. The target function to be minimized is the residual between the experimental structure factor amplitudes and the structure factor amplitudes calculated from the model.

In this study, two different programs were used for structure refinement in the reciprocal space, *phenix.refine* of the *PHENIX* suite (Liebschner et al. 2019) and *Refmac5* of the *CCP4* suite (Murshudov et al. 2011). They are the most used structure refinement programs according to the RCSB Protein Data Bank (<https://www.rcsb.org/stats/distribution-software>). *Coot* (Emsley and Cowtan 2004) was used for model building and real-space refinement.

1.3.7 Difference Fourier map calculation

When a TR crystallography experiment is conducted, it is difficult to trigger the reaction in all proteins within microcrystals using optical pump-probe schemes for TR studies which often represent less than 10% of the total population (Coquelle et al. 2018a; Pande et al. 2016; Woodhouse et al. 2020a). This means that within a crystal there are proteins that undergo structural changes upon light illumination (intermediate-state structure) and proteins that remain in the initial state (dark-state structure). Difference Fourier maps are calculated to visualize structural differences between the light-triggered and the reference structure (Henderson and Moffat 1971; Rould and Carter 2003).

In X-ray crystallography, a difference Fourier map is a difference density map that is calculated using Fourier coefficients. These coefficients represent the differences between the light-triggered structure factor amplitudes and the initial structure factor amplitudes using the phase from the initial model for both terms, since there are no phases available for the light-triggered data. This type of map shows positive electron density at the regions of the model that are not present in the reference data but present in the light-triggered data and negative density map at the regions of the model that are present in reference data but not in the light-triggered data. To calculate such a map, the data should come from isomorphous crystals. Two crystals are called isomorphous when they have the same space group and unit cell parameters, and when the

repetitive unit is at the same position in the asymmetric unit of the crystal. The only structural difference that is tolerated is the small differences deliberately introduced in the light-triggering dataset.

An improved difference Fourier map could be obtained by applying a q-weighting factor (Ursby and Bourgeois 1997). Q-weighting assigns a weight parameter to structure factor amplitude differences based on measurement errors (σ), using Bayesian statistics. In addition, q-weighting improves the signal-to-noise ratio of structure factor amplitude differences. Q-weighted difference Fourier maps have been calculated from synchrotron (Colletier et al. 2007, 2008; Duan et al. 2013; de la Mora et al. 2020) and XFEL data (Colletier et al. 2016; Coquelle et al. 2018a; Woodhouse et al. 2020b). Recently, a software, named *Xtrapol8* that calculates difference Fourier maps for TR crystallography was developed (De Zitter et al. 2022).

1.3.8 Structure factor extrapolation

As it was mentioned previously in Section 1.3.7, differences between light-triggered structure and reference structure can be assessed by calculating the difference Fourier map. This reveals a piece of qualitative information about the differences between the two datasets. In some cases, the perturbation fails to trigger the reaction in all molecules in the crystal. In the end, the crystal contains a mixture of molecules that undergo perturbation and molecules that remain in their initial state.

In such cases, a linear extrapolation of structure factor amplitudes is calculated (Genick 2007). Extrapolated structure factors are generated by adding the computed structure factors for the reference data and the difference structure factors for the light-triggered data, where the difference structure factors come from the difference Fourier map (Genick 2007). This approach treats structure factors as scalars rather than vectors. And this is because it is considered that the phases do not change between the triggered and non-triggered data sets. As a result, the amplitude of the difference in structure factors is amplified to match 100% of the light-triggered state (Genick et al. 1997). As a consequence, the computed extrapolated electron density map only contains information on the intermediate state, the structure of which can be modelled as done into a conventional electron density map.

1.3.9 Figures

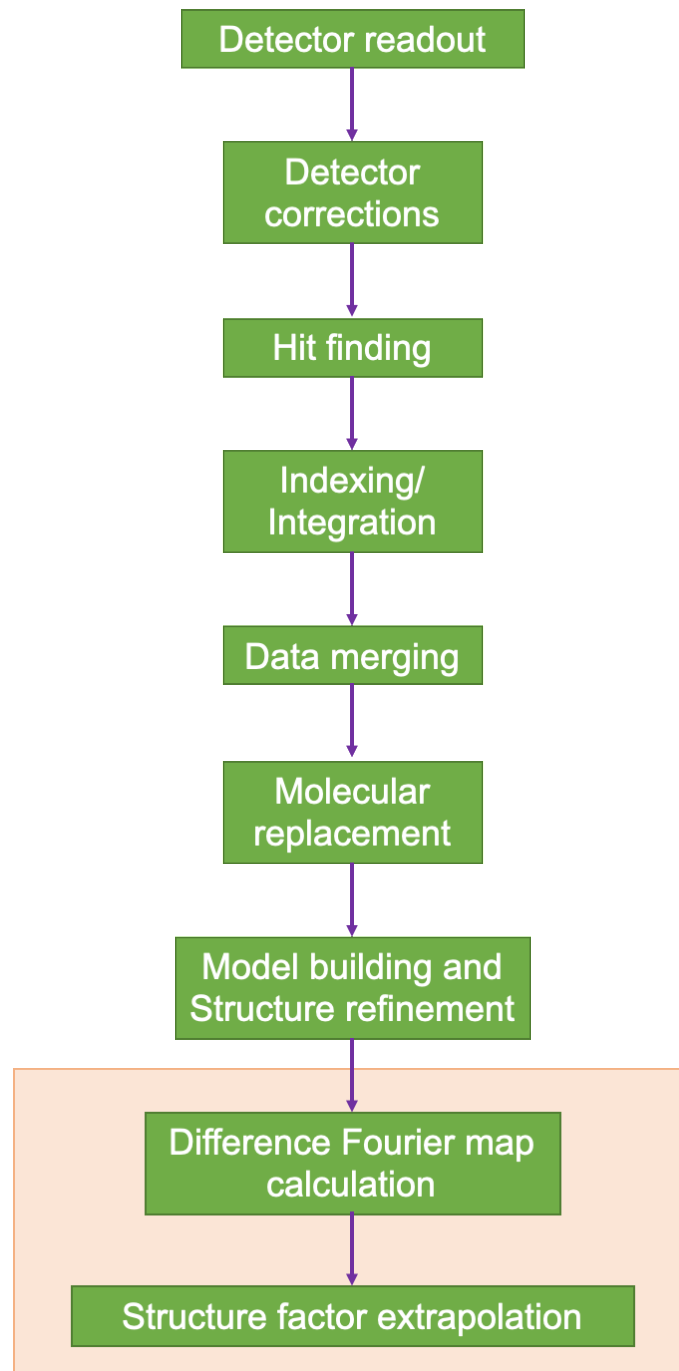


Figure 1.3.1: Flow diagram of serial crystallography data analysis.

Major steps of serial crystallography data processing from detector readout to the structure solution and map calculation. Data-analysis steps for time-resolved crystallography are included in the orange box. Experimental phasing is also possible for SX, but this is not included in the diagram.

Chapter 2
Fatty acid
photodecarboxylase

2.1 Introduction

2.1.1 Enzymes and their reactions

Two molecules can react if they are in the proper orientation and have the right amount of energy. This would need a large amount of energy and time for the reaction to occur. Fortunately, most biological reactions that take place in living organisms are catalyzed by enzymes. They are biological macromolecules within cells that act as catalysts. In other words, without enzymes, the reactions would not take place at a perceptible rate. A catalyst is a compound that accelerates the rate of a chemical reaction by reducing the activation energy without undergoing any irreversible chemical change. Moreover, they do not alter the equilibrium of a reaction they are involved in. In contrast to chemical catalysts, enzymes are highly selective and catalyze specific reactions only. This selectivity arises from the structure and dynamics of the enzyme, and specifically of its active site. The active site is the most critical feature of an enzyme. It is usually a cavity in which the substrate binds and undergoes changes that result in product formation.

Several hypotheses on the enzyme-substrate binding have been proposed. Emil Fischer in 1894 postulated the first and the simplest model to explain an enzyme function is that the substrate simply fits into the active site (Fischer 1894). This approach is called "Lock and Key" (Fischer 1894). According to another concept, namely "Induced Fit", the approaching substrate molecule causes conformational changes in the enzyme and precise orientation of the residues in the active site is needed to cause the reaction (Johnson 2008; Koshland and Neet 1968). Another model that was suggested was based on the preorganization of the reaction environment by the enzyme (Cannon, Singleton, and Benkovic 1996). The amino acids of the enzyme are flexible due to the freedom of single covalent bonds that are predominant in enzymes. Another model was suggested based on molecular mechanisms results, named "near-attack conformation" (Bruice 2002; Bruice and Lightstone 1999). This model proposed that the conformers of the molecules that take part in the reaction have specific interatomic distances and bonding angles and that the transition state is attained via ground-state conformers that strongly resemble the transition state.

Two main hypotheses on the driving force of the catalytic function have been suggested. One proposes that the catalytic function is impacted by dynamical processes (Hay and Scrutton 2012; Karplus 2010) whereas the other proposes that it is derived from preorganized electrostatics (Warshel et al. 2006). Catalytic reactions in the enzymes are assisted by protein dynamics on a wide time scale (van den Bedem and Fraser 2015; Henzler-Wildman and Kern 2007). Precisely, these time scales are described by bond vibrations on the 10-100 fs timescale, rotations of side chains at the protein surface on the 10-100 ps timescale, and protein breathing motions (rotations of side chains at the protein interior; Mariño Pérez et al. 2022) on the micro- to millisecond timescale (Agarwal 2006; Hammes-Schiffer and Benkovic 2006). Preorganized electrostatic model was introduced by Arieh Warshel (Warshel and Bora 2016) and it suggests that the transition state is stabilized by the polar environment of the enzyme via electrostatic interactions which results to lower the energetic barrier (Kamerlin and Warshel 2010; Prah et al. 2019).

Many enzymes contain co-factors. They are chemically diverse and include:

- i. Organic groups or compounds. Examples in this category are the heme molecule that is bound covalently to cytochrome c peroxidase (Poulos et al. 1980) and the vitamins and their derivatives like nicotinamide adenine dinucleotide (NAD/H) that is bound in a non-covalently way to lactate dehydrogenase (Read et al. 2001).
- ii. Metal ions, or metallic clusters that temporally bind to the active site of the enzyme. For instance, nickel ion (Ni^{2+}) is found in the active site of urease (Benini et al. 2014), and Cytochrome bc1 Complex binds an iron-sulfur (2Fe-2S) cluster (Gao et al. 2003).

Enzymes can be regulated by molecules that either increase (activators) or decrease (inhibitors) activity. Various parameters such as temperature and pH may affect enzymatic activity, too. Substrate and enzyme concentrations determine enzyme kinetics, in particular the speed at which a chemical reaction is catalyzed by an enzyme.

Enzymes are most often proteins, but can also be composed of RNA. In the latter case, they are called ribozymes (ex. ribosomes, ribonuclease P, *etc.*) (Weinberg, Weinberg, and Hammann 2019). According to the International Union of Biochemistry and Molecular Biology (IUBMB)

Enzyme Nomenclature, enzymes can be classified into seven categories according to the biochemical reaction they carry out:

- i. Oxidoreductases (EC 1) that catalyze oxidoreduction reactions (ex. peroxidase).
- ii. Transferases (EC 2) that transport a functional group from one molecule to another (ex. methyltransferase).
- iii. Hydrolases (EC 3) that hydrolyse chemical bonds (ex. DNA or RNA nucleases).
- iv. Lyases (EC 4) that break chemical bonds and create new ones (ex. adenyl cyclase).
- v. Isomerases (EC 5) that rearrange the functional groups within a molecule to form isomers (ex. topoisomerases).
- vi. Ligases (EC 6) (or synthases) that allow the junction of two molecules (ex. DNA ligase).
- vii. Translocases (EC 7) that catalyze the movement of ions or small molecules across cellular membranes (e.g. membrane transport protein).

Extended reviews on enzymatic catalysis can be found here (Agarwal 2006, 2019; Hammes-Schiffer and Benkovic 2006).

2.1.2 Photoenzymes

The great majority of enzymatic processes in biological cells are thermally triggered, whereas light-activated reactions are substantially rarer (Björn 2018). In Nature, there are only three enzymes whose catalytic reaction requires a continuous flux of light. So far, two photoenzymes have been well characterized *i.e.* DNA photolyases (Brettel and Byrdin 2010; Sancar 2016; Zhong 2015) and the light-dependent protochlorophyllide oxidoreductase (LPOR) (Gabruk and Mysliwa-Kurdziel, 2015). The third enzyme is the newly discovered fatty acid

photodecarboxylase (FAP), which is involved in lipid metabolism in microalga (Sorigué *et al.*, 2017) and which was studied during my Ph.D. work.

DNA photolyases are omnipresent in Nature (archaea, bacteria, and eukaryotes) (Mei and Dvornyk 2015). However, humans and some other mammals have a copy of the gene of a DNA photolyase that codes a nonfunctional DNA photolyase (Mei and Dvornyk 2015). DNA photolyases are flavoenzymes which are involved in repairing DNA damaged by exposure to far UV light that led to a covalent linkage of two adjacent thymine bases of the same DNA strand. Two products are then formed, cyclobutane pyrimidine dimer (CPD, ~80%) and a less-frequently pyrimidine-pyrimidone (6–4) photoproduct (6–4PP, ~20%) (Liu, Wang, and Zhong 2015; Sancar 2003). Two types of photolyases, CPD photolyase and (6–4) photolyase, recognizing specifically the corresponding photoproduct, have similar primary, secondary and tertiary structures (Liu *et al.* 2015; Sancar 2003). Both DNA photolyases use blue or near UV light and a fully reduced co-factor FADH⁻ to repair DNA damage. The mechanisms of both CPD (Kao *et al.* 2005) and (6-4) (Li *et al.* 2010) DNA photolyase have been studied by transient absorption spectroscopy that shed light on the cyclic electron-transfer reaction photocycle between the co-factor FADH⁻ and either CPD or (6-4) photoproducts. Recently, SFX structure from (6-4) DNA photolyase microcrystals was solved (Cellini *et al.* 2021) paving the way for TR-SFX studies in which the structural intermediate states of the activated (6-4) DNA photolyase can be revealed.

LPOR catalyzes one of the last reactions of chlorophyll biosynthesis and it is involved in the reduction of protochlorophyllide to chlorophyllide upon light absorption. These are tetrapyrrole derivatives. Upon light absorption, LPOR uses a co-factor, a nicotinamide adenine dinucleotide phosphate (NADPH), as an electron donor to reduce one of the double bonds of porphyrin, an unsaturated tetrapyrrole. The chlorophyll molecule's chlorin ring is generated during this process. Chlorins absorb red light more efficiently than porphyrins, which is critical for the conversion of solar energy into chemical energy during photosynthesis (Bröcker, Jahn, and Moser 2012; Gabruk and Mysliwa-Kurdziel 2015). LPORs can be found in many cyanobacteria, green algae, lower plants (like bryophytes), gymnosperms, and angiosperms (like monocotyledons and dicotyledons) (Yang and Cheng 2004). Even though the above-mentioned organisms are oxygen-dependent, it was found that LPROR is also present in *Dinoroseobacter shibae* DFL12T, an α -proteobacterium that is an anoxygenic phototrophic organism.

2.1.3 Fatty acid photodecarboxylase

The third enzyme is the newly discovered fatty acid photodecarboxylase (FAP), which is involved in lipid metabolism in microalga (Sorigué *et al.*, 2017), and decarboxylates free fatty acids to produce hydrocarbons after light absorption from a co-factor, a flavin adenine dinucleotide (FAD) (Figure 2.2.1). FAP was first isolated from the microalgae *Chlorella variabilis* NC64A (Sorigué *et al.* 2016, 2017). *C. variabilis* NC64A is a unicellular photosynthetic green alga and it can be found in marine and brackish waters (Blanc *et al.* 2010). The FAP that is produced by *C. variabilis* is referred to as CvFAP.

This algal enzyme is a member of a subfamily of the glucose-methanol-choline (GMC) oxidoreductase family (Cavener 1992). It is a flavoprotein family that includes a variety of oxidases and dehydrogenases whose functions are diverse and that share a similar fold (Cavener 1992). Some other examples of GMC oxidoreductase are cholesterol oxidase (Li *et al.* 1993), hydroxynitrile lyase (Dreveny *et al.* 2009), pyridoxine oxidase (Mugo *et al.* 2013), glucose dehydrogenase (Yoshida *et al.* 2015), and choline oxidase (Salvi *et al.* 2014) whose substrates are a steroid, benzaldehyde, pyridoxamine, gluconolactone, and glycine betaine, respectively. It is believed that the common ancestor of GMC proteins could bind several of the substrates with more or less low catalytic activity for the above-mentioned substrates (Cavener 1992) and that the substrate specificity might arise upon mutation in the active site of the protein (Cavener 1992).

FAP has a wide range of applications in the green chemistry domain. Photochemical processes, in general, have productivities that are orders of magnitude too low for industrial applicability due to a reactor design based on external illumination with inadequate light penetration in photocatalyst suspensions. This significant limitation was overcome by implementing a novel reactor idea of interior lighting based on small (1 cm diameter) wirelessly powered light emitters (WLEs) (Burek *et al.* 2017). Indeed, utilizing WLEs as a source of heightened internal illumination, the rates of light-induced, FAP-catalyzed decarboxylation of fatty acids were considerably increased (Duong *et al.* 2021). This enzyme is of interest for its ability to convert fatty acids derived from triglycerides to a mixture of straight-chain hydrocarbons that,

depending on their chain lengths, could be used to produce next-generation biofuels such as biodiesel in two steps from waste triglyceride (Ma et al. 2020). Mutant screening of the amino acids in the active site demonstrated a fatty acid chain-length selectivity of the enzyme for short-chain carboxylic acids (Amer et al. 2020; Zhang et al. 2019) and medium to long (C12 to C18) fatty acids (Santner et al. 2021). Transformation of unsaturated fatty acid into enantiomerically secondary fatty alcohols *via* two steps of enzymatic cascade reaction was reported (Zhang et al. 2020). The first step consists of introducing an alcohol functional group using a fatty acid hydratase and the second step consists of decarboxylation of the product of the first step by CvFAP (Zhang et al. 2020).

The first structure of CvFAP was solved at 3.15 Å resolution by cryo-MX (PDB ID: 5NCC) (Sorigué et al. 2017). Even though the crystals were twinned, the structure could be solved by molecular replacement by using two domains from known structures of the GMC oxidoreductase family, a choline oxidase (PDB ID: 2JB) and a glucose dehydrogenase (PDB ID: 4YNT). The 3D structure of the 69-kDa enzyme, revealed a two-domain protein (Figure 2.1.1), one in the N-terminal whose amino acids stabilize the FAD and the other domain forms a hydrophobic tunnel that enables the substrate and product trafficking. In between the two domains, loops prevent the solvent from entering the active site. The hydrophobic tunnel is open to the solvent and ends at the active site in which the isoalloxazine moiety of the FAD resides. The conservation of the majority of the amino acids of the hydrophobic tunnel was evidenced by sequence alignment of the subgroup of the GMC oxidoreductase and FAP (Sorigué et al. 2017).

This chapter is about TR-SFX studies on CvFAP and the contribution of its results to understanding the dynamics and mechanism of FAP reached by a large scientific consortium. Section 2.3 focuses on data analysis of the TR-SFX experiment on CvFAP and describes the difficulties that arose during this step as well as the calculation of extrapolated structure factor amplitudes. This section is currently under review in *Acta Crystallographica D*. Section 2.3 describes my contribution to the publication (Sorigué et al. 2021) that presents a detailed description of CvFAP's photomechanism.

2.1.4 Figures

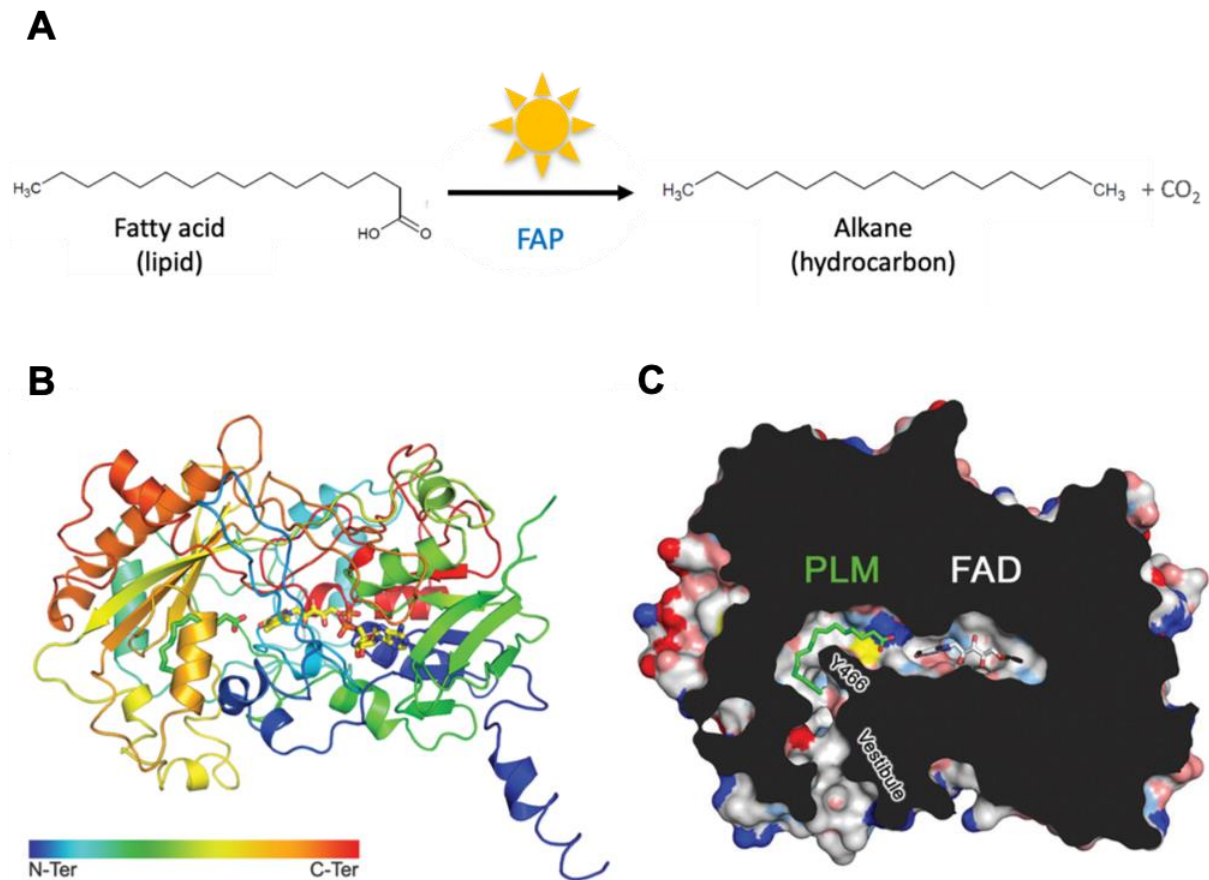


Figure 2.1.1: Mode of action and structural features of CvFAP

(A) FAP is involved in the lipid metabolism in microalgae and catalyzes the decarboxylation of free fatty acids to alkanes or alkenes upon light absorption. (B) The enzyme's overall architecture in complex with FAD co-factor and palmitate (PLM); a fatty acid. The structure is colored from the N- to the C-terminal, with the FAD and palmitic acid represented in sticks (PDB ID: 5NCC). (C) Slice through the electrostatic surface representation of CvFAP. The hydrophobic tunnel (vestibule) is open to one end and leads to the active site with its substrate (PLM) and co-factor (FAD). Figure adapted from (Sorigué et al. 2017).

2.2 Time-resolved SFX studies on fatty acid photodecarboxylase

2.2.1 Introduction

This section describes my contribution to the published paper in *Science*, entitled “Mechanism and dynamics of fatty acid photodecarboxylase” (Sorigué et al. 2021). Specifically, I was involved in microcrystal production for time-resolved SFX (TR-SFX) experiments, microcrystal diffraction quality tests at the ESRF (Grenoble, France), time-resolved emission and absorption spectroscopy experiment on microcrystals, TR-SFX experiment at the LCLS (Stanford, USA), off-line TR-SFX data processing and analysis, SFX structure refinement and Fourier electron density map calculation. The purpose of using SFX was to solve X-ray radiation damage-free structure at room temperature and the one of using TR-SFX to identify the time scale on which decarboxylation of the fatty acid occurs, *i.e.* which of the two proposed scenarios is the right one.

The first publication of CvFAP described a new photocatalytic enzyme from algae that uses blue light to produce hydrocarbons from free fatty acids in one step (Sorigué et al. 2017). The photoenzyme is a biocatalyst that is involved in hydrocarbon synthesis and employs a riboflavin co-factor (FAD) to promote fatty acid decarboxylation via radical-based catalysis (Sorigué et al. 2017). In the following presents two major issues which need to be addressed:

- i) The reported structure of CvFAP was solved at 3.15 Å resolution with twinned crystals (PDB ID: 5NCC) (Sorigué et al. 2017). The structure revealed fatty acid substrate facing the co-factor FAD in the catalytic side and a hydrophobic tunnel open to the solvent which leads to the fatty acid substrate (Figure 2.1.1). To gain more accurate structural insight, a high-resolution crystal structure needed to be solved.
- ii) The catalytic mechanism of CvFAP remained largely unknown. Based on time-resolved optical spectroscopy results, two possible scenarios were envisaged to occur after FAD excitation upon photon absorption (Figure 2.2.1). In the first scenario, substrate decarboxylation is concomitant with forward electron transfer

(fET) from the fatty acid to the photoexcited FAD*. fET occurs within 300 ps and leads to an anionic radical co-factor (FAD^{•-}). In the second scenario, decarboxylation occurs concomitantly with back electron transfer (bET) from FAD^{•-} to the substrate radical within 100 ns.

These two issues were further investigated by an international consortium in which I participated and the results were recently published (Sorigué et al. 2021). The supplementary information of this article can be found here:

<https://www.science.org/doi/10.1126/science.abd5687>

2.2.2 Results and Discussion

High-resolution dark state structure of CvFAP solved by synchrotron cryo-crystallography

It has been reported earlier that the crystals of CvFAP are twinned and the 3D structure was solved at 3.15 Å resolution (PDB ID: 5NCC) (Sorigué et al. 2017). Dr. Pascal Arnoux and the group of Dr. Frédéric Beisson (CEA Cadarache, France) were able to modify the protein expression and crystallization protocol by removing the N-terminal helix (residues 61 to 76) that was involved in crystal packing. Hence, they were able to solve a 3D structure of CvFAP in its dark state at 1.8 Å resolution using cryo-macromolecular crystallography (MX) at the ESRF synchrotron (PDB ID: 6YRU) (Sorigué et al. 2021) (Figure 2.2.2A). This high-resolution structure shows two C18 fatty acids that were co-purified with the CvFAP. One fatty acid is located in the active site and is stabilized by hydrogen bonds between its carboxylate group and two water molecules (Wat1 and Wat2), as well as by interacting with the side chains of Arg451 and Gln575. Conversely, the other enzymes of the GMC family stabilize their substrate near the N5 atom of the isoalloxazine ring of the FAD (Figure S2 in Appendix 6.1). The second fatty acid is located on the surface of the protein in the hydrophobic tunnel. It is stabilized by hydrophobic interactions with the side chains of Leu427, Tyr419, Ile126, Ile416, Leu420, Arg132, and Arg122.

The high-resolution cryo-MX structure of CvFAP in the dark state revealed an intriguing feature, *i.e.* a bent oxidized isoalloxazine ring of the FAD cofactor, whose dihedral angle C4-

N5-N10-C9 deviates by 17.4° from planarity (PDB ID: 6YRU) (Sorigué et al. 2021) (Figure 2.2.2B). Usually, the conformation of the isoalloxazine ring of FAD is planar in the oxidized and bent in the reduced state (Kar, Miller, and Mroginiski 2021). Previously observed FAD bending in X-ray crystal structures was assigned to X-ray-induced reduction during crystallographic data collection (Røhr, Hersleth, and Andersson 2010; Senda et al. 2009). The absorbed X-ray dose for the cryo-MX dark state structure (PDB ID: 6YRU) was estimated to be 154 kGy (Sorigué et al. 2021). Dr. Antoine Royant (IBS, Grenoble) and his team showed by *in crystallo* UV-Vis absorption microspectrophotometry that X-ray induced FAD reduction occurred with a half-dose of 40 kGy (Sorigué et al. 2021). Moreover, a Raman microspectrophotometry experiment at different X-ray doses (from 0 to 1.9 MGy) carried out by the same team suggested that at 100 K the conformation of the isoalloxazine ring of the FAD co-factor did not change between its oxidized and the reduced states (Sorigué et al. 2021). Dr. Pascal Arnoux and Dr. Antoine Royant were able to solve a dark-state crystal structure of CvFAP at room-temperature at 1.9 Å resolution using synchrotron MX at an absorbed dose as low as 37 kGy (PDB ID: 6YRX), yet which is still close to the photoreduction half-dose of FAD (Sorigué et al. 2021). This structure also revealed a bent FAD (bending angle 13.7° (Figure S4 in Appendix 6.1)). Only SFX at an XFEL, providing X-ray damage-free protein structures because of the diffraction-before-destruction principle (Neutze et al. 2000), was then identified as being the ultimate way of revealing whether oxidized FAD in FAP is planar or bent.

Room-temperature SFX structure in the dark state of CvFAP

The DYNAMOP group at the IBS, the group of Prof. Ilme Schlichting at the Max-Planck Institute in Heidelberg, and I used room-temperature SFX at the LCLS (XFEL facility; see below for details) to get a definitive answer on the conformation of the oxidized FAD in FAP. This was the first goal of my project. XFEL radiation offers the possibility to collect radiation damage-free data (Burgie et al. 2020; Hirata et al. 2014; Rose et al. 2021), except if long pulses of the unattenuated beam are used (Nass 2019; Nass et al. 2015). Microcrystals of CvFAP were injected into the vacuum chamber of the CXI end-station of the LCLS XFEL facility in Stanford (USA) (Liang et al. 2015). The structure of this dark-state structure was solved at 2.0 Å resolution (Table 2.2.1). The space group is $P2_1$ with two molecules in the asymmetric unit. At that time, the space group was not unambiguous (see Section 2.3). First, we forced the isoalloxazine ring to be planar. The $F_{\text{obs}}-F_{\text{calc}}$ difference map then showed that the FAD is not

planar but indeed bent (Figure 2.2.3A). Moreover, a $F_{\text{obs}}-F_{\text{calc}}$ omit map of the FAD was calculated showing that the isoalloxazine ring should indeed be modeled in a bent conformation (Figure 2.2.3C). The fully refined SFX dark-state structure featured a bending angle of the FAD isoalloxazine ring of 14.3° which is similar to the bending angle of the synchrotron structures solved at 100 K (PDB ID: 6YRU) and RT at low-dose (PDB ID: 6YRX) (Figure 2.2.4). No other flavoprotein that we are aware of contains a butterfly-bent conformation of the oxidized flavin. Bending conformations were attributed to X-ray-induced reduction (Berkholz et al. 2008; Kort et al. 2004; Mees et al. 2004; Røhr et al. 2010). Future radiation-free structures of oxidized flavoproteins should reveal if the bending is a unique feature of CvFAP.

Investigation on the potential functional relevance of the bent isoalloxazine ring was carried out by Dr. Tatiana Domratcheva (Lomonosov Moscow State University, Russia) using quantum chemical calculations. It was shown that a bent FAD decreased the oxidized-flavin excitation energy easy forward electron transfer (fET) (Sorigué et al. 2021). Specifically, vertical excitation, vertical electron affinity, and adiabatic electron affinity decreased from 3.02; -1.15, and -1.57 eV (planar FAD) to 2.70, -4.00, and -5.44 eV (bent FAD), respectively (Figure 2.2.5A). Vertical excitation is the process of transitioning from the ground state to the excited state without causing structural changes. Vertical electron affinity is defined as the difference in energy between the energy in the neutral form of a molecule and the energy of the corresponding anionic molecule. If molecular geometries are optimized (*i.e.* most stable geometry) in both forms (neutral and anionic), then the electron affinity is called adiabatic electron affinity. In addition, the maximum absorption of the oxidized FAD (ground state) in CvFAP is 467 nm (Figure 2.2.5B). This value is red-shifted regarding the typical values of 445 to 450 nm for other flavoproteins and free FAD. This red-shift is attributed to FAD bending in the enzyme which allows photoexcitation (Sorigué et al. 2021). This is well enough into the so-called “green-gap”, *i.e.* outside the region where chlorophyll strongly absorbs, thus enhancing the light capture capacity of CvFAP.

Time-resolved serial femtosecond crystallography of CvFAP

The second goal of my CvFAP project was to investigate the structural changes occurring after photon absorption to assess whether scenario 1 or scenario 2 is correct (see Section 2.3.1). This was achieved after photoexcitation of CvFAP microcrystals at room temperature and data collection with TR-SFX experiment (Brändén and Neutze 2021; Colletier et al. 2018) using a

pump-probe scheme. Time-resolved fluorescence spectroscopy on CvFAP microcrystals established that the kinetics of fET are the same as in solution (supplementary text S5, fig. S15 in Appendix 6.1). For TR-SFX at the LCLS, FAP microcrystals were photoexcited by pump pulses (400 nm wavelength; 11 $\mu\text{J}/\text{pulse}$, 4 ps (FWHM) pulse length, circularly polarized) and probed by femtosecond XFEL pulses after pump-probe delays of 20 ps, 900 ps, 300 ns, and 2 μs to cover time scales on which FAD reduction and FAD \bullet^- reoxidation occur. The SFX dark-state structure mentioned above was determined from data collected without pump laser excitation. Structural changes after photoexcitation were visualized as positive and negative peaks in difference Fourier electron density maps calculated between the light and dark data sets ($F_{\text{obs}}^{\text{light}_\Delta t} - F_{\text{obs}}^{\text{dark}}$; Figure 2.2.6A) at 2.2 Å resolution. The most prominent difference electron density peaks at all four time points are in the active site, with the highest negative peaks (-5.5 to -10.1 σ , depending on the time point) at the position of the carboxyl group of the substrate, suggesting that light-induced decarboxylation occurred (Figure 2.2.6A).

At 900 ps, decarboxylation has occurred to a considerable extent. This result is in line with the 270 ps time constant determined by multi-scale time-resolved infrared (IR) spectroscopy (Figure 2.2.7) which was carried out by the team of Dr. Marten Vos (Ecole Polytechnique, Palaiseau, France) (Sorigué et al. 2021). This experiment revealed that the amplitude of CO₂ absorption band changed with a time constant of 270 ps, centered at 2337.5 cm^{-1} (Figure 2.2.7, and Figure 2 C - E and supplementary Figure S9 in Appendix 6.1). The initial CO₂ band frequency is 5 cm^{-1} lower than that of ¹²CO₂ in an aqueous solution, a shift being attributed to the protein environment. Following then, the CO₂ signal decreases almost fourfold with a time constant of 100 ns without changing much in shape, followed by an upshift approaching 2342 cm^{-1} , a process with a time constant of 1.5 ms. The latter phase most likely reflects CO₂ migration towards the solvent.

Back to TR-SFX, at 300 ns and 2 μs , a strong negative peak is observed at Wat1 (-5.8 , and -6.2 σ , respectively, Figure 2.2.6A), but not at Wat2. We note the absence of positive difference electron density peaks associated with the photodissociated CO₂ in the vicinity of the substrate carboxyl group. A possible reason could be the small initial displacement of cleaved CO₂ relative to its position in the fatty acid, in line with the structure determined based on an illuminated cryo-cooled crystal ‘100 K light’ (Dr. Pascal Arnoux; see supplementary Figure S13C in Appendix 6.1 for comparison). It is conceivable that the positive difference densities close to Cys432 in the 300 ns and 2 μs data sets (Figure 2.2.6A) correspond to the feature(s)

observed in the data obtained from cryo-cooled crystals illuminated at 150 K (Dr. Pascal Arnoux; Figure 2.2.6B and Fig. 4D in Appendix 6.1) that were tentatively assigned to bicarbonate (see supplementary Figure S14 in Appendix 6.1). In the SFX data, attempts to fit unambiguously this positive difference density with a bicarbonate, a CO₂ molecule, or a mixture thereof remained unsatisfactory (see Section 2.3). The absence of significant difference electron density peaks at the FAD at all four time points suggests that the isoalloxazine ring does not undergo significant light-induced conformational changes.

Reaction cycle of CvFAP

As it was mentioned previously, elucidation of CvFAP's reaction cycle is the fruit of a large international consortium (Sorigué et al. 2021). By combining results from different techniques such as multiscale TR IR spectroscopy, Fourier transform IR spectroscopy, TR-SFX, transient absorption spectroscopy, quantum chemistry calculations, and synchrotron X-ray crystallography, a detailed reaction mechanism of CvFAP was suggested (Sorigué et al. 2021). The evolution of the substrate (fatty acid) to the products [hydrocarbon and CO₂] is described in detail, as well as the role the protein moiety plays in the catalytic process that is suggested to involve a proton-coupled electron-transfer (PCET) mechanism (Figure 2.2.8). The steps of the reaction cycle are as follows:

- i) Excitation of the FAD co-factor upon light absorption.
- ii) Forward electron transfer (fET) from fatty acid to FAD* leads to decarboxylation of the substrate and the formation of an alkyl radical at a time constant of ~300 ps.
- iii) Back electron transfer (bET) from FAD^{•-} to the alkyl radical at a time constant of ~100 ns. Formation of red-shifted FAD. Arg451 is the final proton donor to the alkyl radical. Alkane (first product) and CO₂ (second product) are formed.
- iv) On a longer time scale, 75% of the CO₂ is transformed to HCO₃⁻ (bicarbonate) while the other 25% of the CO₂ is not transformed to HCO₃⁻ and migrates away from the active site.

- v) Red-shifted FAD disappears on the millisecond timescale. CO₂ migrates away from the active site.

- vi) Hydrocarbon product is released.

- vii) A new substrate binds in the active site.

2.2.3 Ongoing work and perspectives

Characterization of X-ray radiation damage to crystalline CvFAP using serial synchrotron crystallography at cryo- and room-temperatures.

Further investigations of X-ray radiation damage on CvFAP using serial synchrotron crystallography (SSX) are ongoing in the DYNAMOP group (IBS, Grenoble). The goal of this project is to study specific and global radiation damage inflicted on crystalline macromolecules. Such an experiment was carried out at the ID13 beamline at the ESRF in November 2017 (proposal CS5103) in which I participated. The ID13 beamline provided one of the highest flux-densities available at third-generation synchrotron sources worldwide (before the upgrade of the ESRF in 2020). Microcrystals (size of 20x20x20 μm) of CvFAP were sandwiched between two Si₃N₄ membranes and presented to an X-ray beam of 3.2 μm (hor. FWHM) × 2 μm (vert. FWHM). Images were collected with 20 frames per spot on the chip with 1.4 ms of exposure time for each spot. Each spot was spaced by 10 μm in both vertical and horizontal directions. A similar experimental setup was used previously by the same team for a radiation damage experiment on HEWL crystals (de la Mora et al. 2020). The hypothesis of this experiment was that the X-ray-induced reduction of the FAD co-factor can cause decarboxylation of the fatty acid (substrate). The data analysis is ongoing by Ronald Ríos Santacruz, a Ph.D. student in the DYNAMOP Group (IBS, Grenoble).

Neutron crystallography on CvFAP macrocrystals

The goal of the neutron project is to study the hydrogen bond network in the active side of CvFAP as well as the ionization and protonation states of the components of the active site in

different intermediates after photon absorption. These intermediates are aimed to be trapped at various cryo-temperatures. This project is a collaboration between the DYNAMOP Group, Dr. Nicolas Coquelle (ESRF, Grenoble), Dr. Damien Sorigué (CEA Cadarache), and Dr. Monica Spano (IBS, Grenoble). I had been involved in this project during the first discussions on the crystal growth of CvFAP suitable for neutron crystallography experiments.

2.2.4 Materials and Methods

Microcrystal growth and injection for TR-SFX

Crystallization screening was performed under red-light conditions at 8°C using 96-wells plates in batch condition. Screening was done by mixing 20 μL of CvFAP in solution 1 (150 mM NaCl, 10 mM Tris pH 8.0, 5% (w/v) glycerol) at different concentrations (3-12 mg mL^{-1}) with 20 μL of mother liquor containing 100 mM Na citrate pH 5.5, 10 mM spermidine and PEG 4000 (12 to 28% w/v). A 1:1 mixture of 19% (w/v) PEG 4000, 0.1 M sodium citrate pH 5.5, 10 mM spermidine (solution 2) and solution 1 at a protein concentration of 6 mg mL^{-1} yielded two types of crystals, hereafter referred to as needle and diamond crystals based on their respective shapes. Efforts to obtain only one crystal form were not successful. The diffraction quality of needle shaped crystals ($30 \times 3 \times 3 \mu\text{m}^3$) was assessed at the microfocus beamline ID23-2 (Flot et al. 2010) of the ESRF (Grenoble) at room temperature (RT; using MicroRT™ mounts from MiTeGen) and at 100 K (in a cryo-loop) after buffer exchange by centrifugation and resuspension in 20% (v/v) glycerol, 23% (w/v) PEG 4000, 100 mM Na citrate pH 5.5 and 10 mM spermidine. The diffraction limit, as judged in the program *Dozor* implemented in *MeshAndCollect* data-collection workflow (Zander et al. 2015) was 2.3 Å at 100 K and 2.6 Å at room temperature. For TR-SFX experiments, large quantities of microcrystals were generated using the batch method by gently mixing 4 mL of solution 1 at a protein concentration of 6 mg mL^{-1} with 4 mL of solution 2 at 8°C. 1.5 grs of CvFAP was crystallized using this approach. Batches consisting mostly of needle shaped crystals ($100 - 200 \times 2 - 5 \times 2 - 5 \mu\text{m}^3$) were selected and stored at 4°C. Prior to injection, they were reduced in size to about $10 \times 2 - 5 \times 2 - 5 \mu\text{m}^3$ (Figure 2.2.9) by flowing a slurry containing 20% (v/v) microcrystals at 2.5 mL min^{-1} successively through a 20 μm and a 10 μm stainless steel filter in tandem. After filtering, the crystal suspension was concentrated to 60% (v/v) by

centrifugation and removal of the supernatant and placed in a stainless steel sample syringe for injection. The syringe was installed on an anti-settling device (Lomb et al. 2012) equipped with a Peltier element-cooled syringe holder at 4°C. The crystals were injected with a gas dynamic virtual nozzle (GDVN (Weierstall, Spence, and Doak 2012)), using sample capillaries with an inner diameter of 75 or 100 μm , into the microfocus vacuum chamber of the CXI end station (Liang et al. 2015) of the Linac Coherent Light Source (LCLS) at the SLAC National Accelerator Laboratory. The sample was injected at flow rates between 35 and 55 $\mu\text{L min}^{-1}$ in a liquid jet of about 5 μm in diameter.

Picosecond pump-laser excitation of FAP microcrystals in TR-SFX experiments

CvFAP microcrystals ($\sim 10 \times 4 \times 4 \mu\text{m}^3$, $P2_1$, two molecules (A,B) in the asymmetric unit) were photoexcited with pulses of a Ti:sapphire laser (400 nm wavelength; 11 μJ / pulse, circularly polarized). The pulse length was 4 ps (FWHM), achieved by detuning the pulse compressor. The pump-laser beam of Gaussian shape was focused to a spot of 155 μm (FWHM), resulting in a peak power density of 10 GW/cm^2 . Under these excitation conditions, and assuming an extinction coefficient of 9250 $\text{M}^{-1}\text{cm}^{-1}$ (estimated from Fig. 3A in Sorigué *et al.* 2017 under the assumption that the extinction coefficient at 467 nm is 11300 $\text{M}^{-1}\text{cm}^{-1}$) 2.8 photons were absorbed on average per FAD chromophore. The number of absorbed photons in the front and the rear of the crystals (Grünbein et al. 2020) do not deviate considerably from the average (Figure 2.2.10) because of the large penetration depth of 400 nm light into the FAP crystals used (1/e penetration depth at 400 nm is 47 μm , see Figure 2.2.10). Excitation-power dependent transient absorption spectroscopy carried out on CvFAP in solution at the pump-power density (10 GW/cm^2) of the TR-SFX experiment (see supplementary Figure S28 in Appendix 6.1) showed that multi-photon processes had decayed by the first TR-SFX time point (20 ps).

TR-SFX data collection and online monitoring

SFX data were collected (LT59, 22, 24 and 25 Nov 2018) in the microfocus chamber of CXI with the LCLS producing X-ray pulses (nominal photon energy 9.5 keV, pulse length 23 fs) at a repetition rate of 120 Hz. The X-ray beam was focused to 1 $\mu\text{m} \times 1 \mu\text{m}$ (FWHM), the nominal pulse energy at the sample position was ~ 1.3 mJ, taking into account a beamline transmission of $> 60\%$. Data were acquired with the CSPAD detector (Blaj et al. 2015)

operating in a dual-gain mode. During data collection, the hutch lights were switched off. On-line monitoring of the diffraction data, such as estimation of the hit rate, the fraction of multiple hits and of the pixel saturation and diffraction resolution, was carried out using the CFEL-ASG Software Suite (CASS) (Foucar et al. 2012)). TR-SFX data were recorded according to a 400-nm pump (see above) – X-ray probe scheme, with pump-probe delays of 20 ps, 900 ps, 300 ns and 2 μ s. Two dark images without laser excitation and 15 light images with laser excitation were collected in a pseudo-randomly interleaved fashion.

SFX data processing

On-line and off-line hit finding and dark vs. light image-sorting (without and with pump-laser excitation, respectively) was performed using NanoPeakCell (Coquelle et al. 2015)). Hit-finding parameters were adjusted after visual inspection of the first diffraction patterns using the NanoPeakCell graphical interface. A total of 8,141,555 images were collected for all five datasets (dark, light_20ps, light_900ps, light_300ns, light_2 μ s), 1,001,248 of which were identified as hits, corresponding to an overall hit-rate of 12.3%.

CrystFEL v.0.8.0 (White 2019) was used for detector geometry optimization, indexing (*Xgandalf* (Gevorkov et al. 2019)), integration (*rings-grad* method) and merging with the Monte Carlo (MC) algorithm *process_hkl*. MC averaging included the scaling option. The sample-to-detector distance was refined iteratively until the unit cell parameters displayed a Gaussian distribution (Nass et al. 2016). The overall indexing rate (indexed images / hits) was about 25%. A resolution cutoff of 2.0 \AA was chosen based on acentric moments of the E distribution except for the light_2 μ s dataset which was cut at 2.2 \AA resolution. The space group is *P2*₁, with two molecules (A, B) in the asymmetric unit. SFX data processing statistics are shown in (Table 2.2.1).

In view of the large number of images used in the data sets, the high values of R_{split} indicate an underlying problem. We explored different space groups but the problem remained, even when a lower symmetry was used, suggesting inherent disorder in the data as the fundamental issue. There are several possible types of disorder that could affect the SFX data. These include inherent variability in the microcrystals, which we cannot exclude at this time, as well as some particular complications arising from the cell parameters of our FAP microcrystals: $a = 61.4 \text{ \AA}$, $b = 60.0 \text{ \AA}$, $c = 182.9 \text{ \AA}$ and $\alpha = 90^\circ$, $\beta = 90.6^\circ$, $\gamma = 90^\circ$. Thus, not only are the cell parameters close to orthorhombic, but also $a \approx b \approx \frac{1}{3}c$. This results in an indexing

ambiguity, as it is possible for an indexing algorithm to confuse the three axes. In addition, there is the possibility of actual pseudomerohedral twinning in the crystals. All of these possible complications would result in a high R_{split} and noisy maps. At present, none of our attempts at resolving this static disorder (whether real or apparent) by reindexing of individual images based on their correlation with the rest of the data set, twin refinement, or the screening of various indexing schemes at the data processing stage, have resulted in a satisfactory solution.

SFX dark structure solution and refinement

The microcrystals used for SFX are of another crystal form than those used for the conventional crystallography experiments; specifically, their space group is $P2_1$ with two molecules in the asymmetric unit as opposed to $I222$ with a single molecule in the asymmetric unit for most of the synchrotron structures (the R451K mutant crystallized in $P2_12_12_1$ (one molecule in the asymmetric unit) with very similar unit cell parameters as the $P2_1$ SFX crystal form). The dark structure corresponding to the data set without laser excitation was phased by molecular replacement with *Phaser* (McCoy et al. 2007) using as a search model the synchrotron ‘100 K dark’ structure of FAP described in this study devoid of all cofactors and water molecules and with atomic B-factors reset to 30 Å². This resulted in an unambiguous solution with two molecules in the asymmetric unit and an excellent electron density map showing clear density for the FAD cofactor as well as the fatty acid molecules. Structure refinement was performed using *Refmac5* (Murshudov et al. 2011) and included positional and isotropic individual B-factor refinement in reciprocal space (25-2 Å resolution range) with local NCS restraints. Model building and real space refinement were performed using *Coot* (Emsley and Cowtan 2004). In the initial model, the isoalloxazine ring of the oxidized FAD cofactor was constrained to be planar. $mF_{\text{obs}} - DF_{\text{calc}}$ peaks clearly indicated a significant deviation from planarity (Figure 2.2.3). Therefore, once refinement of the protein moiety, waters and substrate molecules was completed, the restraints of the isoalloxazine ring were relaxed by increasing the estimated standard deviation of the isoalloxazine torsion angles in the .cif file. In the final model (PDB accession code 6ZH7), the isoalloxazine ring of the FAD cofactor is clearly bent (C4-N5-N10-C9 dihedral angle (butterfly bending angle), deviating from planarity by 14.3° in molecule A and by 11.7° in molecule B; Figure 2.2.4, Figure 2.2.3B and D). Figures were made with *PyMOL* (Schrödinger and DeLano 2020). SFX data-structure refinement statistics are shown in Table 2.2.1.

Calculation of difference Fourier maps between SFX data sets with and without laser excitation

To assess structural changes induced by illumination, q-weighted (Ursby and Bourgeois 1997) difference Fourier electron density maps ($F_{\text{obs}}^{\text{light}_{20\text{ps}}} - F_{\text{obs}}^{\text{dark}}$, $F_{\text{obs}}^{\text{light}_{900\text{ps}}} - F_{\text{obs}}^{\text{dark}}$, $F_{\text{obs}}^{\text{light}_{300\text{ns}}} - F_{\text{obs}}^{\text{dark}}$, $F_{\text{obs}}^{\text{light}_{2\mu\text{s}}} - F_{\text{obs}}^{\text{dark}}$) were calculated in CNS (Brünger et al. 1998) using scripts published in Wickstrand et al. (Wickstrand et al. 2015) and the SFX dark-state structure for phasing. The maps are shown in Figure 2.2.11 for each of the two FAP molecules present in the asymmetric unit (A and B). As described in the main text, the calculated q-weighted difference electron density maps show a different extent of decarboxylation of the fatty acid at the various time delays, as well as various positive and negative peaks throughout the active site and beyond. The maps contain some differences between the two molecules in the asymmetric unit, suggesting either differences in the structural change upon illumination or simply the maps' noise level. We therefore also averaged the maps using a procedure based on local averaging (Nass et al. 2020). This resulted in the maps shown in Figure 2.2.6.

Time-resolved fluorescence spectroscopy of CvFAP crystals

Even though most crystalline proteins are biologically active, their reaction kinetics often differ from the solution state (Mozzarelli and Rossi 1996; Woodhouse et al. 2020a). In preparation for TR-SFX experiments, we assessed the kinetics of FAP in the crystalline and solution state by carrying out fluorescence-decay measurements. For solution experiments, the 6 mg mL⁻¹ FAP solution was diluted to 0.375 mg mL⁻¹ in buffer (50 mM Tris pH 8.5, 100 mM NaCl). Experiments on crystalline FAP were carried out on a suspension of microcrystals (1% (v/v); each about 10 × 2 – 5 × 2 – 5 μm³ in size) in 19% (w/v) PEG 4000, 100 mM Na citrate pH 5.5, 10 mM spermidine. Single photon counting fluorescence experiments were performed using an excitation pulse (400 nm) delivered by doubling (harmonic generator, SHG, APE) a femtosecond Ti:sapphire laser (800 nm, Coherent Chameleon Ultra II, 80 MHz, 180 fs) coupled to a pulse picker (APE, 4 MHz). Emission decays were measured using an FT200 Picoquant spectrometer and analyzed by the *FluoFit* software. By using a low excitation power (100 nW), a small excitation beam size (100 μm) and a large volume (2 mL) of sample that was constantly stirred, fluorescence spectra could be acquired for about 3 min without notable chromophore bleaching (as assessed by a UV-Vis absorption spectrum). The measured emission decay of ¹FAD* at 560 nm (fig. S15) was fitted by a weighted-sum of

three exponentials. For FAP in solution, the retrieved time constants corresponding to three different FAD populations were 318 ps (± 5 ps), 980 ps (± 30 ps) and 3.9 ns (± 40 ps) with contributions of 76%, 16% and 8%, respectively. The first population corresponds to FAD undergoing efficient fET, the second to a population undergoing less efficient fET or being photobleached, and the last to a non-reactive population. For the crystal suspension, similar time constants were retrieved (320 ps, 1.45 ns, 4.8 ns) but with different contributions (62%, 14%, 24%), leading to an overall fluorescence decay that is slower in crystals than in solution (see supplementary Figure S15 in Appendix 6.1). To assess whether the decrease in the population undergoing efficient fET in the crystal suspension (62%) compared to solution (72%) is due to the difference in pH (5.5 in crystals versus 8.5 in solution), the experiment was repeated on a FAP solution (0.375 mg mL^{-1} protein concentration) in the crystal buffer (19% (w/v) PEG 4000, 100 mM Na citrate pH 5.5, 10 mM spermidine). The contribution of the population with a fluorescence decay of 322 ps was 75%, indicating that it is the crystal packing and not the pH value that decreases the efficiency of fET in the microcrystal suspension from 72% to 62%. Most importantly, however, we conclude that fET proceeds on the same timescale in crystals (320 ps) as in solution (318 ps at pH 8.5, 322 ps at pH 5.5).

2.2.5 Figures and Tables

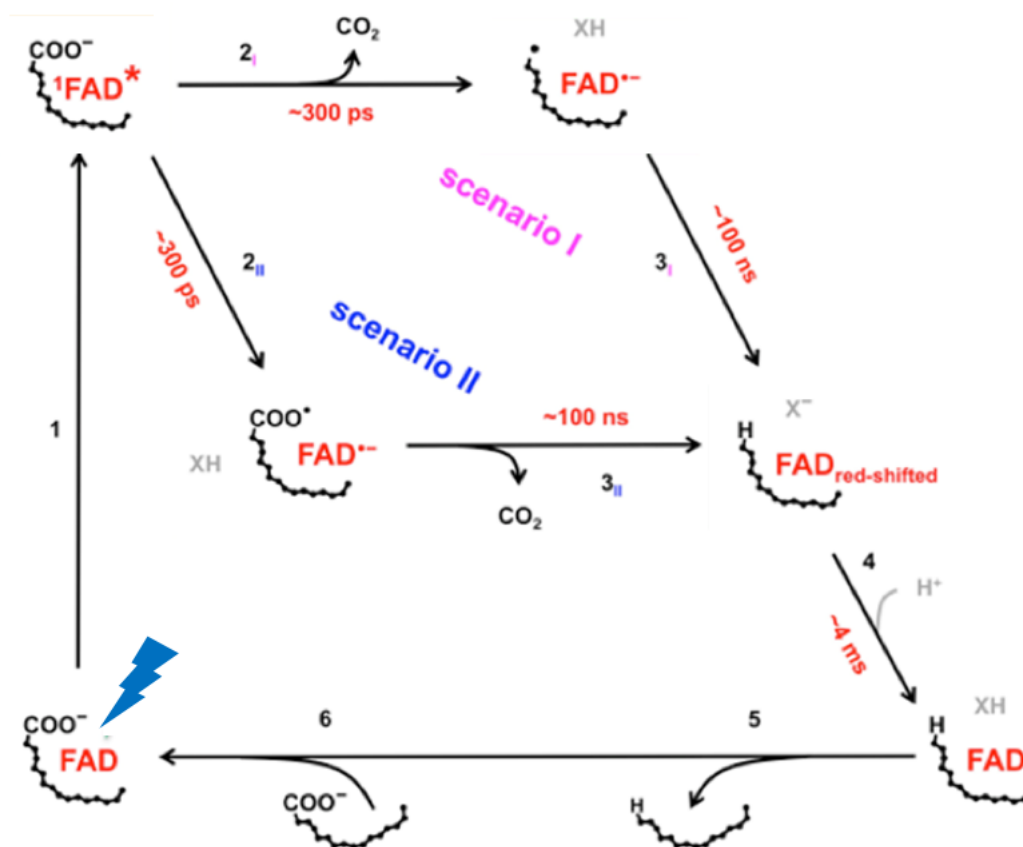


Figure 2.2.1: Suggested model of the CvFAP photocycle (Sorigué et al. 2017)

This figure shows the two possible scenarios that are possible based on (Sorigué et al. 2017). Scenario I: the decarboxylation of the fatty acid is concomitant with forward electron transfer (fET) from the fatty acid to the photoexcited FAD^* within 300 ps. Scenario II: decarboxylation occurs concomitantly with back electron transfer (bET) from $\text{FAD}^{\bullet-}$ to the substrate radical within 100 ns. Figure adapted from (Sorigué et al. 2017).

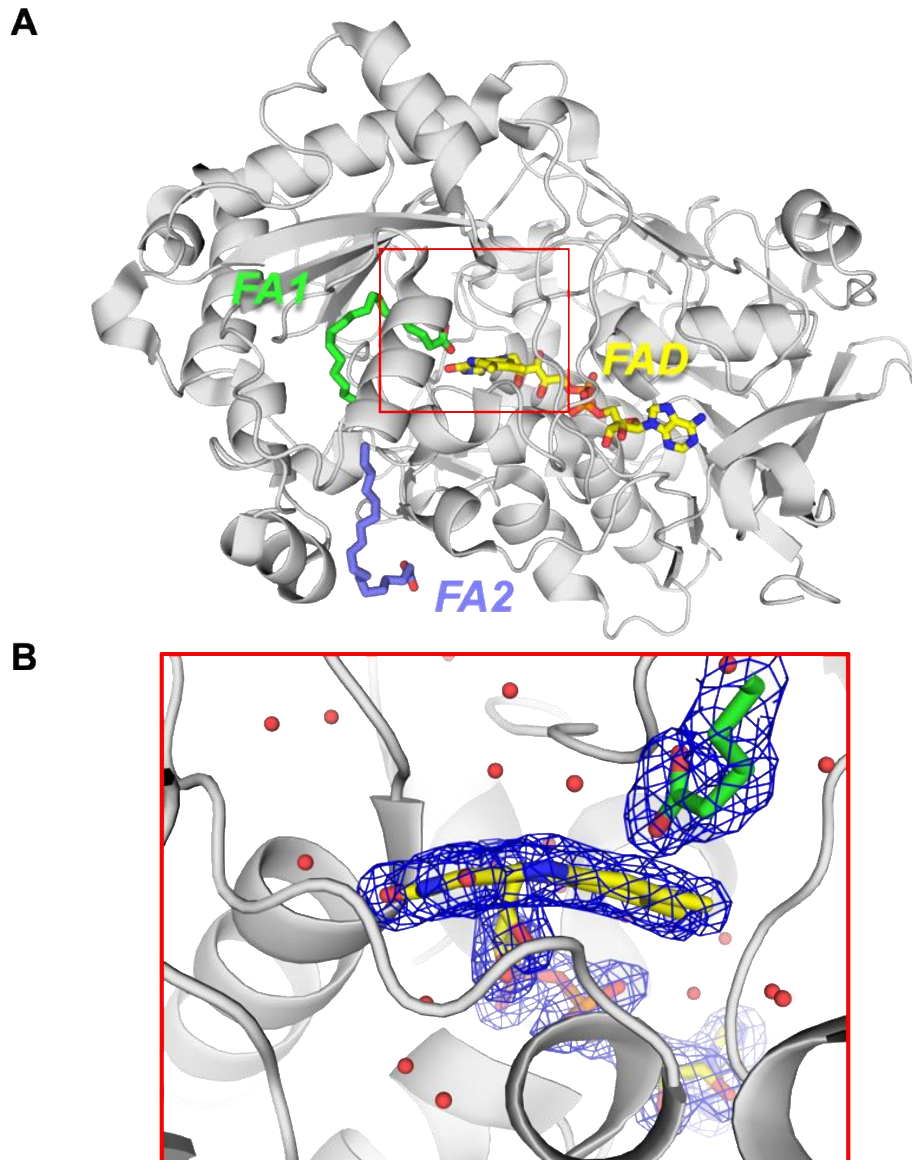


Figure 2.2.2: High-resolution crystal structure of CvFAP

(A) Cryo-MX structure of CvFAP solved at 1.8 Å resolution, including the FAD co-factor (in yellow) and two C18 fatty acids (FA1 and FA2 in green and purple, respectively) (PDB ID: 6YRU). The protein moiety is shown in grey. The active side is delimited by a red rectangle. (B) Zoom in the active site. FA1 faces the bent FAD co-factor. $2F_{obs}-F_{calc}$ map of FAD and FA1 is shown in blue. Dihedral angle C4-N5-N10-C9 of the isoalloxazine ring of the FAD deviates by 17.4° from planarity. Cryo-MX structure of CvFAP was solved by Dr. Pascal Arnoux. Figure adapted from (Sorigué et al. 2021).

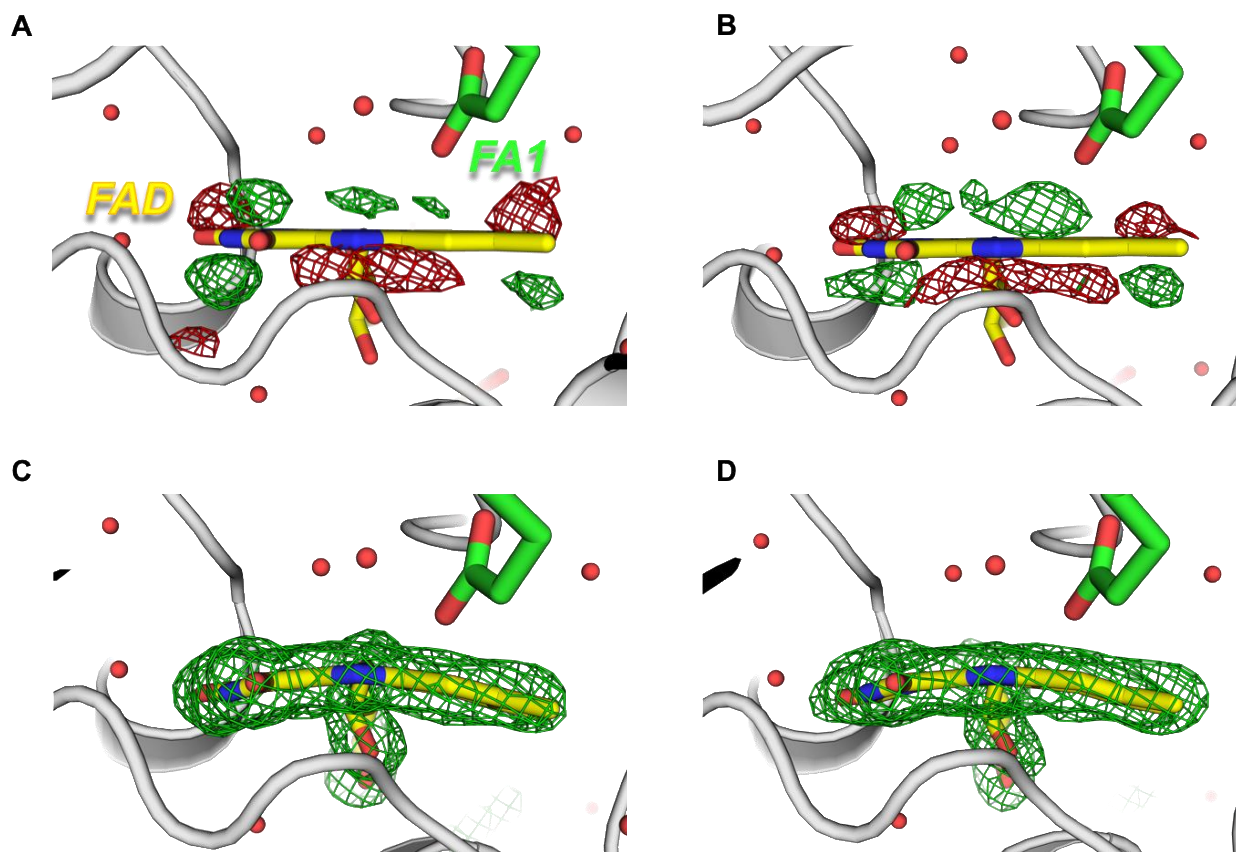


Figure 2.2.3: Residual $mF_{obs} - DF_{calc}$ peaks indicate isoalloxazine rings of the FAD co-factor are not planar in the SFX dark-state structure

When the isoalloxazine ring of the FAD cofactor (yellow stick model) are restrained to be planar in the SFX structure ((A) molecule A, (B) molecule B), peaks in the $mF_{obs} - DF_{calc}$ map ($+3\sigma$ and -3σ in green and red, respectively) indicate bending. The fatty acid is shown in green, the protein moiety in grey. The $mF_{obs} - DF_{calc}$ omit map (3σ , green) indicates bending of the isoalloxazine ring of the FAD cofactor (yellow stick model) in molecules A (C) and B (D). The bending angle is 14.3° and 11.7° in molecule A and B, respectively. The fatty acid is shown in green, the protein moiety in grey. Figure adapted from (Sorigué et al. 2021).

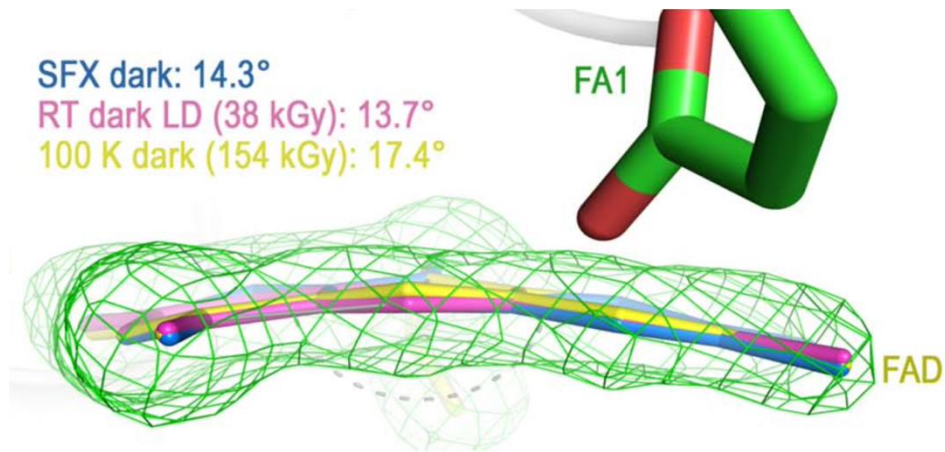


Figure 2.2.4: Bending angle of the isoalloxazine ring of the FAD in the X-ray crystallographic structures

Superposition of the FAD isoalloxazine rings from the SFX dark structure (blue; molecule A; PDB ID: 6ZH7) and the synchrotron structures (pink: RT dark low-dose; PDB ID: 6YRX and yellow: 100 K dark; PDB ID: 6YRU). The SFX $F_{obs} - F_{calc}$ omit map at 3σ (green) is overlaid, and the FAD bending angles are indicated. Figure adapted from (Sorigué et al. 2021).

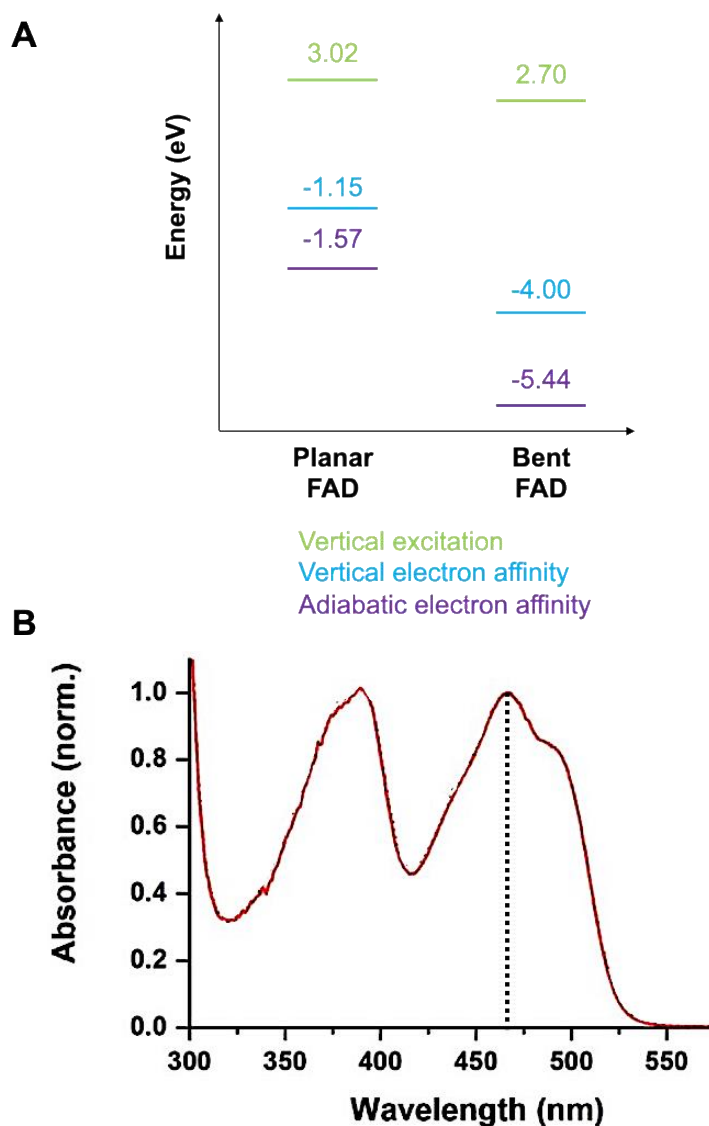


Figure 2.2.5: Flavin butterfly bending energies (A) and UV/Vis absorption spectrum of CvFAP (B)

(A) Flavin bending decreases the vertical excitation, vertical electron affinity, and the adiabatic electron affinity favoring fET. Hence, flavin bending (along with intermolecular interactions) red-shifts the absorbance of the oxidized flavin (B) and facilitates fET. The maximum absorption of CvFAP is 467 nm (compared to the typical values 445 - 450 nm for other flavoproteins and free FAD). The energies compared in this panel are listed in Table S9 in Appendix 6.1 from the work of Dr. Tatjana Domratcheva (Sorigué et al. 2021).

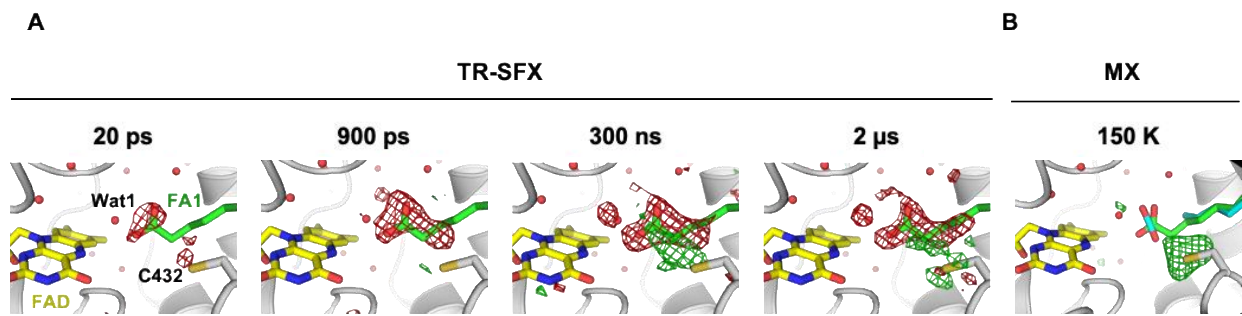


Figure 2.2.6: Time-dependent changes in the CvFAP active site

(A) Locally averaged q -weighted difference Fourier maps calculated between the SFX light and dark datasets ($F_{obs}^{light-\Delta t} - F_{obs}^{dark}$; with $\Delta t = 20$ ps, 900 ps, 300 ns, 2 μ s). The 2.2-Å resolution maps are shown at $+4 \sigma$ (green) and -4σ (red). The SFX dark-state model of molecule B is overlaid, with FAD in yellow, fatty acid in green, and the protein in gray. The q -weighted difference maps for molecules A and B, i.e., without local averaging, are shown in supplementary figure S31 in Appendix 6.1. (B) $F_{obs} - F_{calc}$ electron density (contoured at 3.5σ) of Figure 3E in Appendix 6.1, shown in a different orientation, which features unmodeled positive electron density next to C432 that is reminiscent of a bicarbonate (see Figure 4D and supplementary Figure S14 in Appendix 6.1), in a location similar to where positive difference density is present in the time-resolved maps at 300 ns and 2 μ s. Figure adapted from (Sorigué et al. 2021).

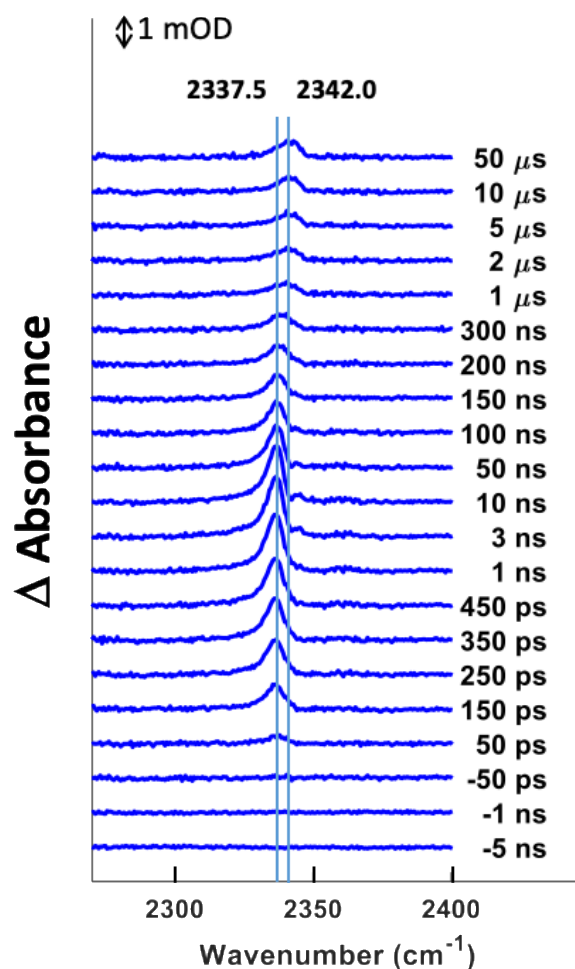


Figure 2.2.7: Time-resolved infrared spectroscopy of CvFAP

Transient infrared spectra in the CO_2 spectral region on the ps- μs time scale. The vertical lines are guides for the eye and correspond to the maximum of released CO_2 in the protein and to the known maximum for CO_2 in aqueous solution, 2342 cm^{-1} (Jones and McLaren 1958). The upper traces correspond to independent steady-state 298 K light-induced FTIR difference spectra with ^{12}C -palmitate and $1\text{-}^{13}\text{C}$ -palmitate substrates (blue trace and red trace, respectively). Time-resolved infrared spectroscopy of CvFAP was performed by Dr. Marten Vos and his colleagues. Figure adapted from (Sorigué et al. 2021).

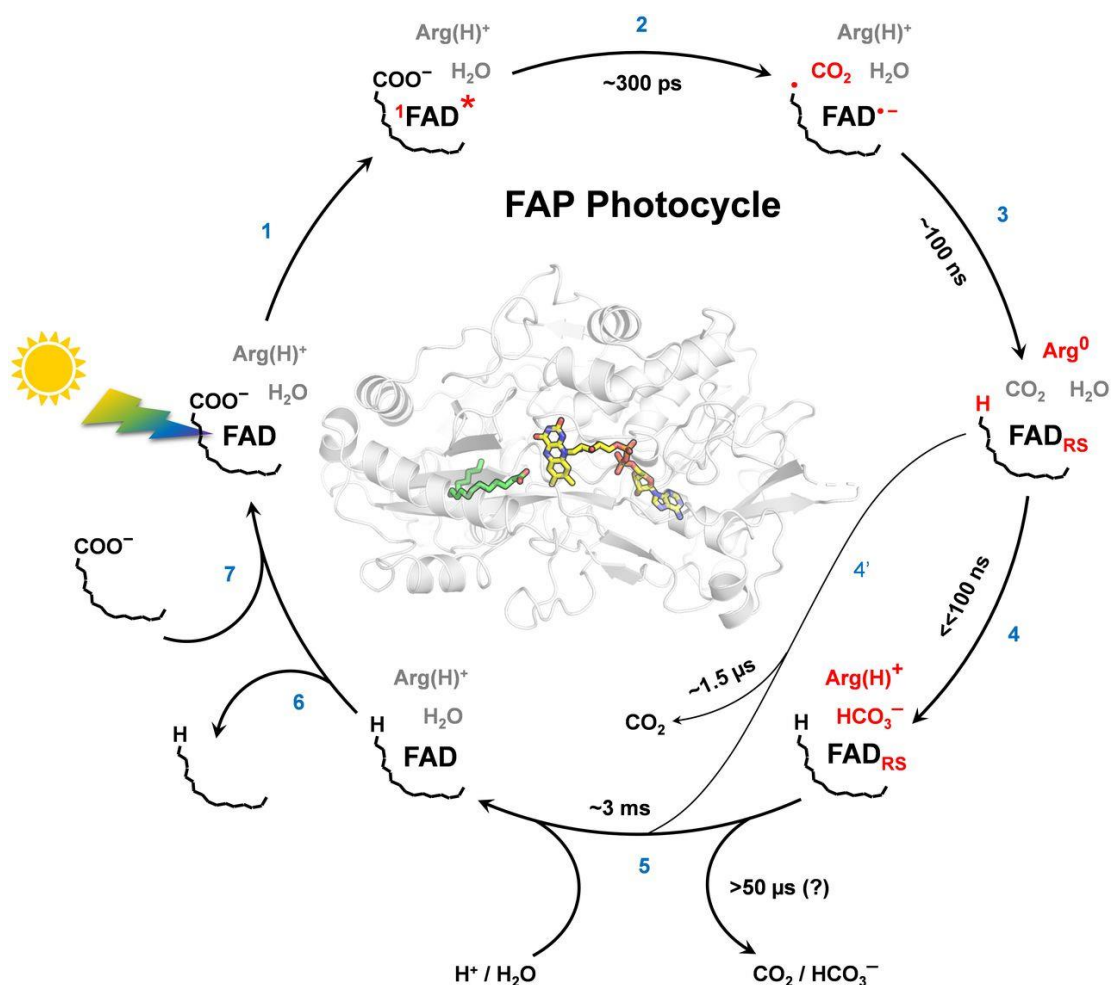


Figure 2.2.8: Suggested CvFAP photocycle

Excitation of the FAD co-factor upon light absorption (1). Forward electron transfer from fatty acid to FAD* leads to decarboxylation of the substrate and the formation of a alkyl radical at a time constant of ~ 300 ps (2). Back electron transfer from FAD \bullet^- to the alkyl radical at a time constant of ~ 100 ns. Formation of red-shifted FAD. Arg451 is the final proton donor to the alkyl radical. Alkane (first product) and CO₂ are formed (3). At a later time scale, 75% of the CO₂ is transformed to HCO₃⁻ (4) while the other 25% of the CO₂ is not transformed to HCO₃⁻ and migrates away from the active site (4'). At millisecond timescale, red-shifted FAD disappears. CO₂ migrates away from the active site (5). Hydrocarbon product is released (6). The new substrate binds the active site (7). Changes after individual steps are marked in red; time constants are for RT. Figure adapted from (Sorigué et al. 2021).

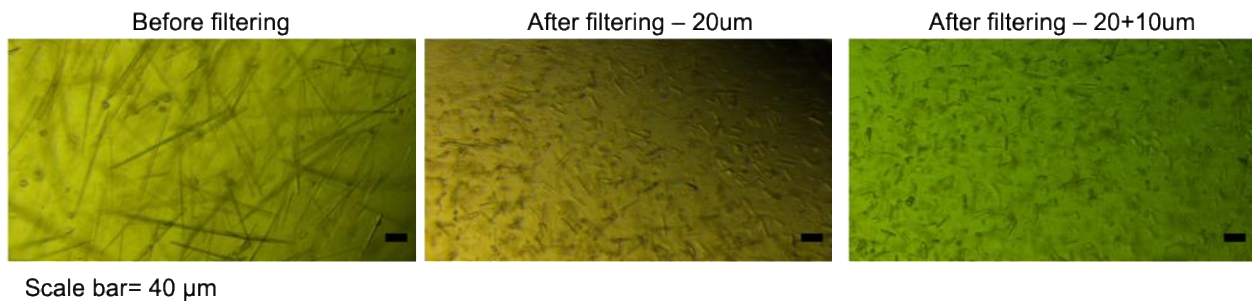


Figure 2.2.9: Filtering effect on FAP microcrystal size.

Before filtering, the crystal size was about $100 - 200 \times 2 - 5 \times 2 - 5 \mu\text{m}^3$ (left). After flowing them through a $20 \mu\text{m}$ (middle) and then a $10 \mu\text{m}$ filter, the size was $10 \times 2 - 5 \times 2 - 5 \mu\text{m}^3$ (right). The scale bar corresponds to $40 \mu\text{m}$. Figure adapted from (Sorigué et al. 2021).

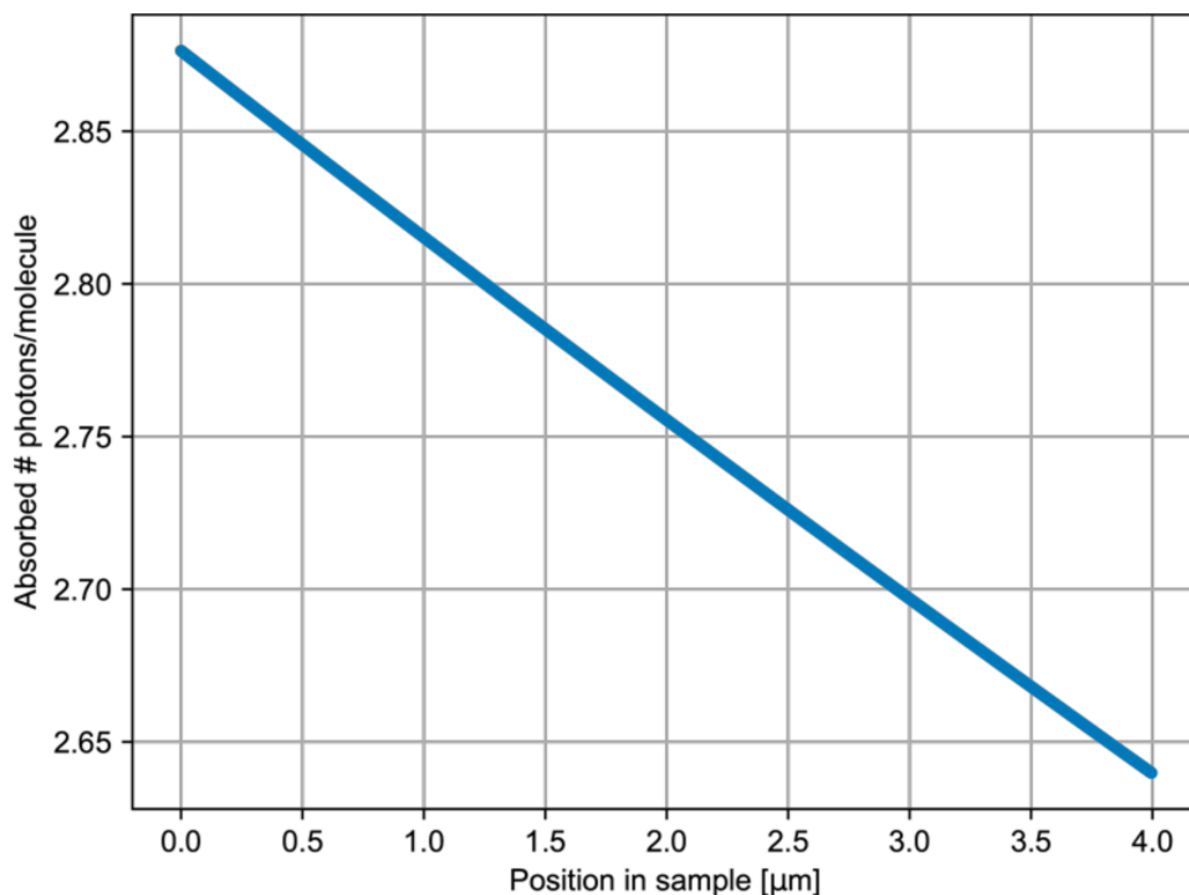


Figure 2.2.10: Depth-dependent photon absorption regimes inside FAP crystals

Depth-dependent photon absorption ($9250 \text{ M}^{-1}\text{cm}^{-1}$ at 400 nm) regime in a $4\text{-}\mu\text{m}$ FAP crystal (FAD concentration 10.3 mM) with pump-laser illumination (4 ps pulse length, $11 \mu\text{J}$ pulse energy, $155 \mu\text{m}$ (FWHM) spot size). The $1/e$ penetration depth is $47 \mu\text{m}$. Figure adapted from (Sorigué et al. 2021).

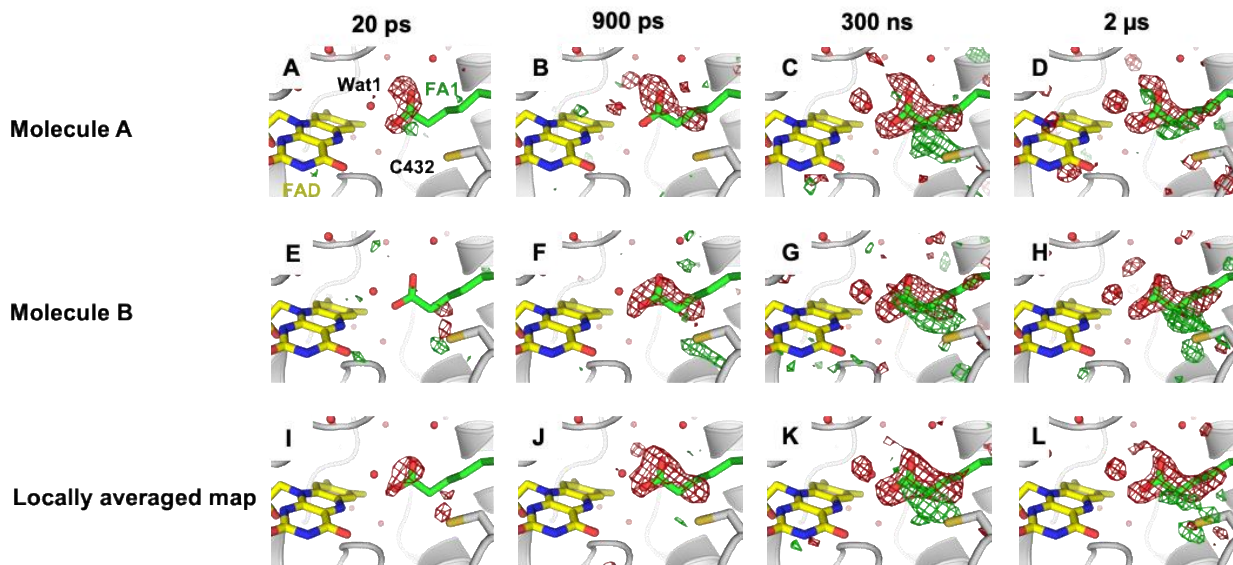


Figure 2.2.11: Time-dependent changes in the CvFAP active site by TR-SFX

Q-weighted difference Fourier electron density maps calculated between the SFX light and dark datasets ($F_{obs}^{light_Δt} - F_{obs}^{dark}$; with $light_Δt=20ps$ (A, E, I), $900ps$ (B, F, J), $300ns$ (C, G, K), $2μs$ (D, H, L)) at 2.2 \AA resolution. Maps corresponding to molecules A (A-D) and B (E-H) are shown at $+3.5 \sigma$ (green) and -3.5σ (red) and locally NCS-averaged maps (I-L) at $+4 \sigma$ (green) and -4σ (red). The SFX dark-state model (FAD in yellow, fatty acid in green, protein moiety in light grey) of molecule A is overlaid in panels A-D and of molecule B in panels E-L. The maps were calculated from 68,421 dark images and 88,919, 50,214, 44,868 and 18,600 light images for $\Delta t = 20 ps$, $900 ps$ and $300 ns$ and $2 \mu s$, respectively. Panels I-L are identical to those in Figure 2.3.6. Figure adapted from (Sorigué et al. 2021).

Table 2.2.1: SFX data processing and refinement statistics

Dataset	dark	light_20ps	light_900ps	light_300ns	light_2 μ s
PDB ID code	6ZH7				
Pump-laser excitation (400 nm)	no	yes	yes	yes	yes
Nominal pump-probe delay	n/a	20 ps	900 ps	300 ns	2 μ s
Space group	$P2_1$	$P2_1$	$P2_1$	$P2_1$	$P2_1$
Unit cell parameters					
a (Å)	61.4 \pm 0.1	61.4 \pm 0.1	61.4 \pm 0.1	61.4 \pm 0.1	61.4 \pm 0.1
b (Å)	60.0 \pm 0.1	60.0 \pm 0.1	60.0 \pm 0.1	60.0 \pm 0.1	60.0 \pm 0.1
c (Å)	182.9 \pm 0.3	182.9 \pm 0.3	182.9 \pm 0.3	182.9 \pm 0.3	182.9 \pm 0.3
β (°)	90.6	90.6	90.6	90.6	90.6
Collected frames	2,579,455	1,625,450	1,728,093	1,298,912	909,645
Hits	264,812	290,962	227,517	151,599	66,358
Indexed images	68,421	88,919	50,214	44,868	18,600
Resolution (Å)	25–2.00 (2.05–2.00)	25–2.00 (2.05–2.00)	25–2.00 (2.05–2.00)	25–2.00 (2.05–2.00)	25–2.20 (2.25–2.20)
Observations	33,069,955 (1,438,474)	42,928,992 (1,869,092)	25,083,092 (1,091,803)	20,934,706 (907,081)	8,076,033 (383,644)
Unique reflections	93,061 (6,086)	93,060 (6,086)	93,064 (6,086)	93,055 (6,086)	70,385 (4,671)
$R_{\text{split}}^{\#}$ (%)	15.1 (68.5)	13.4 (61.3)	18.0 (80.0)	19.4 (84.5)	24.9 (67.8)
CC*	0.996 (0.841)	0.996 (0.869)	0.994 (0.797)	0.992 (0.790)	0.983 (0.816)
$I / \sigma(I)$	5.6 (1.7)	6.40 (1.9)	4.8 (1.4)	4.4 (1.3)	3.7 (1.6)
Completeness (%)	100 (100)	100 (100)	100 (100)	100 (100)	100 (100)
Multiplicity	355 (236)	461 (307)	270 (179)	225 (149)	115 (82)
R_{iso}^S (with respect to dark dataset)	n.a	0.157	0.171	0.174	0.202
Refinement statistics					
Refinement strategy	Classical refinement	n.a	n.a	n.a	n.a
Resolution (Å)	25–2.00 (2.05–2.00)				
R_{free}	0.235				
R_{work}	0.196				
Number of protein atoms	8417				
Number of ligand atoms	166				
Number of water atoms	394				
B-factor protein (Å ²)	31				
r.m.s.d. bond lengths (Å)	0.01				
r.m.s.d. angles (°)	1.8				
Ramachandran favored	95.8 %				
Ramachandran allowed	3.7 %				

Ramachandran outliers	0.2 %				
Rotamer outliers	1.6 %				
C-beta outliers	0				
Clashscore	5				

Values in brackets are for the highest resolution shell

$$\# \cdot R_{split} = \frac{1}{\sqrt{2}} \times \frac{\sum_{hkl} |I_{hkl}^{even} - I_{hkl}^{odd}|}{0.5 \times \sum_{hkl} |I_{hkl}^{even} + I_{hkl}^{odd}|}$$

CC*: see (121)

R_{iso}^{\$} was calculated using *Phenix* up to 2.2 Å resolution

2.3 Time-resolved serial femtosecond crystallography on fatty acid photodecarboxylase: lessons learned

Time-resolved serial femtosecond crystallography on fatty acid photodecarboxylase: lessons learned

Kyprianos Hadjidemetriou¹, Nicolas Coquelle², Thomas R.M. Barends³, Elke De Zitter¹, Ilme Schlichting³, Jacques-Philippe Colletier¹, Martin Weik¹

¹Univ. Grenoble Alpes, CEA, CNRS, Institut de Biologie Structurale, 38000 Grenoble, France.

²European Synchrotron Radiation Facility, 38043 Grenoble, France.

³Max-Planck-Institut für medizinische Forschung, Jahnstrasse 29, 69120 Heidelberg, Germany.

Correspondence: weik@ibs.fr; Ilme.Schlichting@mpimf-heidelberg.mpg.de

2.3.1 Synopsis

We describe crystallographic difficulties encountered in the data processing of recently published time-resolved serial femtosecond crystallography data. We explain the origin of these issues, and how they were circumvented or dealt with. We extend the previously published crystallographic analyses by application of extrapolations methods to determine on the structures of intermediate states.

2.3.2 Abstract

Upon absorption of a blue-light photon, fatty acid photodecarboxylase catalyzes the decarboxylation of free fatty acids to form hydrocarbons (*e.g.* alkanes or alkenes). Major components of the catalytic mechanism have recently been elucidated by combining static and time-resolved serial femtosecond crystallography (TR-SFX), time-resolved vibrational and

electronic spectroscopies, quantum chemical calculations and site-directed mutagenesis (Sorigué *et al.*, 2021). The TR-SFX experiments, carried out at four different ps – μ s pump-probe delays, yielded input for the calculation of Fourier difference maps that demonstrated light-induced decarboxylation. Here, we highlight some of the difficulties encountered during the experiment as well as data processing, in particular regarding space group assignment, describe a pump-laser power titration and extend data analysis by structure factor extrapolation of the TR-SFX data. Structure refinement against extrapolated structure factors reveals a reorientation of the generated hydrocarbon and the formation of a photoproduct close to C432 and R451. Identification of its chemical nature, CO₂ or bicarbonate, was not possible because of limited data quality that we assign to specificities of the crystalline system. Further TR-SFX experiments on a different crystal form are required to identify photoproducts and their movements during the catalytic cycle.

2.3.3 Introduction

Time-resolved serial femtosecond crystallography (SFX) (Boutet *et al.*, 2012) at X-ray free electron lasers (XFEL) presents a powerful means to study structural changes in crystalline biological macromolecules following reaction triggering (Colletier *et al.*, 2018, Branden & Neutze, 2021). Because their activity can conveniently be triggered with light pulses, mostly photo-sensitive proteins have been studied by time-resolved SFX (TR-SFX) so far (Domratcheva & Schlichting, 2018, Poddar *et al.*, 2021), including myoglobin (Barends *et al.*, 2015), photoactive yellow protein (Pande *et al.*, 2016), photosystem II (Suga *et al.*, 2019, Kern *et al.*, 2018), various rhodopsins (Nango *et al.*, 2016, Nass Kovacs *et al.*, 2019, Skopintsev *et al.*, 2020, Oda *et al.*, 2021, Yun *et al.*, 2021, Mous *et al.*, 2022), phytochromes (Claesson *et al.*, 2020), a photosynthetic reaction center (Dods *et al.*, 2021), photoswitchable fluorescent proteins (Coquelle *et al.*, 2018), cytochrome c oxidase (Shimada *et al.*, 2017), photolyase (Maestre-Reyna *et al.*, 2022), as well as P450nor (Tosha *et al.*, 2017, Nomura *et al.*, 2021), using a caged substrate. Most recently, TR-SFX has complemented other experimental and computational approaches to study the catalytic mechanism of fatty acid photodecarboxylase (Sorigue *et al.*, 2021).

Fatty acid photodecarboxylase (FAP), together with protochlorophyllide oxidoreductase (Gabruk & Mysliwa-Kurdziel, 2015) and DNA photolyases (Sancar, 2016), is part of the rare class of photoenzymes that require light to initiate each catalytic event. Absorption of a blue-light photon by the flavin adenine dinucleotide (FAD) cofactor within FAP triggers decarboxylation of the fatty acid substrate which leads to the formation of a hydrocarbon molecule and CO₂ (Sorigue *et al.*, 2017). The recently published high-resolution (1.8 Å) structure of FAP, determined from cryo-crystallographic synchrotron data (see Figure 1 from (Sorigue *et al.*, 2021)) combined with UV-VIS absorbance spectra, revealed a bent oxidized FAD in the dark state. A radiation damage-free dark-state SFX structure (Figure 2.3.1) confirmed the bent nature of the FAD as an unusual feature of the enzyme rather than being the result of X-ray irradiation (Sorigue *et al.*, 2021). In this study, also mechanistic insight into photocatalysis of FAP was obtained, by combining experimental and computational approaches. Forward electron transfer from the fatty-acid substrate to the photoexcited FAD occurs in 300 ps and is accompanied by concomitant decarboxylation of the latter as shown by time-resolved visible and infrared (IR) absorption spectroscopies, respectively. Back electron transfer from the FAD•⁻ radical to the alkyl radical occurs in 100 ns, concomitant with transformation of the generated CO₂ into another molecule - possibly bicarbonate as suggested by FTIR. Fourier difference maps $F_{obs}^{light} - F_{obs}^{dark}$ calculated from TR-SFX data at pump-probe delays of 20 ps, 900 ps, 300 ns and 2 μs indicated that decarboxylation had occurred by the 900 ps time point, in line with the rate determined by TR IR spectroscopy. Intermediate-state structures, however, were not presented in that study.

Here, we summarize the data processing challenges encountered during the TR-SFX data analysis of Sorigué *et al* 2021 and their possible origins. We present additional TR-SFX data collected at a pump-probe delay of 900 ps at three different pump-laser power densities that explain why the particular pump-laser power density has been chosen for the TR-SFX experiment reported by Sorigué *et al* 2021. Furthermore, structure factor extrapolation was carried out for the four time points and controls that assess the quality of the resulting electron density maps. Intermediate-state structures were then refined against extrapolated structure factors for the four time points. At 300 ns, the structure displays repositioning of the hydrocarbon product with respect to the substrate. Different models were tested with the aim to identify the compound that might explain difference density seen at 300 ns in the active site.

2.3.4 Materials and Methods

Brief summary of TR-SFX data collection and processing reported earlier (Sorigué et al. 2021)

Needle-shaped microcrystals ($10 \times 4 \times 4 \mu\text{m}^3$) of *Chlorella variabilis* FAP (CvFAP) in 19 % (w/v) PEG 4000, 0.1 M sodium citrate pH 5.5, 10 mM spermidine were injected with a Gas Dynamic Virtual Nozzle (GDVN)(DePonte *et al.*, 2008) into the microfocus chamber of the CXI end station of the Linac Coherent Light Source (LCLS)(Liang *et al.*, 2015) in November 2018 (proposal LT59). Optical pump (400 nm wavelength; circularly polarized; 4 ps (FWHM) pulse length; 11 μJ / pulse; 155 μm (FWHM) focal spot) – X-ray probe (9.5 keV photon energy; 23 fs pulse length; 1 μm (FWHM)) TR-SFX data were collected at 20 ps, 900 ps, 300 ns and 2 μs time delays. CrystFEL v.0.8.0 was used for indexing (*Xgandalf* (Gevorkov *et al.*, 2019)), integration (*rings-grad* option) and merging with the Monte Carlo (MC) algorithm *process_hkl* (with scaling option). The high-resolution cutoff was 2 Å for all data sets, except for the 2 μs light data set that was set at 2.2 Å . The space group is $P2_1$, with two molecules (A, B) in the asymmetric unit and cell parameters of $a = 61.4 \text{ Å}$, $b = 60.0 \text{ Å}$, $c = 182.9 \text{ Å}$ and $\alpha = 90^\circ$, $\beta = 90.6^\circ$, $\gamma = 90^\circ$ (Supplementary Table S2.3.1).

Pump-power titration at 900 ps

At the start of the previously reported TR-SFX LT59 experiment (Sorigué *et al.*, 2021), a limited pump power titration was carried out at a 900 ps pump-probe delay using 7.5 μJ / pulse (nominally 1.9 absorbed photons / FAD when assuming similar absorption cross-sections for the first and subsequently absorbed photon), 3.7 μJ / pulse (nominally 0.9 photons / FAD) and 11 μJ / pulse (nominally 2.8 photons / FAD). The light data collected with pump-laser excitation at 3.7 and 7.5 and 11 μJ / pulse consisted of 18 704, 34 264 and 50 214 indexed images, respectively, when processed in space group $P2_1$ (Supplementary Table S2.3.2). The decision to carry out the subsequent TR-SFX series at 11 μJ / pulse was taken during the LT59 experiment based on q -weighted (Ursby & Bourgeois, 1997) Fourier difference electron density maps $F_{\text{obs}}^{\text{light}_{900\text{ps}_E}} - F_{\text{obs}}^{\text{dark}}$ (Supplementary Figure S2.3.1) using the then only available 18

430 dark images and 15 574, 12 796 and 19 151 light images (at pump energy values E of 3.7, 7.5 and 11 μJ per pulse, respectively) processed in the $P2_12_12_1$ space group (Supplementary Table S2.3.3) we assumed during the early phase of LT59 (see section 3.1 for a detailed discussion of why the space group was initially assumed to be $P2_12_12_1$ and eventually chosen to be $P2_1$). After completion of the LT59 experiment, the same number (18 704) of indexed images were randomly selected from the three light data sets processed in the correct $P2_1$ space group (Supplementary Table S2.3.2) and $F_{\text{obs}}^{\text{light}_{900\text{ps}_E}} - F_{\text{obs}}^{\text{dark}}$ maps (Figure 2.3.2) calculated with the program *Xtrapol8* (De Zitter *et al.*, 2022) using the 68 421 dark images published earlier (Sorigue *et al.*, 2021). Since certain parts of monomers A and B display significant conformational differences (Supplementary Figure S2.3.2) these maps were averaged using a local averaging procedure (Nass *et al.*, 2020).

Calculation of Fourier difference electron-density maps and structure factor extrapolation at four pump-probe delays

q -weighted Fourier difference electron density maps $F_{\text{obs}}^{\Delta t_{\text{light}}} - F_{\text{obs}}^{\text{dark}}$ were calculated with *Xtrapol8*, using the dark-state structure (including the two fatty acid substrates in the active site and at the protein surface) to phase the maps. As expected, these maps (Figure 2.3.3) are similar to the ones published earlier (Sorigué *et al.*, 2021). We also used *Xtrapol8* to determine the occupancy of the light states and to calculate extrapolated structure factor amplitudes (F_{ext}) using the following formula (Duan *et al.*, 2013, Coquelle *et al.*, 2018):

$$F_{\text{ext}}^{\Delta t_{\text{light}}} = \alpha \times \frac{q}{\langle q \rangle} \times (F_{\text{obs}}^{\Delta t_{\text{light}}} - F_{\text{obs}}^{\text{dark}}) + F_{\text{obs}}^{\text{dark}} \quad (\text{eq. 2.3.1})$$

where α denotes the inverse of the occupancy, q and $\langle q \rangle$ are reflection-specific and average q -weights, and $F_{\text{obs}}^{\text{dark}}$ and $F_{\text{obs}}^{\Delta t_{\text{light}}}$ are the observed structure factor amplitudes for the dark state and the photo-triggered state at a given time delay Δt , respectively. The extrapolation procedure can generate negative F_{ext} that are not usable by refinement programs, resulting in reduced completeness (De Zitter *et al.*, 2022). The number of these reflections depends on the value of α and represents 1.58, 3.50, 6.02 and 2.41% of the extrapolated reflections in the data sets at $\Delta t = 20$ ps, 900 ps, 300ns and 2 μs , respectively, at the determined occupancies given

below. To estimate their positive values, we used the *truncate* option in *Xtrapol8*, whereby a French-Wilson based scaling is applied to all reflections (Evans & Murshudov, 2013). Occupancy determination was carried out using the *difference-map* method, which automates the procedure introduced in (Coquelle *et al.*, 2018) whereby the sum of the integrated values of the highest selected peaks in the $mF_{ext}^{\Delta t_light} - DF_{calc}^{dark}$ that are also present in the q -weighted $F_{obs}^{\Delta t_light} - F_{obs}^{dark}$ map is plotted as a function of the occupancy (Supplementary Figure S2.3.3), and the occupancy value at the maximum peak height considered as correct. In the *difference-map* method, the highest peaks are automatically selected using a Z-scoring of 2 on the normal distribution of all difference peaks in the maps, avoiding possible bias that could skew occupancy determination. In the present case, residues used for occupancy determination included Y466 and C432 and were all located around the fatty acid substrate in the active site. The automatically-determined occupancies lie within a range of 25 to 35 %. The maxima were observed at 35, 30, 25 and 35% for the 20 ps, 900 ps, 300 ns and 2 μ s time delays, respectively, with which the most probable sets of extrapolated structure factor amplitudes were calculated.

Difference density maps using the extrapolated structure factors ($mF_{ext}^{\Delta t_light} - DF_{calc}^{dark}$, Figure 2.3.4), were calculated with the dark-state structure (including the two fatty acid substrates) as a phase model. Both $F_{obs}^{\Delta t_light} - F_{obs}^{dark}$ (Figure 2.3.3) and $mF_{ext}^{\Delta t_light} - DF_{calc}^{dark}$ (Figure 2.3.4) maps indicate structural changes that occurred at the time-delay Δt with respect to the dark-state.

Difference refinement using extrapolated structure factors

In order to model structural changes that had occurred at Δt , difference refinement of the Δt_light structures was performed against $F_{ext}^{\Delta t_light}$ using *phenix.refine* (Afonine *et al.*, 2012), a *PHENIX* suite program (Liebschner *et al.*, 2019). The refinement started from the dark model (PDB entry code 6ZH7) from which the two fatty acid substrates were omitted and the atom coordinates randomized with a mean error value of 0.5 Å using *phenix.pdbtools*. Positional and isotropic individual B-factor refinement was carried out in reciprocal space, using `wxc_scale=0.02` and secondary structure restraints as required for maximum likelihood refinement to converge. Simulated annealing was performed during the first cycle of the

refinement using the default parameters of *phenix.refine*. Manual model building and real space refinement were performed using *Coot* (Emsley & Cowtan, 2004).

Particular attention was paid to modeling the FAD cofactor. When its isoalloxazine rings were forced to be planar or omitted from the model at 300 ns, the $mF_{ext}^{\Delta t_{300ns}} - DF_{calc}$ map displayed peaks indicative of FAD bending (Figure 2.3.5). In the final refined light model at 300 ns, the isoalloxazine ring system deviates from planarity by $\sim 10^\circ$ (C4-N5-N10-C9 dihedral angle, Figure 2.3.5B, D). Similarly, deviation from planarity is 11, 9 and 10° in the refined light models at 20 ps, 900 ps and 2 μ s, respectively. The corresponding angle in the SFX dark state structure has been determined to be 14° (Sorigué *et al.*, 2021).

Before modeling the electron density with potential reaction products, the quality of the extrapolated electron density maps was assessed by omitting a well-ordered water molecule (Wat2) and the rigid active-site side chains of R451 and W479 from the model at 300 ns and calculating $2mF_{ext}^{\Delta t_{300ns}} - DF_{calc}$ and $mF_{ext}^{\Delta t_{300ns}} - DF_{calc}$ maps (Supplementary Figure S2.3.4). Since electron density for both side chains and for Wat2 was present, modeling of reaction products was attempted.

At first, the focus was on modeling the alkane product. We outline the approach again using the 300 ns data as an example. $2mF_{ext}^{\Delta t_{300ns}} - DF_{calc}$ and $mF_{ext}^{\Delta t_{300ns}} - DF_{calc}$ maps were calculated either with the dark-state model (PDB entry code 6ZH7, Figure 2.3.4C,G) or with a model from which the substrate had been omitted (Figure 2.3.6A, B, E, F) suggested a C17 hydrocarbon molecule should be modeled (Figure 2.3.6C, D, G, H). Similarly, a C17 hydrocarbon molecule was modeled at the other three time points (Figure 2.3.7; Supplementary Table S2.3.4).

Before and after modeling the hydrocarbon molecule at 300 ns, there is a strong positive feature next to the side chain of C432 in the $mF_{ext}^{\Delta t_{300ns}} - DF_{calc}$ map in both monomers A (Figure 2.3.8A, B) and B (Figure 2.3.8E, F) at a similar position as a positive peak seen in the $F_{obs}^{300ns_light} - F_{obs}^{dark}$ maps (Figure 2.3.3C, G, K). Two different models were assessed to fit this positive peak: a CO₂ and a water molecule, both at 100% occupancy (Figure 2.3.8C, G) or

a HCO_3^- molecule at 100% occupancy (Figure 2.3.8D, H). The correlation between models of monomer A and B (including either CO_2 and a water or HCO_3^-) and the corresponding map was calculated with *phenix.get_cc_mtz_pdb* using scale option and fixing a 3-Å radius around the atoms of the products.

2.3.5 Results and Discussion

Choice of space group, twinning, data quality

Prior to the TR-SFX experiment described here (LCLS, LT59, Nov. 2018), needle-shaped FAP microcrystals were used in a short test run at the LCLS (LR38, Feb. 2018). The space group was found to be $P2_12_12_1$, with unit cell dimensions of 60, 70 and 115 Å for a , b and c , respectively. During the scale-up phase in preparation for LT59, the imidazole/maleate buffer was replaced by sodium citrate, with all other crystallization parameters unchanged. This replacement allowed the needle-shaped crystals to grow thicker. Due to time restrictions, the crystals could not be tested at a synchrotron prior to the experiment LT59, at the beginning of which we thus assumed the space group to be $P2_12_12_1$. We could indeed index the diffraction patterns according to an orthorhombic lattice type, however unit cell dimensions of 61, 60 and 180 Å indicated a change in crystal form. The observation of two populations of α angles, being distributed sharply around 89.3° and 90.5° (Supplementary Figure S2.3.5A), led us to reindex all data according to a monoclinic lattice and merging intensities specifying $P2_1$, using as unit cell parameters 61.4 Å, 60 Å, 182.9 Å for a , b , and c , and 90°, 90.6°, 90° for α , β , and γ , respectively (Supplementary Figure S2.3.5B).

Indexing nonetheless remained ambiguous, as can be judged from the relatively high R_{split} values reported in Sorigué *et al.* for the dark data set (15.1% and 68.5% for the overall R_{split} and the value in the highest resolution shell, Supplementary Table S2.3.1). Indeed, the lattice displayed higher point group symmetry, mmm , than expected for space group $P2_1$ which would be $2/m$. Because $a \sim b \sim c/3$, an indexing ambiguity can arise from swapping, for example, the a

and b axes or cyclic permutation of the axes. However, if that had happened during indexing or by actual twinning, the former would lead to a peak in the 90° section of the self-rotation function and the latter to a peak in the 120° section, neither of which is observed (not shown). Nevertheless, a small fraction of misindexed patterns would not generate a peak in the self-rotation function but still affect intensity statistics. The only remaining possibility for twinning (or misindexing) is a 180° rotation around a or c , possible because β is close to 90° . Due to the crystallographic two-fold axis, a rotation of 180° around a or c are nearly equivalent and would manifest as peaks in the 180° section of the self-rotation function. These are indeed observed and are of approximately the same height as the crystallographic peak (Supplementary Figure S2.3.6; calculated using MOLREP of the CCP4 suite (Winn *et al.*, 2011)), which could indicate ~50% twinning. Based on the L-test (Padilla & Yeates, 2003), however, twinning could be excluded. However, there is also non-crystallographic symmetry (NCS) relating the two monomers A and B in the asymmetric unit of the monoclinic space group, which is a two-fold rotation (almost) perpendicular to the crystallographic two-fold axis, which results in the creation of a third two-fold, perpendicular to the other two. So, the contents of the unit cell have indeed approximate mmm point group symmetry, and even without twinning the strong peaks in the 180° section of the self-rotation function are expected. Accordingly, the $P2_1$ packing is only a minor deviation from the $P2_12_12_1$ packing (Supplementary Figure S2.3.9).

To further investigate whether the symmetry is $P2_1$ or $P2_12_12_1$, we split the dark images into two equal halves that were integrated separately using $P2_1$ space group symmetry and calculated R_{split} , *i.e.* the R-factor between the two sets of intensities derived from the two half data sets corrected for the drop in number of observations caused by dividing the data into halves (White *et al.*, 2012). We then applied the reindexing operator $h,-k,-l$ (one of the symmetry operations of $P2_12_12_1$) to one of the two half data sets and again calculated R_{split} . This procedure, proposed by an anonymous referee, allows the two possible space group choices to be compared on the basis of R_{split} values calculated using the same number of reflections, which would not be the case when comparing R_{split} values obtained from processing all the data in either $P2_1$ or $P2_12_12_1$. In this case, reindexing one of the two half data sets resulted in much higher values of R_{split} , particularly at high resolution (Figure 2.3.9). Thus, any $h,-k,-l$ symmetry in the data is not perfect, and the true space group symmetry of the data is, therefore, most likely $P2_1$.

Alternatively to merging intensities by Monte Carlo (MC) averaging (Sorigué *et al.*, 2021), merging with *partialator* (--custom-split option) was carried out in *CrystFEL* v.0.8.0 which resulted in a decreased R_{split} of the dark data set of 12.1% (15.1 % for MC), but yielded apparently twinned data, as assessed with *phenix.xtrriage* (not shown). Also, up to ~22 % of measured reflections were discarded by *partialator* suggesting that the gain in precision of the data could lead to reduced accuracy in the estimation of structure factor amplitudes. Therefore, we decided to rely on the merged intensities obtained by MC averaging. Nevertheless, we cannot exclude that use of *partialator* yielded data so much better that real twinning could be detected.

After completion of the LT59 beamtime, diffraction data of single FAP crystals were collected at the SLS beamline PXII – X10SA. The space group varied from crystal to crystal between $P2_12_12_1$ and $P2_1$, sometimes even as a function of the data acquisition location on the long needle shaped crystals.

In summary, the relatively large R_{split} values (see Table S2 in (Sorigue *et al.*, 2021), reproduced as Supplementary Table S2.3.1) likely reflect inherent disorder of the data that most likely stems from indexing ambiguities.

Effect of pump laser energy on Fourier difference maps at 900 ps

The appropriate optical pump-laser energy to use in a TR-SFX experiment is currently a much-debated issue. Motivated by the wish to increase light-induced changes in electron density maps, most studies have been carried out so far at pump-laser energies corresponding to significantly more than one nominally absorbed photon per chromophore, carrying the risk of unwanted multiphoton effects contaminating or even dominating the functionally relevant single-photon processes (Grünbein *et al.*, 2020, Miller *et al.*, 2020). Good practice is thus to carry out a spectroscopic pump-laser power titration on protein crystals or solutions to identify the linear excitation regime (see *e.g.* (Hutchison *et al.*, 2016, Nass Kovacs *et al.*, 2019, Sorigué *et al.*, 2021)), ideally followed by a structural power titration to assess if structural changes can be seen in that regime (see *e.g.* (Claesson *et al.*, 2020)).

Our recent TR-SFX study presented structural data at four pump probe delays (20 ps, 900 ps, 300 ns, 2 μ s) photoexcited with 11 μ J/pulse, an energy corresponding to an average of 2.8 nominally absorbed photons per chromophore (Sorigue *et al.*, 2021). Prior to collecting data at the four time points using this laser energy, a limited number of light images was collected at 900 ps with 3.7 and 7.5 μ J/ pulse (0.9 and 1.9 nominally absorbed photons per chromophore per pulse on average, respectively). Fourier difference maps, $F_{\text{obs}}^{\text{light}_{900\text{ps}_E}} - F_{\text{obs}}^{\text{dark}}$, were calculated between the light and dark data merged in $P2_12_12_1$, *i.e.*, in the space group we assumed at the beginning of the LT59 beamtime (Supplementary Figure S2.3.1), based on 18 430 dark images, and 15574, 12796 and 19151 light images at 3.7, 7.5 and 11 μ J/ pulse, respectively. Negative peaks on the fatty acid carboxyl group are present, whose height increases as a function of the laser energy. This increase motivated our choice of collecting the subsequent TR-SFX data at 11 μ J/pulse. A better-informed decision could have been made if we had integrated the negative difference electron around the fatty acid carboxyl group and plotted the values as a function of pump-laser energy to check whether the signal increases linearly with pump energy.

After completion of the LT59 beamtime, $F_{\text{obs}}^{\text{light}_{900\text{ps}_E}} - F_{\text{obs}}^{\text{dark}}$ maps were calculated again, based on data merged in $P2_1$, *i.e.* in the space group we eventually considered more likely than $P2_12_12_1$ (Figure 2.3.2; Supplementary Table S2.3.2). The maps were calculated with 68 421 dark images and with an equal number of 18 704 light images for the three 900 ps light data sets, which corresponds to a subset of the available 7.5 and 11 μ J/ pulse data, respectively. For the three pump energies negative difference density peaks are observed at different atoms of the fatty acid carboxylate for the A-monomer (Figure 2.3.2A-C); for the B-monomer no peaks are observed (Figure 2.3.2E-G). This is not due to lack of photo-cleavage since strong negative peaks are observed in both monomers, covering almost the entire carboxylate when almost three times more light images (*i.e.* 50 214) are used for map calculation at 11 μ J (Figure 2.3.2H). Together this clearly shows that the data derived from the 18 704 images collected for the power titration are not accurate enough to assess the extent of photolysis with any confidence. Many more images should have been collected (for a discussion of the signal-to-noise ratio as a function of indexed images see (Gorel *et al.*, 2021)).

Fourier difference electron maps, calculated between light and dark data sets, mainly show peaks in the active site (see as an example the 300 ns map covering an entire asymmetric unit, Supplementary Figure S2.3.7) and provide clear evidence for substrate decarboxylation (Figure 2.3.5 in (Sorigue *et al.*, 2021)). Here, Fourier difference electron maps with a very similar content were reproduced with the program *Xtrapol8* (Figure 2.3.3). Two observations are noteworthy. First, the apparent extent of decarboxylation seems to be different at 900 ps (Figure 3B, F) and 300 ns (Figure 2.3.3C, G), a surprising observation given that the decarboxylation time constant of 270 ps determined by TR-IR spectroscopy (Sorigue *et al.*, 2021) suggested otherwise. Three possible explanations can be offered: i) spatial overlap between pump and probe laser changed slightly, ii) the apparent difference reflects the noise level of the data, iii) at 900 ps a positive peak due to photodecarboxylated CO₂ compensates part of the negative peak on the carboxyl group. Second, it is striking that peaks, both in terms of height and temporal evolution, behave differently in monomers A and B. Very likely this reflects noise in the data since the photochemical decarboxylation yield is expected to be the same in both monomers, nevertheless differences in protein dynamics may also be possible due to a different packing environment (Supplementary Figure S2.3.8), which would be in line with conformational differences identified at the protein surface (Supplementary Figure S2.3.2).

In order to model structural changes that had occurred at the different time points, structure factor extrapolation has been carried out using *Xtrapol8* (see Methods section and (De Zitter *et al.*, 2022)) that estimates the structure factor amplitudes F_{ext} that would have been measured for each pump-probe dataset if the photo-triggered intermediate had been present in crystals at 100% occupancy (eq. 2.3.1). The occupancy of intermediate states was determined to be between 25 and 35% for the four time delays. Extrapolated electron density maps $2mF_{ext}^{At_light} - DF_{calc}^{dark}$ and $mF_{ext}^{At_light} - DF_{calc}^{dark}$ maps (Figure 2.3.4) point to qualitatively similar structural changes as the Fourier difference electron maps (Figure 2.3.3) for the four time delays. In particular, a negative $mF_{ext}^{At_light} - DF_{calc}^{dark}$ peak on the substrate reflects light-induced decarboxylation and a nearby positive peak indicates reorientation of the formed hydrocarbon chain (Figure 2.3.4). At 300 ns and 2 μ s, a positive $mF_{ext}^{At_light} - DF_{calc}^{dark}$ peak is visible next to the side chain of C432, in line with the reported observations in Fourier difference electron maps (Sorigue *et al.*, 2021).

Before modeling reaction products, the information content of the extrapolated electron density maps was evaluated by calculating omit maps. The 300 ns data serves as an example: the well-ordered water molecule WAT2 and the side chains of the rigid active site residues R451 and W479 were removed from the dark-state structure and the resulting model used to phase electron density maps using extrapolated structure factors (Supplementary Figure S2.3.4). These maps ($2mF_{ext}^{300ns_light} - DF_{calc}$ and $mF_{ext}^{300ns_light} - DF_{calc}$) show clear electron density for the omitted atoms in both monomers, indicating that the extrapolated structure factors contain sufficient information to correctly locate large, rigid side chains and well-ordered water molecules. Further, the conformation of the isoalloxazine ring of the FAD cofactor, bent in the dark-state structure (Sorigue *et al.*, 2021), was assessed at 300 ns by restraining it to be planar. The resulting $2mF_{ext}^{300ns_light} - DF_{calc}$ and $mF_{ext}^{300ns_light} - DF_{calc}$ maps (Figure 2.3.5A, C) indicated cofactor bending, determined to be 10° in the final refined 300 ns light-state structure (Figure 2.3.5B, D).

To identify and locate reaction products, the initial focus was on the hydrocarbon product (C17), as illustrated again by the 300 ns data. First, $2mF_{ext}^{300ns_light} - DF_{calc}$ and $mF_{ext}^{300ns_light} - DF_{calc}$ maps based on a model without fatty acid substrate or hydrocarbon product were calculated (Figure 2.3.6A, B, E, F). They indicate that the hydrocarbon moves towards the side chain of Y466 (Figure 2.3.6A, E) and recoils (Figure 2.3.6B, F) with respect to the fatty acid position, as evident in the final model (Figure 2.3.6C, D, G, H). Recoil of the hydrocarbon product is accompanied by a small rotation in the side chain of Y466 (Figure 2.3.6D, H) as observed earlier in a synchrotron cryo-crystallography structure (Sorigue *et al.*, 2021). A hydrocarbon chain has then been included in the light models at the 20 ps, 900 ps and 2 μ s time points and refined against extrapolated structure factors (Supplementary Table S2.3.2; Figure 2.3.4). At 20 ps, but not at the other time points, the extrapolated electron density maps indicated that a fatty acid substrate rather than a hydrocarbon product needed to be modelled in the active site (Figure 2.3.4), in line with the decarboxylation time constant of 270 ps determined by TR-IR spectroscopy (Sorigue *et al.*, 2021).

No products other than an alkane molecule were modelled in the light structures at 20 ps and 900 ps because no residual peaks in the $mF_{ext}^{At_light} - DF_{calc}^{dark}$ maps (Figure 2.3.4A,B,E,F) were present that would have indicated the necessity of doing so. At 300 ns, however, further modeling was attempted to assess if structure factor extrapolation could help decide between a

bicarbonate and a CO₂, an ambiguity debated in (Sorigue *et al.*, 2021). Indeed, our earlier report suggested, but did not prove, transient formation of a bicarbonate molecule next to C432 after decarboxylation (Sorigue *et al.*, 2021). In an attempt to test this suggestion, we either modeled a CO₂ and a water molecule (Figure 2.3.8C, G) or a bicarbonate molecule (Figure 2.3.8D, H) at 300 ns and refined against extrapolated structure factors. We note that the bicarbonate position in monomer B (Figure 2.3.8H), but not in monomer A (Figure 2.3.8D), is similar to the one suggested based on cryo MX data (Figure 4D in (Sorigue *et al.*, 2021)). Peaks in the residual $mF_{ext}^{300ns_light} - DF_{calc}$ map do not allow one to clearly discriminate between these two models and the $2mF_{ext}^{300ns_light} - DF_{calc}$ maps tend to support both to a similar level (Figure 2.3.7). The R_{work}/R_{free} values for the CO₂/water (model 1) and HCO₃⁻ (model 2) models, which are 34.9/40.8 and 34.4/40.9, respectively, indicate a minor decrease of the R_{free} value by 0.1 for model 1. Real space correlation between map coefficients and CO₂ or HCO₃⁻ of the monomers A and B in the corresponding structures indicates a slightly better correlation for model 2 (CC=0.724 and 0.57 for monomer A and B, respectively) than for model 1 (CC=0.717 and 0.51 for monomer A and B, respectively). Therefore, electron density maps calculated from extrapolated structure factors do not allow one to resolve the product ambiguity at 300 ns. At 2 μs, further product modeling was not attempted because of peaks next to Cys432 being lower (Figure 2.3.3D,H) than at 300 ns (Figure 2.3.3C,G), possibly due to limited data quality at 2 μs (Supplementary Table S2.3.1 and S2.3.4).

2.3.6 Conclusion

We discussed several lessons learnt in the course of the recently reported TR-SFX study on FAP (Sorigue *et al.*, 2021). First, a minor change in the batch crystallization conditions (sodium citrate instead of imidazole/maleate) during the scale-up phase led to an unexpected change in space group and unit cell dimensions of the needled-shaped crystals. Assessing the diffraction of the final crystal batch at a synchrotron source prior to the TR-SFX experiment could have uncovered some of the problematic features of the needle-shaped FAP microcrystals. Indeed, the peculiar unit cell characteristics ($a \sim b \sim c/3$, β close to 90°) and the non-crystallographic symmetry axis being close to a crystallographic axis probably led to indexing ambiguity that could not be solved and that resulted in poor data statistics, such as high R_{split} values. Furthermore, we learnt that the mandatory pump-laser power titration needs to be based on a

large enough number of images to yield high signal/noise in electron density maps for the feature investigated (here decarboxylation) (Gorel *et al.*, 2021) and on more than the three energies used here. If Fourier difference electron density maps with high signal/noise had been available, peaks could have been integrated and plotted as a function of pump-laser energy to be able to choose conditions that are still in the linear excitation regime.

Here, we extended the study (Sorigue *et al.*, 2021) by carrying out refinement of intermediate state structures against extrapolated structure factors at 20 ps, 900 ps, 300 ns and 2 μ s. A particular focus was on the 300-ns light structure that evidences a reorientation of the hydrocarbon product after photodecarboxylation of the fatty acid substrate and displays a FAD co-factor similarly bent as in the dark-state structure. Refinement against extrapolated structure factors at 300 ns did not allow one to distinguish between two possible products located near C432. This will require further TR-SFX studies on FAP with a less problematic crystal form.

2.3.7 Acknowledgements

We thank the anonymous referee who suggested reindexing one of the half data sets to further investigate space group ambiguity. The study was supported by ANR grants to MW (*BioXFEL*, *SNAPsHOTs*) and JPC (*XinVivo*), an MENESR – Univ. Grenoble Alpes fellowship to KH, a travel grant from the CNRS GOtoXFEL program to MW and an ERC Consolidator Grant 724362 (STePLADDER) to TRMB. This work was partially carried out at the platforms of the Grenoble Instruct-ERIC center (IBS and ISBG; UMS 3518 CNRS-CEA-UGA-EMBL) within the Grenoble Partnership for Structural Biology (PSB). Platform access was supported by FRISBI (ANR-10-INBS-05-02) and GRAL, a project of the University Grenoble Alpes graduate school (Ecoles Universitaires de Recherche) CBH-EUR-GS (ANR-17-EURE-0003). The IBS acknowledges integration into the Interdisciplinary Research Institute of Grenoble (IRIG, CEA). We acknowledge support from the Max Planck Society.

2.3.8 Figures

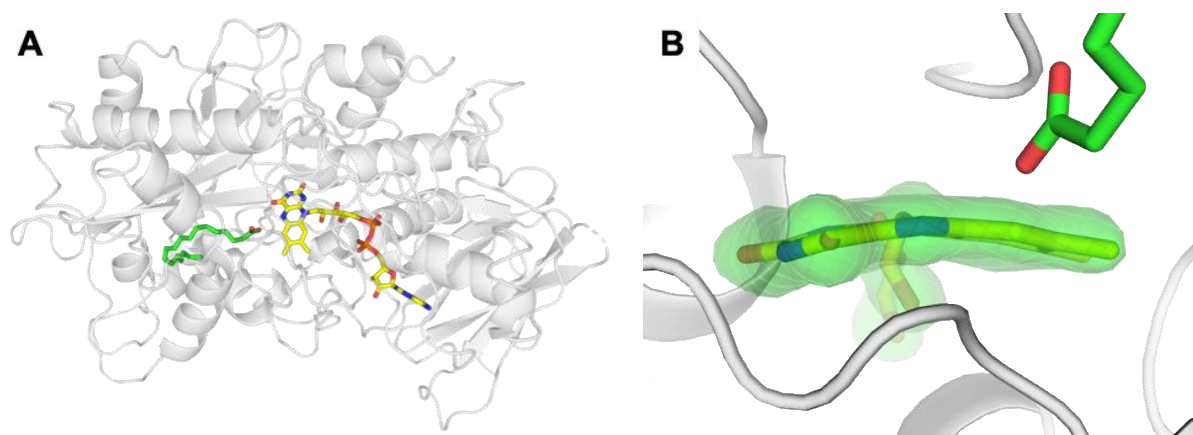


Figure 2.3.1: SFX dark-state crystal structure of CvFAP (PDB entry code 6ZH7)

(A) Structure of CvFAP determined at 2 Å resolution from SFX data at room temperature (Sorigué et al., 2021). (B) FAD is in a bent conformation (C4-N5-N10-C9 dihedral angle is 14°). The $mF_{obs}-DF_{calc}$ omit map at 3 r.m.s.d. (green) is overlaid. FAD and the C18 fatty acid substrate are shown in yellow and green, respectively. The protein of monomer A is shown in grey.

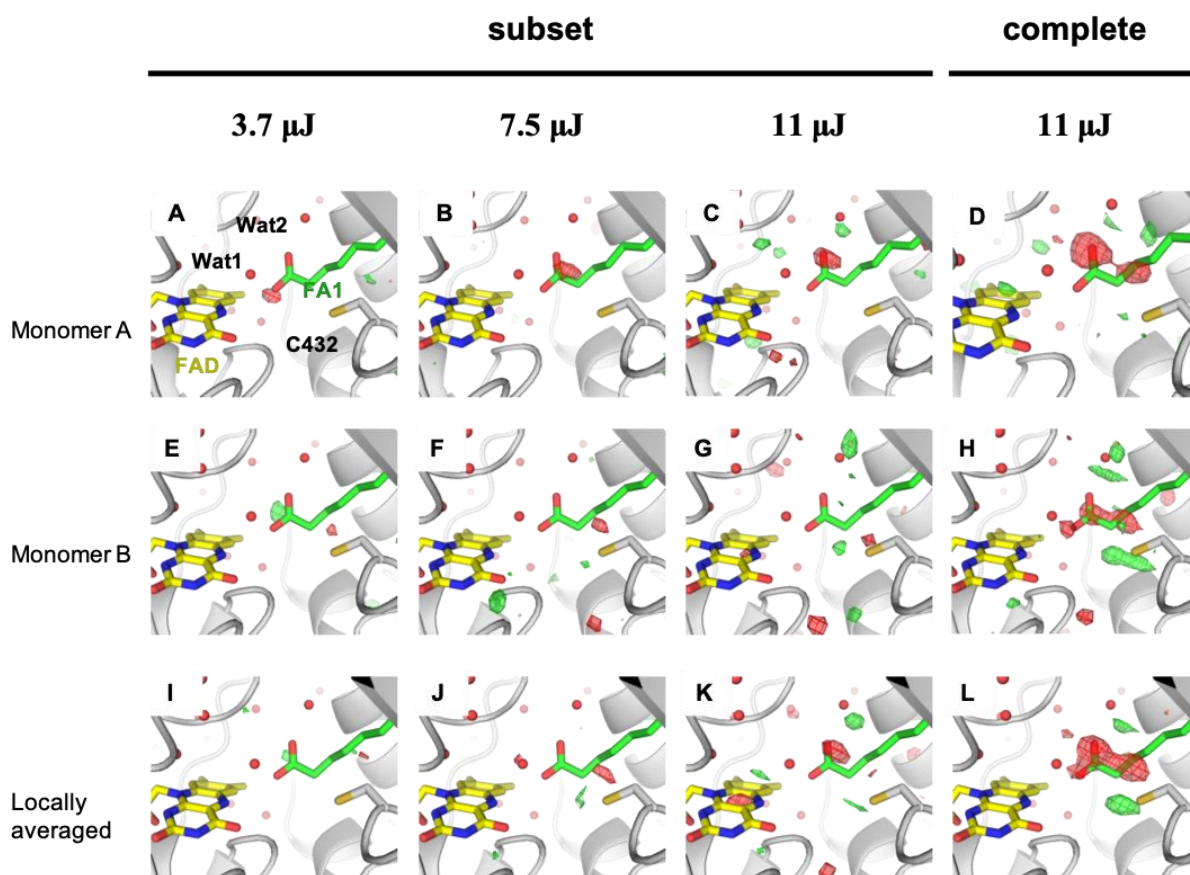


Figure 2.3.2: Fourier difference maps at 900 ps and three different pump-pulse energies using data processed in the $P2_1$ space group

Q -weighted Fourier difference electron density maps calculated between SFX light ($\Delta t = 900$ ps) data sets at different pump-laser energies and the dark data set ($F_{obs}^{light_900ps_E} - F_{obs}^{dark}$, with $E = 3.7 \mu\text{J}$ (A, E, I), $7.5 \mu\text{J}$ (B, F, J), and $11 \mu\text{J}$ (C, D, G, H, K, L) at 2.2 \AA resolution. Maps are contoured at $+3.5 \sigma$ (green) and -3.5σ (red). The SFX dark-state model (PDB entry code 6ZH7) of monomer A is overlaid in panels A-D and of monomer B in panels E-L, with FAD in yellow, the fatty acid substrate in green and the protein moiety in light grey. The maps were calculated with 68 421 dark images, and with 18 704 light images in panels A-C, E-F and I-K (subset) and 50 214 light images in panels D, H and L (complete).

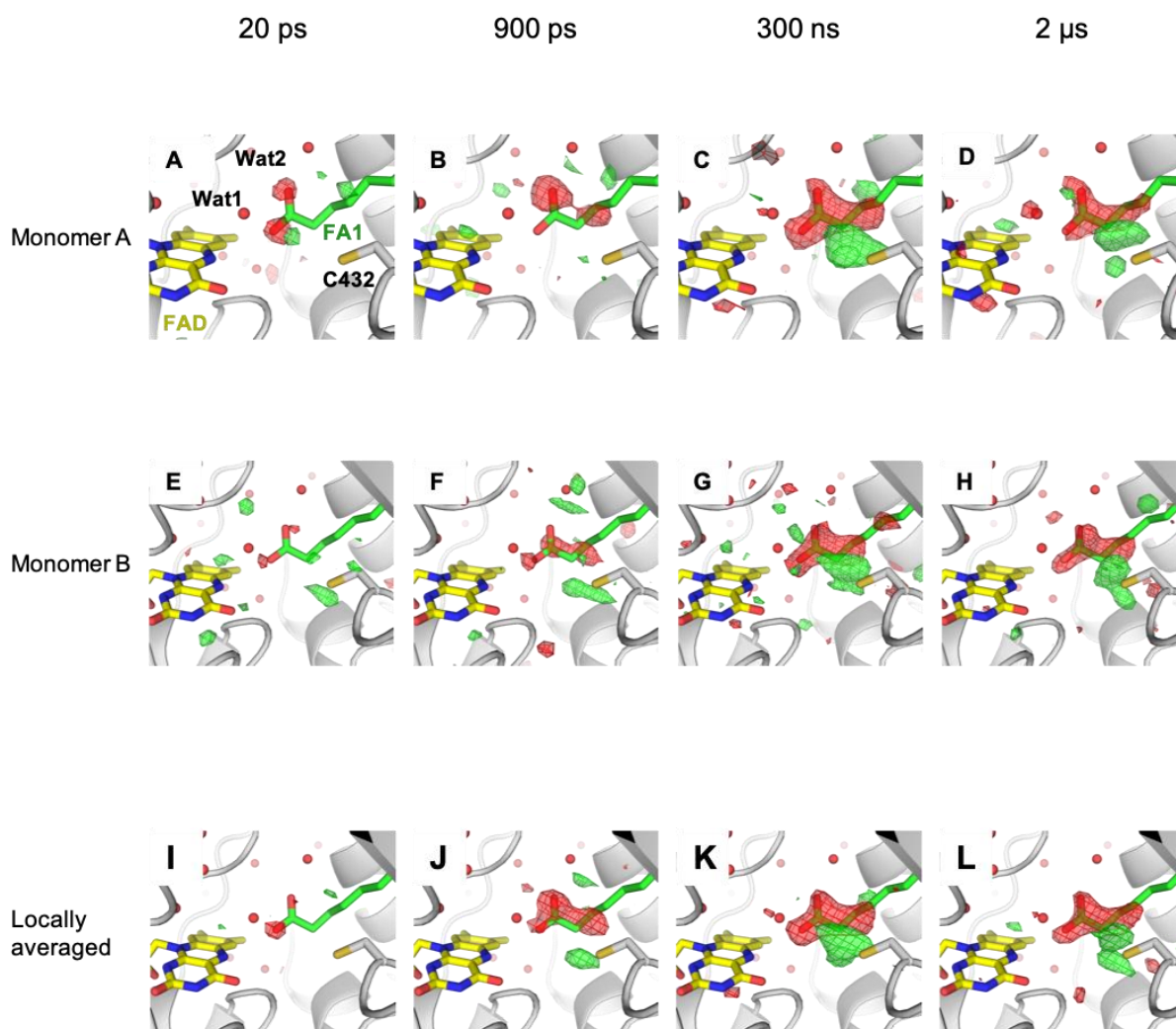


Figure 2.3.3: Fourier difference maps at four different pump-probe time delays

q-weighted Fourier difference electron density maps calculated between the light and dark data sets ($F_{obs}^{\Delta t_light} - F_{obs}^{dark}$); with $\Delta t = 20$ ps (A, E, I), 900 ps (B, F, J), 300 ns (C, G, K) at 2 Å resolution and $\Delta t = 2$ μs (D, H, L) at 2.2 Å resolution. Maps corresponding to monomers A (A-D) and B (E-H) are shown at +3.5 r.m.s.d. (green) and -3.5 r.m.s.d. (red) and locally averaged maps (I-L) are shown at +4.0 r.m.s.d. (green) and -4.0 r.m.s.d. (red).

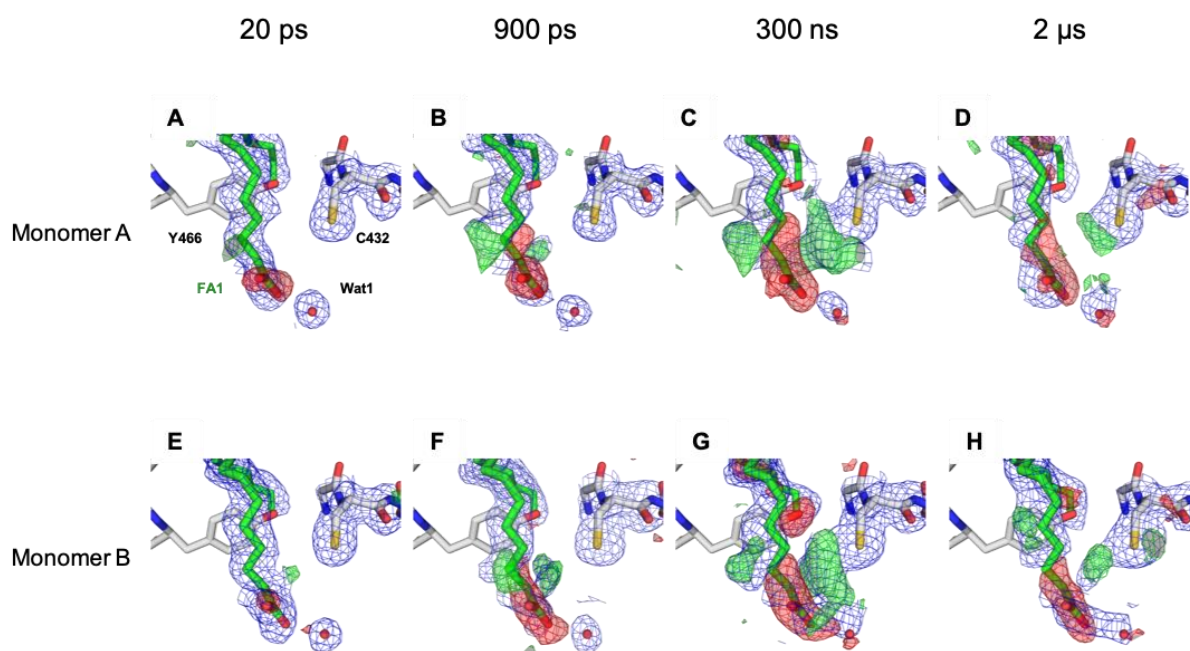


Figure 2.3.4: Extrapolated electron density maps at four different pump-probe time delays calculated using the dark state model

Extrapolated electron density maps $2mF_{ext}^{\Delta t_light} - DF_{calc}^{dark}$; (1 r.m.s.d., blue) and $mF_{ext}^{\Delta t_light} - DF_{calc}^{dark}$ maps (+3 r.m.s.d., green; -3 r.m.s.d., red), calculated between the light and dark data sets, with $\Delta t = 20$ ps (A, E), 900 ps (B, F), 300 ns (C, G) at 2 Å resolution and 2 μs (D, H) at 2.2 Å resolution. Maps are shown around the fatty acid (FA) and C432 of monomer A (A, B, C, D) and monomer B (E, F, G, H) and calculated with the dark structure (including the two fatty acid substrates and Wat1) as a phase model without refinement. The dark state model is represented as sticks, with the carbon atoms of the protein in grey and the fatty acid molecule in light green.

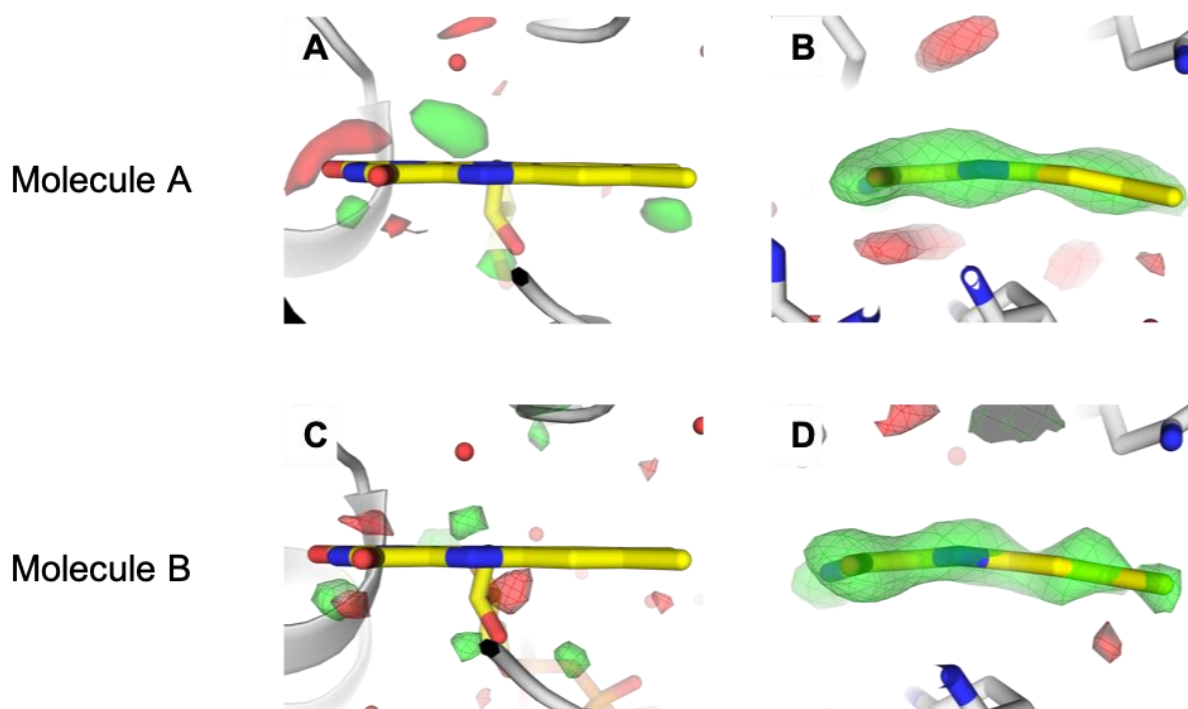


Figure 2.3.5: Conformation of the isoalloxazine ring of the FAD cofactor in the extrapolated structure at 300 ns

Extrapolated electron density map, $mF_{ext}^{\Delta t - 300ns} - DF_{calc}$ maps (+3 r.m.s.d., green; -3 r.m.s.d., red), calculated between the dark and the light data set at 300 ns and phased with a model in which the isoalloxazine rings of the FAD cofactor (yellow) is either restrained to be planar (A, C) or absent (B, D). Superimposed in panels A and C is a model with a planar FAD and in B and D the final refined light model at 300 ns, in which the isoalloxazine bending angle is $\sim 11^\circ$.

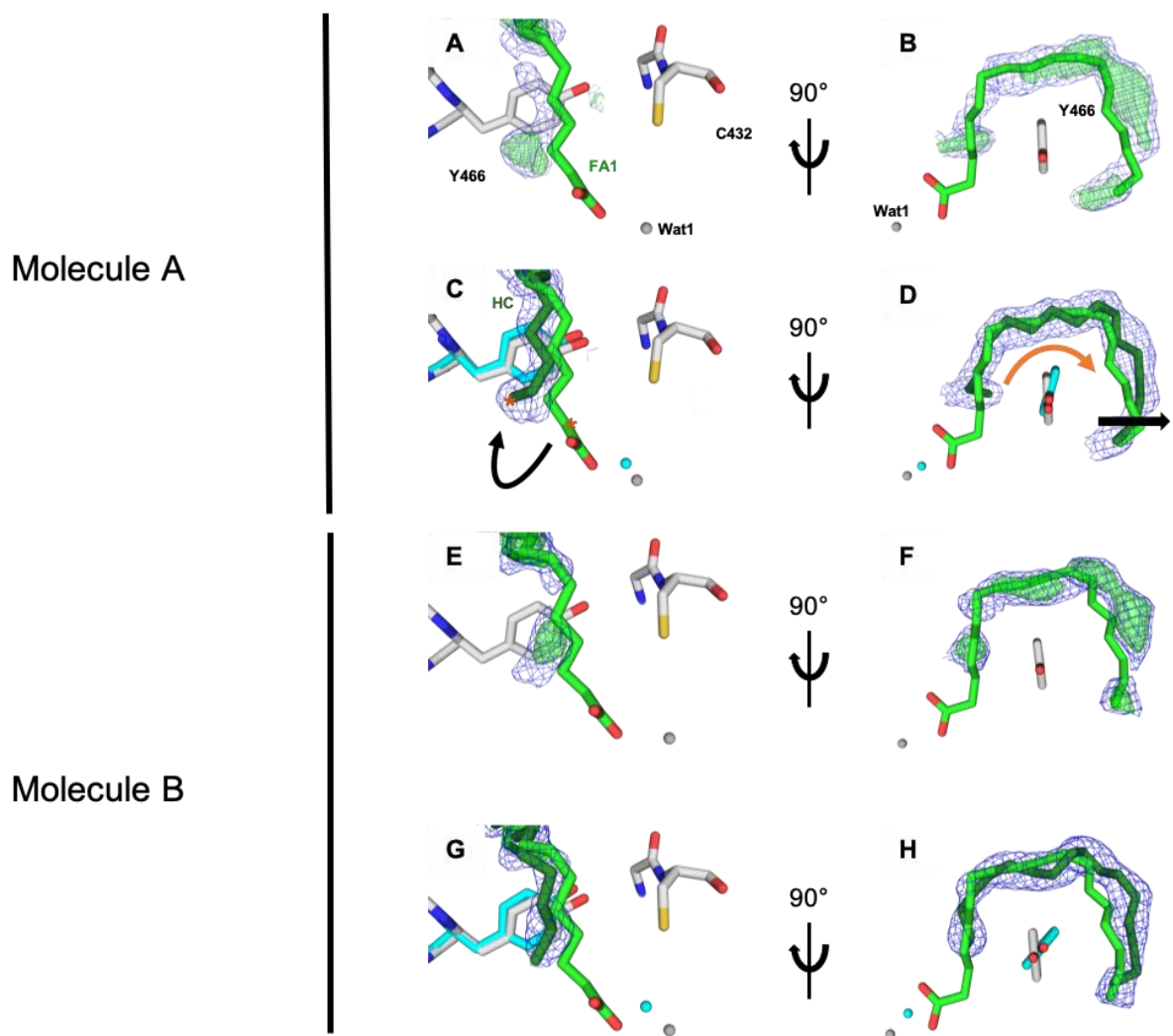


Figure 2.3.6: Hydrocarbon product in the extrapolated structure at 300 ns

(A,B,E,F) q -weighted extrapolated electron density maps, $2mF_{ext}^{\Delta t_{300ns}} - DF_{calc}$ (1 r.m.s.d., blue mesh) and $mF_{ext}^{\Delta t_{300ns}} - DF_{calc}$ (+3 r.m.s.d., green) were calculated with models of monomers A (A,B) and B (E,F) from which the substrate was omitted. (C,D,G,H) Extrapolated electron density maps, $2mF_{ext}^{\Delta t_{300ns}} - DF_{calc}$ (1 r.m.s.d., blue mesh) calculated with models of monomers A (C,D) and B (G,H) without substrate but including a hydrocarbon product (HC; dark green). Dark and 300-ns intermediate state models of monomer A (A,B,C,D) and monomer B (E,F,G,H) are overlaid in grey and cyan, respectively. The fatty acid substrate (FA1) in the dark model is shown in lime green in panels A-H.

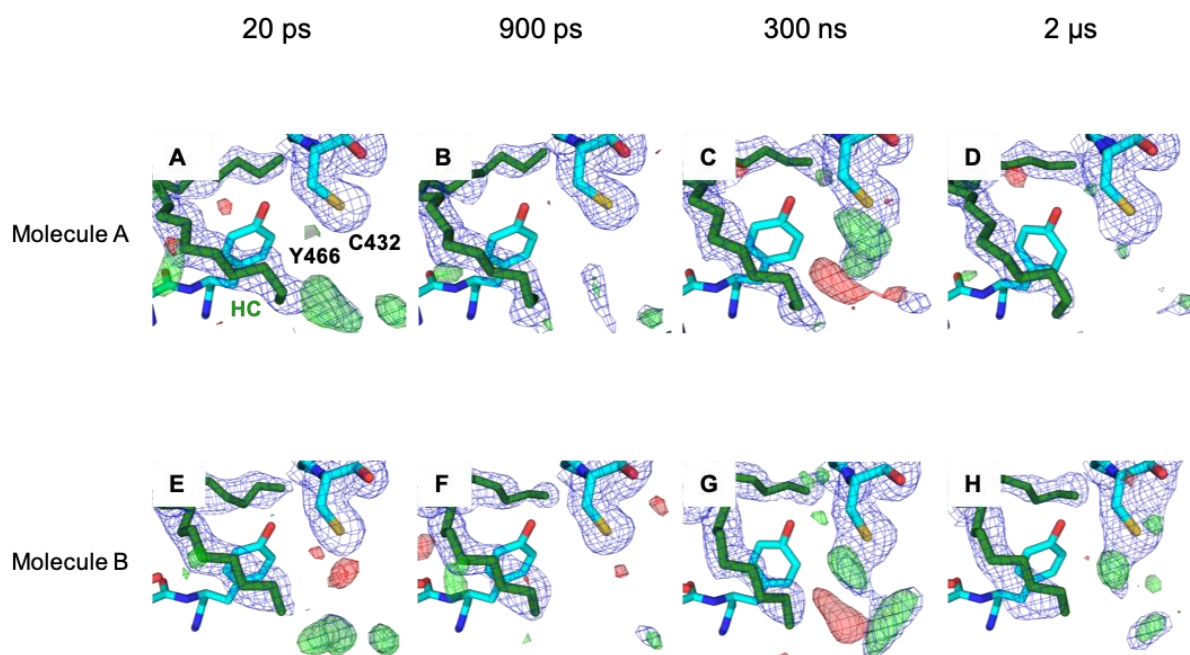


Figure 2.3.7: Extrapolated electron density maps at four different pump-probe time delays calculated using refined models containing a C17 hydrocarbon molecule

Extrapolated electron density maps, $2mF_{ext}^{\Delta t_light} - DF_{calc}^{dark}$ (1 r.m.s.d., blue) and $mF_{ext}^{\Delta t_light} - DF_{calc}^{dark}$ (+3 r.m.s.d., green; -3 r.m.s.d., red), calculated between the light and dark data sets, with $\Delta t = 20$ ps (A, E), 900 ps (B, F), 300 ns (C, G) at 2 Å resolution and 2 μs (D, H) at 2.2 Å resolution. Maps are shown around the fatty acid (FA) and C432 of monomer A (A, B, C, D) and monomer B (E, F, G, H) and calculated with refined models containing a C17 hydrocarbon molecule. The respective refined models are represented as sticks, with the carbon atoms of the protein in cyan and the hydrocarbon in dark green. Note that Wat1 has been excluded from all models.

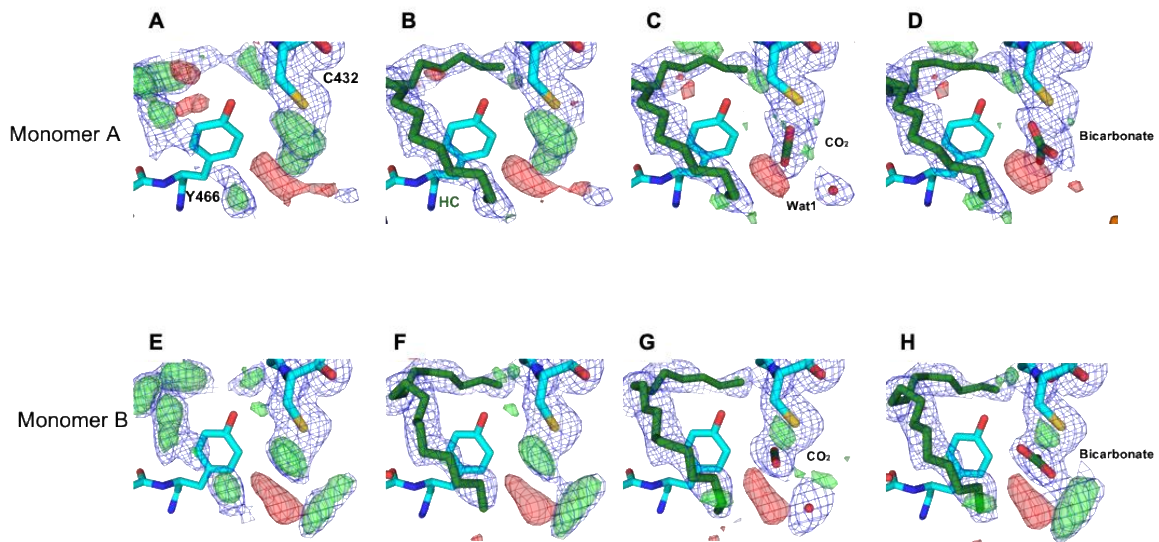


Figure 2.3.8: Attempts to model various molecules next to C432 at 300 ns

Extrapolated electron density maps, $2mF_{ext}^{\Delta t_{300ns}} - DF_{calc}$ (1 r.m.s.d., blue mesh) and $mF_{ext}^{\Delta t_{300ns}} - DF_{calc}$ maps (+3 r.m.s.d., green; -3 r.m.s.d., red), calculated between the dark and the light data set at 300 ns and phased with a model without (A, E) and with (B, F) the hydrocarbon molecule, but without any additional molecule next to C432, or with a CO_2 and water molecule, both at 100% occupancy (C, G), or a HCO_3^- molecule at 100% occupancy (D, H). The corresponding models of monomers A (A, B, C, D) and B (E, F, G, H) are shown. $mF_{ext}^{\Delta t_{300ns}} - DF_{calc}$ map omit maps of the Wat1 are shown in B and F.

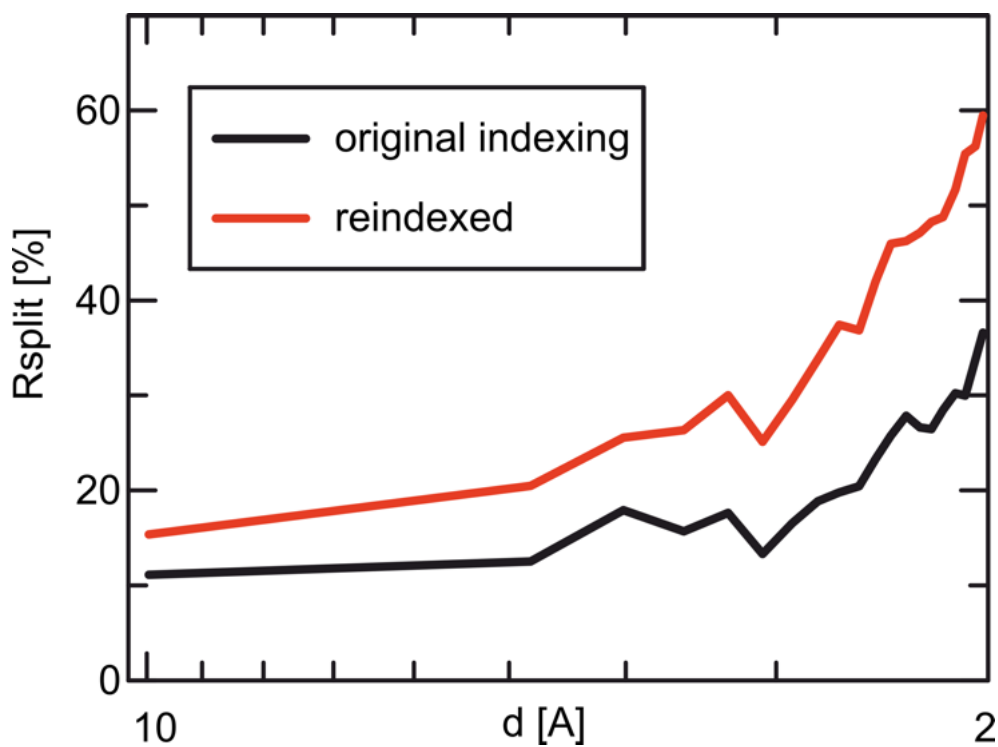


Figure 2.3.9: Comparison of the R-factor intensity distribution between native and reindexing datasets

R_{split} as a function of resolution for the CvFAP dark data, before (black line) and after (red line) reindexing one of the two half-datasets using the operation $h,-k,-l$. Applying this operation, which is a member of the $P2_12_12_1$ space group, results in a noticeable increase in R_{split} suggesting the true symmetry is $P2_1$ rather.

2.3.9 Supporting information

Supplementary Table S2.3.1: Statistics of data processing and of refinement against observed structure factors at 20 ps, 900 ps, 300 ns, 2 μ s as reported in Sorigué et al ((Sorigué et al., 2021))

Dataset	dark	light_20ps	light_900ps	light_300ns	light_2 μ s
PDB ID code	6ZH7				
Pump-laser excitation (400 nm)	no	yes	yes	yes	yes
Pump energy (μ J)	n/a	11	11	11	11
Nominal pump-probe delay	n/a	20 ps	900 ps	300 ns	2 μ s
Space group	$P2_1$	$P2_1$	$P2_1$	$P2_1$	$P2_1$
Unit cell parameters					
a (Å)	61.4 \pm 0.1	61.4 \pm 0.1	61.4 \pm 0.1	61.4 \pm 0.1	61.4 \pm 0.1
b (Å)	60.0 \pm 0.1	60.0 \pm 0.1	60.0 \pm 0.1	60.0 \pm 0.1	60.0 \pm 0.1
c (Å)	182.9 \pm 0.3	182.9 \pm 0.3	182.9 \pm 0.3	182.9 \pm 0.3	182.9 \pm 0.3
β (°)	90.6	90.6	90.6	90.6	90.6
Collected frames	2,579,455	1,625,450	1,728,093	1,298,912	909,645
Hits	264,812	290,962	227,517	151,599	66,358
Indexed images	68,421	88,919	50,214	44,868	18,600
Resolution (Å)	25– 2.00 (2.05 – 2.00)	25– 2.00 (2.05 – 2.00)	25– 2.00 (2.05 – 2.00)	25– 2.00 (2.05 – 2.00)	25– 2.20 (2.25 – 2.20)
Observations	33,069,955 (1,438,474)	42,928,992 (1,869,092)	25,083,092 (1,091,803)	20,934,706 (907,081)	8,076,033 (383,644)
Unique reflections	93,061 (6,086)	93,060 (6,086)	93,064 (6,086)	93,055 (6,086)	70,385 (4,671)
$R_{\text{split}}^{\#}$ (%)	15.1 (68.5)	13.4 (61.3)	18.0 (80.0)	19.4 (84.5)	24.9 (67.8)
CC*	0.996 (0.841)	0.996 (0.869)	0.994 (0.797)	0.992 (0.790)	0.983 (0.816)
$I / \sigma(I)$	5.6 (1.7)	6.40 (1.9)	4.8 (1.4)	4.4 (1.3)	3.7 (1.6)
Completeness (%)	100 (100)	100 (100)	100 (100)	100 (100)	100 (100)

Multiplicity	355 (236)	461 (307)	270 (179)	225 (149)	115 (82)
R _{iso} ^s (with respect to dark dataset)	n.a	0.157	0.171	0.174	0.202
Refinement statistics					
Refinement strategy	Classical refinement	n.a	n.a	n.a	n.a
Resolution (Å)	25– 2.00 (2.05 – 2.00)				
R _{free}	0.235				
R _{work}	0.196				
Number of protein atoms	8417				
Number of ligand atoms	166				
Number of water atoms	394				
B-factor protein (Å ²)	31				
r.m.s.d. bond lengths (Å)	0.01				
r.m.s.d. angles (°)	1.8				
Ramachandran favored	95.8 %				
Ramachandran allowed	3.7 %				
Ramachandran outliers	0.2 %				
Rotamer outliers	1.6 %				
C-beta outliers	0				
Clashscore	5				

Values in brackets are for the highest resolution shell

Supplementary Table S2.3.2: Statistics of pump-power titration SFX data processed in space group $P2_1$

Dataset	Δt_{900} ps	Δt_{900} ps	Δt_{900} ps
Energy (μ J)	3.7	7.5	11
Data collection and processing			
Space group	$P2_1$	$P2_1$	$P2_1$
[§] Unit cell parameters			
a (\AA)	61.4 ± 0.1	61.4 ± 0.1	61.4 ± 0.1
b (\AA)	60.0 ± 0.1	60.0 ± 0.1	60.0 ± 0.1
c (\AA)	182.9 ± 0.3	182.9 ± 0.3	182.9 ± 0.3
β ($^\circ$)	90.6	90.6	90.6
Hits	85,757	141,349	188,288
Indexed image, total	18,704	34,264	50,214
Indexing rate (%)	21.81	24.24	26.67
Indexed images, subset	18,704	18,704	18,704 (*)
Resolution (\AA)	25– 2.20 (2.25 – 2.20)	25– 2.20 (2.25 – 2.20)	25– 2.20 (2.25 – 2.20)
Observations	7,724,496 (365,950)	10,189,805 (490,193)	10,751,282 (515,733)
Unique reflections	70,419 (4,672)	70,420 (4,672)	70,426 (4,672)
# R_{split} (%)	25.7 (73.0)	18.8 (54.5)	18.4 (52.1)
#CC*	0.983 (0.800)	0.991 (0.896)	0.991 (0.897)
# $I / \sigma(I)$	3.6 (1.5)	3.9 (1.7)	3.9 (1.8)
#Completeness (%)	100 (100)	100 (100)	100 (100)
#Multiplicity	109 (78)	145 (105)	153 (110)

(*) statistics refer to the subset of indexed images

(§) all data sets were processed using the same unit cell.

Supplementary Table S2.3.3: Statistics of pump-power titration SFX data processed during the LT59 beamtime in the assumed space group $P2_12_12_1$

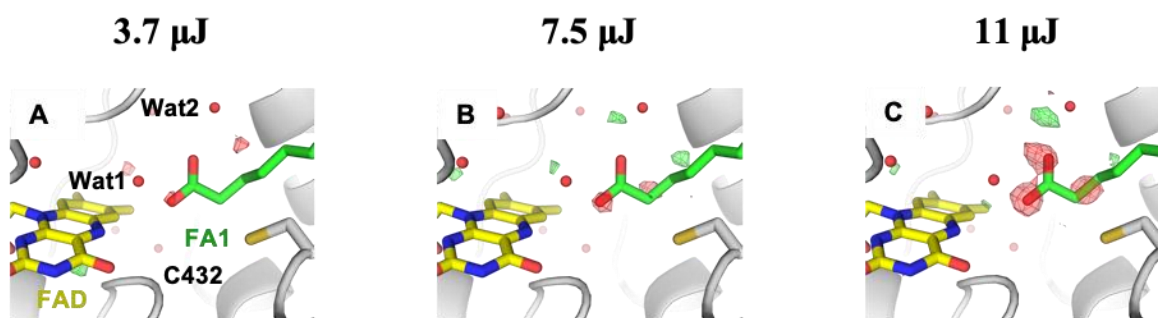
Dataset	Dark	Δt_{900} ps	Δt_{900} ps	Δt_{900} ps
Energy (μJ)	-	3.7	7.5	11
Data collection and processing				
Space group	$P2_12_12_1$	$P2_12_12_1$	$P2_12_12_1$	$P2_12_12_1$
^s Unit cell parameters				
a (\AA)	60.2 ± 0.1	60.2 ± 0.1	60.2 ± 0.1	60.2 ± 0.1
b (\AA)	61.6 ± 0.2	61.6 ± 0.2	61.6 ± 0.2	61.6 ± 0.2
c (\AA)	183.6 ± 0.5	183.6 ± 0.5	183.6 ± 0.5	183.6 ± 0.5
α ($^\circ$)	90	90	90	90
β, γ ($^\circ$)	90	90	90	90
Hits	172,376	135,930	142,757	226,977
Indexed images	18,430	15,574	12,796	19,151
Indexing rate (%)	10.69	11.46	8.96	8.44
Resolution (\AA)	25– 1.80 (1.84 – 1.80)	25– 1.90 (1.95 – 1.90)	25– 1.90 (1.95 – 1.90)	25– 1.90 (1.95 – 1.90)
Observations	9,566,432 (417,017)	6,954,961 (321,119)	6,818,329 (318,313)	10,334,563 (483,927)
Unique reflections	66,176 (4, 349)	56,302 (3,688)	56,301 (3,688)	56,302 (3,688)
Rsplit# (%)	23.6 (113.9)	23.6 (82.4)	27.9 (93.4)	22.4 (71.5)
CC*	0.986 (0.774)	0.984 (0.857)	0.975 (0.850)	0.983 (0.900)
I / σ (I)	4.0 (1.0)	4.1 (1.4)	3.8 (1.2)	4.7 (1.5)
Completeness (%)	100 (100)	100 (100)	100 (100)	100 (100)
Multiplicity	168 (96)	120 (87)	139 (86)	210 (131)
Refinement				
Resolution (\AA)	18 – 1.8 (1.83 – 1.80)			
Number of reflections	63,917 (2,642)			
R _{free}	25.9 (33.0)			
R _{work}	22.2 (31.1)			

Number of protein atoms	4,297			
Number of ligand atoms	80			
Number of water atoms	235			
B-factor protein (\AA^2)	21.96			
r.m.s.d. bond lengths (\AA)	0.006			
r.m.s.d. angles ($^\circ$)	0.813			
Ramachandran favored	96.23			
Ramachandran allowed	3.59			
Ramachandran outliers	0.18			
Rotamer outliers	2.24			
C-beta outliers	0			
Clashscore	2.87			

(^s) All data sets were processed using the same unit cell.

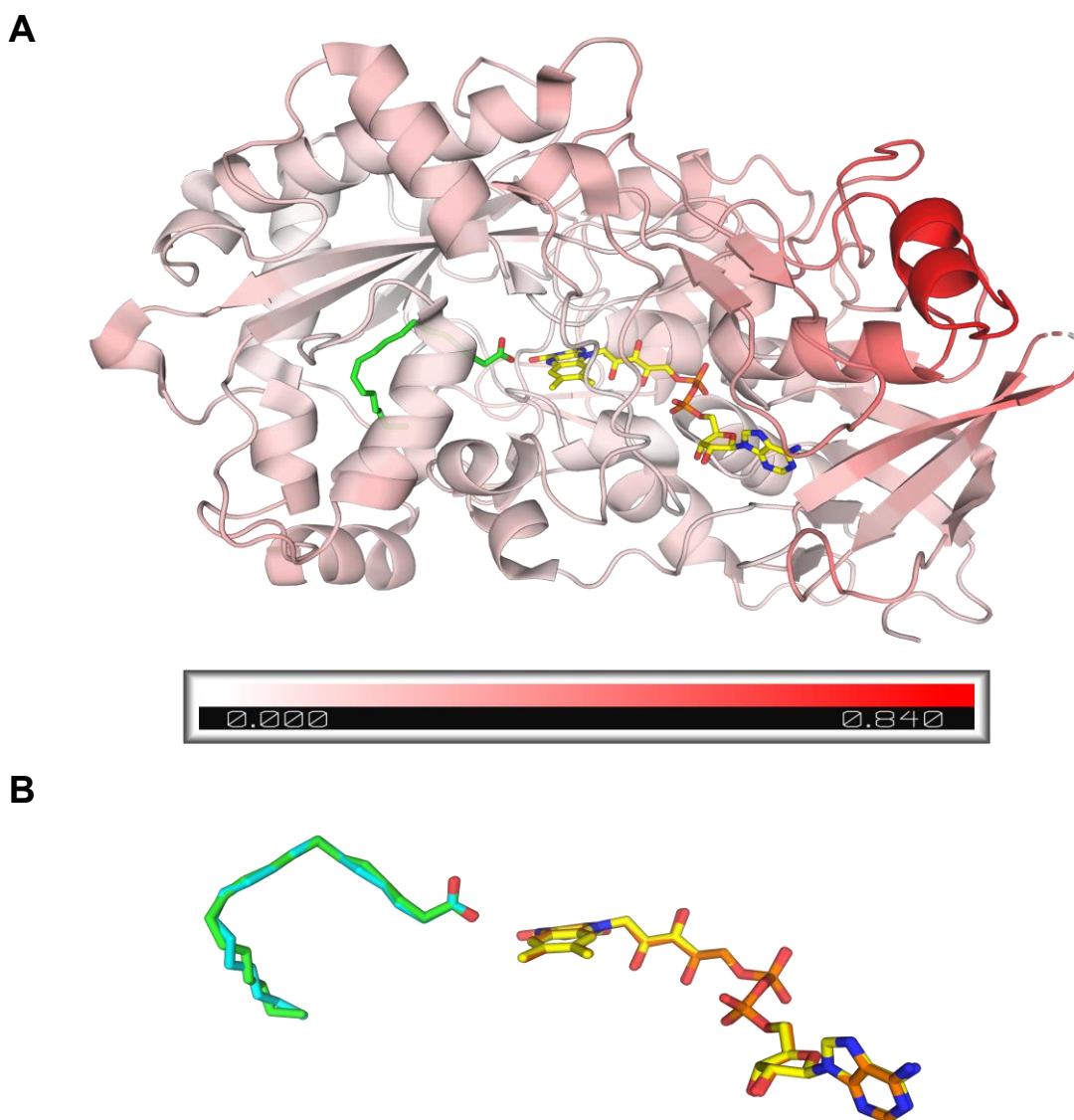
Supplementary Table S2.3.4: Statistics of refinement against extrapolated structure factors at 20 ps, 900 ps, 300 ns, 2 μ s including fatty acid (20 ps) and alkane (900 ps, 300 ns, 2 μ s) and a water molecule (at 20 ps, 900 ps, 300 ns, 2 μ s) in the active site.

Dataset	$\Delta t_{20ps_model_alkane}$	$\Delta t_{900ps_model_alkane}$	$\Delta t_{300ns_model_alkane}$	$\Delta t_{2\mu s_model_alkane}$
PDB ID entry	7R33	7R34	7R35	7R36
Pump energy (μ J)	11	11	11	11
Refinement strategy	Difference refinement	Difference refinement	Difference refinement	Difference refinement
Resolution (\AA)	10– 2.00 (2.02– 2.00)	10– 2.00 (2.02– 2.00)	10– 2.00 (2.02– 2.00)	10– 2.20 (2.23 – 2.20)
Number of reflections	89,568 (2,736)	89,564 (2,749)	89,565 (2,754)	67,248 (2,607)
R_{free}	32.01 (44.91)	37.27 (49.62)	40.94 (48.25)	37.90 (48.63)
R_{work}	26.46 (40.16)	30.63 (42.37)	35.19 (42.78)	29.72 (41.48)
Number of protein atoms	8,630	8,630	8,630	8,630
Number of ligand atoms	160	160	160	160
Number of water atoms	392	392	392	392
B-factor protein (\AA^2)	34.39	34.59	31.98	33.48
r.m.s.d. bond lengths (\AA)	0.008	0.008	0.002	0.009
r.m.s.d. angles ($^\circ$)	1.025	1.026	0.451	1.070
Ramachandran favored	94.70	93.18	94.08	92.91
Ramachandran allowed	4.49	6.01	5.21	5.75
Ramachandran outliers	0.81	0.81	0.72	1.35
Rotamer outliers	5.55	5.99	2.44	7.44
C-beta outliers	0	0	0	0
Clashscore	6.57	9.26	5.54	11.83



Supplementary Figure S2.3.1: Fourier difference maps at 900 ps at three different pump-pulse energies using data processed in the $P2_12_12_1$ space group

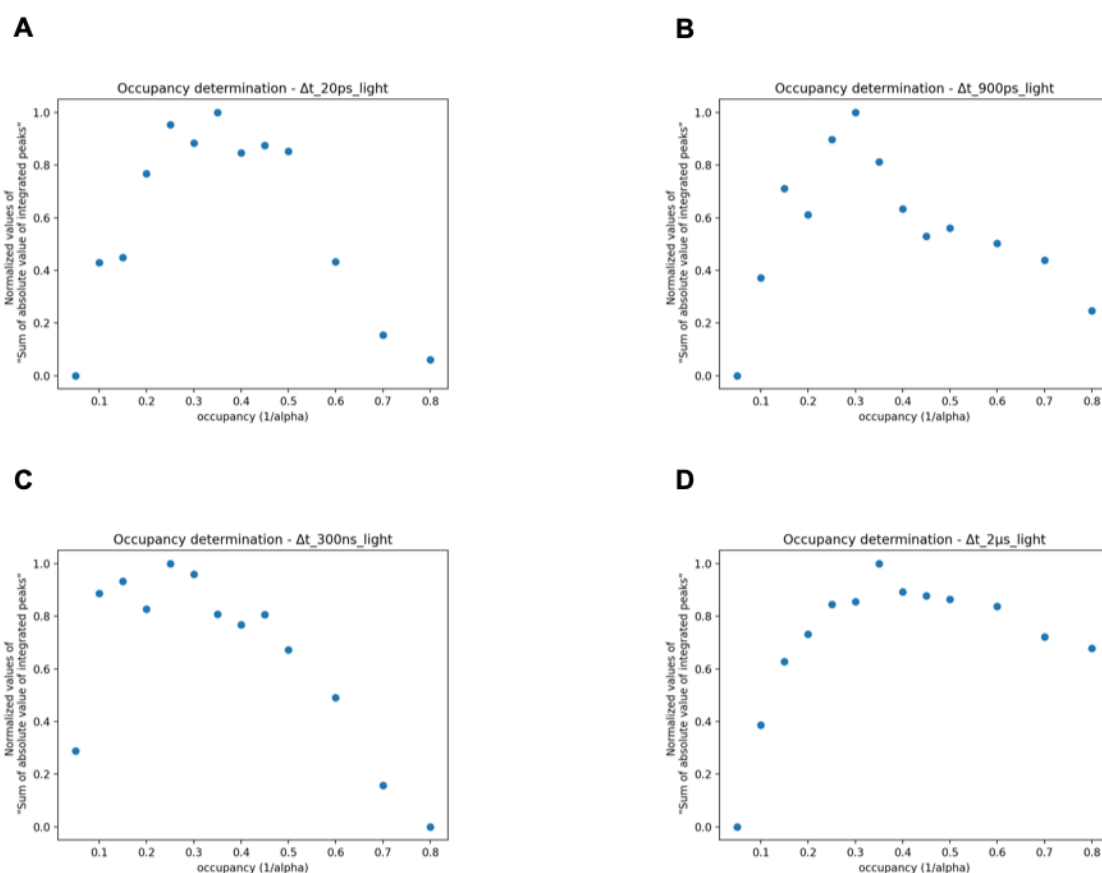
q-weighted Fourier difference electron density maps calculated between SFX light ($\Delta t = 900$ ps) data sets at different pump-laser energies and the dark data set ($F_{obs}^{light_900ps_E} - F_{obs}^{dark}$); with $E = 3.7 \mu J$ (A), $7.5 \mu J$ (B), and $11 \mu J$ (C) at 1.9 \AA resolution. Maps are contoured at $+3.5$ r.m.s.d. (green) and -3 r.m.s.d. (red). The cryo MX dark-state model (PDB entry code 6YRU) is overlaid in panels A-C with FAD in yellow, the fatty acid substrate in green and the protein in light grey. The maps were calculated with 18 430 dark images, and with 15 574, 12 796 and 19 151 light images in panels A-C, respectively.



Supplementary Figure S2.3.2: Conformational differences between monomers A and B in the asymmetric unit

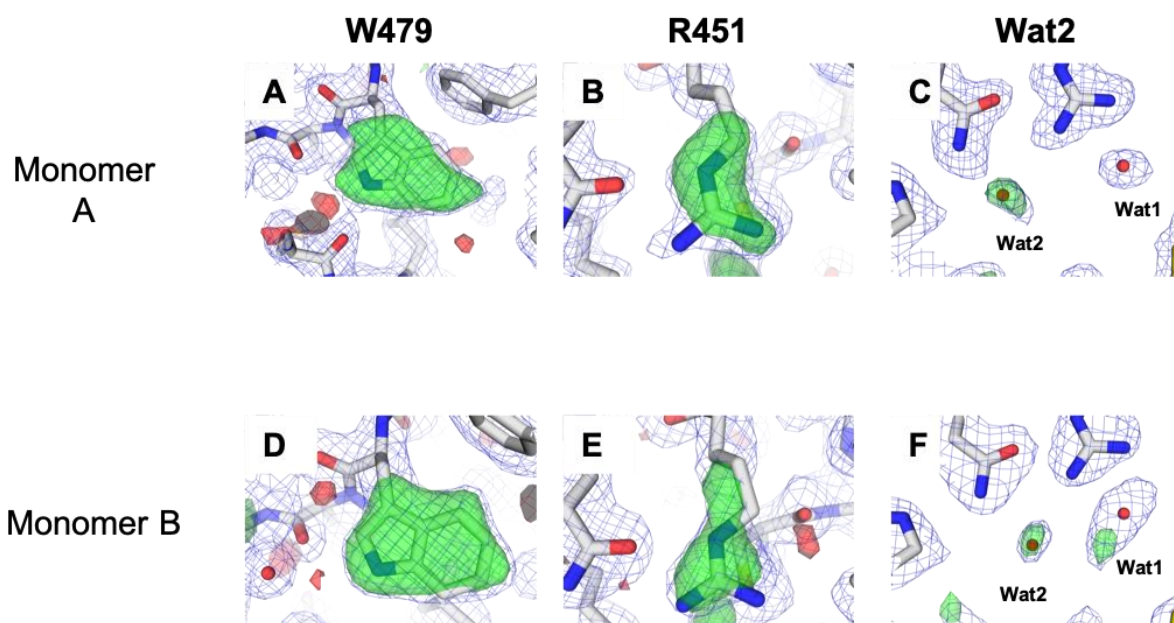
(A) Cartoon model of monomer A, colored according to the distance between equivalent Ca atoms in monomers A and B (distance = $\sqrt{(x_2 - x_1)^2 + (y_2 - y_1)^2 + (z_2 - z_1)^2}$). The color code ranges from white (smaller distances) to red (larger distances; maximum is 0.84 Å) and reflects the distance between equivalent Ca atoms in monomers A and B. Carbon atoms of the fatty acid and the FAD of monomer A are shown as green and yellow sticks, respectively.

(B) Overlay of FAD/substrate of molecule A and B shown in yellow/green and orange/cyan, respectively.



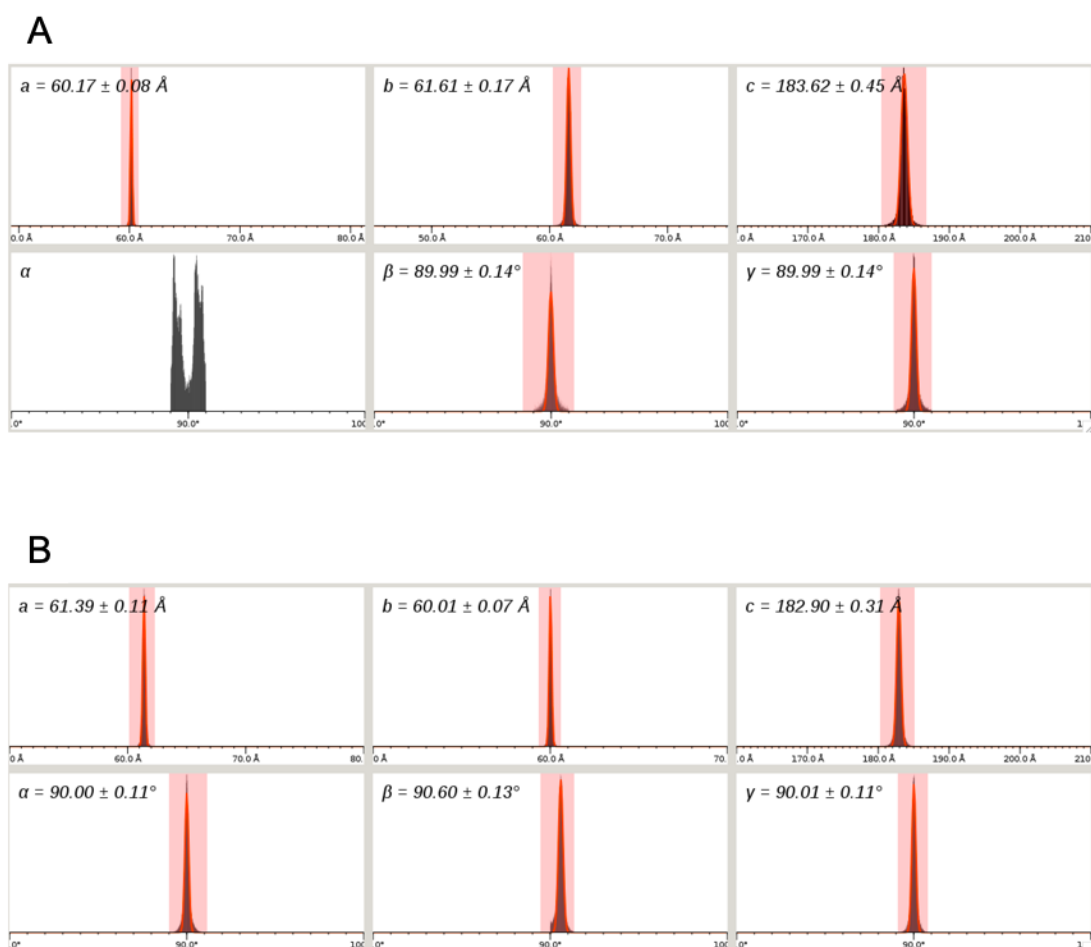
Supplementary Figure S2.3.3: Occupancy determination at the four-time delays

Determination of the occupancy, corresponding to the inverse of the weighting factor α of the Δt_{light} structures with $\Delta t = 20$ ps (A), 900 ps (B), 300 ns (C), at 2 Å resolution and $\Delta t = 2$ μs (D). The ratio of integrated peaks in the $mF_{ext}^{\Delta t_{300ns}} - DF_{calc}^{dark}$ map and of integrated peaks in the $F_{obs}^{\Delta t_{light}} - F_{obs}^{dark}$ maps, normalized to its maximum value, is plotted as a function of the occupancy. Only peaks around the fatty acid in the active site were used for α determination.



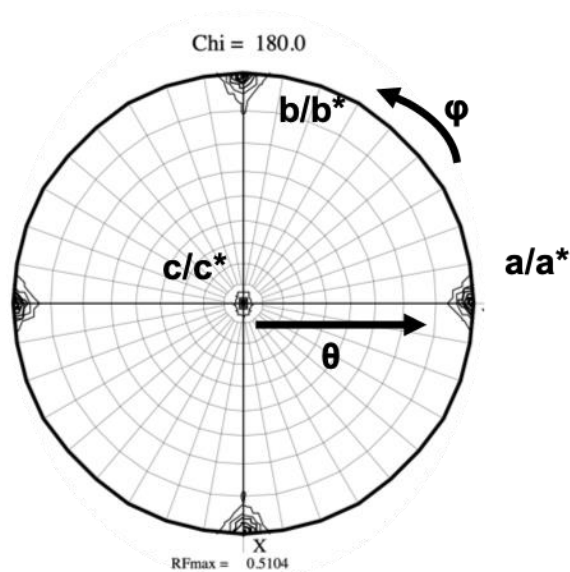
Supplementary Figure S2.3.4: Extrapolated electron density maps at 300 ns after omitting Wat2, and the side chains of W479 and R451

Extrapolated electron density maps $2mF_{ext}^{\Delta t-300ns} - DF_{calc}$ (1 r.m.s.d., blue) and $mqF_{ext}^{\Delta t-300ns} - DF_{calc}$ maps (+3 r.m.s.d., green; -3 r.m.s.d., red), calculated between the dark and the light data set at 300 ns and phased with a refined model from which the side chains of W479 (A, D) or R451 (B, E), or Wat2 (C, F) have been omitted. The dark state model (PDB entry code 6ZH7) is overlaid. Monomers A and B are shown in panels A, B, C and D, E, F respectively.



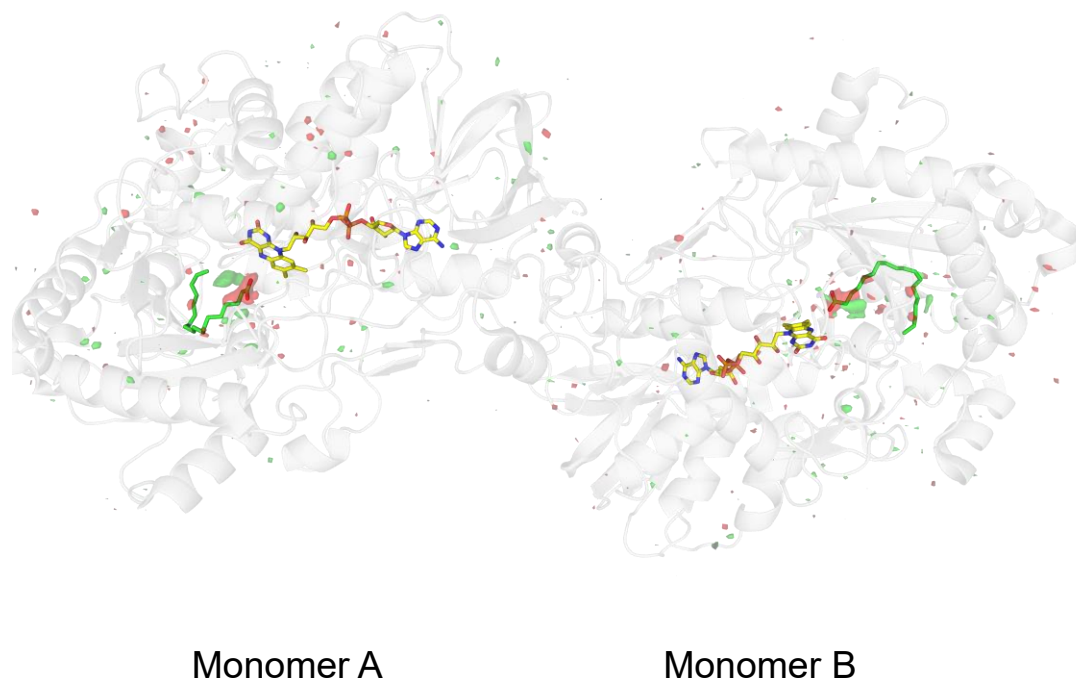
Supplementary Figure S2.3.5: Screenshot of cell_explorer from CrystFEL showing the unit cell parameter distributions for dark datasets resulting from processing with $P2_12_12_1$ (A) and $P2_1$ (B)

All unit cell parameters could be well fitted according to a Gaussian distribution (red line) except for the α angle of the $P2_12_12_1$ data (A) that featured a double peak centered at 89.3° and 90.5° .



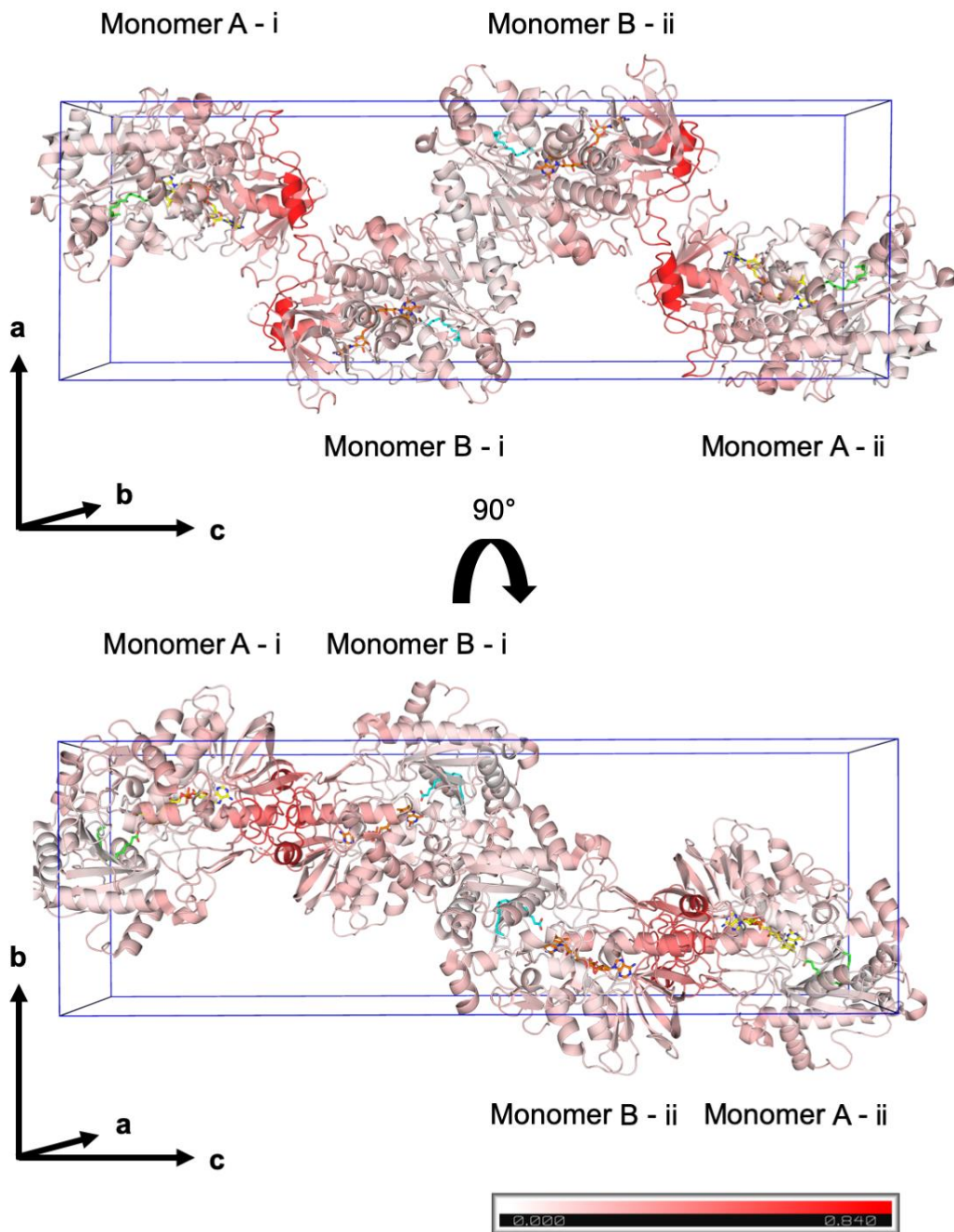
Supplementary Figure S2.3.6: Stereographic projection of the self-rotation function of the dark dataset (PDB code 6ZH7)

The self-rotation function of the FAP crystal was calculated using data in the 10 – 2.5 Å resolution range and the 2-fold ($\chi = 180^\circ$) section plotted above a threshold of 25 σ with increments of 0.9 σ . The crystallographic axes are c/c^* along z (center of the plot), a/a^* along x ($\theta=90$, $\varphi=0$), b/b^* along y ($\theta=90$, $\varphi=90$). The crystallographic axis of $P2_1$ along b/b^* is evident, as well as are peaks of similar height along a/a^* that stem from NCS linking FAP molecules A and B within the asymmetric unit.



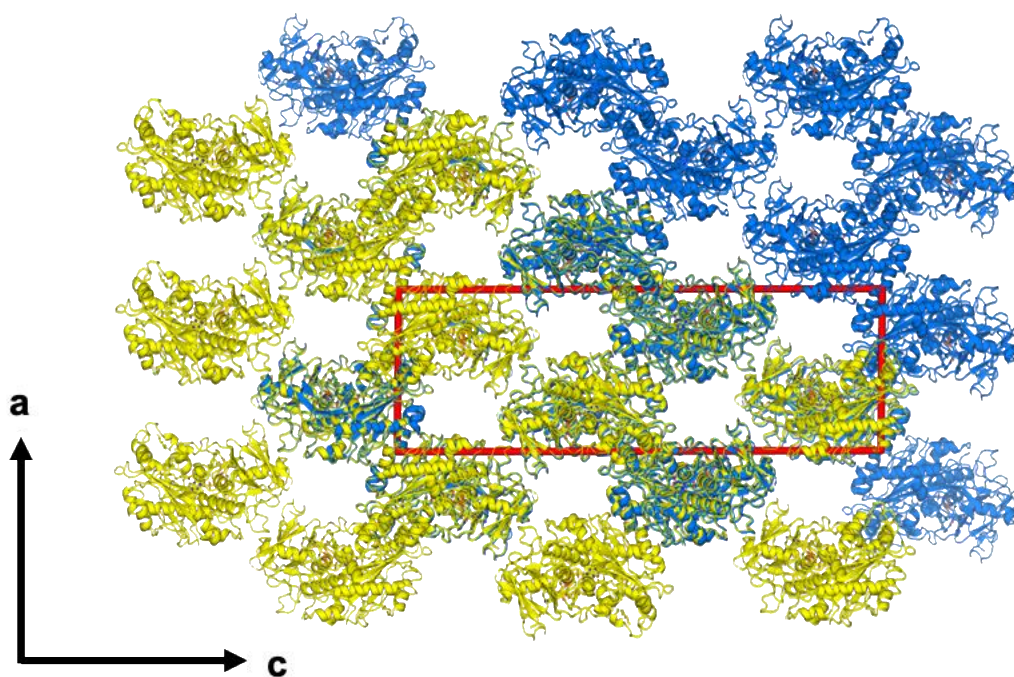
Supplementary Figure S2.3.7: Fourier difference map at 300 ns in the asymmetric unit

q-weighted difference Fourier electron density map calculated between the light and dark data sets $F_{obs}^{\Delta t_{300ns}} - F_{obs}^{dark}$ at 2 Å resolution. The map is shown at +3.5 r.m.s.d. (green) and -3.5 r.m.s.d. (red). FAD and the C18 fatty acid substrate are shown in yellow and green, respectively. The protein of monomer A is shown in grey.

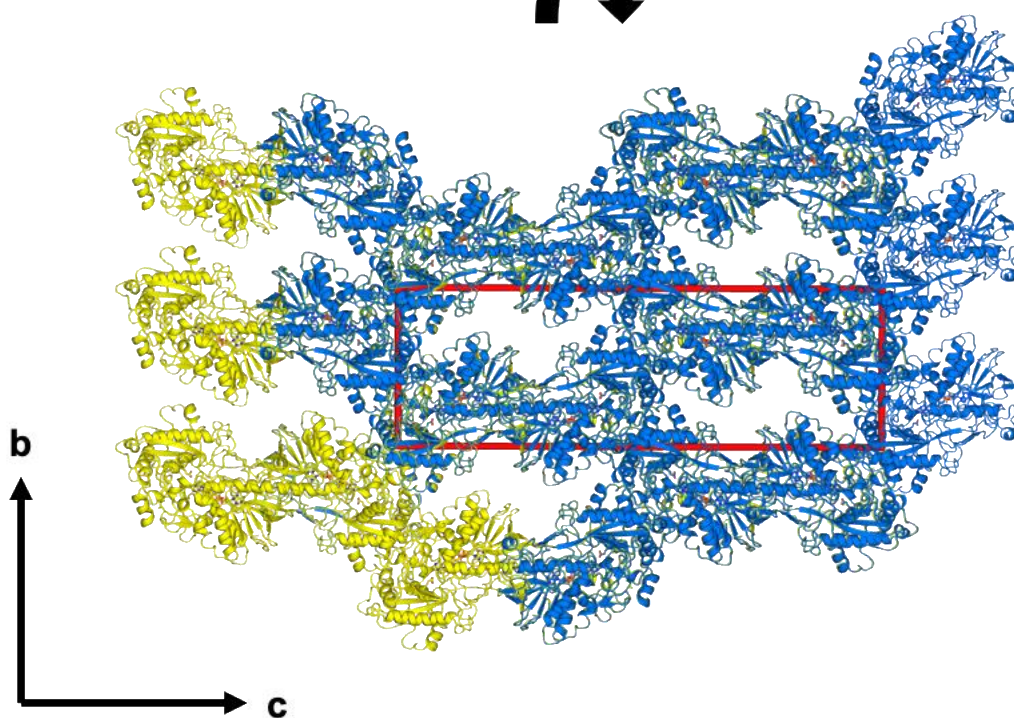


Supplementary Figure S2.3.8: Unit cell content of dark-state CvFAP in the $P2_1$ space group (PDB entry code 6ZH7)

Monomers A and B in the asymmetric units i and ii are shown. The monomers are colored according to the distance between equivalent $C\alpha$ atoms in monomers A and B as in Supplementary Figure S2.



90°



Supplementary Figure S2.3.9: Crystal packing in $P2_1$ and $P2_12_12_1$ space groups

The crystal packings of dark-state CvFAP in the $P2_1$ (yellow) and the $P2_12_12_1$ (blue) space groups are shown. The unit cells are shown in red for both space groups: $a = 61.4 \text{ \AA}$, $b = 60.0 \text{ \AA}$, $c = 182.9 \text{ \AA}$ and $\alpha = 90^\circ$, $\beta = 90.6^\circ$, $\gamma = 90^\circ$ for $P2_1$ (Supplementary table S2.3.1) and $a = 60.2 \text{ \AA}$, $b = 61.6 \text{ \AA}$, $c = 183.6 \text{ \AA}$ and $\alpha, \beta, \gamma = 90^\circ$ for $P2_12_12_1$ (Supplementary table S2.3.3). The superposition indicates that the $P2_1$ packing is only a minor deviation from the $P2_12_12_1$ packing.

2.3.10 References

- Afonine, P. V., Grosse-Kunstleve, R. W., Echols, N., Headd, J. J., Moriarty, N. W., Mustyakimov, M., Terwilliger, T. C., Urzhumtsev, A., Zwart, P. H. & Adams, P. D. (2012). *Acta Crystallographica Section D* **68**, 352-367.
- Barends, T. R., Foucar, L., Ardevol, A., Nass, K., Aquila, A., Botha, S., Doak, R. B., Falahati, K., Hartmann, E., Hilpert, M., Heinz, M., Hoffmann, M. C., Kofinger, J., Koglin, J. E., Kovacsova, G., Liang, M., Milathianaki, D., Lemke, H. T., Reinstein, J., Roome, C. M., Shoeman, R. L., Williams, G. J., Burghardt, I., Hummer, G., Boutet, S. & Schlichting, I. (2015). *Science* **350**, 445-450.
- Boutet, S., Lomb, L., Williams, G. J., Barends, T. R., Aquila, A., Doak, R. B., Weierstall, U., DePonte, D. P., Steinbrener, J., Shoeman, R. L., Messerschmidt, M., Barty, A., White, T. A., Kassemeyer, S., Kirian, R. A., Seibert, M. M., Montanez, P. A., Kenney, C., Herbst, R., Hart, P., Pines, J., Haller, G., Gruner, S. M., Philipp, H. T., Tate, M. W., Hromalik, M., Koerner, L. J., van Bakel, N., Morse, J., Ghonsalves, W., Arnlund, D., Bogan, M. J., Caleman, C., Fromme, R., Hampton, C. Y., Hunter, M. S., Johansson, L. C., Katona, G., Kupitz, C., Liang, M., Martin, A. V., Nass, K., Redecke, L., Stellato, F., Timneanu, N., Wang, D., Zatsepin, N. A., Schafer, D., Defever, J., Neutze, R., Fromme, P., Spence, J. C., Chapman, H. N. & Schlichting, I. (2012). *Science* **337**, 362-364.
- Branden, G. & Neutze, R. (2021). *Science* **373**,
- Claesson, E., Wahlgren, W. Y., Takala, H., Pandey, S., Castillon, L., Kuznetsova, V., Henry, L., Panman, M., Carrillo, M., Kubel, J., Nanekar, R., Isaksson, L., Nimmrich, A., Cellini, A., Morozov, D., Maj, M., Kurttila, M., Bosman, R., Nango, E., Tanaka, R., Tanaka, T., Fangjia, L., Iwata, S., Owada, S., Moffat, K., Groenhof, G., Stojkovic, E. A., Ihalainen, J. A., Schmidt, M. & Westenhoff, S. (2020). *Elife* **9**,
- Colletier, J.-P., Schirò, G. & Weik, M. (2018). *X-ray free electron lasers: A revolution in structural biology*, edited by S. Boutet, P. Fromme & M. S. Hunter, pp. 331-356. Cham: Springer International Publishing.
- Coquelle, N., Sliwa, M., Woodhouse, J., Schirò, G., Adam, V., Aquila, A., Barends, T. R. M., Boutet, S., Byrdin, M., Carbajo, S., De la Mora, E., Doak, R. B., Feliks, M., Fieschi, F., Foucar, L., Guillon, V., Hilpert, M., Hunter, M. S., Jakobs, S., Koglin, J. E., Kovacsova, G., Lane, T. J., Lévy, B., Liang, M., Nass, K., Ridard, J., Robinson, J. S., Roome, C. M., Ruckebusch, C., Seaberg, M., Thepaut, M., Cammarata, M., Demachy, I., Field, M., Shoeman, R. L., Bourgeois, D., Colletier, J.-P., Schlichting, I. & Weik, M. (2018). *Nature Chemistry* **10**, 31-37.
- De Zitter, E., Coquelle, N., Barends, T. R. & Colletier, J.-P. (2022). *bioRxiv* 2022.2001.2009.475568.
- DePonte, D. P., Weierstall, U., Schmidt, K., Warner, J., Starodub, D., Spence, J. C. H. & Doak, R. B. (2008). *Journal of Physics D: Applied Physics* **41**, 195505.
- Dods, R., Båth, P., Morozov, D., Gagnér, V. A., Arnlund, D., Luk, H. L., Kübel, J., Maj, M., Vallejos, A., Wickstrand, C., Bosman, R., Beyerlein, K. R., Nelson, G., Liang, M., Milathianaki, D., Robinson, J., Harimoorthy, R., Berntsen, P., Malmerberg, E., Johansson, L., Andersson, R., Carbajo, S., Claesson, E., Conrad, C. E., Dahl, P., Hammarin, G., Hunter, M. S., Li, C., Lisova, S., Royant, A., Safari, C., Sharma, A.,

- Williams, G. J., Yefanov, O., Westenhoff, S., Davidsson, J., DePonte, D. P., Boutet, S., Barty, A., Katona, G., Groenhof, G., Brändén, G. & Neutze, R. (2021). *Nature* **589**, 310-314.
- Domratheva, T. & Schlichting, I. (2018). *Faraday discussions* **207**, 9-26.
- Duan, C., Adam, V., Byrdin, M., Ridard, J., Kieffer-Jaquinod, S., Morlot, C., Arcizet, D., Demachy, I. & Bourgeois, D. (2013). *Journal of the American Chemical Society* **135**, 15841-15850.
- Emsley, P. & Cowtan, K. (2004). *Acta Crystallogr D Biol Crystallogr.* **60**, 2126-2132. Epub 2004 Nov 2126.
- Gabruk, M. & Mysliwa-Kurziel, B. (2015). *Biochemistry* **54**, 5255-5262.
- Gorel, A., Schlichting, I. & Barends, T. R. M. (2021). *IUCrJ* **8**, 532-543.
- Grünbein, M. L., Stricker, M., Nass Kovacs, G., Kloos, M., Doak, R. B., Shoeman, R. L., Reinstein, J., Lecler, S., Haacke, S. & Schlichting, I. (2020). *Nature Methods* **17**, 681-684.
- Hutchison, C. D. M., Kaucikas, M., Tenboer, J., Kupitz, C., Moffat, K., Schmidt, M. & van Thor, J. J. (2016). *Chemical Physics Letters* **654**, 63-71.
- Kern, J., Chatterjee, R., Young, I. D., Fuller, F. D., Lassalle, L., Ibrahim, M., Gul, S., Fransson, T., Brewster, A. S., Alonso-Mori, R., Hussein, R., Zhang, M., Douthit, L., de Lichtenberg, C., Cheah, M. H., Shevela, D., Wersig, J., Seuffert, I., Sokaras, D., Pastor, E., Weninger, C., Kroll, T., Sierra, R. G., Aller, P., Butryn, A., Orville, A. M., Liang, M., Batyuk, A., Koglin, J. E., Carbajo, S., Boutet, S., Moriarty, N. W., Holton, J. M., Dobbek, H., Adams, P. D., Bergmann, U., Sauter, N. K., Zouni, A., Messinger, J., Yano, J. & Yachandra, V. K. (2018). *Nature* **563**, 421-425.
- Liang, M., Williams, G. J., Messerschmidt, M., Seibert, M. M., Montanez, P. A., Hayes, M., Milathianaki, D., Aquila, A., Hunter, M. S., Koglin, J. E., Schafer, D. W., Guillet, S., Busse, A., Bergan, R., Olson, W., Fox, K., Stewart, N., Curtis, R., Miahnahri, A. A. & Boutet, S. (2015). *Journal of Synchrotron Radiation* **22**, 514-519.
- Liebschner, D., Afonine, P. V., Baker, M. L., Bunkóczi, G., Chen, V. B., Croll, T. I., Hintze, B., Hung, L. W., Jain, S., McCoy, A. J., Moriarty, N. W., Oeffner, R. D., Poon, B. K., Prisant, M. G., Read, R. J., Richardson, J. S., Richardson, D. C., Sammito, M. D., Sobolev, O. V., Stockwell, D. H., Terwilliger, T. C., Urzhumtsev, A. G., Videau, L. L., Williams, C. J. & Adams, P. D. (2019). *Acta Crystallogr D Struct Biol* **75**, 861-877.
- Miller, R. J. D., Pare-Labrosse, O., Sarracini, A. & Besaw, J. E. (2020). *Nature Communications* **11**,
- Mous, S., Gotthard, G., Ehrenberg, D., Sen, S., Weinert, T., Johnson, P. J. M., James, D., Nass, K., Furrer, A., Kekilli, D., Ma, P., Brunle, S., Casadei, C. M., Martiel, I., Dworkowski, F., Gashi, D., Skopintsev, P., Wranik, M., Knopp, G., Panepucci, E., Panneels, V., Cirelli, C., Ozerov, D., Schertler, G., Wang, M., Milne, C., Standfuss, J., Schapiro, I., Heberle, J. & Nogly, P. (2022). *Science* eabj6663.
- Nango, E., Royant, A., Kubo, M., Nakane, T., Wickstrand, C., Kimura, T., Tanaka, T., Tono, K., Song, C., Tanaka, R., Arima, T., Yamashita, A., Kobayashi, J., Hosaka, T.,

- Mizohata, E., Nogly, P., Sugahara, M., Nam, D., Nomura, T., Shimamura, T., Im, D., Fujiwara, T., Yamanaka, Y., Jeon, B., Nishizawa, T., Oda, K., Fukuda, M., Andersson, R., B $\sqrt{\bullet}$ th, P., Dods, R., Davidsson, J., Matsuoka, S., Kawatake, S., Murata, M., Nureki, O., Owada, S., Kameshima, T., Hatsui, T., Joti, Y., Schertler, G., Yabashi, M., Bondar, A.-N., Standfuss, J. r., Neutze, R. & Iwata, S. (2016). *Science* **354**, 1552-1557.
- Nass, K., Gorel, A., Abdullah, M. M., V. Martin, A., Kloos, M., Marinelli, A., Aquila, A., Barends, T. R. M., Decker, F.-J., Bruce Doak, R., Foucar, L., Hartmann, E., Hilpert, M., Hunter, M. S., Jurek, Z., Koglin, J. E., Kozlov, A., Lutman, A. A., Kovacs, G. N., Roome, C. M., Shoeman, R. L., Santra, R., Quiney, H. M., Ziaja, B., Boutet, S. & Schlichting, I. (2020). *Nature Communications* **11**, 1814.
- Nass Kovacs, G., Colletier, J.-P., Grünbein, M. L., Yang, Y., Stensitzki, T., Batyuk, A., Carbajo, S., Doak, R. B., Ehrenberg, D., Foucar, L., Gasper, R., Gorel, A., Hilpert, M., Kloos, M., Koglin, J. E., Reinstein, J., Roome, C. M., Schlesinger, R., Seaberg, M., Shoeman, R. L., Stricker, M., Boutet, S., Haacke, S., Heberle, J., Heyne, K., Domratcheva, T., Barends, T. R. M. & Schlichting, I. (2019). *Nat Commun* **10**, 3177.
- Nomura, T., Kimura, T., Kanematsu, Y., Yamada, D., Yamashita, K., Hirata, K., Ueno, G., Murakami, H., Hisano, T., Yamagiwa, R., Takeda, H., Gopalasingam, C., Kousaka, R., Yanagisawa, S., Shoji, O., Kumasaka, T., Yamamoto, M., Takano, Y., Sugimoto, H., Toshi, T., Kubo, M. & Shiro, Y. (2021). *Proc Natl Acad Sci U S A* **118**,
- Oda, K., Nomura, T., Nakane, T., Yamashita, K., Inoue, K., Ito, S., Vierock, J., Hirata, K., Maturana, A. D., Katayama, K., Ikuta, T., Ishigami, I., Izume, T., Umeda, R., Eguma, R., Oishi, S., Kasuya, G., Kato, T., Kusakizako, T., Shihoya, W., Shimada, H., Takatsuji, T., Takemoto, M., Taniguchi, R., Tomita, A., Nakamura, R., Fukuda, M., Miyauchi, H., Lee, Y., Nango, E., Tanaka, R., Tanaka, T., Sugahara, M., Kimura, T., Shimamura, T., Fujiwara, T., Yamanaka, Y., Owada, S., Joti, Y., Tono, K., Ishitani, R., Hayashi, S., Kandori, H., Hegemann, P., Iwata, S., Kubo, M., Nishizawa, T. & Nureki, O. (2021). *Elife* **10**,
- Pande, K., Hutchison, C. D., Groenhof, G., Aquila, A., Robinson, J. S., Tenboer, J., Basu, S., Boutet, S., DePonte, D. P., Liang, M., White, T. A., Zatsepin, N. A., Yefanov, O., Morozov, D., Oberthuer, D., Gati, C., Subramanian, G., James, D., Zhao, Y., Koralek, J., Brayshaw, J., Kupitz, C., Conrad, C., Roy-Chowdhury, S., Coe, J. D., Metz, M., Xavier, P. L., Grant, T. D., Koglin, J. E., Ketawala, G., Fromme, R., Srajer, V., Henning, R., Spence, J. C., Ourmazd, A., Schwander, P., Weierstall, U., Frank, M., Fromme, P., Barty, A., Chapman, H. N., Moffat, K., van Thor, J. J. & Schmidt, M. (2016). *Science* **352**, 725-729.
- Poddar, H., Heyes, D. J., Schiro, G., Weik, M., Leys, D. & Scrutton, N. S. (2021). *FEBS J*
- Sancar, A. (2016). *Angew Chem Int Ed Engl* **55**, 8502-8527.
- Shimada, A., Kubo, M., Baba, S., Yamashita, K., Hirata, K., Ueno, G., Nomura, T., Kimura, T., Shinzawa-Itoh, K., Baba, J., Hatano, K., Eto, Y., Miyamoto, A., Murakami, H., Kumasaka, T., Owada, S., Tono, K., Yabashi, M., Yamaguchi, Y., Yanagisawa, S., Sakaguchi, M., Ogura, T., Komiyama, R., Yan, J., Yamashita, E., Yamamoto, M., Ago, H., Yoshikawa, S. & Tsukihara, T. (2017). *Science advances* **3**, e1603042.
- Skopintsev, P., Ehrenberg, D., Weinert, T., James, D., Kar, R. K., Johnson, P. J. M., Ozerov, D., Furrer, A., Martiel, I., Dworkowski, F., Nass, K., Knopp, G., Cirelli, C., Arrell, C.,

- Gashi, D., Mous, S., Wranik, M., Gruhl, T., Kekilli, D., Brünle, S., Deupi, X., Schertler, G. F. X., Benoit, R. M., Panneels, V., Nogly, P., Schapiro, I., Milne, C., Heberle, J. & Standfuss, J. (2020). *Nature* **583**, 314-318.
- Sorigue, D., Hadjidemetriou, K., Blangy, S., Gotthard, G., Bonvalet, A., Coquelle, N., Samire, P., Aleksandrov, A., Antonucci, L., Benachir, A., Boutet, S., Byrdin, M., Cammarata, M., Carbajo, S., Cuine, S., Doak, R. B., Foucar, L., Gorel, A., Grunbein, M., Hartmann, E., Hienerwadel, R., Hilpert, M., Kloos, M., Lane, T. J., Legeret, B., Legrand, P., Li-Beisson, Y., Moulin, S. L. Y., Nurizzo, D., Peltier, G., Schiro, G., Shoeman, R. L., Sliwa, M., Solinas, X., Zhuang, B., Barends, T. R. M., Colletier, J. P., Joffre, M., Royant, A., Berthomieu, C., Weik, M., Domratcheva, T., Brettel, K., Vos, M. H., Schlichting, I., Arnoux, P., Muller, P. & Beisson, F. (2021). *Science* **372**,
- Sorigue, D., Legeret, B., Cuine, S., Blangy, S., Moulin, S., Billon, E., Richaud, P., Brugiere, S., Coute, Y., Nurizzo, D., Muller, P., Brettel, K., Pignol, D., Arnoux, P., Li-Beisson, Y., Peltier, G. & Beisson, F. (2017). *Science* **357**, 903-907.
- Suga, M., Akita, F., Yamashita, K., Nakajima, Y., Ueno, G., Li, H., Yamane, T., Hirata, K., Umena, Y., Yonekura, S., Yu, L.-J., Murakami, H., Nomura, T., Kimura, T., Kubo, M., Baba, S., Kumasaka, T., Tono, K., Yabashi, M., Isobe, H., Yamaguchi, K., Yamamoto, M., Ago, H. & Shen, J.-R. (2019). *Science* **366**, 334.
- Tosha, T., Nomura, T., Nishida, T., Saeki, N., Okubayashi, K., Yamagiwa, R., Sugahara, M., Nakane, T., Yamashita, K., Hirata, K., Ueno, G., Kimura, T., Hisano, T., Muramoto, K., Sawai, H., Takeda, H., Mizohata, E., Yamashita, A., Kanematsu, Y., Takano, Y., Nango, E., Tanaka, R., Nureki, O., Shoji, O., Ikemoto, Y., Murakami, H., Owada, S., Tono, K., Yabashi, M., Yamamoto, M., Ago, H., Iwata, S., Sugimoto, H., Shiro, Y. & Kubo, M. (2017). *Nat Commun* **8**, 1585.
- Ursby, T. & Bourgeois, D. (1997). *Acta Crystallographica Section A* **53**, 564-575.
- Winn, M. D., Ballard, C. C., Cowtan, K. D., Dodson, E. J., Emsley, P., Evans, P. R., Keegan, R. M., Krissinel, E. B., Leslie, A. G., McCoy, A., McNicholas, S. J., Murshudov, G. N., Pannu, N. S., Potterton, E. A., Powell, H. R., Read, R. J., Vagin, A. & Wilson, K. S. (2011). *Acta crystallographica. Section D, Biological crystallography* **67**, 235-242.
- Yun, J. H., Li, X., Yue, J., Park, J. H., Jin, Z., Li, C., Hu, H., Shi, Y., Pandey, S., Carbajo, S., Boutet, S., Hunter, M. S., Liang, M., Sierra, R. G., Lane, T. J., Zhou, L., Weierstall, U., Zatsepin, N. A., Ohki, M., Tame, J. R. H., Park, S. Y., Spence, J. C. H., Zhang, W., Schmidt, M., Lee, W. & Liu, H. (2021). *Proc Natl Acad Sci U S A* **118**,

Chapter 3

Reversibly photoswitchable fluorescent proteins

3.1 Introduction

3.1.1 Fluorescent proteins

Fluorescent proteins (FPs) have revolutionized life sciences by being used in optical microscopy to mark biological samples. FPs share many features such as the tertiary structure of the majority of FPs consists of an 11-stranded β -barrel. As the name implies, the structure surrounding a three-amino-acid chromophore is barrel-shaped (Figure 3.1.1). The chromophore core structure is a 4-(p-hydroxybenzylidene)-5-imidazolinone (p-HBI) moiety formed autocatalytically by three amino acids. The first residue may vary while the other two are usually tyrosine and glycine. In the presence of oxygen, the three-residue chromophore matures to a p-HBI chromophore. Specifically, tyrosine is reduced to a hydroxybenzylidene moiety, while glycine is cyclized into an imidazolinone ring. These two aromatic rings, linked by an ethylene bridge, are part of a conjugated system that is common to green-light-emitting FPs. When the first residue of the tripeptide participates in the conjugated system of the chromophore, then the FPs are more likely to be red-shifted.

The 2008 Nobel Prize in Chemistry was awarded to three scientists “*for the discovery and development of the green fluorescent protein, GFP*” (www.nobelprize.org). These three scientists and their contributions were:

- i) Osamu Shimomura first extracted, purified, crystallized, and determined the structure of the GFP from *Aequorea victoria* (a jellyfish) and reported that it shines bright green when exposed to visible light. He was able to denature GFP and applied digestion with papain. He then isolated the only fragment that absorbed UV/vis light above 300 nm and that had a similar absorption spectrum to GFP. Even though this fragment did not fluoresce, it was presumed that this was the chromophore (Head et al. 2000; Shimomura 1979).
- ii) Martin Chalfie demonstrated how GFPs can be a luminescent reporter gene. He managed to express GFP in the transparent worm *Caenorhabditis elegans* and the bacterium *Escherichia coli* (Chalfie et al. 1994).

- iii) Roger Y. Tsien contributed to further the knowledge of GFP fluorescence. He reported that the autocatalytic formation of the chromophore was oxygen-dependent (Heim, Prasher, and Tsien 1994). He also generated genetically modified variants of the GFP which allowed to extend the fluorescence emission colors to a wide range of emission wavelengths throughout the visible spectrum (Shaner et al. 2004; Wang et al. 2004).

The protonation state of the p-hydroxybenzylidene moiety is pivotal for the fluorescence properties of the chromophore that are also affected by its protein environment. The latter is important for the fluorescence properties of the p-HBI which are also affected by the chromophore's environment.

A subclass of FPs, known as phototransformable FPs (or PTFPs), has been developed that undergoes specific phototransformations (Adam et al. 2014). Such phototransformations may be reversible, irreversible, or both, resulting in spectrally and structurally distinct types with far greater adaptability than the standard FPs. The employment of such FPs is the foundation of many breakthroughs in advanced fluorescence microscopy. For instance, cellular trafficking and single-molecule observation and localization within a cell or a tissue are some relevant advanced applications. So far, PTFPs have been discovered in the *Anthozoa* class (e.g. stony corals). They have also been engineered using FPs from another class of *Cnidaria* phylum, the *Hydrozoa* (e.g. jellyfish). PTFPs fall into three categories:

- i) Photoactivable FPs (PAFPs). Upon light absorption, PAFP undergo an irreversible activation from a non-fluorescent native state (dark state) to a fluorescent state (light-emitting state). An example is the green-emitting GFP-derived PA-GFP (for photo and activatable GFP) (Patterson and Lippincott-Schwartz 2002). After light excitation, decarboxylation of Glu222 close to the chromophore, together with the rotation of Thr203, stabilizes the anionic, fluorescent form of the chromophore. (Patterson and Lippincott-Schwartz 2002).
- ii) Photoconvertible FPs (PCFPs). In this category of PTFPs, the chromophore is altered chemically in an irreversible manner upon UV/violet light irradiation. Taking the example of the first-ever discovered PCFP, Kaede (Ando et al. 2002)

which is a green-to-red PCFP was isolated from a stony coral, *Trachyphyllia geoffroyi*. In its native state, the FP emits green light and is photoconverted to a red-emitting state. The mechanism is described by a β -elimination that involves the carboxylic acid of the Glu212 side chain, C $_{\alpha}$ of His62 (first residue of the chromophore triplet), and a water molecule in the vicinity of His62 (Hayashi et al. 2007; Mizuno et al. 2003). This leads to the backbone cleavage between His62 and Phe61, changing the structure of the chromophore and expanding the conjugated π -system of the latter.

- iii) Reversibly photoswitchable FPs (RSFPs). The characteristic of the RSFPs is that their chromophore has two conformational states, the fluorescent (*on*-state) and the non-fluorescent (*off*-state), and two protonation states, the anionic and the protonated. The chromophore can be reversibly toggled between them by light activation. This photoisomerization is described by a strong variation of the chromophore's twist and tilt dihedral angles (φ and τ dihedral angles). Photoswitching is an intrinsic feature of the triplet of amino acids composing the chromophore (Yang et al. 2008).

The current study focuses on RSFPs that we will thus introduce more in-depth in the following section.

3.1.2 Reversibly photoswitchable fluorescent proteins

RSFPs' chromophores can undergo *trans*-to-*cis* and *cis*-to-*trans* isomerization upon light absorption. They are classified into two categories depending on their resting state, *i.e.* "negative" and "positive" switchers. In negative RSFPs, the chromophore switches to the *off*-state following light absorption of the *on*-state, whereas in positive RSFPs, the chromophore undergoes *on*-switching upon illumination of the *off*-state (Jensen et al. 2020). At neutral pH, the resting state of negative RSFPs is the fluorescent state (*on*-state) and the chromophore is in the *cis* conformation and with an anionic state. Photoswitching to its non-fluorescent state (*off*-state) leads to a protonated *trans* conformation which is a less stable state. From the *off*-state, the *on*-state can be reached either by light illumination or by thermal conversion. Positive

RSFPs have the opposite properties. An exception in negative RSFPs is rsGamilus whose *off*-switching event is accompanied by *trans*-to-*cis* isomerization coupled with protonation of the chromophore (Shinoda et al. 2019). Dronpa (Ando, Mizuno, and Miyawaki 2004) (PDB ID: 2IE2) which is a negative RSFP was the first green RSFP engineered from *Echinophyllia* a stony coral. Faster photoswitchable RSFPs evolved from Dronpa are Dronpa2 (M159T) and Dronpa3 (V157I and M159T) as well as rsFastLime (V157G) (Ando et al. 2007; Andresen et al. 2008; Stiel et al. 2007). Dronpa and its mutants share the same chromophore triplet of amino acids, *i.e.* Cys-Tyr-Gly, but they differ in their chromophore pocket as the mutations occur in the vicinity of the chromophore. Another example of negative RSFP designed from Anthozoan FP is the blue-emitting mTFP0.7 (Henderson et al. 2007) and the red-emitting rsCherryRev (Stiel et al. 2008). Padron (Stiel et al. 2007), a Dronpa mutant, is a positive RSFP that exhibits the reverse action compared to its parental protein. Other positive RSFPs of the Anthozoan class are the red-emitting asFP595 (Lukyanov et al. 2000) and rsCherry (Stiel et al. 2008). RSFPs, especially “negative” ones, are also engineered from Hydrozoan FPs and specifically from *A. victoria* and thus from GFP. Examples of green-emitting RSFPs are Mut2Q (Abbruzzetti et al. 2005), rsFolder, and rsFolder2 (El Khatib et al. 2016), rsEGFP (Grotjohann et al. 2011a), rsEGFP2 (Grotjohann et al. 2012a) whose chromophore triad is Ala-Tyr-Gly, except for rsEGFP that is Thr-Tyr-Gly. The first yellow-emitting RSFP is EYQ1 (Bizzarri et al. 2010) that was evolved from EYFP; referred to as clone 10C in (Ormö et al. 1996). An extensive literature on RSFPs is found in the following reviews (Adam 2014; Adam et al. 2014; Bourgeois and Adam 2012; Bourgeois, Regis-Faro, and Adam 2012; Duan et al. 2014; Jensen et al. 2020; Zhou and Lin 2013).

In the present Ph.D. work, structural and functional aspects of rsEGFP2 were studied with the aim to reach a structural understanding of the switching mechanism as a marker in super-resolution microscopy and especially in REversible Saturable Optical Fluorescence Transitions (RESOLFT) fluorescent microscopy (A. Schwentker et al. 2007; Dedecker et al. 2007; Hell, Jakobs, and Kastrup 2003; Hofmann et al. 2005).

3.1.3 Super-resolution microscopy

Ernst Abbe, who was a physicist, contemplated a physical limit for the highest resolution of the conventional lens-based optical microscope in 1873 (Abbe 1873). A microscope's resolution is defined as the shortest distance between two spots on an image that can still be identified as two distinct objects on the sample, corresponding at best to half the wavelength of visible light ($\lambda/2 > 200\text{nm}$, known as Abbe's diffraction limit).

The development of electron microscopy led to an increase in resolution. Another German physicist Ernst Ruska, who was awarded the Nobel Prize in Physics in 1938, designed and developed the prototype of the electron microscope (Ruska 1934). Since then, the resolution limit of such instruments has been pushed up to 0.5 Å (Smith 2008). As far as the biological samples are concerned, 1 Å resolution was only recently reached for apoferritin, a 474-kDa globular multidomain protein, by using single-particle cryo-electron microscopy (Nakane et al. 2020; Yip et al. 2020).

Circumvention of the above-mentioned diffraction limit in optical microscopy was suggested by Eric Betzig, Stefan W. Hell, William E. Moerner who were awarded the Nobel Prize in Chemistry in 2014. The work of these scientists led to the increase of the resolution of optical microscopy by using fluorescent molecules. Hence, applications have been broadened to label biomolecules within the cell and track biological processes such as cell division (Sahl, Hell, and Jakobs 2017). Studying biological samples at the nanoscale landmarked the so-called nanoscopy or super-resolution microscopy whose resolution can reach 1 nm (Balzarotti et al. 2017).

RSFPs are used as molecular markers in many super-resolution microscopy techniques such as RESOLFT (Reversible Saturable Optical Fluorescence Transition (A. Schwentker et al. 2007; Dedeker et al. 2007; Hell et al. 2003; Hofmann et al. 2005)), NL-SIM (Non-Linear Structured Illumination Microscopy (Gustafsson 2005)), SOFI (Super-resolution Optical Fluctuation Imaging (Dertinger et al. 2009)) and PALM (Photo Activated Localization Microscopy (Shroff et al. 2007)). Extended literature on the applications of super-resolution microscopy in cell biology can be found in the following reviews (Jacquemet et al. 2020; Jensen et al. 2020; Jing et al. 2021; Khater, Nabi, and Hamarneh 2020; Schubert 2017; Valli et al. 2021).

The RESOLFT technique is based on the same concept as the stimulated emission depletion (STED) microscopy (Hell and Wichmann 1994; Vicidomini, Bianchini, and Diaspro 2018).

Yet, in contrast to STED, which needs a powerful depletion laser, RESOLFT was designed to operate at a low saturation intensity, allowing for substantially decreased phototoxic damage (Grotjohann et al. 2011). An important element of RESOLFT is that it takes advantage of the relatively stable states of RSFPs (*on*- and *off*-states) that are interchanged upon light illumination. Such states are characterized by the structural conformation (*cis* and *trans*) and by the protonation state of the chromophore. This light-driven process of photoswitching involves different metastable intermediate states of the chromophore that are characterized by their capability to be fluorescent or non-fluorescent. For an experiment with rsEGFP2, RESOLFT set-up requires a confocal scanner that includes a 405-nm focal beam and two 491-nm focal beams for the *on*- and *off*-switching of the chromophore, respectively. The two 491-nm beams are (i) a conventional Gaussian-shaped beam that reads out the fluorescence and (ii) a doughnut-shaped beam whose central intensity is minimum (or “zero”) and the focal periphery has maximum intensity. Using a pulse method, each image is taken pixel by pixel. The sample is first irradiated by the 405-nm beam for ~100 μ s activating the rsEGFP2 molecules within the focal area. Next, the 491-nm beam is employed for tens of ms to enable *off*-switching of rsEGFP2 molecules. As the latter beam is doughnut-shaped, the molecules in the center of the beam (zero intensity) remain active, whose fluorescence is then read out by the Gaussian-shaped 491-nm beam for a few ms. The procedure is repeated to scan the whole sample (Grotjohann et al. 2011a, 2012a; Testa et al. 2012). RESOLFT super-resolution microscopy is suitable for *in vivo* imaging due to its low light intensities. Alternatively to RSFPs, organic dyes like the Cy3-Alexa67 heterodimer can also be used in RESOLFT super-resolution microscopy (Kwon et al. 2015).

3.1.4 rsEGFP2

A UV/Vis absorption spectrum from *av*GFP includes two peaks. A major peak at 395 nm and a minor peak at 475 nm. The former peak is attributed to the neutral (or protonated) form of the chromophore whereas the latter peak corresponds to the anionic form of the chromophore (Tsien 1998). Enhanced Green Fluorescent Protein (EGFP) was first reported in 1995, deviating by a single point mutation (S65T) from *av*GFP (Heim, Cubitt, and Tsien 1995). Specifically, the excitation spectrum showed a single peak at 490 nm and an emission peak at 510 nm with an amplitude nearly six-fold higher than that of the wild-type protein. In EGFP, the excitation

maximum is red-shifted by about 100 nm with respect to the *avGFP* spectrum. Moreover, the EGFPs folded more efficiently than the *avGFP* when expressed in *Escherichia coli*. The two above-mentioned properties induce the increase of the fluorescence intensity (Cormack, Valdivia, and Falkow 1996). The fluorescence quantum yield (FQY) of EGFP is 0.6 and the extinction coefficient (ϵ) is $55900 \text{ M}^{-1} \text{ cm}^{-1}$ at 488 nm (<https://www.fpbases.org/protein/egfp/>) while the respective values for the *avGFP* are 0.79 and $25000 \text{ M}^{-1} \text{ cm}^{-1}$ at 395 nm (<https://www.fpbases.org/protein/avgfp/>). Moreover, a double mutation of the GFP chromophore (F64L and S65T) shows an approximately 35-fold higher cellular brightness than the *avGFP* allowing the use of EGFP in imaging of mammalian cells (Zhang, Gurtu, and Kain 1996).

rsEGFP is a reversibly switchable EGFP that can be switched on at $\lambda = 405 \text{ nm}$ and off at $\lambda = 491 \text{ nm}$. In the *on*-state, rsEGFP has an absorption peak at $\lambda = 491 \text{ nm}$ due to an anionic phenol group of the chromophore, while the *off*-state corresponds to the neutral state of the chromophore and has an absorption peak at $\lambda = 396 \text{ nm}$. The *on*-state is characterized by a FQY of 0.36, an ϵ of $47000 \text{ M}^{-1} \text{ cm}^{-1}$ at 491 nm, and a chromophore maturation time of 180 min (Grotjohann et al. 2011b). The ϵ of the *off*-state is $17900 \text{ M}^{-1} \text{ cm}^{-1}$ at 405 nm (Duwé et al. 2015). The half-time for spontaneous conversion from the *off*- to the *on*-state is approximately 23 min (Grotjohann et al. 2011b). sEGFP2 was generated to provide faster switching between the *on*- and *off*-state and to shorten the recording time with RESOLFT (Grotjohann et al. 2012b) (Figure 3.1.2). The excitation and emission peaks of rsEGFP2 are located at $\lambda = 478 \text{ nm}$ and $\lambda = 503 \text{ nm}$, respectively. When the *on*-state of rsEGFP2 is irradiated with a 488 nm light, fluorescence is induced and the rsEGFP2 moves to the *off*-state, whereas irradiation at 405 nm switches the protein back to the *on*-state. Photoswitching involves isomerization (*cis* in *on*; *trans* in *off*) and a change in protonation state (anionic in *on*; neutral in *off*) of the chromophore and reorganization of residues in the chromophore pocket. The quantum yield (QY) of *off*-to-*on* switching (0.23) is higher than the one of *on*-to-*off* switching (0.0093) (Adam et al. 2021).

Both structures, the *on*-state (*cis*), and *off*-state (*trans*) were solved by cryo-macromolecular synchrotron crystallography at 1.45 (PDB ID: 5DTX) and 1.5 Å (PDB ID: 5DTY) resolution, respectively. (El Khatib et al. 2016). Structure elucidation of rsEGFP2 established that the *cis-trans* isomerization mechanism is similar in Hydrozoan and Anthozoan RSFPs (El Khatib et al. 2016). As rsEGFP2 is a negative RSFP, its resting state is the *on*-state. To obtain the *off*-state structure of rsEGFP2, the crystals were illuminated by a laser at 488 nm provoking an *on*-to-

off switching. Nevertheless, there are some notable differences in the *cis-trans* isomerization of RSFPs from Hydrozoan and Anthozoan. For comparison, two negative RSFPs, Dronpa (Anthozoan) and rsEGFP2 (Hydrozoan) are briefly described in the following. In Dronpa (Figure 3.1.3), upon *off*-switching the *trans* conformation (PDB ID: 2POX (Andresen et al. 2007)), the Glu144-Arg66-Glu211 triad replaces the H-bonded Glu144-His193-Glu211 triad in the *cis* conformation (PDB ID: 4EMQ (Nguyen Bich et al. 2012)). Moreover, the chromophore is stabilized by His193 or Arg66 and Arg91 *via* π -snacking or cation- π interactions with the p-hydroxybenzylidene moiety in the *cis* or *trans* conformations, respectively (Bourgeois and Adam 2012; El Khatib et al. 2016). In rsEGFP2, on the other hand, major rearrangements are observed in the vicinity of the p-hydroxybenzylidene part of the chromophore. Particularly, in the *cis* conformation (*on*-state), the oxygen of the phenolate group interacts *via* H-bonds with the side chains of His149 and Thr204 and a water molecule. On the contrary, in the *trans* conformation (*off*-state), the phenol oxygen is only H-bonded to a water molecule that is not present in the *on*-state (Figure 3.3.7). Additionally, the side chain of Glu223 binds imidazolinone moiety *via* H-bond in the *off*-state but not in the *on*-state. Structural information of rsEGFP2 in both *on*- and *off*-states was confirmed by serial femtosecond crystallography (SFX) at room temperature (RT) (Coquelle et al. 2018b). However, *off*-state heterogeneity of rsEGFP2 has been detected by SFX at RT in a more recent study (Woodhouse et al. 2020a). In addition to the previously mentioned *trans* conformation (or *trans1*), a second *trans* conformation (*trans2*) was characterized (Woodhouse et al. 2020a), whose conformation resembles the *trans* conformation of the chromophore of rsFolder2 in its *off*-state (*cf.* Section 3.3).

This chapter is divided into three sections:

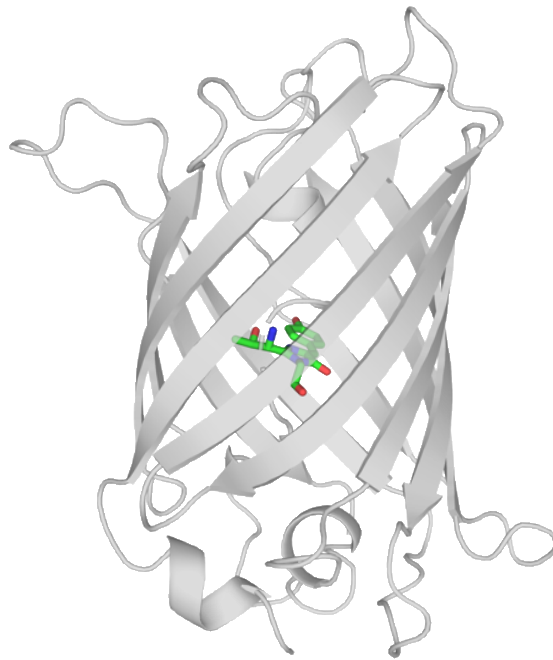
- i) Time-resolved (TR) SFX studies on rsEGFP2 mutants, V151A and V151L (Section 3.2). The amino acid in position 151 was suggested to be a steric obstacle in the *off*-to-*on* isomerization pathway (*see* Supplementary Movie 1 in (Coquelle et al. 2018b)). To test this hypothesis, a rsEGFP2 variant with a shorter (V151A; (Coquelle et al. 2018b)) and larger (V151L; (Adam et al. 2021)) amino acid side chain were generated. TR-SFX experiments at a nanosecond pump-probe delay were able to characterize ground-state intermediate structures in both mutants.

- ii) Rational control of *off*-state heterogeneity in a photoswitchable fluorescent protein provides switching contrast enhancement (Section 3.3). In-depth investigation of the *off*-state heterogeneity in the RSFPs by static SFX, cryo-MX, *in vitro* and *in vivo* photophysical characterization, UV-visible absorption spectroscopy, RESOLFT experiments, and quantum chemical calculations. This part of my work was published in (Adam et al. 2021).

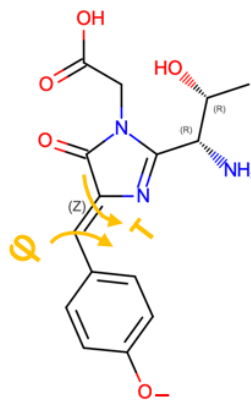
- iii) Comparison of synchrotron and XFEL room-temperature serial crystallography data using microcrystals of parental rsEGFP2 with size as low as $3 \times 3 \times 3 \mu^3$ (Section 3.3).

3.1.5 Figures

a



b



c

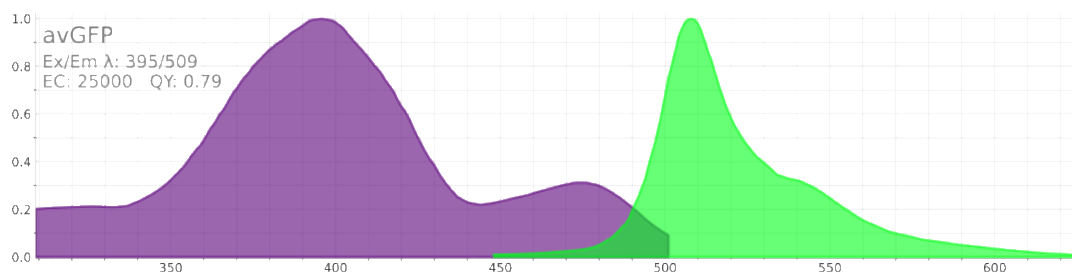
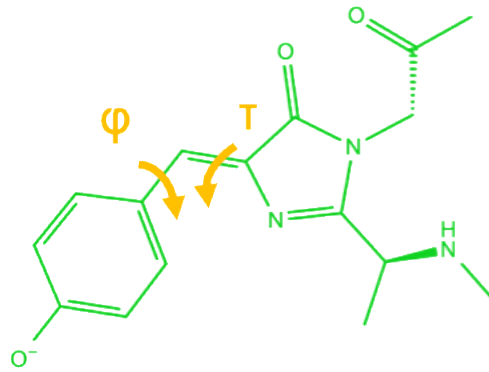


Figure 3.3.1: Structure of the GFP from *Aequorea victoria* (avGFP) and its chromophore
(a) Crystal structure of the avGFP (PDB ID: 1EMA, 1.9 Å resolution) showcasing an 11-stranded β -barrel that surrounds a chromophore. High transparency of the beta-sheets is set for better visualization of the chromophore. (b) The chromophore of avGFP is formed from

three amino acids, Ser65-Tyr66-Gly67. The two dihedral angles (τ and φ) are shown in orange. "R" and "Z" stand for Rectus and Zusammen. (c) Excitation (purple) and emission spectra (green) of avGFP. The maximum excitation and emission wavelengths are at 395 and 509 nm, respectively. The excitation coefficient is $25\,000\text{ M}^{-1}\cdot\text{cm}^{-1}$ and the FQY is 0.79. Spectra and photophysical parameters are collected from the FP base website (<https://www.fpbase.org/>) (Lambert 2019).

on-state



cis, anionic

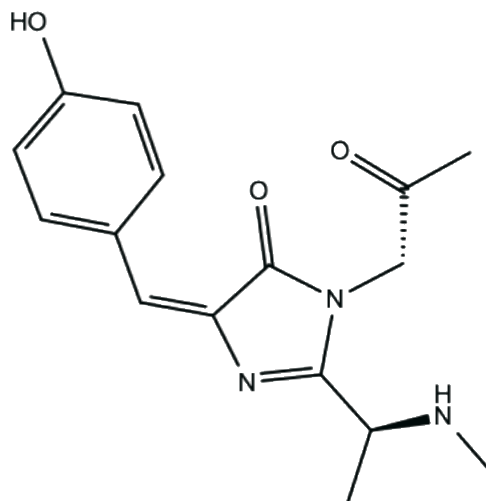
405 nm
Q.Y. = 0.23



488 nm
Q.Y. = 0.0093



off-state



trans, neutral

Figure 3.1.2: Photoswitching cycle of rsEGFP2

Chromophore in the fluorescent on-state (*cis*, anionic; upper panel) and the non-fluorescent off-state (*trans*, neutral; lower panel). The two dihedral angles (τ and φ) are shown in orange. Photoisomerization occurs after irradiating the on-state at 488 nm (*cis*-to-*trans*) and the off-state at 400 nm (*trans*-to-*cis*). The size of the arrows indicates the proportionality of the switching QY (0.23 for off-to-on and 0.0093 for on-to-off (Adam et al. 2021)).

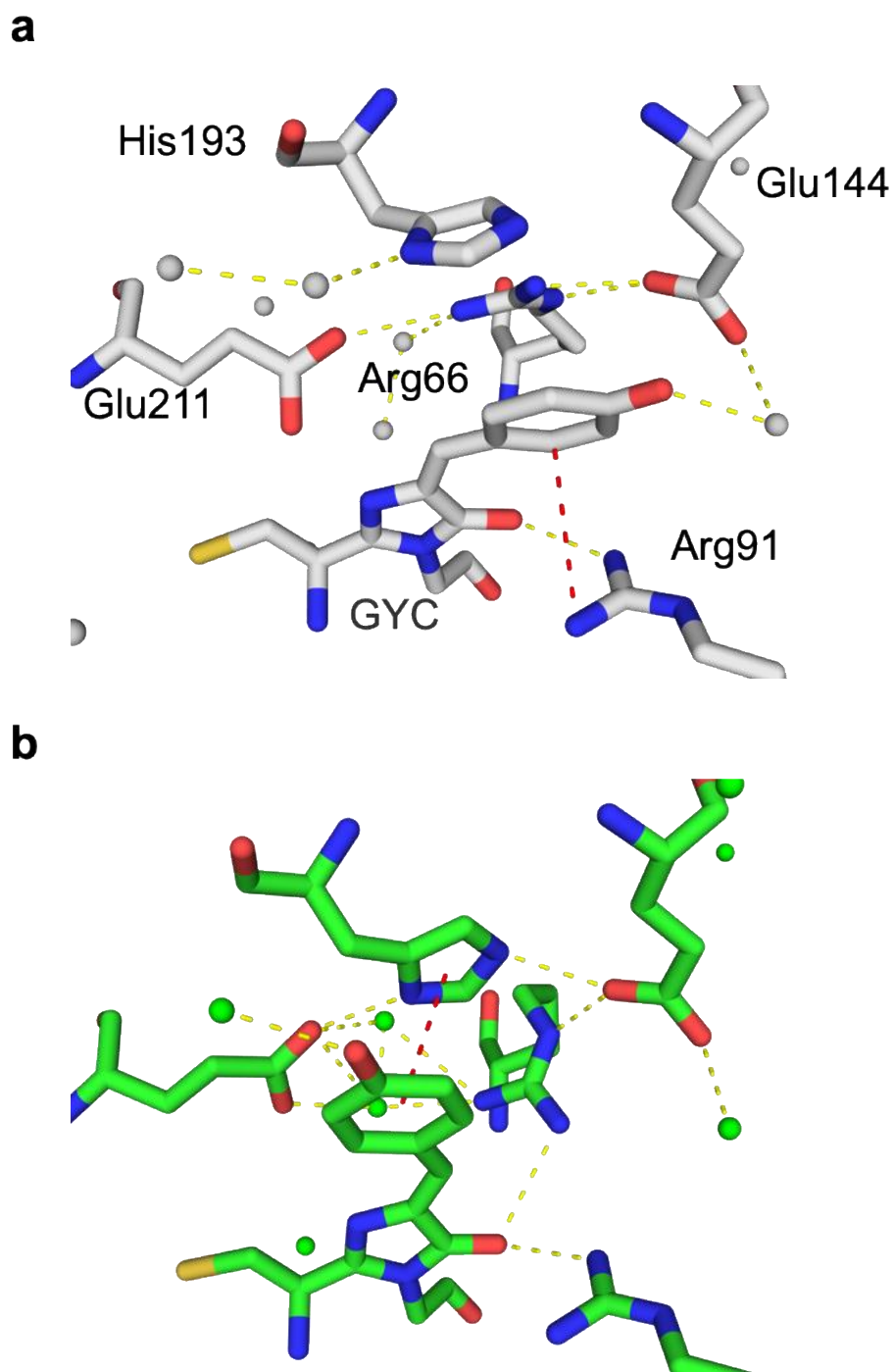


Figure 3.1.3: Chromophore pocket of the off- and on-state structures of Dronpa

Off- (a; PDB ID: 2POX (Andresen et al. 2007)) and on- (b; PDB ID: 4EMQ (Nguyen Bich et al. 2012)) state structures of Dronpa. Hydrogen and π -stacking or cation- π interactions are shown in yellow and red dashed lines, respectively. The amino acid composition of the GYC chromophore is Gly-Tyr-Cis.

3.2 Time-resolved SFX studies on rsEGFP2 mutants

3.2.1 Introduction

This section describes my contribution to a paper in preparation entitled “Trans to cis photoisomerization in fluorescent proteins is independent of the free volume”. I was involved in all steps of protein expression, microcrystallization, TR-SFX experiments and data analysis on rsEGFP2 mutants, V151A and V151L. The complete author list of this paper is:

L. M. Uriarte[#], K. Hadjidemetriou[#], A.-S. Banneville, T. R. M. Barends, N. Coquelle, R. B. Doak, F. Fieschi, L. Foucar, A. Gorel, M. Hilpert, M. Kloos, C. M. Roome, R. L. Shoeman, S. Owada, G. Schirò, M. Stricker, M. Thépaut, K. Ueda, D. You, N. Zala, A. Lukacs; G. Greetham; I. Sazanovich; K. Tono; S. R. Meech; I. Schlichting; J.-P. Colletier, M. Weik; M. Sliwa

Recently, time-resolved serial femtosecond crystallography (TR-SFX) was used to study the *off*-to-*on* switching mechanism of rsEGFP2 (Coquelle et al. 2018b; Woodhouse et al. 2020a). As the quantum yield of the *on*-to-*off* switching is 10 times lower than that of *off*-to-*on* switching, only the study of the latter mechanism is in practice possible by crystallography. During those TR-SFX experiments, a pump-probe scheme (Figure 3.2.1) was used which consisted of an optical laser at 400 nm for triggering *on*-switching and an XFEL beam to record diffraction patterns from the microcrystals after a certain time delay. As the resting state of the rsEGFP2 is the *on*-state (*cis* conformation of the chromophore), the microcrystals had to be photoswitched from the *on*- to the *off*-state by an inline cw laser (488 nm) before the injection into the XFEL beam (Schirò et al. 2017).

The excited-state intermediate structure revealed a twisted chromophore at 3% occupancy (model T) halfway between the *trans* and *cis* isomers at 1 ps after photon absorption (PDB ID: 5O8B) (Coquelle et al. 2018b). In addition to the model T, a second planar conformation (model P) of the chromophore was observed at the 1ps-intermediate state at occupancy of 4% (PDB ID: 5O8B). The main structural changes in the vicinity of the chromophore between the structures in the *off*-state and after 1 ps of light triggering were (Coquelle et al. 2018b):

- (i) a hydrogen bond of Arg97 with the imidazolinone ring of the chromophore in the *on*- and *off*-state while this interaction is absent in the excited intermediate state.
- (ii) displacement of about 1 Å of the side chain of His149 maintaining the hydrogen bond with the side chain of the Tyr146 as was the case in the *off*-state structure.
- (iii) different rotamers for the Val151 and Thr204 side chains that are coupled with the movement of the p-hydroxybenzylidene moiety of the chromophore.
- (iv) the twisting conformation of the chromophore is accompanied by a displacement along the barrel axis of the α -helix in the N-terminal of the chromophore.

Inspection of the excited-state structure 1 ps after photoexcitation indicated that steric hindrance of the valine residue in position 151 might hinder *off*-to-*on* switching (Supplementary Movie 1 in (Coquelle et al. 2018b)). To test this hypothesis, two variants of rsEGFP2, V151A, and V151L were generated. Photophysical characterization of the two variants was carried out by Dr. Virgile Adam (DYNAMOP/IBS, Grenoble), static macromolecular X-ray structures were solved by Dr. Joyce Woodhouse (DYNAMOP/IBS, Grenoble) (Adam et al. 2021). rsEGFP2-V151A had a similar *off*-to-*on* switching $QY = 2.5 \times 10^{-3}$ than parental rsEGFP2 whose value was 2.3×10^{-3} (Adam et al. 2021). Surprisingly, rsEGFP2-V151A had a better switching contrast (119) than parental rsEGFP2 (43). Regarding the rsEGFP2-V151L variant, it was shown that its brightness was higher than the one of rsEGFP2, but that the *off*-to-*on* switching QY and contrast were lower (see Section 3.3 for more information). TR-SFX, together with femtosecond transient absorption spectroscopy in solution, thus suggested that the *trans*-to-*cis* isomerization takes place in the excited state on the picosecond time scale and that a ground-state proton transfer occurs at later stages of photoswitching (Coquelle et al. 2018b). This is in accordance with what was observed in Dronpa (Warren et al. 2013; Yadav et al. 2015), an anthozoan RSFP. Moreover, transient absorption spectroscopy in D₂O confirmed that proton transfer does not occur in the excited state (Coquelle et al. 2018b).

A follow-up TR-SFX experiment on *trans*-to-*cis* isomerization in parental rsEGFP2 triggered by 400-nm laser illumination was performed with a pump-probe delay of 10 ns (Woodhouse et al. 2020a). The crystal structure (PDB ID: 6T3A) revealed a *cis* chromophore in a protein

pocket different from the *on*-state structure. Specifically, the water molecule that is H-bounded to the *cis* isomer is also present in both 10-ns intermediate and *on*-state structures. His149 in the 10-ns intermediate structure is displaced by ~ 1 Å compared to the position of the same amino acid in the *off*-state structure. Concerning the side chain of Glu223, one of its oxygen atoms of the carboxylic group forms a hydrogen bond with the imidazolinone moiety of the chromophore. In the *off*-state structure, Glu223 also forms a hydrogen bond with imidazolinone moiety of the chromophore but not in the *on*-state structure. Time-resolved UV/Vis absorption spectroscopy showed that ground-state deprotonation of the chromophore occurred on the μ s timescale, suggesting that the chromophore in the 10-ns intermediate structure is in its protonated state (Woodhouse et al. 2020a). Furthermore, spectroscopy suggested that deprotonation of the phenolate group is concomitant with the movement of the His149 side chain in its final position as it is modeled in the *on*-state structure of the rsEGFP2.

The above described TR-SFX experiment on rsEGFP2 took place in 2015 at SACLA (Woodhouse et al. 2020a). The goal of a follow-up experiment was to determine ground-state structures formed after excited-state decay of the rsEGFP2-V151A and V151L variants starting from their *off*-state. The experiment took place at BL3-EH4c at SACLA in Japan from July 27th to July 29th 2018 (proposal SACLA2018A8026) during which I participated.

3.2.2 Results and Discussion

Off-state structures of rsEGFP2 V151A and V151L variants

Prior to the injection, microcrystals of the variants V151A and V151L, whose size was about $3 \times 3 \times 3 \mu\text{m}^3$, were pre-illuminated with a 488-nm laser to generate the *off*-state by photoisomerization of the chromophore from *cis* to *trans*. The *off*-state structures of rsEGFP2-V151A and -V151L variants are described in Section 3.4 of the current manuscript (Adam et al. 2021). Briefly, when the side chain at position 151 is reduced (V151A) or increased (V151L), it results to only one *off*-state conformations with higher and lower photoswitching contrast, respectively, when compared to parental rsEGFP2.

Intermediate state structures of *rsEGFP2-V151A* and *-V151L* variants 10 ns after photoexcitation

TR-SFX data were collected according to a pump-probe scheme (Figure 3.2.1) at a 10 ns time delay for both variants. The pump-laser energy that was used was 2 and 5 μJ for the variants V151A and V151L, respectively. A pump-probe delay of 10 ns was chosen for comparison purposes with the corresponding 10-ns intermediate structure of rsEGFP2 (Woodhouse et al. 2020a).

The structural traits that emerge within 10 ns after photoexcitation may be distinguished from the *off*-state structure in a q-weighted (Ursby and Bourgeois 1997) Fourier difference map $F_{\text{obs}}^{10\text{ns-state}} - F_{\text{obs}}^{\text{off-state}}$ for both datasets (Figure 3.2.2) at 1.95 and 2.1 \AA resolution for V151A and V151L, respectively. *Xtrapol8* was used to generate these maps (De Zitter et al. 2022). The highest positive and negative peaks were observed at the positions of *cis* and *trans* chromophores, respectively, for both V151A and V151L variants (Figure 3.2.2). Peaks on the *cis* and *trans* conformations are respectively at +8.9 and -7.5 σ (+5.5 and -5.6 σ) for V151A (V151L). The chromophore movement suggested to occur from the negative to the positive peak is more noticeable in V151A than in V151L because of the proximity of the *trans* and *cis* chromophore conformations so that part of the positive and negative signals cancel out. $F_{\text{obs}}^{10\text{ns-state}} - F_{\text{obs}}^{\text{off-state}}$ maps also display important peaks on side chains in the vicinity of the chromophore. In V151A, $F_{\text{obs}}^{10\text{ns-state}} - F_{\text{obs}}^{\text{off-state}}$ peaks are detected on alternative conformations of the Tyr146 side chain that correspond to the *off*- (-4.7 σ) and *on*- state (+5.0 σ) conformations and on the side chain of Ala151 (+5.0 σ). In V151L, there is a positive peak (+4.0 σ) on the *on*-state conformation of the Leu151 side chain.

Structure refinement against extrapolated structure factor amplitudes ($F_{\text{ext}}^{\Delta t_{10\text{ns}}}$) was performed for both V151A and V151L datasets. Occupancies of 0.20 and 0.25, respectively, were estimated by *Xtrapol8* (Figure 3.2.3). Briefly, the similarity between the $F_{\text{ext}}^{10\text{ns-state}} - F_{\text{cal}}^{\text{off-state}}$ maps calculated at different occupancies and the $F_{\text{obs}}^{10\text{ns-state}} - F_{\text{obs}}^{\text{off-state}}$ map was estimated, and the occupancies were set at the value in which the similarity between the two types of maps was at its highest. A continuous density englobes the totality if the chromophore is observed in the $2F_{\text{ext}}^{10\text{ns-state}} - F_{\text{cal}}^{\text{off-state}}$ maps of both V151A and V151L 10-ns intermediate structures (Figure 3.2.4). The main and side chains of amino acids are also well defined in the extrapolated electron density maps, except for the side chain of His149 that is not well defined in the $2F_{\text{ext}}^{10\text{ns-}}$

$^{state} - F_{cal}^{off-state}$ maps for both V151A and V151L. The main difference between the *off*-state structure and the 10-ns intermediate structure in both variants is the chromophore isomerization state (Figure 3.2.5). Additionally, His149NE2 is displaced from the respective *off*-state conformation by 1.5 and 1.0 Å respectively for the intermediate structure of V151A and V151L (Figure 3.2.5). Tyr146 in the intermediate structure is displaced by 2.1 and 1.3 Å from the corresponding *off*-state structure of V151A and V151L (Figure 3.2.5). Comparison of V151A and V151L *on*-state structures with the respective intermediate structures shows that they are globally superimposable at the position of the chromophore as well as at the position of the amino acids in the chromophore pocket, except for His149 (Figure 3.2.6). Ten ns after photoexcitation, His149 has thus not reached its final *on*-state position.

A similar hydrogen bond network is observed between the 10-ns intermediate structures of the two variants (Figure 3.2.7). An exception is the hydrogen bond between the chromophore and the His149. In V151A variant (V151L variant), the chromophore makes an H-bond with His149NE2 (His149ND1) at 2.5 Å (3.3 Å) (Figure 3.2.7). The same structural observations were made with the parental rsEGFP2 concerning the chromophore and the chromophore pocket in the 10-ns intermediate structure (Woodhouse et al. 2020a). An assumption was made for the parental rsEGFP2 that the protonation state of His149 would not change between the 10-ns intermediate state and the *on*-state and that the p-hydroxybenzylidene group of the chromophore was a donor and the His149 was an acceptor of the hydrogen bond. This suggested that the chromophore of the parental rsEGFP2 was in a protonated state (Woodhouse et al. 2020a).

Furthermore, unpublished time-resolved UV/Vis and infrared spectroscopy results by Dr. Lucas M. Uriarte and Dr. Michel Sliwa from Université de Lille in France, showed by using time-resolved absorption UV/Vis spectroscopy that the protonation transfer occurs at μ s-ms time scale (Figure 3.2.8). The experiments were carried out in solution at 50 mM HEPES pH 8, 50 mM NaCl. The time-resolved difference spectrum of the V151A variant shows at 100 ns a positive band centered at 430 nm (Figure 3.2.8a, c). This positive peak evolves as a function of time and at a millisecond time scale, two bands are observed, one negative at 400 nm and one positive at 480 nm. Time-resolved difference spectrum of V151L mutant shows at 100 ns one positive band centered at 380 nm and one negative band centered at 440 nm (Figure 3.2.8b, d). At the millisecond time scale, the two peaks evolve, and new peaks appear, one positive centered at 480 nm and one negative centered at 410 nm. Experiments carried out in D₂O

solution (50 mM HEPES pD 8, 50 mM NaCl) for V151A (V151L), yielded time constants of 1.76 μ s, 20.91 μ s, 251 μ s, and 3.95 ms (4.59 μ s, 33.05 μ s, and 1.4 ms). The isotope effects are assigned to the last time constant, $k_H/k_D = 3.46$ (for the two last time constants, $k_H/k_D = 1.77$ and 2.22, respectively) (Figure 3.2.8e-h). This indicates that the last and the two evolutions in V151A and V151L variants, respectively, can be assigned to proton transfer steps. In summary, the protonation state from the *off*-state to the 10 ns after photoexcitation does not change. In other words, the chromophore at *cis* conformation after 10 ns of pump-probe delay is protonated. Moreover, time-resolved absorption UV/Vis spectroscopy suggested the absence of excited-state proton transfer. Briefly, no isotopic effect for the lifetime of excited states species was detected in time-resolved absorption UV/Vis spectroscopy measurements performed in D₂O compared with H₂O buffers (results not shown). Dr. Lucas M. Uriarte and Dr. Michel Sliwa also concluded that after 10 ns the chromophore is in its ground state as the excited state has decayed to the ground state (time delay > 10 ps) (results not shown).

3.2.3 Conclusions and Perspectives

In summary, both V151A and V151L intermediate structures solved by TR-SFX feature the same changes after 10 ns of photoexcitation which are isomerized from *trans* to *cis* of the chromophore, amino acid side chains in the chromophore pocket are in the same position as in the *on*-state structure and the only exception is His149 whose position is closer to the *off*-state structure than to the *on*-state structure. Time-resolved absorption UV/Vis spectroscopy suggested that chromophore in the 10-ns intermediate structures in both mutants is protonated and that the deprotonation of the chromophore takes place in later steps of photoisomerization (μ s-ms range) *via* ground state proton transfer process.

Further investigation of the *off*-to-*on* photoswitching of the V151A and V151L mutants is currently undergoing to capture excited-state structures by TR-SFX. Unpublished time-resolved UV/Vis and infrared spectroscopy results by Dr. Lucas M. Uriarte and Dr. Michel Sliwa suggested an excited-state isomerization (like the parental rsEGFP2 (Woodhouse et al. 2020a)) and their isomerization time-constants are approximately identical, 0.72 and 0.70 ps for V151A and V151L, respectively (results not shown). Therefore, a pump-probe delay of 1 ps at TR-SFX would reveal an excited-state structure for both mutants. Concerning the V151A

variant, a TR-SFX experiment was performed at SwissFEL in Switzerland (proposal: p17808) between May 28th and 31st, 2019 in which I participated. Data analysis is currently ongoing. A TR-SFX experiment on the V151L variant took place between February 17th and 20th, 2022 at the LCLS in the USA (proposal: LW61) during which the excited state structure 500 fs after photon absorption could be determined (not shown). Together with Ninon Zala, I expressed, purified and crystallized several grams of the V151L variant for that experiment, in which I participated remotely. Resolving the excited-state structures of both variants will clear up the *off-to-on* photoswitching of the RSFPs and allow understanding of the involvement of the chromophore pocket composition in the process (Figure 3.2.9). Shortening and lengthening the side chain of the amino acid in position 151 may or may not influence the *off-to-on* photoswitching mechanism and how this position stabilizes a twisted conformation in the excited-state structure of the parental rsEGFP2.

3.2.4 Materials and Methods

The different steps described in the “Materials and Methods” section are summarized in Table 3.2.1. The indicated steps for this project were performed in collaboration with other members of the DYNAMOP group. Steps 1 to 4 are the same as they were described previously (Ando et al. 2007; Andresen et al. 2008; Stiel et al. 2007). Here, a brief description is presented along with the input provided by colleagues:

- Plasmid construction (Step 1) was performed by Dr. Virgile Adam.
- Bacterial transformation (Step 2) was performed by Dr. Anne-Sophie Banneville and Ninon Zala.
- Bacterial culture and protein purification (Steps 3 and 4) were performed by Ninon Zala, Dr. Anne-Sophie Banneville, and myself.
- Microcrystallization (Step 5) was performed mainly by myself with the help of Dr. Joyce Woodhouse.
- Time-resolved serial femtosecond crystallography (Step 6): I participated in XFEL experiments on rsEGFP2 (LCLS, LR38, February 22nd – 26th, 2018; SACLA, SACLA2018A026, July 28th – 30th, 2018; SwissFEL, p17808, May 28th – 31st, 2019) and on FAP (LCLS, LT59, November 22nd – 25th, 2018). The full list and the

contribution of the people who participated in the TR-SFX experiments are available in Appendix 6.2 .

- All the following steps (Steps 7 to 10) were performed by myself under the guidance of Dr. Nicolas Coquelle, Dr. Jacques-Philippe Colletier, and Dr. Martin Weik.

The information that is described in the following steps regarding V151A and V151L variants is the same as they are described in (Adam et al. 2021). For more information, see Section 3.3 of the current manuscript.

Step 1: Plasmid production, site-directed mutagenesis

Site-directed mutagenesis was performed to produce V151A and V151L variants of rsEGFP2 using the primers 5'-CAACAGCCACAACGCCTATATCATGGCC-3' and 5'-CTACAACAGCCACAACCTCTATATCATGGCCG-3', respectively. The plasmid coding for rsEGFP2 was provided by Prof. Stefan Jakobs (MPI for Biophysical Chemistry, Göttingen, Germany) and was used for mutagenesis. The pQE1 plasmid is suitable for expression in *E. coli* having a gene expressing the resistance for ampicillin. It expresses either V151A or V151L variants of rsEGFP2 fused to an N-terminal His-tag. The plasmid map that was used for this project is shown in Figure 3.2.10.

Steps 2 and 3: Bacterial transformation, induction, and bacterial culture

pQE31_rsEGFP2(-V151A or -V151L) plasmids were transformed in BL21 (DE) strain of *E. coli* using heat shock (42°C for 45 s). In a Petri dish, transformed bacteria were then spread on the surface of a semi-solid, agar-based lysogeny broth (LB) medium (Bertani 1951, 2004) in the presence of ampicillin. The Petri dish was incubated at 37°C overnight. The result is shown in Figure 3.2.10 in which the bacteria transformed with the plasmid of interest appear green under blue light. This observation is the same for the transformed bacteria coding for both V151A and V151L variants of rsEGFP2. Bacteria were grown in LB medium (Auto Induction Medium) (Sezonov, Joseleau-Petit, and D'Ari 2007) for 24 hours at 37°C.

Step 4: Purification of rsEGFP2-V151A and rsEGFP2-V151L variants

Protein purification was carried out as described previously (El Khatib et al. 2016). rsEGFP2 mutants fused to an N-terminal polyhistidine tag are expressed in the cytoplasmic compartment of *E. coli* BL21 cells. Cell lysis was performed using mechanical or sonication methods. During this step, the cells were broken open to access the intracellular content. After centrifugation, the supernatant containing the soluble cell components was collected. The pellet containing the broken membrane parts of the cells or any unbroken cells was disposed of. The supernatant then underwent two consecutive chromatography steps. The first consisted in immobilized metal-affinity chromatography (IMAC) using Ni(II)-nitrilotriacetic acid (NTA) agarose (QIAGEN) as stationary phase (Hochuli, Döbeli, and Schacher 1987). Immobilized NTA resin has four coordination interactions with Ni²⁺. The remaining two coordination positions of the octahedral Ni²⁺ are accessible by two imidazole rings that are part of the histidine side chains of the His-tag part of the recombinant protein. Thus, the recombinant protein of interest is specifically bound to the stationary phase of the column whereas the other proteins that are present in the soluble lysate are not bound to the column. The recombinant protein is then eluted in the presence of free imidazole molecules whose affinity is higher than the one of the polyhistidine tag. The following step consisted in size exclusion chromatography (SEC) (Barth, Jackson, and Boyes 1994) that separates biological macromolecules according to their molecular weight. The separation of the macromolecules is based on their relative size or their hydrodynamic volume with respect to the average pore size of the packing of the column. Small macromolecules easily pass through the pores, whereas large macromolecules don't. Thus, large and small macromolecules are eluted in small and large volumes, respectively. The columns that were used for the purification of V151A and V151L variants were HiLoad[®] 16/600 Superdex[®] 75 (GE Healthcare) and HiLoad[®] 26/600 Superdex[®] 75 (GE Healthcare), respectively. After the protein purification steps, ~250 mg and ~350 mg of V151A and V151L variants, were obtained per liter of bacterial culture. In total, about eight and two grams of V151A and V151L variants were produced, respectively. The V151A mutant was purified using the SEC method at the MP3 platform (IBS, Grenoble). A significant fraction of the purified protein of the V151A variant was used for other TR-SFX experiments (LR38, LCLS, and p17808, SwissFEL) which are not described in this section. The protein was concentrated at 50 mg.mL⁻¹ and the sample was stored in 50 mM HEPES pH 7.5 and 50 mM NaCl at 4°C.

Step 5: Protein microcrystallization by seeded batch

The microcrystallization protocol was set up by Prof. Ilme Schlichting (MPI Heidelberg, Germany) and used already for producing rsEGFP2 microcrystals for earlier TR-SFX experiments (Coquelle et al. 2018b; Woodhouse et al. 2020a). The seeded batch microcrystallization method was optimized by Dr. Joyce Woodhouse (Woodhouse 2018) and used for microcrystallizing the V151A and V151L variants.

The seeded batch microcrystallization method consists of two parts: i) preparation of seeds, and ii) batch crystallization. To produce seeds, we first need to produce macrocrystals of V151A and V151L variants with vapor diffusion method using the same protocol as it was described previously for parental rsEGFP2 (El Khatib et al. 2016). Then, these macrocrystals were crushed. Three consecutive cycles of crystal crushing were performed using 1.5-, 1.0-, 0.5-mm zirconium beads contained in BeadBug™ 2.0-mL prefilled tubes (Sigma-Aldrich) using a BeadBug™ microtube homogenizer (Sigma-Aldrich). Each cycle consisted of crystal crushing for 45 s at 4,000 rpm, followed by cooling for 45 s in a stirred ice bath. The cooling step is important to keep the overall temperature of the sample as stable as possible because heating during crystal crushing may cause protein denaturation and/or crystal dissolution. Subsequently, the crushed crystals were successively filtered manually through PCTFE stainless steel frits with pore sizes of 10.0, 2.0, and 0.5 μm (IDEX Health & Science LLC) contained in the filter assembly (IDEX Health & Science LLC). Filtering ensured that the crushed crystals, to be used as seeds, had a homogeneous size of less than 0.5 μm . The seeds were stored in 2 M ammonium sulfate and 100 mM HEPES pH 8 at room temperature, protected from light. Microcrystals were obtained as described below:

- i) 1.2 mL of 3.33 M ammonium sulfate and 170 mM HEPES pH 8 (crystallization solution) were added in a 15-mL Falcon® tube.
- ii) 20 μL of seeds at 100 % (v/v) were then added to the crystallization solution accompanied by rapid mixing with a P200 pipette.
- iii) In the end, 0.8 mL of protein at 50 $\text{mg}\cdot\text{mL}^{-1}$ in 50 mM HEPES pH 7.5 and 50 mM NaCl was rapidly mixed with P1000 pipette with the crystallization solution including the seeds.

The final batch of ~2 mL contained 20 mg.mL⁻¹ of protein, 2 M ammonium sulfate, 120 mM HEPES pH 8, and 20 mM NaCl. Once microcrystals had grown and settled within 2 - 3 days, the supernatant of the batch solution was removed and a new solution was added at 2 M ammonium sulfate and 100 mM HEPES pH 8 (final crystallization buffer). The added volume was calculated to get a concentration of settled microcrystals of 10 % (v/v). The final size of microcrystals was 3 × 3 × 3 μm³ for both variants. This procedure was repeated multiple times to crystallize the total quantity of the V151A and V151L mutants in solution. The microcrystals were then stored at room temperature and protected from light.

Step 6: Data collection and online monitoring

The TR-SFX experiment was carried out at the BL2 – EH3 experimental station of SACLA (Yabashi, Tanaka, and Ishikawa 2015) (SACLA 2018A8026, 27 – 29 July 2018). Before the injection, microcrystals were resuspended to the final crystallization buffer (2 M ammonium sulfate and 100 mM HEPES pH 8) at a concentration of 6.6 % (v/v). Then, microcrystals were filtered manually through PCTFE stainless steel frits of a 20 μm pore size (IDEX Health & Science LLC). Filtering was carried out to eliminate large blocks of microcrystals so as to avoid any potential clogging of the injection system. The samples (typically 4 mL volume) were loaded into a stainless-steel sample syringe, which was then installed on an anti-settling device (Lomb et al. 2012) onto a Peltier element-cooled (20°C) syringe holder (during the experiment the hutch temperature was about 27 – 29 °C). Crystals were injected at a flow rate of 40 μL.min⁻¹ with a gas dynamic virtual nozzle (GDVN) (DePonte et al. 2008), using sample capillaries with an inner diameter of 75 μm into the helium-filled Diverse Application Platform for hard X-ray Diffraction (*DAPHNIS*) chamber (Tono et al. 2015)) at SACLA.

The objective of our TR-SFX experiment was to study photointermediates during the *off-to-on* isomerization. Since the resting state of both V151A and V151L variants is the *on*-state, the chromophore within the microcrystalline proteins needed to be switched to the *off*-state prior to the TR-SFX experiment. The required pre-illumination was carried out using a 488 nm laser (200 mW nominal power, 25 ms transit time, 300 W.cm⁻²). However, the *on-to-off* quantum yields ($\varphi_{on-to-off}$) of both V151A and V151L mutants are 11.4×10^{-3} and 6.5×10^{-3} , respectively (*cf.* Table 1 in Appendix 6.2). The pre-illumination was performed using a custom-made device inserted 2 m upstream of the GDVN nozzle into the injection tubing (Schirò et al. 2017) and the residual amount of the remaining *on*-state (or pre-illumination efficiency) state

was assessed by absorption spectroscopy on microcrystals using a Nanodrop 2000c spectrometer. Spectra analysis is described in Section 3.4.5 of the current manuscript. In the case of rsEGFP2-V151A (Figure 3.3.5b) and V151L (Figure 3.3.5c), 85% and 77% (accuracy is estimated to be approximately 10%) were switched to the *off*-state, respectively, so that 15% and 23% remained in the *on*-state, respectively.

TR-SFX data collection on rsEGFP2-V151A and -V151L variants was performed using X-ray pulses (nominal photon energy 7.6 keV, pulse length ≤ 10 fs) at a repetition rate of 30 Hz. The X-ray beam was focused to $1.3 \mu\text{m}$ (H) \times $1.4 \mu\text{m}$ (V) (FWHM), the pulse energy was $\sim 400 \mu\text{J}$. The reaction was initiated using optical laser pulses (wavelength of 400 nm, pulse length at 6 ns) at a repetition rate of 15 Hz. The pump laser had a circularly polarized beam whose spot size was about $180 \mu\text{m}$ (FWHM) and an energy per pulse of 2 (0.8 absorbed photons per chromophore; $0.91 \text{ MW}\cdot\text{cm}^{-2}$ of laser power density) and 5 μJ (2.4 absorbed photons per chromophore; $2.3 \text{ MW}\cdot\text{cm}^{-2}$ of laser power density) for the experiments on V151A and V151L variants, respectively. The pump-probe delay was set to 10 ns. Data were acquired with the octal-MPCCD detector (Kameshima et al. 2014) with eight sensor modules positioned 50 mm away from the sample. The CFEL–ASG Software Suite (CASS (Foucar et al. 2012)) was used for online monitoring of diffraction data, such as diffraction resolution, hit rate, the fraction of multiple hits, and pixel saturation.

Step 7: Data processing

NanoPeakCell (Coquelle et al. 2015) was used for the *off*-line hit finding. Hit-finding parameters were adjusted after visual inspection of the first diffraction patterns using the NanoPeakCell graphical interface.

For rsEGFP2-V151A in the 10-ns intermediate and the *off*-state, and rsEGFP2-V151L in the 10-ns intermediate and the *off*-state, 8350, 10794, 3346, and 4930 images were indexed, respectively (Table 3.2.2). The CrystFEL v.0.7.0 suite (White 2019) was used for further data processing. The data were indexed with *Mosflm* and integrated using the rings-nocen option for all datasets. Merging was performed using CrystFEL v.0.8.0 with *partialator* using the xsphere partiality model with one cycle of scaling and post-refinement for all datasets. A resolution cut-off of 1.95 and 2.1 Å for both light and dark datasets were chosen based on SNR, R_{split} , and CC* statistics (Table 3.2.2) for V151A and V151L variant datasets, respectively.

Step 8: SFX structure solution and refinement

The *off*-state SFX structures were phased by molecular replacement with *Phaser* (McCoy *et al.* 2007). As a search model was used the SFX *off*-state structure of parental rsEGFP2 (PDB entry 6T39 (Woodhouse *et al.* 2020a)) for both structures of rsEGFP2-V151A (PDB entry 7O7X) and -V151L (PDB entry 7O7W) in the *off*-state (Adam *et al.* 2021).

Refinement included positional and isotropic individual B-factor refinement in reciprocal space in *Refmac5* (Murshudov *et al.* 2011) for all structures. Model building and real-space refinement were performed with *Coot* (Emsley and Cowtan 2004). Initially, the chromophore had been omitted from the model and subsequently included and modeled as described below. Once the chromophore had been included, its position and isotropic individual B-factors were refined in reciprocal space, while the protein moiety remained fixed.

For rsEGFP2-V151A in the *off*-state, the chromophore was first modeled at 100% occupancy in the *trans1* conformation of the parent rsEGFP2 (PDB entry 7O7U (Adam *et al.* 2021)) resulting in negative $F_{\text{obs}} - F_{\text{calc}}$ peaks on the chromophore and the side chains of Tyr146 and H149 (not shown). Then, the chromophore (*cis*) and Tyr146 and H149 conformations of the rsEGFP2-V151A SFX *off*-state model (PDB entry 7O7X (Adam *et al.* 2021)) were added and their occupancies set manually. Several cycles of positional and isotropic individual B-factor refinements in reciprocal space were carried out. No major features remained in the resulting $F_{\text{obs}} - F_{\text{calc}}$ map when the *cis* and *trans1* chromophores were occupied at 20 and 80%, respectively (Figure 3.3.5b), in accordance with spectroscopy (Figure Figure 3.3.6c) that indicated 85% of the molecules were switched to the *off*-state.

For rsEGFP2-V151L in the *off*-state, the *trans2* chromophore of parental rsEGFP2 (PDB entry 7O7U (Adam *et al.* 2021)) and the *cis* chromophore of the rsEGFP2-V151L cryo-MX *on*-state model (PDB entry 7O7E (Adam *et al.* 2021)) were inserted and their respective occupancies varied manually. The resulting $F_{\text{obs}} - F_{\text{calc}}$ map was featureless when the *cis* and *trans2* chromophores were occupied at 25 and 75%, respectively (Figure 3.3.5c), in accordance with spectroscopy (Figure 3.3.6d) that indicated 77% of the molecules were switched to the *off*-state.

Step 9: Difference electron density maps

Assessment of structural changes that occurred 10 ns after pump laser excitation in both variants was performed by calculating q-weighted (qW) (Ursby and Bourgeois 1997) difference electron density maps ($F_{\text{obs}}^{10\text{-ns_state}} - F_{\text{obs}}^{\text{off-state}}$). The effect of the ambiguous structure factor value was reduced *via* q-weighting which employs Bayesian statistics. Such maps were obtained using the *Xtrapol8* program (De Zitter et al. 2022). Difference structure factors were phased using the corresponding *off*-state model from both variants. The range from low- and high-resolution cutoffs were set from 24 to 1.95 and 2.1 Å for V151A and V151L variants, respectively. The isotropic B-factor scaling method was used to scale *10 ns*-state to the *off*-state datasets.

Step 10: Structure factor extrapolation

For further investigation and characterization of the *10ns*-intermediate states in the V151A and V151L variants, extrapolated structure factors ($F_{\text{ext}}^{10\text{ns-state}}$) (Genick 2007) were calculated. This technique relies on the structure factor amplitude differences (Coquelle et al. 2018b) as stated by the following equation:

$$F_{\text{ext}}^{10\text{ns-state}} = \alpha \times (F_{\text{obs}}^{10\text{ns-state}} - F_{\text{obs}}^{\text{off-state}}) + F_{\text{obs}}^{\text{off-state}} \quad (\text{eq. 3.2.1})$$

where α is the inverse of the occupancy of this intermediate, $F_{\text{obs}}^{10\text{ns-state}}$ and $F_{\text{obs}}^{\text{off-state}}$ are the observed structure factor amplitudes of the *10ns* intermediate state and the *off*-state, respectively.

Extrapolated structure factors ($F_{\text{ext}}^{10\text{ns-state}}$) for V151A and V151L variants were phased with the corresponding *off*-state model. The occupancy, in this case, reflects the fraction of the proteins within the crystals that structurally changed upon laser irradiation at 10 ns. The same approach, as stated before, was utilized to determine α (*i. e.* 1/occupancy) (Coquelle et al. 2018b; Woodhouse et al. 2020a). Briefly, several $F_{\text{ext}}^{10\text{ns-state}}$ were calculated by varying α in eq. 3.2.1. $mF_{\text{ext}}^{10\text{ns-state}} - DF_{\text{calc}}^{\text{off-state}}$, for each α value (1/occupancy), and $F_{\text{obs}}^{10\text{ns-state}} - F_{\text{obs}}^{\text{off-state}}$ peaks at and around the chromophore were integrated. The ratio of these integrated peaks was plotted as a function of occupancy (Figure 3.2.3). Only peaks on the chromophore were considered. The value of occupancy (1/ α) was determined at the maximum of the ratio between

$mF_{\text{ext}}^{10\text{ns-state}} - DF_{\text{calc}}^{\text{off-state}}$ and $F_{\text{obs}}^{10\text{ns-state}} - F_{\text{obs}}^{\text{off-state}}$. Occupancies of 0.20 and 0.25 were estimated for V151A and V151L variants, respectively.

The V151A and V151L 10-ns intermediate state structures were refined using reciprocal and real-space refinement. Alternated cycles between *Refmac5* (Murshudov et al. 2011) and model building with *Coot* (Emsley and Cowtan 2004) were performed starting from the respective *off*-state models against the extrapolated structure factor amplitudes.

3.2.5 Figures and Tables

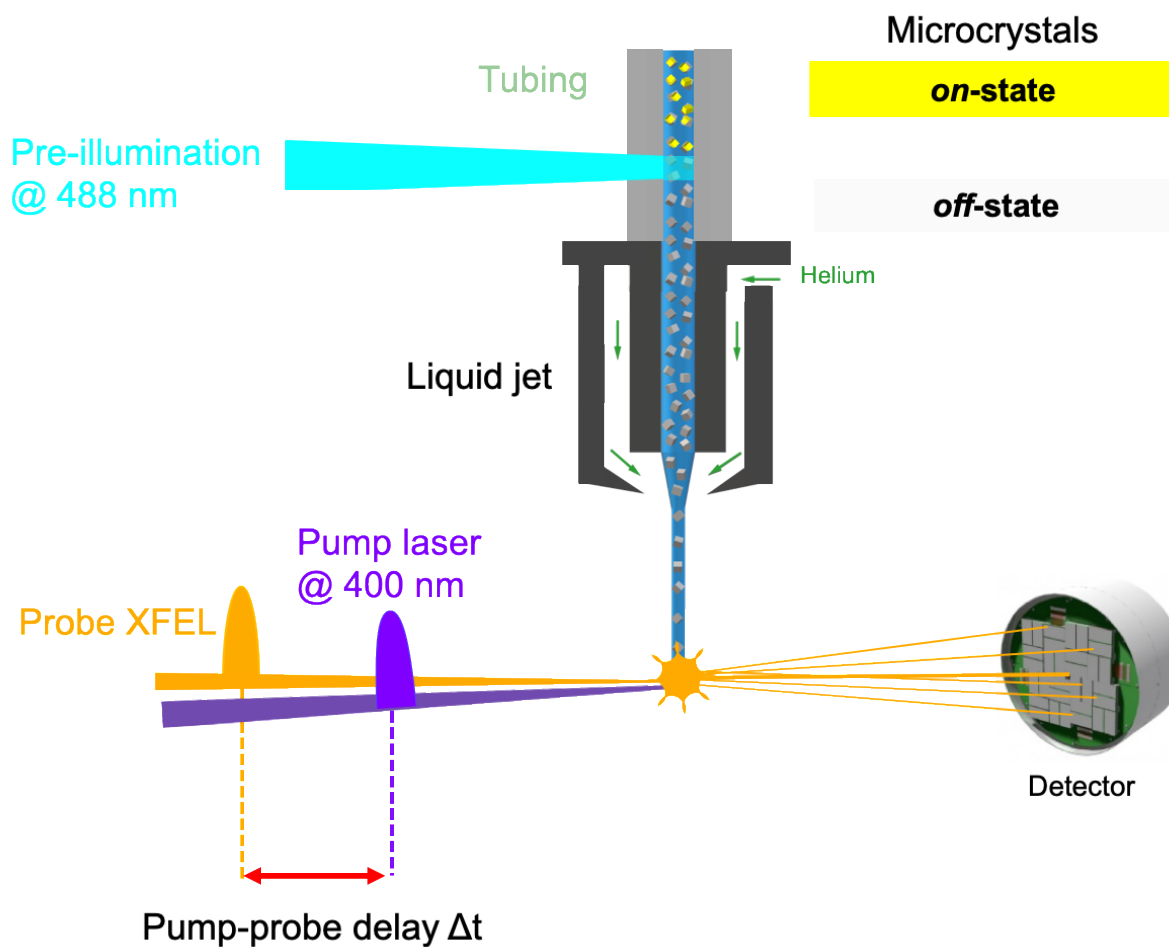


Figure 3.2.1: TR-SFX pump-probe scheme to study *rsEGFP2 -V151A* and *-V151L* intermediate states

The resting state of the microcrystalline protein is in the on-state. A pre-illumination laser at 488 nm switches the proteins to the off-state prior to sample injection. Optical pump pulses trigger photoswitching and XFEL probe pulses generate diffraction patterns that allow the determination of intermediate-state structures. The pump-probe delay was set to 10 ns.

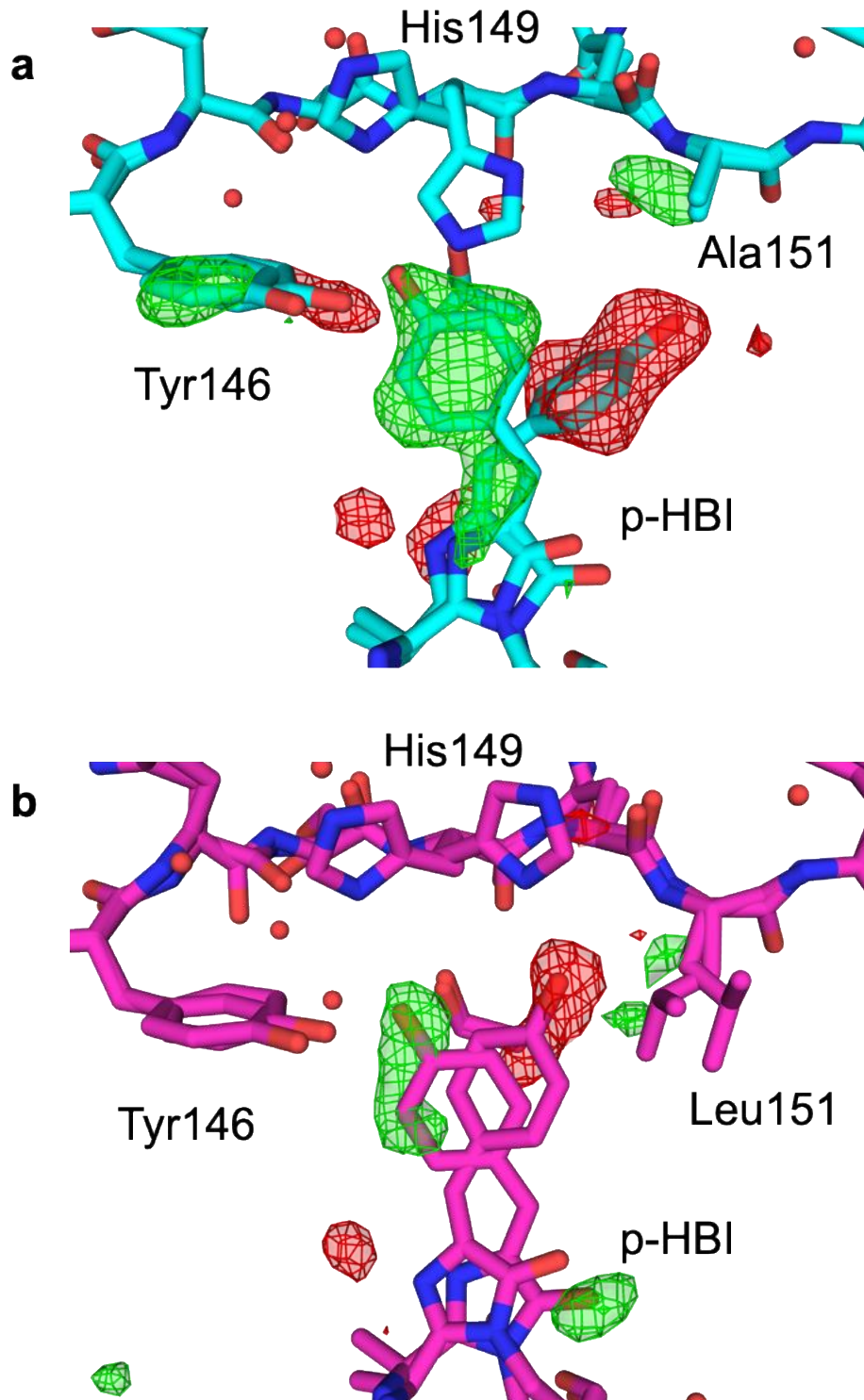


Figure 3.2.2: Fourier difference maps of rsEGFP2-V151A -V151L 10 ns after photoexcitation

Evolution of the chromophore after pumping at 400 nm at 10 ns time delays of rsEGFP2-V151A (a) and of rsEGFP2-V151L (b). q -weighted Fourier difference maps $F_{obs}^{\Delta t, 10ns} - F_{obs}^{off-state}$ ($+3.5 \sigma$ (green) and -3.5σ (red)) of the two variants are shown. In off-state structures

rsEGFP2-V151A (PDB ID: 7O7V) and V151L (PDB ID: 7O7X), cis and trans conformations are 85% and 15 %, and 77% and 23 %, respectively. The maps were generated at 1.95 and 2.1 Å resolution for V151A and V151L, respectively.

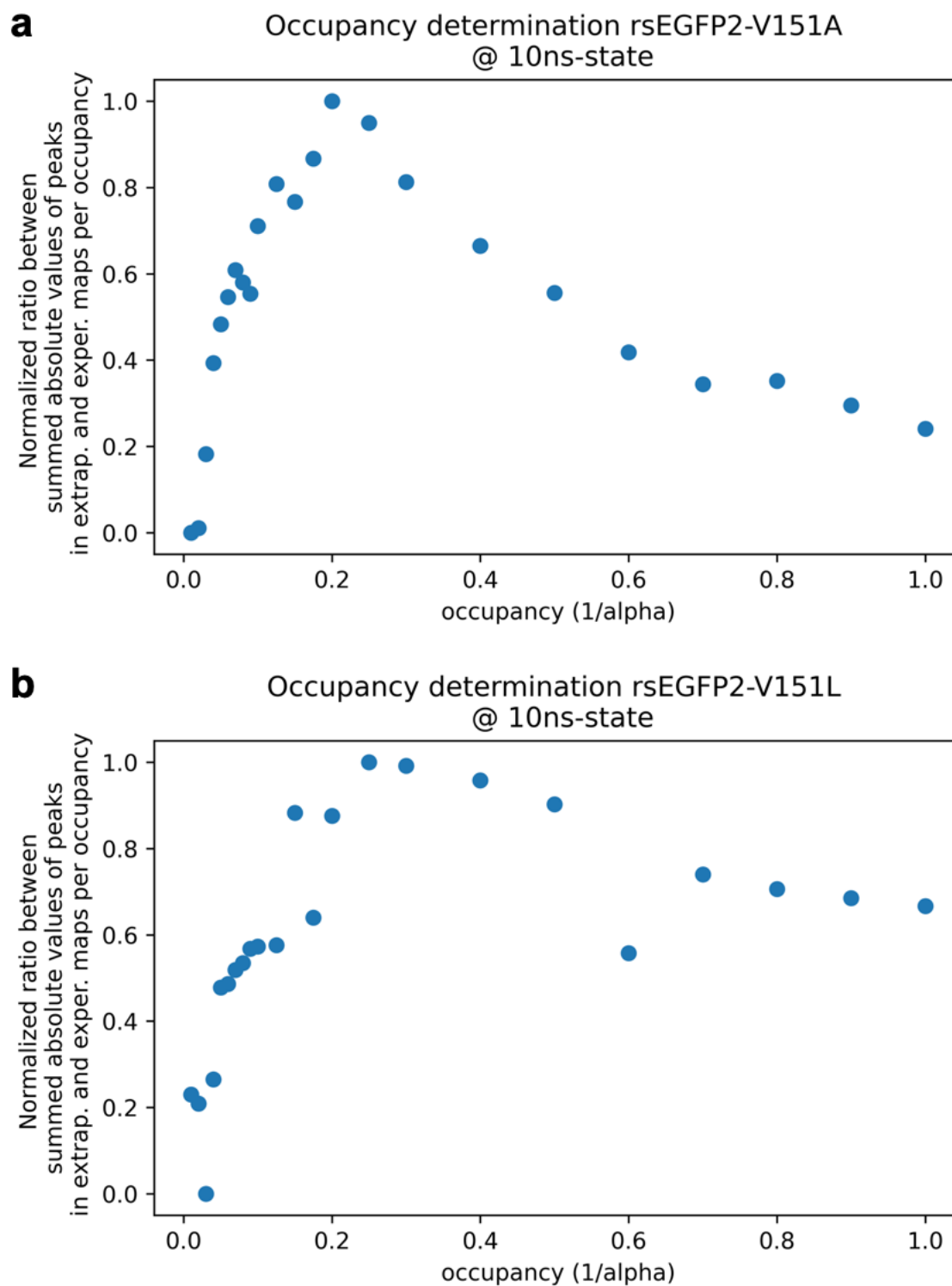


Figure 3.2.3: Occupancy determination of the extrapolated structure of the 10-ns intermediates for V151A and V151L variants

Determination of the occupancy, corresponding to the inverse of the weighting factor α of the 10ns structures for V151A (a) and V151L (b) at 1.95 and 2.1 Å resolution, respectively. The

ratio of integrated peaks in the $F_{ext}^{10ns_state} - F_{calc}^{off_state}$ map and of integrated peaks in the $F_{obs}^{\Delta t_10ns} - F_{obs}^{off_state}$ map, normalized to its maximum value, is plotted as a function of the occupancy. Occupancies of 0.20 and 0.25 were estimated for V151A and V151L, respectively. Only peaks around the chromophore were used for α determination.

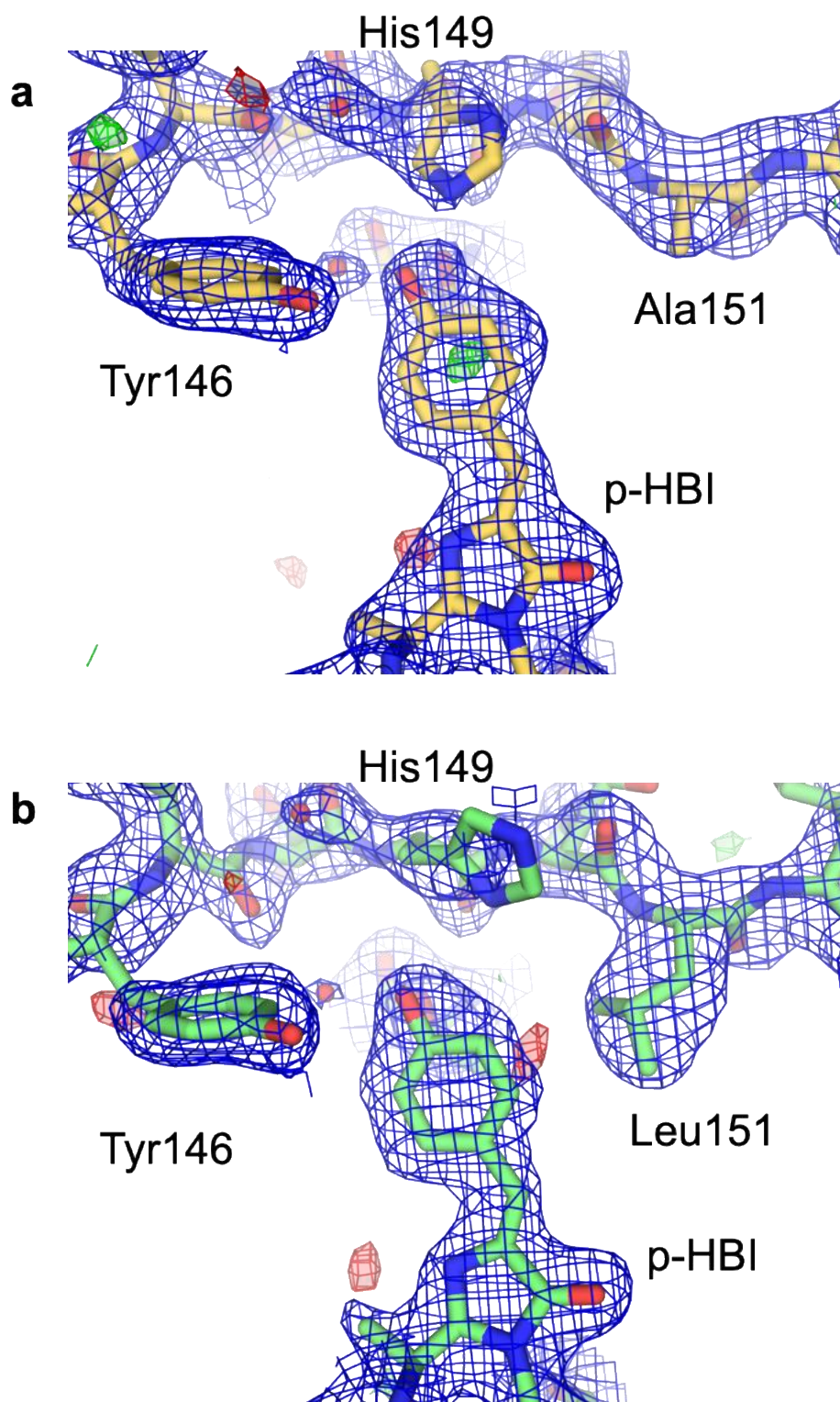


Figure 3.2.4: Extrapolated structures of 10-ns intermediates of rsEGFP2-V151A and V151L variants 10 ns after photoexcitation of the off-state

Refined extrapolated structures for V151A (a) and V151L (b) 10 ns after photoexcitation. Extrapolated structure factor amplitudes were calculated at 1.95 and 2.1 Å resolution and with

occupancies of 0.20 and 0.25 for V151A and V151L, respectively. $2F_{\text{ext}}^{\Delta t-10\text{ns}} - F_{\text{cal}}^{\text{off-state}}$ are contoured at 1σ (blue) and $F_{\text{ext}}^{\Delta t-10\text{ns}} - F_{\text{cal}}^{\text{off-state}}$ at $+3 \sigma$ (green) and -3σ (red).

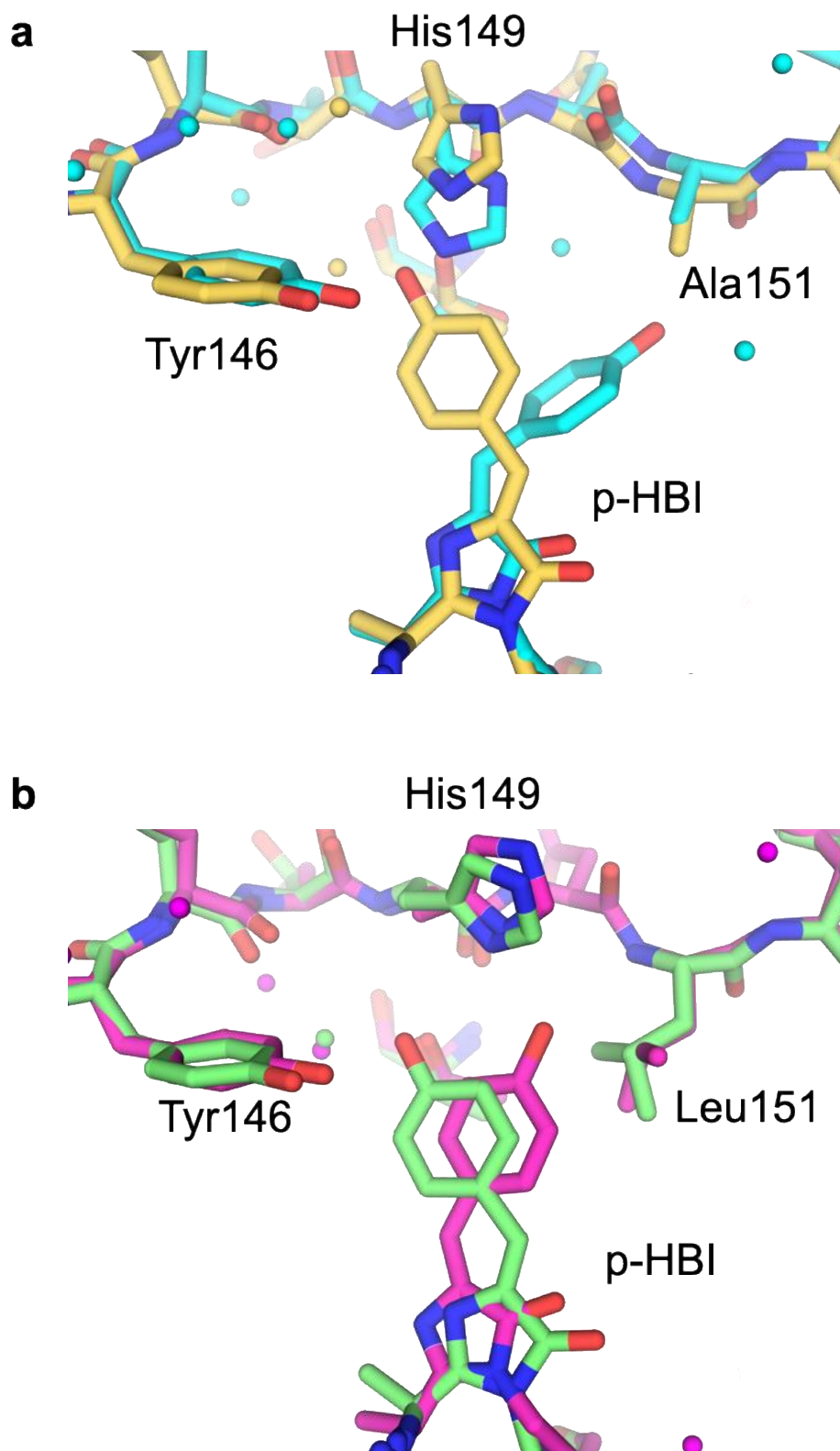


Figure 3.2.5: Overlay of 10-ns intermediate-state models of rsEGFP2-V151A and -V151L and their corresponding off-state models

Chromophore pocket of V151A (a) and V151L (b). Off-state models are shown in cyan and magenta for V151A (PDB ID: 7O7V) and V151L (PDB ID: 7O7X), respectively. 10-ns

intermediate-state models are shown in yellow and light green for V151A and V151L, respectively. The alternate conformations that correspond to the remaining on-state were excluded from the off-state models.

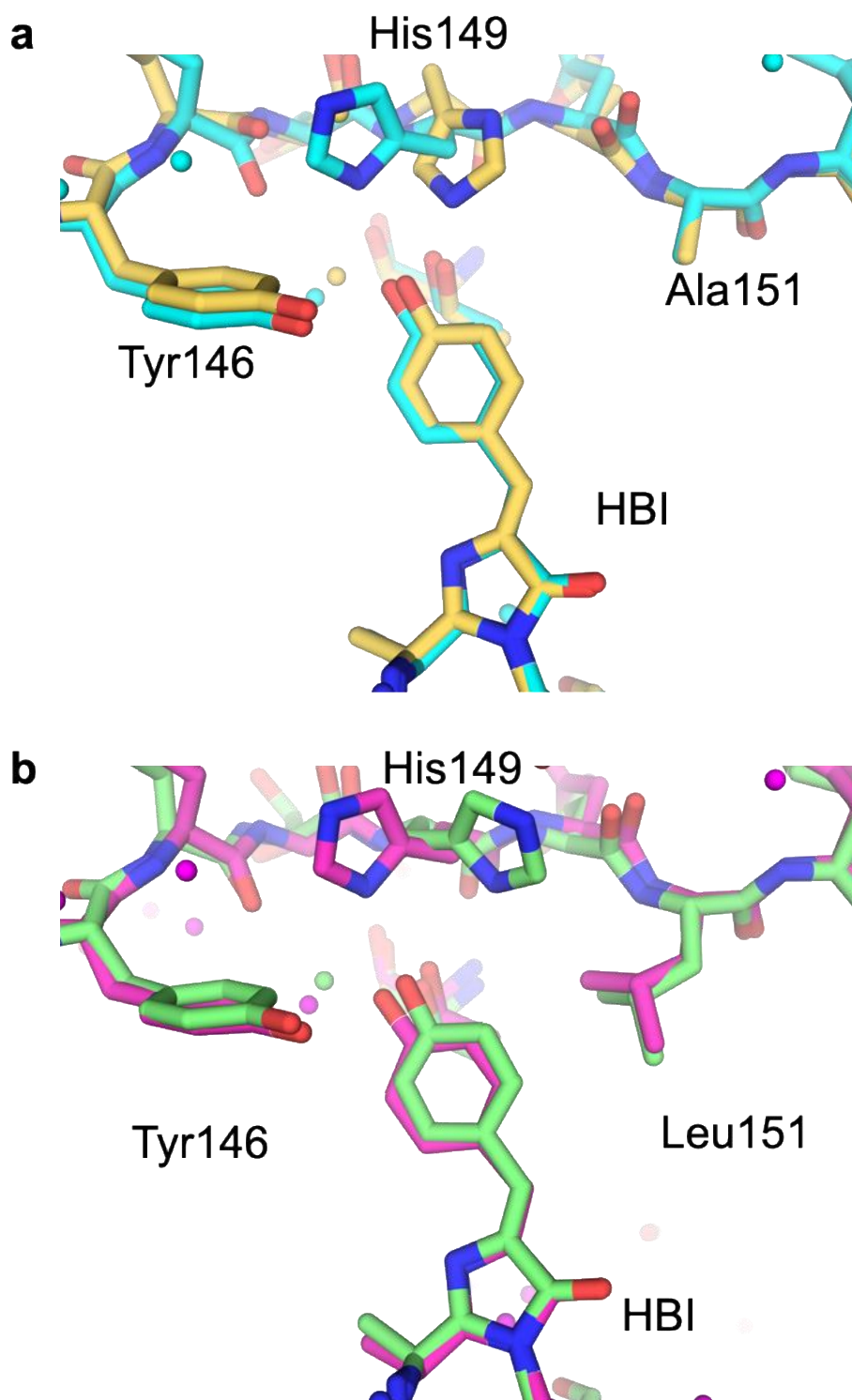
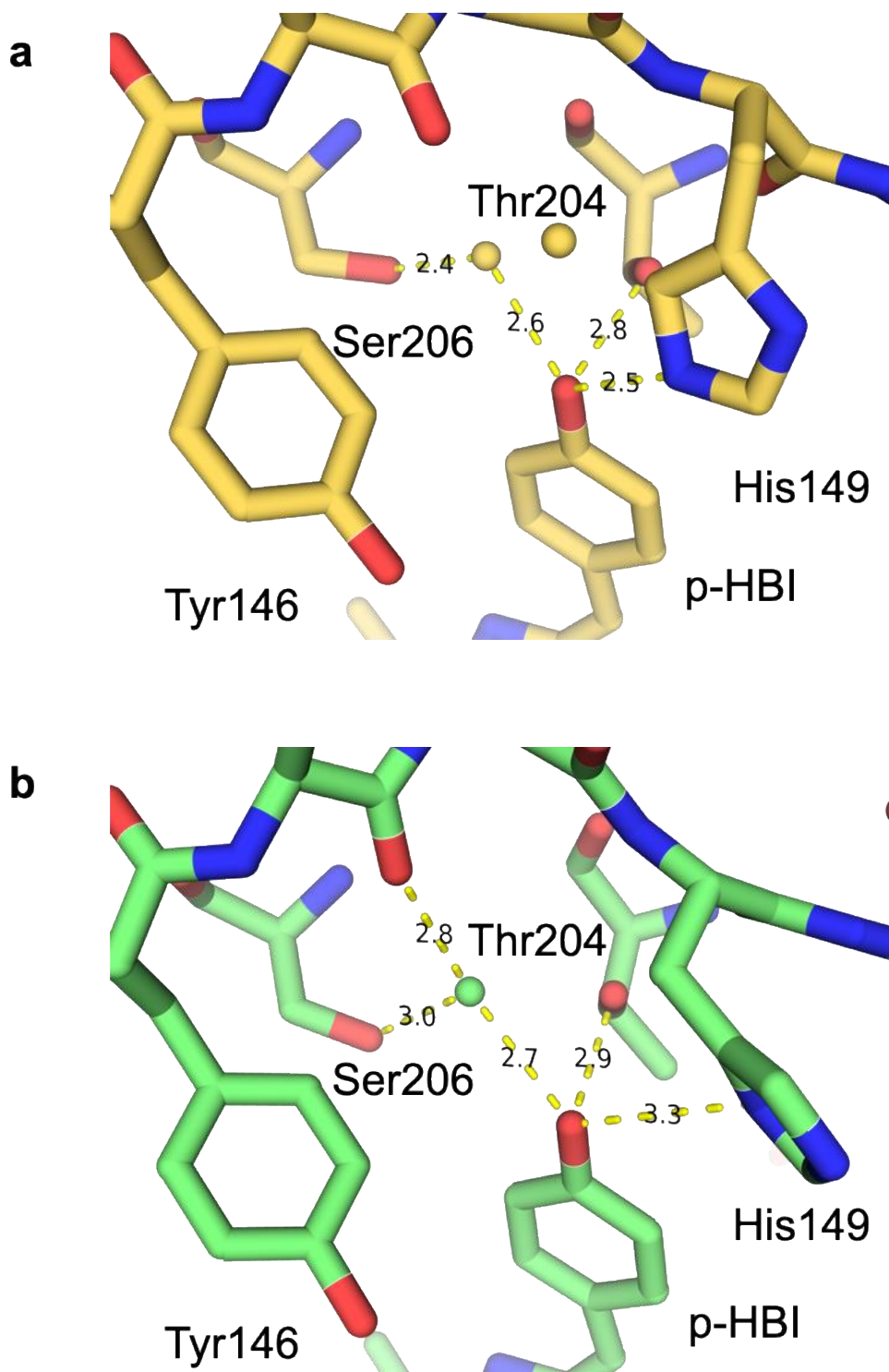


Figure 3.2.6: Overlay of 10-ns intermediate-state models of rsEGFP2-V151A and -V151L and their corresponding on-state models

Chromophore pocket of the V151A (a) and V151L (b). On-state models are shown in cyan and magenta for V151A (PDB ID: 7O7V) and V151L (PDB ID: 7O7X), respectively. 10-ns

intermediate-state models are shown in yellow and light green for V151A and V151L, respectively.



*Figure 3.2.7: Hydrogen bonding distances in the vicinity of the *p*-hydroxybenzylidene group of the chromophore in the 10-ns intermediate-state models of rsEGFP2-V151A and -V151L. The environment of the chromophore pocket in its 10-ns intermediate-state structure of V151A (a) and V151L (b). Water molecules are shown as spheres. Distances are in Angstrom.*

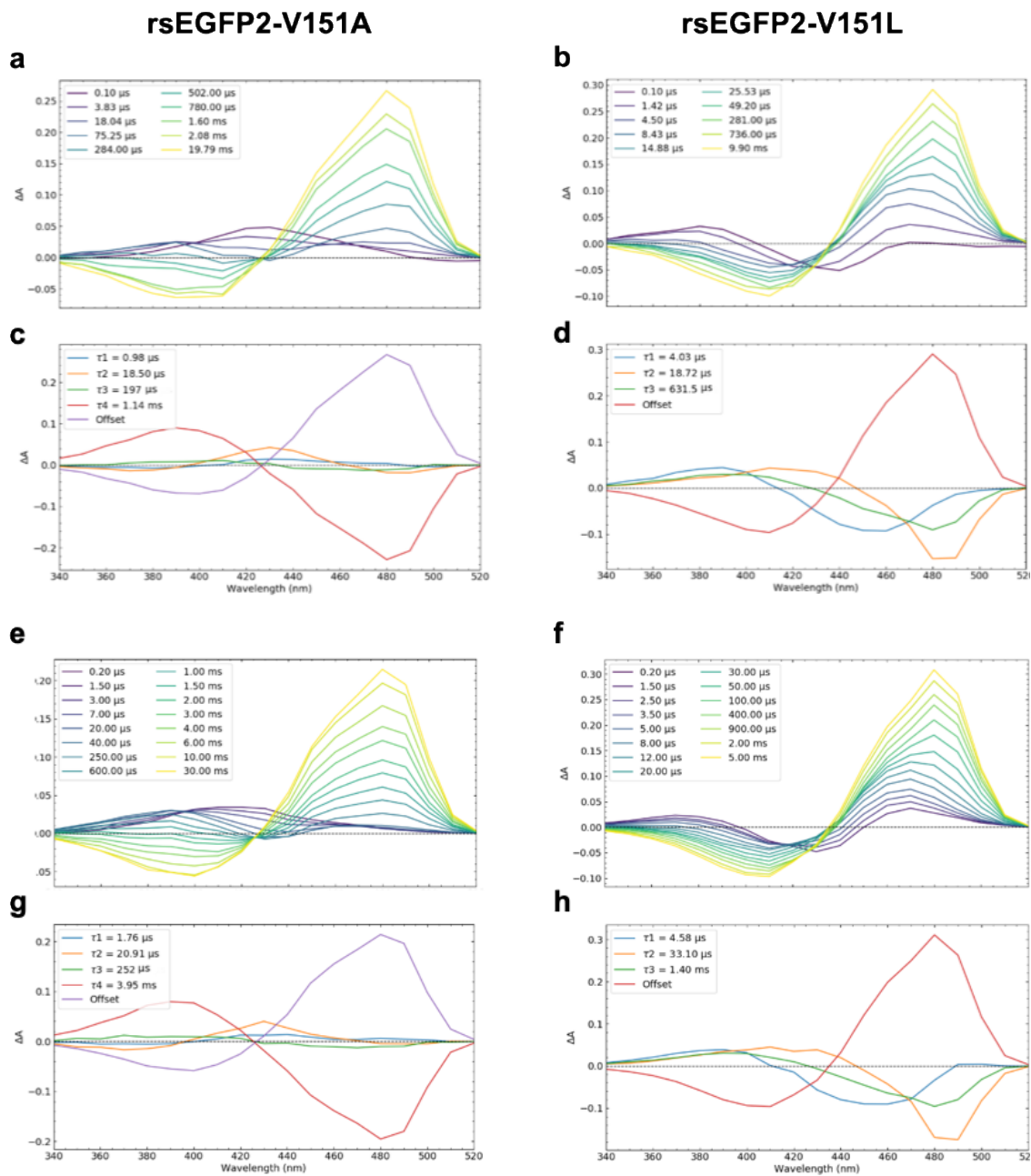


Figure 3.2.8: Time-resolved absorption UV/Vis spectroscopy of V151A and V151L mutants in solution

Time-resolved difference absorption spectra between 100 ns to 10 ms, recorded after a 410 nm nanosecond excitation of the off-state for the V151A (a) and V151L (b) (50 mM HEPES pH 8, 50 mM NaCl). The panels c (V151A) and d (V151L) correspond to the decay associated spectra reconstructed using the pre-exponential factors obtained from the global fit analysis of the raw data with a weighted sum of exponential decay functions. Time-resolved difference absorption spectra from 200 ns to the ms range in D₂O solution (50 mM HEPES pD 8, 50 mM NaCl) were recorded after a 410 nm nanosecond excitation of the off-state for the V151A (e) and V151L (f)

variants. The panels g (V151A) and h (V151L) correspond to the decay-associated spectra obtained from global fitting the raw data with a weighted sum of exponential decay function. The spectra without laser excitation were subtracted to calculate the difference spectra.

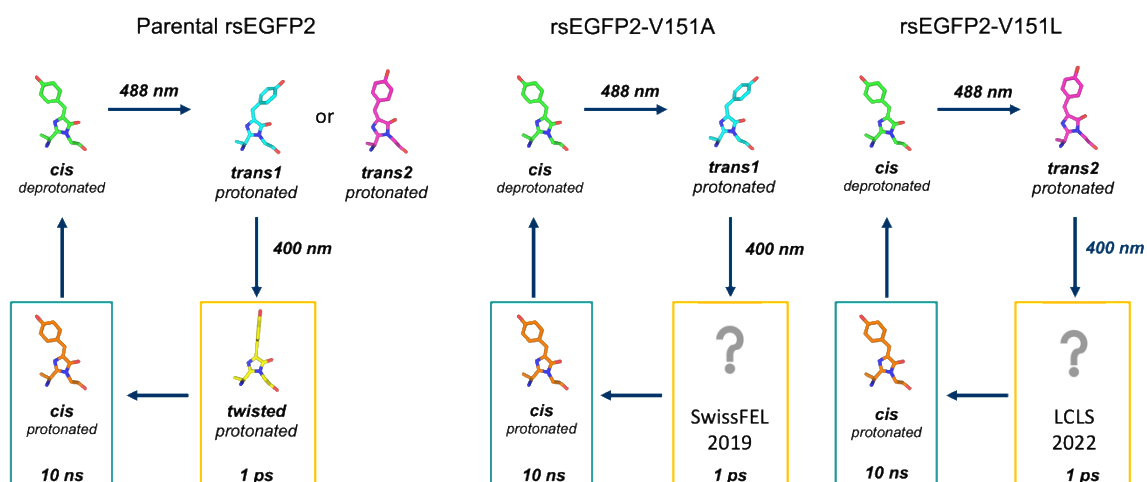


Figure 3.2.9: off-to-on isomerization mechanism in parental rsEGFP2 and its mutants V151A and V151L

TR and static SFX structures of parental rsEGFP2 and its mutants V151A and V151L allow understanding photoswitching mechanism in RSFPs. Complete off-to-on isomerization mechanism of parental rsEGFP2 was suggested previously resolving excited-state structure at 1 ps (Coquelle et al. 2018b) and ground-state structure at 10 ns (Woodhouse et al. 2020a) as well as on- and off-state structures (Woodhouse 2018; Woodhouse et al. 2020a). Static structures of on- and off-state of the V151A and V151L were resolved recently (Adam et al. 2021). Ground-state structures of both mutants at 10 ns are described in this section. The off-to-on isomerization mechanism in both mutants will be completed by resolving the excited-state structures at 1 ps. For V151A, the TR-SFX experiment took place in SwissFEL (proposal: p17808) in 2019, and data analysis is ongoing. For V151L, the TR-SFX experiment took place in February 2022 at the LCLS (proposal: LW61). Static structures in the off-state for parental rsEGFP2 and its mutants are discussed in Section 3.4.

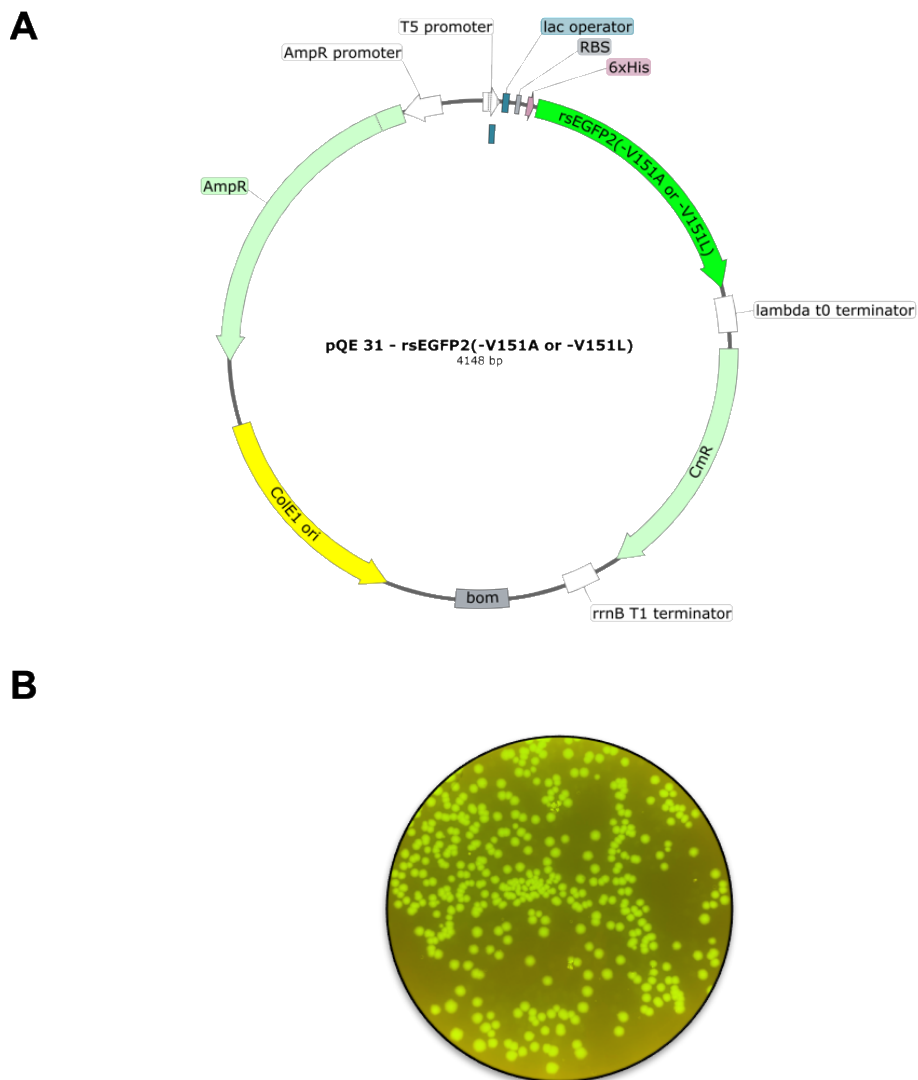


Figure 3.2.10: Plasmid design for rsEGFP2-V151A and -V151L, and transformed bacteria. (A) T5 promoter: bacteriophage T5 promoter for *E. coli* RNA polymerase with embedded lac operator; RSB: strong bacterial ribosome binding site; 6 xHis: His-Tag; rsEGFP2(-V151A or -V151L): gene coding for rsEGFP2-V151A or -V151L; Lambda t0 terminator: Transcription terminator from phage lambda; CmR: Chloramphenicol-resistance gene; rrnB T1 terminator: Termination region T1 of the rrnB gene coding for ribosomal RNA in *E. coli*; AmpR promoter: promoter for ampicillin resistance; AmpR: transcriptional regulator for the *Citrobacter freundii* ampC β -lactamase gene; ColE1 ori: ColE1 origin of replication; bom: basis of mobility. The figure was prepared by SnapGene Viewer software (from Insightful Science; available at snapgene.com). (B) Bacterial cultures on Petri dish expressing the rsEGFP2-V151L that appear green under blue light. Same observation as rsEGFP2-V151A.

Step 1	Plasmid Construction
Step 2	Bacterial Transformation
Step 3	Bacterial Culture
Step 4	Protein Purification
Step 5	Microcrystallization
Step 6	Serial Femtosecond Crystallography
Step 7	Data Analysis
Step 8	Model Building And Structure Refinement
Step 9	Fourier Difference Map
Step 10	Structure Factor Extrapolation

Table 3.2.1: Summary of the steps described in the Materials and Methods section

Dataset	rsEGFP2-V151A	rsEGFP2-V151L
Pump-probe delay	10 ns	10 ns
Data collection and processing		
Space group	$P2_12_12_1$	$P2_12_12_1$
Unit cell parameters		
a (Å)	51.8 ± 0.2	51.8 ± 0.2
b (Å)	62.7 ± 0.2	62.9 ± 0.2
c (Å)	71.6 ± 0.3	71.9 ± 0.3
Indexed images	8,350	3,346
Resolution (Å)	24– 1.95 (2.00 – 1.95)	24– 2.10 (2.15 – 2.10)
Observations	1,621,917 (59,384)	601,559 (21,612)
Unique reflections	18,182 (1,176)	14,733 (958)
R _{split} [#] (%)	8.0 (81.5)	14.1 (80.0)
CC*	0.999 (0.826)	0.996 (0.799)
I / σ(I)	6.3 (1.3)	4.5 (1.4)
Completeness (%)	100 (100)	100 (100)
Multiplicity	115 (50)	52 (23)
Refinement strategy	Difference refinement	Difference refinement
Resolution (Å)	10– 1.95 (2.00 – 1.95)	24 – 2.1 (2.15 – 2.10)
Number of reflections	16,582 (1,237)	13,421 (977)
R _{free}	39.7 (51.6)	39.8 (51.2)
R _{work}	26.9 (49.8)	31.3 (40.8)
Number of protein atoms	2,096	2,107
Number of ligand atoms	20	20
Number of water atoms	111	60
B-factor protein (Å ²)	42.85	39.39
r.m.s.d. bond lengths (Å)	0.01	0.01
r.m.s.d. angles (°)	1.717	1.796
Ramachandran favored	95.20	94.32
Ramachandran allowed	4.80	4.74
Ramachandran outliers	0.87	0.44
Rotamer outliers	13.14	10.92
C-beta outliers	0	0
Clashscore	13.33	18.72
Riso,free	10.37	13,04
Riso,work	9.89	13,82
CCiso,free	0.9924	0,9820
CCiso,work	0.9933	0,9817

Table 3.2.2: TR-SFX data collection and refinement against extrapolated structure factor amplitudes statistics of the structures of V151A and V151L.

3.3 Rational control of *off*-state heterogeneity in a photoswitchable fluorescent protein

3.3.1 Introduction

This section describes my contribution to the preprint paper entitled “Rational control of structural *off*-state heterogeneity in a photoswitchable fluorescent protein provides switching contrast enhancement” (Appendix 6.2) and how my results complement those of my colleagues. Specifically, I was involved in all steps of SFX experiments on parental rsEGFP2 as well as its mutants V151A and V151L. Finally, I carried out the final structure refinement and validation steps of the rsEGFP2-V151A and -V151L variants determined from cryo-MX data collected at the ESRF synchrotron.

Several factors determine a given RSFP's usability for live-cell RESOLFT nanoscopy. On the one hand, any relevant RSFP must be a suitable fusion tag with a low dimerization proclivity and a rapid maturation rate. It must also display a suitable set of photophysical characteristics. There are five parameters that are crucial for RESOLFT imaging. These are the brightness in the *on*-state, photoswitching speed, residual fluorescence in the *off*-state, photoswitching fatigue and photoswitching contrast (Figure 3.3.1). These parameters are discussed below (Adam et al. 2021; Jensen et al. 2020):

- i) Brightness. It is calculated by multiplying the extinction coefficient by the fluorescence quantum yield.
- ii) Photoswitching speed. This parameter specifies the time necessary to convert the proteins from maximum to minimum fluorescence intensity (from *on*- to *off*-state) or *vice versa*.
- iii) Residual fluorescence in the *off*-state.
- iv) Photoswitching fatigue. It refers to the percentage of proteins that are degraded after a specific number of photocycles. A highly photostable RSFP, for example, may be switched thousands of times before losing half of its initial brightness.

- v) Photoswitching contrast. It is defined as the ratio of the *on*-state fluorescence to the residual *off*-state fluorescence.

This section represents new insights on reversibly photoswitchable fluorescent protein (RSFP) structure and function. It is described as a relationship between the photoswitching contrast and the chromophore conformation in the non-fluorescent *off*-state. Photoswitching contrast is a critical parameter that substantially determines the resolution limit in super-resolution microscopy. Structural heterogeneity in the *off*-state was reported previously (Woodhouse et al. 2020a), consisting of two chromophore conformations, named *trans1* and *trans2* (Figure 1 in (Woodhouse et al. 2020a)) revealed by room temperature SFX. Both conformers differ in their twist and tilt dihedral angles (ϕ and τ dihedral angles (Figure 3.1.2)) as well as in protein environment and H-bonding network. When crystals with a contracted unit cell were studied, cryo-crystallographic synchrotron data revealed a comparable *trans2* isomer following *off*-switching of an rsEGFP2 variation carrying a monochlorinated chromophore, whereas crystals with a larger unit cell had a conformation similar to *trans1* (Chang, Romei, and Boxer 2019). As revealed by static SFX, *trans1* and *trans2* conformers are found on each side of the Val151 side chain (Woodhouse et al. 2020a). Moreover, the same amino acid was suggested to be a steric obstacle in the *off*-to-*on* isomerization pathway (*see* Supplementary Movie 1 in (Coquelle et al. 2018b)). To test this hypothesis, a rsEGFP2 variant with a shorter amino acid side chain in position 151 was generated, *i.e.* the valine was replaced with alanine (V151A variant; Coquelle et al. 2018).

The study englobes contributions of a large consortium from different disciplines such as X-ray crystallography at synchrotrons and XFELs, *in vitro* and *in vivo* photophysical characterization, UV-visible absorption spectroscopy, RESOLFT experiments, and quantum chemical calculations.

3.3.2 Results

Structural heterogeneity in the off-state of parental rsEGFP2

To corroborate the observation of a second *trans* isomer in parental rsEGFP2 (Woodhouse et al. 2020a), a follow-up SFX experiment was carried out at the Linac Coherent Light Source (LCLS) using microcrystals of parental rsEGFP2 of the same crystal batch used earlier (Coquelle et al. 2018b; Woodhouse et al. 2020a). The *on*-state crystals were photoswitched by 488 nm light (Schirò et al. 2017) and the room-temperature (RT) structure of the resulting *off*-state was solved at 1.7 Å resolution (PDB entry 7O7U). Both *trans1* and *trans2* chromophore conformations are again present (Figure 3.3.2, Table 3.3.1). They agree well with those observed earlier (Woodhouse et al. 2020a), as well as with those observed in cryo-crystallographic structures of a rsEGFP2 variant containing a monochlorinated chromophore (Chang et al. 2019) (Figure 3.3.3). The *trans2* conformation is similar to the one adopted by rsFolder in its *off*-state (El Khatib et al. 2016) (Figure 3.3.4).

Structural heterogeneity bisected in the off-states of parental rsEGFP2 V151A and V151L variants

Given that the *trans1* and *trans2* chromophore conformations lie on either side of the V151 side chain in parental rsEGFP2 (Figures 3.3.2-4), we reasoned that this residue could also control the *off*-state heterogeneity. In addition to the rsEGFP2 variant with a shortened side chain (V151A (Coquelle et al. 2018b)), one with an enlarged (V151L) side chain was therefore generated and non-fluorescent *off*-state structures of both variants were solved from RT SFX data collected at the SPring-8 Angstrom Compact free electron Laser (SACLA) from microcrystals after 488 nm light illumination (Figure 3.3.5, Table 3.3.1).

The *off*-state structures (V151A: PDB entry 7O7X, V151L: PDB entry 7O7W) display only one chromophore conformation: *trans1* for V151A (Figure 3.3.6a) and *trans2* for V151L (Figure 3.3.6b). Absorption spectroscopy indicates that about 85% and 77% of microcrystalline rsEGFP2-V151A and -V151L chromophores have switched from the *on*- to the *off*-state, respectively (Figure 3.3.6c and 6d). *trans1* and *trans2* chromophore conformations were modelled at 80% (75%) occupancy in rsEGFP2-V151A (-V151L) and the residual *cis* conformer at 20% (25%). Spectroscopic and crystallographic *on*- and *off*-state occupancies are thus consistent. In addition to differences in chromophore conformations, the *off*-states of the two variants also differ in their His149 and Tyr146 conformations.

In the *off*-state of the V151A variant, His149 forms a hydrogen bond with Tyr146 and the *trans1* chromophore forms a hydrogen bond with a water molecule (distance: 2.7 Å, Figure 3.3.6a, Figure 3.3.7c), whereas in the *off*-state of the V151L variant His149 is hydrogen-bonded to the *trans2* chromophore (distance of 2.5 Å between the chromophore phenol group and His149ND1; Figure 3.3.6b, Figure 3.3.7b). Synchrotron cryo-crystallography structures of rsEGFP2-V151A (*off*-state: PDB entry 7O7C, *on*-state: PDB entry 7O7D) and -V151L (*off*-state: PDB entry 7O7H, *on*-state: PDB entry 7O7E) also feature a *trans1* and *trans2* chromophore in their *off*-state, respectively (Figure 3.3.8b, d; Table 3.3.2) and a *cis* chromophore in the *on*-state (Figure 3.3.8a, c; Table 3.3.2).

Overall, the RT SFX structures strongly suggest that the conformational *off*-state heterogeneity (*trans1*, *trans2*) seen in parental rsEGFP2 is eliminated in the rsEGFP2-V151A and -V151L variants, with *trans1* being occupied in the former and *trans2* in the latter. Thus, the residue at position 151 controls the *off*-state chromophore conformations.

3.3.3 Discussion

Comparison of trans1 and trans2 off-state chromophore conformations in parental rsEGFP2 determined from data collected during three different SFX experiments

In addition to the well-documented *trans1* conformation of the *off*-state chromophore (Coquelle et al. 2018b; El Khatib et al. 2016), a second conformation, *trans2*, has been reported for crystalline parental rsEGFP2 (Chang et al. 2019; Woodhouse et al. 2020a). Here, we confirm the observation of *trans2* in parental rsEGFP2 (Figures 3.3.3-4) and provide evidence for its existence in rsFolder2 (Supplementary figure S6 of Appendix 6.2). rsFolder2 is a super folding variant of rsEGFP2 and it has eight amino acid mutations compared to parental rsEGFP2.

Occupancies of chromophore conformations differ in *off*-state structures determined from data collected during three different SFX experiments, *i.e.* 10%, 90%, and 0% (Coquelle et al. 2018b), 10%, 65%, and 25% (Woodhouse et al. 2020a), 30%, 40% and 30% (present work) for *cis*, *trans1* and *trans2*, respectively (Figure 3.3.9). The pre-illumination efficiency differed in the above-mentioned SFX experiments as assessed by absorption spectroscopy with 10 %

(Supplementary figure 15 in (Coquelle et al. 2018b)), 10% (Woodhouse et al. 2020), and 30% (present work ; (Supplementary figure S13 in Appendix 6.2)) of the molecules remaining in the *on*-state after pre-illumination at 488 nm, in Coquelle et al. 2018, Woodhouse et al. 2020 and the present work, respectively, which could be linked to the observed variation in *off*-state heterogeneity. Alternatively, aging of the crystalline proteins might be at the origin of *trans2* being increasingly populated in *off*-state structures of parental rsEGFP2 determined by SFX under identical buffer conditions on microcrystals of the same batch (0% in May 2015 (Coquelle et al. 2018b), 25% in July 2015 (Woodhouse et al. 2020a) and 30% in June 2016 (present work)).

Given the above, we suggest that the variation in the population of *trans2* conformer in parental rsEGFP2 and rsFolder2 is caused by experimental and/or environmental parameters. Upon *on-to-off* isomerization, a low, environment-dependent barrier in the protein conformational landscape allows access to either *trans1* or *trans2*, or the exchange between the two conformations. We refer to this observation as “*switching fragility*” (a concept coined by Dominique Bourgeois). This fragility may have an impact on super-resolution microscopy applications in which labeling occurs in different cellular compartments with varied physicochemical environments (*e.g.* viscosity, ionic strength, or nature of the recombinant protein).

Modulation of conformational off-state heterogeneity

We show that the occupancy of *trans1* and *trans2* conformations can be controlled by modifying the steric constraints imposed by the side-chain of residue 151, a residue retracting transiently during *off-to-on* photoswitching (Coquelle et al. 2018b). Upon *on-to-off* switching, only *trans1* forms in the rsEGFP2-V151A variant, whereas only *trans2* seems to be occupied in the V151L variant (Figure 3.3.6).

Interestingly, only the *trans2* conformation is observed in rsFolder, although it has a valine at position 151 (El Khatib et al. 2016). rsFolder displays a phenylalanine at position 146 instead of a tyrosine in parental rsEGFP2 and rsFolder2 that cannot form an H-bond to the critical His149 in the *off*-state (El Khatib et al. 2016; Woodhouse et al. 2020a). Consequently, it seems plausible that His149 is free to form an H-bond with the protonated *off*-state chromophore that during *on-to-off* switching then adopts the *trans2* conformer, instead of the *trans1* conformer

that is not H-bonded to His149 in parental rsEGFP2 and rsFolder2. Thus, access to *trans1* and *trans2* is controlled by residues located either on the *cis* or the *trans* side of the chromophore pocket, although it appears that the presence of an alanine at position 151 has a dominant effect on the presence of the *trans1* isomer.

Correlation between off-state conformations, switching contrast, and absorbance spectra

In the associated publication (see Appendix 3.6), we have been able to establish a causal relationship between the *off*-state conformational heterogeneity of parental rsEGFP2 and rsFolder2 and photoswitching contrast determined during an extensive photophysical characterization. Briefly, *trans1* (V151A variant) and *trans2* (V151L variant) conformers exhibit higher and lower photoswitching contrast, respectively, compared to parental rsEGFP2 and rsFolder2, both *in vivo* and *in vitro* (Table 1 and Figure 6 in Appendix 6.2).

By comparing fluorescence switching kinetics (Figure 3.3.4 and Supplementary figure S8) and the *off*-state UV/Vis absorption spectra (Figure 4 in Appendix 6.2) of the V151A and V151L variants, Virgile Adam and Dominique Bourgeois (IBS) suggested that changes in the photoswitching contrasts of the variants are caused by the red- and blue-shifted absorption spectra of *trans2* and *trans1*, respectively.

Quantum chemical calculations by Tatjana Domratcheva (Moscow State University) showed that *trans1* and *trans2* differ in the length of the phenolic OH bond as well as of the conjugated π system. The *trans1* conformer has a stronger bonding of the phenolic proton, coupled with a reduced π -conjugation compared to *trans2*. Thus, the S_0 - S_1 energy is higher in the case of *trans1* than of *trans2* (Figure 3.3.6 and Supplementary Table S4 in Appendix 6.2).

All the above correlates with the differences in the chromophore dihedral angles, *i.e.* τ and φ , and thus the planarity of the *trans1* and *trans2* chromophores (Table 3). The red-shifted absorption spectra are consistent with a more extended electron delocalization in the quasi-planar *trans2* conformation of the chromophore. On the other hand, the blue-shifted absorption spectra of *trans1* is compatible with the stabilization of the protonated form by charge transfer from Y146, activated by H-bonding to H149, which is absent for *trans2* (Figure 3.3.8).

RESOLFT experiments on rsFolder2-V151A

Based on *in vivo* switching properties carried out by Nickels Jensen and Stefan Jakobs (MPI Göttingen), both parental rsEGFP2- and rsFolder2-V151A variants appeared to be suitable for RESOLFT super-resolution microscopy (Table 1 and Figure 6 in Appendix 6.2). A fusion protein of the cytoskeletal protein Keratin with rsFolder2-V151A was expressed in cultured human HeLa cells and imaged on the RESOLFT microscope by Nickels Jensen and Stefan Jakobs (Figure 7 in Appendix 6.2). The choice of rsFolder2-V151A was based on the higher photoswitching contrast *in vitro* (Table 1 in Appendix 6.2) and *in vivo* (Figure 6 in Appendix 6.2) in comparison with rsEGFP2-V151A and that rsFolder2-V151A has super folding properties that may be interesting in nanoscopy applications. Despite the increased switching contrast of the V151A variant, the recorded RESOLFT images do not show a significant increase in resolution compared to the parent protein. This is most probably due to the lower molecular and cellular brightness of this variant compared to the parents (Table 1 in Appendix 6.2).

3.3.4 Ongoing work and perspectives

Further investigation is required, in particular, to identify the parameters influencing *trans2* formation in the *off*-state. In our ongoing work, we try to vary the pre-illumination time at 488 nm (*cis*-to-*trans* isomerization) of parental rsEGFP2 microcrystals and then collect data using room-temperature serial synchrotron crystallography. The goal is to see whether the pre-illumination conditions changes the occupancy of the *trans2* conformer in the *off*-state.

The reported rsEGFP2-V151A and rsFolder2-V151A variants are promising leads for the next-generation RSFPs, for which the fluorescence brightness has to be increased while maintaining the enhanced switching contrast as described here.

3.3.5 Materials and Methods

Expression, purification, and microcrystallization of parental rsEGFP2 and its V151A and V151L variants

Transformation, expression, purification, and microcrystallization of parental rsEGFP2 were performed as described previously (Coquelle et al. 2018b; Woodhouse et al. 2020a). Microcrystals of $3 \times 3 \times 3 \mu\text{m}^3$ were obtained by the seeded batch method established by Ilme Schlichting (MPI Heidelberg). The final protein, precipitant, salt, and buffer concentrations were 20 mg/mL, 2 M ammonium sulfate, 20 mM, 120 mM HEPES pH 8, respectively. Purification and microcrystallization took place in April 2015 and were carried out by Joyce Woodhouse and Virgile Adam (IBS). The parental rsEGFP2 microcrystal batch was the same as the one used for earlier SFX experiments (Coquelle et al. 2018b; Woodhouse et al. 2020a). The corresponding information for rsEGFP2-V151A and -V151L is described in Section 3.2 of the current manuscript.

Injection for SFX data collection and pre-illumination to induce on-to-off switching

Before injection, sedimented parental rsEGFP2 microcrystals were resuspended in 2.5 M ammonium sulfate, 100 mM HEPES pH 8 and 5 – 10 % (v/v) of finely crushed parental rsEGFP2 microcrystals were added to reduce aggregation of microcrystals, and the resulting clogging of the injector tubing. All microcrystal suspensions were filtered through a 20- μm stainless steel filter using a sample loop and a manually-driven syringe. They were loaded into a stainless-steel sample syringe, which was then installed on an anti-settling device (Lomb et al. 2012) onto a Peltier element-cooled (20°C) syringe holder. Crystals were injected at flow rates between 30 – 40 $\mu\text{L min}^{-1}$ with a gas dynamic virtual nozzle (GDVN (Weierstall et al. 2012)), using sample capillaries with an inner diameter of 75 μm . For *off*-state data collections, parental rsEGFP2 microcrystals were injected at a concentration of 20-30% (v/v) into the microfocus vacuum chamber of the CXI instrument (Liang et al. 2015) at the LCLS (proposal LM47, 23 – 27 June 2016). For *on*-state data collection of the rsEGFP2-V151A variant, the sample was injected at 5 % (v/v) into the microfocus vacuum back-chamber of the CXI instrument at the LCLS (proposal LR38, 22 – 26 February 2018). The corresponding information for rsEGFP2-V151A and -V151L was described in Section 3.2 of the current manuscript.

For *off*-state data collections, microcrystals were pre-illuminated during transit from the sample syringe to the injector with 488 nm laser light (200 mW nominal power, 25 ms transit time, 300 W cm^{-2}) within a custom-made device (Schirò et al. 2017) to switch them from the resting *on*-state to the *off*-state. The pre-illumination efficiency, *i.e.* the ratio of generated *off*-state and the

residual amount of remaining *on*-state was assessed by absorption spectroscopy using a Nanodrop 2000c spectrometer. The spectra after 488 nm illumination contain contributions from *off*- and *on*-state chromophores and are distorted by scattering effects. They were modeled by Lucas Uriarte and Michel Sliwa (University Lille) by a sum of two Gaussians (Gaussian 1 at 400 nm and Gaussian 2 at 482 nm) and an exponential function. Baseline distortions due to scattering were subtracted and the spectrum smoothed with a Savitzky-Golay filter and normalized at 280 nm. The absorbance of Gaussian 2 at 482 nm relative to the absorbance at 482 nm of the spectrum before 488 nm illumination (assumed to correspond to 100% *on*-state) represents the pre-illumination efficiency. For parental rsEGFP2 (LCLS experiment LM47), only 66% were switched to the *off*-state and 34% remained in the *on*-state (Supplementary figure S13a in Appendix 6.2), *i.e.* less than during earlier SFX experiments (Coquelle et al. 2018b; Woodhouse et al. 2020a), where 90% (Coquelle et al. 2018b) and 84% (SACLA experiment in 2015 (2015A8031(Woodhouse et al. 2020a)) (Supplementary figure S13b in Appendix 6.2) of parental rsEGFP2 was switched to the *off*-state. Robert Shoeman (MPI Heidelberg) noticed after the LM47 experiment on parental rsEGFP2 that the SMA fiber within the high-performance liquid chromatography (HPLC) tee union of the pre-illumination device (see Figure 2 in (Schirò et al. 2017)) was dirty or damaged, leading to a 50% drop in laser power at the sample position. The corresponding information for rsEGFP2-V151A and -V151L was described in Section 3.2 of the current manuscript.

Room-temperature data collection and online monitoring

SFX data on parental rsEGFP2 in the *off*-state were acquired with the CSPAD detector (Blaj et al. 2015) operating in a dual-gain mode in the microfocus vacuum chamber of the CXI instrument at the LCLS operating at 120 Hz, with X-ray pulses of 35 fs in length and photon energy of nominally 9.1 keV (LM47). The X-ray beam was focused to 1 – 2 μm (FWHM). rsEGFP2- V151A *on*-state data (LR38) were collected in the vacuum back chamber of CXI (focus 5 – 10 μm (FWHM); photon energy 9.8 keV). The CFEL–ASG Software Suite (CASS) (Foucar 2016) was used for online monitoring of diffraction data, such as diffraction resolution, hit rate, the fraction of multiple hits, and pixel saturation. The corresponding information for rsEGFP2-V151A and -V151L is described in Section 3.2 of the current manuscript.

SFX data processing

NanoPeakCell (Coquelle et al. 2015) was used for the *on*- and *off*-line hit finding. Hit-finding parameters were adjusted after visual inspection of the first diffraction patterns using the NanoPeakCell graphical interface.

For parental rsEGFP2 and rsEGFP2-V151A in the *on*-state, 80 605 and 17 538 images were indexed, respectively (Table 3.3.2). The CrystFEL suite (White 2019) was used for further data processing. The data were indexed with *Mosflm* and integrated with *ring-nocen* using v.0.6.2 for parent rsEGFP2 and v.0.6.3 for rsEGFP2-V151A in the *on*-state. Merging was performed using CrystFEL v.0.8.0 with the Monte Carlo algorithm, *process_hkl*, for the parental rsEGFP2 *off*-state dataset and with *partialator* using the xsphere partiality model with one cycle of scaling and post-refinement for rsEGFP2-V151A variant. A resolution cut-off of 1.7 and 1.9 Å was chosen based on SNR, R_{split} , and CC^* statistics (Table 3.3.2) for parental rsEGFP2 and rsEGFP2-V151A in the *on*-state, respectively. The corresponding information for rsEGFP2-V151A and -V151L is described in Section 3.2 of the current manuscript.

SFX structure solution and refinement

The SFX structures were phased by molecular replacement with *Phaser* (McCoy et al. 2007). As a search model was used the SFX *off*-state structure of parental rsEGFP2 (PDB entry 6T39 (Woodhouse et al. 2020a)) for the structure of parental rsEGFP2 in the *off*-state (PDB entry 7O7U). The SFX parental rsEGFP2 *on*-state structure (PDB entry 5O89 (Coquelle et al. 2018b)) was used as a search model for the structure of rsEGFP2-V151A in the *on*-state (PDB entry 7O7V).

Refinement with *Refmac5* (Murshudov et al. 2011) included positional and isotropic individual B-factor refinement in reciprocal space for both structures. Model building and real-space refinement were performed in *Coot* (Emsley and Cowtan 2004). Initially, the chromophore had been omitted from the model and subsequently included and modeled as described below. Once the chromophore had been included, its position and isotropic individual B-factors were refined in reciprocal space, while the protein moiety remained fixed. Both structures were superposed to the parental rsEGFP2 *off*-state structure (PDB entry 6T39 (Woodhouse et al. 2020a)) using the CCP4 program *superpose* which is a structural alignment tool based on secondary structure matching.

For parental rsEGFP2 in the *off*-state, the chromophores were modeled in a *trans1* conformation at 70% occupancy and the *on*-state *cis* conformation at 30% according to spectroscopy (Supplementary figure S13a in Appendix 6.2). The resulting $F_{\text{obs}} - F_{\text{calc}}$ map showed a positive peak indicating the presence of *trans2* (Figure 3.3.9a). When the occupancy of *cis*, *trans2*, and *trans1* was set to 30%, 30%, and 40% occupancy the resulting $F_{\text{obs}} - F_{\text{calc}}$ map was featureless in the chromophore region (Figure 3.3.9b). That a considerable fraction (30%) of the chromophore was in the *trans2* conformation was also confirmed by a $F_{\text{obs}} - F_{\text{calc}}$ map in which the hydroxybenzylidene moiety was omitted (Figure 3.3.9c). We note that the chromophore occupancies were different from the ones in parental rsEGFP2 in the *off*-state reported earlier (PDB ID 6T39 (Woodhouse et al. 2020a), 10% *cis*, 25% *trans,2*, and 65% *trans1*), in agreement with spectroscopy (Supplementary figure S13 in the Appendix 6.2).

For rsEGFP2-V151A in the *on*-state, the *cis* chromophore of rsEGFP2 was included at 100% occupancy.

The corresponding information for rsEGFP2-V151A and -V151L *off*-state SFX structures is described in Section 3.2 of the current manuscript.

Crystallization, synchrotron cryo-crystallographic data collection, and structure solution, and refinement of rsEGFP2-V151A and -V151L variants in their on- and off-states

These steps were carried out before I arrived in the team and they were performed by Joyce Woodhouse and Virgile Adam (IBS, Grenoble). I was involved during the last steps of structure refinement, validation, and deposition of rsEGFP2-V151A *on*- (PDB ID 7O7C) and *off*-states (PDB ID 7O7D) and -V151L variants in its *on*- (PDB ID 7O7E) and *off*-states (PDB ID 7O7H).

3.3.6 Figure and Tables

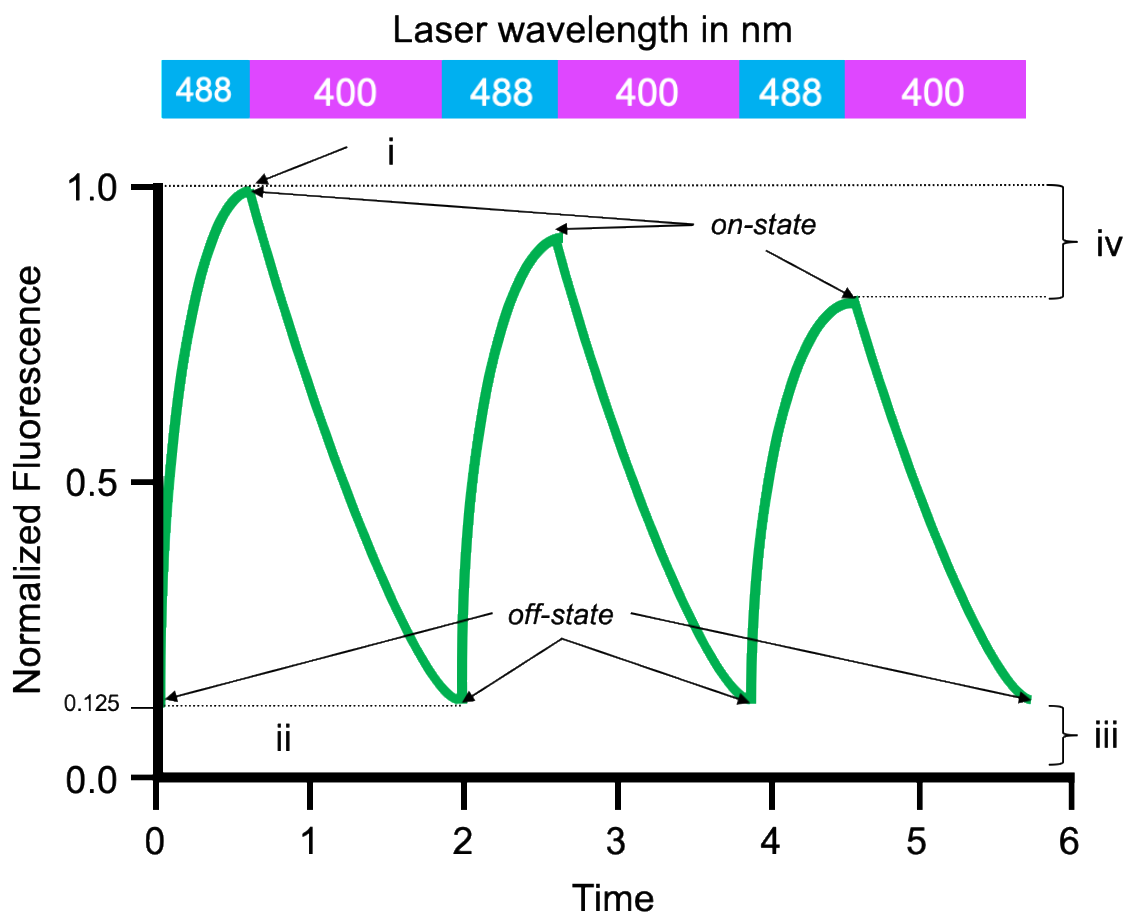


Figure 3.3.1: Photophysical parameters revealed from fluorescence switching curves

Theoretical fluorescence curve of an ensemble of rsEGFP2 in solution. Plotted is the emitted fluorescence after on-switching (488 nm) and off-switching (400 nm) as a function of time. Five important photophysical parameters can be determined from such curves like brightness (i), photoswitching speed (ii), residual fluorescence in the off-state (iii), photoswitching fatigue (iv), and photoswitching contrast (8) (ratio between the maximum fluorescence signal (i) (1.00) and the residual signal (iii) (0.125)). The figure was adapted from (Jensen et al. 2020).

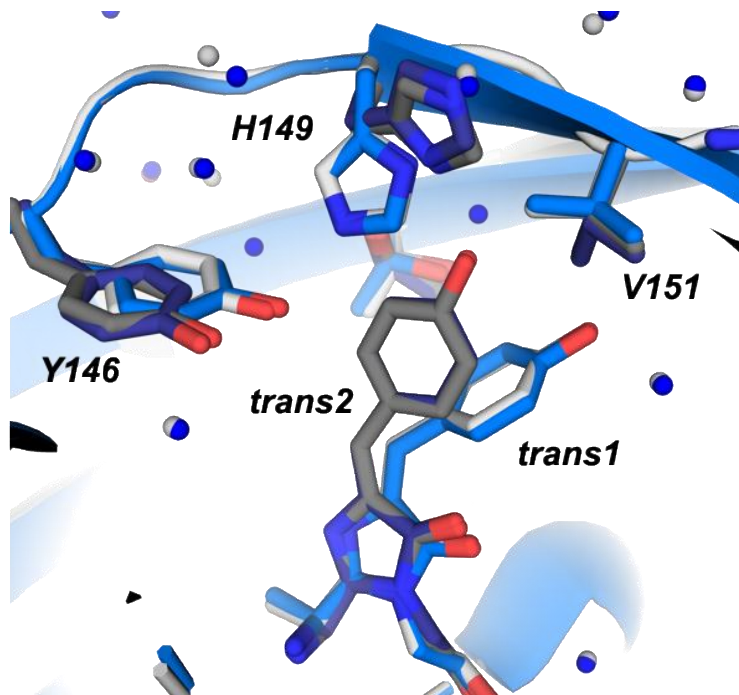


Figure 3.3.2: Off-state conformations in parental rsEGFP2

Structures of parental rsEGFP2 in its off-state solved from RT SFX data. Off-state models of parental rsEGFP2 solved from RT SFX data published earlier (PDB entry 6T39 (Woodhouse et al. 2020a)) and data described here (PDB entry 7O7U). Trans1 and trans2 conformers are occupied at 40% (light grey) and 30% (dark grey) in parental rsEGFP2 (this work) and at 65% (light blue) and 25% (dark blue) in 6T39, respectively. The figure was adapted from (Adam et al. 2021).

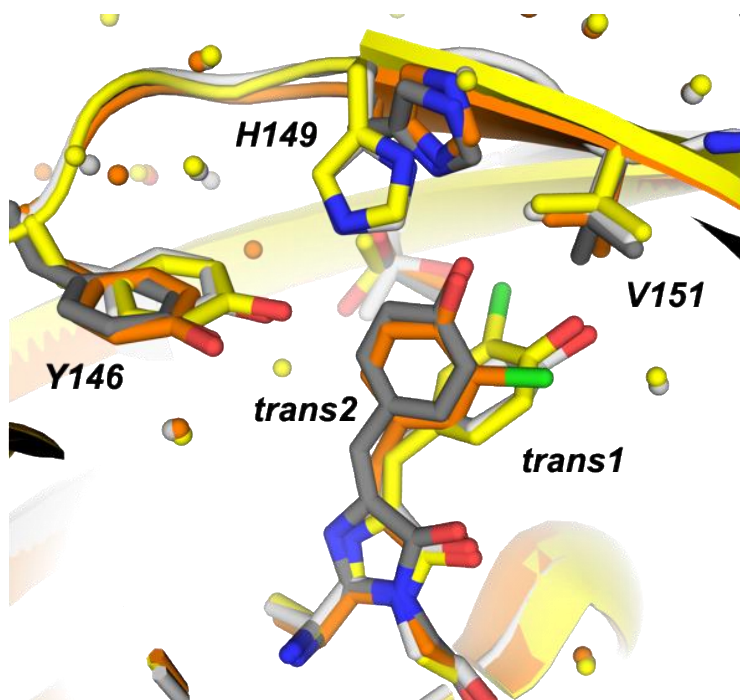


Figure 3.3.3: Comparison of off-state conformations in parental rsEGFP2 with those in rsEGFP2 with a monochlorinated chromophore

Off-state models of parental rsEGFP2 solved from RT SFX data in this work (light and dark grey; same information as in Figure 3.3.2), overlaid with trans conformations in synchrotron structures of parental rsEGFP2 containing a monochlorinated chromophore (Chang et al. 2019) solved from crystals with looser (yellow) and tighter (orange) crystal packings. The figure was adapted from (Adam et al. 2021).

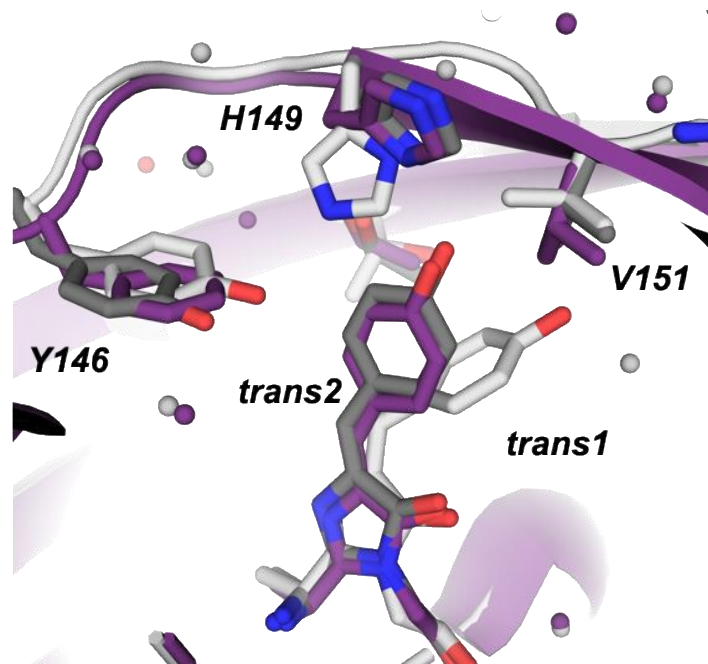


Figure 3.3.4: Comparison of off-state conformations in parental rsEGFP2 and in rsFolder
Off-state models of parental rsEGFP2 solved from RT SFX data in this work (light and dark grey), overlaid with trans conformations in synchrotron structures of the off-state model of rsFolder (PDB entry 5DU0 (El Khatib et al. 2016)) in purple. The figure was adapted from (Adam et al. 2021).

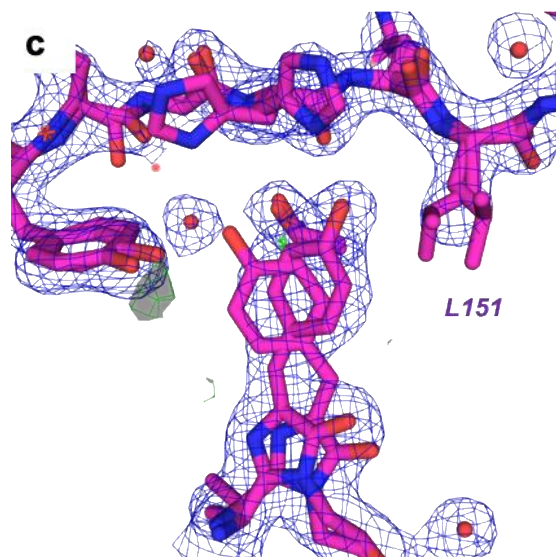
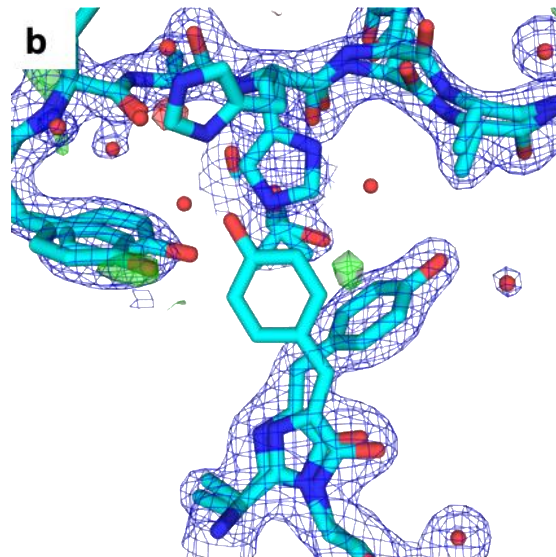
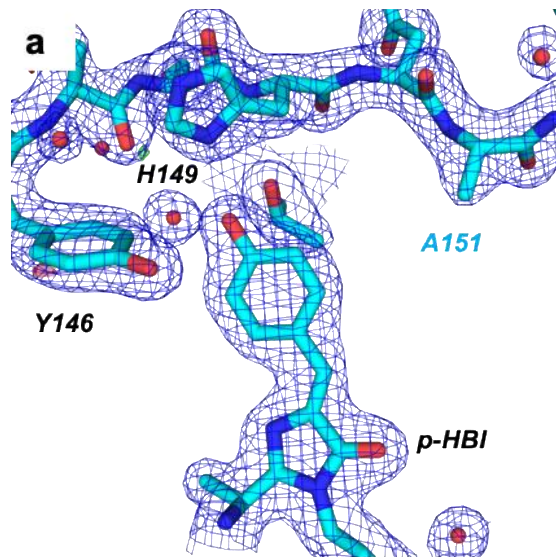


Figure 3.3.5: Structures of the rsEGFP2-V151A variant in its on- and off-states and of -V151L in its off-state solved from RT SFX data

Zoom on the chromophore (*p*-hydroxybenzylidene imidazolinone, *p*-HBI) region in crystal structures of (a) the rsEGFP2-V151A variant in its on- (PDB entry 7O7V) and (b) off-state (PDB entry 7O7X) and (c) the V151L variant in its off-state (PDB entry 7O7W) solved from SFX data collected at room temperature. $2F_{obs} - F_{calc}$ (1σ) and $F_{obs} - F_{calc}$ ($\pm 3\sigma$) electron density maps are shown in blue and green/red, respectively. The figure was adapted from (Adam et al. 2021).

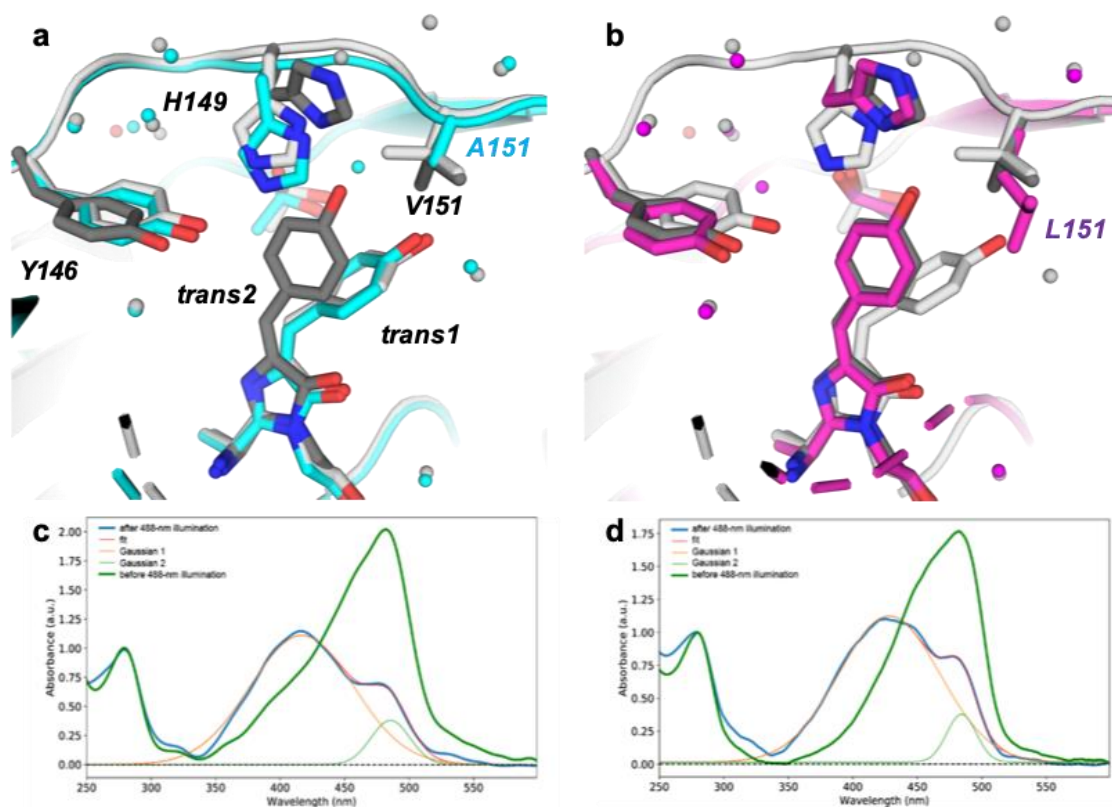


Figure 3.3.6: Comparison between parental rsEGFP2 and its V151A and V151L variants in their off-states solved from RT SFX data.

Off-state models of (a) rsEGFP2-V151A (cyan; PDB entry 7O7X) and (b) -V151L (purple; PDB entry 7O7W) variants are superimposed on the model of parental rsEGFP2 in the off-state solved from RT SFX data (PDB entry 7O7U), featuring trans1 in light grey and trans2 in dark grey. Trans1 and trans2 are occupied at 80% and 75% in rsEGFP2 V151A and V151L, respectively. The cis conformers were removed for clarity. Absorption spectra of rsEGFP2-V151A (c) and -V151L (d) microcrystals before (green) and after having been pre-illuminated (blue) at a laser power of nominally 200 mW within a custom-made device (Schirò et al. 2017) during an SFX experiment after background subtraction, smoothing with a Savitzky-Golay filter and normalization at 280 nm. The spectrum after 488 nm illumination was modeled by a sum of two Gaussians (Gaussian 1 at 400 nm in orange and Gaussian 2 at 482 nm in light green). The absorbance of Gaussian 2 at 482 nm relative to the absorbance at 482 nm of the spectrum before 488 nm illumination (assumed to correspond to 100% on-state) indicates that 85% (77%) were switched to the off-state for rsEGFP2-V151A (V151L) and 15% (23%) remained in the on-state. The figure was adapted from (Adam et al. 2021).

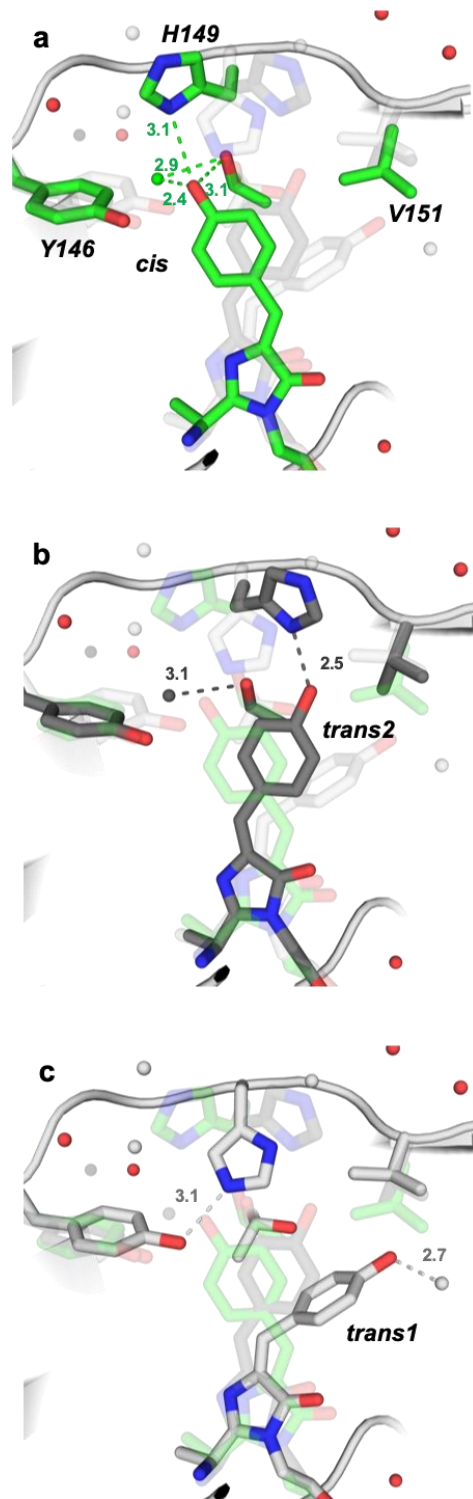


Figure 3.3.7: Hydrogen bonds in the chromophore pocket

The environment of the chromophore in its cis (a; green), trans2 (b; dark grey), and trans1 (c; light grey) conformation in the parental rsEGFP2 off-state structure (PDB entry 7O7U). Water molecules belonging to all three chromophore conformations are shown in red. Hydrogen-bond lengths are in Ångstrom. The figure was adapted from (Adam et al. 2021).

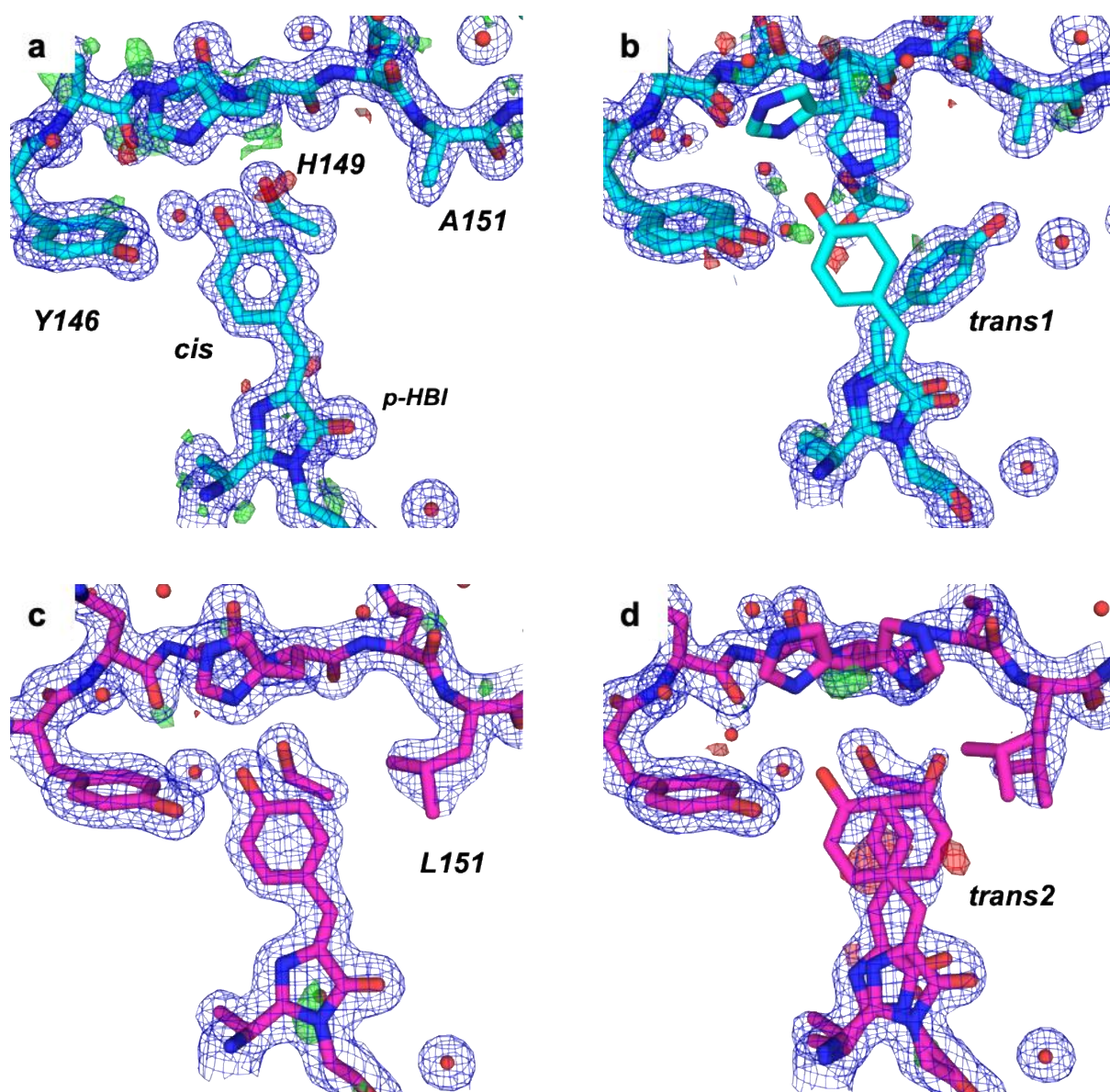


Figure 3.3.8: Structures of rsEGFP2 -V151A and -V151L variants in their on- and off-states solved using data from synchrotron cryo-crystallography

Zoom on the chromophore (*p*-hydroxybenzylidene imidazolinone, *p*-HBI) region in crystal structures of rsEGFP2 variants V151A (cyan) and V151L (purple) in their on- and off-states solved from synchrotron data collected at cryo-temperatures. (a, b) Electron density maps (mesh) and models of the rsEGFP2-V151A variant in the (a) on- (PDB entry 7O7D) and (b) off-state (PDB entry 7O7C). (c, d) Electron density maps (mesh) and models of the rsEGFP2-V151L variant in the (c) on- (PDB entry 7O7E) and (d) off-state (PDB entry 7O7H). In (b) and (d) an alternate conformation of the chromophore corresponding to the *cis* isomer of the on-

state remains in the off-state. $2F_{obs}-F_{calc}$ (1σ) and $F_{obs}-F_{calc}$ ($\pm 3 \sigma$) electron density maps are shown in blue and green/red, respectively. The figure was adapted from (Adam et al. 2021).

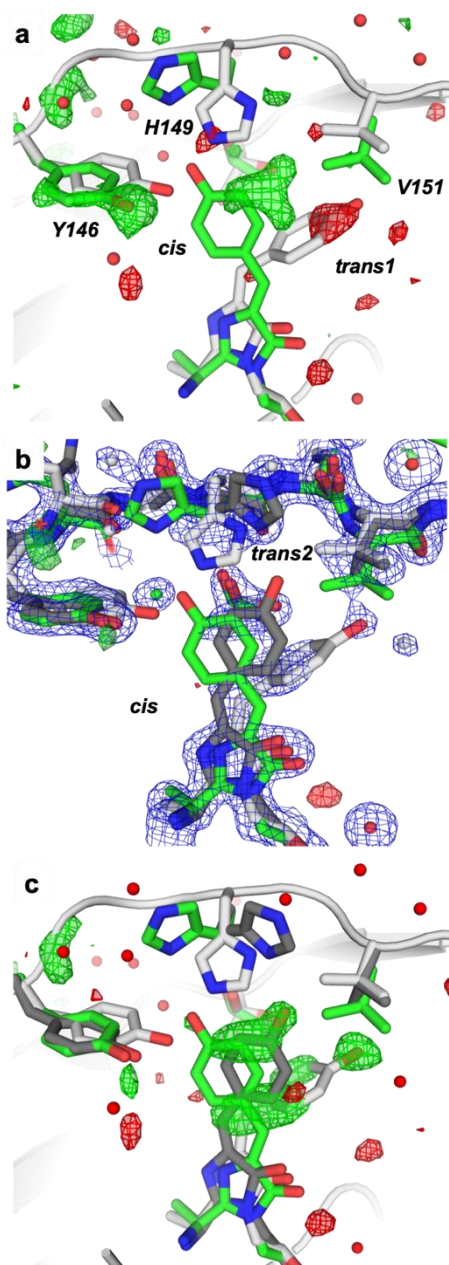


Figure 3.3.9: Structure refinement strategy of parental rsEGFP2 in its off-state solved from RT SFX data.

(a) Residual $F_{obs} - F_{calc}$ map (green, 3σ ; red, -3σ) of the rsEGFP2 in the off-state calculated with a model containing a cis (light green) and a trans1 chromophore (light grey) at an occupancy of 30 and 70%, respectively. (b) Final model of parental rsEGFP2 in the off-state (PDB entry 7O7U) with occupancies of cis (green), trans1 (light grey), and trans2 (dark grey) chromophore conformations of 30%, 40%, and 30%, respectively. Superimposed are the $2F_{obs} - F_{calc}$ (blue, 1σ) and $F_{obs} - F_{calc}$ maps (green, 3σ ; red, -3σ). (c) $F_{obs} - F_{calc}$ map (green, 3σ ; red, -3σ), calculated with a model from which the hydroxybenzylidene moiety was omitted,

overlaid with the model of parental rsEGFP2 in the off-state (PDB entry 7O7U). The figure was adapted from (Adam et al. 2021).

Dataset	Parental rsEGFP2 <i>off</i>	rsEGFP2-V151A <i>on</i>	rsEGFP2-V151A <i>off</i>	rsEGFP2-V151L <i>off</i>
PDB entry	7O7U	7O7V	7O7X	7O7W
Data collection and processing				
Space group	<i>P</i> 2 ₁ 2 ₁ 2 ₁	<i>P</i> 2 ₁ 2 ₁ 2 ₁	<i>P</i> 2 ₁ 2 ₁ 2 ₁	<i>P</i> 2 ₁ 2 ₁ 2 ₁
Unit cell parameters				
a (Å)	51.7 ± 0.1	51.9 ± 0.2	51.8 ± 0.2	51.8 ± 0.2
b (Å)	63.1 ± 0.2	62.7 ± 0.3	62.7 ± 0.2	62.9 ± 0.2
c (Å)	73.5 ± 0.2	72.0 ± 0.4	71.6 ± 0.3	71.9 ± 0.3
Collected frames Hits				
Indexed images	80,605	17,538	10,794	4,930
Resolution (Å)	17– 1.70 (1.74 – 1.70)	24 – 1.9 (1.95 – 1.90)	24– 1.95 (2.00 – 1.95)	24– 2.10 (2.15 – 2.10)
Observations	22,894,347 (991,284)	2,916,477 (100,602)	2,044,776 (75,714)	778,314 (28,668)
Unique reflections	27,394 (1,810)	19,739 (1,293)	18,181 (1,176)	14,734 (958)
R _{split} [#] (%)	6.8 (56.3)	6.3 (73.6)	7.7 (58.4)	14.0 (53.4)
CC*	0.999 (0.924)	0.999 (0.891)	0.999 (0.904)	0.996 (0.891)
I / σ(I)	10.0 (1.9)	7.8 (1.4)	7.0 (1.8)	4.9 (1.9)
Completeness (%)	100 (100)	100 (100)	100 (100)	100 (100)
Multiplicity	835 (548)	148 (78)	112 (64)	53 (30)
Refinement statistics				
Refinement strategy	Classical refinement	Classical refinement	Classical refinement	Classical refinement
Resolution (Å)	17– 1.70 (1.74 – 1.70)	24 – 1.9 (1.95 – 1.90)	31 – 1.95 (2.00 – 1.95)	31– 2.10 (2.15 – 2.10)
Number of reflections	26368 (2,661)	19,091 (2,543)	17,600 (2,739)	14,284 (2,661)
R _{free}	21.5 (38.0)	19.2 (27.14)	20.1 (31.0)	21.3 (22.0)
R _{work}	18.0 (37.0)	14.9 (21.16)	15.7 (26.0)	17.3 (29.0)
Number of protein atoms	2,443	2,005	2,182	2,193
Number of ligand atoms	60	20	40	40
Number of water atoms	177	111	125	58
B-factor protein (Å ²)	22.81	48.5	43.41	38.97
r.m.s.d. bond lengths (Å)	0.01	0.01	0.008	0.008
r.m.s.d. angles (°)	1.728	1.609	1.547	1.566
Ramachandran favored	97.00	97.90	97.83	97.41
Ramachandran allowed	3.00	2.10	2.17	2.59
Ramachandran outliers	0.00	0.00	0.00	0.00
Rotamer outliers	4.01	1.80	1.22	0.81
C-beta outliers	0	0	0	0
Clashscore	6.23	2.51	5	6.78

Table 3.3.1: *RT SFX data collection and refinement statistics of the structures of parental rsEGFP2 and its V151A and V151L variants. Values in brackets correspond to the highest resolution shell. The table was adapted from (Adam et al. 2021).*

Data collection and processing				
Dataset	rsEGFP2 V151A <i>on</i>	rsEGFP2 V151A <i>off</i>	rsEGFP2 V151L <i>on</i>	rsEGFP2 V151L <i>off</i>
PDB entry	7O7D	7O7C	7O7E	7O7H
Illumination (488 nm)	No	Yes	No	Yes
Space group	P2 ₁ 2 ₁ 2 ₁	P2 ₁ 2 ₁ 2 ₁	P2 ₁ 2 ₁ 2 ₁	P2 ₁ 2 ₁ 2 ₁
Unit cell parameters				
a (Å)	60.0	51.2	51.1	51.3
b (Å)	62.1	60.3	62.5	61.2
c (Å)	69.4	66.6	70.4	70.3
Collected frames	1050	547	794	950
Observations	166,004 (12,182)*	89,498 (6,540)	91,956 (14,602)	84,740 (13,701)
Resolution (Å)	46.28 - 1.4 (1.44-1.4)	40.57 - 1.55 (1.59-1.55)	41.38 - 1.8 (1.91-1.8)	46.16 - 1.7 (1.81-1.7)
R _{meas} (%)	4.8 (42.5)	4.5 (60.6)	6.5 (46.6)	4.7 (42.8)
CC ½ (%)	99.9 (85.3)	99.9 (70.7)	99.9 (91.6)	99.9 (87.1)
I/σI	17.26 (3.23)	14.82 (2.26)	14.17 (2.72)	15.5 (2.9)
Completeness (%)	97.4 (96.7)	97.0 (98.4)	98.3 (98.3)	97.2 (98.5)
Multiplicity	3.9 (3.9)	3.0 (3.0)	4.3 (4.3)	3.5 (3.5)
Refinement statistics				
Resolution (Å)	46.28 - 1.4 (1.43-1.40)	40.57 - 1.55 (1.60-1.55)	41.38 - 1.8 (1.88-1.80)	46.16 - 1.7 (1.77-1.70)
Number of reflections	42,980 (2,669)	29,619 (2,528)	21,205 (2,482)	24,184 (2,539)
R _{free} (%)	17.90 (25.39)	19.61 (28.60)	20.76 (29.05)	19.70 (26.05)
R _{work} (%)	15.21 (21.80)	16.40 (24.46)	15.92 (24.97)	15.70 (22.17)
Number of protein atoms	2,066	2,096	1,977	2,129
Number of solvent atoms	353	275	317	298
B-factor protein (Å ²)	16.11	19.12	29.12	29.66
r.m.s.d bond lengths (Å)	0.006	0.008	0.006	0.01
r.m.s.d angles (°)	0.902	0.997	0.847	1.031
Ramachandran favored (%)	99.12	98.68	98.70	97.84
Ramachandran allowed (%)	0.88	1.32	1.30	2.16
Ramachandran outliers (%)	0.00	0.00	0.00	0.00
Rotamer outliers (%)	1.29	1.28	1.79	2.08
C-beta outliers	0	0	0	0
Clashscore	4.32	5.66	3.29	5.81

Table 3.3.2: Cryo-crystallographic synchrotron data collection and refinement statistics of rsEGFP2-V151A, and rsEGFP2-V151L structures in their on- and off-states. Values in brackets correspond to the highest resolution shell. The table was adapted from (Adam et al. 2021).

Method	Protein	State	PDB ID	Conformer	* ϕ (°)	# τ (°)
Synchrotron cryo-crystallography	rsEGFP2-V151A	<i>off</i> -state	707C	<i>cis</i>	174	-166
			707C	<i>trans1</i>	-54	16
		<i>on</i> -state	707D	<i>cis</i>	174	-166
	rsEGFP2-V151L	<i>off</i> -state	707H	<i>cis</i>	171	-169
			707H	<i>trans2</i>	7	-3
		<i>on</i> -state	707E	<i>cis</i>	171	-169
	rsFolder2	<i>on</i> -state	7AMB	<i>cis</i>	175	-178
		<i>off</i> -state	7AMF	<i>cis</i>	170	-176
			7AMF	<i>trans1</i>	-44	17
	Cl-rsEGFP2 (24)	<i>on</i> -state	6PFR	expanded <i>cis</i>	167	-166
			6PFS	contracted <i>cis</i>	142	-169
		<i>off</i> -state	6PFT	expanded <i>trans</i>	-32 [§]	2
			6PFU	contracted <i>trans</i>	43	-30
RT SFX	parental rsEGFP2	<i>off</i> -state	707U	<i>cis</i>	168	-167
			707U	<i>trans1</i>	-48	7
			707U	<i>trans2</i>	7	-4
	rsEGFP2-V151A	<i>off</i> -state	707X	<i>cis</i>	173	-172
			707X	<i>trans1</i>	-50	9
	rsEGFP2-V151L	<i>off</i> -state	707V	<i>cis</i>	178	-170
			707W	<i>cis</i>	173	-151
			707W	<i>trans2</i>	10	-18
Comput. B3LYP-D3 geometry optimization	rsEGFP2	<i>off</i> -state	(6T39) ^{&}	<i>trans1</i>	-31	-5
		<i>off</i> -state	(6T39) ^{&}	<i>trans2</i>	-7	-10
	rsEGFP2-V151A	<i>off</i> -state	(6T39) ^{&}	<i>trans1</i>	-27	-6
	rsEGFP2-V151L	<i>off</i> -state	(6T39) ^{&}	<i>trans2</i>	-8	-10

*CA2-CB2-CG2-CD2 (for numbering see Supplementary figure 16c in (Coquelle et al. 2018b))

#C2-CA2-CB2-CG2

§CA2-CB2-CG2-CD1 (due to the flip of the chromophore around CB2-CG2 in PDB ID 6PFT)

&starting coordinates of the computational models were taken from PDB 6T39

Table 3.3.3: Chromophore dihedral angles from crystallographic models and after computational geometry optimization. The table was adapted from (Adam et al. 2021).

3.4 Comparison of synchrotron and XFEL room-temperature serial crystallography data collected on protein crystals 3 μm in diameter

Kyprianos Hadjidemetriou^{1,#}, Nicolas Coquelle^{2,#}, Joyce Woodhouse^{1,#}, Eugenio de la Mora¹, Anastasya Shilova², Martin Rosenthal², Thomas R. M. Barends³, Ilme Schlichting³, Manfred Burghammer², Jacques-Philippe Colletier¹, Martin Weik¹

¹Institut de Biologie Structurale, Univ. Grenoble Alpes, CEA, CNRS, F-38044 Grenoble, France

²European Synchrotron Radiation Facility, Grenoble, France.

³Max Planck Institute for Medical Research, Jahnstrasse 29, D-69120 Heidelberg, Germany

equal contribution

Correspondence: weik@ibs.fr, colletier@ibs.fr

Abstract

The development of serial crystallography has boosted the revival of room temperature data collection by outrunning and minimizing chemical and structural radiation damage through femtosecond pulses at XFELs and by distributing the X-ray dose over a myriad of crystals at synchrotrons, respectively. The mitigation of damage by a serial approach means micrometer-sized protein crystals can now be studied at both XFELs and more routinely at synchrotrons. Whereas exploring the ultrafast dynamics by time-resolved studies will continue to require XFELs, motions on the μs -ms time-scale will increasingly be studied at third and fourth generation synchrotrons. If light-sensitive proteins are to be studied by time-resolved serial crystallography, the crystal size should not exceed the $1/e$ penetration depth of trigger light into the crystals to avoid unwanted multiphoton effects. In the case of the reversibly photoswitchable fluorescent protein rsEGFP2, crystals as small as 3 μm are required to comply with this condition. Here we address the question as to whether such small protein microcrystals diffract better at an XFEL and if yes, by how much. We collected room-temperature serial femtosecond crystallography (SFX) and serial synchrotron crystallography (SSX) data on the same batch of rsEGFP2 crystals using GDVN and solid support sample presentation methods, respectively. The data sets, consisting of the same number of indexed images, were processed

identically and the solved structures were compared. The SFX and SSX datasets extended to 1.8 and 2.0 Å resolution, respectively. Electron density maps are of comparable quality and difference Fourier maps do not show any signs of radiation damage. We conclude that for rsEGFP2 microcrystals that are 3 μm in diameter, there is only a marginal improvement in diffraction quality and resolution when comparing the SFX to the SSX data set. Even on protein microcrystals that small, time-resolved serial crystallography experiments can thus be envisaged at synchrotrons, except for ultrafast studies requiring femtosecond pulses from an XFEL. With the multiplication of fourth-generation synchrotrons, the possibilities for using SSX will further grow and the complementarity with SFX increased.

3.4.1 Introduction

Serial crystallography emerged with the advent of X-ray free-electron lasers (XFELs) whose extremely bright femtosecond pulses enable diffraction-before-destruction experiments (Neutze et al. 2000), the so-called serial femtosecond crystallography (SFX (Boutet et al. 2012; Chapman et al. 2011)). During the femtosecond exposure, the protein crystal of uncontrolled orientation effectively stands still and a diffraction pattern is recorded before chemical and structural damage has had the time to develop. Eventually, the crystal is destroyed so that the sample needs to be replenished constantly employing a liquid or a viscous jet (Grünbein and Nass Kovacs 2019) or by raster-scanning of a solid support (Martiel et al. 2019). An SFX data set is then assembled from typically tens of thousands of indexed diffraction images. Owing to the high peak brilliance and shortness of XFEL pulses, SFX data can be collected from sub-micron-sized crystals (Chapman et al. 2011), including naturally occurring nanocrystals (see e.g. Colletier et al. 2016), allowing damage-free structures of radiation-sensitive proteins to be determined (see e.g. (Ebrahim et al. 2019)) and time-resolved studies on the ultrafast timescale can be carried out (Brändén and Neutze 2021; Colletier et al. 2018).

The rise of SFX benefitted from developments in macromolecular crystallography (MX) at synchrotrons over the past decades and now, in turn, benefits wider spread implementation of serial and multi-crystal data collections at synchrotrons (Hough and Owen 2021; Mehrabi et al. 2021; Schulz et al. 2022). Various sample presentation methods and data-collection schemes emerged in the past years. In the first study, helical line scans were carried out on a large number

of microcrystals held in a cryo-loop at 100 K (Gati et al. 2014). Subsequently, RT serial diffraction data were collected on crystals flowing across the beam in a quartz capillary (Stellato et al. 2014), injected in a lipidic cubic phase (LCP) (Nogly et al. 2015) or slowly extruded after embedding in various viscous media (Botha et al. 2015). In an alternative approach based on solid supports, microcrystals were sandwiched between silicon nitride windows (Coquelle et al. 2015) or mylar sheets (Doak et al. 2018) or deposited on silicon chips (Meents et al. 2017; Owen et al. 2017) and serial diffraction data were collected at RT in a raster-scanning mode. Microcrystals were also presented to the synchrotron beam through a tape drive (Beyerlein et al. 2017a; Roessler et al. 2016) and microfluidic devices (Monteiro et al. 2020). In serial synchrotron crystallography (SSX) approaches, crystals stand still or are translated during exposure, so that all Bragg reflections are only partially measured, hence a large number of images are required for sufficient sampling of reciprocal space. In multi-crystal collection schemes, at variance, oscillation data are collected over a few degrees on many crystals and those partial data sets are merged. Such an approach was used to collect data at 100 K *in situ* on membrane proteins grown in LCP (Huang et al. 2016) and on crystals deposited in micron-sized well-mounts (Guo et al. 2018) or at RT on crystals deposited on silicon chips (Roedig et al. 2016), sandwiched between two Kapton foils (Schubert et al. 2016) or grown in a microfluidic device (Heymann et al. 2014). The main difference between the two approaches is that multi-crystal data collection relies on the averaging and scaling of partial data sets with mostly fully measured reflections, whereas partial reflections from a large number of diffraction images are scaled and merged in serial crystallography. Multi-crystal data collection thus requires fewer crystals to be measured but is less amenable to time-resolved studies. Specific sample presentation (Mehrabi et al. 2020) and reaction initiation methods (Mehrabi, Schulz, Agthe, et al. 2019; Schulz et al. 2018) have recently been developed that now allow for time-resolved SSX experiments to be carried out (reviewed in (Pearson and Mehrabi 2020)), examples being the study of bacteriorhodopsin's photocycle (Weinert et al. 2019) and catalytic steps in the enzyme fluoroacetate dehalogenase (Mehrabi, Schulz, Dsouza, et al. 2019).

X-ray radiation damage is particularly pronounced at RT, with a decrease in crystal lifetime of about two orders of magnitude compared to 100 K (Nave and Hill 2005), and when microcrystals are used, for which a larger number of incident photons is required to reach the same diffraction intensity than those of larger crystals (Yamamoto et al. 2017). By distributing the absorbed dose over a multitude of crystals, serial or multi-crystal data collection schemes mitigate the problem of X-ray radiation damage at synchrotron sources and thus ease room-

temperature microcrystallography (Ebrahim et al. 2019; de la Mora et al. 2020). Room temperature crystallography offers at least three advantages over cryo-crystallography, namely the preservation of functionally relevant conformational heterogeneity of proteins (Fraser et al. 2011), the possibility to carry out time-resolved experiments, and the unnecessary use of cryo-protectants.

When protein microcrystals do not grow large enough for structure solution by cryo-MX at a synchrotron (see *e.g.* (Zhang et al. 2015)) or when microcrystals ought to be used in time-resolved experiments for efficient reaction initiation while minimizing multi-photon effects, the question arises whether serial crystallography at an XFEL or a synchrotron source should be envisaged. Answering this question depends on the relative diffraction power of microcrystals at both sources. Several reports have been published that compare the quality of SFX versus SSX data sets and in particular their respective resolution limit. Data sets obtained on microcrystals of cathepsin B by SFX at RT and by serial helical line scans at 100 K were at 2.1 Å and 3 Å, respectively (Gati et al. 2014). Lysozyme crystals diffracted to 1.9 Å resolution in both an SFX (GDVN injection, crystal size $1 \times 1 \times 3 \mu\text{m}^3$) (Boutet et al. 2012) and an SSX experiment (high-viscosity extrusion injection of crystals ($10 - 15 \times 10 - 15 \times 30 - 60 \mu\text{m}^3$) embedded in LCP) (Botha et al. 2015). SFX and SSX data sets collected both at RT on bacteriorhodopsin crystals in LCP were at 2.3 and 2.4 Å resolution, respectively (Nango et al. 2016). The crystals were larger in the SSX than the SFX experiment ($5 - 40 \times 5 - 40 \times 1 - 5 \mu\text{m}^3$ versus $3 - 15 \times 3 - 15 \times 1 - 3 \mu\text{m}^3$). Crystals of the human G protein-coupled adenosine receptor of the same size ($30 \times 30 \times 5 \mu\text{m}^3$) in LCP were used to obtain SFX and SSX data sets at 1.7 and 2.1 Å resolution, respectively (Weinert et al. 2017). The SFX and SSX data sets consisted of 3,565 and 128,086 indexed images, respectively. In another study, SFX and cryo-MX data sets and structures have been compared, yet differing in two parameters, namely data collection temperature (RT in the former, cryo in the latter) and crystal size (microcrystals in the former, macrocrystals in the latter (Naitow et al. 2017)). A first systematic comparison of SFX and SSX data sets consisting of the same number of indexed images and obtained by using microcrystals of the same size has recently been carried out and showed that both techniques can yield data of equivalent quality (Mehrabi et al. 2021). The crystals were $20 \times 20 \times 10 \mu\text{m}^3$ in size. A similar study of much smaller protein microcrystals remains elusive. Such a small size might be required for time-resolved SFX and SSX studies on optically dense microcrystals

of light-responding proteins that demand the size of the crystals (Mehrabi et al. 2021) to match the $1/e$ light penetration depth (Grünbein et al. 2020).

Here we compare SFX and SSX data sets of almost 14,000 indexed images each, collected at RT on rsEGFP2 microcrystals of the same size ($3 \times 3 \times 3 \mu\text{m}^3$) (Figure 3.4.1a). rsEGFP2 is a reversibly photoswitchable fluorescent protein that serves as a molecular marker in super-resolution microscopy (Grotjohann et al. 2012a). The SFX data is a subset of diffraction data collected using a GDVN liquid jet at CXI/LCLS and reported earlier (Coquelle et al. 2018b) and the SSX data sets were collected on solid supports in raster-scanning mode at the ESRF ID13 beamline. The SFX and SSX data sets were at 1.8 and 2.0 Å resolution, respectively, from which protein structures of similar quality were refined.

3.4.2 Results and Discussion

This study provides a systematic comparison of serial X-ray crystallography data collected at a synchrotron source (SSX) and an XFEL facility (SFX). SFX and SSX datasets were collected on microcrystals of rsEGFP2 in the *on*-state. The microcrystals for SFX and SSX were $3 \times 3 \times 3 \mu\text{m}^3$ in size (Figure 3.4.1a) and originated from the same crystallization batch (Coquelle et al. 2018b; Woodhouse et al. 2020a). Liquid jet injection and solid-support raster scanning were used in SFX and SSX, respectively (Figure 3.4.1b and c). Diffraction data were processed identically and the two data sets were composed of the same number of indexed images for a most meaningful comparison.

Comparison of SSX and SFX datasets

The most striking difference between the two data sets obtained is the estimated resolution reached (Table 1). A CC^* (Karplus and Diederichs 2012) of about 0.88 was used as the criterion for high-resolution cut-off, being 1.8 Å for the SFX and 2.0 Å for the SSX data set. Closer inspection of data processing statistics shows that globally the SSX data set is of slightly higher quality than the SFX one (Figure 3.4.2 and Table 3.4.1). The overall R_{split} is lower for the SSX (12.5%) than for the SFX data set (18.1%). Moreover, the Wilson B factor is 36.5 Å² for SSX data whereas the corresponding value for SFX data is 33.7 Å² (Table 3.4.1). In low-resolution

bins, up to ~ 3 Å, the quality is higher for the SSX than the SFX data set, whereas in higher resolution bins (from 3 Å to the high-resolution cut-off) the situation is reversed (Figure 3.4.2c). At 2 Å resolution, for example, R_{split} is 65 and 18 % for the SSX and SFX datasets, respectively. Since both data sets are complete and have been collected on crystals from the same batch, the difference in data quality is either due to differences in the X-ray source (synchrotron vs. XFEL) and/or the sample delivery method (solid support vs. GDVN) and/or the detector used (Eiger X 4M vs. CSPAD).

Comparison of the rsEGFP2 on-state structures determined by SSX and SFX

The model of rsEGFP2 in the *on*-state (PDB ID: 5O89) was refined against the SFX and SSX data sets at 1.8 and 2.0 Å resolution, respectively (Figure 3.4.4a and 3.4.4b). The refined models are superimposable (Figure 3.4.4c). No significant differences are observed in the chromophore pocket (Figure 3.4.4). All-atom root-mean-square deviations (r.m.s.d.) between the two models is 0.43 Å.

B-factor distribution is similar in both structures but with somewhat larger values in the SSX than in the SFX structure (Figure 3.4.5a), possibly echoing the difference in Wilson B factors (Figure 3.4.3). Figure 3.4.5b shows the difference distance matrix (DDM) which is the difference (in Å) between each $C\alpha$ of the SSX model and paired to every possible $C\alpha$ of the SFX model. The DDM reveals a relative expansion downstream of β -sheet 7 of the SSX versus the SFX structure (Figure 3.4.5b). In Figure 3.4.5c, it can be seen that the difference in distance values is more noticeable closer to the C-terminal of the structures.

A q-weighted Fourier difference map was calculated at 2.0 Å resolution using observed structure factor amplitudes of the SSX and SFX data sets (Figure 3.4.6). Most peaks are in the region that is indicated with asterisks in Figures 3.4.6a and b. The highest peak (-6.73σ) is located on the side chain of the His149 (Figure 3.4.6c), indicating a loss of definition of that residue in the SSX compared to the SFX structure. A decrease below the nominal pH value (8.0) of crystals prior to collecting the SSX data set might have increased the residual fraction of protonated chromophores (pK_a 6) leading to an increased disorder of the His149 side chain. No features are observable on the chromophore (Figure 3.4.6c) known to be highly radiation-sensitive (Adam et al. 2009), suggesting that the SSX structure is devoid of specific radiation damage, given that the SFX structure is radiation damage-free.

Further analysis was performed by calculating molecular van der Waals and Void volumes in proteins (Table 3.4.2). SSX model has a larger protein total volume than the SFX model. Both Void and van der Waals (VDW) volumes are greater in the SSX model than in the SFX model. Even if the difference in VDM volume between both structures is only 62.979 \AA^3 , the difference in Void volume is much higher of about 474.727 \AA^3 indicating that the difference in protein volume is due to the increase of the Void volume in the SSX model.

3.4.3 Conclusion and Perspectives

Here, we report a comparison of SSX and SFX datasets collected from the same batch of microcrystals whose size is about 3 \mu m in diameter. The SSX experiment during which the sample was sealed in a Si_3N_4 sandwich and there was no replenishment of crystallization buffer during data collection. On the other hand, during the SFX experiment (GDVN), the sample was constantly surrounded by the crystallization buffer until the delivery of the sample to the interaction point. Merging statistics suggests a higher resolution cut-off for the SFX (1.8 \AA) than for the SSX data set (2 \AA). Structures after refinement showed a slight variation in the volume of the protein in the SSX model compared to the SFX model. The differences in data statistics and structures might be attributed to the differences in radiation sources (synchrotron *versus* XFEL), detectors used (EIGER X 4M *versus* CSPAD), or sample presentation method (solid support *versus* GDVN).

Remarkably, high-quality SSX data can be collected from protein crystals as small as 3 \mu m . Crystals of such a small size might be required in time-resolved SSX experiments to match a small penetration depth of the pump laser in optically dense crystals of light-sensitive proteins (Grünbein et al. 2020). The $1/e$ penetration depth of 488-nm light into crystals of rsEGFP2 in the *on*-state is 2.5 \mu m (assuming a molar extinction coefficient of $60807 \text{ M}^{-1}\text{cm}^{-1}$ and a protein concentration in the crystal of 29 mM), hence requiring such a small crystal size for efficient reaction initiation, while minimizing the risk of multiphoton artifacts.

Synergetic studies involving XFEL and synchrotron radiation sources for elucidating ultrafast or ms intermediate structures would be more straightforward when minimization of the

variation in experimental parameters is considered, *i.e.* to use the same microcrystal batch, the same sample delivery method, and the same detector. In a recent study (Mehrabi et al. 2021) in which a comparison of SSX and SFX data sets was made, the authors used the same parameters but they used different detectors for SFX (MP-CCP in SACLA) and SSX datasets (EIGER 6M in DESY).

3.4.4 Materials and Methods

Expression, purification, and microcrystallization of rsEGFP2

rsEGFP2 was expressed and purified as previously described (El Khatib et al. 2016). Briefly, competent *E. coli* BL21(DE3) cells were transformed. Bacteria were grown in a self-inducible medium at 37 °C. After cell lysis, the protein fused to an N-terminal polyhistidine tag was purified by affinity chromatography using Ni-NTA beads followed by a size-exclusion chromatography step. Microcrystals from the same batch as the one used by Coquelle and co-workers (Coquelle et al. 2018) were used for SSX experiments (Figure 3.4.1a). They were generated by microseeded batch crystallization (Ilme Schlichting, unpublished) and the final condition was 2 M ammonium sulfate, 115.4 mM HEPES pH 8, 12.3 mM NaCl, 20 mg ml⁻¹ protein, and a final seed dilution in the batch of 1/50 (v/v). Microcrystals with a size of 3 µm in diameter appeared within 12 – 24 h at 20°C.

Sample preparation, data collection, and processing for SSX

The supernatant above the settled rsEGFP2 microcrystals was removed and the crystals were washed and stored in 2.5 M ammonium sulfate, 100 mM HEPES pH 8. After settling, solid support for the sample delivery was prepared as described previously (Coquelle et al. 2015; de la Mora et al. 2020). Microcrystals were centrifuged for ~1 min at 4000 rpm. About 500 nL from the pellet were pipetted onto a 500 nm thick and 2.5 × 2.5 mm² large Si₃N₄ membrane (Silson Northampton, England: <http://www.silson.com>) before adding another membrane in a *back-to-back* fashion to form sandwich-like solid support. The membranes were sealed using Araldite[®] glue to avoid sample dehydration, a procedure that took typically 15 – 20 s. The solid support was fixed using SuperGlue (LOCOTITE[®]) onto a small piece of glass, itself attached

to a magnetic crystal mount. Data on microcrystalline rsEGFP2 in their *on*-state (*i.e.* without prior pre-illumination at 488 nm) were collected at RT on the ID13-EH2 microfocuss beamline at the European Synchrotron Radiation Facility (ESRF) in March 2016. The membrane was scanned in lines with an X-ray beam (photon energy 13 keV) focused to $1.7 \times 2 \mu\text{m}^2$ (FWHM). Neighboring exposure positions were spaced by 10 μm , both horizontally and vertically. An EIGER X 4M (DECTRIS[®]) detector was used for data acquisition with a 2 ms exposure time at each position. Frames were recorded at 46,200 positions. NanoPeakCell (Coquelle et al. 2015) was used for hit finding. Finally, 13719 frames were indexed with CrystFEL 0.6.2 (White et al. 2016), using *MOSFLM* (Powell 1999), *DirAx* (Duisenberg 1992), and *XDS* (Kabsch 1988, 2010b, 2010a) as indexing methods. Integration was performed using the *ring-nocen* module. Merging was performed using the *partialator* algorithm using the *unity* partiality model with one cycle of scaling and post-refinement (White 2014; White et al. 2016).

Sample preparation, data collection, and processing for SFX

SFX data were recorded on CXI at the LCLS (proposal LI56) and have been published (Coquelle et al. 2018b). Briefly, a suspension containing 2 – 10 % (v/v) of rsEGFP2 microcrystals in 2 M ammonium sulfate, 100 mM HEPES pH 8 was filtered through a 20- μm stainless steel frit using an HPLC pump system before being transferred into a syringe mounted on an anti-settling device (Lomb et al. 2012) and injected in the CXI vacuum chamber using a gas dynamic virtual nozzle (GDVN) injector (DePonte et al. 2008). SFX data were acquired with Cornell-SLAC Pixel Array detector (CSPAD) (Blaj et al. 2015) at RT on rsEGFP2 crystals in the *on*-state, *i.e.* without pre-illumination and pump-laser triggering. Indexing was performed with CrystFEL 0.6.2 using *MOSFLM*, *DirAx*, and *XDS*, and integration was performed using the *ring-nocen* method. Merging was performed using the *partialator* algorithm using the *unity* partiality model with one cycle of scaling and post-refinement. For the sake of comparing SFX and SSX data sets, the same number of indexed frames as the one composing the SSX data set (*i.e.* 13,719) were randomly extracted from the 34,715 indexed frames of the *on*-state reference data set (Coquelle et al. 2018b) and underwent the same data processing protocol.

SFX and SSX structure solution and refinement

Both structures underwent the same molecular replacement and refinement protocols. Molecular replacement was performed with *Phaser* (McCoy et al. 2007) starting from the *on-state* structure of rsEGFP2 determined by RT SFX (PDB ID: 5O89 (Coquelle et al. 2018b)). Before structure refinement, B-factors were set to the corresponding values calculated from Wilson plots (Table 3.4.1). Reciprocal space refinement was performed using *Refmac5* (Murshudov et al. 2011) and included positional and isotropic individual B-factor refinement. Manual model building and real-space refinement were carried out using *Coot* (Emsley and Cowtan 2004). Figures were produced with *PyMOL* (Schrödinger and DeLano 2020).

Structure comparison

RMSD between the SSX and SFX models was calculated using the least-squares algorithm implemented in *Coot* (Emsley and Cowtan 2004). *Phenix.model_model_distances* program was used to calculate the pair-to-pair distance difference for *Ca*, all and backbone atoms. DDM was calculated by a Python script provided by Dr. Nicolas Coquelle from the ESRF (Grenoble, France).

Calculation of Fourier difference maps between SSX and SFX data sets

Q-weighted (Ursby and Bourgeois 1997) Fourier difference electron density maps of the SSX data against the SFX data ($F_{obs}^{SSX} - F_{obs}^{SFX}$) were calculated using the software *Xtrapol8* (De Zitter et al. 2022).

Calculation of absorbed X-ray dose

the absorbed X-ray dose was calculated with RADDPOSE-3D version 4 (Bury et al. 2018) and RADDPOSE-XFEL (Dickerson et al. 2020) for SSX and SFX data sets, respectively. Input parameters were 3 μm crystal dimensions, 3.3 voxels/ μm , unit cell parameters as they are specified in Table 3.4.1, four monomers in the unit cell (P2₁2₁2₁ space group), 239 amino acids, seven sulfur atoms in the protein, 2100 mM and 2600 mM (ammonium sulfate and HEPES; see Sample preparation in Materials and Methods) for sulfur elements present in the solvent, fraction of the unit cell occupied of the solvent of 0.403. Photoelectron escape from the crystal and influx from the surrounding material into the crystal, and fluorescent-photon escape were considered. Beam specifications for the SSX data set were Gaussian profile, a flux of 1×10^{12} , 1.7 (H) and 2.0 μm

FWHM, photon energy at 13 keV. The start and end rotational angles were set to 0, as still images were collected. The exposure time was 2 ms. Beam specifications for the SFX data set were Gaussian profile, 1.3 (H) and 1.3 μm FWHM, photon, and pulse energy at 9.5 keV and 0.3 mJ. The start and end rotational angles were set to 0, as still images were collected and as it was suggested for other SFX datasets (Dickerson et al. 2020). The exposure time was 35 fs. For the radiation dose estimation, 18 runs with 250,000 photons were used as for other SFX datasets (Dickerson et al. 2020).

3.4.5 Figures and Tables

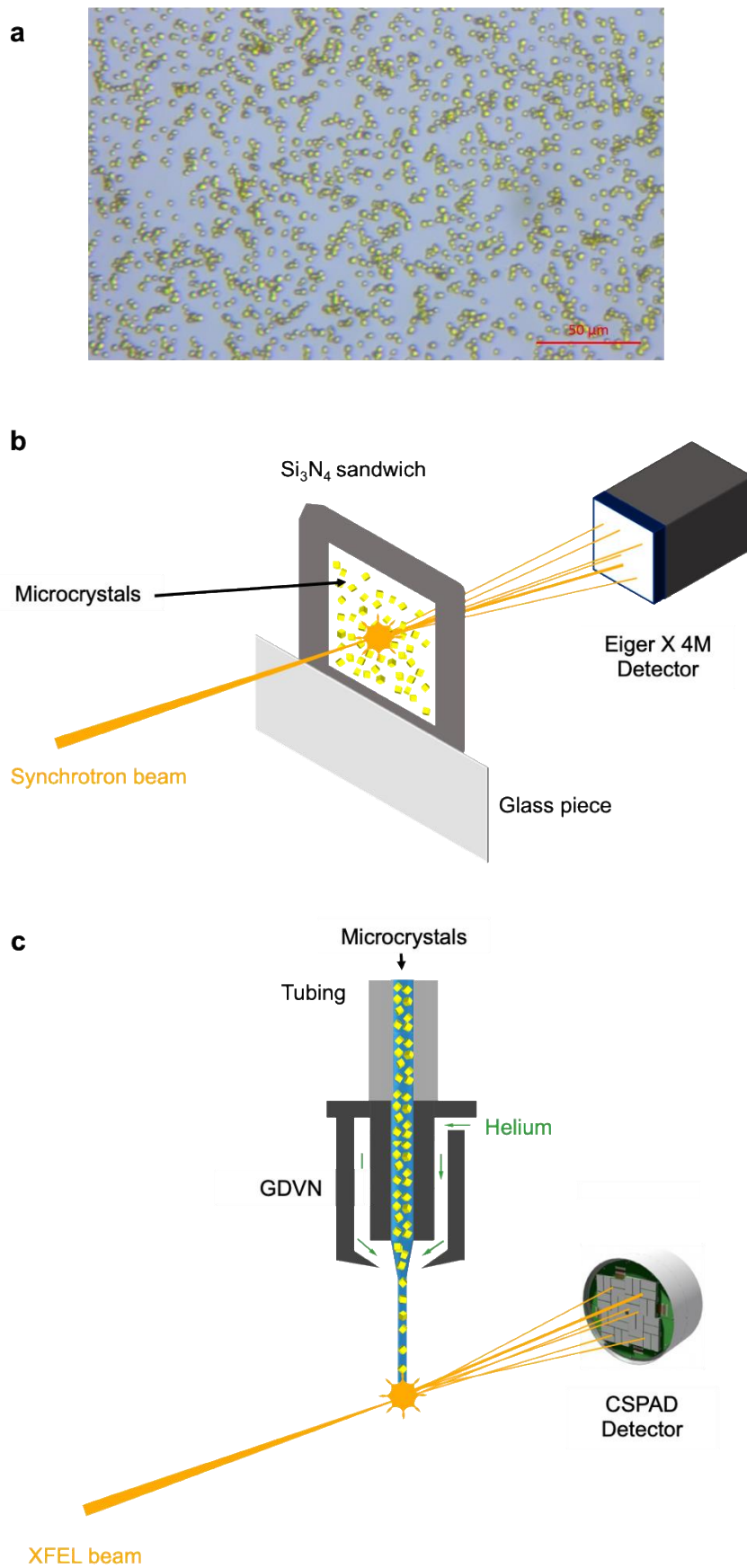


Figure 3.4.1: Crystals and experimental setups for serial crystallography

Microcrystals (a) used for the experimental setups that were used for SSX (b) and SFX (c) data collection. (a) rsEGFP2 crystals were about 3 μm in size. The image was taken using an optical microscope (Zeiss SteREO Discovery.V12) using an Achromat S 1.5 \times objective. (b) Raster scan setup. Microcrystals are loaded on a silicon nitride sandwich that is presented to the X-ray beam. (c) GDVN setup. Microcrystals are pumped through a capillary and the jet is focused by helium gas through the nozzle aperture.

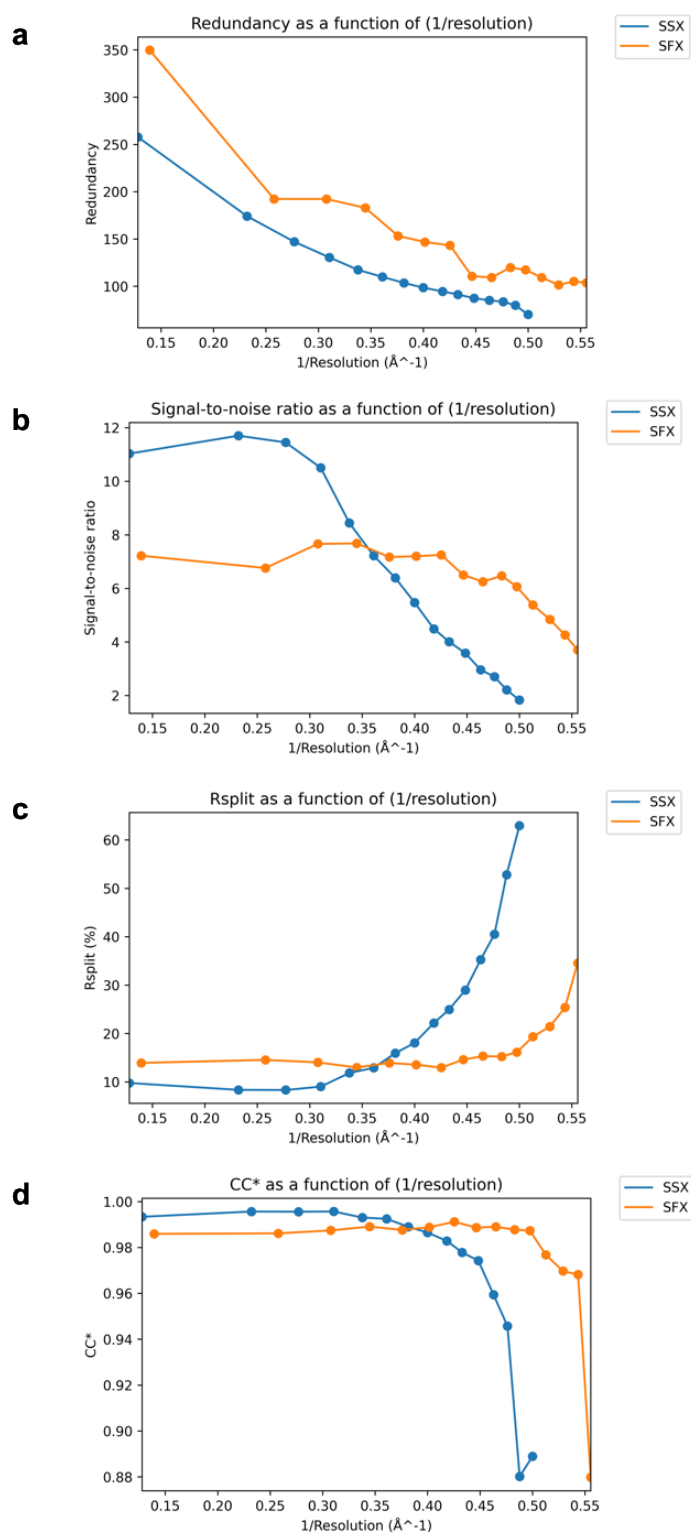


Figure 3.4.2: Data processing statistics as a function of resolution

Redundancy (a), signal-to-noise ratio (SNR) (b), R_{split} (c) and CC^* (d) as a function of $1/resolution$ for SFX (orange) and SSX (blue) datasets. High-resolution cut-offs are set to 1.8 and 2.0 Å for SFX and SSX datasets, respectively.

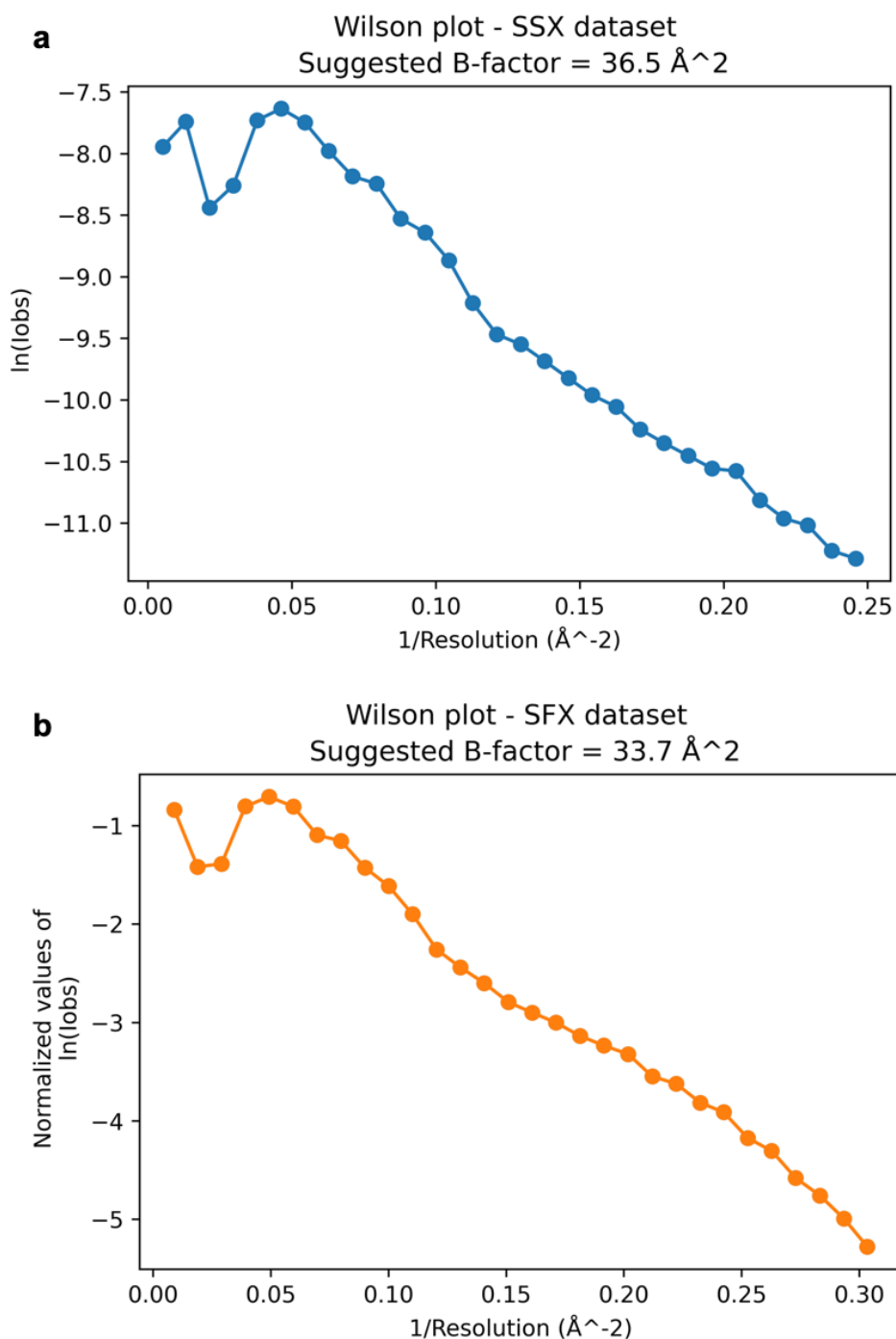


Figure 3.4.3: Wilson plots of SSX and SFX datasets

Plots showing intensities as a function of resolution for SSX (a) and SFX (b) datasets. Wilson B was estimated at 36.5 and 33.7 \AA^2 considering intensities from 4.5 \AA up to the highest resolution for each dataset (Table 3.4.1). Wilson B plots and factors were calculated using truncate from the CCP4 suite.

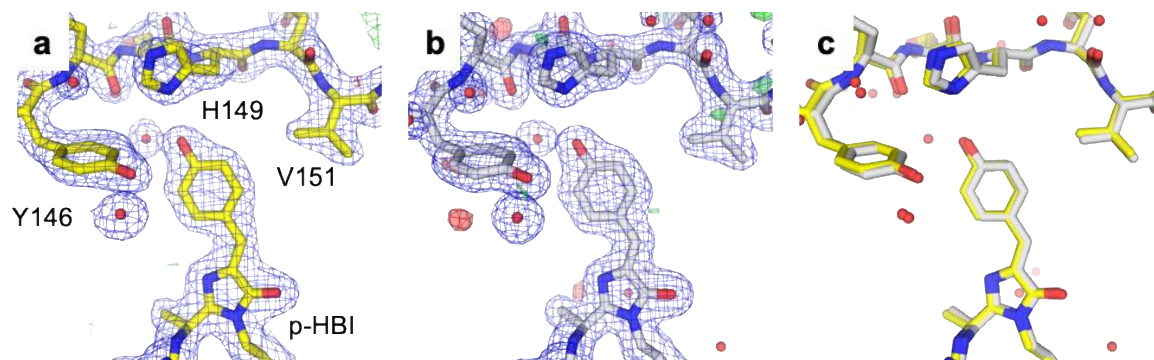


Figure 3.4.4: SSX and SFX structures of rsEGFP2

Models and maps of rsEGFP2 in the on-state based on SSX (a) and SFX (b) data. Overlay of the two models (c). SSX and SFX models are shown in yellow and grey respectively. $2F_{obs}-F_{calc}$ maps at 1σ are displayed in blue and $F_{obs}-F_{calc}$ maps at $\pm 3 \sigma$ are displayed in green/red.

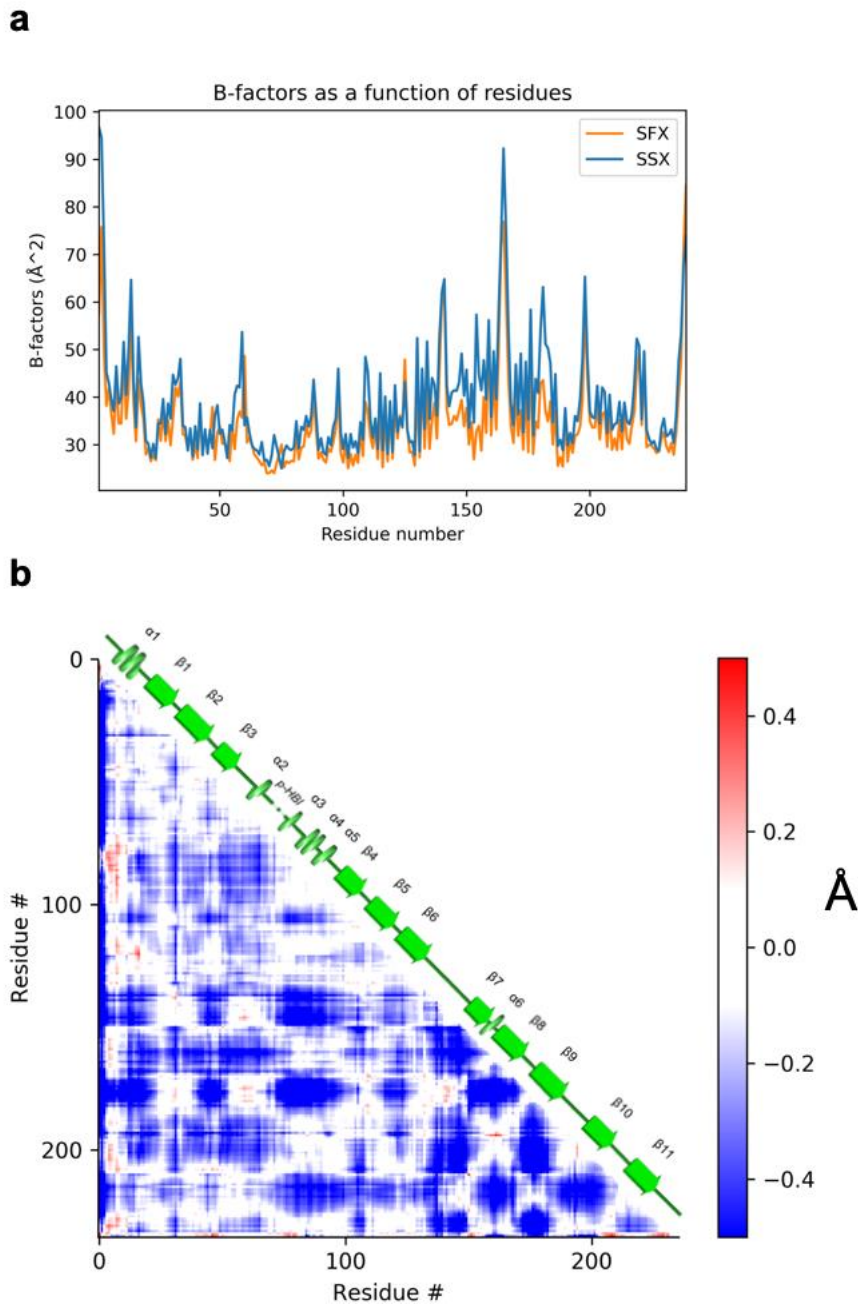


Figure 3.4.5: B-factors and difference distance matrix between SSX and SFX structures

(a) Averaged overall B-factors (main and side-chain) distribution of the amino acids in the SSX (orange) and SFX (blue) structures. (b) Difference distance matrix (DDM) between the pairs of Ca atoms of both structures, where red indicates greater distances in the SFX than the SSX structure and blue greater distances in the SSX than the SFX structures. rsEGFP2 secondary structure elements are represented as green spirals and arrows for α -helices and β -sheets, respectively.

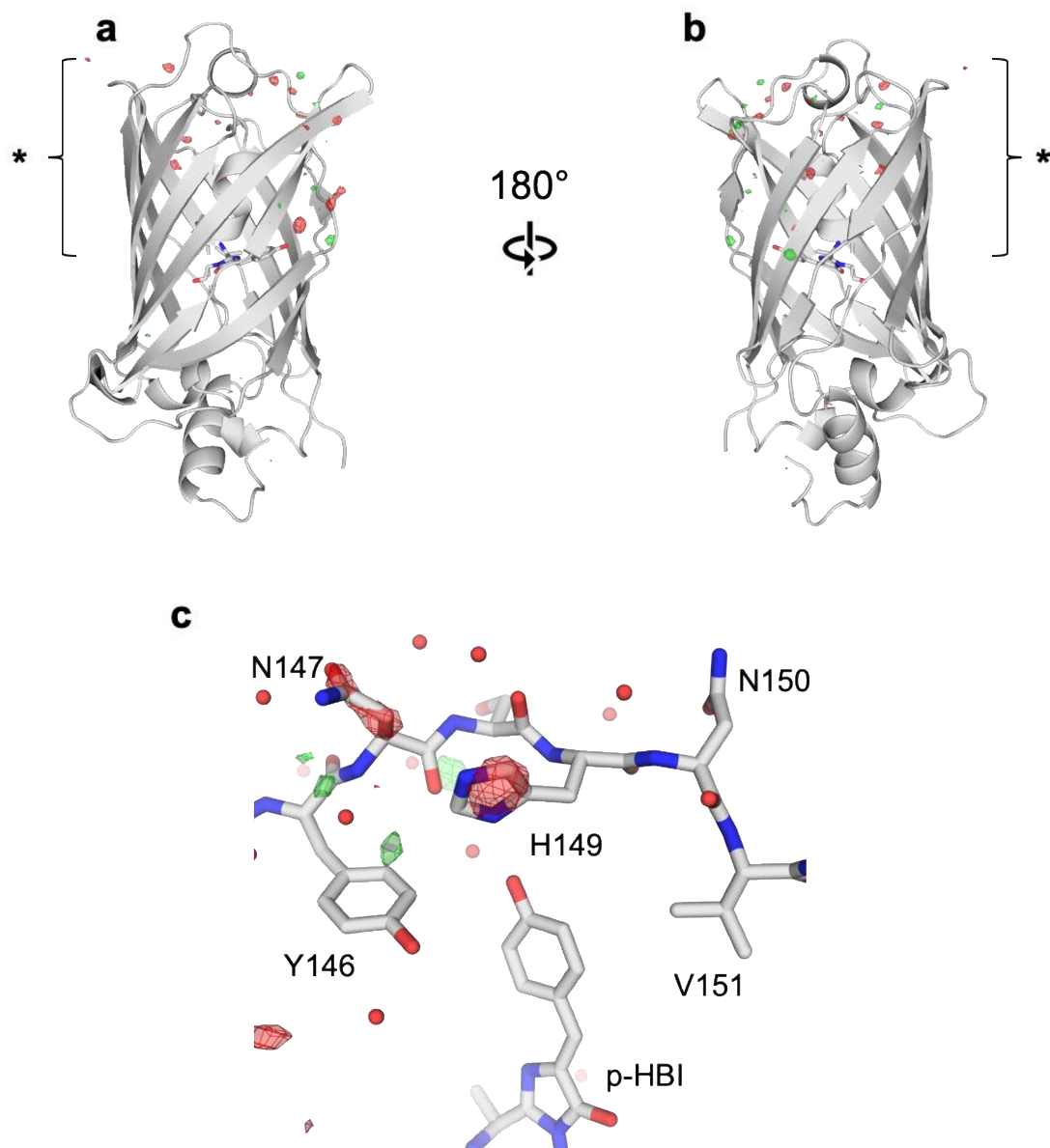


Figure 3.4.6: Fourier difference map computed using SSX and SFX datasets

Q-weighted Fourier difference map calculated at 2.0 Å resolution using observed structure factor amplitudes of the SSX and SFX datasets ($F_{obs}^{SSX} - F_{obs}^{SFX}$), contoured at $+4\sigma$ (green) and -4σ (red) and overlaid onto the model determined from the SFX dataset. (a, b) entire SFX model and (c) zoom (asterisk) into the chromophore pocket, where the highest peak (-6.73σ) is located on the H149 site chain.

Dataset	SSX	SFX
Space group	P2 ₁ 2 ₁ 2 ₁	P2 ₁ 2 ₁ 2 ₁
Unit cell parameters		
a (Å)	51.67	
b (Å)	62.26	
c (Å)	71.88	
Indexed frames	13,719	13,719
Observations	1,953,974	3,445,787
Resolution (Å)	17.00 – 2.00 (2.05 – 2.00)	17.00– 1.80 (1.84 – 1.80)
R _{split} (%)	10.65 (62.94)	14.17 (34.54)
CC*	0.996 (0.889)	0.992 (0.880)
I / σ(I)	6.34 (1.83)	6.31 (3.70)
Completeness (%)	100 (100)	100 (100)
Redundancy	116.8 (70.1)	150.7 (103.7)
Wilson B factor (Å ²)	36.5	33.7
R _{iso, free} (% , with respect to SFX dataset) [§]	25.10	n.a
R _{iso, work} (% , with respect to SFX dataset) [§]	25.66	n.a
CC _{iso, free} (% , with respect to SFX dataset) [§]	93.21	n.a
CC _{iso, work} (% , with respect to SFX dataset) [§]	92.97	n.a
Absorbed dose (MGy)	0.07 [§]	31.65 ^{&}
Refinement statistics		
Resolution (Å)	17.00 – 2.00 (2.05 – 2.00)	17.00– 1.80 (1.84 – 1.80)
Number of reflections	15,359 (1,088)	20,941 (1,504)
R _{free} (%)	19.1 (31.3)	18.2 (22.8)
R _{work} (%)	14.7 (24.1)	14.7 (21.6)
Number of protein atoms	1961	1951

Number of water atoms	128	234
B-factor protein (\AA^2)	39.85	34.13
r.m.s.d. bond lengths (\AA)	0.0098	0.013
r.m.s.d. angles ($^\circ$)	1.66	1.80
Ramachandran favored (%)	98.7	98.3
Ramachandran allowed (%)	1.3	1.7
Ramachandran outliers (%)	0.0	0.0
Rotamer outliers (%)	1.8	1.8
C-beta outliers (%)	0.0	0.0
Clashscore	3.60	3.87

^s Average Diffraction Weighted Dose (ADWD) calculated with RADDPOSE-3D (Bury et al. 2018)

[&] Average Dose Exposed Region (ADER) calculated with RADDPOSE-XFEL (Dickerson et al. 2020)

Table 3.4.1: Data collection, processing, and refinement statistics

Protein	Total Volume (Å ³)	Void Volume (Å ³)	VDW Volume (Å ³)	Packing	Density
<i>SSX model</i>	33451.220	9521.701	23929.519	0.715	85060
<i>SFX model</i>	32912.424	9045.974	23866.450	0.725	86397

Table 3.4.2: Protein volume calculation for SSX and SFX models

4 Summary

My Ph.D. thesis describes the study of two light-sensitive proteins, the photoenzyme fatty acid photodecarboxylase (FAP), and the reversibly photoswitchable fluorescent protein rsEGFP2 by using X-ray free-electron lasers (XFELs). XFELs offer the possibility to capture short-lived intermediates from microcrystals using time-resolved (TR) serial femtosecond crystallography (SFX).

FAP is a photoenzyme from microalga that converts free fatty acids to the corresponding hydrocarbons and releases a CO₂ molecule whose catalytic reaction requires light. My Ph.D. work confirmed the unusual bending conformation of the oxidized light-capturing co-factor, FAD by a radiation-damage free SFX structure of the dark-state solved at 2 Å resolution. Moreover, characterization of light-captured intermediates at 20 ps, 900 ps, 300 ns at 2 Å resolution, and 2 μs at 2.2 Å resolution was carried out with the aim to follow the fate of the two products, the hydrocarbon, and the CO₂ molecule. To do so, difference Fourier maps and extrapolated structure factors were calculated and intermediate-state structures refined. Only the hydrocarbon molecule, but not the CO₂ molecule, could be identified in the extrapolated electron density maps. Challenges encountered before and during the TR-SFX experiment are described in detail. My Ph.D. work on FAP, *i.e.* characterization of the radiation damage-free dark-state structure, as well as difference Fourier maps of the intermediate structures, complemented results from various experimental and computational results obtained by an international consortium that allowed proposing a detailed mechanism for the FAP photocycle.

rsEGFP2 is a photoswitchable fluorescent protein that is used for nanoscopy applications. rsEGFP2 undergoes *cis-to-trans* isomerization upon light absorption. When the *on*-state (*cis* chromophore conformation) of rsEGFP2 is irradiated with 488 nm light, fluorescence is induced and rsEGFP2 transits to the *off*-state (*trans*), whereas irradiation at 405 nm switches the protein back to the *on*-state. My Ph.D. work on rsEGFP2 was focused on elucidation and characterization of the parental rsEGFP2 and its V151A and V151L variants by static SFX and of rsEGFP2-V151A and -V151L by TR-SFX on the nanosecond time scale. Static SFX structures on the parental rsEGFP2 and its variants showed that the structural heterogeneity of the chromophore in the *off*-state that was reported previously for the parental protein was suppressed in its variants. Intermediate structures of the V151A and V151L variants have been

solved by nanosecond TR-SFX. Ten ns after photoexcitation, both structures feature a chromophore that isomerized from *trans* to *cis* and indicate that amino acid side chains in the chromophore pocket are in the same position as in the *on*-state structure, the only exception being His149 whose position is closer to the one in the *off*-state structure rather than the *on*-state structure. To prepare for TR-SSX experiments to be carried out in the future, a systematic comparison has been carried out of SSX and SFX data collected on rsEGFP2 microcrystals. Such a TR-SSX experiment, carried out on the micro- to millisecond time scale, will allow characterizing the movement of His149 beyond the 10 ns time point.

The perpetual development of TR-SFX and TR-SSX allow the elucidation of intermediate structures in biological macromolecules and the ability to make what is called “molecular movies”. The understanding of the structure of the biomolecules gives the opportunity to improve, tailor and specify the protein function and also to expand their applications.

5 References

- A. Schwentker, Miriam, Hannes Bock, Michael Hofmann, Stefan Jakobs, Jörg Bewersdorf, Christian Eggeling, and Stefan W. Hell. 2007. “Wide-Field Subdiffraction RESOLFT Microscopy Using Fluorescent Protein Photoswitching.” *Microscopy Research and Technique* 70(3):269–80. doi: 10.1002/jemt.20443.
- Abbe, E. 1873. “Beiträge zur Theorie des Mikroskops und der mikroskopischen Wahrnehmung.” *Archiv für Mikroskopische Anatomie* 9(1):413–68. doi: 10.1007/BF02956173.
- Abbruzzetti, Stefania, Elena Grandi, Cristiano Viappiani, Sara Bologna, Barbara Campanini, Samanta Raboni, Stefano Bettati, and Andrea Mozzarelli. 2005. “Kinetics of Acid-Induced Spectral Changes in the GFPmut2 Chromophore.” *Journal of the American Chemical Society* 127(2):626–35. doi: 10.1021/ja045400r.
- Adam, Virgile. 2014. “Phototransformable Fluorescent Proteins: Which One for Which Application?” *Histochemistry and Cell Biology* 142(1):19–41. doi: 10.1007/s00418-014-1190-5.
- Adam, Virgile, Romain Berardozi, Martin Byrdin, and Dominique Bourgeois. 2014. “Phototransformable Fluorescent Proteins: Future Challenges.” *Current Opinion in Chemical Biology* 20:92–102. doi: 10.1016/j.cbpa.2014.05.016.
- Adam, Virgile, Philippe Carpentier, Sebastien Violot, Mickaël Lelimosin, Claudine Darnault, G. Ulrich Nienhaus, and Dominique Bourgeois. 2009. “Structural Basis of X-Ray-Induced Transient Photobleaching in a Photoactivatable Green Fluorescent Protein.” *Journal of the American Chemical Society* 131(50):18063–65. doi: 10.1021/ja907296v.
- Adam, Virgile, Kyprianos Hadjidemetriou, Nickels Jensen, Robert L. Shoeman, Joyce Woodhouse, Andrew Aquila, Anne-Sophie Banneville, Thomas R. M. Barends, Victor Bezchastnov, Sebastien Boutet, Martin Byrdin, Marco Cammarata, Sergio Carbajo, Nina-Eleni Christou, Nicolas Coquelle, Eugenio De la Mora, Mariam El Khatib, Tadeo Moreno Chicano, R. Bruce Doak, Franck Fieschi, Lutz Foucar, Oleksandr Glushonkov, Alexander Gorel, Marie-Luise Grunbein, Mario Hilpert, Mark Hunter, Marco Kloos, Jason E. Koglin, Thomas J. Lane, Mengning Liang, Angela Mantovanelli, Karol Nass, Gabriela Nass Kovacs, Shigeki Owada, Christopher M. Roome, Giorgio Schiro, Matthew Seaberg, Miriam Stricker, Michel Thepaut, Kensuke Tono, Kiyoshi Ueda, Lucas M. Uriarte, Daehyun You, Ninon Zala, Tatiana Domratcheva, Stefan Jakobs, Michel Sliwa, Ilme Schlichting, Jacques-Philippe Colletier, Dominique Bourgeois, and Martin Weik. 2021. “Rational Control of Structural Off-State Heterogeneity in a Photoswitchable Fluorescent Protein Provides Switching Contrast Enhancement.” *BioRxiv* 2021.11.05.462999. doi: 10.1101/2021.11.05.462999.
- Agarwal, Pratul K. 2006. “Enzymes: An Integrated View of Structure, Dynamics and Function.” *Microbial Cell Factories* 5(1):2. doi: 10.1186/1475-2859-5-2.
- Agarwal, Pratul K. 2019. “A Biophysical Perspective on Enzyme Catalysis.” *Biochemistry* 58(6):438–49. doi: 10.1021/acs.biochem.8b01004.

- Altarelli, M. 2011. "The European X-Ray Free-Electron Laser Facility in Hamburg." *Nuclear Instruments and Methods in Physics Research Section B: Beam Interactions with Materials and Atoms* 269(24):2845–49. doi: 10.1016/j.nimb.2011.04.034.
- Altarelli, M. 2015. "The European X-Ray Free-Electron Laser: Toward an Ultra-Bright, High Repetition-Rate x-Ray Source." *High Power Laser Science and Engineering* 3:e18. doi: 10.1017/hpl.2015.17.
- Amer, Mohamed, Emilia Z. Wojcik, Chenhao Sun, Robin Hoeven, John M. X. Hughes, Matthew Faulkner, Ian Sofian Yunus, Shirley Tait, Linus O. Johannissen, Samantha J. O. Hardman, Derren J. Heyes, Guo-Qiang Chen, Michael H. Smith, Patrik R. Jones, Helen S. Toogood, and Nigel S. Scrutton. 2020. "Low Carbon Strategies for Sustainable Bio-Alkane Gas Production and Renewable Energy." *Energy & Environmental Science* 13(6):1818–31. doi: 10.1039/D0EE00095G.
- Ando, R., H. Hama, M. Yamamoto-Hino, H. Mizuno, and A. Miyawaki. 2002. "An Optical Marker Based on the UV-Induced Green-to-Red Photoconversion of a Fluorescent Protein." *Proceedings of the National Academy of Sciences* 99(20):12651–56. doi: 10.1073/pnas.202320599.
- Ando, Ryoko, Cristina Flors, Hideaki Mizuno, Johan Hofkens, and Atsushi Miyawaki. 2007. "Highlighted Generation of Fluorescence Signals Using Simultaneous Two-Color Irradiation on Dronpa Mutants." *Biophysical Journal* 92(12):L97–99. doi: 10.1529/biophysj.107.105882.
- Ando, Ryoko, Hideaki Mizuno, and Atsushi Miyawaki. 2004. "Regulated Fast Nucleocytoplasmic Shuttling Observed by Reversible Protein Highlighting." *Science* 306(5700):1370–73. doi: 10.1126/science.1102506.
- Andresen, M., A. C. Stiel, S. Trowitzsch, G. Weber, C. Eggeling, M. C. Wahl, S. W. Hell, and S. Jakobs. 2007. "Structural Basis for Reversible Photoswitching in Dronpa." *Proceedings of the National Academy of Sciences* 104(32):13005–9. doi: 10.1073/pnas.0700629104.
- Andresen, Martin, Andre C. Stiel, Jonas Fölling, Dirk Wenzel, Andreas Schönle, Alexander Egner, Christian Eggeling, Stefan W. Hell, and Stefan Jakobs. 2008. "Photoswitchable Fluorescent Proteins Enable Monochromatic Multilabel Imaging and Dual Color Fluorescence Nanoscopy." *Nature Biotechnology* 26(9):1035–40. doi: 10.1038/nbt.1493.
- Aquila, Andrew, Mark S. Hunter, R. Bruce Doak, Richard A. Kirian, Petra Fromme, Thomas A. White, Jakob Andreasson, David Arnlund, Saša Bajt, Thomas R. M. Barends, Miriam Barthelmess, Michael J. Bogan, Christoph Bostedt, Hervé Bottin, John D. Bozek, Carl Caleman, Nicola Coppola, Jan Davidsson, Daniel P. DePonte, Veit Elser, Sascha W. Epp, Benjamin Erk, Holger Fleckenstein, Lutz Foucar, Matthias Frank, Raimund Fromme, Heinz Graafsma, Ingo Grotjohann, Lars Gumprecht, Janos Hajdu, Christina Y. Hampton, Andreas Hartmann, Robert Hartmann, Stefan Hau-Riege, Günter Hauser, Helmut Hirsemann, Peter Holl, James M. Holton, André Hömke, Linda Johansson, Nils Kimmel, Stephan Kassemeyer, Faton Krasniqi, Kai-Uwe Kühnel, Mengning Liang, Lukas Lomb, Erik Malmerberg, Stefano Marchesini, Andrew V. Martin, Filipe R. N. C. Maia, Marc Messerschmidt, Karol Nass, Christian Reich,

- Richard Neutze, Daniel Rolles, Benedikt Rudek, Artem Rudenko, Ilme Schlichting, Carlo Schmidt, Kevin E. Schmidt, Joachim Schulz, M. Marvin Seibert, Robert L. Shoeman, Raymond Sierra, Heike Soltau, Dmitri Starodub, Francesco Stellato, Stephan Stern, Lothar Strüder, Nicusor Timneanu, Joachim Ullrich, Xiaoyu Wang, Garth J. Williams, Georg Weidenspointner, Uwe Weierstall, Cornelia Wunderer, Anton Barty, John C. H. Spence, and Henry N. Chapman. 2012. “Time-Resolved Protein Nanocrystallography Using an X-Ray Free-Electron Laser.” *Optics Express* 20(3):2706. doi: 10.1364/OE.20.002706.
- Aumonier, Sylvain, Gianluca Santoni, Guillaume Gotthard, David von Stetten, Gordon A. Leonard, and Antoine Royant. 2020. “Millisecond Time-Resolved Serial Oscillation Crystallography of a Blue-Light Photoreceptor at a Synchrotron.” *IUCrJ* 7(4):728–36. doi: 10.1107/S2052252520007411.
- Ayyer, Kartik, Oleksandr M. Yefanov, Dominik Oberthür, Shatabdi Roy-Chowdhury, Lorenzo Galli, Valerio Mariani, Shibom Basu, Jesse Coe, Chelsie E. Conrad, Raimund Fromme, Alexander Schaffer, Katerina Dörner, Daniel James, Christopher Kupitz, Markus Metz, Garrett Nelson, Paulraj Lourdu Xavier, Kenneth R. Beyerlein, Marius Schmidt, Iosifina Sarrou, John C. H. Spence, Uwe Weierstall, Thomas A. White, Jay-How Yang, Yun Zhao, Mengning Liang, Andrew Aquila, Mark S. Hunter, Joseph S. Robinson, Jason E. Koglin, Sébastien Boutet, Petra Fromme, Anton Barty, and Henry N. Chapman. 2016. “Macromolecular Diffractive Imaging Using Imperfect Crystals.” *Nature* 530(7589):202–6. doi: 10.1038/nature16949.
- Baker, P. J., G. W. Farrants, T. J. Stillman, K. L. Britton, J. R. Helliwell, and D. W. Rice. 1990. “Isomorphous Replacement with Optimized Anomalous Scattering Applied to Protein Crystallography.” *Acta Crystallographica Section A Foundations of Crystallography* 46(9):721–25. doi: 10.1107/S0108767390005153.
- Balzarotti, Francisco, Yvan Eilers, Klaus C. Gwosch, Arvid H. Gynnå, Volker Westphal, Fernando D. Stefani, Johan Elf, and Stefan W. Hell. 2017. “Nanometer Resolution Imaging and Tracking of Fluorescent Molecules with Minimal Photon Fluxes.” *Science* 355(6325):606–12. doi: 10.1126/science.aak9913.
- Barends, Thomas R. M., Lutz Foucar, Albert Ardevol, Karol Nass, Andrew Aquila, Sabine Botha, R. Bruce Doak, Konstantin Falahati, Elisabeth Hartmann, Mario Hilpert, Marcel Heinz, Matthias C. Hoffmann, Jürgen Köfinger, Jason E. Koglin, Gabriela Kovacsova, Mengning Liang, Despina Milathianaki, Henrik T. Lemke, Jochen Reinstein, Christopher M. Roome, Robert L. Shoeman, Garth J. Williams, Irene Burghardt, Gerhard Hummer, Sébastien Boutet, and Ilme Schlichting. 2015. “Direct Observation of Ultrafast Collective Motions in CO Myoglobin upon Ligand Dissociation.” *Science* 350(6259):445. doi: 10.1126/science.aac5492.
- Barends, Thomas R. M., Lutz Foucar, Sabine Botha, R. Bruce Doak, Robert L. Shoeman, Karol Nass, Jason E. Koglin, Garth J. Williams, Sébastien Boutet, Marc Messerschmidt, and Ilme Schlichting. 2014. “De Novo Protein Crystal Structure Determination from X-Ray Free-Electron Laser Data.” *Nature* 505(7482):244–47. doi: 10.1038/nature12773.
- Barends, Thomas R. M., Lutz Foucar, Robert L. Shoeman, Sadia Bari, Sascha W. Epp, Robert Hartmann, Gunter Hauser, Martin Huth, Christian Kieser, Lukas Lomb, Koji Motomura, Kiyonobu Nagaya, Carlo Schmidt, Rafael Strecker, Denis Anielski,

- Rebecca Boll, Benjamin Erk, Hironobu Fukuzawa, Elisabeth Hartmann, Takaki Hatsui, Peter Holl, Yuichi Inubushi, Tetsuya Ishikawa, Stephan Kassemeyer, Christian Kaiser, Frank Koeck, Naoki Kunishima, Moritz Kurka, Daniel Rolles, Benedikt Rudek, Artem Rudenko, Takahiro Sato, Claus-Dieter Schroeter, Heike Soltau, Lothar Strueder, Tomoyuki Tanaka, Tadashi Togashi, Kensuke Tono, Joachim Ullrich, Satoshi Yase, Shin-ichi Wada, Makoto Yao, Makina Yabashi, Kiyoshi Ueda, and Ilme Schlichting. 2013. “Anomalous Signal from S Atoms in Protein Crystallographic Data from an X-Ray Free-Electron Laser.” *Acta Crystallographica Section D Biological Crystallography* 69(5):838–42. doi: 10.1107/S0907444913002448.
- Barkla, C. G., and C. A. Sadler. 1909. “LXIX. *The Absorption of Röntgen Rays.*” *The London, Edinburgh, and Dublin Philosophical Magazine and Journal of Science* 17(101):739–60. doi: 10.1080/14786440508636650.
- Barth, Howard G., Christian Jackson, and Barry E. Boyes. 1994. “Size Exclusion Chromatography.” *Analytical Chemistry* 66(12):595–620. doi: 10.1021/ac00084a022.
- Barty, Anton, Carl Caleman, Andrew Aquila, Nicusor Timneanu, Lukas Lomb, Thomas A. White, Jakob Andreasson, David Arnlund, Saša Bajt, Thomas R. M. Barends, Miriam Barthelmess, Michael J. Bogan, Christoph Bostedt, John D. Bozek, Ryan Coffee, Nicola Coppola, Jan Davidsson, Daniel P. DePonte, R. Bruce Doak, Tomas Ekeberg, Veit Elser, Sascha W. Epp, Benjamin Erk, Holger Fleckenstein, Lutz Foucar, Petra Fromme, Heinz Graafsma, Lars Gumprecht, Janos Hajdu, Christina Y. Hampton, Robert Hartmann, Andreas Hartmann, Günter Hauser, Helmut Hirsemann, Peter Holl, Mark S. Hunter, Linda Johansson, Stephan Kassemeyer, Nils Kimmel, Richard A. Kirian, Mengning Liang, Filipe R. N. C. Maia, Erik Malmerberg, Stefano Marchesini, Andrew V. Martin, Karol Nass, Richard Neutze, Christian Reich, Daniel Rolles, Benedikt Rudek, Artem Rudenko, Howard Scott, Ilme Schlichting, Joachim Schulz, M. Marvin Seibert, Robert L. Shoeman, Raymond G. Sierra, Heike Soltau, John C. H. Spence, Francesco Stellato, Stephan Stern, Lothar Strüder, Joachim Ullrich, X. Wang, Georg Weidenspointner, Uwe Weierstall, Cornelia B. Wunderer, and Henry N. Chapman. 2012. “Self-Terminating Diffraction Gates Femtosecond X-Ray Nanocrystallography Measurements.” *Nature Photonics* 6(1):35–40. doi: 10.1038/nphoton.2011.297.
- Barty, Anton, Richard A. Kirian, Filipe R. N. C. Maia, Max Hantke, Chun Hong Yoon, Thomas A. White, and Henry Chapman. 2014. “*Cheetah*: Software for High-Throughput Reduction and Analysis of Serial Femtosecond X-Ray Diffraction Data.” *Journal of Applied Crystallography* 47(3):1118–31. doi: 10.1107/S1600576714007626.
- Batyuk, Alexander, Lorenzo Galli, Andrii Ishchenko, Gye Won Han, Cornelius Gati, Petr A. Popov, Ming-Yue Lee, Benjamin Stauch, Thomas A. White, Anton Barty, Andrew Aquila, Mark S. Hunter, Mengning Liang, Sébastien Boutet, Mengchen Pu, Zhi-jie Liu, Garrett Nelson, Daniel James, Chufeng Li, Yun Zhao, John C. H. Spence, Wei Liu, Petra Fromme, Vsevolod Katritch, Uwe Weierstall, Raymond C. Stevens, and Vadim Cherezov. 2016. “Native Phasing of X-Ray Free-Electron Laser Data for a G Protein–Coupled Receptor.” *Science Advances* 2(9):e1600292. doi: 10.1126/sciadv.1600292.
- van den Bedem, Henry, and James S. Fraser. 2015. “Integrative, Dynamic Structural Biology at Atomic Resolution—It’s about Time.” *Nature Methods* 12(4):307–18. doi: 10.1038/nmeth.3324.

- Benini, Stefano, Michele Cianci, Luca Mazzei, and Stefano Ciurli. 2014. "Fluoride Inhibition of Sporosarcina Pasteurii Urease: Structure and Thermodynamics." *JBIC Journal of Biological Inorganic Chemistry* 19(8):1243–61. doi: 10.1007/s00775-014-1182-x.
- Berkholz, Donald S., H. Richard Faber, Savvas N. Savvides, and P. Andrew Karplus. 2008. "Catalytic Cycle of Human Glutathione Reductase Near 1 Å Resolution." *Journal of Molecular Biology* 382(2):371–84. doi: 10.1016/j.jmb.2008.06.083.
- Berson, D. M. 2002. "Phototransduction by Retinal Ganglion Cells That Set the Circadian Clock." *Science* 295(5557):1070–73. doi: 10.1126/science.1067262.
- Bertani, G. 1951. "Studies on Lysogenesis. I. The Mode of Phage Liberation by Lysogenic Escherichia Coli." *Journal of Bacteriology* 62(3):293–300. doi: 10.1128/jb.62.3.293-300.1951.
- Bertani, Giuseppe. 2004. "Lysogeny at Mid-Twentieth Century: P1, P2, and Other Experimental Systems." *Journal of Bacteriology* 186(3):595–600. doi: 10.1128/JB.186.3.595-600.2004.
- Beyerlein, Kenneth R., Dennis Dierksmeyer, Valerio Mariani, Manuela Kuhn, Iosifina Sarrou, Angelica Ottaviano, Salah Awel, Juraj Knoska, Silje Fuglerud, Olof Jönsson, Stephan Stern, Max O. Wiedorn, Oleksandr Yefanov, Luigi Adriano, Richard Bean, Anja Burkhardt, Pontus Fischer, Michael Heymann, Daniel A. Horke, Katharina E. J. Jungnickel, Elena Kovaleva, Olga Lorbeer, Markus Metz, Jan Meyer, Andrew Morgan, Kanupriya Pande, Saravanan Panneerselvam, Carolin Seuring, Aleksandra Tolstikova, Julia Lieske, Steve Aplin, Manfred Roessle, Thomas A. White, Henry N. Chapman, Alke Meents, and Dominik Oberthuer. 2017a. "Mix-and-Diffuse Serial Synchrotron Crystallography." *IUCrJ* 4(6):769–77. doi: 10.1107/S2052252517013124.
- Beyerlein, Kenneth R., Dennis Dierksmeyer, Valerio Mariani, Manuela Kuhn, Iosifina Sarrou, Angelica Ottaviano, Salah Awel, Juraj Knoska, Silje Fuglerud, Olof Jönsson, Stephan Stern, Max O. Wiedorn, Oleksandr Yefanov, Luigi Adriano, Richard Bean, Anja Burkhardt, Pontus Fischer, Michael Heymann, Daniel A. Horke, Katharina E. J. Jungnickel, Elena Kovaleva, Olga Lorbeer, Markus Metz, Jan Meyer, Andrew Morgan, Kanupriya Pande, Saravanan Panneerselvam, Carolin Seuring, Aleksandra Tolstikova, Julia Lieske, Steve Aplin, Manfred Roessle, Thomas A. White, Henry N. Chapman, Alke Meents, and Dominik Oberthuer. 2017b. "Mix-and-Diffuse Serial Synchrotron Crystallography." *IUCrJ* 4(Pt 6):769–77. doi: 10.1107/S2052252517013124.
- Bielecki, Johan, Max F. Hantke, Benedikt J. Daurer, Hemanth K. N. Reddy, Dirk Hasse, Daniel S. D. Larsson, Laura H. Gunn, Martin Svenda, Anna Munke, Jonas A. Sellberg, Leonie Flueckiger, Alberto Pietrini, Carl Nettelblad, Ida Lundholm, Gunilla Carlsson, Kenta Okamoto, Nicusor Timneanu, Daniel Westphal, Olena Kulyk, Akifumi Higashiura, Gijs van der Schot, Ne-Te Duane Loh, Taylor E. Wysong, Christoph Bostedt, Tais Gorkhover, Bianca Iwan, M. Marvin Seibert, Timur Osipov, Peter Walter, Philip Hart, Maximilian Bucher, Anatoli Ulmer, Dipanwita Ray, Gabriella Carini, Ken R. Ferguson, Inger Andersson, Jakob Andreasson, Janos Hajdu, and Filipe R. N. C. Maia. 2019. "Electrospray Sample Injection for Single-Particle Imaging with x-Ray Lasers." *Science Advances* 5(5):eaav8801. doi: 10.1126/sciadv.aav8801.

- Bizzarri, Ranieri, Michela Serresi, Francesco Cardarelli, Stefania Abbruzzetti, Barbara Campanini, Cristiano Viappiani, and Fabio Beltram. 2010. "Single Amino Acid Replacement Makes *Aequorea Victoria* Fluorescent Proteins Reversibly Photoswitchable." *Journal of the American Chemical Society* 132(1):85–95. doi: 10.1021/ja9014953.
- Björn, Lars Olof. 2018. "Photoenzymes and Related Topics: An Update." *Photochemistry and Photobiology* 94(3):459–65. doi: 10.1111/php.12892.
- Blaj, Gabriel, Pietro Caragiulo, Gabriella Carini, Sebastian Carron, Angelo Dragone, Dietrich Freytag, Gunther Haller, Philip Hart, Jasmine Hasi, Ryan Herbst, Sven Herrmann, Chris Kenney, Bojan Markovic, Kurtis Nishimura, Shawn Osier, Jack Pines, Benjamin Reese, Julie Segal, Astrid Tomada, and Matt Weaver. 2015. "X-Ray Detectors at the Linac Coherent Light Source." *Journal of Synchrotron Radiation* 22(3):577–83. doi: 10.1107/S1600577515005317.
- Blanc, Guillaume, Garry Duncan, Irina Agarkova, Mark Borodovsky, James Gurnon, Alan Kuo, Erika Lindquist, Susan Lucas, Jasmyn Pangilinan, Juergen Polle, Asaf Salamov, Astrid Terry, Takashi Yamada, David D. Dunigan, Igor V. Grigoriev, Jean-Michel Claverie, and James L. Van Etten. 2010. "The *Chlorella Variabilis* NC64A Genome Reveals Adaptation to Photosymbiosis, Coevolution with Viruses, and Cryptic Sex." *The Plant Cell* 22(9):2943–55. doi: 10.1105/tpc.110.076406.
- Blume, Christine, Corrado Garbazza, and Manuel Spitschan. 2019. "Effects of Light on Human Circadian Rhythms, Sleep and Mood." *Somnologie* 23(3):147–56. doi: 10.1007/s11818-019-00215-x.
- Bonifacio, R., C. Pellegrini, and L. M. Narducci. 1984. "Collective Instabilities and High-Gain Regime in a Free Electron Laser." *Optics Communications* 50(6):373–78. doi: 10.1016/0030-4018(84)90105-6.
- Botha, S., D. Baitan, K. E. J. Jungnickel, D. Oberthür, C. Schmidt, S. Stern, M. O. Wiedorn, M. Perbandt, H. N. Chapman, and C. Betzel. 2018. "De Novo Protein Structure Determination by Heavy-Atom Soaking in Lipidic Cubic Phase and SIRAS Phasing Using Serial Synchrotron Crystallography." *IUCrJ* 5(5):524–30. doi: 10.1107/S2052252518009223.
- Botha, Sabine, Karol Nass, Thomas R. M. Barends, Wolfgang Kabsch, Beatrice Latz, Florian Dworkowski, Lutz Foucar, Ezequiel Panepucci, Meitian Wang, Robert L. Shoeman, Ilme Schlichting, and R. Bruce Doak. 2015. "Room-Temperature Serial Crystallography at Synchrotron X-Ray Sources Using Slowly Flowing Free-Standing High-Viscosity Microstreams." *Acta Crystallographica Section D Biological Crystallography* 71(2):387–97. doi: 10.1107/S1399004714026327.
- Bourgeois, D., and M. Weik. 2009. "Kinetic Protein Crystallography: A Tool to Watch Proteins in Action." *Crystallography Reviews* 15(2):87–118. doi: 10.1080/08893110802604868.
- Bourgeois, Dominique, and Virgile Adam. 2012. "Reversible Photoswitching in Fluorescent Proteins: A Mechanistic View." *IUBMB Life* 64(6):482–91. doi: 10.1002/iub.1023.

- Bourgeois, Dominique, Aline Regis-Faro, and Virgile Adam. 2012. "Photoactivated Structural Dynamics of Fluorescent Proteins." *Biochemical Society Transactions* 40(3):531–38. doi: 10.1042/BST20120002.
- Bourgeois, Dominique, and Martin Weik. 2008. "Kinetic Protein Crystallography Using Caged Compounds." P. fa19 in *Protein Science Encyclopedia*, edited by A. R. Fersht. Weinheim, Germany: Wiley-VCH Verlag GmbH & Co. KGaA.
- Boutet, Sébastien, Lukas Lomb, Garth J. Williams, Thomas R. M. Barends, Andrew Aquila, R. Bruce Doak, Uwe Weierstall, Daniel P. DePonte, Jan Steinbrener, Robert L. Shoeman, Marc Messerschmidt, Anton Barty, Thomas A. White, Stephan Kassemeyer, Richard A. Kirian, M. Marvin Seibert, Paul A. Montanez, Chris Kenney, Ryan Herbst, Philip Hart, Jack Pines, Gunther Haller, Sol M. Gruner, Hugh T. Philipp, Mark W. Tate, Marianne Hromalik, Lucas J. Koerner, Niels van Bakel, John Morse, Wilfred Ghonsalves, David Arnlund, Michael J. Bogan, Carl Caleman, Raimund Fromme, Christina Y. Hampton, Mark S. Hunter, Linda C. Johansson, Gergely Katona, Christopher Kupitz, Mengning Liang, Andrew V. Martin, Karol Nass, Lars Redecke, Francesco Stellato, Nicusor Timneanu, Dingjie Wang, Nadia A. Zatsepin, Donald Schafer, James Deфеver, Richard Neutze, Petra Fromme, John C. H. Spence, Henry N. Chapman, and Ilme Schlichting. 2012. "High-Resolution Protein Structure Determination by Serial Femtosecond Crystallography." *Science (New York, N.Y.)* 337(6092):362–64. doi: 10.1126/science.1217737.
- Bragg, William Henry, and William Lawrence Bragg. 1913. "The Reflection of X-Rays by Crystals." *Proceedings of the Royal Society of London. Series A, Containing Papers of a Mathematical and Physical Character* 88(605):428–38. doi: 10.1098/rspa.1913.0040.
- Brändén, Gisela, and Richard Neutze. 2021. "Advances and Challenges in Time-Resolved Macromolecular Crystallography." *Science* 373(6558):eaba0954. doi: 10.1126/science.aba0954.
- Brettel, Klaus, and Martin Byrdin. 2010. "Reaction Mechanisms of DNA Photolyase." *Current Opinion in Structural Biology* 20(6):693–701. doi: 10.1016/j.sbi.2010.07.003.
- Bröcker, Markus J., Dieter Jahn, and Jürgen Moser. 2012. "94 Key Enzymes of Chlorophyll Biosynthesis." Pp. 1–43 in *Handbook of Porphyrin Science (Volume 20)*. Vol. 20, *Handbook of Porphyrin Science*. World Scientific Publishing Company.
- Bruice, Thomas C. 2002. "A View at the Millennium: The Efficiency of Enzymatic Catalysis." *Accounts of Chemical Research* 35(3):139–48. doi: 10.1021/ar0001665.
- Bruice, Thomas C., and Felice C. Lightstone. 1999. "Ground State and Transition State Contributions to the Rates of Intramolecular and Enzymatic Reactions." *Accounts of Chemical Research* 32(2):127–36. doi: 10.1021/ar960131y.
- Brünger, A. T., P. D. Adams, G. M. Clore, W. L. DeLano, P. Gros, R. W. Grosse-Kunstleve, J. S. Jiang, J. Kuszewski, M. Nilges, N. S. Pannu, R. J. Read, L. M. Rice, T. Simonson, and G. L. Warren. 1998. "Crystallography & NMR System: A New Software Suite for Macromolecular Structure Determination." *Acta Crystallographica Section D Biological Crystallography* 54(5):905–21. doi: 10.1107/S0907444998003254.

- Burek, B. O., A. Sutor, D. W. Bahnemann, and J. Z. Bloh. 2017. “Completely Integrated Wirelessly-Powered Photocatalyst-Coated Spheres as a Novel Means to Perform Heterogeneous Photocatalytic Reactions.” *Catal. Sci. Technol.* 7(21):4977–83. doi: 10.1039/C7CY01537B.
- Burgie, E. Sethe, Jonathan A. Clinger, Mitchell D. Miller, Aaron S. Brewster, Pierre Aller, Agata Butryn, Franklin D. Fuller, Sheraz Gul, Iris D. Young, Cindy C. Pham, In-Sik Kim, Asmit Bhowmick, Lee J. O’Riordan, Kyle D. Sutherlin, Joshua V. Heinemann, Alexander Batyuk, Roberto Alonso-Mori, Mark S. Hunter, Jason E. Koglin, Junko Yano, Vittal K. Yachandra, Nicholas K. Sauter, Aina E. Cohen, Jan Kern, Allen M. Orville, George N. Phillips, and Richard D. Vierstra. 2020. “Photoreversible Interconversion of a Phytochrome Photosensory Module in the Crystalline State.” *Proceedings of the National Academy of Sciences* 117(1):300–307. doi: 10.1073/pnas.1912041116.
- Bury, Charles S., Jonathan C. Brooks-Bartlett, Steven P. Walsh, and Elspeth F. Garman. 2018. “Estimate Your Dose: RADDPOSE-3D: RADDPOSE-3D.” *Protein Science* 27(1):217–28. doi: 10.1002/pro.3302.
- Calvey, George D., Andrea M. Katz, Chris B. Schaffer, and Lois Pollack. 2016. “Mixing Injector Enables Time-Resolved Crystallography with High Hit Rate at X-Ray Free Electron Lasers.” *Structural Dynamics* 3(5):054301. doi: 10.1063/1.4961971.
- Cannon, William R., Scott F. Singleton, and Stephen J. Benkovic. 1996. “A Perspective on Biological Catalysis.” *Nature Structural & Molecular Biology* 3(10):821–33. doi: 10.1038/nsb1096-821.
- Carrillo, Melissa, Suraj Pandey, Juan Sanchez, Moraima Noda, Ishwor Poudyal, Luis Aldama, Tek Narsingh Malla, Elin Claesson, Weixiao Yuan Wahlgren, Denisse Feliz, Vukica Šrajcar, Michał Maj, Leticia Castillon, So Iwata, Eriko Nango, Rie Tanaka, Tomoyuki Tanaka, Luo Fangjia, Kensuke Tono, Shigeki Owada, Sebastian Westenhoff, Emina A. Stojković, and Marius Schmidt. 2021. “High-Resolution Crystal Structures of Transient Intermediates in the Phytochrome Photocycle.” *Structure* S0969212621000770. doi: 10.1016/j.str.2021.03.004.
- Cavener, Douglas R. 1992. “GMC Oxidoreductases.” *Journal of Molecular Biology* 223(3):811–14. doi: 10.1016/0022-2836(92)90992-S.
- Cellini, Andrea, Weixiao Yuan Wahlgren, Léocadie Henry, Suraj Pandey, Swagatha Ghosh, Leticia Castillon, Elin Claesson, Heikki Takala, Joachim Kübel, Amke Nimmrich, Valentyna Kuznetsova, Eriko Nango, So Iwata, Shigeki Owada, Emina A. Stojković, Marius Schmidt, Janne A. Ihalainen, and Sebastian Westenhoff. 2021. “The Three-Dimensional Structure of *Drosophila Melanogaster* (6–4) Photolyase at Room Temperature.” *Acta Crystallographica Section D Structural Biology* 77(8):1001–9. doi: 10.1107/S2059798321005830.
- Chalfie, Martin, Yuan Tu, Ghia Euskirchen, William W. Ward, and Douglas C. Prasher. 1994. “Green Fluorescent Protein as a Marker for Gene Expression.” *Science* 263(5148):802–5. doi: 10.1126/science.8303295.

- Chang, Jeffrey, Matthew G. Romei, and Steven G. Boxer. 2019. "Structural Evidence of Photoisomerization Pathways in Fluorescent Proteins." *Journal of the American Chemical Society* 141(39):15504–8. doi: 10.1021/jacs.9b08356.
- Chapman, Henry N., Carl Caleman, and Nicusor Timneanu. 2014. "Diffraction before Destruction." *Philosophical Transactions of the Royal Society B: Biological Sciences* 369(1647):20130313. doi: 10.1098/rstb.2013.0313.
- Chapman, Henry N., Petra Fromme, Anton Barty, Thomas A. White, Richard A. Kirian, Andrew Aquila, Mark S. Hunter, Joachim Schulz, Daniel P. DePonte, Uwe Weierstall, R. Bruce Doak, Filipe R. N. C. Maia, Andrew V. Martin, Ilme Schlichting, Lukas Lomb, Nicola Coppola, Robert L. Shoeman, Sascha W. Epp, Robert Hartmann, Daniel Rolles, Artem Rudenko, Lutz Foucar, Nils Kimmel, Georg Weidenspointner, Peter Holl, Mengning Liang, Miriam Barthelmeß, Carl Caleman, Sébastien Boutet, Michael J. Bogan, Jacek Krzywinski, Christoph Bostedt, Saša Bajt, Lars Gumprecht, Benedikt Rudek, Benjamin Erk, Carlo Schmidt, André Hömke, Christian Reich, Daniel Pietschner, Lothar Strüder, Günter Hauser, Hubert Gorke, Joachim Ullrich, Sven Herrmann, Gerhard Schaller, Florian Schopper, Heike Soltau, Kai-Uwe Kühnel, Marc Messerschmidt, John D. Bozek, Stefan P. Hau-Riege, Matthias Frank, Christina Y. Hampton, Raymond G. Sierra, Dmitri Starodub, Garth J. Williams, Janos Hajdu, Nicusor Timneanu, M. Marvin Seibert, Jakob Andreasson, Andrea Rocker, Olof Jönsson, Martin Svenda, Stephan Stern, Karol Nass, Robert Andritschke, Claus-Dieter Schröter, Faton Krasniqi, Mario Bott, Kevin E. Schmidt, Xiaoyu Wang, Ingo Grotjohann, James M. Holton, Thomas R. M. Barends, Richard Neutze, Stefano Marchesini, Raimund Fromme, Sebastian Schorb, Daniela Rupp, Marcus Adolph, Tais Gorkhover, Inger Andersson, Helmut Hirsemann, Guillaume Potdevin, Heinz Graafsma, Björn Nilsson, and John C. H. Spence. 2011. "Femtosecond X-Ray Protein Nanocrystallography." *Nature* 470(7332):73–77. doi: 10.1038/nature09750.
- Cheng, Robert KY. 2020. "Towards an Optimal Sample Delivery Method for Serial Crystallography at XFEL." *Crystals* 10(3):215. doi: 10.3390/cryst10030215.
- Christie, R. M., ed. 2001. "The Physical and Chemical Basis of Colour." Pp. 12–44 in *Colour Chemistry*. The Royal Society of Chemistry.
- Claesson, Elin, Weixiao Yuan Wahlgren, Heikki Takala, Suraj Pandey, Leticia Castillon, Valentyna Kuznetsova, Léocadie Henry, Matthijs Panman, Melissa Carrillo, Joachim Kübel, Rahul Nanekar, Linnéa Isaksson, Amke Nimrich, Andrea Cellini, Dmitry Morozov, Michał Maj, Moona Kurttila, Robert Bosman, Eriko Nango, Rie Tanaka, Tomoyuki Tanaka, Luo Fangjia, So Iwata, Shigeki Owada, Keith Moffat, Gerrit Groenhof, Emina A. Stojković, Janne A. Ihalainen, Marius Schmidt, and Sebastian Westenhoff. 2020. "The Primary Structural Photoresponse of Phytochrome Proteins Captured by a Femtosecond X-Ray Laser." *ELife* 9:e53514. doi: 10.7554/eLife.53514.
- Cohen, Aina E., S. Michael Soltis, Ana González, Laura Aguila, Roberto Alonso-Mori, Christopher O. Barnes, Elizabeth L. Baxter, Winnie Brehmer, Aaron S. Brewster, Axel T. Brunger, Guillermo Calero, Joseph F. Chang, Matthieu Chollet, Paul Ehrensberger, Thomas L. Eriksson, Yiping Feng, Johan Hattne, Britt Hedman, Michael Hollenbeck, James M. Holton, Stephen Keable, Brian K. Kobilka, Elena G. Kovaleva, Andrew C. Kruse, Henrik T. Lemke, Guowu Lin, Artem Y. Lyubimov, Aashish Manglik, Irimpan I. Mathews, Scott E. McPhillips, Silke Nelson, John W. Peters, Nicholas K. Sauter,

- Clyde A. Smith, Jinhu Song, Hilary P. Stevenson, Yingsu Tsai, Monarin Uervirojnangkoorn, Vladimir Vinetsky, Soichi Wakatsuki, William I. Weis, Oleg A. Zadovnyy, Oliver B. Zeldin, Diling Zhu, and Keith O. Hodgson. 2014. “Goniometer-Based Femtosecond Crystallography with X-Ray Free Electron Lasers.” *Proceedings of the National Academy of Sciences* 111(48):17122–27. doi: 10.1073/pnas.1418733111.
- Collaborative Computational Project, Number 4. 1994. “The CCP4 Suite: Programs for Protein Crystallography.” *Acta Crystallographica Section D Biological Crystallography* 50(5):760–63. doi: 10.1107/S0907444994003112.
- Colletier, J. P., D. Bourgeois, B. Sanson, D. Fournier, J. L. Sussman, I. Silman, and M. Weik. 2008. “Shoot-and-Trap: Use of Specific x-Ray Damage to Study Structural Protein Dynamics by Temperature-Controlled Cryo-Crystallography.” *Proceedings of the National Academy of Sciences* 105(33):11742–47. doi: 10.1073/pnas.0804828105.
- Colletier, Jacques-Philippe, Antoine Royant, Alexandre Specht, Benoît Sanson, Florian Nachon, Patrick Masson, Giuseppe Zaccai, Joel L. Sussman, Maurice Goeldner, Israel Silman, Dominique Bourgeois, and Martin Weik. 2007. “Use of a ‘caged’ Analogue to Study the Traffic of Choline within Acetylcholinesterase by Kinetic Crystallography.” *Acta Crystallographica Section D Biological Crystallography* 63(11):1115–28. doi: 10.1107/S0907444907044472.
- Colletier, Jacques-Philippe, Michael R. Sawaya, Mari Gingery, Jose A. Rodriguez, Duilio Cascio, Aaron S. Brewster, Tara Michels-Clark, Robert H. Hice, Nicolas Coquelle, Sébastien Boutet, Garth J. Williams, Marc Messerschmidt, Daniel P. DePonte, Raymond G. Sierra, Hartawan Laksmono, Jason E. Koglin, Mark S. Hunter, Hyun-Woo Park, Monarin Uervirojnangkoorn, Dennis K. Bideshi, Axel T. Brunger, Brian A. Federici, Nicholas K. Sauter, and David S. Eisenberg. 2016. “De Novo Phasing with X-Ray Laser Reveals Mosquito Larvicide BinAB Structure.” *Nature* 539(7627):43–47. doi: 10.1038/nature19825.
- Colletier, Jacques-Philippe, Giorgio Schirò, and Martin Weik. 2018. “Time-Resolved Serial Femtosecond Crystallography, Towards Molecular Movies of Biomolecules in Action.” Pp. 331–56 in *X-ray Free Electron Lasers*, edited by S. Boutet, P. Fromme, and M. S. Hunter. Cham: Springer International Publishing.
- Conrad, Chelsie E., Shibom Basu, Daniel James, Dingjie Wang, Alexander Schaffer, Shatabdi Roy-Chowdhury, Nadia A. Zatsepin, Andrew Aquila, Jesse Coe, Cornelius Gati, Mark S. Hunter, Jason E. Koglin, Christopher Kupitz, Garrett Nelson, Ganesh Subramanian, Thomas A. White, Yun Zhao, James Zook, Sébastien Boutet, Vadim Cherezov, John C. H. Spence, Raimund Fromme, Uwe Weierstall, and Petra Fromme. 2015. “A Novel Inert Crystal Delivery Medium for Serial Femtosecond Crystallography.” *IUCrJ* 2(4):421–30. doi: 10.1107/S2052252515009811.
- Coquelle, Nicolas, Aaron S. Brewster, Ulrike Kapp, Anastasya Shilova, Britta Weinhausen, Manfred Burghammer, and Jacques-Philippe Colletier. 2015. “Raster-Scanning Serial Protein Crystallography Using Micro- and Nano-Focused Synchrotron Beams.” *Acta Crystallographica Section D Biological Crystallography* 71(5):1184–96. doi: 10.1107/S1399004715004514.

- Coquelle, Nicolas, Michel Sliwa, Joyce Woodhouse, Giorgio Schirò, Virgile Adam, Andrew Aquila, Thomas R. M. Barends, Sébastien Boutet, Martin Byrdin, Sergio Carbajo, Eugenio De la Mora, R. Bruce Doak, Mikolaj Feliks, Franck Fieschi, Lutz Foucar, Virginia Guillon, Mario Hilpert, Mark S. Hunter, Stefan Jakobs, Jason E. Koglin, Gabriela Kovacsova, Thomas J. Lane, Bernard Lévy, Mengning Liang, Karol Nass, Jacqueline Ridard, Joseph S. Robinson, Christopher M. Roome, Cyril Ruckebusch, Matthew Seaberg, Michel Thepaut, Marco Cammarata, Isabelle Demachy, Martin Field, Robert L. Shoeman, Dominique Bourgeois, Jacques-Philippe Colletier, Ilme Schlichting, and Martin Weik. 2018a. “Chromophore Twisting in the Excited State of a Photoswitchable Fluorescent Protein Captured by Time-Resolved Serial Femtosecond Crystallography.” *Nature Chemistry* 10(1):31–37. doi: 10.1038/nchem.2853.
- Coquelle, Nicolas, Michel Sliwa, Joyce Woodhouse, Giorgio Schirò, Virgile Adam, Andrew Aquila, Thomas R. M. Barends, Sébastien Boutet, Martin Byrdin, Sergio Carbajo, Eugenio De la Mora, R. Bruce Doak, Mikolaj Feliks, Franck Fieschi, Lutz Foucar, Virginia Guillon, Mario Hilpert, Mark S. Hunter, Stefan Jakobs, Jason E. Koglin, Gabriela Kovacsova, Thomas J. Lane, Bernard Lévy, Mengning Liang, Karol Nass, Jacqueline Ridard, Joseph S. Robinson, Christopher M. Roome, Cyril Ruckebusch, Matthew Seaberg, Michel Thepaut, Marco Cammarata, Isabelle Demachy, Martin Field, Robert L. Shoeman, Dominique Bourgeois, Jacques-Philippe Colletier, Ilme Schlichting, and Martin Weik. 2018b. “Chromophore Twisting in the Excited State of a Photoswitchable Fluorescent Protein Captured by Time-Resolved Serial Femtosecond Crystallography.” *Nature Chemistry* 10(1):31–37. doi: 10.1038/nchem.2853.
- Cormack, Brendan P., Raphael H. Valdivia, and Stanley Falkow. 1996. “FACS-Optimized Mutants of the Green Fluorescent Protein (GFP).” *Gene* 173(1):33–38. doi: 10.1016/0378-1119(95)00685-0.
- Dasgupta, Medhanjali, Dominik Budday, Saulo H. P. de Oliveira, Peter Madzellan, Darya Marchany-Rivera, Javier Seravalli, Brandon Hayes, Raymond G. Sierra, Sébastien Boutet, Mark S. Hunter, Roberto Alonso-Mori, Alexander Batyuk, Jennifer Wierman, Artem Lyubimov, Aaron S. Brewster, Nicholas K. Sauter, Gregory A. Applegate, Virendra K. Tiwari, David B. Berkowitz, Michael C. Thompson, Aina E. Cohen, James S. Fraser, Michael E. Wall, Henry van den Bedem, and Mark A. Wilson. 2019. “Mix-and-Inject XFEL Crystallography Reveals Gated Conformational Dynamics during Enzyme Catalysis.” *Proceedings of the National Academy of Sciences* 116(51):25634–40. doi: 10.1073/pnas.1901864116.
- Daurer, Benedikt J., Max F. Hantke, Carl Nettelblad, and Filipe R. N. C. Maia. 2016. “Hummingbird: Monitoring and Analyzing Flash X-Ray Imaging Experiments in Real Time.” *Journal of Applied Crystallography* 49(3):1042–47. doi: 10.1107/S1600576716005926.
- De Zitter, Elke, Nicolas Coquelle, Thomas RM Barends, and Jacques-Philippe Colletier. 2022. *Xtrapol8: Automatic Elucidation of Low-Occupancy Intermediate-States in Crystallographic Studies. preprint*. Biophysics. doi: 10.1101/2022.01.09.475568.
- Dedecker, Peter, Jun-ichi Hotta, Cristina Flors, Michel Sliwa, Hiroshi Uji-i, Maarten B. J. Roeffaers, Ryoko Ando, Hideaki Mizuno, Atsushi Miyawaki, and Johan Hofkens. 2007. “Subdiffraction Imaging through the Selective Donut-Mode Depletion of Thermally Stable Photoswitchable Fluorophores: Numerical Analysis and Application to the

- Fluorescent Protein Dronpa.” *Journal of the American Chemical Society* 129(51):16132–41. doi: 10.1021/ja076128z.
- DePonte, D. P., U. Weierstall, K. Schmidt, J. Warner, D. Starodub, J. C. H. Spence, and R. B. Doak. 2008. “Gas Dynamic Virtual Nozzle for Generation of Microscopic Droplet Streams.” *Journal of Physics D: Applied Physics* 41(19):195505. doi: 10.1088/0022-3727/41/19/195505.
- Dertinger, T., R. Colyer, G. Iyer, S. Weiss, and J. Enderlein. 2009. “Fast, Background-Free, 3D Super-Resolution Optical Fluctuation Imaging (SOFI).” *Proceedings of the National Academy of Sciences* 106(52):22287–92. doi: 10.1073/pnas.0907866106.
- Dickerson, Joshua L., Patrick T. N. McCubbin, and Elspeth F. Garman. 2020. “RADDPOSE-XFEL: Femtosecond Time-Resolved Dose Estimates for Macromolecular X-Ray Free-Electron Laser Experiments.” *Journal of Applied Crystallography* 53(2):549–60. doi: 10.1107/S1600576720000643.
- Diederichs, Kay, and Meitian Wang. 2017. “Serial Synchrotron X-Ray Crystallography (SSX).” Pp. 239–72 in *Protein Crystallography*. Vol. 1607, *Methods in Molecular Biology*, edited by A. Wlodawer, Z. Dauter, and M. Jaskolski. New York, NY: Springer New York.
- Doak, R. Bruce, Gabriela Nass Kovacs, Alexander Gorel, Lutz Foucar, Thomas R. M. Barends, Marie Luise Grünbein, Mario Hilpert, Marco Kloos, Christopher M. Roome, Robert L. Shoeman, Miriam Stricker, Kensuke Tono, Daehyun You, Kiyoshi Ueda, Darren A. Sherrell, Robin L. Owen, and Ilme Schlichting. 2018. “Crystallography on a Chip - without the Chip: Sheet-on-Sheet Sandwich.” *Acta Crystallographica. Section D, Structural Biology* 74(Pt 10):1000–1007. doi: 10.1107/S2059798318011634.
- Dods, Robert, Petra Båth, Dmitry Morozov, Viktor Ahlberg Gagnér, David Arnlund, Hoi Ling Luk, Joachim Kübel, Michał Maj, Adams Vallejos, Cecilia Wickstrand, Robert Bosman, Kenneth R. Beyerlein, Garrett Nelson, Mengning Liang, Despina Milathianaki, Joseph Robinson, Rajiv Harimoorthy, Peter Berntsen, Erik Malmerberg, Linda Johansson, Rebecka Andersson, Sergio Carbajo, Elin Claesson, Chelsie E. Conrad, Peter Dahl, Greger Hammarin, Mark S. Hunter, Chufeng Li, Stella Lisova, Antoine Royant, Cecilia Safari, Amit Sharma, Garth J. Williams, Oleksandr Yefanov, Sebastian Westenhoff, Jan Davidsson, Daniel P. DePonte, Sébastien Boutet, Anton Barty, Gergely Katona, Gerrit Groenhof, Gisela Brändén, and Richard Neutze. 2021. “Ultrafast Structural Changes within a Photosynthetic Reaction Centre.” *Nature* 589(7841):310–14. doi: 10.1038/s41586-020-3000-7.
- Dreveny, Ingrid, Aleksandra S. Andryushkova, Anton Glieder, Karl Gruber, and Christoph Kratky. 2009. “Substrate Binding in the FAD-Dependent Hydroxynitrile Lyase from Almond Provides Insight into the Mechanism of Cyanohydrin Formation and Explains the Absence of Dehydrogenation Activity.” *Biochemistry* 48(15):3370–77. doi: 10.1021/bi802162s.
- Duan, Chenxi, Virgile Adam, Martin Byrdin, and Dominique Bourgeois. 2014. “Structural Basis of Photoswitching in Fluorescent Proteins.” Pp. 177–202 in *Photoswitching Proteins*. Vol. 1148, *Methods in Molecular Biology*, edited by S. Cambridge. New York, NY: Springer New York.

- Duan, Chenxi, Virgile Adam, Martin Byrdin, Jacqueline Ridard, Sylvie Kieffer-Jaquinod, Cécile Morlot, Delphine Arcizet, Isabelle Demachy, and Dominique Bourgeois. 2013. “Structural Evidence for a Two-Regime Photobleaching Mechanism in a Reversibly Switchable Fluorescent Protein.” *Journal of the American Chemical Society* 135(42):15841–50. doi: 10.1021/ja406860e.
- Duisenberg, A. J. M. 1992. “Indexing in Single-Crystal Diffractometry with an Obstinate List of Reflections.” *Journal of Applied Crystallography* 25(2):92–96. doi: 10.1107/S0021889891010634.
- Dunne, Mike. 2020. “LCLS Strategic Facility Development Plan, https://lcls.slac.stanford.edu/sites/lcls.slac.stanford.edu/files/lcls_strategic_development_plan.pdf.”
- Duong, Hong T., Yinqi Wu, Alexander Sutor, Bastien O. Burek, Frank Hollmann, and Jonathan Z. Bloh. 2021. “Intensification of Photobiocatalytic Decarboxylation of Fatty Acids for the Production of Biodiesel.” *ChemSusChem* 14(4):1053–56. doi: 10.1002/cssc.202002957.
- Duwé, Sam, Elke De Zitter, Vincent Gielen, Benjamien Moeyaert, Wim Vandenberg, Tim Grotjohann, Koen Clays, Stefan Jakobs, Luc Van Meervelt, and Peter Dedecker. 2015. “Expression-Enhanced Fluorescent Proteins Based on Enhanced Green Fluorescent Protein for Super-Resolution Microscopy.” *ACS Nano* 9(10):9528–41. doi: 10.1021/acsnano.5b04129.
- Ebrahim, Ali, Tadeo Moreno-Chicano, Martin V. Appleby, Amanda K. Chaplin, John H. Beale, Darren A. Sherrell, Helen M. E. Duyvesteyn, Shigeki Owada, Kensuke Tono, Hiroshi Sugimoto, Richard W. Strange, Jonathan A. R. Worrall, Danny Axford, Robin L. Owen, and Michael A. Hough. 2019. “Dose-Resolved Serial Synchrotron and XFEL Structures of Radiation-Sensitive Metalloproteins.” *IUCrJ* 6(4):543–51. doi: 10.1107/S2052252519003956.
- El Khatib, Mariam, Alexandre Martins, Dominique Bourgeois, Jacques-Philippe Colletier, and Virgile Adam. 2016. “Rational Design of Ultrastable and Reversibly Photoswitchable Fluorescent Proteins for Super-Resolution Imaging of the Bacterial Periplasm.” *Scientific Reports* 6(1):18459. doi: 10.1038/srep18459.
- Emma, P., R. Akre, J. Arthur, R. Bionta, C. Bostedt, J. Bozek, A. Brachmann, P. Bucksbaum, R. Coffee, F. J. Decker, Y. Ding, D. Dowell, S. Edstrom, A. Fisher, J. Frisch, S. Gilevich, J. Hastings, G. Hays, Ph. Hering, Z. Huang, R. Iverson, H. Loos, M. Messerschmidt, A. Miahnahri, S. Moeller, H. D. Nuhn, G. Pile, D. Ratner, J. Rzepiela, D. Schultz, T. Smith, P. Stefan, H. Tompkins, J. Turner, J. Welch, W. White, J. Wu, G. Yocky, and J. Galayda. 2010. “First Lasing and Operation of an Ångström-Wavelength Free-Electron Laser.” *Nature Photonics* 4(9):641–47. doi: 10.1038/nphoton.2010.176.
- Emsley, Paul, and Kevin Cowtan. 2004. “Coot: Model-Building Tools for Molecular Graphics.” *Acta Crystallographica Section D Biological Crystallography* 60(12):2126–32. doi: 10.1107/S0907444904019158.

- Ernst, Oliver P., David T. Lodowski, Marcus Elstner, Peter Hegemann, Leonid S. Brown, and Hideki Kandori. 2014. "Microbial and Animal Rhodopsins: Structures, Functions, and Molecular Mechanisms." *Chemical Reviews* 114(1):126–63. doi: 10.1021/cr4003769.
- Evans, Philip, and Airlie McCoy. 2008. "An Introduction to Molecular Replacement." *Acta Crystallographica Section D Biological Crystallography* 64(1):1–10. doi: 10.1107/S0907444907051554.
- Feldhaus, J., J. Arthur, and J. B. Hastings. 2005. "X-Ray Free-Electron Lasers." *Journal of Physics B: Atomic, Molecular and Optical Physics* 38(9):S799–819. doi: 10.1088/0953-4075/38/9/023.
- Fischer, Emil. 1894. "Einfluss Der Configuration Auf Die Wirkung Der Enzyme." *Berichte Der Deutschen Chemischen Gesellschaft* 27(3):2985–93. doi: 10.1002/cber.18940270364.
- Flot, David, Trevor Mairs, Thierry Giraud, Matias Guijarro, Marc Lesourd, Vicente Rey, Denis van Brussel, Christian Morawe, Christine Borel, Olivier Hignette, Joel Chavanne, Didier Nurizzo, Sean McSweeney, and Edward Mitchell. 2010. "The ID23-2 Structural Biology Microfocus Beamline at the ESRF." *Journal of Synchrotron Radiation* 17(1):107–18. doi: 10.1107/S0909049509041168.
- Foucar, Lutz. 2016. "CFEL-ASG Software Suite (CASS): Usage for Free-Electron Laser Experiments with Biological Focus." *Journal of Applied Crystallography* 49(4):1336–46. doi: 10.1107/S1600576716009201.
- Foucar, Lutz, Anton Barty, Nicola Coppola, Robert Hartmann, Peter Holl, Uwe Hoppe, Stephan Kassemeyer, Nils Kimmel, Jochen Küpper, Mirko Scholz, Simone Techert, Thomas A. White, Lothar Strüder, and Joachim Ullrich. 2012. "CASS—CFEL-ASG Software Suite." *Computer Physics Communications* 183(10):2207–13. doi: 10.1016/j.cpc.2012.04.023.
- Fraser, J. S., H. van den Bedem, A. J. Samelson, P. T. Lang, J. M. Holton, N. Echols, and T. Alber. 2011. "Accessing Protein Conformational Ensembles Using Room-Temperature X-Ray Crystallography." *Proceedings of the National Academy of Sciences* 108(39):16247–52. doi: 10.1073/pnas.1111325108.
- Friedrich, W., P. Knipping, and M. Laue. 1913. "Interferenzerscheinungen bei Röntgenstrahlen." *Annalen der Physik* 346(10):971–88. doi: 10.1002/andp.19133461004.
- Fromme, Raimund, Andrii Ishchenko, Markus Metz, Shatabdi Roy Chowdhury, Shibom Basu, Sébastien Boutet, Petra Fromme, Thomas A. White, Anton Barty, John C. H. Spence, Uwe Weierstall, Wei Liu, and Vadim Cherezov. 2015. "Serial Femtosecond Crystallography of Soluble Proteins in Lipidic Cubic Phase." *IUCrJ* 2(5):545–51. doi: 10.1107/S2052252515013160.
- Fukuda, Yohta, Ka Man Tse, Takanori Nakane, Toru Nakatsu, Mamoru Suzuki, Michihiro Sugahara, Shigeyuki Inoue, Tetsuya Masuda, Fumiaki Yumoto, Naohiro Matsugaki, Eriko Nango, Kensuke Tono, Yasumasa Joti, Takashi Kameshima, Changyong Song, Takaki Hatsui, Makina Yabashi, Osamu Nureki, Michael E. P. Murphy, Tsuyoshi Inoue, So Iwata, and Eiichi Mizohata. 2016. "Redox-Coupled Proton Transfer Mechanism in

- Nitrite Reductase Revealed by Femtosecond Crystallography.” *Proceedings of the National Academy of Sciences* 113(11):2928–33. doi: 10.1073/pnas.1517770113.
- Fuller, Franklin D., Sheraz Gul, Ruchira Chatterjee, E. Sethe Burgie, Iris D. Young, Hugo Lebrette, Vivek Srinivas, Aaron S. Brewster, Tara Michels-Clark, Jonathan A. Clinger, Babak Andi, Mohamed Ibrahim, Ernest Pastor, Casper de Lichtenberg, Rana Hussein, Christopher J. Pollock, Miao Zhang, Claudiu A. Stan, Thomas Kroll, Thomas Fransson, Clemens Weninger, Markus Kubin, Pierre Aller, Louise Lassalle, Philipp Bräuer, Mitchell D. Miller, Muhamed Amin, Sergey Koroidov, Christian G. Roessler, Marc Allaire, Raymond G. Sierra, Peter T. Docker, James M. Glowonia, Silke Nelson, Jason E. Koglin, Diling Zhu, Matthieu Chollet, Sanghoon Song, Henrik Lemke, Mengning Liang, Dimosthenis Sokaras, Roberto Alonso-Mori, Athina Zouni, Johannes Messinger, Uwe Bergmann, Amie K. Boal, J. Martin Bollinger, Carsten Krebs, Martin Högbom, George N. Phillips, Richard D. Vierstra, Nicholas K. Sauter, Allen M. Orville, Jan Kern, Vittal K. Yachandra, and Junko Yano. 2017. “Drop-on-Demand Sample Delivery for Studying Biocatalysts in Action at X-Ray Free-Electron Lasers.” *Nature Methods* 14(4):443–49. doi: 10.1038/nmeth.4195.
- Gabruk, Michal, and Beata Mysliwa-Kurdziel. 2015. “Light-Dependent Protochlorophyllide Oxidoreductase: Phylogeny, Regulation, and Catalytic Properties.” *Biochemistry* 54(34):5255–62. doi: 10.1021/acs.biochem.5b00704.
- Gao, Xiugong, Xiaoling Wen, Lothar Esser, Byron Quinn, Linda Yu, Chang-An Yu, and Di Xia. 2003. “Structural Basis for the Quinone Reduction in the Bc1 Complex: A Comparative Analysis of Crystal Structures of Mitochondrial Cytochrome Bc1 with Bound Substrate and Inhibitors at the Qi Site.” *Biochemistry* 42(30):9067–80. doi: 10.1021/bi0341814.
- Garman, Elspeth F. 2010. “Radiation Damage in Macromolecular Crystallography: What Is It and Why Should We Care?” *Acta Crystallographica Section D Biological Crystallography* 66(4):339–51. doi: 10.1107/S0907444910008656.
- Garman, Elspeth F., and Robin Leslie Owen. 2006. “Cryocooling and Radiation Damage in Macromolecular Crystallography.” *Acta Crystallographica Section D Biological Crystallography* 62(1):32–47. doi: 10.1107/S0907444905034207.
- Gati, Cornelius, Gleb Bourenkov, Marco Klinge, Dirk Rehders, Francesco Stellato, Dominik Oberthür, Oleksandr Yefanov, Benjamin P. Sommer, Stefan Mogk, Michael Duszynski, Christian Betzel, Thomas R. Schneider, Henry N. Chapman, and Lars Redecke. 2014. “Serial Crystallography on *in Vivo* Grown Microcrystals Using Synchrotron Radiation.” *IUCrJ* 1(2):87–94. doi: 10.1107/S2052252513033939.
- Geloni, Gianluca, Zhirong Huang, and Claudio Pellegrini. 2017. “CHAPTER 1. The Physics and Status of X-Ray Free-Electron Lasers.” Pp. 1–44 in *Energy and Environment Series*, edited by U. Bergmann, V. Yachandra, and J. Yano. Cambridge: Royal Society of Chemistry.
- Geloni, Gianluca, Vitali Kocharyan, and Evgeni Saldin. 2011. “Circular Polarization Control for the European XFEL in the Soft X-Ray Regime.” *ArXiv:1106.1776 [Physics]*.

- Genick, Ulrich K. 2007. “Structure-Factor Extrapolation Using the Scalar Approximation: Theory, Applications and Limitations.” *Acta Crystallographica Section D Biological Crystallography* 63(10):1029–41. doi: 10.1107/S0907444907038164.
- Genick, Ulrich K., Gloria E. O. Borgstahl, Kingman Ng, Zhong Ren, Claude Pradervand, Patrick M. Burke, Vukica Šrajer, Tsu-Yi Teng, Wilfried Schildkamp, Duncan E. McRee, Keith Moffat, and Elizabeth D. Getzoff. 1997. “Structure of a Protein Photocycle Intermediate by Millisecond Time-Resolved Crystallography.” *Science* 275(5305):1471–75. doi: 10.1126/science.275.5305.1471.
- Gevorkov, Yaroslav, Oleksandr Yefanov, Anton Barty, Thomas A. White, Valerio Mariani, Wolfgang Brehm, Aleksandra Tolstikova, Rolf-Rainer Grigat, and Henry N. Chapman. 2019. “XGANDALF – Extended Gradient Descent Algorithm for Lattice Finding.” *Acta Crystallographica Section A Foundations and Advances* 75(5):694–704. doi: 10.1107/S2053273319010593.
- Gicquel, Yannig, Robin Schubert, Svetlana Kapis, Gleb Bourenkov, Thomas Schneider, Markus Perbandt, Christian Betzel, Henry N. Chapman, and Michael Heymann. 2018. “Microfluidic Chips for In Situ Crystal X-Ray Diffraction and In Situ Dynamic Light Scattering for Serial Crystallography.” *Journal of Visualized Experiments* (134):57133. doi: 10.3791/57133.
- Gisriel, Chris, Jesse Coe, Romain Letrun, Oleksandr M. Yefanov, Cesar Luna-Chavez, Natasha E. Stander, Stella Lisova, Valerio Mariani, Manuela Kuhn, Steve Aplin, Thomas D. Grant, Katerina Dörner, Tokushi Sato, Austin Echelmeier, Jorvani Cruz Villarreal, Mark S. Hunter, Max O. Wiedorn, Juraj Knoska, Victoria Mazalova, Shatabdi Roy-Chowdhury, Jay-How Yang, Alex Jones, Richard Bean, Johan Bielecki, Yoonhee Kim, Grant Mills, Britta Weinhausen, Jose D. Meza, Nasser Al-Qudami, Saša Bajt, Gerrit Brehm, Sabine Botha, Djelloul Boukhelef, Sandor Brockhauser, Barry D. Bruce, Matthew A. Coleman, Cyril Danilevski, Erin Discianno, Zachary Dobson, Hans Fangohr, Jose M. Martin-Garcia, Yaroslav Gevorkov, Steffen Hauf, Ahmad Hosseinizadeh, Friederike Januschek, Gihan K. Ketawala, Christopher Kupitz, Luis Maia, Maurizio Manetti, Marc Messerschmidt, Thomas Michelat, Jyotirmoy Mondal, Abbas Ourmazd, Gianpietro Previtali, Iosifina Sarrou, Silvan Schön, Peter Schwander, Megan L. Shelby, Alessandro Silenzi, Jolanta Sztuk-Dambietz, Janusz Szuba, Monica Turcato, Thomas A. White, Krzysztof Wrona, Chen Xu, Mohamed H. Abdellatif, James D. Zook, John C. H. Spence, Henry N. Chapman, Anton Barty, Richard A. Kirian, Matthias Frank, Alexandra Ros, Marius Schmidt, Raimund Fromme, Adrian P. Mancuso, Petra Fromme, and Nadia A. Zatsepin. 2019. “Membrane Protein Megahertz Crystallography at the European XFEL.” *Nature Communications* 10(1):5021. doi: 10.1038/s41467-019-12955-3.
- Grotjohann, Tim, Ilaria Testa, Marcel Leutenegger, Hannes Bock, Nicolai T. Urban, Flavie Lavoie-Cardinal, Katrin I. Willig, Christian Eggeling, Stefan Jakobs, and Stefan W. Hell. 2011a. “Diffraction-Unlimited All-Optical Imaging and Writing with a Photochromic GFP.” *Nature* 478(7368):204–8. doi: 10.1038/nature10497.
- Grotjohann, Tim, Ilaria Testa, Marcel Leutenegger, Hannes Bock, Nicolai T. Urban, Flavie Lavoie-Cardinal, Katrin I. Willig, Christian Eggeling, Stefan Jakobs, and Stefan W. Hell. 2011b. “Diffraction-Unlimited All-Optical Imaging and Writing with a Photochromic GFP.” *Nature* 478(7368):204–8. doi: 10.1038/nature10497.

- Grotjohann, Tim, Ilaria Testa, Matthias Reuss, Tanja Brakemann, Christian Eggeling, Stefan W. Hell, and Stefan Jakobs. 2012a. “RsEGFP2 Enables Fast RESOLFT Nanoscopy of Living Cells.” *ELife* 1:e00248. doi: 10.7554/eLife.00248.
- Grotjohann, Tim, Ilaria Testa, Matthias Reuss, Tanja Brakemann, Christian Eggeling, Stefan W. Hell, and Stefan Jakobs. 2012b. “RsEGFP2 Enables Fast RESOLFT Nanoscopy of Living Cells” edited by X. Zhuang. *ELife* 1:e00248. doi: 10.7554/eLife.00248.
- Grünbein, Marie Luise, Johan Bielecki, Alexander Gorel, Miriam Stricker, Richard Bean, Marco Cammarata, Katerina Dörner, Lars Fröhlich, Elisabeth Hartmann, Steffen Hauf, Mario Hilpert, Yoonhee Kim, Marco Kloos, Romain Letrun, Marc Messerschmidt, Grant Mills, Gabriela Nass Kovacs, Marco Ramilli, Christopher M. Roome, Tokushi Sato, Matthias Scholz, Michel Sliwa, Jolanta Sztuk-Dambietz, Martin Weik, Britta Weinhausen, Nasser Al-Qudami, Djelloul Boukhelef, Sandor Brockhauser, Wajid Ehsan, Moritz Emons, Sergey Esenov, Hans Fangohr, Alexander Kaukher, Thomas Kluyver, Max Lederer, Luis Maia, Maurizio Manetti, Thomas Michelat, Astrid Münnich, Florent Pallas, Guido Palmer, Gianpietro Previtali, Natascha Raab, Alessandro Silenzi, Janusz Szuba, Sandhya Venkatesan, Krzysztof Wrona, Jun Zhu, R. Bruce Doak, Robert L. Shoeman, Lutz Foucar, Jacques-Philippe Colletier, Adrian P. Mancuso, Thomas R. M. Barends, Claudiu A. Stan, and Ilme Schlichting. 2018. “Megahertz Data Collection from Protein Microcrystals at an X-Ray Free-Electron Laser.” *Nature Communications* 9(1):3487. doi: 10.1038/s41467-018-05953-4.
- Grünbein, Marie Luise, and Gabriela Nass Kovacs. 2019. “Sample Delivery for Serial Crystallography at Free-Electron Lasers and Synchrotrons.” *Acta Crystallographica Section D* 75(2):178–91. doi: 10.1107/S205979831801567X.
- Grünbein, Marie Luise, Miriam Stricker, Gabriela Nass Kovacs, Marco Kloos, R. Bruce Doak, Robert L. Shoeman, Jochen Reinstein, Sylvain Lecler, Stefan Haacke, and Ilme Schlichting. 2020. “Illumination Guidelines for Ultrafast Pump-Probe Experiments by Serial Femtosecond Crystallography.” *Nature Methods* 17(7):681–84. doi: 10.1038/s41592-020-0847-3.
- Guo, Gongrui, Martin R. Fuchs, Wuxian Shi, John Skinner, Evanna Berman, Craig M. Ogata, Wayne A. Hendrickson, Sean McSweeney, and Qun Liu. 2018. “Sample Manipulation and Data Assembly for Robust Microcrystal Synchrotron Crystallography.” *IUCrJ* 5(3):238–46. doi: 10.1107/S2052252518005389.
- Gustafsson, M. G. L. 2005. “Nonlinear Structured-Illumination Microscopy: Wide-Field Fluorescence Imaging with Theoretically Unlimited Resolution.” *Proceedings of the National Academy of Sciences* 102(37):13081–86. doi: 10.1073/pnas.0406877102.
- Hajdu, J., K. R. Acharya, D. I. Stuart, D. Barford, and L. N. Johnson. 1988. “Catalysis in Enzyme Crystals.” *Trends in Biochemical Sciences* 13(3):104–9. doi: 10.1016/0968-0004(88)90051-5.
- Hajdu, Janos, Richard Neutze, Tove Sjögren, Karl Edman, Abraham Szöke, Rupert C. Wilmouth, and Carrie M. Wilmot. 2000. “Analyzing Protein Functions in Four Dimensions.” *Nature Structural Biology* 7(11):1006–12. doi: 10.1038/80911.

- Halsted, Thomas P., Keitaro Yamashita, Kunio Hirata, Hideo Ago, Go Ueno, Takehiko Tosha, Robert R. Eady, Svetlana V. Antonyuk, Masaki Yamamoto, and S. Samar Hasnain. 2018. “An Unprecedented Dioxygen Species Revealed by Serial Femtosecond Rotation Crystallography in Copper Nitrite Reductase.” *IUCrJ* 5(1):22–31. doi: 10.1107/S2052252517016128.
- Hammes-Schiffer, Sharon, and Stephen J. Benkovic. 2006. “Relating Protein Motion to Catalysis.” *Annual Review of Biochemistry* 75(1):519–41. doi: 10.1146/annurev.biochem.75.103004.142800.
- Hattne, Johan, Nathaniel Echols, Rosalie Tran, Jan Kern, Richard J. Gildea, Aaron S. Brewster, Roberto Alonso-Mori, Carina Glöckner, Julia Hellmich, Hartawan Laksmono, Raymond G. Sierra, Benedikt Lassalle-Kaiser, Alyssa Lampe, Guangye Han, Sheraz Gul, Dörte DiFiore, Despina Milathianaki, Alan R. Fry, Alan Miahnahri, William E. White, Donald W. Schafer, M. Marvin Seibert, Jason E. Koglin, Dimosthenis Sokaras, Tsu-Chien Weng, Jonas Sellberg, Matthew J. Latimer, Pieter Glatzel, Petrus H. Zwart, Ralf W. Grosse-Kunstleve, Michael J. Bogan, Marc Messerschmidt, Garth J. Williams, Sébastien Boutet, Johannes Messinger, Athina Zouni, Junko Yano, Uwe Bergmann, Vittal K. Yachandra, Paul D. Adams, and Nicholas K. Sauter. 2014. “Accurate Macromolecular Structures Using Minimal Measurements from X-Ray Free-Electron Lasers.” *Nature Methods* 11(5):545–48. doi: 10.1038/nmeth.2887.
- Hay, Sam, and Nigel S. Scrutton. 2012. “Good Vibrations in Enzyme-Catalysed Reactions.” *Nature Chemistry* 4(3):161–68. doi: 10.1038/nchem.1223.
- Hayashi, Ikuko, Hideaki Mizuno, Kit I. Tong, Toshiaki Furuta, Fujie Tanaka, Masato Yoshimura, Atsushi Miyawaki, and Mitsuhiro Ikura. 2007. “Crystallographic Evidence for Water-Assisted Photo-Induced Peptide Cleavage in the Stony Coral Fluorescent Protein Kaede.” *Journal of Molecular Biology* 372(4):918–26. doi: 10.1016/j.jmb.2007.06.037.
- Head, James F., Satoshi Inouye, Katsunori Teranishi, and Osamu Shimomura. 2000. “The Crystal Structure of the Photoprotein Aequorin at 2.3 Å Resolution.” *Nature* 405(6784):372–76. doi: 10.1038/35012659.
- Heim, R., D. C. Prasher, and R. Y. Tsien. 1994. “Wavelength Mutations and Posttranslational Autoxidation of Green Fluorescent Protein.” *Proceedings of the National Academy of Sciences* 91(26):12501–4. doi: 10.1073/pnas.91.26.12501.
- Heim, Roger, Andrew B. Cubitt, and Roger Y. Tsien. 1995. “Improved Green Fluorescence.” *Nature* 373(6516):663–64. doi: 10.1038/373663b0.
- Hekstra, Doeke R., K. Ian White, Michael A. Socolich, Robert W. Henning, Vukica Šrajer, and Rama Ranganathan. 2016. “Electric-Field-Stimulated Protein Mechanics.” *Nature* 540(7633):400–405. doi: 10.1038/nature20571.
- Hell, S. W., S. Jakobs, and L. Kastrop. 2003. “Imaging and Writing at the Nanoscale with Focused Visible Light through Saturable Optical Transitions.” *Applied Physics A: Materials Science & Processing* 77(7):859–60. doi: 10.1007/s00339-003-2292-4.

- Hell, Stefan W., and Jan Wichmann. 1994. "Breaking the Diffraction Resolution Limit by Stimulated Emission: Stimulated-Emission-Depletion Fluorescence Microscopy." *Optics Letters* 19(11):780. doi: 10.1364/OL.19.000780.
- Henderson, J. N., H. -w. Ai, R. E. Campbell, and S. J. Remington. 2007. "Structural Basis for Reversible Photobleaching of a Green Fluorescent Protein Homologue." *Proceedings of the National Academy of Sciences* 104(16):6672–77. doi: 10.1073/pnas.0700059104.
- Henderson, R., and J. K. Moffat. 1971. "The Difference Fourier Technique in Protein Crystallography: Errors and Their Treatment." *Acta Crystallographica Section B Structural Crystallography and Crystal Chemistry* 27(7):1414–20. doi: 10.1107/S0567740871004060.
- Hendrickson, Wayne A. 2014. "Anomalous Diffraction in Crystallographic Phase Evaluation." *Quarterly Reviews of Biophysics* 47(1):49–93. doi: 10.1017/S0033583514000018.
- Henrich, B., J. Becker, R. Dinapoli, P. Goettlicher, H. Graafsma, H. Hirsemann, R. Klanner, H. Krueger, R. Mazzocco, A. Mozzanica, H. Perrey, G. Potdevin, B. Schmitt, X. Shi, A. K. Srivastava, U. Trunk, and C. Youngman. 2011. "The Adaptive Gain Integrating Pixel Detector AGIPD a Detector for the European XFEL." *Nuclear Instruments and Methods in Physics Research Section A: Accelerators, Spectrometers, Detectors and Associated Equipment* 633:S11–14. doi: 10.1016/j.nima.2010.06.107.
- Henzler-Wildman, Katherine, and Dorothee Kern. 2007. "Dynamic Personalities of Proteins." *Nature* 450(7172):964–72. doi: 10.1038/nature06522.
- Heymann, Michael, Achini Opathalage, Jennifer L. Wierman, Sathish Akella, Doletta M. E. Szebenyi, Sol M. Gruner, and Seth Fraden. 2015. "Room-Temperature Serial Crystallography Using a Kinetically Optimized Microfluidic Device for Protein Crystallization and on-Chip X-Ray Diffraction. Corrigendum." *IUCrJ* 2(5):601–601. doi: 10.1107/S205225251501492X.
- Heymann, Michael, Achini Opathalage, Jennifer L. Wierman, Sathish Akella, Doletta M. E. Szebenyi, Sol M. Gruner, and Seth Fraden. 2014. "Room-Temperature Serial Crystallography Using a Kinetically Optimized Microfluidic Device for Protein Crystallization and on-Chip X-Ray Diffraction." *IUCrJ* 1(5):349–60. doi: 10.1107/S2052252514016960.
- Hirata, Kunio, Kyoko Shinzawa-Itoh, Naomine Yano, Shuhei Takemura, Koji Kato, Miki Hatanaka, Kazumasa Muramoto, Takako Kawahara, Tomitake Tsukihara, Eiki Yamashita, Kensuke Tono, Go Ueno, Takaaki Hikima, Hironori Murakami, Yuichi Inubushi, Makina Yabashi, Tetsuya Ishikawa, Masaki Yamamoto, Takashi Ogura, Hiroshi Sugimoto, Jian-Ren Shen, Shinya Yoshikawa, and Hideo Ago. 2014. "Determination of Damage-Free Crystal Structure of an X-Ray-Sensitive Protein Using an XFEL." *Nature Methods* 11(7):734–36. doi: 10.1038/nmeth.2962.
- Hochuli, E., H. Döbeli, and A. Schacher. 1987. "New Metal Chelate Adsorbent Selective for Proteins and Peptides Containing Neighbouring Histidine Residues." *Journal of Chromatography A* 411:177–84. doi: 10.1016/S0021-9673(00)93969-4.
- Hofmann, M., C. Eggeling, S. Jakobs, and S. W. Hell. 2005. "Breaking the Diffraction Barrier in Fluorescence Microscopy at Low Light Intensities by Using Reversibly

- Photoswitchable Proteins.” *Proceedings of the National Academy of Sciences* 102(49):17565–69. doi: 10.1073/pnas.0506010102.
- Hough, Michael A., and Robin L. Owen. 2021. “Serial Synchrotron and XFEL Crystallography for Studies of Metalloprotein Catalysis.” *Current Opinion in Structural Biology* 71:232–38. doi: 10.1016/j.sbi.2021.07.007.
- Huang, Chia Ying, Vincent Olieric, Pikyee Ma, Nicole Howe, Lutz Vogeley, Xiangyu Liu, Rangana Warshamanage, Tobias Weinert, Ezequiel Panepucci, Brian Kobilka, Kay Diederichs, Meitian Wang, and Martin Caffrey. 2016. “In Meso in Situ Serial X-Ray Crystallography of Soluble and Membrane Proteins at Cryogenic Temperatures.” *Acta Crystallographica. Section D, Structural Biology* 72(Pt 1):93–112. doi: 10.1107/S2059798315021683.
- Huang, Chia-Ying, Vincent Olieric, Nicole Howe, Rangana Warshamanage, Tobias Weinert, Ezequiel Panepucci, Lutz Vogeley, Shibom Basu, Kay Diederichs, Martin Caffrey, and Meitian Wang. 2018. “In Situ Serial Crystallography for Rapid de Novo Membrane Protein Structure Determination.” *Communications Biology* 1(1):124. doi: 10.1038/s42003-018-0123-6.
- Hunter, Mark S., Brent Segelke, Marc Messerschmidt, Garth J. Williams, Nadia A. Zatsepin, Anton Barty, W. Henry Benner, David B. Carlson, Matthew Coleman, Alexander Graf, Stefan P. Hau-Riege, Tommaso Pardini, M. Marvin Seibert, James Evans, Sébastien Boutet, and Matthias Frank. 2014. “Fixed-Target Protein Serial Microcrystallography with an x-Ray Free Electron Laser.” *Scientific Reports* 4:6026. doi: 10.1038/srep06026.
- Hunter, Mark S., Chun Hong Yoon, Hasan DeMirici, Raymond G. Sierra, E. Han Dao, Radman Ahmadi, Fulya Aksit, Andrew L. Aquila, Halilibrahim Ciftci, Serge Guillet, Matt J. Hayes, Thomas J. Lane, Meng Liang, Ulf Lundström, Jason E. Koglin, Paul Mgbam, Yashas Rao, Lindsey Zhang, Soichi Wakatsuki, James M. Holton, and Sébastien Boutet. 2016. “Selenium Single-Wavelength Anomalous Diffraction de Novo Phasing Using an X-Ray-Free Electron Laser.” *Nature Communications* 7(1):13388. doi: 10.1038/ncomms13388.
- Hwu, Yeukuang, and Giorgio Margaritondo. 2021. “Synchrotron Radiation and X-Ray Free-Electron Lasers (X-FELs) Explained to All Users, Active and Potential.” *Journal of Synchrotron Radiation* 28(3):1014–29. doi: 10.1107/S1600577521003325.
- Ibrahim, Mohamed, Thomas Fransson, Ruchira Chatterjee, Mun Hon Cheah, Rana Hussein, Louise Lassalle, Kyle D. Sutherland, Iris D. Young, Franklin D. Fuller, Sheraz Gul, In-Sik Kim, Philipp S. Simon, Casper de Lichtenberg, Petko Chervnev, Isabel Bogacz, Cindy C. Pham, Allen M. Orville, Nicholas Saichek, Trent Northen, Alexander Batyuk, Sergio Carbajo, Roberto Alonso-Mori, Kensuke Tono, Shigeki Owada, Asmit Bhowmick, Robert Bolotovskiy, Derek Mendez, Nigel W. Moriarty, James M. Holton, Holger Dobbek, Aaron S. Brewster, Paul D. Adams, Nicholas K. Sauter, Uwe Bergmann, Athina Zouni, Johannes Messinger, Jan Kern, Vittal K. Yachandra, and Junko Yano. 2020. “Untangling the Sequence of Events during the $S_2 \rightarrow S_3$ Transition in Photosystem II and Implications for the Water Oxidation Mechanism.” *Proceedings of the National Academy of Sciences* 117(23):12624–35. doi: 10.1073/pnas.2000529117.

- Ishigami, Izumi, Ariel Lewis-Ballester, Austin Echelmeier, Gerrit Brehm, Nadia A. Zatsepin, Thomas D. Grant, Jesse D. Coe, Stella Lisova, Garrett Nelson, Shangji Zhang, Zachary F. Dobson, Sébastien Boutet, Raymond G. Sierra, Alexander Batyuk, Petra Fromme, Raimund Fromme, John C. H. Spence, Alexandra Ros, Syun-Ru Yeh, and Denis L. Rousseau. 2019. “Snapshot of an Oxygen Intermediate in the Catalytic Reaction of Cytochrome *c* Oxidase.” *Proceedings of the National Academy of Sciences* 116(9):3572–77. doi: 10.1073/pnas.1814526116.
- Jacquemet, Guillaume, Alexandre F. Carisey, Hellyeh Hamidi, Ricardo Henriques, and Christophe Leterrier. 2020. “The Cell Biologist’s Guide to Super-Resolution Microscopy.” *Journal of Cell Science* 133(11):jcs240713. doi: 10.1242/jcs.240713.
- Jensen, Nickels A., Isabelle Jansen, Maria Kamper, and Stefan Jakobs. 2020. “Reversibly Switchable Fluorescent Proteins for RESOLFT Nanoscopy.” Pp. 241–61 in *Nanoscale Photonic Imaging*. Vol. 134, *Topics in Applied Physics*, edited by T. Salditt, A. Egner, and D. R. Luke. Cham: Springer International Publishing.
- Jing, Yingying, Chenshuang Zhang, Bin Yu, Danying Lin, and Junle Qu. 2021. “Super-Resolution Microscopy: Shedding New Light on In Vivo Imaging.” *Frontiers in Chemistry* 9:746900. doi: 10.3389/fchem.2021.746900.
- Johansson, Linda C., David Arnlund, Gergely Katona, Thomas A. White, Anton Barty, Daniel P. DePonte, Robert L. Shoeman, Cecilia Wickstrand, Amit Sharma, Garth J. Williams, Andrew Aquila, Michael J. Bogan, Carl Caleman, Jan Davidsson, R. Bruce Doak, Matthias Frank, Raimund Fromme, Lorenzo Galli, Ingo Grotjohann, Mark S. Hunter, Stephan Kassemeyer, Richard A. Kirian, Christopher Kupitz, Mengning Liang, Lukas Lomb, Erik Malmerberg, Andrew V. Martin, Marc Messerschmidt, Karol Nass, Lars Redecke, M. Marvin Seibert, Jennie Sjöhamn, Jan Steinbrener, Francesco Stellato, Dingjie Wang, Weixiao Y. Wahlgren, Uwe Weierstall, Sebastian Westenhoff, Nadia A. Zatsepin, Sébastien Boutet, John C. H. Spence, Ilme Schlichting, Henry N. Chapman, Petra Fromme, and Richard Neutze. 2013. “Structure of a Photosynthetic Reaction Centre Determined by Serial Femtosecond Crystallography.” *Nature Communications* 4(1):2911. doi: 10.1038/ncomms3911.
- Johansson, Linda C., David Arnlund, Thomas A. White, Gergely Katona, Daniel P. DePonte, Uwe Weierstall, R. Bruce Doak, Robert L. Shoeman, Lukas Lomb, Erik Malmerberg, Jan Davidsson, Karol Nass, Mengning Liang, Jakob Andreasson, Andrew Aquila, Saša Bajt, Miriam Barthelmess, Anton Barty, Michael J. Bogan, Christoph Bostedt, John D. Bozek, Carl Caleman, Ryan Coffee, Nicola Coppola, Tomas Ekeberg, Sascha W. Epp, Benjamin Erk, Holger Fleckenstein, Lutz Foucar, Heinz Graafsma, Lars Gumprecht, Janos Hajdu, Christina Y. Hampton, Robert Hartmann, Andreas Hartmann, Günter Hauser, Helmut Hirsemann, Peter Holl, Mark S. Hunter, Stephan Kassemeyer, Nils Kimmel, Richard A. Kirian, Filipe R. N. C. Maia, Stefano Marchesini, Andrew V. Martin, Christian Reich, Daniel Rolles, Benedikt Rudek, Artem Rudenko, Ilme Schlichting, Joachim Schulz, M. Marvin Seibert, Raymond G. Sierra, Heike Soltau, Dmitri Starodub, Francesco Stellato, Stephan Stern, Lothar Strüder, Nicusor Timneanu, Joachim Ullrich, Weixiao Y. Wahlgren, Xiaoyu Wang, Georg Weidenspointner, Cornelia Wunderer, Petra Fromme, Henry N. Chapman, John C. H. Spence, and Richard Neutze. 2012. “Lipidic Phase Membrane Protein Serial Femtosecond Crystallography.” *Nature Methods* 9(3):263–65. doi: 10.1038/nmeth.1867.

- Johnson, Kenneth A. 2008. "Role of Induced Fit in Enzyme Specificity: A Molecular Forward/Reverse Switch." *Journal of Biological Chemistry* 283(39):26297–301. doi: 10.1074/jbc.R800034200.
- Jones, Llewellyn H., and Eugene McLaren. 1958. "Infrared Absorption Spectra of SO₂ and CO₂ in Aqueous Solution." *The Journal of Chemical Physics* 28(5):995–995. doi: 10.1063/1.1744329.
- Kabsch, W. 1988. "Evaluation of Single-Crystal X-Ray Diffraction Data from a Position-Sensitive Detector." *Journal of Applied Crystallography* 21(6):916–24. doi: 10.1107/S0021889888007903.
- Kabsch, Wolfgang. 2010a. "Integration, Scaling, Space-Group Assignment and Post-Refinement." *Acta Crystallographica Section D Biological Crystallography* 66(2):133–44. doi: 10.1107/S0907444909047374.
- Kabsch, Wolfgang. 2010b. "XDS." *Acta Crystallographica Section D Biological Crystallography* 66(2):125–32. doi: 10.1107/S0907444909047337.
- Kabsch, Wolfgang. 2014. "Processing of X-Ray Snapshots from Crystals in Random Orientations." *Acta Crystallographica. Section D, Biological Crystallography* 70(Pt 8):2204–16. doi: 10.1107/S1399004714013534.
- Kamerlin, Shina C. L., and Arieh Warshel. 2010. "At the Dawn of the 21st Century: Is Dynamics the Missing Link for Understanding Enzyme Catalysis?: Critically Examining the Dynamical Proposal." *Proteins: Structure, Function, and Bioinformatics* 78(6):1339–75. doi: 10.1002/prot.22654.
- Kameshima, Takashi, Shun Ono, Togo Kudo, Kyosuke Ozaki, Yoichi Kirihara, Kazuo Kobayashi, Yuichi Inubushi, Makina Yabashi, Toshio Horigome, Andrew Holland, Karen Holland, David Burt, Hajime Murao, and Takaki Hatsui. 2014. "Development of an X-Ray Pixel Detector with Multi-Port Charge-Coupled Device for X-Ray Free-Electron Laser Experiments." *Review of Scientific Instruments* 85(3):033110. doi: 10.1063/1.4867668.
- Kang, Heung-Sik, Chang-Ki Min, Hoon Heo, Changbum Kim, Haeryong Yang, Gyujin Kim, Inhyuk Nam, Soung Youl Baek, Hyo-Jin Choi, Geonyeong Mun, Byoung Ryul Park, Young Jin Suh, Dong Cheol Shin, Jinyul Hu, Juho Hong, Seonghoon Jung, Sang-Hee Kim, KwangHoon Kim, Donghyun Na, Soung Soo Park, Yong Jung Park, Jang-Hui Han, Young Gyu Jung, Seong Hun Jeong, Hong Gi Lee, Sangbong Lee, Sojeong Lee, Woul-Woo Lee, Bonggi Oh, Hyung Suck Suh, Yong Woon Parc, Sung-Ju Park, Min Ho Kim, Nam-Suk Jung, Young-Chan Kim, Mong-Soo Lee, Bong-Ho Lee, Chi-Won Sung, Ik-Su Mok, Jung-Moo Yang, Chae-Soon Lee, Hocheol Shin, Ji Hwa Kim, Yongsam Kim, Jae Hyuk Lee, Sang-Youn Park, Jangwoo Kim, Jaeku Park, Intae Eom, Seungyu Rah, Sunam Kim, Ki Hyun Nam, Jaehyun Park, Jaehun Park, Sangsoo Kim, Soonam Kwon, Sang Han Park, Kyung Sook Kim, Hyojung Hyun, Seung Nam Kim, Seonghan Kim, Sun-min Hwang, Myong Jin Kim, Chae-yong Lim, Chung-Jong Yu, Bong-Soo Kim, Tai-Hee Kang, Kwang-Woo Kim, Seung-Hwan Kim, Hee-Seock Lee, Heung-Soo Lee, Ki-Hyeon Park, Tae-Yeong Koo, Dong-Eon Kim, and In Soo Ko. 2017. "Hard X-Ray Free-Electron Laser with Femtosecond-Scale Timing Jitter." *Nature Photonics* 11(11):708–13. doi: 10.1038/s41566-017-0029-8.

- Kantardjieff, Katherine A., and Bernhard Rupp. 2003. “Matthews Coefficient Probabilities: Improved Estimates for Unit Cell Contents of Proteins, DNA, and Protein-Nucleic Acid Complex Crystals.” *Protein Science: A Publication of the Protein Society* 12(9):1865–71. doi: 10.1110/ps.0350503.
- Kao, Y. T., C. Saxena, L. Wang, A. Sancar, and D. Zhong. 2005. “Direct Observation of Thymine Dimer Repair in DNA by Photolyase.” *Proceedings of the National Academy of Sciences* 102(45):16128–32. doi: 10.1073/pnas.0506586102.
- Kar, Rajiv K., Anne-Frances Miller, and Maria-Andrea Mroginski. 2021. “Understanding Flavon Electronic Structure and Spectra.” *WIREs Computational Molecular Science*. doi: 10.1002/wcms.1541.
- Karplus, Martin. 2010. “Role of Conformation Transitions in Adenylate Kinase.” *Proceedings of the National Academy of Sciences* 107(17). doi: 10.1073/pnas.1002180107.
- Karplus, P. A., and K. Diederichs. 2012. “Linking Crystallographic Model and Data Quality.” *Science* 336(6084):1030–33. doi: 10.1126/science.1218231.
- Keedy, Daniel A., Lillian R. Kenner, Matthew Warkentin, Rahel A. Woldeyes, Jesse B. Hopkins, Michael C. Thompson, Aaron S. Brewster, Andrew H. Van Benschoten, Elizabeth L. Baxter, Monarin Uervirojnangkoorn, Scott E. McPhillips, Jinhua Song, Roberto Alonso-Mori, James M. Holton, William I. Weis, Axel T. Brunger, S. Michael Soltis, Henrik Lemke, Ana Gonzalez, Nicholas K. Sauter, Aina E. Cohen, Henry van den Bedem, Robert E. Thorne, and James S. Fraser. 2015. “Mapping the Conformational Landscape of a Dynamic Enzyme by Multitemperature and XFEL Crystallography.” *ELife* 4:e07574. doi: 10.7554/eLife.07574.
- Kern, J., R. Alonso-Mori, J. Hellmich, R. Tran, J. Hattne, H. Laksmono, C. Glockner, N. Echols, R. G. Sierra, J. Sellberg, B. Lassalle-Kaiser, R. J. Gildea, P. Glatzel, R. W. Grosse-Kunstleve, M. J. Latimer, T. A. McQueen, D. DiFiore, A. R. Fry, M. Messerschmidt, A. Miahnahri, D. W. Schafer, M. M. Seibert, D. Sokaras, T. C. Weng, P. H. Zwart, W. E. White, P. D. Adams, M. J. Bogan, S. Boutet, G. J. Williams, J. Messinger, N. K. Sauter, A. Zouni, U. Bergmann, J. Yano, and V. K. Yachandra. 2012. “Room Temperature Femtosecond X-Ray Diffraction of Photosystem II Microcrystals.” *Proceedings of the National Academy of Sciences* 109(25):9721–26. doi: 10.1073/pnas.1204598109.
- Kern, Jan, Roberto Alonso-Mori, Rosalie Tran, Johan Hattne, Richard J. Gildea, Nathaniel Echols, Carina Glöckner, Julia Hellmich, Hartawan Laksmono, Raymond G. Sierra, Benedikt Lassalle-Kaiser, Sergey Koroidov, Alyssa Lampe, Guangye Han, Sheraz Gul, Dörte DiFiore, Despina Milathianaki, Alan R. Fry, Alan Miahnahri, Donald W. Schafer, Marc Messerschmidt, M. Marvin Seibert, Jason E. Koglin, Dimosthenis Sokaras, Tsu-Chien Weng, Jonas Sellberg, Matthew J. Latimer, Ralf W. Grosse-Kunstleve, Petrus H. Zwart, William E. White, Pieter Glatzel, Paul D. Adams, Michael J. Bogan, Garth J. Williams, Sébastien Boutet, Johannes Messinger, Athina Zouni, Nicholas K. Sauter, Vittal K. Yachandra, Uwe Bergmann, and Junko Yano. 2013. “Simultaneous Femtosecond X-Ray Spectroscopy and Diffraction of Photosystem II at Room Temperature.” *Science (New York, N.Y.)* 340(6131):491–95. doi: 10.1126/science.1234273.

- Kern, Jan, Ruchira Chatterjee, Iris D. Young, Franklin D. Fuller, Louise Lassalle, Mohamed Ibrahim, Sheraz Gul, Thomas Fransson, Aaron S. Brewster, Roberto Alonso-Mori, Rana Hussein, Miao Zhang, Lacey Douthit, Casper de Lichtenberg, Mun Hon Cheah, Dmitry Shevela, Julia Wersig, Ina Seuffert, Dimosthenis Sokaras, Ernest Pastor, Clemens Weninger, Thomas Kroll, Raymond G. Sierra, Pierre Aller, Agata Butryn, Allen M. Orville, Mengning Liang, Alexander Batyuk, Jason E. Koglin, Sergio Carbajo, Sébastien Boutet, Nigel W. Moriarty, James M. Holton, Holger Dobbek, Paul D. Adams, Uwe Bergmann, Nicholas K. Sauter, Athina Zouni, Johannes Messinger, Junko Yano, and Vittal K. Yachandra. 2018. “Structures of the Intermediates of Kok’s Photosynthetic Water Oxidation Clock.” *Nature* 563(7731):421–25. doi: 10.1038/s41586-018-0681-2.
- Kern, Jan, Rosalie Tran, Roberto Alonso-Mori, Sergey Koroidov, Nathaniel Echols, Johan Hattne, Mohamed Ibrahim, Sheraz Gul, Hartawan Laksmono, Raymond G. Sierra, Richard J. Gildea, Guangye Han, Julia Hellmich, Benedikt Lassalle-Kaiser, Ruchira Chatterjee, Aaron S. Brewster, Claudiu A. Stan, Carina Glöckner, Alyssa Lampe, Dörte DiFiore, Despina Milathianaki, Alan R. Fry, M. Marvin Seibert, Jason E. Koglin, Erik Gallo, Jens Uhlig, Dimosthenis Sokaras, Tsu-Chien Weng, Petrus H. Zwart, David E. Skinner, Michael J. Bogan, Marc Messerschmidt, Pieter Glatzel, Garth J. Williams, Sébastien Boutet, Paul D. Adams, Athina Zouni, Johannes Messinger, Nicholas K. Sauter, Uwe Bergmann, Junko Yano, and Vittal K. Yachandra. 2014. “Taking Snapshots of Photosynthetic Water Oxidation Using Femtosecond X-Ray Diffraction and Spectroscopy.” *Nature Communications* 5(1):4371. doi: 10.1038/ncomms5371.
- Khater, Ismail M., Ivan Robert Nabi, and Ghassan Hamarneh. 2020. “A Review of Super-Resolution Single-Molecule Localization Microscopy Cluster Analysis and Quantification Methods.” *Patterns* 1(3):100038. doi: 10.1016/j.patter.2020.100038.
- Kirian, Richard A., Xiaoyu Wang, Uwe Weierstall, Kevin E. Schmidt, John C. H. Spence, Mark Hunter, Petra Fromme, Thomas White, Henry N. Chapman, and James Holton. 2010. “Femtosecond Protein Nanocrystallography—Data Analysis Methods.” *Optics Express* 18(6):5713. doi: 10.1364/OE.18.005713.
- Konold, Patrick E., Enis Arik, Jörn Weißenborn, Jos C. Arents, Klaas J. Hellingwerf, Ivo H. M. van Stokkum, John T. M. Kennis, and Marie Louise Groot. 2020. “Confinement in Crystal Lattice Alters Entire Photocycle Pathway of the Photoactive Yellow Protein.” *Nature Communications* 11(1):4248. doi: 10.1038/s41467-020-18065-9.
- Kort, Remco, Hirofumi Komori, Shin-ichi Adachi, Kunio Miki, and Andre Eker. 2004. “DNA Apophotolyase from *Anacystis Nidulans* : 1.8 Å Structure, 8-HDF Reconstitution and X-Ray-Induced FAD Reduction.” *Acta Crystallographica Section D Biological Crystallography* 60(7):1205–13. doi: 10.1107/S0907444904009321.
- Koshland, D. E., and K. E. Neet. 1968. “The Catalytic and Regulatory Properties of Enzymes.” *Annual Review of Biochemistry* 37(1):359–411. doi: 10.1146/annurev.bi.37.070168.002043.
- Kováčsová, Gabriela, Marie Luise Grünbein, Marco Kloos, Thomas R. M. Barends, Ramona Schlesinger, Joachim Heberle, Wolfgang Kabsch, Robert L. Shoeman, R. Bruce Doak, and Ilme Schlichting. 2017. “Viscous Hydrophilic Injection Matrices for Serial Crystallography.” *IUCrJ* 4(4):400–410. doi: 10.1107/S2052252517005140.

- Kovalev, Kirill, Roman Astashkin, Ivan Gushchin, Philipp Orekhov, Dmytro Volkov, Egor Zinovev, Egor Marin, Maksim Rulev, Alexey Alekseev, Antoine Royant, Philippe Carpentier, Svetlana Vaganova, Dmitrii Zabelskii, Christian Baeken, Ilya Sergeev, Taras Balandin, Gleb Bourenkov, Xavier Carpena, Roeland Boer, Nina Maliar, Valentin Borshchevskiy, Georg Büldt, Ernst Bamberg, and Valentin Gordeliy. 2020. “Molecular Mechanism of Light-Driven Sodium Pumping.” *Nature Communications* 11(1):2137. doi: 10.1038/s41467-020-16032-y.
- Kragh, Helge. 2018. “The Lorenz-Lorentz Formula: Origin and Early History.” *Substantia* 7-18 Pages. doi: 10.13128/SUBSTANTIA-56.
- Kubota, Y., M. Suzuki, T. Katayama, K. Yamamoto, K. Tono, Y. Inubushi, T. Seki, K. Takashi, H. Wadati, and M. Yabashi. 2019. “Polarization Control with an X-Ray Phase Retarder for High-Time-Resolution Pump–Probe Experiments at SACLA.” *Journal of Synchrotron Radiation* 26(4):1139–43. doi: 10.1107/S1600577519006222.
- Kupitz, Christopher, Shibom Basu, Ingo Grotjohann, Raimund Fromme, Nadia A. Zatsepin, Kimberly N. Rendek, Mark S. Hunter, Robert L. Shoeman, Thomas A. White, Dingjie Wang, Daniel James, Jay-How Yang, Danielle E. Cobb, Brenda Reeder, Raymond G. Sierra, Haiguang Liu, Anton Barty, Andrew L. Aquila, Daniel Deponte, Richard A. Kirian, Sadia Bari, Jesse J. Bergkamp, Kenneth R. Beyerlein, Michael J. Bogan, Carl Caleman, Tzu-Chiao Chao, Chelsie E. Conrad, Katherine M. Davis, Holger Fleckenstein, Lorenzo Galli, Stefan P. Hau-Riege, Stephan Kassemeyer, Hartawan Laksmono, Mengning Liang, Lukas Lomb, Stefano Marchesini, Andrew V. Martin, Marc Messerschmidt, Despina Milathianaki, Karol Nass, Alexandra Ros, Shatabdi Roy-Chowdhury, Kevin Schmidt, Marvin Seibert, Jan Steinbrener, Francesco Stellato, Lifan Yan, Chunhong Yoon, Thomas A. Moore, Ana L. Moore, Yulia Pushkar, Garth J. Williams, Sébastien Boutet, R. Bruce Doak, Uwe Weierstall, Matthias Frank, Henry N. Chapman, John C. H. Spence, and Petra Fromme. 2014. “Serial Time-Resolved Crystallography of Photosystem II Using a Femtosecond X-Ray Laser.” *Nature* 513(7517):261–65. doi: 10.1038/nature13453.
- Kupitz, Christopher, Jose L. Olmos, Mark Holl, Lee Tremblay, Kanupriya Pande, Suraj Pandey, Dominik Oberthür, Mark Hunter, Mengning Liang, Andrew Aquila, Jason Tenboer, George Calvey, Andrea Katz, Yujie Chen, Max O. Wiedorn, Juraj Knoska, Alke Meents, Valerio Majrjani, Tyler Norwood, Ishwor Poudyal, Thomas Grant, Mitchell D. Miller, Weijun Xu, Aleksandra Tolstikova, Andrew Morgan, Markus Metz, Jose M. Martin-Garcia, James D. Zook, Shatabdi Roy-Chowdhury, Jesse Coe, Nirupa Nagarathnam, Domingo Meza, Raimund Fromme, Shibom Basu, Matthias Frank, Thomas White, Anton Barty, Sasa Bajt, Oleksandr Yefanov, Henry N. Chapman, Nadia Zatsepin, Garrett Nelson, Uwe Weierstall, John Spence, Peter Schwander, Lois Pollack, Petra Fromme, Abbas Ourmazd, George N. Phillips, and Marius Schmidt. 2017. “Structural Enzymology Using X-Ray Free Electron Lasers.” *Structural Dynamics* 4(4):044003. doi: 10.1063/1.4972069.
- Kwon, Jiwoong, Jihee Hwang, Jaewan Park, Gi Rim Han, Kyu Young Han, and Seong Keun Kim. 2015. “RESOLFT Nanoscopy with Photoswitchable Organic Fluorophores.” *Scientific Reports* 5(1):17804. doi: 10.1038/srep17804.
- Lambert, Talley J. 2019. “FPbase: A Community-Editable Fluorescent Protein Database.” *Nature Methods* 16(4):277–78. doi: 10.1038/s41592-019-0352-8.

- Landau, E. M., and J. P. Rosenbusch. 1996. "Lipidic Cubic Phases: A Novel Concept for the Crystallization of Membrane Proteins." *Proceedings of the National Academy of Sciences of the United States of America* 93(25):14532–35. doi: 10.1073/pnas.93.25.14532.
- von Laue, Max. 1915. "Concerning the Detection of X-Ray Interferences." *Nobel Lecture* 13.
- Li, J., A. Vrielink, P. Brick, and D. M. Blow. 1993. "Crystal Structure of Cholesterol Oxidase Complexed with a Steroid Substrate: Implications for Flavin Adenine Dinucleotide Dependent Alcohol Oxidases." *Biochemistry* 32(43):11507–15.
- Li, Jiang, Zheyun Liu, Chuang Tan, Xunmin Guo, Lijuan Wang, Aziz Sancar, and Dongping Zhong. 2010. "Dynamics and Mechanism of Repair of Ultraviolet-Induced (6–4) Photoproduct by Photolyase." *Nature* 466(7308):887–90. doi: 10.1038/nature09192.
- Liang, Mengning, Garth J. Williams, Marc Messerschmidt, M. Marvin Seibert, Paul A. Montanez, Matt Hayes, Despina Milathianaki, Andrew Aquila, Mark S. Hunter, Jason E. Koglin, Donald W. Schafer, Serge Guillet, Armin Busse, Robert Bergan, William Olson, Kay Fox, Nathaniel Stewart, Robin Curtis, Alireza Alan Miahnahri, and Sébastien Boutet. 2015. "The Coherent X-Ray Imaging Instrument at the Linac Coherent Light Source." *Journal of Synchrotron Radiation* 22(3):514–19. doi: 10.1107/S160057751500449X.
- Liebschner, Dorothee, Pavel V. Afonine, Matthew L. Baker, Gábor Bunkóczi, Vincent B. Chen, Tristan I. Croll, Bradley Hintze, Li-Wei Hung, Swati Jain, Airlie J. McCoy, Nigel W. Moriarty, Robert D. Oeffner, Billy K. Poon, Michael G. Prisant, Randy J. Read, Jane S. Richardson, David C. Richardson, Massimo D. Sammito, Oleg V. Sobolev, Duncan H. Stockwell, Thomas C. Terwilliger, Alexandre G. Urzhumtsev, Lizbeth L. Videau, Christopher J. Williams, and Paul D. Adams. 2019. "Macromolecular Structure Determination Using X-Rays, Neutrons and Electrons: Recent Developments in *Phenix*." *Acta Crystallographica Section D Structural Biology* 75(10):861–77. doi: 10.1107/S2059798319011471.
- Liu, W., D. Wacker, C. Gati, G. W. Han, D. James, D. Wang, G. Nelson, U. Weierstall, V. Katritch, A. Barty, N. A. Zatsepin, D. Li, M. Messerschmidt, S. Boutet, G. J. Williams, J. E. Koglin, M. M. Seibert, C. Wang, S. T. A. Shah, S. Basu, R. Fromme, C. Kupitz, K. N. Rendek, I. Grotjohann, P. Fromme, R. A. Kirian, K. R. Beyerlein, T. A. White, H. N. Chapman, M. Caffrey, J. C. H. Spence, R. C. Stevens, and V. Cherezov. 2013. "Serial Femtosecond Crystallography of G Protein-Coupled Receptors." *Science* 342(6165):1521–24. doi: 10.1126/science.1244142.
- Liu, Zheyun, Lijuan Wang, and Dongping Zhong. 2015. "Dynamics and Mechanisms of DNA Repair by Photolyase." *Physical Chemistry Chemical Physics* 17(18):11933–49. doi: 10.1039/C4CP05286B.
- Lomb, Lukas, Thomas R. M. Barends, Stephan Kassemeyer, Andrew Aquila, Sascha W. Epp, Benjamin Erk, Lutz Foucar, Robert Hartmann, Benedikt Rudek, Daniel Rolles, Artem Rudenko, Robert L. Shoeman, Jakob Andreasson, Sasa Bajt, Miriam Barthelmeß, Anton Barty, Michael J. Bogan, Christoph Bostedt, John D. Bozek, Carl Caleman, Ryan Coffee, Nicola Coppola, Daniel P. DePonte, R. Bruce Doak, Tomas Ekeberg, Holger Fleckenstein, Petra Fromme, Maike Gebhardt, Heinz Graafsma, Lars Gumprecht,

- Christina Y. Hampton, Andreas Hartmann, Günter Hauser, Helmut Hirsemann, Peter Holl, James M. Holton, Mark S. Hunter, Wolfgang Kabsch, Nils Kimmel, Richard A. Kirian, Mengning Liang, Filipe R. N. C. Maia, Anton Meinhart, Stefano Marchesini, Andrew V. Martin, Karol Nass, Christian Reich, Joachim Schulz, M. Marvin Seibert, Raymond Sierra, Heike Soltau, John C. H. Spence, Jan Steinbrener, Francesco Stellato, Stephan Stern, Nicusor Timneanu, Xiaoyu Wang, Georg Weidenspointner, Uwe Weierstall, Thomas A. White, Cornelia Wunderer, Henry N. Chapman, Joachim Ullrich, Lothar Strüder, and Ilme Schlichting. 2011. “Radiation Damage in Protein Serial Femtosecond Crystallography Using an X-Ray Free-Electron Laser.” *Physical Review B* 84(21):214111. doi: 10.1103/PhysRevB.84.214111.
- Lomb, Lukas, Jan Steinbrener, Sadia Bari, Daniel Beisel, Daniel Berndt, Christian Kieser, Martin Lukat, Niklas Neef, and Robert L. Shoeman. 2012. “An Anti-Settling Sample Delivery Instrument for Serial Femtosecond Crystallography.” *Journal of Applied Crystallography* 45(4):674–78. doi: 10.1107/S0021889812024557.
- Lomelino, Carrie L., Jin Kyun Kim, Cheol Lee, Seon Woo Lim, Jacob T. Andring, Brian P. Mahon, Moses Chung, Chae Un Kim, and Robert McKenna. 2018. “Carbonic Anhydrase II Microcrystals Suitable for XFEL Studies.” *Acta Crystallographica Section F Structural Biology Communications* 74(6):327–30. doi: 10.1107/S2053230X18006118.
- Lukyanov, Konstantin A., Arkady F. Fradkov, Nadya G. Gurskaya, Mikhail V. Matz, Yulii A. Labas, Aleksandr P. Savitsky, Mikhail L. Markelov, Andrey G. Zaraisky, Xiaoning Zhao, Yu Fang, Wenyan Tan, and Sergey A. Lukyanov. 2000. “Natural Animal Coloration Can Be Determined by a Nonfluorescent Green Fluorescent Protein Homolog.” *Journal of Biological Chemistry* 275(34):25879–82. doi: 10.1074/jbc.C000338200.
- Lutman, Alberto A., James P. MacArthur, Markus Ilchen, Anton O. Lindahl, Jens Buck, Ryan N. Coffee, Georgi L. Dakovski, Lars Dammann, Yuantao Ding, Hermann A. Dürr, Leif Glaser, Jan Grünert, Gregor Hartmann, Nick Hartmann, Daniel Higley, Konstantin Hirsch, Yurii I. Levashov, Agostino Marinelli, Tim Maxwell, Ankush Mitra, Stefan Moeller, Timur Osipov, Franz Peters, Marc Planas, Ivan Shevchuk, William F. Schlotter, Frank Scholz, Jörn Seltmann, Jens Viefhaus, Peter Walter, Zachary R. Wolf, Zhirong Huang, and Heinz-Dieter Nuhn. 2016. “Polarization Control in an X-Ray Free-Electron Laser.” *Nature Photonics* 10(7):468–72. doi: 10.1038/nphoton.2016.79.
- Ma, Yunjian, Xizhen Zhang, Wuyuan Zhang, Peilin Li, Yongru Li, Frank Hollmann, and Yonghua Wang. 2020. “Photoenzymatic Production of Next Generation Biofuels from Natural Triglycerides Combining a Hydrolase and a Photodecarboxylase.” *ChemPhotoChem* 4(1):39–44. doi: 10.1002/cptc.201900205.
- Madey, John M. J. 1971. “Stimulated Emission of Bremsstrahlung in a Periodic Magnetic Field.” *Journal of Applied Physics* 42(5):1906–13. doi: 10.1063/1.1660466.
- Margaritondo, G., and Primož Rebernik Ribic. 2011. “A Simplified Description of X-Ray Free-Electron Lasers.” *Journal of Synchrotron Radiation* 18(2):101–8. doi: 10.1107/S090904951004896X.

- Mariani, Valerio, Andrew Morgan, Chun Hong Yoon, Thomas J. Lane, Thomas A. White, Christopher O'Grady, Manuela Kuhn, Steve Aplin, Jason Koglin, Anton Barty, and Henry N. Chapman. 2016. "OnDA : Online Data Analysis and Feedback for Serial X-Ray Imaging." *Journal of Applied Crystallography* 49(3):1073–80. doi: 10.1107/S1600576716007469.
- Marman, Hugh, Connie Darmanin, and Brian Abbey. 2018. "The Influence of Photoelectron Escape in Radiation Damage Simulations of Protein Micro-Crystallography." *Crystals* 8(7):267. doi: 10.3390/cryst8070267.
- Martiel, Isabelle, Henrike M. Müller-Werkmeister, and Aina E. Cohen. 2019. "Strategies for Sample Delivery for Femtosecond Crystallography." *Acta Crystallographica Section D Structural Biology* 75(2):160–77. doi: 10.1107/S2059798318017953.
- Martin-Garcia, Jose M. 2021. "Protein Dynamics and Time Resolved Protein Crystallography at Synchrotron Radiation Sources: Past, Present and Future." *Crystals* 11(5):521. doi: 10.3390/cryst11050521.
- Martin-Garcia, Jose M., Chelsie E. Conrad, Garrett Nelson, Natasha Stander, Nadia A. Zatsepin, James Zook, Lan Zhu, James Geiger, Eugene Chun, David Kissick, Mark C. Hilgart, Craig Ogata, Andrii Ishchenko, Nirupa Nagaratnam, Shatabdi Roy-Chowdhury, Jesse Coe, Ganesh Subramanian, Alexander Schaffer, Daniel James, Gihan Ketwala, Nagarajan Venugopalan, Shenglan Xu, Stephen Corcoran, Dale Ferguson, Uwe Weierstall, John C. H. Spence, Vadim Cherezov, Petra Fromme, Robert F. Fischetti, and Wei Liu. 2017. "Serial Millisecond Crystallography of Membrane and Soluble Protein Microcrystals Using Synchrotron Radiation." *IUCrJ* 4(4):439–54. doi: 10.1107/S205225251700570X.
- Matthews, B. W. 1968. "Solvent Content of Protein Crystals." *Journal of Molecular Biology* 33(2):491–97. doi: 10.1016/0022-2836(68)90205-2.
- Maxwell, James Clerk. 1865. "VIII. A Dynamical Theory of the Electromagnetic Field." *Philosophical Transactions of the Royal Society of London* 155:459–512. doi: 10.1098/rstl.1865.0008.
- McCoy, Airlie J., Ralf W. Grosse-Kunstleve, Paul D. Adams, Martyn D. Winn, Laurent C. Storoni, and Randy J. Read. 2007. "Phaser Crystallographic Software." *Journal of Applied Crystallography* 40(4):658–74. doi: 10.1107/S0021889807021206.
- Meents, A., M. O. Wiedorn, V. Srajer, R. Henning, I. Sarrou, J. Bergtholdt, M. Barthelmess, P. Y. A. Reinke, D. Dierksmeyer, A. Tolstikova, S. Schaible, M. Messerschmidt, C. M. Ogata, D. J. Kissick, M. H. Taft, D. J. Manstein, J. Lieske, D. Oberthuer, R. F. Fischetti, and H. N. Chapman. 2017. "Pink-Beam Serial Crystallography." *Nature Communications* 8(1):1281. doi: 10.1038/s41467-017-01417-3.
- Mees, Alexandra, Tobias Klar, Petra Gnau, Ulrich Hennecke, Andre P. M. Eker, Thomas Carell, and Lars-Oliver Essen. 2004. "Crystal Structure of a Photolyase Bound to a CPD-Like DNA Lesion After in Situ Repair." *Science* 306(5702):1789–93. doi: 10.1126/science.1101598.
- Mehrabi, P., R. Bücker, G. Bourenkov, H. M. Ginn, D. von Stetten, H. M. Müller-Werkmeister, A. Kuo, T. Morizumi, B. T. Eger, W. L. Ou, S. Oghbaey, A. Sarracini, J. E. Besaw, O.

- Pare´-Labrosse, S. Meier, H. Schikora, F. Tellkamp, A. Marx, D. A. Sherrell, D. Axford, R. L. Owen, O. P. Ernst, E. F. Pai, E. C. Schulz, and R. J. D. Miller. 2021. “Serial Femtosecond and Serial Synchrotron Crystallography Can Yield Data of Equivalent Quality: A Systematic Comparison.” *Science Advances* 7(12):eabf1380. doi: 10.1126/sciadv.abf1380.
- Mehrabi, Pedram, Henrike M. Müller-Werkmeister, Jan-Philipp Leimkohl, Hendrik Schikora, Jelena Ninkovic, Silvia Krivokuca, Ladislav Andriček, Sascha W. Epp, Darren Sherrell, Robin L. Owen, Arwen R. Pearson, Friedjof Tellkamp, Eike C. Schulz, and R. J. Dwayne Miller. 2020. “The HARE Chip for Efficient Time-Resolved Serial Synchrotron Crystallography.” *Journal of Synchrotron Radiation* 27(2):360–70. doi: 10.1107/S1600577520000685.
- Mehrabi, Pedram, Eike C. Schulz, Michael Agthe, Sam Horrell, Gleb Bourenkov, David von Stetten, Jan-Philipp Leimkohl, Hendrik Schikora, Thomas R. Schneider, Arwen R. Pearson, Friedjof Tellkamp, and R. J. Dwayne Miller. 2019. “Liquid Application Method for Time-Resolved Analyses by Serial Synchrotron Crystallography.” *Nature Methods* 16(10):979–82. doi: 10.1038/s41592-019-0553-1.
- Mehrabi, Pedram, Eike C. Schulz, Raison Dsouza, Henrike M. Müller-Werkmeister, Friedjof Tellkamp, R. J. Dwayne Miller, and Emil F. Pai. 2019. “Time-Resolved Crystallography Reveals Allosteric Communication Aligned with Molecular Breathing.” *Science* 365(6458):1167–70. doi: 10.1126/science.aaw9904.
- Mei, Qiming, and Volodymyr Dvornyk. 2015. “Evolutionary History of the Photolyase/Cryptochrome Superfamily in Eukaryotes” edited by N. S. Foulkes. *PLOS ONE* 10(9):e0135940. doi: 10.1371/journal.pone.0135940.
- Milne, Christopher, Thomas Schietinger, Masamitsu Aiba, Arturo Alarcon, Jürgen Alex, Alexander Anghel, Vladimir Arsov, Carl Beard, Paul Beaud, Simona Bettoni, Markus Bopp, Helge Brands, Manuel Brönnimann, Ingo Brunnenkant, Marco Calvi, Alessandro Citterio, Paolo Craievich, Marta Csatari Divall, Mark Dällenbach, Michael D’Amico, Andreas Dax, Yunpei Deng, Alexander Dietrich, Roberto Dinapoli, Edwin Divall, Sladana Dordevic, Simon Ebner, Christian Erny, Hansrudolf Fitze, Uwe Flechsig, Rolf Follath, Franziska Frei, Florian Gärtner, Romain Ganter, Terence Garvey, Zheqiao Geng, Ishkhan Gorgisyan, Christopher Gough, Andreas Hauff, Christoph Hauri, Nicole Hiller, Tadej Humar, Stephan Hunziker, Gerhard Ingold, Rasmus Ischebeck, Markus Janousch, Pavle Juranić, Mario Jurcevic, Maik Kaiser, Babak Kalantari, Roger Kalt, Boris Keil, Christoph Kittel, Gregor Knopp, Waldemar Koprek, Henrik Lemke, Thomas Lippuner, Daniel Llorente Sancho, Florian Löhl, Carlos Lopez-Cuenca, Fabian Märki, Fabio Marcellini, Goran Marinkovic, Isabelle Martiel, Ralf Menzel, Aldo Mozzanica, Karol Nass, Gian Orlandi, Cigdem Ozkan Loch, Ezequiel Panepucci, Martin Paraliiev, Bruce Patterson, Bill Pedrini, Marco Pedrozzi, Patrick Pollet, Claude Pradervand, Eduard Prat, Peter Radi, Jean-Yves Raguin, Sophie Redford, Jens Rehanek, Julien Réhault, Sven Reiche, Matthias Ringele, Jochen Rittmann, Leonid Rivkin, Albert Romann, Marie Ruat, Christian Ruder, Leonardo Sala, Lionel Schebacher, Thomas Schilcher, Volker Schlott, Thomas Schmidt, Bernd Schmitt, Xintian Shi, Markus Stadler, Lukas Stingelin, Werner Sturzenegger, Jakub Szlachetko, Dhanya Thattil, Daniel Treyer, Alexandre Trisorio, Wolfgang Tron, Seraphin Vetter, Carlo Vicario, Didier Voulot, Meitian Wang, Thierry Zamofing, Christof Zellweger, Riccardo Zennaro, Elke Zimoch, Rafael Abela, Luc Patthey, and Hans-Heinrich Braun. 2017.

- “SwissFEL: The Swiss X-Ray Free Electron Laser.” *Applied Sciences* 7(7):720. doi: 10.3390/app7070720.
- Mizuno, Hideaki, Tapas Kumar Mal, Kit I. Tong, Ryoko Ando, Toshiaki Furuta, Mitsuhiro Ikura, and Atsushi Miyawaki. 2003. “Photo-Induced Peptide Cleavage in the Green-to-Red Conversion of a Fluorescent Protein.” *Molecular Cell* 12(4):1051–58. doi: 10.1016/S1097-2765(03)00393-9.
- Moffat, Keith. 2001. “Time-Resolved Biochemical Crystallography: A Mechanistic Perspective.” *Chemical Reviews* 101(6):1569–82. doi: 10.1021/cr990039q.
- Moffat, Keith. 2019. “Laue Diffraction and Time-Resolved Crystallography: A Personal History.” *Philosophical Transactions of the Royal Society A: Mathematical, Physical and Engineering Sciences* 377(2147):20180243. doi: 10.1098/rsta.2018.0243.
- Monteiro, Diana C. F., Emmanuel Amoah, Cromarte Rogers, and Arwen R. Pearson. 2021. “Using Photocaging for Fast Time-Resolved Structural Biology Studies.” *Acta Crystallographica Section D Structural Biology* 77(10):1218–32. doi: 10.1107/S2059798321008809.
- Monteiro, Diana C. F., David von Stetten, Claudia Stohrer, Marta Sans, Arwen R. Pearson, Gianluca Santoni, Peter van der Linden, and Martin Trebbin. 2020. “3D-MiXD: 3D-Printed X-Ray-Compatible Microfluidic Devices for Rapid, Low-Consumption Serial Synchrotron Crystallography Data Collection in Flow.” *IUCrJ* 7(2):207–19. doi: 10.1107/S2052252519016865.
- de la Mora, Eugenio, Nicolas Coquelle, Charles S. Bury, Martin Rosenthal, James M. Holton, Ian Carmichael, Elspeth F. Garman, Manfred Burghammer, Jacques-Philippe Colletier, and Martin Weik. 2020. “Radiation Damage and Dose Limits in Serial Synchrotron Crystallography at Cryo- and Room Temperatures.” *Proceedings of the National Academy of Sciences* 117(8):4142–51. doi: 10.1073/pnas.1821522117.
- Moseley, H. G. J. 1914. “LXXX. *The High-Frequency Spectra of the Elements. Part II.*” *The London, Edinburgh, and Dublin Philosophical Magazine and Journal of Science* 27(160):703–13. doi: 10.1080/14786440408635141.
- Motz, H. 1951. “Applications of the Radiation from Fast Electron Beams.” *Journal of Applied Physics* 22(5):527–35. doi: 10.1063/1.1700002.
- Motz, H., W. Thon, and R. N. Whitehurst. 1953. “Experiments on Radiation by Fast Electron Beams.” *Journal of Applied Physics* 24(7):826–33. doi: 10.1063/1.1721389.
- Mous, Sandra, Guillaume Gotthard, David Ehrenberg, Saumik Sen, Tobias Weinert, Philip J. M. Johnson, Daniel James, Karol Nass, Antonia Furrer, Demet Kekilli, Pikyee Ma, Steffen Brünle, Cecilia Maria Casadei, Isabelle Martiel, Florian Dworkowski, Dardan Gashi, Petr Skopintsev, Maximilian Wranik, Gregor Knopp, Ezequiel Panepucci, Valerie Panneels, Claudio Cirelli, Dmitry Ozerov, Gebhard F. X. Schertler, Meitian Wang, Chris Milne, Joerg Standfuss, Igor Schapiro, Joachim Heberle, and Przemyslaw Nogly. 2022. “Dynamics and Mechanism of a Light-Driven Chloride Pump.” *Science* 375(6583):845–51. doi: 10.1126/science.abj6663.

- Mozzanica, A., M. Andrä, R. Barten, A. Bergamaschi, S. Chiriotti, M. Brückner, R. Dinapoli, E. Fröjdh, D. Greiffenberg, F. Leonarski, C. Lopez-Cuenca, D. Mezza, S. Redford, C. Ruder, B. Schmitt, X. Shi, D. Thattil, G. Tinti, S. Vetter, and J. Zhang. 2018. “The JUNGFRÄU Detector for Applications at Synchrotron Light Sources and XFELs.” *Synchrotron Radiation News* 31(6):16–20. doi: 10.1080/08940886.2018.1528429.
- Mozzarelli, A., and G. L. Rossi. 1996. “Protein Function in the Crystal.” *Annual Review of Biophysics and Biomolecular Structure* 25(1):343–65. doi: 10.1146/annurev.bb.25.060196.002015.
- Mugo, Andrew Njagi, Jun Kobayashi, Taiji Yamasaki, Bunzo Mikami, Kouhei Ohnishi, Yu Yoshikane, and Toshiharu Yagi. 2013. “Crystal Structure of Pyridoxine 4-Oxidase from *Mesorhizobium Loti*.” *Biochimica et Biophysica Acta (BBA) - Proteins and Proteomics* 1834(6):953–63. doi: 10.1016/j.bbapap.2013.03.004.
- Murphy, J.B., and C. Pellegrini. 1985. “Free Electron Lasers for the XUV Spectral Region.” *Nuclear Instruments and Methods in Physics Research Section A: Accelerators, Spectrometers, Detectors and Associated Equipment* 237(1–2):159–67. doi: 10.1016/0168-9002(85)90344-4.
- Murphy, J. B., and C. Pellegrini. 1985. “Generation of High-Intensity Coherent Radiation in the Soft-x-Ray and Vacuum-Ultraviolet Region.” *Journal of the Optical Society of America B* 2(1):259. doi: 10.1364/JOSAB.2.000259.
- Murray, Thomas D., Artem Y. Lyubimov, Craig M. Ogata, Huy Vo, Monarin Uervirojnangkoorn, Axel T. Brunger, and James M. Berger. 2015. “A High-Transparency, Micro-Patternable Chip for X-Ray Diffraction Analysis of Microcrystals under Native Growth Conditions.” *Acta Crystallographica. Section D, Biological Crystallography* 71(Pt 10):1987–97. doi: 10.1107/S1399004715015011.
- Murshudov, Garib N., Pavol Skubák, Andrey A. Lebedev, Navraj S. Pannu, Roberto A. Steiner, Robert A. Nicholls, Martyn D. Winn, Fei Long, and Alexei A. Vagin. 2011. “REFMAC 5 for the Refinement of Macromolecular Crystal Structures.” *Acta Crystallographica Section D Biological Crystallography* 67(4):355–67. doi: 10.1107/S0907444911001314.
- Naitow, Hisashi, Yoshinori Matsuura, Kensuke Tono, Yasumasa Joti, Takashi Kameshima, Takaki Hatsui, Makina Yabashi, Rie Tanaka, Tomoyuki Tanaka, Michihiro Sugahara, Jun Kobayashi, Eriko Nango, So Iwata, and Naoki Kunishima. 2017. “Protein–Ligand Complex Structure from Serial Femtosecond Crystallography Using Soaked Thermolysin Microcrystals and Comparison with Structures from Synchrotron Radiation.” *Acta Crystallographica Section D Structural Biology* 73(8):702–9. doi: 10.1107/S2059798317008919.
- Nakane, Takanori, Shinya Hanashima, Mamoru Suzuki, Haruka Saiki, Taichi Hayashi, Keisuke Kakinouchi, Shigeru Sugiyama, Satoshi Kawatake, Shigeru Matsuoka, Nobuaki Matsumori, Eriko Nango, Jun Kobayashi, Tatsuro Shimamura, Kanako Kimura, Chihiro Mori, Naoki Kunishima, Michihiro Sugahara, Yoko Takakyu, Shigeyuki Inoue, Tetsuya Masuda, Toshiaki Hosaka, Kensuke Tono, Yasumasa Joti, Takashi Kameshima, Takaki Hatsui, Makina Yabashi, Tsuyoshi Inoue, Osamu Nureki, So Iwata, Michio Murata, and Eiichi Mizohata. 2016. “Membrane Protein Structure Determination by SAD, SIR, or

- SIRAS Phasing in Serial Femtosecond Crystallography Using an Iododetergent.” *Proceedings of the National Academy of Sciences* 113(46):13039–44. doi: 10.1073/pnas.1602531113.
- Nakane, Takanori, Abhay Kotecha, Andrija Sente, Greg McMullan, Simonas Masiulis, Patricia M. G. E. Brown, Ioana T. Grigoras, Lina Malinauskaite, Tomas Malinauskas, Jonas Miehling, Tomasz Uchański, Lingbo Yu, Dimple Karia, Evgeniya V. Pechnikova, Erwin de Jong, Jeroen Keizer, Maarten Bischoff, Jamie McCormack, Peter Tiemeijer, Steven W. Hardwick, Dimitri Y. Chirgadze, Garib Murshudov, A. Radu Aricescu, and Sjors H. W. Scheres. 2020. “Single-Particle Cryo-EM at Atomic Resolution.” *Nature* 587(7832):152–56. doi: 10.1038/s41586-020-2829-0.
- Nakane, Takanori, Changyong Song, Mamoru Suzuki, Eriko Nango, Jun Kobayashi, Tetsuya Masuda, Shigeyuki Inoue, Eiichi Mizohata, Toru Nakatsu, Tomoyuki Tanaka, Rie Tanaka, Tatsuro Shimamura, Kensuke Tono, Yasumasa Joti, Takashi Kameshima, Takaki Hatsui, Makina Yabashi, Osamu Nureki, So Iwata, and Michihiro Sugahara. 2015. “Native Sulfur/Chlorine SAD Phasing for Serial Femtosecond Crystallography.” *Acta Crystallographica Section D Biological Crystallography* 71(12):2519–25. doi: 10.1107/S139900471501857X.
- Nam, Ki Hyun. 2020a. “Approach of Serial Crystallography.” *Crystals* 10(10):854. doi: 10.3390/cryst10100854.
- Nam, Ki Hyun. 2020b. “Lard Injection Matrix for Serial Crystallography.” *International Journal of Molecular Sciences* 21(17):5977. doi: 10.3390/ijms21175977.
- Nam, Ki Hyun. 2022. “Beef Tallow Injection Matrix for Serial Crystallography.” *Scientific Reports* 12(1):694. doi: 10.1038/s41598-021-04714-6.
- Nango, Eriko, Antoine Royant, Minoru Kubo, Takanori Nakane, Cecilia Wickstrand, Tetsunari Kimura, Tomoyuki Tanaka, Kensuke Tono, Changyong Song, Rie Tanaka, Toshi Arima, Ayumi Yamashita, Jun Kobayashi, Toshiaki Hosaka, Eiichi Mizohata, Przemyslaw Nogly, Michihiro Sugahara, Daewoong Nam, Takashi Nomura, Tatsuro Shimamura, Dohyun Im, Takaaki Fujiwara, Yasuaki Yamanaka, Byeonghyun Jeon, Tomohiro Nishizawa, Kazumasa Oda, Masahiro Fukuda, Rebecka Andersson, Petra Båth, Robert Dods, Jan Davidsson, Shigeru Matsuoka, Satoshi Kawatake, Michio Murata, Osamu Nureki, Shigeki Owada, Takashi Kameshima, Takaki Hatsui, Yasumasa Joti, Gebhard Schertler, Makina Yabashi, Ana-Nicoleta Bondar, Jörg Standfuss, Richard Neutze, and So Iwata. 2016. “A Three-Dimensional Movie of Structural Changes in Bacteriorhodopsin.” *Science* 354(6319):1552–57. doi: 10.1126/science.aah3497.
- Nass, Karol. 2019. “Radiation Damage in Protein Crystallography at X-Ray Free-Electron Lasers.” *Acta Crystallographica Section D Structural Biology* 75(2):211–18. doi: 10.1107/S2059798319000317.
- Nass, Karol, Lutz Foucar, Thomas R. M. Barends, Elisabeth Hartmann, Sabine Botha, Robert L. Shoeman, R. Bruce Doak, Roberto Alonso-Mori, Andrew Aquila, Saša Bajt, Anton Barty, Richard Bean, Kenneth R. Beyerlein, Maïke Bublitz, Nikolaj Drachmann, Jonas Gregersen, H. Olof Jönsson, Wolfgang Kabsch, Stephan Kassemeyer, Jason E. Koglin, Michael Krumrey, Daniel Mattle, Marc Messerschmidt, Poul Nissen, Linda Reinhard,

- Oleg Sitsel, Dimosthenis Sokaras, Garth J. Williams, Stefan Hau-Riege, Nicusor Timneanu, Carl Caleman, Henry N. Chapman, Sébastien Boutet, and Ilme Schlichting. 2015. “Indications of Radiation Damage in Ferredoxin Microcrystals Using High-Intensity X-FEL Beams.” *Journal of Synchrotron Radiation* 22(2):225–38. doi: 10.1107/S1600577515002349.
- Nass, Karol, Alexander Gorel, Malik M. Abdullah, Andrew V. Martin, Marco Kloos, Agostino Marinelli, Andrew Aquila, Thomas R. M. Barends, Franz-Josef Decker, R. Bruce Doak, Lutz Foucar, Elisabeth Hartmann, Mario Hilpert, Mark S. Hunter, Zoltan Jurek, Jason E. Koglin, Alexander Kozlov, Alberto A. Lutman, Gabriela Nass Kovacs, Christopher M. Roome, Robert L. Shoeman, Robin Santra, Harry M. Quiney, Beata Ziaja, Sébastien Boutet, and Ilme Schlichting. 2020. “Structural Dynamics in Proteins Induced by and Probed with X-Ray Free-Electron Laser Pulses.” *Nature Communications* 11(1):1814. doi: 10.1038/s41467-020-15610-4.
- Nass, Karol, Anton Meinhart, Thomas R. M. Barends, Lutz Foucar, Alexander Gorel, Andrew Aquila, Sabine Botha, R. Bruce Doak, Jason Koglin, Mengning Liang, Robert L. Shoeman, Garth Williams, Sebastien Boutet, and Ilme Schlichting. 2016. “Protein Structure Determination by Single-Wavelength Anomalous Diffraction Phasing of X-Ray Free-Electron Laser Data.” *IUCrJ* 3(3):180–91. doi: 10.1107/S2052252516002980.
- Nass Kovacs, Gabriela, Jacques-Philippe Colletier, Marie Luise Grünbein, Yang Yang, Till Stensitzki, Alexander Batyuk, Sergio Carbajo, R. Bruce Doak, David Ehrenberg, Lutz Foucar, Raphael Gasper, Alexander Gorel, Mario Hilpert, Marco Kloos, Jason E. Koglin, Jochen Reinstein, Christopher M. Roome, Ramona Schlesinger, Matthew Seaberg, Robert L. Shoeman, Miriam Stricker, Sébastien Boutet, Stefan Haacke, Joachim Heberle, Karsten Heyne, Tatiana Domratcheva, Thomas R. M. Barends, and Ilme Schlichting. 2019. “Three-Dimensional View of Ultrafast Dynamics in Photoexcited Bacteriorhodopsin.” *Nature Communications* 10(1):3177. doi: 10.1038/s41467-019-10758-0.
- Navaza, J. 1994. “AMoRe: An Automated Package for Molecular Replacement.” *Acta Crystallographica Section A Foundations of Crystallography* 50(2):157–63. doi: 10.1107/S0108767393007597.
- Nave, Colin, and Mark A. Hill. 2005. “Will Reduced Radiation Damage Occur with Very Small Crystals?” *Journal of Synchrotron Radiation* 12(3):299–303. doi: 10.1107/S0909049505003274.
- Neutze, Richard, Remco Wouts, David van der Spoel, Edgar Weckert, and Janos Hajdu. 2000. “Potential for Biomolecular Imaging with Femtosecond X-Ray Pulses.” *Nature* 406(6797):752–57. doi: 10.1038/35021099.
- Nguyen Bich, Ngan, Benjamien Moeyaert, Kristof Van Hecke, Peter Dedecker, Hideaki Mizuno, Johan Hofkens, and Luc Van Meervelt. 2012. “Structural Basis for the Influence of a Single Mutation K145N on the Oligomerization and Photoswitching Rate of Dronpa.” *Acta Crystallographica Section D Biological Crystallography* 68(12):1653–59. doi: 10.1107/S0907444912039686.

- Nogly, Przemyslaw, Daniel James, Dingjie Wang, Thomas A. White, Nadia Zatsepin, Anastasya Shilova, Garrett Nelson, Haiguang Liu, Linda Johansson, Michael Heymann, Kathrin Jaeger, Markus Metz, Cecilia Wickstrand, Wenting Wu, Petra Båth, Peter Berntsen, Dominik Oberthuer, Valerie Panneels, Vadim Cherezov, Henry Chapman, Gebhard Schertler, Richard Neutze, John Spence, Isabel Moraes, Manfred Burghammer, Joerg Standfuss, and Uwe Weierstall. 2015. “Lipidic Cubic Phase Serial Millisecond Crystallography Using Synchrotron Radiation.” *IUCrJ* 2(2):168–76. doi: 10.1107/S2052252514026487.
- Nogly, Przemyslaw, Tobias Weinert, Daniel James, Sergio Carbajo, Dmitry Ozerov, Antonia Furrer, Dardan Gashi, Veniamin Borin, Petr Skopintsev, Kathrin Jaeger, Karol Nass, Petra Båth, Robert Bosman, Jason Koglin, Matthew Seaberg, Thomas Lane, Demet Kekilli, Steffen Brünle, Tomoyuki Tanaka, Wenting Wu, Christopher Milne, Thomas White, Anton Barty, Uwe Weierstall, Valerie Panneels, Eriko Nango, So Iwata, Mark Hunter, Igor Schapiro, Gebhard Schertler, Richard Neutze, and Jörg Standfuss. 2018. “Retinal Isomerization in Bacteriorhodopsin Captured by a Femtosecond X-Ray Laser.” *Science (New York, N.Y.)* 361(6398). doi: 10.1126/science.aat0094.
- Nomura, Takashi, Tetsunari Kimura, Yusuke Kanematsu, Daichi Yamada, Keitaro Yamashita, Kunio Hirata, Go Ueno, Hironori Murakami, Tamao Hisano, Raika Yamagiwa, Hanae Takeda, Chai Gopalasingam, Ryota Kousaka, Sachiko Yanagisawa, Osami Shoji, Takashi Kumasaka, Masaki Yamamoto, Yu Takano, Hiroshi Sugimoto, Takehiko Tosha, Minoru Kubo, and Yoshitsugu Shiro. 2021. “Short-Lived Intermediate in N₂O Generation by P450 NO Reductase Captured by Time-Resolved IR Spectroscopy and XFEL Crystallography.” *Proceedings of the National Academy of Sciences* 118(21):e2101481118. doi: 10.1073/pnas.2101481118.
- Oberthür, Dominik. 2018. “Biological Single-Particle Imaging Using XFELs – towards the next Resolution Revolution.” *IUCrJ* 5(6):663–66. doi: 10.1107/S2052252518015129.
- Oda, Kazumasa, Takashi Nomura, Takanori Nakane, Keitaro Yamashita, Keiichi Inoue, Shota Ito, Johannes Vierock, Kunio Hirata, Andrés D. Maturana, Kota Katayama, Tatsuya Ikuta, Itsuki Ishigami, Tamaki Izume, Rie Umeda, Ryuun Eguma, Satomi Oishi, Go Kasuya, Takafumi Kato, Tsukasa Kusakizako, Wataru Shihoya, Hiroto Shimada, Tomoyuki Takatsuji, Mizuki Takemoto, Reiya Taniguchi, Atsushi Tomita, Ryoki Nakamura, Masahiro Fukuda, Hirotake Miyauchi, Yongchan Lee, Eriko Nango, Rie Tanaka, Tomoyuki Tanaka, Michihiro Sugahara, Tetsunari Kimura, Tatsuro Shimamura, Takaaki Fujiwara, Yasuaki Yamanaka, Shigeki Owada, Yasumasa Joti, Kensuke Tono, Ryuichiro Ishitani, Shigehiko Hayashi, Hideki Kandori, Peter Hegemann, So Iwata, Minoru Kubo, Tomohiro Nishizawa, and Osamu Nureki. 2021. “Time-Resolved Serial Femtosecond Crystallography Reveals Early Structural Changes in Channelrhodopsin.” *ELife* 10:e62389. doi: 10.7554/eLife.62389.
- Oghbaey, Saeed, Antoine Sarracini, Helen M. Ginn, Olivier Pare-Labrosse, Anling Kuo, Alexander Marx, Sascha W. Epp, Darren A. Sherrell, Bryan T. Eger, Yinpeng Zhong, Rolf Loch, Valerio Mariani, Roberto Alonso-Mori, Silke Nelson, Henrik T. Lemke, Robin L. Owen, Arwen R. Pearson, David I. Stuart, Oliver P. Ernst, Henrike M. Mueller-Werkmeister, and R. J. Dwayne Miller. 2016. “Fixed Target Combined with Spectral Mapping: Approaching 100% Hit Rates for Serial Crystallography.” *Acta Crystallographica. Section D, Structural Biology* 72(Pt 8):944–955. doi: 10.1107/s2059798316010834.

- Olmos, Jose L., Suraj Pandey, Jose M. Martin-Garcia, George Calvey, Andrea Katz, Juraj Knoska, Christopher Kupitz, Mark S. Hunter, Mengning Liang, Dominik Oberthuer, Oleksandr Yefanov, Max Wiedorn, Michael Heyman, Mark Holl, Kanupriya Pande, Anton Barty, Mitchell D. Miller, Stephan Stern, Shatabdi Roy-Chowdhury, Jesse Coe, Nirupa Nagaratnam, James Zook, Jacob Verburgt, Tyler Norwood, Ishwor Poudyal, David Xu, Jason Koglin, Matthew H. Seaberg, Yun Zhao, Saša Bajt, Thomas Grant, Valerio Mariani, Garrett Nelson, Ganesh Subramanian, Euiyoung Bae, Raimund Fromme, Russell Fung, Peter Schwander, Matthias Frank, Thomas A. White, Uwe Weierstall, Nadia Zatsepin, John Spence, Petra Fromme, Henry N. Chapman, Lois Pollack, Lee Tremblay, Abbas Ourmazd, George N. Phillips, and Marius Schmidt. 2018. “Enzyme Intermediates Captured ‘on the Fly’ by Mix-and-Inject Serial Crystallography.” *BMC Biology* 16(1):59. doi: 10.1186/s12915-018-0524-5.
- O’Neill, Peter, David L. Stevens, and Elspeth F. Garman. 2002. “Physical and Chemical Considerations of Damage Induced in Protein Crystals by Synchrotron Radiation: A Radiation Chemical Perspective.” *Journal of Synchrotron Radiation* 9(6):329–32. doi: 10.1107/S0909049502014553.
- Ormö, Mats, Andrew B. Cubitt, Karen Kallio, Larry A. Gross, Roger Y. Tsien, and S. James Remington. 1996. “Crystal Structure of the *Aequorea Victoria* Green Fluorescent Protein.” *Science* 273(5280):1392–95. doi: 10.1126/science.273.5280.1392.
- Owen, R. L., E. Rudino-Pinera, and E. F. Garman. 2006. “Experimental Determination of the Radiation Dose Limit for Cryocooled Protein Crystals.” *Proceedings of the National Academy of Sciences* 103(13):4912–17. doi: 10.1073/pnas.0600973103.
- Owen, Robin L., Danny Axford, Darren A. Sherrell, Anling Kuo, Oliver P. Ernst, Eike C. Schulz, R. J. Dwayne Miller, and Henrike M. Mueller-Werkmeister. 2017. “Low-Dose Fixed-Target Serial Synchrotron Crystallography.” *Acta Crystallographica Section D Structural Biology* 73(4):373–78. doi: 10.1107/S2059798317002996.
- Pande, K., C. D. M. Hutchison, G. Groenhof, A. Aquila, J. S. Robinson, J. Tenboer, S. Basu, S. Boutet, D. P. DePonte, M. Liang, T. A. White, N. A. Zatsepin, O. Yefanov, D. Morozov, D. Oberthuer, C. Gati, G. Subramanian, D. James, Y. Zhao, J. Koralek, J. Brayshaw, C. Kupitz, C. Conrad, S. Roy-Chowdhury, J. D. Coe, M. Metz, P. L. Xavier, T. D. Grant, J. E. Koglin, G. Ketawala, R. Fromme, V. rاجر, R. Henning, J. C. H. Spence, A. Ourmazd, P. Schwander, U. Weierstall, M. Frank, P. Fromme, A. Barty, H. N. Chapman, K. Moffat, J. J. van Thor, and M. Schmidt. 2016. “Femtosecond Structural Dynamics Drives the Trans/Cis Isomerization in Photoactive Yellow Protein.” *Science* 352(6286):725–29. doi: 10.1126/science.aad5081.
- Pandey, Suraj, Richard Bean, Tokushi Sato, Ishwor Poudyal, Johan Bielecki, Jorvani Cruz Villarreal, Oleksandr Yefanov, Valerio Mariani, Thomas A. White, Christopher Kupitz, Mark Hunter, Mohamed H. Abdellatif, Saša Bajt, Valerii Bondar, Austin Echelmeier, Diandra Doppler, Moritz Emons, Matthias Frank, Raimund Fromme, Yaroslav Gevorkov, Gabriele Giovanetti, Man Jiang, Daihyun Kim, Yoonhee Kim, Henry Kirkwood, Anna Klimovskaia, Juraj Knoska, Faisal H. M. Koua, Romain Letrun, Stella Lisova, Luis Maia, Victoria Mazalova, Domingo Meza, Thomas Michelat, Abbas Ourmazd, Guido Palmer, Marco Ramilli, Robin Schubert, Peter Schwander, Alessandro Silenzi, Jolanta Sztuk-Dambietz, Alexandra Tolstikova, Henry N. Chapman, Alexandra Ros, Anton Barty, Petra Fromme, Adrian P. Mancuso, and Marius Schmidt. 2020.

- “Time-Resolved Serial Femtosecond Crystallography at the European XFEL.” *Nature Methods* 17(1):73–78. doi: 10.1038/s41592-019-0628-z.
- Park, Jaehyun, Sehan Park, Jangwoo Kim, Gisu Park, Yunje Cho, and Ki Hyun Nam. 2019. “Polyacrylamide Injection Matrix for Serial Femtosecond Crystallography.” *Scientific Reports* 9(1):2525. doi: 10.1038/s41598-019-39020-9.
- Patterson, George H., and Jennifer Lippincott-Schwartz. 2002. “A Photoactivatable GFP for Selective Photolabeling of Proteins and Cells.” *Science* 297(5588):1873–77. doi: 10.1126/science.1074952.
- Pearson, Arwen R., and Pedram Mehrabi. 2020. “Serial Synchrotron Crystallography for Time-Resolved Structural Biology.” *Current Opinion in Structural Biology* 65:168–74. doi: 10.1016/j.sbi.2020.06.019.
- Poddar, Harshwardhan, Derren J. Heyes, Giorgio Schirò, Martin Weik, David Leys, and Nigel S. Scrutton. 2021. “A Guide to Time-resolved Structural Analysis of Light-activated Proteins.” *The FEBS Journal* febs.15880. doi: 10.1111/febs.15880.
- Poulos, Thomas L., S. T. Freer, Richard A. Alden, Steven L. Edwards, U. Skogland, Koji Takio, Birgitta Eriksson, Nguyen-huu Xuong, Takashi Yonetani, and Joseph Kraut. 1980. “The Crystal Structure of Cytochrome c Peroxidase.” *The Journal of Biological Chemistry* 255 2:575–80.
- Powell, Harold R. 1999. “The Rossmann Fourier Autoindexing Algorithm in *MOSFLM*.” *Acta Crystallographica Section D Biological Crystallography* 55(10):1690–95. doi: 10.1107/S09074444999009506.
- Prah, Alja, Eric Frančišković, Janez Mavri, and Jernej Stare. 2019. “Electrostatics as the Driving Force Behind the Catalytic Function of the Monoamine Oxidase A Enzyme Confirmed by Quantum Computations.” *ACS Catalysis* 9(2):1231–40. doi: 10.1021/acscatal.8b04045.
- Raimondi, Pantaleo. 2017. “Hybrid Multi Bend Achromat: From SuperB to EBS.” *Proceedings of the 8th Int. Particle Accelerator Conf.* IPAC2017:6 pages, 3.578 MB. doi: 10.18429/JACOW-IPAC2017-THPPA3.
- Ramakrishnan, Saminathan, Jason R. Stagno, Chelsie E. Conrad, Jienyu Ding, Ping Yu, Yuba R. Bhandari, Yun-Tzai Lee, Gary Pauly, Oleksandr Yefanov, Max O. Wiedorn, Juraj Knoska, Dominik Oberthür, Thomas A. White, Anton Barty, Valerio Mariani, Chufeng Li, Wolfgang Brehm, William F. Heinz, Valentin Magidson, Stephen Lockett, Mark S. Hunter, Sébastien Boutet, Nadia A. Zatsepin, Xiaobing Zuo, Thomas D. Grant, Suraj Pandey, Marius Schmidt, John C. H. Spence, Henry N. Chapman, and Yun-Xing Wang. 2021. “Synchronous RNA Conformational Changes Trigger Ordered Phase Transitions in Crystals.” *Nature Communications* 12(1):1762. doi: 10.1038/s41467-021-21838-5.
- Read, J. A., V. J. Winter, C. M. Eszes, R. B. Sessions, and R. L. Brady. 2001. “Structural Basis for Altered Activity of M- and H-isozyme Forms of Human Lactate Dehydrogenase.” *Proteins: Structure, Function, and Bioinformatics* 43(2):175–85. doi: 10.1002/1097-0134(20010501)43:2<175::AID-PROT1029>3.0.CO;2-#.

- Redecke, L., K. Nass, D. P. DePonte, T. A. White, D. Rehders, A. Barty, F. Stellato, M. Liang, T. R. M. Barends, S. Boutet, G. J. Williams, M. Messerschmidt, M. M. Seibert, A. Aquila, D. Arnlund, S. Bajt, T. Barth, M. J. Bogan, C. Caleman, T. C. Chao, R. B. Doak, H. Fleckenstein, M. Frank, R. Fromme, L. Galli, I. Grotjohann, M. S. Hunter, L. C. Johansson, S. Kassemeyer, G. Katona, R. A. Kirian, R. Koopmann, C. Kupitz, L. Lomb, A. V. Martin, S. Mogk, R. Neutze, R. L. Shoeman, J. Steinbrener, N. Timneanu, D. Wang, U. Weierstall, N. A. Zatsepin, J. C. H. Spence, P. Fromme, I. Schlichting, M. Duszynko, C. Betzel, and H. N. Chapman. 2013. “Natively Inhibited Trypanosoma Brucei Cathepsin B Structure Determined by Using an X-Ray Laser.” *Science* 339(6116):227–30. doi: 10.1126/science.1229663.
- Ren, Zhong, Medine Ayhan, Sepalika Bandara, Kalinga Bowatte, Indika Kumarapperuma, Semini Gunawardana, Heewhan Shin, Cong Wang, Xiaoli Zeng, and Xiaojing Yang. 2018. “Crystal-on-Crystal Chips for *in Situ* Serial Diffraction at Room Temperature.” *Lab on a Chip* 18(15):2246–56. doi: 10.1039/C8LC00489G.
- Ren, Zhong, Cong Wang, Heewhan Shin, Sepalika Bandara, Indika Kumarapperuma, Michael Y. Ren, Weijia Kang, and Xiaojing Yang. 2020. “An Automated Platform for *in Situ* Serial Crystallography at Room Temperature.” *IUCrJ* 7(6). doi: 10.1107/S2052252520011288.
- Roedig, P., I. Vartiainen, R. Duman, S. Panneerselvam, N. Stübe, O. Lorbeer, M. Warmer, G. Sutton, D. I. Stuart, E. Weckert, C. David, A. Wagner, and A. Meents. 2015. “A Micro-Patterned Silicon Chip as Sample Holder for Macromolecular Crystallography Experiments with Minimal Background Scattering.” *Scientific Reports* 5(1):10451. doi: 10.1038/srep10451.
- Roedig, Philip, Ramona Duman, Juan Sanchez-Weatherby, Ismo Vartiainen, Anja Burkhardt, Martin Warmer, Christian David, Armin Wagner, and Alke Meents. 2016. “Room-Temperature Macromolecular Crystallography Using a Micro-Patterned Silicon Chip with Minimal Background Scattering.” *Journal of Applied Crystallography* 49(3):968–75. doi: 10.1107/S1600576716006348.
- Roessler, Christian G., Rakhi Agarwal, Marc Allaire, Roberto Alonso-Mori, Babak Andi, José F. R. Bachega, Martin Bommer, Aaron S. Brewster, Michael C. Browne, Ruchira Chatterjee, Eunsun Cho, Aina E. Cohen, Matthew Cowan, Sammy Datwani, Victor L. Davidson, Jim Defever, Brent Eaton, Richard Ellson, Yiping Feng, Lucien P. Ghislain, James M. Glownia, Guangye Han, Johan Hattne, Julia Hellmich, Annie Héroux, Mohamed Ibrahim, Jan Kern, Anthony Kuczewski, Henrik T. Lemke, Pinghua Liu, Lars Majlof, William M. McClintock, Stuart Myers, Silke Nelsen, Joe Olechno, Allen M. Orville, Nicholas K. Sauter, Alexei S. Soares, S. Michael Soltis, Heng Song, Richard G. Stearns, Rosalie Tran, Yingssu Tsai, Monarin Uervirojnangkoorn, Carrie M. Wilmot, Vittal Yachandra, Junko Yano, Erik T. Yukl, Diling Zhu, and Athina Zouni. 2016. “Acoustic Injectors for Drop-On-Demand Serial Femtosecond Crystallography.” *Structure* 24(4):631–40. doi: 10.1016/j.str.2016.02.007.
- Røhr, Åsmund Kjendseth, Hans-Petter Hersleth, and K. Kristoffer Andersson. 2010. “Tracking Flavin Conformations in Protein Crystal Structures with Raman Spectroscopy and QM/MM Calculations.” *Angewandte Chemie International Edition* 49(13):2324–27. doi: 10.1002/anie.200907143.

- Röntgen, W. C. 1898. “Ueber eine neue Art von Strahlen.” *Annalen der Physik* 300(1):12–17. doi: 10.1002/andp.18983000103.
- Rose, Samuel L., Svetlana V. Antonyuk, Daisuke Sasaki, Keitaro Yamashita, Kunio Hirata, Go Ueno, Hideo Ago, Robert R. Eady, Takehiko Tosha, Masaki Yamamoto, and S. Samar Hasnain. 2021. “An Unprecedented Insight into the Catalytic Mechanism of Copper Nitrite Reductase from Atomic-Resolution and Damage-Free Structures.” *Science Advances* 7(1):eabd8523. doi: 10.1126/sciadv.abd8523.
- Rosenbaum, D. M., V. Cherezov, M. A. Hanson, S. G. F. Rasmussen, F. S. Thian, T. S. Kobilka, H. J. Choi, X. J. Yao, W. I. Weis, R. C. Stevens, and B. K. Kobilka. 2007. “GPCR Engineering Yields High-Resolution Structural Insights into 2-Adrenergic Receptor Function.” *Science* 318(5854):1266–73. doi: 10.1126/science.1150609.
- Rosenbaum, G., K. C. Holmes, and J. Witz. 1971. “Synchrotron Radiation as a Source for X-Ray Diffraction.” *Nature* 230(5294):434–37. doi: 10.1038/230434a0.
- Rossmann, M. G. 1990. “The Molecular Replacement Method.” *Acta Crystallographica Section A Foundations of Crystallography* 46(2):73–82. doi: 10.1107/S0108767389009815.
- Rossmann, Michael G., and Cornelis G. van Beek. 1999. “Data Processing.” *Acta Crystallographica Section D Biological Crystallography* 55(10):1631–40. doi: 10.1107/S0907444999008379.
- Rould, Mark A., and Charles W. Carter. 2003. “Isomorphous Difference Methods.” Pp. 145–63 in *Methods in Enzymology*. Vol. 374. Elsevier.
- Roussel, Eléonore, Enrico Allaria, Carlo Callegari, Marcello Coreno, Riccardo Cucini, Simone Mitri, Bruno Diviacco, Eugenio Ferrari, Paola Finetti, David Gauthier, Giuseppe Penco, Lorenzo Raimondi, Cristian Svetina, Marco Zangrando, Andreas Beckmann, Leif Glaser, Gregor Hartmann, Frank Scholz, Joern Seltmann, Ivan Shevchuk, Jens Viehhaus, and Luca Giannessi. 2017. “Polarization Characterization of Soft X-Ray Radiation at FERMI FEL-2.” *Photonics* 4(4):29. doi: 10.3390/photonics4020029.
- Ruska, E. 1934. “Über Fortschritte im Bau und in der Leistung des magnetischen Elektronenmikroskops.” *Zeitschrift für Physik* 87(9–10):580–602. doi: 10.1007/BF01333326.
- Rysselberghe, Pierre Van. 1932. “Remarks Concerning the Clausius-Mossotti Law.” *The Journal of Physical Chemistry* 36(4):1152–55. doi: 10.1021/j150334a007.
- Sahl, Steffen J., Stefan W. Hell, and Stefan Jakobs. 2017. “Fluorescence Nanoscopy in Cell Biology.” *Nature Reviews Molecular Cell Biology* 18(11):685–701. doi: 10.1038/nrm.2017.71.
- Salvi, Francesca, Yuan-Fang Wang, Irene T. Weber, and Giovanni Gadda. 2014. “Structure of Choline Oxidase in Complex with the Reaction Product Glycine Betaine.” *Acta Crystallographica Section D Biological Crystallography* 70(2):405–13. doi: 10.1107/S1399004713029283.

- Sancar, Aziz. 2003. "Structure and Function of DNA Photolyase and Cryptochrome Blue-Light Photoreceptors." *Chemical Reviews* 103(6):2203–38. doi: 10.1021/cr0204348.
- Sancar, Aziz. 2016. "Mechanisms of DNA Repair by Photolyase and Excision Nuclease (Nobel Lecture)." *Angewandte Chemie International Edition* 55(30):8502–27. doi: 10.1002/anie.201601524.
- Santner, Paul, László Krisztián Szabó, Santiago Nahuel Chanquia, Aske Høj Merrild, Frank Hollmann, Selin Kara, and Bekir Engin Eser. 2021. "Optimization and Engineering of Fatty Acid Photodecarboxylase for Substrate Specificity." *ChemCatChem* 13(18):4038–46. doi: 10.1002/cctc.202100840.
- Sauter, Nicholas K., Johan Hattne, Ralf W. Grosse-Kunstleve, and Nathaniel Echols. 2013. "New Python-Based Methods for Data Processing." *Acta Crystallographica Section D Biological Crystallography* 69(7):1274–82. doi: 10.1107/S0907444913000863.
- Sawaya, M. R., D. Cascio, M. Gingery, J. Rodriguez, L. Goldschmidt, J. P. Colletier, M. M. Messerschmidt, S. Boutet, J. E. Koglin, G. J. Williams, A. S. Brewster, K. Nass, J. Hattne, S. Botha, R. B. Doak, R. L. Shoeman, D. P. DePonte, H. W. Park, B. A. Federici, N. K. Sauter, I. Schlichting, and D. S. Eisenberg. 2014. "Protein Crystal Structure Obtained at 2.9 Å Resolution from Injecting Bacterial Cells into an X-Ray Free-Electron Laser Beam." *Proceedings of the National Academy of Sciences* 111(35):12769–74. doi: 10.1073/pnas.1413456111.
- Schirò, Giorgio, Joyce Woodhouse, Martin Weik, Ilme Schlichting, and Robert L. Shoeman. 2017. "Simple and Efficient System for Photoconverting Light-Sensitive Proteins in Serial Crystallography Experiments." *Journal of Applied Crystallography* 50(3):932–39. doi: 10.1107/S1600576717006264.
- Schlichting, I., and R. S. Goody. 1997. "Triggering Methods in Crystallographic Enzyme Kinetics." *Methods in Enzymology* 277:467–90. doi: 10.1016/s0076-6879(97)77026-5.
- Schmidt, Marius. 2013. "Mix and Inject: Reaction Initiation by Diffusion for Time-Resolved Macromolecular Crystallography." *Advances in Condensed Matter Physics* 2013:1–10. doi: 10.1155/2013/167276.
- Schmidt, Marius. 2020. "Reaction Initiation in Enzyme Crystals by Diffusion of Substrate." *Crystals* 10(2):116. doi: 10.3390/cryst10020116.
- Schmidt, Marius, Hyotcherl Ihee, Reinhard Pahl, and Vukica Srajer. 2005. "Protein–Ligand Interaction Probed by Time-Resolved Crystallography." Pp. 115–54 in *Protein-Ligand Interactions*. Vol. 305. New Jersey: Humana Press.
- Schrödinger, LLC, and Warren DeLano. 2020. *PyMOL* [computer program]. Version 2.4.0. <http://www.pymol.org/pymol>.
- Schubert, Robin, Svetlana Kapis, Yannig Gicquel, Gleb Bourenkov, Thomas R. Schneider, Michael Heymann, Christian Betzel, and Markus Perbandt. 2016. "A Multicrystal Diffraction Data-Collection Approach for Studying Structural Dynamics with Millisecond Temporal Resolution." *IUCrJ* 3(Pt 6):393–401. doi: 10.1107/S2052252516016304.

- Schubert, Veit. 2017. “Super-Resolution Microscopy – Applications in Plant Cell Research.” *Frontiers in Plant Science* 8. doi: 10.3389/fpls.2017.00531.
- Schulz, Eike C., Pedram Mehrabi, Henrike M. Müller-Werkmeister, Friedjof Tellkamp, Ajay Jha, William Stuart, Elke Persch, Raoul De Gasparo, François Diederich, Emil F. Pai, and R. J. Dwayne Miller. 2018. “The Hit-and-Return System Enables Efficient Time-Resolved Serial Synchrotron Crystallography.” *Nature Methods* 15(11):901–4. doi: 10.1038/s41592-018-0180-2.
- Schulz, Eike C., Briony A. Yorke, Arwen R. Pearson, and Pedram Mehrabi. 2022. “Best Practices for Time-Resolved Serial Synchrotron Crystallography.” *Acta Crystallographica Section D Structural Biology* 78(1):14–29. doi: 10.1107/S2059798321011621.
- Senda, Toshiya, Miki Senda, Shigenobu Kimura, and Tetsuo Ishida. 2009. “Redox Control of Protein Conformation in Flavoproteins.” *Antioxidants & Redox Signaling* 11(7):1741–66. doi: 10.1089/ars.2008.2348.
- Sezonov, Guennadi, Danièle Joseleau-Petit, and Richard D’Ari. 2007. “Escherichia Coli Physiology in Luria-Bertani Broth.” *Journal of Bacteriology* 189(23):8746–49. doi: 10.1128/JB.01368-07.
- Shaner, Nathan C., Robert E. Campbell, Paul A. Steinbach, Ben N. G. Giepmans, Amy E. Palmer, and Roger Y. Tsien. 2004. “Improved Monomeric Red, Orange and Yellow Fluorescent Proteins Derived from Discosoma Sp. Red Fluorescent Protein.” *Nature Biotechnology* 22(12):1567–72. doi: 10.1038/nbt1037.
- Shapiro, D. A., H. N. Chapman, D. DePonte, R. B. Doak, P. Fromme, G. Hembree, M. Hunter, S. Marchesini, K. Schmidt, J. Spence, D. Starodub, and U. Weierstall. 2008. “Powder Diffraction from a Continuous Microjet of Submicrometer Protein Crystals.” *Journal of Synchrotron Radiation* 15(6):593–99. doi: 10.1107/S0909049508024151.
- Shelby, M. L., D. Gilbale, T. D. Grant, C. Seuring, B. W. Segelke, W. He, A. C. Evans, T. Pakendorf, P. Fischer, M. S. Hunter, A. Batyuk, M. Barthelmess, A. Meents, M. A. Coleman, T. L. Kuhl, and M. Frank. 2020. “A Fixed-Target Platform for Serial Femtosecond Crystallography in a Hydrated Environment.” *IUCrJ* 7(1):30–41. doi: 10.1107/S2052252519014003.
- Shimada, Atsuhiko, Minoru Kubo, Seiki Baba, Keitaro Yamashita, Kunio Hirata, Go Ueno, Takashi Nomura, Tetsunari Kimura, Kyoko Shinzawa-Itoh, Junpei Baba, Keita Hatano, Yuki Eto, Akari Miyamoto, Hironori Murakami, Takashi Kumasaka, Shigeki Owada, Kensuke Tono, Makina Yabashi, Yoshihiro Yamaguchi, Sachiko Yanagisawa, Miyuki Sakaguchi, Takashi Ogura, Ryo Komiya, Jiwang Yan, Eiki Yamashita, Masaki Yamamoto, Hideo Ago, Shinya Yoshikawa, and Tomitake Tsukihara. 2017. “A Nanosecond Time-Resolved XFEL Analysis of Structural Changes Associated with CO Release from Cytochrome c Oxidase.” *Science Advances* 3(7):e1603042. doi: 10.1126/sciadv.1603042.
- Shimomura, O. 1979. “Structure of the Chromophore of *Aequorea* Green Fluorescent Protein.” *FEBS Letters* 104(2):220–22. doi: 10.1016/0014-5793(79)80818-2.

- Shinoda, Hajime, Kai Lu, Ryosuke Nakashima, Tetsuichi Wazawa, Kosuke Noguchi, Tomoki Matsuda, and Takeharu Nagai. 2019. “Acid-Tolerant Reversibly Switchable Green Fluorescent Protein for Super-Resolution Imaging under Acidic Conditions.” *Cell Chemical Biology* 26(10):1469-1479.e6. doi: 10.1016/j.chembiol.2019.07.012.
- Shroff, Hari, Catherine G. Galbraith, James A. Galbraith, Helen White, Jennifer Gillette, Scott Olenych, Michael W. Davidson, and Eric Betzig. 2007. “Dual-Color Superresolution Imaging of Genetically Expressed Probes within Individual Adhesion Complexes.” *Proceedings of the National Academy of Sciences* 104(51):20308–13. doi: 10.1073/pnas.0710517105.
- Sierra, Raymond G., Cornelius Gati, Hartawan Laksmono, E. Han Dao, Sheraz Gul, Franklin Fuller, Jan Kern, Ruchira Chatterjee, Mohamed Ibrahim, Aaron S. Brewster, Iris D. Young, Tara Michels-Clark, Andrew Aquila, Mengning Liang, Mark S. Hunter, Jason E. Koglin, Sébastien Boutet, Elia A. Junco, Brandon Hayes, Michael J. Bogan, Christina Y. Hampton, Elisabetta V. Puglisi, Nicholas K. Sauter, Claudiu A. Stan, Athina Zouni, Junko Yano, Vittal K. Yachandra, S. Michael Soltis, Joseph D. Puglisi, and Hasan DeMirici. 2016. “Concentric-Flow Electrokinetic Injector Enables Serial Crystallography of Ribosome and Photosystem II.” *Nature Methods* 13(1):59–62. doi: 10.1038/nmeth.3667.
- Sierra, Raymond G., Hartawan Laksmono, Jan Kern, Rosalie Tran, Johan Hattne, Roberto Alonso-Mori, Benedikt Lassalle-Kaiser, Carina Glöckner, Julia Hellmich, Donald W. Schafer, Nathaniel Echols, Richard J. Gildea, Ralf W. Grosse-Kunstleve, Jonas Sellberg, Trevor A. McQueen, Alan R. Fry, Marc M. Messerschmidt, Alan Miahnahri, M. Marvin Seibert, Christina Y. Hampton, Dmitri Starodub, N. Duane Loh, Dimosthenis Sokaras, Tsu-Chien Weng, Petrus H. Zwart, Pieter Glatzel, Despina Milathianaki, William E. White, Paul D. Adams, Garth J. Williams, Sébastien Boutet, Athina Zouni, Johannes Messinger, Nicholas K. Sauter, Uwe Bergmann, Junko Yano, Vittal K. Yachandra, and Michael J. Bogan. 2012. “Nanoflow Electrospinning Serial Femtosecond Crystallography.” *Acta Crystallographica Section D Biological Crystallography* 68(11):1584–87. doi: 10.1107/S0907444912038152.
- Skopintsev, Petr, David Ehrenberg, Tobias Weinert, Daniel James, Rajiv K. Kar, Philip J. M. Johnson, Dmitry Ozerov, Antonia Furrer, Isabelle Martiel, Florian Dworkowski, Karol Nass, Gregor Knopp, Claudio Cirelli, Christopher Arrell, Dardan Gashi, Sandra Mous, Maximilian Wranik, Thomas Gruhl, Demet Kekilli, Steffen Brünle, Xavier Deupi, Gebhard F. X. Schertler, Roger M. Benoit, Valerie Panneels, Przemyslaw Nogly, Igor Schapiro, Christopher Milne, Joachim Heberle, and Jörg Standfuss. 2020. “Femtosecond-to-Millisecond Structural Changes in a Light-Driven Sodium Pump.” *Nature* 583(7815):314–18. doi: 10.1038/s41586-020-2307-8.
- Smith, David J. 2008. “Ultimate Resolution in the Electron Microscope?” *Materials Today* 11:30–38. doi: 10.1016/S1369-7021(09)70005-7.
- Sommerfeld, Arnold. 1912. “Über Die Beugung Der Röntgenstrahlen.” *Annalen Der Physik* 343(8):473–506.
- Son, Sang-Kil, Henry N. Chapman, and Robin Santra. 2011. “Multiwavelength Anomalous Diffraction at High X-Ray Intensity.” *Physical Review Letters* 107(21):218102. doi: 10.1103/PhysRevLett.107.218102.

- Sorigué, D., K. Hadjidemetriou, S. Blangy, G. Gotthard, A. Bonvalet, N. Coquelle, P. Samire, A. Aleksandrov, L. Antonucci, A. Benachir, S. Boutet, M. Byrdin, M. Cammarata, S. Carbajo, S. Cuiné, R. B. Doak, L. Foucar, A. Gorel, M. Grünbein, E. Hartmann, R. Hienerwadel, M. Hilpert, M. Kloos, T. J. Lane, B. Légeret, P. Legrand, Y. Li-Beisson, S. L. Y. Moulin, D. Nurizzo, G. Peltier, G. Schirò, R. L. Shoeman, M. Sliwa, X. Solinas, B. Zhuang, T. R. M. Barends, J. P. Colletier, M. Joffre, A. Royant, C. Berthomieu, M. Weik, T. Domratcheva, K. Brettel, M. H. Vos, I. Schlichting, P. Arnoux, P. Müller, and F. Beisson. 2021. “Mechanism and Dynamics of Fatty Acid Photodecarboxylase.” *Science* 372(6538):eabd5687. doi: 10.1126/science.abd5687.
- Sorigué, Damien, Bertrand Légeret, Stéphan Cuiné, Stéphanie Blangy, Solène Moulin, Emmanuelle Billon, Pierre Richaud, Sabine Brugière, Yohann Couté, Didier Nurizzo, Pavel Müller, Klaus Brettel, David Pignol, Pascal Arnoux, Yonghua Li-Beisson, Gilles Peltier, and Fred Beisson. 2017. “An Algal Photoenzyme Converts Fatty Acids to Hydrocarbons.” *Science* 357(6354):903–7. doi: 10.1126/science.aan6349.
- Sorigué, Damien, Bertrand Légeret, Stéphan Cuiné, Pablo Morales, Boris Mirabella, Geneviève Guédeney, Yonghua Li-Beisson, Reinhard Jetter, Gilles Peltier, and Fred Beisson. 2016. “Microalgae Synthesize Hydrocarbons from Long-Chain Fatty Acids via a Light-Dependent Pathway.” *Plant Physiology* pp.00462.2016. doi: 10.1104/pp.16.00462.
- Spence, J. C. H., and R. B. Doak. 2004. “Single Molecule Diffraction.” *Physical Review Letters* 92(19):198102. doi: 10.1103/PhysRevLett.92.198102.
- Spence, John C. H., Richard A. Kirian, Xiaoyu Wang, Uwe Weierstall, Kevin E. Schmidt, Thomas White, Anton Barty, Henry N. Chapman, Stefano Marchesini, and James Holton. 2011. “Phasing of Coherent Femtosecond X-Ray Diffraction from Size-Varying Nanocrystals.” *Optics Express* 19(4):2866. doi: 10.1364/OE.19.002866.
- Sprenger, W. W., W. D. Hoff, J. P. Armitage, and K. J. Hellingwerf. 1993. “The Eubacterium *Ectothiorhodospira Halophila* Is Negatively Phototactic, with a Wavelength Dependence That Fits the Absorption Spectrum of the Photoactive Yellow Protein.” *Journal of Bacteriology* 175(10):3096–3104. doi: 10.1128/jb.175.10.3096-3104.1993.
- Stagno, J. R., Y. Liu, Y. R. Bhandari, C. E. Conrad, S. Panja, M. Swain, L. Fan, G. Nelson, C. Li, D. R. Wendel, T. A. White, J. D. Coe, M. O. Wiedorn, J. Knoska, D. Oberthuer, R. A. Tuckey, P. Yu, M. Dyba, S. G. Tarasov, U. Weierstall, T. D. Grant, C. D. Schwieters, J. Zhang, A. R. Ferré-D’Amaré, P. Fromme, D. E. Draper, M. Liang, M. S. Hunter, S. Boutet, K. Tan, X. Zuo, X. Ji, A. Barty, N. A. Zatsepin, H. N. Chapman, J. C. H. Spence, S. A. Woodson, and Y. X. Wang. 2017. “Structures of Riboswitch RNA Reaction States by Mix-and-Inject XFEL Serial Crystallography.” *Nature* 541(7636):242–46. doi: 10.1038/nature20599.
- Stellato, Francesco, Dominik Oberthür, Mengning Liang, Richard Bean, Cornelius Gati, Oleksandr Yefanov, Anton Barty, Anja Burkhardt, Pontus Fischer, Lorenzo Galli, Richard A. Kirian, Jan Meyer, Saravanan Panneerselvam, Chun Hong Yoon, Fedor Chervinskii, Emily Speller, Thomas A. White, Christian Betzel, Alke Meents, and Henry N. Chapman. 2014. “Room-Temperature Macromolecular Serial Crystallography Using Synchrotron Radiation.” *IUCrJ* 1(4):204–12. doi: 10.1107/S2052252514010070.

- Stiel, Andre C., Martin Andresen, Hannes Bock, Michael Hilbert, Jessica Schilde, Andreas Schönle, Christian Eggeling, Alexander Egner, Stefan W. Hell, and Stefan Jakobs. 2008. "Generation of Monomeric Reversibly Switchable Red Fluorescent Proteins for Far-Field Fluorescence Nanoscopy." *Biophysical Journal* 95(6):2989–97. doi: 10.1529/biophysj.108.130146.
- Stiel, Andre C., Simon Trowitzsch, Gert Weber, Martin Andresen, Christian Eggeling, Stefan W. Hell, Stefan Jakobs, and Markus C. Wahl. 2007. "1.8 Å Bright-State Structure of the Reversibly Switchable Fluorescent Protein Dronpa Guides the Generation of Fast Switching Variants." *Biochemical Journal* 402(1):35–42. doi: 10.1042/BJ20061401.
- Stoddard, Barry L. 1996. "Intermediate Trapping and Laue X-Ray Diffraction: Potential for Enzyme Mechanism, Dynamics, and Inhibitor Screening." *Pharmacology & Therapeutics* 70(3):215–56. doi: 10.1016/0163-7258(96)00058-7.
- Stoddard, Barry L. 2001. "Trapping Reaction Intermediates in Macromolecular Crystals for Structural Analyses." *Methods* 24(2):125–38. doi: 10.1006/meth.2001.1174.
- Stoddard, Barry L., Bruce E. Cohen, Michael Brubaker, Andrew D. Mesecar, and Daniel E. Koshland Jr. 1998. "Millisecond Laue Structures of an Enzyme–Product Complex Using Photocaged Substrate Analogs." *Nature Structural Biology* 5(10):891–97. doi: 10.1038/2331.
- Suga, Michihiro, Fusamichi Akita, Kunio Hirata, Go Ueno, Hironori Murakami, Yoshiki Nakajima, Tetsuya Shimizu, Keitaro Yamashita, Masaki Yamamoto, Hideo Ago, and Jian-Ren Shen. 2015. "Native Structure of Photosystem II at 1.95 Å Resolution Viewed by Femtosecond X-Ray Pulses." *Nature* 517(7532):99–103. doi: 10.1038/nature13991.
- Suga, Michihiro, Fusamichi Akita, Michihiro Sugahara, Minoru Kubo, Yoshiki Nakajima, Takanori Nakane, Keitaro Yamashita, Yasufumi Umena, Makoto Nakabayashi, Takahiro Yamane, Takamitsu Nakano, Mamoru Suzuki, Tetsuya Masuda, Shigeyuki Inoue, Tetsunari Kimura, Takashi Nomura, Shinichiro Yonekura, Long-Jiang Yu, Tomohiro Sakamoto, Taiki Motomura, Jing-Hua Chen, Yuki Kato, Takumi Noguchi, Kensuke Tono, Yasumasa Joti, Takashi Kameshima, Takaki Hatsui, Eriko Nango, Rie Tanaka, Hisashi Naitow, Yoshinori Matsuura, Ayumi Yamashita, Masaki Yamamoto, Osamu Nureki, Makina Yabashi, Tetsuya Ishikawa, So Iwata, and Jian-Ren Shen. 2017. "Light-Induced Structural Changes and the Site of O=O Bond Formation in PSII Caught by XFEL." *Nature* 543(7643):131–35. doi: 10.1038/nature21400.
- Suga, Michihiro, Fusamichi Akita, Keitaro Yamashita, Yoshiki Nakajima, Go Ueno, Hongjie Li, Takahiro Yamane, Kunio Hirata, Yasufumi Umena, Shinichiro Yonekura, Long-Jiang Yu, Hironori Murakami, Takashi Nomura, Tetsunari Kimura, Minoru Kubo, Seiki Baba, Takashi Kumasaka, Kensuke Tono, Makina Yabashi, Hiroshi Isobe, Kizashi Yamaguchi, Masaki Yamamoto, Hideo Ago, and Jian-Ren Shen. 2019. "An Oxyl/Oxo Mechanism for Oxygen-Oxygen Coupling in PSII Revealed by an x-Ray Free-Electron Laser." *Science* 366(6463):334–38. doi: 10.1126/science.aax6998.
- Suga, Michihiro, Atsuhiko Shimada, Fusamichi Akita, Jian-Ren Shen, Takehiko Tosha, and Hiroshi Sugimoto. 2020. "Time-Resolved Studies of Metalloproteins Using X-Ray Free Electron Laser Radiation at SACLA." *Biochimica et Biophysica Acta (BBA) - General Subjects* 1864(2):129466. doi: 10.1016/j.bbagen.2019.129466.

- Sugahara, Michihiro, Eiichi Mizohata, Eriko Nango, Mamoru Suzuki, Tomoyuki Tanaka, Tetsuya Masuda, Rie Tanaka, Tatsuro Shimamura, Yoshiki Tanaka, Chiyo Suno, Kentaro Ihara, Dongqing Pan, Keisuke Kakinouchi, Shigeru Sugiyama, Michio Murata, Tsuyoshi Inoue, Kensuke Tono, Changyong Song, Jaehyun Park, Takashi Kameshima, Takaki Hatsui, Yasumasa Joti, Makina Yabashi, and So Iwata. 2015. “Grease Matrix as a Versatile Carrier of Proteins for Serial Crystallography.” *Nature Methods* 12(1):61–63. doi: 10.1038/nmeth.3172.
- Sugahara, Michihiro, Takanori Nakane, Tetsuya Masuda, Mamoru Suzuki, Shigeyuki Inoue, Changyong Song, Rie Tanaka, Toru Nakatsu, Eiichi Mizohata, Fumiaki Yumoto, Kensuke Tono, Yasumasa Joti, Takashi Kameshima, Takaki Hatsui, Makina Yabashi, Osamu Nureki, Keiji Numata, Eriko Nango, and So Iwata. 2017. “Hydroxyethyl Cellulose Matrix Applied to Serial Crystallography.” *Scientific Reports* 7(1):703. doi: 10.1038/s41598-017-00761-0.
- Sugahara, Michihiro, Changyong Song, Mamoru Suzuki, Tetsuya Masuda, Shigeyuki Inoue, Takanori Nakane, Fumiaki Yumoto, Eriko Nango, Rie Tanaka, Kensuke Tono, Yasumasa Joti, Takashi Kameshima, Takaki Hatsui, Makina Yabashi, Osamu Nureki, Keiji Numata, and So Iwata. 2016. “Oil-Free Hyaluronic Acid Matrix for Serial Femtosecond Crystallography.” *Scientific Reports* 6(1):24484. doi: 10.1038/srep24484.
- Sui, Shuo, Yuxi Wang, Kristopher W. Kolewe, Vukica Srajer, Robert Henning, Jessica D. Schiffman, Christos Dimitrakopoulos, and Sarah L. Perry. 2016. “Graphene-Based Microfluidics for Serial Crystallography.” *Lab on a Chip* 16(16):3082–96. doi: 10.1039/C6LC00451B.
- Tenboer, Jason, Shibom Basu, Nadia Zatsepin, Kanupriya Pande, Despina Milathianaki, Matthias Frank, Mark Hunter, Sébastien Boutet, Garth J. Williams, Jason E. Koglin, Dominik Oberthuer, Michael Heymann, Christopher Kupitz, Chelsie Conrad, Jesse Coe, Shatabdi Roy-Chowdhury, Uwe Weierstall, Daniel James, Dingjie Wang, Thomas Grant, Anton Barty, Oleksandr Yefanov, Jennifer Scales, Cornelius Gati, Carolin Seuring, Vukica Srajer, Robert Henning, Peter Schwander, Raimund Fromme, Abbas Ourmazd, Keith Moffat, Jasper J. Van Thor, John C. H. Spence, Petra Fromme, Henry N. Chapman, and Marius Schmidt. 2014. “Time-Resolved Serial Crystallography Captures High-Resolution Intermediates of Photoactive Yellow Protein.” *Science* 346(6214):1242–46. doi: 10.1126/science.1259357.
- Testa, Ilaria, Nicolai T. Urban, Stefan Jakobs, Christian Eggeling, Katrin I. Willig, and Stefan W. Hell. 2012. “Nanoscopy of Living Brain Slices with Low Light Levels.” *Neuron* 75(6):992–1000. doi: 10.1016/j.neuron.2012.07.028.
- Tetreau, Guillaume, Anne-Sophie Banneville, Elena A. Andreeva, Aaron S. Brewster, Mark S. Hunter, Raymond G. Sierra, Jean-Marie Teulon, Iris D. Young, Niamh Burke, Tilman A. Grünwald, Joël Beaudouin, Irina Snigireva, Maria Teresa Fernandez-Luna, Alister Burt, Hyun-Woo Park, Luca Signor, Jayesh A. Bafna, Rabia Sadir, Daphna Fenel, Elisabetta Boeri-Erba, Maria Bacia, Ninon Zala, Frédéric Laporte, Laurence Després, Martin Weik, Sébastien Boutet, Martin Rosenthal, Nicolas Coquelle, Manfred Burghammer, Duilio Cascio, Michael R. Sawaya, Mathias Winterhalter, Enrico Gratton, Irina Gutsche, Brian Federici, Jean-Luc Pellequer, Nicholas K. Sauter, and Jacques-Philippe Colletier. 2020. “Serial Femtosecond Crystallography on in Vivo-

Grown Crystals Drives Elucidation of Mosquitocidal Cyt1Aa Bioactivation Cascade.” *Nature Communications* 11(1):1153. doi: 10.1038/s41467-020-14894-w.

- Thompson, Michael C., Benjamin A. Barad, Alexander M. Wolff, Hyun Sun Cho, Friedrich Schotte, Daniel M. C. Schwarz, Philip Anfinrud, and James S. Fraser. 2019. “Temperature-Jump Solution X-Ray Scattering Reveals Distinct Motions in a Dynamic Enzyme.” *Nature Chemistry* 11(11):1058–66. doi: 10.1038/s41557-019-0329-3.
- Tono, K., T. Togashi, Y. Inubushi, T. Sato, T. Katayama, K. Ogawa, H. Ohashi, H. Kimura, S. Takahashi, K. Takeshita, H. Tomizawa, S. Goto, T. Ishikawa, and M. Yabashi. 2013. “Beamline, Experimental Stations and Photon Beam Diagnostics for the Hard x-Ray Free Electron Laser of SACLA.” *New Journal of Physics* 15(8):083035. doi: 10.1088/1367-2630/15/8/083035.
- Tono, Kensuke, Eriko Nango, Michihiro Sugahara, Changyong Song, Jaehyun Park, Tomoyuki Tanaka, Rie Tanaka, Yasumasa Joti, Takashi Kameshima, Shun Ono, Takaki Hatsui, Eiichi Mizohata, Mamoru Suzuki, Tatsuro Shimamura, Yoshiki Tanaka, So Iwata, and Makina Yabashi. 2015. “Diverse Application Platform for Hard X-Ray Diffraction in SACLA (DAPHNIS): Application to Serial Protein Crystallography Using an X-Ray Free-Electron Laser.” *Journal of Synchrotron Radiation* 22(3):532–37. doi: 10.1107/S1600577515004464.
- Tosha, Takehiko, Takashi Nomura, Takuma Nishida, Naoya Saeki, Kouta Okubayashi, Raika Yamagiwa, Michihiro Sugahara, Takanori Nakane, Keitaro Yamashita, Kunio Hirata, Go Ueno, Tetsunari Kimura, Tamao Hisano, Kazumasa Muramoto, Hitomi Sawai, Hanae Takeda, Eiichi Mizohata, Ayumi Yamashita, Yusuke Kanematsu, Yu Takano, Eriko Nango, Rie Tanaka, Osamu Nureki, Osami Shoji, Yuka Ikemoto, Hironori Murakami, Shigeki Owada, Kensuke Tono, Makina Yabashi, Masaki Yamamoto, Hideo Ago, So Iwata, Hiroshi Sugimoto, Yoshitsugu Shiro, and Minoru Kubo. 2017. “Capturing an Initial Intermediate during the P450_{nor} Enzymatic Reaction Using Time-Resolved XFEL Crystallography and Caged-Substrate.” *Nature Communications* 8(1):1585. doi: 10.1038/s41467-017-01702-1.
- Tsien, Roger Y. 1998. “THE GREEN FLUORESCENT PROTEIN.” *Annual Review of Biochemistry* 67(1):509–44. doi: 10.1146/annurev.biochem.67.1.509.
- Ursby, T., and D. Bourgeois. 1997. “Improved Estimation of Structure-Factor Difference Amplitudes from Poorly Accurate Data.” *Acta Crystallographica Section A Foundations of Crystallography* 53(5):564–75. doi: 10.1107/S0108767397004522.
- Usón, Isabel, and George M. Sheldrick. 1999. “Advances in Direct Methods for Protein Crystallography.” *Current Opinion in Structural Biology* 9(5):643–48. doi: 10.1016/S0959-440X(99)00020-2.
- Vagin, A., and A. Teplyakov. 1997. “MOLREP: An Automated Program for Molecular Replacement.” *Journal of Applied Crystallography* 30(6):1022–25. doi: 10.1107/S0021889897006766.
- Valli, Jessica, Adrian Garcia-Burgos, Liam M. Rooney, Beatriz Vale de Melo e Oliveira, Rory R. Duncan, and Colin Rickman. 2021. “Seeing beyond the Limit: A Guide to Choosing

- the Right Super-Resolution Microscopy Technique.” *Journal of Biological Chemistry* 297(1):100791. doi: 10.1016/j.jbc.2021.100791.
- Vicidomini, Giuseppe, Paolo Bianchini, and Alberto Diaspro. 2018. “STED Super-Resolved Microscopy.” *Nature Methods* 15(3):173–82. doi: 10.1038/nmeth.4593.
- Wang, L., W. C. Jackson, P. A. Steinbach, and R. Y. Tsien. 2004. “Evolution of New Nonantibody Proteins via Iterative Somatic Hypermutation.” *Proceedings of the National Academy of Sciences* 101(48):16745–49. doi: 10.1073/pnas.0407752101.
- Warren, Mark M., Marius Kaucikas, Ann Fitzpatrick, Paul Champion, J. Timothy Sage, and Jasper J. van Thor. 2013. “Ground-State Proton Transfer in the Photoswitching Reactions of the Fluorescent Protein Dronpa.” *Nature Communications* 4(1):1461. doi: 10.1038/ncomms2460.
- Warshel, Arieh, and Ram Prasad Bora. 2016. “Perspective: Defining and Quantifying the Role of Dynamics in Enzyme Catalysis.” *The Journal of Chemical Physics* 144(18):180901. doi: 10.1063/1.4947037.
- Warshel, Arieh, Pankaj K. Sharma, Mitsunori Kato, Yun Xiang, Hanbin Liu, and Mats H. M. Olsson. 2006. “Electrostatic Basis for Enzyme Catalysis.” *Chemical Reviews* 106(8):3210–35. doi: 10.1021/cr0503106.
- Weierstall, U., J. C. H. Spence, and R. B. Doak. 2012. “Injector for Scattering Measurements on Fully Solvated Biospecies.” *Review of Scientific Instruments* 83(3):035108. doi: 10.1063/1.3693040.
- Weierstall, Uwe, Daniel James, Chong Wang, Thomas A. White, Dingjie Wang, Wei Liu, John C. H. Spence, R. Bruce Doak, Garrett Nelson, Petra Fromme, Raimund Fromme, Ingo Grotjohann, Christopher Kupitz, Nadia A. Zatsepin, Haiguang Liu, Shibom Basu, Daniel Wacker, Gye Won Han, Vsevolod Katritch, Sébastien Boutet, Marc Messerschmidt, Garth J. Williams, Jason E. Koglin, M. Marvin Seibert, Markus Klinker, Cornelius Gati, Robert L. Shoeman, Anton Barty, Henry N. Chapman, Richard A. Kirian, Kenneth R. Beyerlein, Raymond C. Stevens, Dianfan Li, Syed T. A. Shah, Nicole Howe, Martin Caffrey, and Vadim Cherezov. 2014. “Lipidic Cubic Phase Injector Facilitates Membrane Protein Serial Femtosecond Crystallography.” *Nature Communications* 5(1):3309. doi: 10.1038/ncomms4309.
- Weinberg, Christina E., Zasha Weinberg, and Christian Hammann. 2019. “Novel Ribozymes: Discovery, Catalytic Mechanisms, and the Quest to Understand Biological Function.” *Nucleic Acids Research* 47(18):9480–94. doi: 10.1093/nar/gkz737.
- Weinert, Tobias, Natacha Olieric, Robert Cheng, Steffen Brünle, Daniel James, Dmitry Ozerov, Dardan Gashi, Laura Vera, May Marsh, Kathrin Jaeger, Florian Dworkowski, Ezequiel Panepucci, Shibom Basu, Petr Skopintsev, Andrew S. Doré, Tian Geng, Robert M. Cooke, Mengning Liang, Andrea E. Prota, Valerie Panneels, Przemyslaw Nogly, Ulrich Ermler, Gebhard Schertler, Michael Hennig, Michel O. Steinmetz, Meitian Wang, and Jörg Standfuss. 2017. “Serial Millisecond Crystallography for Routine Room-Temperature Structure Determination at Synchrotrons.” *Nature Communications* 8(1):542. doi: 10.1038/s41467-017-00630-4.

- Weinert, Tobias, Petr Skopintsev, Daniel James, Florian Dworkowski, Ezequiel Panepucci, Demet Kekilli, Antonia Furrer, Steffen Brünle, Sandra Mous, Dmitry Ozerov, Przemyslaw Nogly, Meitian Wang, and Jörg Standfuss. 2019. “Proton Uptake Mechanism in Bacteriorhodopsin Captured by Serial Synchrotron Crystallography.” *Science* 365(6448):61–65. doi: 10.1126/science.aaw8634.
- White, Thomas A. 2014. “Post-Refinement Method for Snapshot Serial Crystallography.” *Philosophical Transactions of the Royal Society B: Biological Sciences* 369(1647):20130330. doi: 10.1098/rstb.2013.0330.
- White, Thomas A. 2019. “Processing Serial Crystallography Data with *CrystFEL*: A Step-by-Step Guide.” *Acta Crystallographica Section D Structural Biology* 75(2):219–33. doi: 10.1107/S205979831801238X.
- White, Thomas A., Richard A. Kirian, Andrew V. Martin, Andrew Aquila, Karol Nass, Anton Barty, and Henry N. Chapman. 2012. “*CrystFEL*: A Software Suite for Snapshot Serial Crystallography.” *Journal of Applied Crystallography* 45(2):335–41. doi: 10.1107/S0021889812002312.
- White, Thomas A., Valerio Mariani, Wolfgang Brehm, Oleksandr Yefanov, Anton Barty, Kenneth R. Beyerlein, Fedor Chervinskii, Lorenzo Galli, Cornelius Gati, Takanori Nakane, Alexandra Tolstikova, Keitaro Yamashita, Chun Hong Yoon, Kay Diederichs, and Henry N. Chapman. 2016. “Recent Developments in *CrystFEL*.” *Journal of Applied Crystallography* 49(2):680–89. doi: 10.1107/S1600576716004751.
- Wickstrand, Cecilia, Robert Dods, Antoine Royant, and Richard Neutze. 2015. “Bacteriorhodopsin: Would the Real Structural Intermediates Please Stand Up?” *Biochimica et Biophysica Acta (BBA) - General Subjects* 1850(3):536–53. doi: 10.1016/j.bbagen.2014.05.021.
- Wiedorn, Max O., Salah Awel, Andrew J. Morgan, Kartik Ayyer, Yaroslav Gevorkov, Holger Fleckenstein, Nils Roth, Luigi Adriano, Richard Bean, Kenneth R. Beyerlein, Joe Chen, Jesse Coe, Francisco Cruz-Mazo, Tomas Ekeberg, Rita Graceffa, Michael Heymann, Daniel A. Horke, Juraj Knoška, Valerio Mariani, Reza Nazari, Dominik Oberthür, Amit K. Samanta, Raymond G. Sierra, Claudiu A. Stan, Oleksandr Yefanov, Dimitrios Rompotis, Jonathan Correa, Benjamin Erk, Rolf Treusch, Joachim Schulz, Brenda G. Hogue, Alfonso M. Gañán-Calvo, Petra Fromme, Jochen Küpper, Andrei V. Rode, Saša Bajt, Richard A. Kirian, and Henry N. Chapman. 2018. “Rapid Sample Delivery for Megahertz Serial Crystallography at X-Ray FELs.” *IUCrJ* 5(5):574–84. doi: 10.1107/S2052252518008369.
- Wiedorn, Max O., Dominik Oberthür, Richard Bean, Robin Schubert, Nadine Werner, Brian Abbey, Martin Aepfelbacher, Luigi Adriano, Aschkan Allahgholi, Nasser Al-Qudami, Jakob Andreasson, Steve Aplin, Salah Awel, Kartik Ayyer, Saša Bajt, Imrich Barák, Sadia Bari, Johan Bielecki, Sabine Botha, Djelloul Boukhelef, Wolfgang Brehm, Sandor Brockhauser, Igor Cheviakov, Matthew A. Coleman, Francisco Cruz-Mazo, Cyril Danilevski, Connie Darmanin, R. Bruce Doak, Martin Domaracky, Katerina Dörner, Yang Du, Hans Fangohr, Holger Fleckenstein, Matthias Frank, Petra Fromme, Alfonso M. Gañán-Calvo, Yaroslav Gevorkov, Klaus Giewekemeyer, Helen Mary Ginn, Heinz Graafsma, Rita Graceffa, Dominic Greiffenberg, Lars Gumprecht, Peter Göttlicher, Janos Hajdu, Steffen Hauf, Michael Heymann, Susannah Holmes, Daniel A.

- Horke, Mark S. Hunter, Siegfried Imlau, Alexander Kaukher, Yoonhee Kim, Alexander Klyuev, Juraj Knoška, Bostjan Kobe, Manuela Kuhn, Christopher Kupitz, Jochen Küpper, Janine Mia Lahey-Rudolph, Torsten Laurus, Karoline Le Cong, Romain Letrun, P. Lourdu Xavier, Luis Maia, Filipe R. N. C. Maia, Valerio Mariani, Marc Messerschmidt, Markus Metz, Davide Mezza, Thomas Michelat, Grant Mills, Diana C. F. Monteiro, Andrew Morgan, Kerstin Mühlig, Anna Munke, Astrid Münnich, Julia Nette, Keith A. Nugent, Theresa Nuguid, Allen M. Orville, Suraj Pandey, Gisel Pena, Pablo Villanueva-Perez, Jennifer Poehlsen, Gianpietro Previtali, Lars Redecke, Winnie Maria Riekehr, Holger Rohde, Adam Round, Tatiana Safenreiter, Iosifina Sarrou, Tokushi Sato, Marius Schmidt, Bernd Schmitt, Robert Schönherr, Joachim Schulz, Jonas A. Sellberg, M. Marvin Seibert, Carolin Seuring, Megan L. Shelby, Robert L. Shoeman, Marcin Sikorski, Alessandro Silenzi, Claudiu A. Stan, Xintian Shi, Stephan Stern, Jola Sztuk-Dambietz, Janusz Szuba, Aleksandra Tolstikova, Martin Trebbin, Ulrich Trunk, Patrik Vagovic, Thomas Ve, Britta Weinhausen, Thomas A. White, Krzysztof Wrona, Chen Xu, Oleksandr Yefanov, Nadia Zatsepin, Jiaguo Zhang, Markus Perbandt, Adrian P. Mancuso, Christian Betzel, Henry Chapman, and Anton Barty. 2018. “Megahertz Serial Crystallography.” *Nature Communications* 9(1):4025. doi: 10.1038/s41467-018-06156-7.
- Wien, W. 1907. “Ueber Eine Berechnung Der Wellenlänge Der Röntgenstrahlen Aus Dem Planckschen Energie- Element.” *Nachrichten von Der Gesellschaft Der Wissenschaften Zu Göttingen, Mathematisch-Physikalische Klasse* 1907:598–601.
- Winkler, F. K., C. E. Schutt, and S. C. Harrison. 1979. “The Oscillation Method for Crystals with Very Large Unit Cells.” *Acta Crystallographica Section A* 35(6):901–11. doi: 10.1107/S0567739479002035.
- Woodhouse, Joyce. 2018. “Studying a Reversibly Switchable Fluorescent Protein by Time-Resolved Crystallography Using the X-Ray Free Electron Lasers.” *Biological Physics*, Université Grenoble Alpes, 2018. English.
- Woodhouse, Joyce, Gabriela Nass Kovacs, Nicolas Coquelle, Lucas M. Uriarte, Virgile Adam, Thomas R. M. Barends, Martin Byrdin, Eugenio de la Mora, R. Bruce Doak, Mikolaj Feliks, Martin Field, Franck Fieschi, Virginia Guillon, Stefan Jakobs, Yasumasa Joti, Pauline Macheboeuf, Koji Motomura, Karol Nass, Shigeki Owada, Christopher M. Roome, Cyril Ruckebusch, Giorgio Schirò, Robert L. Shoeman, Michel Thepaut, Tadashi Togashi, Kensuke Tono, Makina Yabashi, Marco Cammarata, Lutz Foucar, Dominique Bourgeois, Michel Sliwa, Jacques-Philippe Colletier, Ilme Schlichting, and Martin Weik. 2020a. “Photoswitching Mechanism of a Fluorescent Protein Revealed by Time-Resolved Crystallography and Transient Absorption Spectroscopy.” *Nature Communications* 11(1):741. doi: 10.1038/s41467-020-14537-0.
- Woodhouse, Joyce, Gabriela Nass Kovacs, Nicolas Coquelle, Lucas M. Uriarte, Virgile Adam, Thomas R. M. Barends, Martin Byrdin, Eugenio de la Mora, R. Bruce Doak, Mikolaj Feliks, Martin Field, Franck Fieschi, Virginia Guillon, Stefan Jakobs, Yasumasa Joti, Pauline Macheboeuf, Koji Motomura, Karol Nass, Shigeki Owada, Christopher M. Roome, Cyril Ruckebusch, Giorgio Schirò, Robert L. Shoeman, Michel Thepaut, Tadashi Togashi, Kensuke Tono, Makina Yabashi, Marco Cammarata, Lutz Foucar, Dominique Bourgeois, Michel Sliwa, Jacques-Philippe Colletier, Ilme Schlichting, and Martin Weik. 2020b. “Photoswitching Mechanism of a Fluorescent Protein Revealed

- by Time-Resolved Crystallography and Transient Absorption Spectroscopy.” *Nature Communications* 11(1):741. doi: 10.1038/s41467-020-14537-0.
- Yabashi, Makina, Hitoshi Tanaka, and Tetsuya Ishikawa. 2015. “Overview of the SACLA Facility.” *Journal of Synchrotron Radiation* 22(3):477–84. doi: 10.1107/S1600577515004658.
- Yadav, Dheerendra, Fabien Lacomat, Nadia Dozova, Fabrice Rappaport, Pascal Plaza, and Agathe Espagne. 2015. “Real-Time Monitoring of Chromophore Isomerization and Deprotonation during the Photoactivation of the Fluorescent Protein Dronpa.” *The Journal of Physical Chemistry B* 119(6):2404–14. doi: 10.1021/jp507094f.
- Yamamoto, Masaki, Kunio Hirata, Keitaro Yamashita, Kazuya Hasegawa, Go Ueno, Hideo Ago, and Takashi Kumasaka. 2017. “Protein Microcrystallography Using Synchrotron Radiation.” *IUCrJ* 4(5):529–39. doi: 10.1107/S2052252517008193.
- Yamashita, Keitaro, Naoyuki Kuwabara, Takanori Nakane, Tomohiro Murai, Eiichi Mizohata, Michihiro Sugahara, Dongqing Pan, Tetsuya Masuda, Mamoru Suzuki, Tomomi Sato, Atsushi Kodan, Tomohiro Yamaguchi, Eriko Nango, Tomoyuki Tanaka, Kensuke Tono, Yasumasa Joti, Takashi Kameshima, Takaki Hatsui, Makina Yabashi, Hiroshi Many, Tamao Endo, Ryuichi Kato, Toshiya Senda, Hiroaki Kato, So Iwata, Hideo Ago, Masaki Yamamoto, Fumiaki Yumoto, and Toru Nakatsu. 2017. “Experimental Phase Determination with Selenomethionine or Mercury-Derivatization in Serial Femtosecond Crystallography.” *IUCrJ* 4(5):639–47. doi: 10.1107/S2052252517008557.
- Yamashita, Keitaro, Dongqing Pan, Tomohiko Okuda, Michihiro Sugahara, Atsushi Kodan, Tomohiro Yamaguchi, Tomohiro Murai, Keiko Gomi, Naoki Kajiyama, Eiichi Mizohata, Mamoru Suzuki, Eriko Nango, Kensuke Tono, Yasumasa Joti, Takashi Kameshima, Jaehyun Park, Changyong Song, Takaki Hatsui, Makina Yabashi, So Iwata, Hiroaki Kato, Hideo Ago, Masaki Yamamoto, and Toru Nakatsu. 2015. “An Isomorphous Replacement Method for Efficient de Novo Phasing for Serial Femtosecond Crystallography.” *Scientific Reports* 5(1):14017. doi: 10.1038/srep14017.
- Yang, J., and Q. Cheng. 2004. “Origin and Evolution of the Light-Dependent Protochlorophyllide Oxidoreductase (LPOR) Genes.” *Plant Biology* 6(5):537–44. doi: 10.1055/s-2004-821270.
- Yang, Jye-Shane, Guan-Jhih Huang, Yi-Hung Liu, and Shie-Ming Peng. 2008. “Photoisomerization of the Green Fluorescence Protein Chromophore and the Meta- and Para-Amino Analogues.” *Chemical Communications* (11):1344. doi: 10.1039/b717714c.
- Yip, Ka Man, Niels Fischer, Elham Paknia, Ashwin Chari, and Holger Stark. 2020. “Atomic-Resolution Protein Structure Determination by Cryo-EM.” *Nature* 587(7832):157–61. doi: 10.1038/s41586-020-2833-4.
- Yoshida, Hiromi, Genki Sakai, Kazushige Mori, Katsuhiko Kojima, Shigehiro Kamitori, and Koji Sode. 2015. “Structural Analysis of Fungus-Derived FAD Glucose Dehydrogenase.” *Scientific Reports* 5(1):13498. doi: 10.1038/srep13498.

- Yoshizawa, Toru, and George Wald. 1967. "Photochemistry of Iodopsin." *Nature* 214(5088):566–71. doi: 10.1038/214566a0.
- Young, Iris D., Mohamed Ibrahim, Ruchira Chatterjee, Sheraz Gul, Franklin D. Fuller, Sergey Koroidov, Aaron S. Brewster, Rosalie Tran, Roberto Alonso-Mori, Thomas Kroll, Tara Michels-Clark, Hartawan Laksmono, Raymond G. Sierra, Claudiu A. Stan, Rana Hussein, Miao Zhang, Lacey Douthit, Markus Kubin, Casper de Lichtenberg, Long Vo Pham, Håkan Nilsson, Mun Hon Cheah, Dmitriy Shevela, Claudio Saracini, Mackenzie A. Bean, Ina Seuffert, Dimosthenis Sokaras, Tsu-Chien Weng, Ernest Pastor, Clemens Weninger, Thomas Fransson, Louise Lassalle, Philipp Bräuer, Pierre Aller, Peter T. Docker, Babak Andi, Allen M. Orville, James M. Glowina, Silke Nelson, Marcin Sikorski, Diling Zhu, Mark S. Hunter, Thomas J. Lane, Andy Aquila, Jason E. Koglin, Joseph Robinson, Mengning Liang, Sébastien Boutet, Artem Y. Lyubimov, Monarin Uervirojnangkoorn, Nigel W. Moriarty, Dorothee Liebschner, Pavel V. Afonine, David G. Waterman, Gwyndaf Evans, Philippe Wernet, Holger Dobbek, William I. Weis, Axel T. Brunger, Petrus H. Zwart, Paul D. Adams, Athina Zouni, Johannes Messinger, Uwe Bergmann, Nicholas K. Sauter, Jan Kern, Vittal K. Yachandra, and Junko Yano. 2016. "Structure of Photosystem II and Substrate Binding at Room Temperature." *Nature* 540(7633):453–57. doi: 10.1038/nature20161.
- Yun, Ji-Hye, Xuanxuan Li, Jianing Yue, Jae-Hyun Park, Zeyu Jin, Chufeng Li, Hao Hu, Yingchen Shi, Suraj Pandey, Sergio Carbajo, Sébastien Boutet, Mark S. Hunter, Mengning Liang, Raymond G. Sierra, Thomas J. Lane, Liang Zhou, Uwe Weierstall, Nadia A. Zatsepin, Mio Ohki, Jeremy R. H. Tame, Sam-Yong Park, John C. H. Spence, Wenkai Zhang, Marius Schmidt, Weontae Lee, and Haiguang Liu. 2021. "Early-Stage Dynamics of Chloride Ion-Pumping Rhodopsin Revealed by a Femtosecond X-Ray Laser." *Proceedings of the National Academy of Sciences* 118(13):e2020486118. doi: 10.1073/pnas.2020486118.
- Zander, Ulrich, Gleb Bourenkov, Alexander N. Popov, Daniele de Sanctis, Olof Svensson, Andrew A. McCarthy, Ekaterina Round, Valentin Gordeliy, Christoph Mueller-Dieckmann, and Gordon A. Leonard. 2015. "*MeshAndCollect*: An Automated Multi-Crystal Data-Collection Workflow for Synchrotron Macromolecular Crystallography Beamlines." *Acta Crystallographica Section D Biological Crystallography* 71(11):2328–43. doi: 10.1107/S1399004715017927.
- Zeldin, O. B., S. Brockhauser, J. Bremridge, J. M. Holton, and E. F. Garman. 2013. "Predicting the X-Ray Lifetime of Protein Crystals." *Proceedings of the National Academy of Sciences* 110(51):20551–56. doi: 10.1073/pnas.1315879110.
- Zeldin, Oliver B., Markus Gerstel, and Elspeth F. Garman. 2013. "*RADDOSE-3D*: Time- and Space-Resolved Modelling of Dose in Macromolecular Crystallography." *Journal of Applied Crystallography* 46(4):1225–30. doi: 10.1107/S0021889813011461.
- Zhang, G., V. Gurtu, and S. R. Kain. 1996. "An Enhanced Green Fluorescent Protein Allows Sensitive Detection of Gene Transfer in Mammalian Cells." *Biochemical and Biophysical Research Communications* 227(3):707–11. doi: 10.1006/bbrc.1996.1573.
- Zhang, Tao, Deqiang Yao, Jiawei Wang, Yuanxin Gu, and Haifu Fan. 2015. "Serial Crystallographic Analysis of Protein Isomorphous Replacement Data from a Mixture of

- Native and Derivative Microcrystals.” *Acta Crystallographica Section D Biological Crystallography* 71(12):2513–18. doi: 10.1107/S139900471501603X.
- Zhang, Wuyuan, Jeong-Hoo Lee, Sabry H. H. Younes, Fabio Tonin, Peter-Leon Hagedoorn, Harald Pichler, Yoonjin Baeg, Jin-Byung Park, Robert Kourist, and Frank Hollmann. 2020. “Photobiocatalytic Synthesis of Chiral Secondary Fatty Alcohols from Renewable Unsaturated Fatty Acids.” *Nature Communications* 11(1):2258. doi: 10.1038/s41467-020-16099-7.
- Zhang, Wuyuan, Ming Ma, Mieke M. E. Huijbers, Georgy A. Filonenko, Evgeny A. Pidko, Morten van Schie, Sabrina de Boer, Bastien O. Burek, Jonathan Z. Bloh, Willem J. H. van Berkel, Wilson A. Smith, and Frank Hollmann. 2019. “Hydrocarbon Synthesis via Photoenzymatic Decarboxylation of Carboxylic Acids.” *Journal of the American Chemical Society* 141(7):3116–20. doi: 10.1021/jacs.8b12282.
- Zhong, Dongping. 2015. “Electron Transfer Mechanisms of DNA Repair by Photolyase.” *Annual Review of Physical Chemistry* 66(1):691–715. doi: 10.1146/annurev-physchem-040513-103631.
- Zhou, Xin X., and Michael Z. Lin. 2013. “Photoswitchable Fluorescent Proteins: Ten Years of Colorful Chemistry and Exciting Applications.” *Current Opinion in Chemical Biology* 17(4):682–90. doi: 10.1016/j.cbpa.2013.05.031.

6 Appendices

6.1 Mechanism and dynamics of fatty acid photodecarboxylase

RESEARCH ARTICLE SUMMARY

PHOTOENZYMES

Mechanism and dynamics of fatty acid photodecarboxylase

D. Sorigué, K. Hadjidemetriou, S. Blangy, G. Gotthard, A. Bonvalet, N. Coquelle, P. Samire, A. Aleksandrov, L. Antonucci, A. Benachir, S. Boutet, M. Byrdin, M. Cammarata, S. Carbajo, S. Cuiné, R. B. Doak, L. Foucar, A. Gorel, M. Grünbein, E. Hartmann, R. Hienerwadel, M. Hilpert, M. Kloos, T. J. Lane, B. Légeret, P. Legrand, Y. Li-Beisson, S. L. Y. Moulin, D. Nurizzo, G. Peltier, G. Schirò, R. L. Shoeman, M. Sliwa, X. Solinas, B. Zhuang, T. R. M. Barends, J.-P. Colletier, M. Joffre, A. Royant, C. Berthomieu*, M. Weik*, T. Domratcheva*, K. Brettel, M. H. Vos*, I. Schlichting*, P. Arnoux*, P. Müller*, F. Beisson*

INTRODUCTION: Photoenzymes are rare biocatalysts driven by absorption of a photon at each catalytic cycle; they inspire development of artificial photoenzymes with valuable activities. Fatty acid photodecarboxylase (FAP) is a natural photoenzyme that has potential applications in the bio-based production of hydrocarbons, yet its mechanism is far from fully understood.

RATIONALE: To elucidate the mechanism of FAP, we studied the wild-type (WT) enzyme from *Chlorella variabilis* (CvFAP) and variants with altered active-site residues using a wealth of techniques, including static and time-resolved crystallography and spectroscopy, as well as biochemical and computational approaches.

RESULTS: A 1.8-Å-resolution CvFAP x-ray crystal structure revealed a dense hydrogen-bonding network positioning the fatty acid carboxyl group in the vicinity of the flavin adenine dinucleotide (FAD) cofactor. Structures solved from free electron laser and low-dose synchrotron x-ray crystal data further highlighted an

unusual bent shape of the oxidized flavin chromophore, and showed that the bending angle (14°) did not change upon photon absorption (step 1) or throughout the photocycle. Calculations showed that bending substantially affected the energy levels of the flavin. Structural and spectroscopic analysis of WT and mutant proteins targeting two conserved active-site residues, R451 and C432, demonstrated that both residues were crucial for proper positioning of the substrate and water molecules and for oxidation of the fatty acid carboxylate by $^1\text{FAD}^*$ (~300 ps in WT FAP) to form $\text{FAD}^{\bullet-}$ (step 2). Time-resolved infrared spectroscopy demonstrated that decarboxylation occurred quasi-instantaneously upon this forward electron transfer, consistent with barrierless bond cleavage predicted by quantum chemistry calculations and with snapshots obtained by time-resolved crystallography. Transient absorption spectroscopy in H_2O and D_2O buffers indicated that back electron transfer from $\text{FAD}^{\bullet-}$ was coupled to and limited by transfer of an exchangeable proton or hydrogen atom

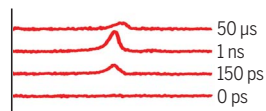
(step 3). Unexpectedly, concomitant with $\text{FAD}^{\bullet-}$ reoxidation (to a red-shifted form FAD_{RS}) in 100 ns, most of the CO_2 product was converted, most likely into bicarbonate (as inferred from FTIR spectra of the cryotrapped FAD_{RS} intermediate). Calculations indicated that this catalytic transformation involved an active-site water molecule. Cryo-Fourier transform infrared spectroscopy studies suggested that bicarbonate formation (step 4) was preceded by deprotonation of an arginine residue (step 3). At room temperature, the remaining CO_2 left the protein in 1.5 μs (step 4'). The observation of residual electron density close to C432 in electron density maps derived from time-resolved and cryocrystallography data suggests that this residue may play a role in stabilizing CO_2 and/or bicarbonate. Three routes for alkane formation were identified by quantum chemistry calculations; the one shown in the figure is favored by the ensemble of experimental data.

CONCLUSION: We provide a detailed and comprehensive characterization of light-driven hydrocarbon formation by FAP, which uses a remarkably complex mechanism including unique catalytic steps. We anticipate that our results will help to expand the green chemistry toolkit. ■

The list of author affiliations is available in the full article online.
*Corresponding author. Email: frederic.beisson@cea.fr (F.B.), pavel.muller@i2bc.paris-saclay.fr (P.M.), pascal.arnoux@cea.fr (P.A.), ilme.schlichting@mpimf-heidelberg.mpg.de (I.S.), marten.vos@polytechnique.edu (M.H.V.), tatjana.domratcheva@mpimf-heidelberg.mpg.de (T.D.), martin.weik@ibs.fr (M.W.), catherine.berthomieu@cea.fr (C.B.)
Cite this article as D. Sorigué et al., *Science* 372, eabd5687 (2021). DOI: 10.1126/science.abd5687

S READ THE FULL ARTICLE AT <https://doi.org/10.1126/science.abd5687>

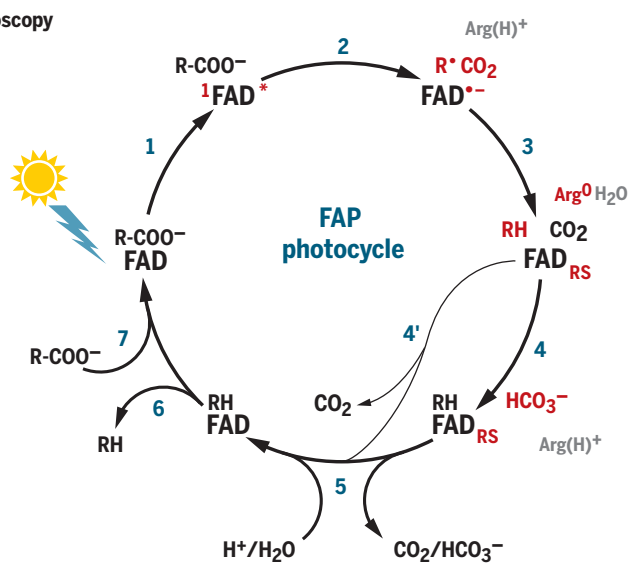
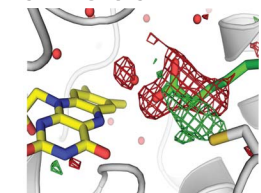
Multiscale time-resolved infrared spectroscopy



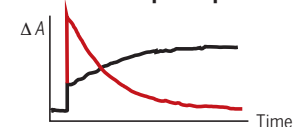
Fourier transform infrared spectroscopy



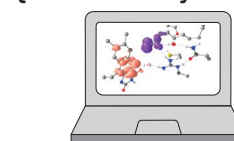
Time-resolved serial femtosecond crystallography



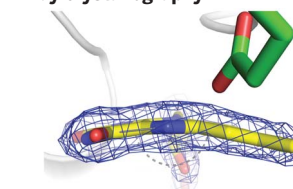
Transient absorption spectroscopy



Quantum chemistry



X-ray crystallography



Elucidation of the FAP photocycle by combining spectroscopic, biochemical, crystallographic, and computational studies.

RESEARCH ARTICLE

PHOTOENZYMES

Mechanism and dynamics of fatty acid photodecarboxylase

D. Sorigué¹, K. Hadjidemetriou², S. Blangy¹, G. Gotthard³, A. Bonvalet⁴, N. Coquelle⁵, P. Samire^{1,6}, A. Aleksandrov⁴, L. Antonucci⁴, A. Benachir⁴, S. Boutet⁷, M. Byrdin², M. Cammarata^{8,†}, S. Carbajo⁷, S. Cuiné¹, R. B. Doak⁹, L. Foucar⁹, A. Gorel⁹, M. Grünbein⁹, E. Hartmann⁹, R. Hienerwadel¹, M. Hilpert⁹, M. Kloos^{9,‡}, T. J. Lane⁷, B. Légeret¹, P. Legrand¹⁰, Y. Li-Beisson¹, S. L. Y. Moulin¹, D. Nurizzo³, G. Peltier¹, G. Schirò², R. L. Shoeman⁹, M. Sliwa¹¹, X. Solinas⁴, B. Zhuang^{4,6}, T. R. M. Barends⁹, J.-P. Colletier², M. Joffre⁴, A. Royant^{2,3}, C. Berthomieu^{1*}, M. Weik^{2*}, T. Domratheva^{9,12*}, K. Brettel⁶, M. H. Vos^{4*}, I. Schlichting^{9*}, P. Arnoux^{1*}, P. Müller^{6*}, F. Beisson^{1*}

Fatty acid photodecarboxylase (FAP) is a photoenzyme with potential green chemistry applications. By combining static, time-resolved, and cryotrapping spectroscopy and crystallography as well as computation, we characterized *Chlorella variabilis* FAP reaction intermediates on time scales from subpicoseconds to milliseconds. High-resolution crystal structures from synchrotron and free electron laser x-ray sources highlighted an unusual bent shape of the oxidized flavin chromophore. We demonstrate that decarboxylation occurs directly upon reduction of the excited flavin by the fatty acid substrate. Along with flavin reoxidation by the alkyl radical intermediate, a major fraction of the cleaved carbon dioxide unexpectedly transformed in 100 nanoseconds, most likely into bicarbonate. This reaction is orders of magnitude faster than in solution. Two strictly conserved residues, R451 and C432, are essential for substrate stabilization and functional charge transfer.

By far most enzymatic reactions in living cells are thermally activated, whereas reactions driven by light are much less common (1). Apart from photosynthetic reaction centers, three natural photoenzymes have been identified to date: DNA photolyases, which are involved in the repair of UV-damaged DNA (2); light-dependent prochlorophyllide oxidoreductase (LPOR), which is required for the maturation of chlorophyll (3); and the recently discovered fatty acid photodecarboxylase (FAP, EC 4.1.1.106), which converts fatty acids to hydrocarbons and CO₂ (4).

Photoenzymes require a photon for each turnover of a substrate molecule and offer the possibility to trigger and monitor catalytic steps and associated structural changes on very short time scales that are generally not accessible for thermally activated enzymes (5). Thus, over the past 20 years, the photochemical mechanism has been studied in detail for DNA photolyases (6–8) and has started to be identified for LPOR (9–13). Because of its readily available substrate, FAP may become a model of choice to understand catalytic steps that occur in enzymology.

Light-driven enzymes are also interesting for practical applications. Increasing our understanding and the repertoire of photoenzymatic mechanisms may help in the design of catalysts performing new reactions (14, 15) or in the development of new light-controlled proteins for optogenetics (16). FAP has potential biotechnological applications in green chemistry because hydrocarbons are important as cosmetics emollients, chemical synthons, solvents, and fuels (17–19). FAP complements routes previously identified for bio-based synthesis of hydrocarbons (20) by providing a one-step light-driven pathway from fatty acids. Rational design approaches have recently allowed improvement of the efficiency of FAP on high-value functionalized carboxylic acids (21) and on short-chain fatty acids to produce liquefied petroleum gas (20). Understanding the reaction mechanism of FAP in detail is thus of utmost importance, both from a fundamental research and an application point of view.

FAP is an algae-specific enzyme from the glucose-methanol-choline (GMC) oxidoreductase family harboring a flavin adenine dinucleotide (FAD) cofactor. It allows the decarboxylation

of C16–C18 free (nonesterified) fatty acids to the corresponding *n*-alka(e)nes (4). These hydrocarbon products are mostly located in chloroplast thylakoids, but their exact role is still unknown (22, 23). The initial spectroscopic characterization of FAP, which was based on monitoring the electronic state of the flavin after excitation by a laser flash, led to the first model of the FAP photocycle (4). The cycle starts with the quenching of the singlet excited state by forward electron transfer (fET) from bound fatty acid R-CO₂⁻ in ~300 ps (with a quantum yield >80%), forming a flavin anion radical FAD^{•-} and a fatty acid radical R-CO₂[•]. The latter decarboxylates, yielding an alkyl radical R[•] and CO₂. FAD^{•-} is reoxidized in ~100 ns by back electron transfer (bET), which ultimately provides the electron for the reduction of R[•] to the alkane RH. FAD^{•-} reoxidation results in a transiently red-shifted flavin state FAD_{RS} that reverts to the initial state in 4 ms.

Despite this insight, several open questions remained, including: Which structural features of the FAP active site promote substrate stabilization and favor the fET? Is decarboxylation instantaneous upon this fET step or is it slowed by an activation barrier? Does conversion of R[•] to the alkane RH occur by bET from FAD^{•-} coupled to a proton transfer (PT/PCET) or by hydrogen atom transfer (HAT) from a nearby amino acid (4, 24)? What is the origin of the proton or the hydrogen atom? Here, we report a high-resolution structure of FAP and characterize key steps along the FAP photocycle using a wealth of static and time-resolved crystallographic and spectroscopic techniques, as well as computational approaches. Our detailed characterization of FAP reveals unforeseen mechanistic complexity.

High-resolution structure of CvFAP

Crystals of FAP from *C. variabilis* NC64A (CvFAP), diffracting x-rays to high resolution and without the twinning fault reported earlier (4), were obtained upon removal of the N-terminal helix involved in crystal packing (residues 61 to 76) in native CvFAP. The resulting structure, solved at 1.8-Å resolution (table S1), now provides a detailed view of the active-site architecture (Fig. 1, A to D, and fig. S1). Although no substrate was added during protein purification and crystallization, two C18 fatty acids copurified with FAP were clearly identified, one in the active site and the other

¹Aix-Marseille University, CEA, CNRS, Institute of Biosciences and Biotechnologies, BIAM Cadarache, 13108 Saint-Paul-lez-Durance, France. ²Université Grenoble Alpes, CEA, CNRS, Institut de Biologie Structurale, 38000 Grenoble, France. ³European Synchrotron Radiation Facility, 38043 Grenoble, France. ⁴LOB, CNRS, INSERM, Ecole Polytechnique, Institut Polytechnique de Paris, 91128 Palaiseau, France. ⁵Large-Scale Structures Group, Institut Laue Langevin, 38042 Grenoble Cedex 9, France. ⁶Université Paris-Saclay, CEA, CNRS, Institute for Integrative Biology of the Cell (I2BC), 91198 Gif-sur-Yvette, France. ⁷Linac Coherent Light Source (LCLS), SLAC National Accelerator Laboratory, Menlo Park, CA 94025, USA. ⁸Department of Physics, UMR URI-CNRS 6251, University of Rennes 1, F-Rennes, France. ⁹Max-Planck-Institut für medizinische Forschung, Jahnstrasse 29, 69120 Heidelberg, Germany. ¹⁰Synchrotron SOLEIL, L'Orme des Merisiers Saint-Aubin, BP 48, 91192 Gif-sur-Yvette, France. ¹¹Univ. Lille, CNRS, UMR 8516, LASIRE, Laboratoire de Spectroscopie pour les Interactions, la Réactivité et l'Environnement, 59000 Lille, France. ¹²Department of Chemistry, Lomonosov Moscow State University, Moscow 119991, Russia.

†Present address: European Synchrotron Radiation Facility (ESRF), F-38043 Grenoble, France. ‡Present address: Sample Environment and Characterization European XFEL, 22869 Schenefeld, Germany.

*Corresponding author. Email: frederic.beisson@cea.fr (F.B.); pavel.muller@i2bc.paris-saclay.fr (P.M.); pascal.arnoux@cea.fr (P.A.); ilme.schlichting@mpimf-heidelberg.mpg.de (I.S.); marten.vos@polytechnique.edu (M.H.V.); tatjana.domratheva@mpimf-heidelberg.mpg.de (T.D.); martin.weik@ibs.fr (M.W.); catherine.berthomieu@cea.fr (C.B.)

on the surface of the protein. The latter is stabilized by hydrophobic interactions with nonpolar side chains (L427, Y419, I126, I416, and L420), as well as the aliphatic parts of R132 and R122. In the active site, the carboxyl group of the fatty acid is stabilized by hydrogen bonds with water molecules (Wat1 and Wat2) and the side chains of R451 and N575 (Fig. 1D). The fatty acid substrate is also stabilized on the dimethylbenzene side of FAD, in contrast to other GMC oxidoreductase enzymes, which have their substrate stabilized near the N5 atom of FAD (fig. S2).

Conformation of oxidized FAD in CvFAP

In the high-resolution dark-state structure of FAP obtained from synchrotron data “100 K dark,” the isoalloxazine ring of the FAD cofactor was found to be bent, with the dihedral angle C4-N5-N10-C9 (butterfly bending angle) deviating by 17.4° from planarity (Fig. 1E and fig. S2A). Such bending is usually interpreted as being caused by x-ray photoreduction con-

verting supposedly planar oxidized flavin to the bent reduced form (8, 25, 26). For FAP, however, in crystallo ultraviolet-visible (UV-Vis) absorption microspectrophotometry (fig. S3), low-dose crystallography, (fig. S4A and table S1), Raman microspectrophotometry (fig. S4, B and C), and molecular dynamics simulations (fig. S5, A and B) using a recent flavin force field (27) indicated that the FAD cofactor is bent in its oxidized form (supplementary text S1). To obtain a definite answer concerning the conformation of the oxidized FAD in FAP, we performed room temperature (RT) serial femtosecond crystallography (SFX) at an x-ray free-electron laser (XFEL; see below for details), which allows collecting essentially radiation damage-free diffraction data (28, 29). This SFX dark-state structure of FAP (“SFX dark”), solved at 2.0-Å resolution (table S2), features a FAD with a similar bending angle (14.3°) as observed in the synchrotron 100 K dark and the “RT dark low-dose” structures (Fig. 1E and figs. S4, S6, and S7), supporting

the notion that in FAP, the FAD cofactor is in a bent conformation in the oxidized state. To our knowledge, a butterfly bent conformation of the oxidized flavin has not been firmly established for any other flavoprotein. In fact, bent conformations were either not discussed in the literature or were attributed to x-ray-induced flavin reduction. Future radiation-damage-free structures of oxidized flavoproteins should reveal whether the bending is a feature specific to FAP.

New insights into the CvFAP photocycle by time-resolved spectroscopy

Our previous single-shot fluorescence and transient absorption experiments in the presence of substrate, with 100 ps and 10 ns temporal resolution, respectively, showed a decay of the singlet excited flavin ($^1\text{FAD}^*$) in ~ 300 ps and formation of $\text{FAD}^{\bullet-}$ within 10 ns (4). Here, we extended the fluorescence and visible absorption experiments to the ultrafast time scale with 100-fs-resolution pump-probe spectroscopy (Fig. 2, A and B, and fig. S8A), showing that no faster $^1\text{FAD}^*$ decay phases occurred [only an ~ 2 -ps thermal relaxation phase was observed in the fluorescence as in other flavoproteins (30)] and that, as predicted (4), $\text{FAD}^{\bullet-}$ is formed concomitantly with $^1\text{FAD}^*$ decay (fig. S8B).

We investigated whether the carboxylate of the fatty acid is cleaved off concomitantly with electron transfer from the fatty acid to $^1\text{FAD}^*$ (~ 300 ps), after this oxidation, or accompanying the bET from flavin (~ 100 ns). Light-induced Fourier transform infrared (FTIR) difference spectroscopy performed at 298 K showed a CO_2 band at 2342 cm^{-1} (Fig. 2C), corresponding to CO_2 in solution (31). The kinetics of CO_2 formation in FAP were monitored by picosecond to microsecond time-resolved infrared spectroscopy (TR-IR) in a frequency range centered around 2350 cm^{-1} and arbitrary detuning asynchronous optical sampling (ADASOPS) (32, 33). This experiment showed the appearance of a CO_2 absorption band centered at 2337.5 cm^{-1} with a time constant of ~ 270 ps (Fig. 2, C to E, and fig. S9). We conclude that decarboxylation is rate-limited by electron transfer from substrate to $^1\text{FAD}^*$, occurring in ~ 300 ps. The initial CO_2 band frequency is $\sim 5\text{ cm}^{-1}$ down-shifted with respect to that of $^{12}\text{CO}_2$ in aqueous solution, a finding that we assign to the protein environment. Subsequently, the CO_2 signal diminishes about fourfold with a time constant of 100 ns without changing much in shape, followed by an upshift toward 2342 cm^{-1} , a process fitted with a time constant of $\sim 1.5\text{ }\mu\text{s}$. The latter process likely reflects migration of CO_2 toward the solvent. The data indicate that the 100-ns process implies transformation of $\sim 75\%$ of the initially formed CO_2 within the protein into another molecule, possibly bicarbonate, concomitant with flavin reoxidation to the red-shifted form FAD_{RS} (see next

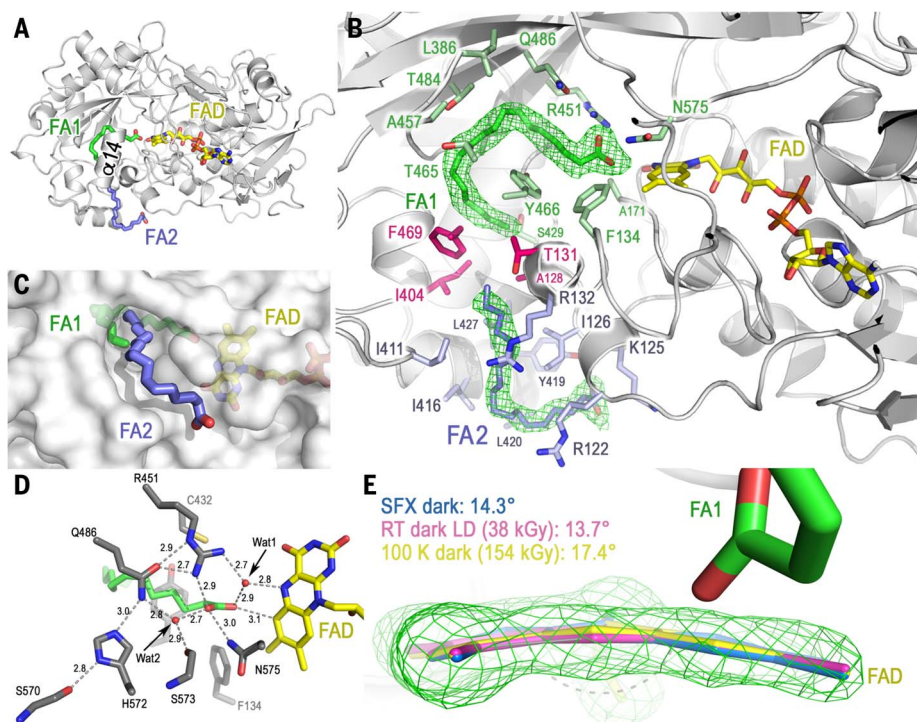


Fig. 1. High-resolution crystal structures of CvFAP. (A) Structure of CvFAP determined from synchrotron data at 100 K (100 K dark), including the FAD cofactor and two C18 fatty acid substrates (FA1 and FA2). (B) Binding of the two substrate molecules. The “omit” electron density map (5.0 σ contour level) is shown as a green mesh, and amino acid side chains in a radius of 4 Å around the binding site are shown as sticks (green: active site, blue: secondary binding site, purple: between sites). (C) Position of the peripheral substrate (FA2) partly obstructing the channel leading to the active site tunnel. (D) Close-up view of the catalytic site showing the water molecules Wat1 and Wat2 and the interactions with FAD (yellow sticks) and the substrate in the active site FA1 (green sticks). Distances are indicated in angstroms. The shortest distance between the substrate and the FAD cofactor (carboxylate O1-isoalloxazine C6) is 3.1 Å. The tail of the peripheral substrate points toward the entrance of a tunnel leading to the active site that is lined by A128, T131, I404, and F469. (E) Superposition of the FAD isoalloxazine rings from the SFX dark structure (blue; molecule A) and the synchrotron structures (pink: RT dark low-dose; yellow: 100 K dark). The SFX $F_{\text{obs}} - F_{\text{calc}}$ omit map at 3 σ (green) is overlaid, and the FAD bending angles are indicated.

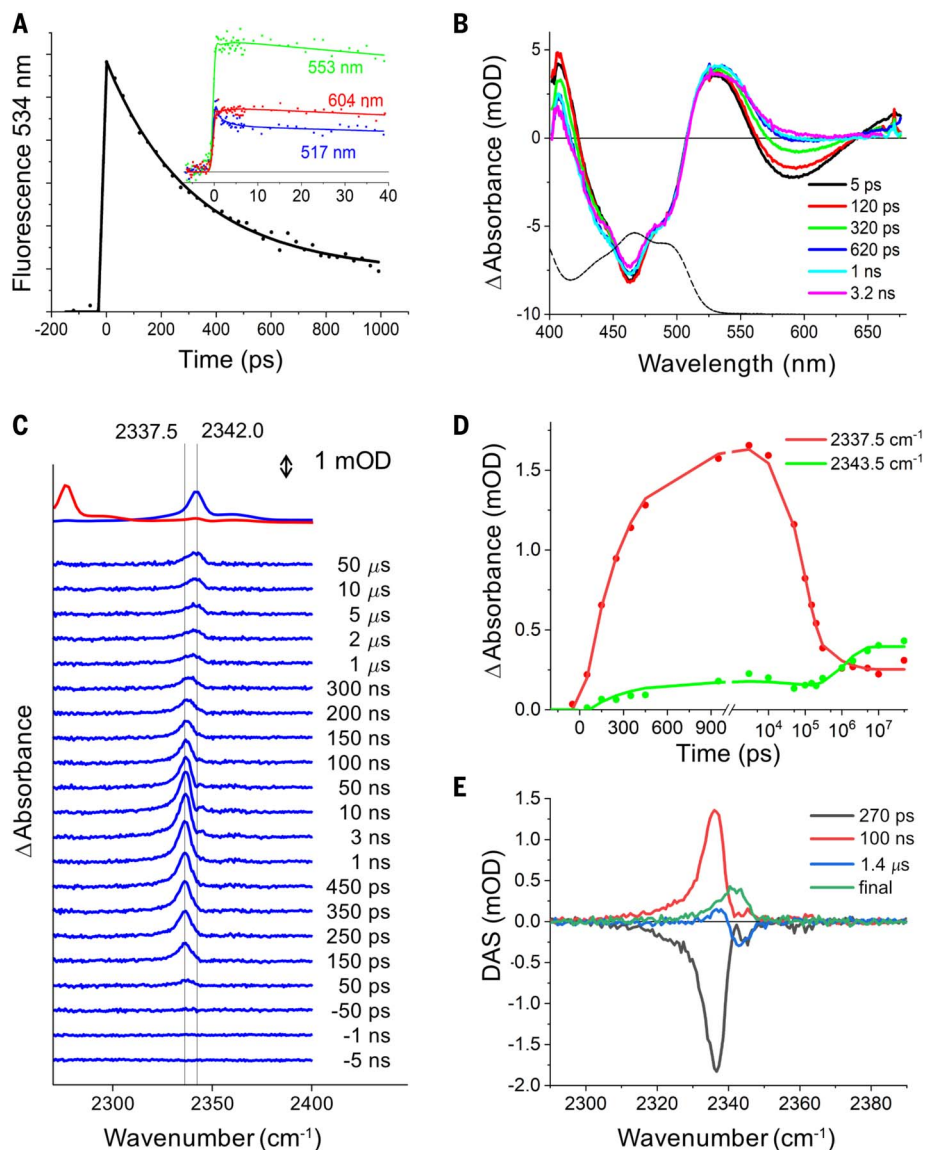


Fig. 2. Time-resolved infrared and UV-Vis spectroscopies of CvFAP. (A) Fluorescence kinetics reflecting $^1\text{FAD}^*$ decay. The solid line is a fit with time constants of 300 ps (85%) and 5 ns [the latter time constant was imposed according to (4)]. The inset shows an additional ~ 2 ps wavelength-dependent phase reflecting red shifting of the fluorescence spectrum caused by excited-state relaxation. (B) Transient visible absorption spectra at different delay times in the same time domain. The negative absorption features reflect bleaching of the FAD_{ox} resting state (<525 nm, the black dashed line is the ground state absorption spectrum) and stimulated emission (550 to 650 nm). Full transient fluorescence spectra and global analysis of the transient absorption spectra are shown in fig. S8. (C) Transient infrared spectra in the CO_2 spectral region on the picosecond-microsecond time scale. The vertical lines are guides for the eye and correspond to the maximum of released CO_2 in the protein and to the known maximum for CO_2 in aqueous solution, 2342 cm^{-1} (31). The upper traces correspond to independent steady-state 298 K light-induced FTIR difference spectra with ^{12}C -palmitate and ^{13}C -palmitate substrates (blue trace and red trace, respectively). (D) Kinetics at frequencies close to the initial and final maxima of released CO_2 . The lines are the result of a global fit. The time scale is linear up to 1 ns and logarithmic thereafter. (E) Decay-associated spectra (DAS) corresponding to a global fit of the data with three exponential phases (time constants of the fit are indicated) and a constant phase.

section on the red-shifted intermediate). This process was not foreseen in our previously proposed reaction scheme (4). Whereas our present data covering six orders of magnitude in time can be reasonably well described with

these three exponential processes and a constant phase (Fig. 2E), it is possible that an additional phase of CO_2 release into the solvent occurs on a time scale exceeding $50\ \mu\text{s}$, the temporal window of our present experiments.

To determine whether any of the reaction steps are coupled to or directly reflect PT or HAT, we compared the kinetics of all steps observable by continuous-probe time-resolved fluorescence or transient absorption spectroscopy in H_2O and D_2O buffers. The biphasic fluorescence signal showing the decay of $^1\text{FAD}^*$ [caused by quenching by ET from the substrate (300 ps phase; $>80\%$) and by the intersystem-crossing to a nonreactive triplet state (~ 6.5 ns phase; $<20\%$)] was not visibly affected by the isotope exchange (Fig. 3A), as expected for reactions that are not substantially coupled to movements of exchangeable hydrogen species [e.g., back-ET from Q_A^- to P680^+ in photosystem II (34)]. By contrast, the kinetics of FAD^* -reoxidation to FAD_{RS} observed by transient absorption spectroscopy at three characteristic wavelengths slowed down by a factor of ~ 2 , from ~ 100 ns in H_2O to ~ 200 ns in D_2O (Fig. 3B), suggesting that this bET step is coupled to and limited by transfer of an exchangeable proton or hydrogen atom. Change of buffer pH in the interval between 7.5 and 9.1 had no effect on the kinetics of this step (fig. S10A), indicating that the proton or hydrogen atom donor involved in the reaction has a pK_a value >9.1 (where K_a is the acid dissociation constant). The significantly lower kinetic isotope effect (KIE) of 1.2 reported by Heyes *et al.* (24) might be due to insufficient time-resolution of their experiment (see supplementary text S4).

The last step observable by transient absorption spectroscopy was the disappearance of the transient red shift of reoxidized FAD occurring in a few milliseconds. This process was previously (4) assigned to reprotonation of X^- , the conjugate base of XH , an unidentified proton donor to the alkyl radical. Kinetics of this process also slowed down from ~ 3 to ~ 10 ms when H_2O in the buffer was replaced by D_2O (Fig. 3C). Consistent with this observation and the recent report of a pH increase (in an unbuffered solution) associated with this step (24), this process apparently reflects a proton transfer from bulk solvent. Again, change of buffer pH in the interval between 7.5 and 9.1 had no effect on the kinetics of this step (fig. S10B), nor did the consumption of the native substrate (fig. S10C). Time-resolved spectroscopic findings are summarized in fig. S11.

Photodecarboxylation and characterization of the red-shifted intermediate at cryogenic temperatures

Our time-resolved spectroscopic results predicted that a fraction of the CO_2 product is present in the active site in the red-shifted photoproduct intermediate. For a detailed characterization by static methods, we tried to stabilize this intermediate using cryotrapping. UV-Vis absorption spectra of CvFAP crystals

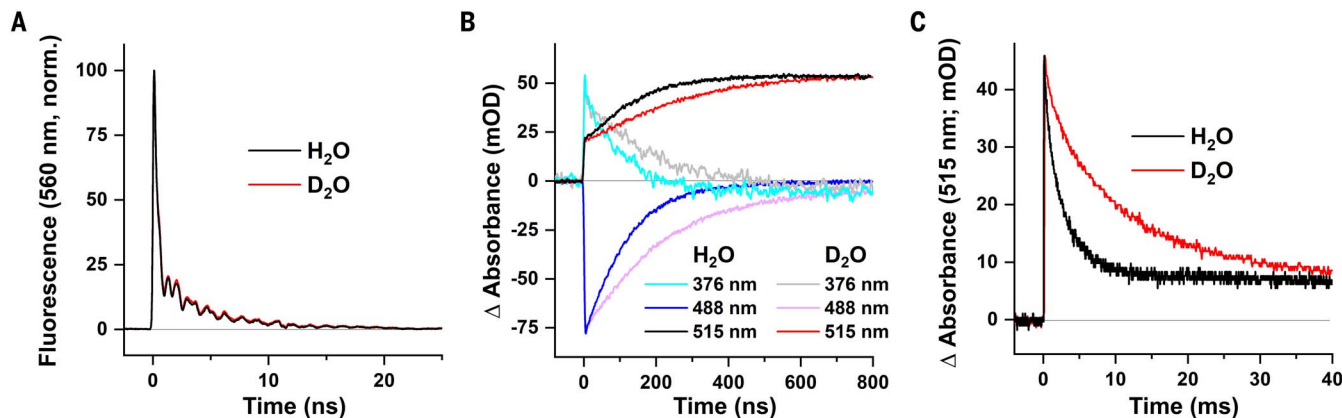


Fig. 3. Effects of H₂O-D₂O exchange on time-resolved fluorescence and UV-Vis spectroscopy of CvFAP. (A) Normalized signals of time-resolved fluorescence of ¹FAD* at 560 nm in H₂O and D₂O buffers. (B) Effect of H₂O-to-D₂O exchange on the kinetics of FAD* reoxidation to FAD_{RS}, followed by transient absorption spectroscopy at selected wavelengths on a submicrosecond time scale. (C) Effect of H₂O to D₂O buffer exchange on the decay of FAD_{RS} measured at 515 nm on the millisecond time scale.

and solutions exposed to increasing amounts of blue light at 100 K indeed revealed the gradual conversion into a red-shifted form similar to that previously observed at RT [(4) and fig. S12]. These conditions were used to further characterize the red-shifted intermediate using light-induced FTIR difference spectroscopy. To identify IR modes of the substrate and products of the reaction, we replaced the native substrate with ¹⁻¹²C or ¹⁻¹³C palmitate. The identification of characteristic ¹³C-sensitive IR bands of carboxylate in the FTIR difference spectra at 1541 and 1391 cm⁻¹ shows that the substrate initially was in the deprotonated form (Fig. 4A, i and ii; details supporting all IR bands assignments mentioned below are given in supplementary text S2). A peak at 2340 cm⁻¹ (Fig. 4A, v) was assigned to formation of CO₂ from ¹⁻¹²C-palmitate and at 2274 cm⁻¹ from ¹⁻¹³C-palmitate. When comparing FTIR spectra recorded with FAP samples containing ¹⁻¹²C- and ¹⁻¹³C-palmitate, small bands were also observed at 1356 to 1335 cm⁻¹ and 1312 cm⁻¹ (Fig. 4A, iii), which is indicative of the formation of trace amounts of ¹²C and ¹³C bicarbonate, respectively. We repeated the FTIR experiments at 150 K. At this temperature, the CO₂ band was small (Fig. 4A, v), whereas large positive bands at 1646 (1614) and 1352 (1318) cm⁻¹ were detected that could be unambiguously assigned to IR modes of ¹²C- (¹³C-) bicarbonate (Fig. 4A, iv). The FTIR data thus demonstrate the buildup of bicarbonate at 150 K and indicate that its formation at 100 K is limited by an energy barrier.

The structure derived from a CvFAP crystal exposed to 470 nm light at 100 K (“100 K light”) featured FAP trapped in a FAD_{RS} state, as shown by in crystallo microspectrophotometry (fig. S12). The difference electron density map between 100 K light and 100 K dark displays strong and significant peaks only

around the substrate and FAD cofactor. These peaks can be fitted with a CO₂ molecule in addition to the alkyl chain stabilized in the active site (Fig. 4, B and C, and fig. S13, A to C). The positive difference electron density along the aliphatic tail of the substrate (from C13 to C15) and the 8° rotation of the side chain of Y466 indicates a correlated motion consistent with the strong electronic coupling observed by quantum chemistry between the substrate and Y466. To reflect the optimum pH of FAP in solution [pH 8.5 (4)] and to overcome thermal activation barriers, a FAP crystal was soaked at pH 8.5 and illuminated at 150 K (“150 K light”). After modeling alkane and a CO₂ molecule, the residual $F_o - F_c$ electron density map showed a positive density with a triangular shape close to C432, which we tentatively attributed to bicarbonate with 30% occupancy (Fig. 4D and fig. S14).

Time-resolved serial femtosecond crystallography of CvFAP

We investigated the structural changes occurring in FAP after photoexcitation at RT by a time-resolved SFX (TR-SFX) experiment (35) using a pump-probe scheme. Time-resolved fluorescence spectroscopy on FAP microcrystals established that the kinetics of fET are the same as in solution (supplementary text S5 and fig. S15). For TR-SFX at the Linac Coherent Light Source (LCLS), FAP microcrystals were photoexcited by picosecond 400-nm pump pulses and probed by femtosecond XFEL pulses after pump-probe delays of 20 ps, 900 ps, 300 ns, and 2 μs to cover time scales on which FAD reduction and FAD* reoxidation occur. The SFX dark state structure mentioned above was determined from the data in the absence of a pump laser pulse. Structural changes after photoexcitation were visualized as positive and negative peaks in difference Fourier electron density maps calculated between the

light and dark datasets ($F_{\text{obs}}^{\text{light}, \Delta t} - F_{\text{obs}}^{\text{dark}}$; Fig. 5A) at 2.2-Å resolution. The most prominent difference electron density peaks at all four time points were at the active site, with the highest negative peak (-5.5 to -10.1 σ, depending on the time point) at the position of the carboxyl group of the substrate, showing that light-induced decarboxylation occurred (Fig. 5A). At 900 ps, decarboxylation had occurred to a considerable extent, consistent with the 270-ps time constant determined by multiscale time-resolved IR spectroscopy (Fig. 2, C to E). At 300 ns and 2 μs, a strong negative peak was observed at Wat1 (-5.8, and -6.2 σ, respectively; Fig. 5A), but not on Wat2. We note the absence of positive difference electron density peaks associated with the photo-dissociated CO₂ in the vicinity of the substrate carboxyl group. A possible reason could be the small initial displacement of cleaved CO₂ relative to its position in the fatty acid, consistent with the structure determined based on an illuminated cryocooled crystal 100 K light (see fig. S13C for comparison). It is conceivable that the positive difference densities close to C432 in the 300-ns and 2-μs datasets (Fig. 5A) correspond to the feature(s) observed in the data obtained from cryocooled crystals illuminated at 150 K (Figs. 5B and 4D), tentatively assigned to a bicarbonate (fig. S14). In the SFX data, attempts to fit unambiguously this positive difference density with a bicarbonate, a CO₂ molecule, or a mixture thereof remained unsatisfactory. The absence of significant difference electron density peaks at the FAD at all four time points suggests that the isoalloxazine ring does not undergo significant light-induced conformational changes.

Quantum chemistry study of CvFAP

We performed quantum chemistry calculations for the decarboxylation reaction in the active site of FAP, considering electronic

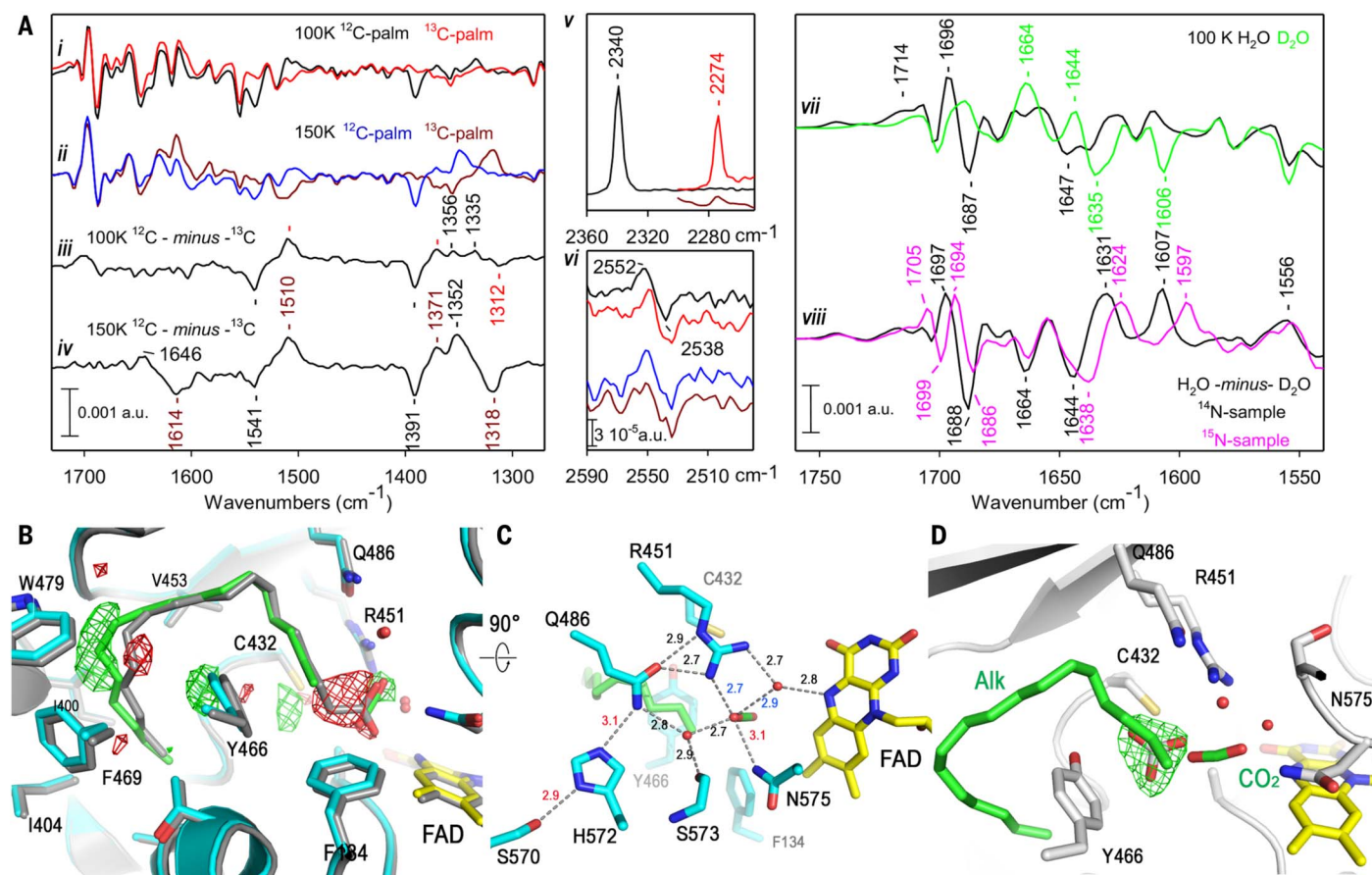


Fig. 4. Characterization of the CvFAP red-shifted intermediate at cryogenic temperatures. (A) Light-induced FTIR difference spectra recorded from FAP solutions (i) and (ii) and corresponding ^{12}C - minus ^{13}C difference spectra (iii) and (iv). The 2360 to 2260 cm^{-1} and 2590 to 2490 cm^{-1} regions of the spectra in (i) and (ii) are shown in (v) and (vi). For the spectrum in black, the FTIR spectrometer was continuously purged with N_2 to avoid contamination by gaseous CO_2 that might originate from a dry air purge. This was not the case for spectra recorded from FAP samples with ^{13}C -palmitate; these were cut off above 2300 cm^{-1} to avoid bands from gaseous CO_2 . (vii) Overlay of the spectra recorded at 100 K from FAP with ^{12}C -palmitate in H_2O (black) and in D_2O (green). (viii) H_2O - D_2O difference spectra calculated for ^{14}N - and ^{15}N -labeled FAP samples. (B) Experimental difference

density map ($F_{\text{light}} - F_{\text{dark}}$, 100 K data) contoured at $\pm 4\sigma$ around the active-site substrate superimposed on the refined structures of the dark state (gray) and the red-shifted form (cyan, with FAD in yellow and alkane and CO_2 in green). The cleavage of the C1-C2 bond is clearly visible. (C) Details of the active site of FAP_{RS} formed upon illumination (UV-Vis spectra in fig. S12). All distances shorter than 3.2 Å are labeled, except the fatty acid O1-FAD C6 distance, which increases from 3.1 Å in the dark to 3.6 Å upon illumination (in CO_2). (D) $F_{\text{o}} - F_{\text{c}}$ electron density omit map (3.5 σ) derived from crystals kept at 150 K and pH 8.5, showing positive difference electron density next to C432, consistent with a bicarbonate. Its potential interactions with the environment are shown in fig. S14. Uncleaved fatty acid (~30% occupancy) is omitted for clarity.

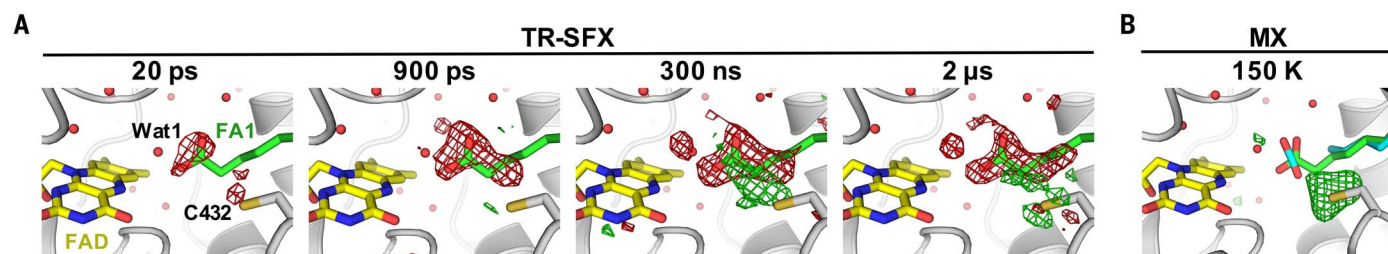


Fig. 5. Time-dependent changes in the CvFAP active site followed by TR-SFX. (A) Locally averaged q-weighted difference Fourier maps calculated between the SFX light and dark datasets ($F_{\text{obs}}^{\text{light}, \Delta t} - F_{\text{obs}}^{\text{dark}}$; with $\Delta t = 20$ ps, 900 ps, 300 ns, 2 μs). The 2.2-Å resolution maps are shown at $+4\sigma$ (green) and -4σ (red). The SFX dark-state model of molecule B is overlaid, with FAD in yellow, fatty acid in green, and the protein in gray. The q-weighted difference

maps for molecules A and B, i.e., without local averaging, are shown in fig. S31. (B) $F_{\text{obs}} - F_{\text{calc}}$ electron density (contoured at 3.5 σ) of Fig. 3E, shown in a different orientation, which features unmodeled positive electron density next to C432 that is reminiscent of a bicarbonate (Fig. 4D and fig. S14, see text), in a location similar to where positive difference density is present in the time-resolved maps at 300 ns and 2 μs .

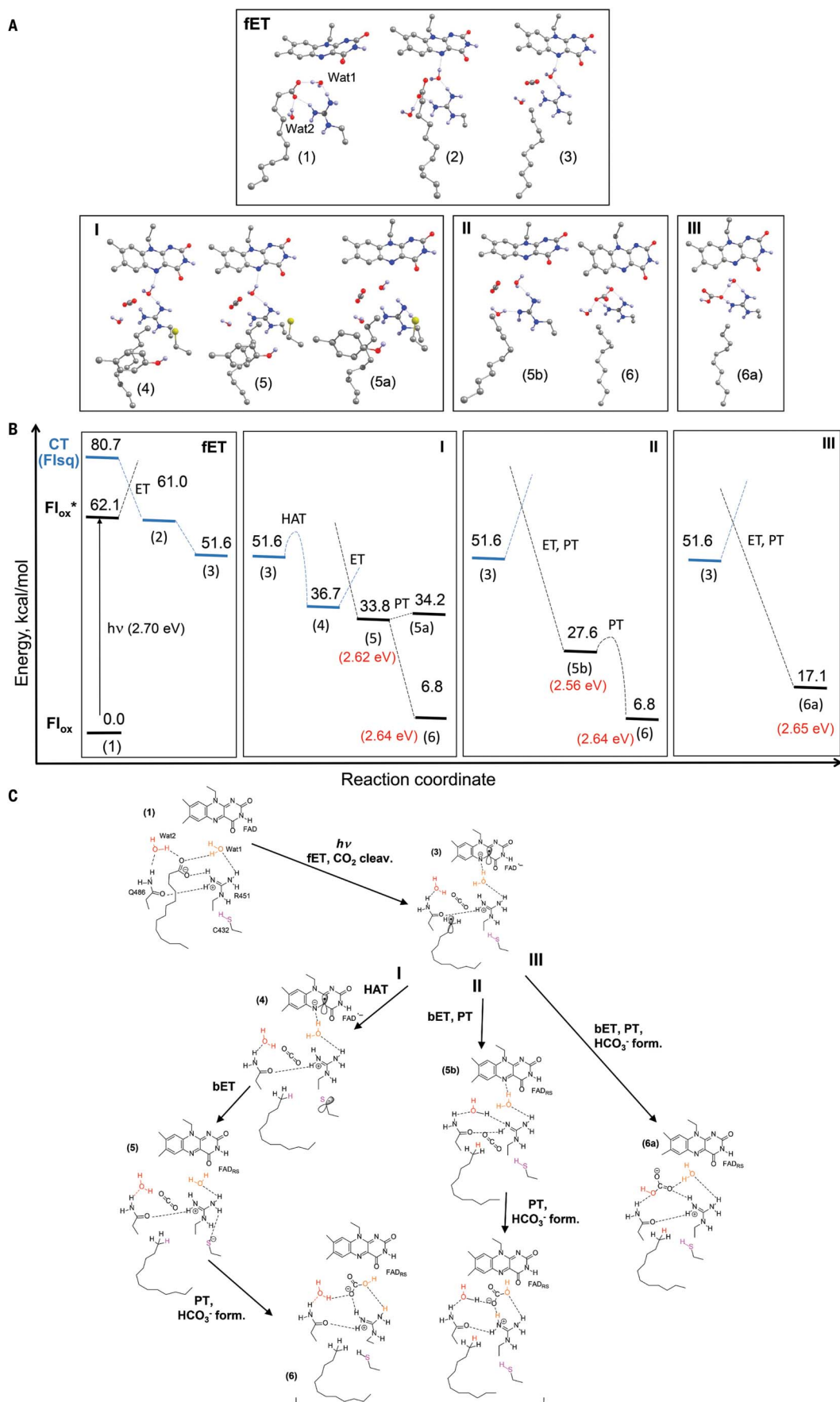


Fig. 6. Plausible CvFAP photoreaction pathways according to quantum chemistry calculations.

(A) Structural changes accompanying decarboxylation and alkane formation in the FAP active site. Flavin butterfly-bending angle is 15° and 19° in the oxidized and semiquinone states, respectively. For clarity, only a small part of the active-site model is shown. The complete model is presented in fig. S16. **(B)** Energies of the reactants, intermediates, and products indicated in (A). Common to all pathways is fET mediated by Wat1 rearrangement (1) → (2) followed by CO₂ cleavage (2) → (3). Alkane formation occurs either

through HAT (pathway I) or PCET (pathways II and III). Pathway I consist of alkane formation through HAT from C432 (3) → (4), flavin reoxidation by the C432 radical (4) → (5), and C432 reprotonation and bicarbonate formation (5) → (6). Pathway II involves alkane formation through bET coupled to PT from Wat2 and subsequent R451 deprotonation (3) → (5b). Bicarbonate formation from CO₂ and Wat1 recovers protonated R451 (5b) → (6). In pathway III, bET is coupled to Wat2 deprotonation and formation of bicarbonate (3) → (6a). **(C)** Chemical scheme detailing intermediate states of fET and pathways I to III.

states relevant for flavin photoexcitation, electron transfer, decarboxylation, and alkane formation, as well as the effects of flavin bending (see supplementary text S6). To perform the reaction pathway calculations, a large active-site model (consisting of 272 atoms; fig. S16) was prepared using the coordinates of the high-resolution crystal structure of the dark state (Fig. 1D). Unexpectedly, computations indicated multiple routes to form an alkane in the FAP active site, as summarized in Fig. 6.

Common to all routes, photoexcitation triggered charge transfer (CT) from the substrate to the flavin. Interactions with two water molecules stabilized the anionic carboxylate substrate (1) (Fig. 6A). Removing these water molecules from the active site or rearranging Wat1 to form a hydrogen bond with flavin substantially decreased the energy of the CT state, i.e., of the flavin radical anion and the fatty acid radical (table S6). After Wat1 rearrangement, the CT energy was 15 kcal/mol lower than the excited-flavin energy (table S6). Concomitantly, electronic coupling between the flavin and substrate increased almost threefold, reaching 47 meV (table S7), thus favoring the transfer of an electron from the carboxylate. The formed carboxylic radical underwent a barrierless decarboxylation (fig. S17), affording the alkyl radical (3). The energy of the alkyl radical intermediate was 52 kcal/mol above the dark state (1), which corresponds to >80% of the photon energy (Fig. 6B). CO₂ dissociation increased the distance separation in the radical pair, and, accordingly, the electronic coupling between the alkyl and flavin radicals was only 7 meV (table S7).

From the alkyl radical (3), the alkane product (6/6a) can be formed through several reaction pathways (Fig. 6, pathways I to III). The chemical changes characterizing pathways I to III are summarized in Fig. 6C. HAT from a nearby residue has been discussed previously (4, 24). Our results indicate strong interactions with the Y466 phenolic side chain (electronic coupling 142 meV; table S7) that may facilitate migration of the alkyl radical toward Y466 and C432. The HAT reaction from C432 (Fig. 6, pathway I) proceeded through an energy barrier (9 kcal/mol; fig. S18) and led to a Cys-radical state (4) with a 15 kcal/mol lower energy than that of the alkyl radical intermediate (3). Reoxidation of the flavin by C432 (5) further reduced the energy by 3 kcal/mol (Fig. 6B). The

resulting thiolate anion was stabilized by a hydrogen bond with positively charged R451; however, proton transfer from R451 to C432 in (5) along the hydrogen bond yielding (5a) did not further reduce the energy (table S5). Therefore, it is likely that C432 reprotonation proceeds by a different mechanism (see below).

Alternatively to the HAT reaction involving C432, a proton can be transferred from Wat2, which stabilizes the alkyl radical (3). The shift of the negative charge from the flavin to the alkane by bET coupled to proton transfer from Wat2 led to a transient formation of a hydroxyl anion which either interacted with CO₂, forming bicarbonate (6a) directly (Fig. 6, pathway III), or deprotonated R451 (5b) (Fig. 6, pathway II). The presence of CO₂ and water molecules in the active site, in particular Wat1, allows R451 reprotonation concomitant with bicarbonate formation (6), even after the alkane was formed, with a small activation energy (4 kcal/mol; fig. S19). The bicarbonate product derived from Wat1 (6) was 10 kcal/mol lower than the bicarbonate originating from Wat2 (6a), rendering pathway II more energetically favorable than pathway III (Fig. 6B). Energy lowering by bicarbonate formation may also further stabilize product (5) of the HAT reaction (pathway I); in the first step, the thiolate C432 obtains a proton from R451 and/or Wat1 and in the second step, bicarbonate is formed from CO₂ and OH⁻ derived from Wat1 (6).

In view of the experimentally observed red-shifted reoxidized flavin intermediate, we compared the flavin excitation energy of the species resulting from the bET reaction and that of the initial dark state (Fig. 6B and table S8). Our computations suggest that the red shift can be explained by formation of various species in which the initial negative charge of the deprotonated carboxylate (1) is either neutralized by formation of CO₂ and deprotonated R451 (5) or shifted away from the flavin by formation of the anionic bicarbonate (6) and (6a) (fig. S20). Additionally, a red-shifted spectrum is caused by hydrogen-bonding interactions of Wat1 with flavin in (5a).

Consistent with the x-ray structures, all active-site models contained the butterfly-bending conformation of the flavin isoalloxazine ring. Flavin bending persisted during geometry optimization of the FAP active-site models (Fig. 6A), in contrast to the essentially

planar optimized geometry of the oxidized and semireduced forms obtained in computations of flavins (36). The significant bending angle in the optimized FAP active-site structures is consistent with the notion that interactions with the protein modulate flavin bending (37). As previously discussed, this bending biases the energy levels of the flavin, favoring flavin reduction (36) and decreasing the excitation energy (table S9), with possible functional implications. In particular, bending diminishes the vertical electron affinity even more than the excited-flavin energy (fig. S21) and thus preferentially reduces the CT-state energy, which should facilitate fET. Thus, flavin bending explains the strongly red-shifted (20-nm) ground-state FAD absorption spectrum of FAP in the dark state compared with free FAD or most flavoproteins, allowing photoexcitation and facile fET up to as far as 530 nm. This is well into the so-called “green gap” (between 500 and 600 nm) in the absorption spectra of chlorophylls that dominate the absorption of algae, thus enhancing the net light-harvesting capacities of FAP.

Role of conserved amino acids in the FAP active site

The active site of CvFAP contains three residues (Y466, C432, and R451) that are strictly conserved and specific to FAPs compared with other GMC oxidoreductases (fig. S23). Y466 and C432 were previously considered as hydrogen atom donor to the alkyl radical R• (followed by bET from FAD⁻ to the tyrosyl or cysteinyl radical) or, alternatively, proton donor in a proton-coupled back-ET from FAD⁻ to R• (4, 24). Our quantum chemical calculations additionally suggest R451 as a potential proton donor. To identify the proton donor experimentally, we performed FTIR; in particular, we analyzed possible contributions from deprotonated forms of these three residues in the cryotrapped red-shifted intermediate. Light-induced FTIR difference spectra of CvFAP recorded at 100 K showed only a shift of a ν (S-H) IR mode of cysteine, and no changes in D₂O compared with H₂O that could be assigned to tyrosine vibrations, which does not support deprotonation of either of the two residues under conditions in which the flavin red shift was observed (Fig. 4A, vi, and supplementary text S2). However, a strong negative band was observed at 1606 cm⁻¹ in

FTIR difference spectra recorded in D₂O (Fig. 4A, vii). In ¹⁵N-labeled FAP samples, this band downshifted to 1597 cm⁻¹ (Fig. 4A, viii). Both observations support assignment of the band to the guanidium IR mode of an arginine side chain. Absence of a positive counterpart of this band after illumination is indicative of arginine deprotonation in the FAD_{RS} state at 100 K (see supplementary text S2).

To gain further insight into the role of Y466, C432, and R451, we prepared Y466F, C432S, R451A, and R451K mutants and performed activity measurements and extensive structural and spectroscopic characterization (UV-Vis absorption spectra are shown in fig. S24). Mutation of Y466 to phenylalanine affected the catalytic activity only slightly (Fig. 7A), consistent with a previous report (24). The kinetics of both fET to FAD and bET from FAD^{•-} did not differ much from wild-type (WT) CvFAP (fig. S25C). Furthermore, almost identical FTIR difference spectra were obtained with WT CvFAP and the Y466F mutant (fig.

S26A). Altogether, these results suggest that Y466 does not directly participate in any PT/HAT or ET step in the FAP photocycle, and its role is only briefly discussed in the supplementary text S4.

Mutation of C432 to serine (a much poorer proton and hydrogen atom donor) strongly affected the catalytic activity (Fig. 7A), as reported earlier by Heyes *et al.*, who considered it indicative of HAT from C432 to the alkyl radical R[•] in the WT protein (24). In contrast to these authors, we detected a low but significant catalytic activity (~10% of WT) for the C432S mutant. Because impairment of the catalytic activity by a point mutation may result from structural changes rather than suppression of a direct function of the replaced residue, we examined the C432S mutant protein in more detail. The dark-state crystal structure of C432S was highly similar to WT except for a new water molecule, Wat3, interacting with S432 (2.7 Å) and the O1 oxygen atom of the fatty acid carboxylate (2.5 Å),

which was rotated by ~42° (Fig. 7D). The distance of the carboxylate O2 the flavin N5 increased from 4.0 Å in WT to 5.0 Å.

The time-resolved fluorescence signal of C432S resembled that of WT after the consumption of native substrate(s); however, the fluorescence decay was slightly (~10%) accelerated (Fig. 7B), indicating that the signal reflects mostly intrinsic ¹FAD* decay [mostly because of intersystem crossing (ISC) (4)], with only a small contribution of competing fET to ¹FAD*. The intrinsic fET rate was ~10× slower than ¹FAD* decay in this mutant (see supplementary text S3). Transient absorption signals on the submillisecond time scale were thus dominated by the triplet (fig. S25F), and the formation of FAD_{RS} could not be resolved. There was, however, a small (~15% of WT) long-lived absorption change at 515 nm (where the transient flavin red shift is most prominent in the WT). About two-thirds of it decayed in a few milliseconds, i.e., with similar kinetics as FAD_{RS} in WT [see upper inset of fig.

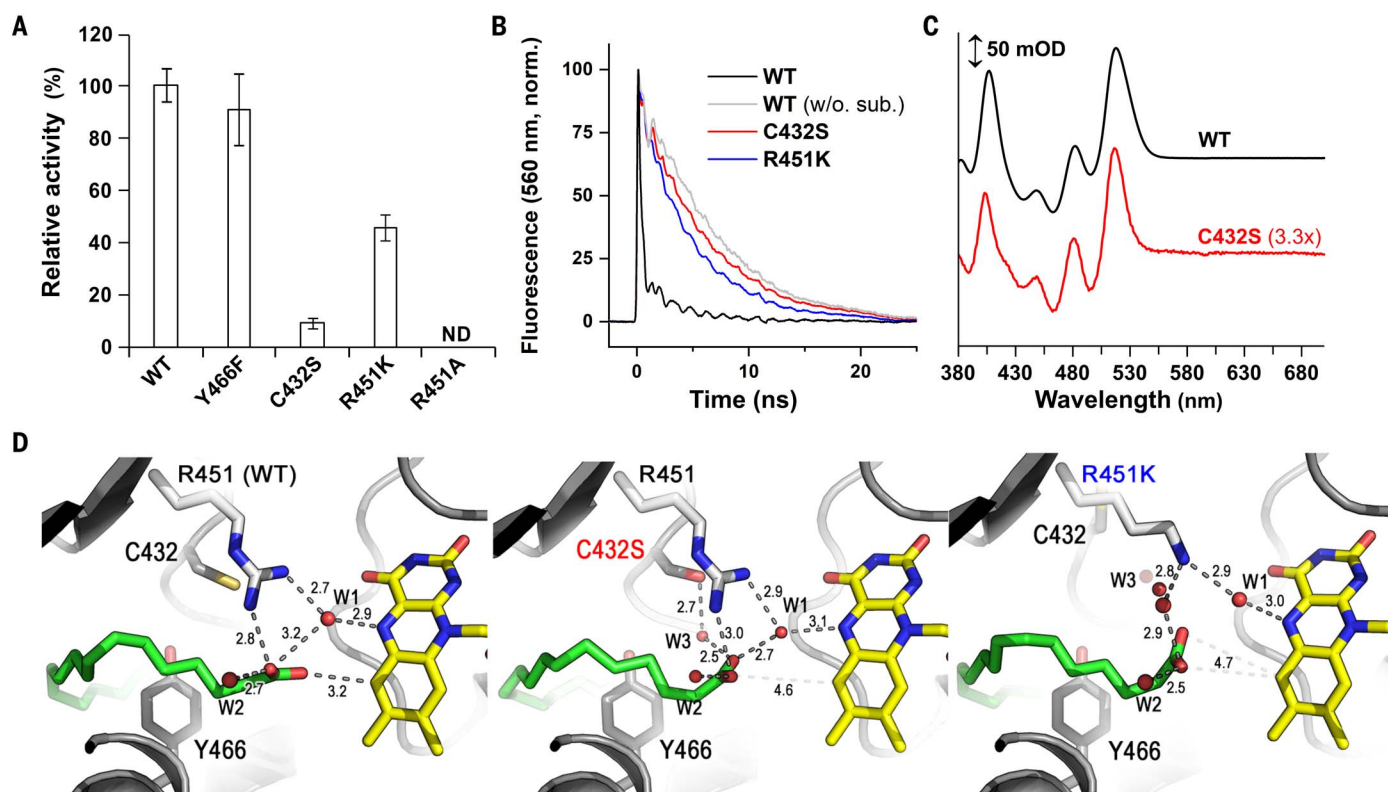
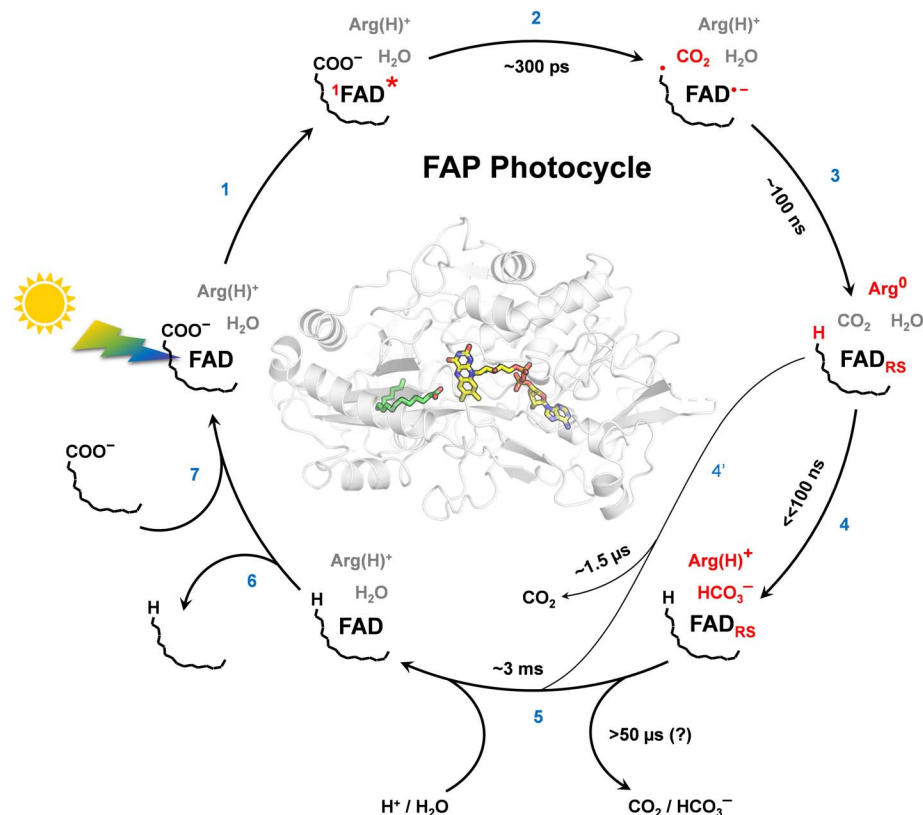


Fig. 7. Impact of mutations of conserved residues on CvFAP activity, ¹FAD* fluorescence decay, spectrum of cryotrapped FAD_{RS}, and active-site structure.

(A) Activities of purified recombinant mutant CvFAPs relative to WT (measured by gas chromatography coupled with mass spectrometry for the Y466F, R451K, and R451A mutants) in the presence of *cis*-vaccenic acid as substrate. Relative activity of the C432S mutant was measured by membrane inlet mass spectrometry to avoid activity underestimation due to low photostability of this particular mutant under continuous illumination conditions. All activities were normalized to FAD content. Mean ± SD is shown (*n* = 5 repeats). ND, not detected. (B) Normalized time-resolved

fluorescence at 560 nm of WT, C432S, and R451K CvFAP in the presence of native substrates (and after their consumption in WT); for Y466F and R451A mutants, see fig. S25B. (C) Light minus dark spectrum of WT and mutant C432S at 200K obtained by cryo-UV-Vis spectroscopy and normalized on FAD content. (D) Structure of the active site of the WT (left), C432S (middle), and R451K (right) mutants. Distances (in angstroms) between substrate (green), FAD (yellow), water molecules (red), and amino acid residues (white or gray) are shown. Compared with WT, in the C432S and R451K mutants, the FA carboxylate is rotated ~50° around an axis defined by the fatty acid atoms O2 and C2.

Fig. 8. Suggested CvFAP photocycle. Upon light excitation (1), fET in ~ 300 ps from the fatty acid anion to ${}^1\text{FAD}^*$ (observed by ultrafast fluorescence and transient absorption spectroscopies) leads to its quasi-instantaneous decarboxylation (2), as observed by TR-IR and TR-SFX and supported by the computed absence of an energy barrier. bET in ~ 100 ns from $\text{FAD}^{\bullet-}$ (presumably to the alkyl radical) results in formation of red-shifted (re-) oxidized flavin FAD_{RS} ; the H/D KIE suggests that bET is coupled to and/or limited by PT. Cryotrapping FTIR experiments suggest arginine as the final proton donor to the alkyl (3). Concomitantly, most CO_2 ($\sim 75\%$) is transformed (4) to bicarbonate as indicated by TR-IR and cryotrapping FTIR. FAD_{RS} disappears in ~ 3 ms (5) with a H/D KIE > 3 , indicating coupling to PT. Upon alkane release (6), new substrate binds (7). About 25% of the formed CO_2 is not transformed to bicarbonate, likely because it migrates away from the active site within 100 ns, leaving the protein in ~ 1.5 μs (4'). In this minor fraction, arginine (R451) should reprotonate at latest in the ~ 3 ms step (5). Changes after individual steps are marked in red; time constants are for RT.



S25F or figure 3D in [24]). With these indirect indications of FAD_{RS} formation in C432S, we attempted to accumulate this species at a cryogenic temperature. Illumination of the sample at 200 K yielded a spectrum with similar shape (but lower amplitude) as the FAD_{RS} spectrum obtained with WT FAP (Fig. 7C).

When R451 was mutated to alanine, the enzymatic activity was completely abolished (Fig. 7A) and no fET was observed (fig. S25B); in fact, the structure showed that the fatty acid was oriented very differently from that in the WT (see fig. S26D and supplementary text S3 and S4 for details).

When R451 was replaced by lysine (which is also positively charged), the catalytic activity amounted to $\sim 45\%$ of WT (Fig. 7A). The fluorescence decay (Fig. 7B) was distinctly faster (~ 4.5 ns) than in WT without substrate (~ 6.5 ns), consistent with fET occurring for $\sim 30\%$ of the excited flavins. Reoxidation of $\text{FAD}^{\bullet-}$ and formation of FAD_{RS} was clearly resolved and found to be markedly faster (~ 30 ns; fig. S25D) than in WT (~ 100 ns; Fig. 3B, fig. S10A, and supplementary text S3 and S4). The acceleration of the (proton-coupled) bET would be consistent with lysine being a better proton donor than arginine (solution $\text{p}K_{\text{a}}$ of Lys is 10.7 versus 12.1 for Arg).

To better understand how R451 affects the active-site architecture, we determined the crystal structure of the R451K mutant in its

dark state at 100 K (Fig. 7D and fig. S26C). The R451K mutant structure differed significantly from WT: Whereas a new water molecule mimicked the NH_2 group of R451 and thereby retained the interaction with the O2 oxygen atom of the fatty acid carboxylate (2.5 Å), the interaction between K451 and the fatty acid O1 oxygen atom induced an $\sim 54^\circ$ rotation of the carboxylate and an increase by 0.6 Å of the distance of the fatty acid O2 to the flavin N5 compared with WT. This created space for a new water molecule, Wat3, akin to the situation in C432S, located between the fatty acid O1 atom (2.4 Å) and K451 (2.8 Å). The close distance of Wat3 and C432 induced a flip of the amino acid stretch T430 to G435, pushing C432 out of the active site and bringing in an additional water molecule. These large structural changes may explain the very different FTIR spectra obtained with the R451K mutant compared with WT (fig. S26B).

Reaction cycle of FAP

Consistent with the strict conservation of C432 and R451 in FAP sequences, even conservative substitutions of these residues resulted in drastic reductions in catalytic activity, in both cases by strongly reducing fET. Unexpectedly, the R451K and C432S mutants shared significant structural modifications with respect to the WT: the presence of a new water molecule, Wat3, close to the fatty acid carboxylate, a rotation of

the carboxylate by $\sim 50^\circ$, a significant elongation of the distance of the fatty acid carboxylate to the flavin N5, as well as small changes in Wat1 location. Quantum chemistry calculations showed that in the C432S mutant, the CT energy increased by 0.2 eV and the electronic coupling reduced fivefold, which is consistent with a much slower observed fET (see supplementary text 6.7 and fig. S22).

These mutants provide important insights into the molecular constraints affording FAP activity: The active site of the WT enzyme is arranged such as to optimize the configuration of the fatty acid carboxylate for fET. Each carboxylate oxygen atom interacts with catalytically important groups (O1: Wat1, O2: R451 and Wat2) while avoiding an inactivating bidentate interaction with R451.

Three possible routes toward alkane formation in FAP were suggested by quantum chemistry (Fig. 6C). Our experimental findings allow assessing the suggested pathways. Pathway I, involving a HAT mechanism to reduce the alkyl radical, as also suggested previously (4, 24), is chemically plausible. However, a number of experimental findings argue against it. First, the C432S mutant retains significant enzymatic activity, suggesting that C432 is not essential for catalysis. Second, in the FAD_{RS} state, only a shift of a thiol S-H vibration is observed by FTIR but no cysteine deprotonation. Third, despite the fact that C432 is

rotated out of the active site in the R451K mutant, this variant is quite active. Although it is possible that C432 rotates back into the active site upon changes in the water structure after CO₂ cleavage, this would not explain the threefold faster bET in R451K. Reaction pathway I (Fig. 6C) seems unlikely, although we cannot rule out that the C432S mutant uses a different mechanism than the WT enzyme. The observation of residual electron density consistent with bicarbonate close to C432 suggests that C432 may stabilize reaction products such as CO₂ and/or bicarbonate away from the original position of the substrate carboxylate.

The other two pathways proceed through PCET (Fig. 6C). Pathway III implies a catalytic role of Wat2 in bicarbonate formation. This mechanism is unlikely, as no changes were observed for Wat2 in the electron density maps derived by TR-SFX. By contrast, 300 ns after photoexcitation, a significant loss of electron density of Wat1 was observed, supporting pathway II. With the cleaved CO₂ present in the active site, as evidenced by cryocrystallography and IR spectroscopy, Wat2 can serve as a proton donor. The transiently deprotonated R451 activates Wat1, resulting in bicarbonate formation in <100 ns. This transformation of CO₂ to bicarbonate is orders of magnitude faster than in solution [tens of seconds (38)], indicating a strong catalytic effect.

R451's role as transient proton donor was a priori unexpected because proton transfers from and to arginine residues are rare (39, 40) due to their relatively high pK_a values. In FAP, the strong basicity of OH⁻ formed from Wat2 by proton-coupled ET to the alkyl radical may allow proton transfer from R451. In addition to this catalytic function, R451 is crucial for the FAP active-site architecture by precisely positioning and orienting the fatty acid head group with respect to FAD and stabilizing the carboxylate in the catalytically active deprotonated form.

Fig. 8 and its legend summarize our comprehensive understanding of the very complex cycle. By combining results obtained by a multitude of experimental techniques and computations, we provide a detailed mechanistic description of the evolution of the reactant (fatty acid) to the products [alka(e)ne and CO₂] and the role of the protein moiety involving a proton-coupled electron-transfer mechanism. We demonstrate partly unexpected structural and dynamic properties of FAP, including features that have not been observed in other flavoproteins and other enzymatic reactions in general. Understanding these catalytic features is an important step in incorporating FAP into the green chemistry toolkit.

Materials and methods summary

The FAP used in all experiments corresponds to residues 76 to 654 of the full-length C_vFAP

(or single mutants thereof obtained by site-directed mutagenesis). WT C_vFAP and C_vFAP mutants expressed in *Escherichia coli* and purified were studied by x-ray crystallography (static and TR-SFX), spectroscopy in solution (FTIR, TR-IR on picosecond to microsecond time scales, time-resolved fluorescence spectroscopy on picosecond to nanosecond time scales, transient absorption spectroscopy on nanosecond to millisecond time scales, and ultrafast visible absorption and fluorescence spectroscopy) and spectroscopy on single crystals (UV-Vis and Raman). Activity assays were based on quantification of hydrocarbons formed (by gas chromatography coupled to mass spectrometry) or CO₂ released (by membrane inlet mass spectrometry). Computational studies involved molecular dynamics simulations and quantum chemistry calculations on C_vFAP and multiple alignments of GMC oxidoreductase protein sequences. Detailed materials and methods are available in the supplementary materials.

REFERENCES AND NOTES

- L. O. Bjorn, "Photoactive proteins," in *Photobiology: The Science of Light and Life* (Springer, ed. 3, 2015), pp. 139–150.
- A. Sancar, Mechanisms of DNA repair by photolysis and excision nuclease (Nobel Lecture). *Angew. Chem. Int. Ed.* **55**, 8502–8527 (2016). doi: [10.1002/anie.201601524](https://doi.org/10.1002/anie.201601524); pmid: [27337655](https://pubmed.ncbi.nlm.nih.gov/27337655/)
- M. Gabruk, B. Mysliwa-Kurziel, Light-dependent protochlorophyllide oxidoreductase: phylogeny, regulation, and catalytic properties. *Biochemistry* **54**, 5255–5262 (2015). doi: [10.1021/acs.biochem.5b00704](https://doi.org/10.1021/acs.biochem.5b00704); pmid: [26230427](https://pubmed.ncbi.nlm.nih.gov/26230427/)
- D. Sorigué et al., An algal photoenzyme converts fatty acids to hydrocarbons. *Science* **357**, 903–907 (2017). doi: [10.1126/science.aan6349](https://doi.org/10.1126/science.aan6349); pmid: [28860382](https://pubmed.ncbi.nlm.nih.gov/28860382/)
- D. Zhong, Ultrafast catalytic processes in enzymes. *Curr. Opin. Chem. Biol.* **11**, 174–181 (2007). doi: [10.1016/j.cbpa.2007.02.034](https://doi.org/10.1016/j.cbpa.2007.02.034); pmid: [17353141](https://pubmed.ncbi.nlm.nih.gov/17353141/)
- M. J. Maul et al., Crystal structure and mechanism of a DNA (6-4) photolyase. *Angew. Chem. Int. Ed.* **47**, 10076–10080 (2008). doi: [10.1002/anie.200804268](https://doi.org/10.1002/anie.200804268); pmid: [18956392](https://pubmed.ncbi.nlm.nih.gov/18956392/)
- P. Müller, J. Yamamoto, R. Martin, S. Iwai, K. Brettel, Discovery and functional analysis of a 4th electron-transferring tryptophan conserved exclusively in animal cytochromes and (6-4) photolyases. *Chem. Commun. (Camb.)* **51**, 15502–15505 (2015). doi: [10.1039/C5CC06276D](https://doi.org/10.1039/C5CC06276D); pmid: [26355419](https://pubmed.ncbi.nlm.nih.gov/26355419/)
- A. Mees et al., Crystal structure of a photolyase bound to a CPD-like DNA lesion after in situ repair. *Science* **306**, 1789–1793 (2004). doi: [10.1126/science.1101598](https://doi.org/10.1126/science.1101598); pmid: [15576622](https://pubmed.ncbi.nlm.nih.gov/15576622/)
- D. J. Heyes, C. N. Hunter, I. H. M. van Stokkum, R. van Grondelle, M. L. Groot, Ultrafast enzymatic reaction dynamics in protochlorophyllide oxidoreductase. *Nat. Struct. Mol. Biol.* **10**, 491–492 (2003). doi: [10.1038/nsb929](https://doi.org/10.1038/nsb929); pmid: [12730687](https://pubmed.ncbi.nlm.nih.gov/12730687/)
- N. S. Scrutton, M. L. Groot, D. J. Heyes, Excited state dynamics and catalytic mechanism of the light-driven enzyme protochlorophyllide oxidoreductase. *Phys. Chem. Chem. Phys.* **14**, 8818–8824 (2012). doi: [10.1039/c2cp23789j](https://doi.org/10.1039/c2cp23789j); pmid: [22419074](https://pubmed.ncbi.nlm.nih.gov/22419074/)
- D. J. Heyes et al., Excited-state charge separation in the photochemical mechanism of the light-driven enzyme protochlorophyllide oxidoreductase. *Angew. Chem. Int. Ed.* **54**, 1512–1515 (2015). doi: [10.1002/anie.201409881](https://doi.org/10.1002/anie.201409881); pmid: [25488797](https://pubmed.ncbi.nlm.nih.gov/25488797/)
- S. Zhang et al., Structural basis for enzymatic photocatalysis in chlorophyll biosynthesis. *Nature* **574**, 722–725 (2019). doi: [10.1038/s41586-019-1685-2](https://doi.org/10.1038/s41586-019-1685-2); pmid: [31645759](https://pubmed.ncbi.nlm.nih.gov/31645759/)
- C.-S. Dong et al., Crystal structures of cyanobacterial light-dependent protochlorophyllide oxidoreductase. *Proc. Natl. Acad. Sci. U.S.A.* **117**, 8455–8461 (2020). doi: [10.1073/pnas.1920244117](https://doi.org/10.1073/pnas.1920244117); pmid: [32234783](https://pubmed.ncbi.nlm.nih.gov/32234783/)

- M. A. Emmanuel, N. R. Greenberg, D. G. Oblinsky, T. K. Hyster, Accessing non-natural reactivity by irradiating nicotinamide-dependent enzymes with light. *Nature* **540**, 414–417 (2016). doi: [10.1038/nature20569](https://doi.org/10.1038/nature20569); pmid: [27974767](https://pubmed.ncbi.nlm.nih.gov/27974767/)
- N. S. Scrutton, Enzymes make light work of hydrocarbon production. *Science* **357**, 872–873 (2017). doi: [10.1126/science.aao4399](https://doi.org/10.1126/science.aao4399); pmid: [28860372](https://pubmed.ncbi.nlm.nih.gov/28860372/)
- T. Courtney, A. Deiters, Recent advances in the optical control of protein function through genetic code expansion. *Curr. Opin. Chem. Biol.* **46**, 99–107 (2018). doi: [10.1016/j.cbpa.2018.07.011](https://doi.org/10.1016/j.cbpa.2018.07.011); pmid: [30056281](https://pubmed.ncbi.nlm.nih.gov/30056281/)
- S. Moulin et al., Continuous photoproduction of hydrocarbon drop-in fuel by microbial cell factories. *Sci. Rep.* **9**, 13713 (2019). doi: [10.1038/s41598-019-50261-6](https://doi.org/10.1038/s41598-019-50261-6); pmid: [31548626](https://pubmed.ncbi.nlm.nih.gov/31548626/)
- W. Zhang et al., Hydrocarbon synthesis via photoenzymatic decarboxylation of carboxylic acids. *J. Am. Chem. Soc.* **141**, 3116–3120 (2019). doi: [10.1021/jacs.8b12282](https://doi.org/10.1021/jacs.8b12282); pmid: [30673222](https://pubmed.ncbi.nlm.nih.gov/30673222/)
- M. Am et al., Low carbon strategies for sustainable bio-alkane gas production and renewable energy. *Energy Environ. Sci.* (2020).
- N. A. Herman, W. Zhang, Enzymes for fatty acid-based hydrocarbon biosynthesis. *Curr. Opin. Chem. Biol.* **35**, 22–28 (2016). doi: [10.1016/j.cbpa.2016.08.009](https://doi.org/10.1016/j.cbpa.2016.08.009); pmid: [27573483](https://pubmed.ncbi.nlm.nih.gov/27573483/)
- J. Xu et al., Light-driven kinetic resolution of α -functionalized carboxylic acids enabled by an engineered fatty acid photodecarboxylase. *Angew. Chem. Int. Ed.* **58**, 8474–8478 (2019). doi: [10.1002/anie.201903165](https://doi.org/10.1002/anie.201903165); pmid: [31033108](https://pubmed.ncbi.nlm.nih.gov/31033108/)
- D. Sorigué et al., Microalgae synthesize hydrocarbons from long-chain fatty acids via a light-dependent pathway. *Plant Physiol.* **171**, 2393–2405 (2016). doi: [10.1104/pp.16.00462](https://doi.org/10.1104/pp.16.00462); pmid: [27288359](https://pubmed.ncbi.nlm.nih.gov/27288359/)
- S. Moulin, A. Beyly, S. Blangy, B. Légeret, M. Floriani, A. Burlacot, D. Sorigué, Y. Li-Beisson, G. Peltier, F. Beisson, Fatty acid photodecarboxylation is an ancient photoenzyme responsible for hydrocarbon formation in the thylakoid membranes of algae. *bioRxiv* 166330 [Preprint]. 23 June 2020. <https://doi.org/10.1101/2020.06.23.166330>
- D. J. Heyes et al., Photochemical mechanism of light-driven fatty acid photodecarboxylase. *ACS Catal.* **10**, 6691–6696 (2020). doi: [10.1021/acscatal.0c01684](https://doi.org/10.1021/acscatal.0c01684); pmid: [32905273](https://pubmed.ncbi.nlm.nih.gov/32905273/)
- T. Senda, M. Senda, S. Kimura, T. Ishida, Redox control of protein conformation in flavoproteins. *Antioxid. Redox Signal.* **11**, 1741–1766 (2009). doi: [10.1089/ars.2008.2348](https://doi.org/10.1089/ars.2008.2348); pmid: [19243237](https://pubmed.ncbi.nlm.nih.gov/19243237/)
- A. K. Rohr, H.-P. Hersleth, K. K. Andersson, Tracking flavin conformations in protein crystal structures with Raman spectroscopy and QM/MM calculations. *Angew. Chem. Int. Ed.* **49**, 2324–2327 (2010). doi: [10.1002/anie.200907143](https://doi.org/10.1002/anie.200907143); pmid: [20187055](https://pubmed.ncbi.nlm.nih.gov/20187055/)
- A. Aleksandrov, A molecular mechanics model for flavins. *J. Comput. Chem.* **40**, 2834–2842 (2019). doi: [10.1002/jcc.26061](https://doi.org/10.1002/jcc.26061); pmid: [31471978](https://pubmed.ncbi.nlm.nih.gov/31471978/)
- H. N. Chapman et al., Femtosecond X-ray protein nanocrystallography. *Nature* **470**, 73–77 (2011). doi: [10.1038/nature09750](https://doi.org/10.1038/nature09750); pmid: [21293373](https://pubmed.ncbi.nlm.nih.gov/21293373/)
- K. Hirata et al., Determination of damage-free crystal structure of an X-ray-sensitive protein using an XFEL. *Nat. Methods* **11**, 734–736 (2014). doi: [10.1038/nmeth.2962](https://doi.org/10.1038/nmeth.2962); pmid: [24813624](https://pubmed.ncbi.nlm.nih.gov/24813624/)
- S. P. Laptinok et al., Ultrafast real-time visualization of active site flexibility of flavoenzyme thymidylate synthase ThyX. *Proc. Natl. Acad. Sci. U.S.A.* **110**, 8924–8929 (2013). doi: [10.1073/pnas.1218729110](https://doi.org/10.1073/pnas.1218729110); pmid: [23671075](https://pubmed.ncbi.nlm.nih.gov/23671075/)
- L. H. Jones, E. McLaren, Infrared Absorption Spectra of SO₂ and CO₂ in Aqueous Solution. *J. Chem. Phys.* **28**, 995 (1958). doi: [10.1063/1.1744329](https://doi.org/10.1063/1.1744329)
- L. Antonucci, A. Bonvalet, X. Solinas, L. Daniault, M. Joffre, Arbitrary-detuning asynchronous optical sampling with amplified laser systems. *Opt. Express* **23**, 27931–27940 (2015). doi: [10.1364/OE.23.027931](https://doi.org/10.1364/OE.23.027931); pmid: [26480451](https://pubmed.ncbi.nlm.nih.gov/26480451/)
- X. Solinas, L. Antonucci, A. Bonvalet, M. Joffre, Multiscale control and rapid scanning of time delays ranging from picosecond to millisecond. *Opt. Express* **25**, 17811–17819 (2017). doi: [10.1364/OE.25.017811](https://doi.org/10.1364/OE.25.017811); pmid: [28789272](https://pubmed.ncbi.nlm.nih.gov/28789272/)
- B. A. Diner, D. A. Force, D. W. Randall, R. D. Britt, Hydrogen bonding, solvent exchange, and coupled proton and electron transfer in the oxidation and reduction of redox-active tyrosine Y(2) in Mn-depleted core complexes of photosystem II. *Biochemistry* **37**, 17931–17943 (1998). doi: [10.1021/bi981894r](https://doi.org/10.1021/bi981894r); pmid: [9922161](https://pubmed.ncbi.nlm.nih.gov/9922161/)
- J.-P. Colletier, G. Schirò, M. Weik, "Time-resolved serial femtosecond crystallography, towards molecular movies of

- biomolecules in action," in *X-Ray Free Electron Lasers: A Revolution in Structural Biology*, S. Boutet, P. Fromme, M. S. Hunter, Eds. (Springer, 2018), pp. 331–356.
36. J. D. Walsh, A.-F. Miller, Flavin reduction potential tuning by substitution and bending. *J. Mol. Struct. THEOCHEM* **623**, 185–195 (2003). doi: [10.1016/S0166-1280\(02\)00719-4](https://doi.org/10.1016/S0166-1280(02)00719-4)
37. B. W. Lennon, C. H. Williams Jr., M. L. Ludwig, Crystal structure of reduced thioredoxin reductase from *Escherichia coli*: Structural flexibility in the isoalloxazine ring of the flavin adenine dinucleotide cofactor. *Protein Sci.* **8**, 2366–2379 (1999). doi: [10.1110/ps.8.11.2366](https://doi.org/10.1110/ps.8.11.2366); pmid: [10595539](https://pubmed.ncbi.nlm.nih.gov/10595539/)
38. N. McCann *et al.*, Kinetics and mechanism of carbamate formation from CO₂(aq), carbonate species, and monoethanolamine in aqueous solution. *J. Phys. Chem. A* **113**, 5022–5029 (2009). doi: [10.1021/jp810564z](https://doi.org/10.1021/jp810564z); pmid: [19338322](https://pubmed.ncbi.nlm.nih.gov/19338322/)
39. Y. Xiao, M. S. Hutson, M. Belenky, J. Herzfeld, M. S. Braiman, Role of arginine-82 in fast proton release during the bacteriorhodopsin photocycle: A time-resolved FT-IR study of purple membranes containing ¹⁵N-labeled arginine. *Biochemistry* **43**, 12809–12818 (2004). doi: [10.1021/bi049238g](https://doi.org/10.1021/bi049238g); pmid: [15461453](https://pubmed.ncbi.nlm.nih.gov/15461453/)
40. P. J. Silva, C. Schulz, D. Jahn, M. Jahn, M. J. Ramos, A tale of two acids: When arginine is a more appropriate acid than H₃O⁺. *J. Phys. Chem. B* **114**, 8994–9001 (2010). doi: [10.1021/jp100961s](https://doi.org/10.1021/jp100961s); pmid: [20553007](https://pubmed.ncbi.nlm.nih.gov/20553007/)

ACKNOWLEDGMENTS

We thank J. Woodhouse for help with microcrystallization, L. Uriarte for help with spectroscopy experiments on crystals, G. Nass Kovacs for preparation of injection conditions, M. Tarnawski for FAP stability measurements, F. Maia for helpful discussions and uploading the SFX data to CXIDB.org, M. Philibert and the GRAP platform for custom manufacturing of scientific equipment. The ESRF is acknowledged for access to beamlines via its in-house research program. This work used the iCOS Laboratory, which is a platform of the Grenoble Instruct-ERIC Centre (ISBG; UMS 3518 CNRS-CEA-UJF-EMBL) within the Grenoble Partnership for Structural Biology (PSB). The IBS acknowledges integration into the Interdisciplinary Research Institute of Grenoble (IRIG, CEA) and financial support by the CEA, the CNRS, and the UGA. The present work has benefited from the platform of Biophysics of I2BC supported by French

Infrastructure for Integrated Structural Biology (FRISBI) ANR-10-INBS-05 and from the platform Heliobiotec (BIAM). The experiments were performed at the Linac Coherent Light Source (LCLS), SLAC National Accelerator Laboratory. Use of the LCLS is supported by the U.S. Department of Energy, Office of Science, Office of Basic Energy Sciences under Contract no. DE-AC02-76SF00515. Part of the sample injector used at LCLS for this research was funded by the National Institutes of Health, P41GM103393, formerly P41RR001209. **Funding:** This work was supported by ANR SNAPsHOTs to F.B., M.W., P.M., K.B., M.H.V., P.A., R.H., and C.B.; ANR Photoalkane to G.P.; ANR SignalBioRNJ to Y.L.-B.; ANR BioXFEL to M.W.; ERC Consolidator Grant STepLADDER (724362) to T.R.M.B.; a Chinese Scholarship Council fellowship to B.Z.; and a MENESR–Univ. Grenoble Alpes fellowship to K.H.; a grant from the Chevreul Institute and the Ministère de l'Enseignement Supérieur et de la Recherche and the Région Nord-Pas de Calais (FEDER) to M.S. **Author contributions:** F.B., M.W., P.A., P.M., I.S., K.B., M.H.V., C.B., and T.D. designed and organized the project. J.-P.C., M.J., T.R.M.B., and A.R. supervised parts of the project. D.S., S. Blangy, P.S., S. Cuiñé, B.L., S.M., Y.L.-B., G.P., E.H., and F.B. analyzed FAP sequences, generated mutants, expressed and purified the FAPs, and performed activity assays. D.S., S. Blangy, E.H., and P.A. produced crystals for synchrotron experiments. P.A., G.G., A.R., D.N., P.L., I.S., and D.S. acquired synchrotron diffraction data. G.G., P.A., and A.R. performed *in crystallo* optical spectroscopies, and P.A., I.S., G.G., P.L., and A.R. interpreted these data. D.S., R.H., and C.B. built the setup for cryogenic light-induced FTIR difference spectroscopy and acquired and analyzed the data. A. Bonvalet, A. Benachir, and D.S. optimized and performed multiscale TR-IR experiments. L.A., X.S., A. Bonvalet, and M.J. conceived and developed multiscale TR-IR spectroscopy and adapted for FAP experiments. A. Bonvalet., L.A., M.J., and M.H.V. analyzed TR-IR data. M.H.V. performed and analyzed femtosecond pump-probe absorption and fluorescence spectroscopy. B.Z. and M.H.V. performed and analyzed picosecond-pump power dependence spectroscopy. A.A. performed molecular dynamics simulations. D.S., S. Blangy, and K.H. produced microcrystals for SFX experiments, and K.H., J.-P.C., and M.W. tested their diffraction quality at the ESRF. M.S., K.H., and D.S. performed time-resolved emission and absorption spectroscopy on microcrystals. T.R.M.B., M.C., S. Boutet, J.-P.C., N.C., R.B.D.,

L.F., A.G., M.L.G., K.H., M.H., M.K., T.J.L., G.S., I.S., R.L.S., and M.W. performed SFX experiments. R.L.S., R.B.D., M.L.G., and M.K. performed sample injection. S. Carbajo, G.S. and M.C. carried out laser work at the LCLS. S. Boutet and T.J.L. prepared and performed SFX data collection. L.F., M.H., N.C., J.P.C., and T.R.M.B. performed online SFX data analysis. K.H., N.C., J.-P.C., A.G., and T.R.M.B. performed offline SFX data processing. K.H., J.-P.C., N.C., M.W., T.R.M.B., and I.S. analyzed SFX data. M.B., K.B., and P.M. built the setups for picosecond-nanosecond time-resolved fluorescence and nanosecond-millisecond transient absorption spectroscopy. D.S., P.S., B.Z., P.M., and K.B. performed the measurements. P.M. and K.B. analyzed the data. T.D. performed quantum chemistry calculations and provided mechanistic insight. F.B., P.M., K.B., M.H.V., I.S., P.A., T.D., M.W., C.B., and D.S. wrote the paper. All authors discussed the results. **Competing interests:** L.A., X.S., A. Bonvalet, and M.J. are authors of a patent describing the general principle of ADASOPS (FR1155799, US10190972B2). The authors declare no other competing interests. **Data and materials availability:** All data are available in the manuscript, the supplementary materials, or at publicly accessible repositories. Atomic coordinates of protein structures have been deposited in the Protein Data Bank under accession nos. 6YRU, 6YRV, 6YRX, 6YRZ, 6YS1, 6YS2, 6ZH7, and 7AV4. SFX diffraction images of FAP microcrystals have been deposited in the Coherent X-ray Imaging Data Bank website (CXIDB) with accession ID 177 (<https://cxidb.org/id-177.html>).

SUPPLEMENTARY MATERIALS

science.sciencemag.org/content/372/6538/eabd5687/suppl/DC1
Materials and Methods
Supplementary Text S1 to S6
Figs. S1 to S31
Tables S1 to S11
References (41–121)
MDAR Reproducibility Checklist

[View/request a protocol for this paper from Bio-protocol.](#)

29 June 2020; accepted 17 February 2021
10.1126/science.abd5687

Mechanism and dynamics of fatty acid photodecarboxylase

D. Sorigué, K. Hadjidemetriou, S. Blangy, G. Gotthard, A. Bonvalet, N. Coquelle, P. Samire, A. Aleksandrov, L. Antonucci, A. Benachir, S. Boutet, M. Byrdin, M. Cammarata, S. Carbajo, S. Cuiñé, R. B. Doak, L. Foucar, A. Gorel, M. Grünbein, E. Hartmann, R. Hienerwadel, M. Hilpert, M. Kloos, T. J. Lane, B. Légeret, P. Legrand, Y. Li-Beisson, S. L. Y. Moulin, D. Nurizzo, G. Peltier, G. Schirò, R. L. Shoeman, M. Sliwa, X. Solinas, B. Zhuang, T. R. M. Barends, J.-P. Colletier, M. Joffre, A. Royant, C. Berthomieu, M. Weik, T. Domratcheva, K. Brettel, M. H. Vos, I. Schlichting, P. Arnoux, P. Müller and F. Beisson

Science **372** (6538), eabd5687.
DOI: 10.1126/science.abd5687

Light makes light work of fatty acids

Photosynthetic organisms are notable for their ability to capture light energy and use it to power biosynthesis. Some algae have gone a step beyond photosynthesis and can use light to initiate enzymatic photodecarboxylation of fatty acids, producing long-chain hydrocarbons. To understand this transformation, Sorigué *et al.* brought to bear an array of structural, computational, and spectroscopic techniques and fully characterized the catalytic cycle of the enzyme. These experiments are consistent with a mechanism starting with electron transfer from the fatty acid to a photoexcited oxidized flavin cofactor. Decarboxylation yields an alkyl radical, which is then reduced by back electron transfer and protonation rather than hydrogen atom transfer. The wealth of experimental data explains how algae harness light energy to produce alka(e)nes and provides an appealing model system for understanding enzyme-catalyzed photochemistry more generally.

Science, this issue p. eabd5687

ARTICLE TOOLS

<http://science.sciencemag.org/content/372/6538/eabd5687>

SUPPLEMENTARY MATERIALS

<http://science.sciencemag.org/content/suppl/2021/04/07/372.6538.eabd5687.DC1>

REFERENCES

This article cites 113 articles, 7 of which you can access for free
<http://science.sciencemag.org/content/372/6538/eabd5687#BIBL>

PERMISSIONS

<http://www.sciencemag.org/help/reprints-and-permissions>

Use of this article is subject to the [Terms of Service](#)

Science (print ISSN 0036-8075; online ISSN 1095-9203) is published by the American Association for the Advancement of Science, 1200 New York Avenue NW, Washington, DC 20005. The title *Science* is a registered trademark of AAAS.

Copyright © 2021 The Authors, some rights reserved; exclusive licensee American Association for the Advancement of Science. No claim to original U.S. Government Works

Rational Control of Off-State Heterogeneity in a Photoswitchable Fluorescent Protein Provides Switching Contrast Enhancement**

Virgile Adam⁺,^[a] Kyprianos Hadjidemetriou⁺,^[a] Nickels Jensen⁺,^[b] Robert L. Shoeman⁺,^[c] Joyce Woodhouse⁺,^[a] Andrew Aquila,^[d] Anne-Sophie Banneville,^[a] Thomas R. M. Barends,^[c] Victor Bezchastnov,^[c] Sébastien Boutet,^[d] Martin Byrdin,^[a] Marco Cammarata,^[e] Sergio Carbajo,^[d] Nina Eleni Christou,^[a] Nicolas Coquelle,^[a] Eugenio De la Mora,^[a] Mariam El Khatib,^[a] Tadeo Moreno Chicano,^[a] R. Bruce Doak,^[c] Franck Fieschi,^[a] Lutz Foucar,^[c] Oleksandr Glushonkov,^[a] Alexander Gorel,^[c] Marie Luise Grünbein,^[c] Mario Hilpert,^[c] Mark Hunter,^[d] Marco Kloos,^[c] Jason E. Koglin,^[d] Thomas J. Lane,^[d] Mengning Liang,^[d] Angela Mantovanelli,^[a] Karol Nass,^[c] Gabriela Nass Kovacs,^[c] Shigeki Owada,^[f, g] Christopher M. Roome,^[c] Giorgio Schirò,^[a] Matthew Seaberg,^[d] Miriam Stricker,^[c] Michel Thépaut,^[a] Kensuke Tono,^[f, g] Kiyoshi Ueda,^[h] Lucas M. Uriarte,^[i] Daehyun You,^[h] Ninon Zala,^[a] Tatiana Domratheva,^{*, [c, j]} Stefan Jakobs,^[b] Michel Sliwa,^[i] Ilme Schlichting,^[c] Jacques-Philippe Colletier,^[a] Dominique Bourgeois,^{*, [a]} and Martin Weik^{*, [a]}

Reversibly photoswitchable fluorescent proteins are essential markers for advanced biological imaging, and optimization of their photophysical properties underlies improved performance and novel applications. Here we establish a link between photoswitching contrast, one of the key parameters that dictate the achievable resolution in nanoscopy applications, and chromophore conformation in the non-fluorescent state of rsEGFP2, a widely employed label in REversible Saturable Optical Fluorescence Transitions (RESOLFT) microscopy. Upon illumination, the *cis* chromophore of rsEGFP2 isomerizes to two

distinct *off*-state conformations, *trans1* and *trans2*, located on either side of the V151 side chain. Reducing or enlarging the side chain at this position (V151A and V151L variants) leads to single *off*-state conformations that exhibit higher and lower switching contrast, respectively, compared to the rsEGFP2 parent. The combination of structural information obtained by serial femtosecond crystallography with high-level quantum chemical calculations and with spectroscopic and photophysical data determined *in vitro* suggests that the changes in switching contrast arise from blue- and red-shifts of the absorption bands

[a] Dr. V. Adam,⁺ Dr. K. Hadjidemetriou,⁺ Dr. J. Woodhouse,⁺ Dr. A.-S. Banneville, Dr. M. Byrdin, Dr. N. Eleni Christou, Dr. N. Coquelle, Dr. E. De la Mora, Dr. M. El Khatib, Dr. T. Moreno Chicano, Prof. Dr. F. Fieschi, Dr. O. Glushonkov, A. Mantovanelli, Dr. G. Schirò, M. Thépaut, N. Zala, Dr. J.-P. Colletier, Dr. D. Bourgeois, Dr. M. Weik
Univ. Grenoble Alpes, CEA, CNRS, Institut de Biologie Structurale, F-38044 Grenoble, France
E-mail: dominique.bourgeois@ibs.fr
weik@ibs.fr

[b] Dr. N. Jensen,⁺ Prof. Dr. S. Jakobs
Department of NanoBiophotonics, Max Planck Institute for Biophysical Chemistry, Göttingen, Germany and University Medical Center of Göttingen, Clinic for Neurology, Göttingen, Germany

[c] Dr. R. L. Shoeman,⁺ Dr. T. R. M. Barends, Dr. V. Bezchastnov, Prof. Dr. R. Bruce Doak, Dr. L. Foucar, A. Gorel, Dr. M. L. Grünbein, M. Hilpert, Dr. M. Kloos, Dr. K. Nass, Dr. G. Nass Kovacs, C. M. Roome, M. Stricker, Dr. T. Domratheva, Prof. Dr. I. Schlichting
Max-Planck-Institut für medizinische Forschung, Jahnstrasse 29, 69120 Heidelberg, Germany
E-mail: t.domratheva@lcc.chem.msu.ru

[d] Dr. A. Aquila, Dr. S. Boutet, Prof. Dr. S. Carbajo, Dr. M. Hunter, Dr. J. E. Koglin, Dr. T. J. Lane, Dr. M. Liang, Dr. M. Seaberg
Linac Coherent Light Source (LCLS), SLAC National Accelerator Laboratory, 2575, Sand Hill Road, Menlo Park, CA 94025, USA

[e] Dr. M. Cammarata
Department of Physics, UMR UR1-CNRS 6251, University of Rennes 1, Rennes, France

[f] Dr. S. Owada, Dr. K. Tono
RIKEN SPring-8 Center, Sayo, Japan

[g] Dr. S. Owada, Dr. K. Tono
Japan Synchrotron Radiation Research Institute, 1-1-1 Kouto, Sayo-cho, Sayo-gun, Hyogo 679-5198, Japan


[h] Prof. Dr. K. Ueda, Dr. D. You
Institute of Multidisciplinary Research for Advanced Materials, Tohoku University, Sendai 980-8577, Japan


[i] Dr. L. M. Uriarte, Dr. M. Sliwa
Univ. Lille, CNRS, UMR 8516, LASIR, Laboratoire de Spectroscopie pour les Interactions, la Réactivité et l'Environnement, Lille 59000, France

[j] Dr. T. Domratheva
Department of Chemistry, Lomonosov Moscow State University, Moscow 119991, Russia

[⁺] These authors contributed equally to this work

[**] A previous version of this manuscript has been deposited on a preprint server (DOI: <https://doi.org/10.1101/2021.11.05.462999>)

 Supporting information for this article is available on the WWW under <https://doi.org/10.1002/cphc.202200192>

 © 2022 The Authors. ChemPhysChem published by Wiley-VCH GmbH. This is an open access article under the terms of the Creative Commons Attribution Non-Commercial License, which permits use, distribution and reproduction in any medium, provided the original work is properly cited and is not used for commercial purposes.

6.2 Rational control of structural off-state heterogeneity in a photoswitchable fluorescent protein provides switching contrast enhancement

associated to *trans1* and *trans2*, respectively. Thus, due to elimination of *trans2*, the V151A variants of rsEGFP2 and its superfolder variant rsFolder2 display a more than two-fold higher switching contrast than their respective parent proteins, both *in vitro* and in *E. coli* cells. The application of the rsFolder2-

V151A variant is demonstrated in RESOLFT nanoscopy. Our study rationalizes the connection between structural and photophysical chromophore properties and suggests a means to rationally improve fluorescent proteins for nanoscopy applications.

Introduction

Reversibly switchable fluorescent proteins (RSFPs^[1,2]) are photochromic markers that are key to multiple super-resolution microscopy (nanoscopy) schemes including RESOLFT (Reversible Saturable Optical Fluorescence Transition^[3–5]), NL-SIM (Non Linear Structured Illumination Microscopy^[6]), SOFI (Super resolution Optical Fluctuation Imaging^[7]) and multicolor PALM (Photo Activated Localization Microscopy^[8]). They are also central tools in contrast enhancing approaches such as OLID (Optical Lock-In Detection microscopy^[9]) and in single channel multicolor approaches such as OPIOM (Out-of-Phase Imaging after Optical Modulation^[10]). With the exception of Dreiklang^[5] and its variant SPOON,^[11] RSFPs typically switch between a fluorescent *on*- and a non-fluorescent *off*-state through light-induced *cis-trans* isomerization of their p-hydroxybenzylidene

imidazolinone chromophore.^[1,12, 13] Depending on whether the same wavelength that induces fluorescence switches the RSFP from the *on*- to the *off*-state or *vice versa*, they are said to be negative or positive, respectively.^[14] At neutral pH, the chromophore of negative RSFPs (such as rsEGFP2 and its rsFolder variants studied here) is generally *cis*-anionic in the *on*-state and *trans*-protonated in the *off*-state, although exceptions have been reported in rsGamillus.^[15] *Off*-switching is promoted by illumination with wavelengths near the fluorescence excitation maximum (typically 488 nm) while *on*-switching requires illumination in the near UV region (typically 405 nm, Figure 1a).

In all nanoscopy applications relying on RSFPs as labels, image quality and the achievable spatial resolution are mainly determined by the following photophysical characteristics:^[14] i) the fluorescence brightness, being defined as the product of the extinction coefficient of the *on*-state and the fluorescence quantum yield, ii) the ensemble switching speed, *i.e.* the time required to switch the ensemble from the *on*- to the *off*-state, or *vice versa*, iii) the switching fatigue, being defined as the fraction of an RSFP ensemble being photobleached per full switching cycle, and iv) the switching contrast, that is, the ratio between the fluorescence signal after *on*-switching and the residual signal after *off*-switching. Such residual fluorescence after *off*-switching mainly originates from back switching of the *off*-state chromophore by the *off*-switching light.^[16] Among these characteristics, a high switching contrast is most critical for achieving high spatial resolution, and engineering efforts have thus been recently conducted to maximize it.^[15,17] If we neglect the possibility that the chromophore is not fully in the fluorescent *cis*-anionic state after *on*-switching,^[18] the switching contrast is a function of the *on*-to-*off* and *off*-to-*on* switching quantum yields and the extinction coefficients of both the *on*- and *off*-states at the *off*-switching wavelength (see eq. 1 in the Results section). In recent experimental^[19,20] and computational^[21] studies, it was proposed that the switching contrast is controlled by the relative stability of RSFPs in their *on*- and *off*-states *via* the number of hydrogen bonds between the chromophore and the protein pocket and its water molecules in each state. Here, focusing on rsEGFP2 and its rsFolder variants, we expand this view by showing how different conformations of the *off*-state chromophore modulate switching contrast, opening the door to rational optimization of RSFPs for enhanced nanoscopy applications.

rsEGFP2 (Figure 1a) has been generated based on EGFP and is widely applied in RESOLFT microscopy thanks to its fast maturation and favorable balance between fluorescence brightness, switching quantum yields, photofatigue resistance and switching contrast.^[22] Recently, evidence for conformational heterogeneity in the *off*-state of rsEGFP2 at room temperature was provided by serial femtosecond crystallography (SFX),

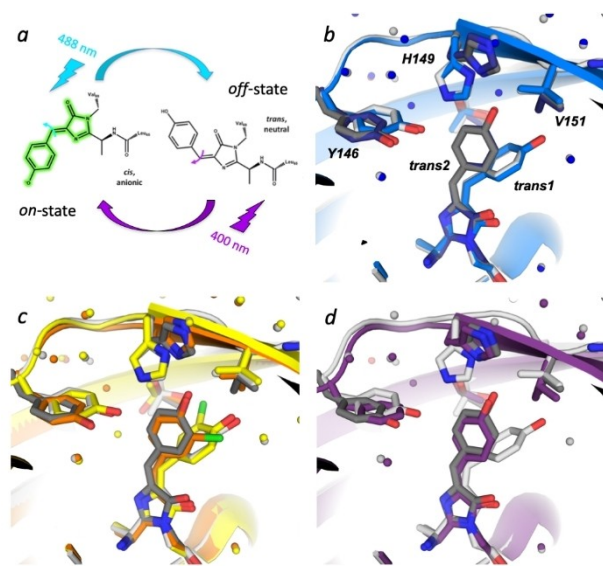


Figure 1. Photoswitching and *off*-state conformations in parental rsEGFP2. (a) rsEGFP2 can be photoswitched from the fluorescent *on*-state (anionic *cis* chromophore) to the non-fluorescent *off*-state (neutral *trans* chromophore) by illumination with 488 nm light, and back by illumination with 405 nm light. Photoswitching involves chromophore isomerization (blue and purple arrows on chromophore methylene bridge) and a change in protonation state of the phenol group. (b) Structures of parental rsEGFP2 in its *off*-state solved from RT SFX data. *Off*-state models of parental rsEGFP2 solved from RT SFX data earlier (PDB entry 6T39^[23]) and in this work (PDB entry 7O7U). *Trans1* and *trans2* are occupied at 40% (light grey) and 30% (dark grey) in parental rsEGFP2 (this work) and at 65% (light blue) and 25% (dark blue) in 6T39, respectively. (c, d) *Off*-state models of parental rsEGFP2 solved from RT SFX data in this work (light and dark grey), overlaid with *trans* conformations in synchrotron structures of rsEGFP2 containing a monochlorinated chromophore^[24] solved from crystals with looser (yellow) and tighter (orange) crystal packings^[24] (c) and with the *off*-state model of rsFolder (PDB entry 5DU0^[26]) in purple (d).

where in addition to the major *trans* state (*trans1* conformer), a hitherto unobserved *trans* isomer (*trans2* conformer) was observed,^[23] which displays different twist and tilt dihedral angles (ϕ and τ dihedral angles; see also Supplementary table S3), protein environment and H-bonding network (Supplementary Figure S1). Interestingly, cryo-crystallographic synchrotron data revealed a similar *trans2* isomer upon *off*-switching of an rsEGFP2 variant containing a monochlorinated chromophore when crystals with a contracted unit cell were examined, whereas a conformation similar to *trans1* was populated in crystals with a larger unit cell.^[24] *Trans1* and *trans2* conformers are located on either side of the V151 side chain (Supplementary Figure S1), a residue that needs to transiently retract for the chromophore to switch between its *cis* and *trans* conformations (see supplementary movie in^[25]) as suggested by time-resolved SFX.^[25] To start addressing the role of this residue in photoswitching, a variant with more space was generated by mutating V151 to an alanine.^[25] During the preliminary photophysical characterization^[25] neither the switching contrast or the structure of the rsEGFP2-V151A variant was analyzed nor was the sEGFP2-V151L control with a more bulkier side chain generated.

The *trans2* conformation in rsEGFP2 is also very similar to the *trans* conformation observed in the *off*-state of rsFolder, a superfolder variant of rsEGFP2 that harbors a phenylalanine instead of a tyrosine at position 146 and that was designed to facilitate RESOLFT microscopy in “hostile” environments such as the bacterial periplasm.^[26] Strikingly, rsFolder has a much lower switching contrast than rsEGFP2 and rsFolder2, a single mutant of rsFolder with a tyrosine at position 146 and thus the same chromophore pocket as rsEGFP2.^[26] This observation suggests a possible link between the presence of *trans2* and a reduced switching contrast, raising the intriguing hypothesis that removal of the *trans2* fraction in rsEGFP2 could further enhance its switching contrast.

Here, we investigate the structural *off*-state heterogeneity in rsEGFP2 and eliminated it in V151A and V151L variants by shortening or lengthening the amino-acid side chain at position 151, respectively. The V151A variant exhibits only the *trans1* conformation and a substantially higher switching contrast compared to the rsEGFP2 parent, whereas the V151L variant shows only the *trans2* conformation and a lower contrast. The effects of the V151A and V151L mutations on the switching contrast are reproduced in rsFolder2. We show that changes in switching contrast between the investigated variants mainly result from differences in extinction coefficients of the corresponding *off*-states at the *off*-switching illumination wavelength. Furthermore, we postulate rapid exchange dynamics between *trans1* and *trans2* in parental rsEGFP2 and in rsFolder2 and suggest that the achieved equilibrium depends on environmental factors, a notion we refer to as “photoswitching fragility”. Finally, we show that the V151A variants maintain their gain in switching contrast *in vivo* and investigate the potential of rsFolder2-V151A for RESOLFT nanoscopy.

Results

Structural Heterogeneity in the Off-State of Parental rsEGFP2

In order to corroborate the observation of a second *trans* isomer in parental rsEGFP2,^[23] a follow-up SFX experiment was carried out at the Linac Coherent Light Source (LCLS) using microcrystals of parental rsEGFP2 of the same crystal batch used earlier.^[23,25] The *on*-state crystals were photoswitched by 488 nm light^[27] and the room-temperature (RT) structure of the resulting *off*-state solved at 1.7 Å resolution (PDB entry 7O7U; see SI for details). Both *trans1* and *trans2* chromophore conformations are again present (Figure 1b, Supplementary Figure S2). They agree well with those observed earlier,^[23] as well as with those observed in cryo-crystallographic structures of an rsEGFP2 variant containing a monochlorinated chromophore^[24] (Figure 1c, Supplementary table S3). The *trans2* conformation is similar to the one adopted by rsFolder in its *off*-state^[26] (Figure 1d).

Structural Heterogeneity Bisected in the Off-States of rsEGFP2 V151A and V151L Variants

Given that the *trans1* and *trans2* chromophore conformations lie on either side of the V151 side chain (Figure 1b–d), we reasoned that this residue could also control the *off*-state heterogeneity. In addition to the rsEGFP2 variant with a shortened side chain (V151A^[25]), one with an enlarged (V151L) side chain was therefore generated and non-fluorescent *off*-state structures of both solved from RT SFX data collected at the SPring-8 Angstrom Compact free electron Laser (SACLA) from microcrystals after 488 nm light illumination^[27] (Figure 2, Supplementary Figure S3, Supplementary table S2). The *off*-state structures (V151A: PDB entry 7O7X, V151L: PDB entry 7O7W) display only one chromophore conformation: *trans1* for V151A (Figure 2a) and *trans2* for V151L (Figure 2b). Absorption spectroscopy indicates that about 85% and 77% of microcrystalline rsEGFP2-V151A and -V151L chromophores have

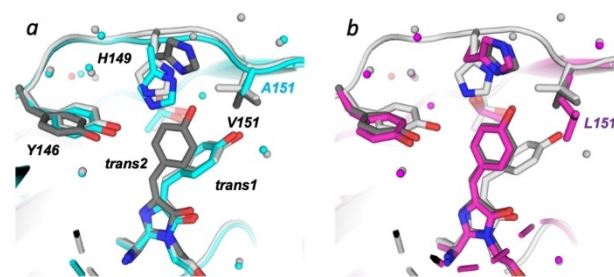


Figure 2. Structures of rsEGFP2 and its V151A and V151L variants in their *off*-states solved from RT SFX data. *Off*-state models of (a) rsEGFP2-V151A (cyan; PDB entry 7O7X) and (b) -V151L (purple; PDB entry 7O7W) variants are superimposed on the model of parental rsEGFP2 in the *off*-state solved from RT SFX data (PDB entry 7O7U), featuring *trans1* in light grey and *trans2* in dark grey. *Trans1* and *trans2* are occupied at 80% and 75% in rsEGFP2 V151A and V151L, respectively. The *cis* conformers were removed for clarity.

switched from the *on*- to the *off*-state, respectively (for details see Supplementary Figure S4 and its legend). *Trans1* and *trans2* chromophore conformations were modelled at 80% (75%) occupancy in rsEGFP2-V151A (V151L) and the residual *cis* conformer at 20% (25%). Spectroscopic and crystallographic *on*- and *off*-state occupancies are thus consistent. In addition to differences in chromophore conformations, the *off*-states of the two variants also differ in their His149 and Tyr146 conformations. In the V151A variant His149 forms a hydrogen bond with Tyr146 and the *trans1* chromophore forms a hydrogen bond with a water molecule (distance: 2.7 Å, Supplementary Figure S1c, Figure 2a), whereas in the V151L variant His149 is hydrogen bonded to the *trans2* chromophore (distance of 2.5 Å between the chromophore phenol group and His149ND1; Supplementary Figure S1b, Figure 2b). Synchrotron cryo-crystallography structures of rsEGFP2-V151A (*off*-state: PDB entry 7O7C, *on*-state: PDB entry 7O7D) and -V151L (*off*-state: PDB entry 7O7H, *on*-state: PDB entry 7O7E) also feature a *trans1* and *trans2* chromophore in their *off*-state, respectively (Supplementary Figure S5b, d) and a *cis* chromophore in the *on*-state (Supplementary Figure S5a, c).

Overall, the RT SFX structures strongly suggest that the conformational *off*-state heterogeneity (*trans1*, *trans2*) seen in parental rsEGFP2 is eliminated in the rsEGFP2-V151A and -V151L variants, with *trans1* being occupied in the former and *trans2* in the latter. Thus, the residue at position 151 controls the *off*-state chromophore conformations (for a discussion of the modulation of conformational *off*-state heterogeneity see Supplementary Text S4).

Occupancies of Trans1 and Trans2 Conformations in Parental rsEGFP2 and rsFolder2 are Sensitive to Experimental Conditions

A puzzling observation is that the relative occupancies of the *trans1* and *trans2* conformations differ in *off*-state crystal structures of rsEGFP2 determined from three different SFX data sets, although the same batch of microcrystals was used (Supplementary text S1). In addition, attempts to observe the *trans2* conformation in macrocrystals of parental rsEGFP2 upon RT illumination at various intensities by synchrotron cryo-crystallography remained unsuccessful (see Supplementary text S2). In contrast, the rsFolder2 *off*-state structure determined by synchrotron cryo-crystallography (PDB entry 7AMF) showed residual occupancy of the *trans2* chromophore in addition to a mainly occupied *trans1* (Supplementary Figure S6), similarly to the parental rsEGFP2 structures determined by RT SFX. These results suggest that relative occupancies of the two *off*-state conformations may change depending on even subtle differences in experimental conditions (see also^[24]) or possibly the age of the crystalline proteins. In contrast, the rsEGFP2-V151A and -V151L structures in their *off*-states determined by SFX (Figure 2) are similar to those derived from cryo-crystallographic data we collected from macrocrystals at the European Synchrotron Radiation Facility (ESRF) (Supplementary table S1; Supplementary Figure S5).

Determination of Switching Contrast, Switching Quantum Yields and Extinction Coefficients of rsEGFP2, rsFolder2 and Their Variants Embedded in Polyacrylamide Gels

To explore a possible correlation between the *off*-state chromophore conformations and the switching contrast, we measured the switching kinetics of rsEGFP2-V151A, rsEGFP2-V151L and parental rsEGFP2 that contain either *trans1*, *trans2*, or both conformations, respectively. We also investigated rsFolder and rsFolder2, as well as the two variants rsFolder2-V151A and rsFolder2-V151L.

We embedded the seven investigated variants in polyacrylamide gels and recorded their fluorescence switching curves under laser illumination at 488 nm, using a wide field fluorescence microscope (Figure 3). The switching contrast was calculated as the ratio of the initial fluorescence in the *on*-state after illumination at 405 nm divided by the residual steady-state fluorescence after *off*-switching with 488 nm light (Table 1). We found that for both rsEGFP2 and rsFolder2 the switching contrast is reduced ($\times \sim 0.33$) in the V151L variants and increased ($\times \sim 2.6$) in the V151A variants compared to the parent proteins. The switching contrasts measured in the V151L variants (~ 15) are similar to that of rsFolder (~ 20), whereas that measured for both V151A variants exceeds 100.

To explore the underlying reason for the modified switching contrasts, we examined the photoswitching kinetics of all variants in more detail. Neglecting the slow thermal relaxation in RSFPs (\sim hour range) in view of the timescale of our experiments (\sim second range), the switching contrast SC at wavelength λ can be approximated by:

$$SC(\lambda) \simeq \frac{k_{\text{on} \rightarrow \text{off}}}{k_{\text{off} \rightarrow \text{on}}} = \frac{\epsilon_{\lambda, \text{on}} \times Q_{\text{on} \rightarrow \text{off}}}{\epsilon_{\lambda, \text{off}} \times Q_{\text{off} \rightarrow \text{on}}} \quad (1)$$

where $k_{\text{on} \rightarrow \text{off}}$ and $k_{\text{off} \rightarrow \text{on}}$ are the *on*-to-*off* and *off*-to-*on* switching rates, $Q_{\text{on} \rightarrow \text{off}}$ and $Q_{\text{off} \rightarrow \text{on}}$ are the *on*-to-*off* and *off*-to-*on* switching quantum yields, respectively, and $\epsilon_{\lambda, \text{on}}$ and $\epsilon_{\lambda, \text{off}}$ are the extinction coefficients of both the *on* and *off* states at the *off*-switching wavelength, respectively. Eq. 1 thus results from the photochemically-driven equilibrium between *on* and *off* states, assuming that the *off* states do not fluoresce. Changes in the switching contrast can thus be due to changes in switching quantum yields^[19,20] and/or extinction coefficients of the *on*- and/or *off*-states. For the proteins in the present study, the *off*-switching wavelength is 488 nm. Whereas $\epsilon_{488, \text{on}}$ was measured using the Ward method^[28] $\varphi_{\text{on} \rightarrow \text{off}}$, $\varphi_{\text{off} \rightarrow \text{on}}$, $\epsilon_{488, \text{off}}$ values were calculated by fitting the experimental fluorescence switching curves (Figure 3) with a kinetic model (see Supplementary methods section and Supplementary text S3). Overall, the dominating effect underlying variations between the observed switching contrasts in the studied variants follows from significant differences in *off*-to-*on* (rather than *on*-to-*off*) switching brightness at 488 nm (Table 1): the V151A variants switch *on* significantly less efficiently at 488 nm than the parent proteins, while the V151L variants switch *on* much more efficiently. The observed differences in the *off*-to-*on* switching brightness are mainly due to differences in $\epsilon_{488, \text{off}}$ (reduced ~ 2.4

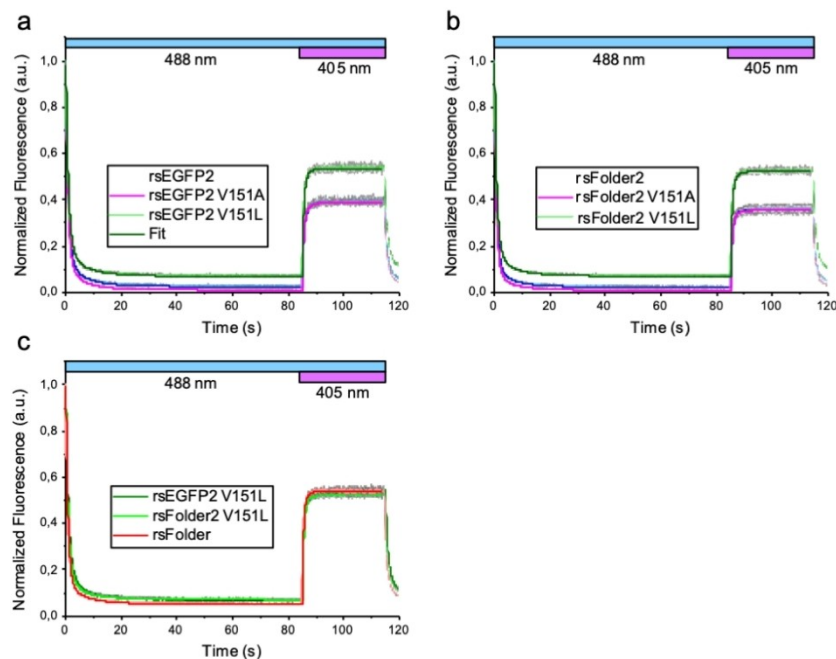


Figure 3. Fluorescence switching curves. (a, b) Fluorescence switching curves for rsEGFP2 and rsFolder2 proteins together with their V151A and V151L variants. (c) Switching curve for rsFolder compared to V151L variants of rsEGFP2 and rsFolder2. Data obtained from *in-vitro* measurements of purified proteins, embedded in polyacrylamide gel (pH 8.0), on an epifluorescence microscope using 488 nm (0.27 W/cm^2) illumination throughout data acquisition, and additional 405 nm (0.03 W/cm^2) during *off-to-on* switching. Pale colors stand for the mean values calculated from six measurements with standard deviations shown in grey, whereas dark solid lines represent the fits from the used kinetic model.

fold in rsEGFP2-V151A, and increased ~ 1.9 fold in rsEGFP2-V151L compared to parental rsEGFP2) and only to a minor extend to differences in *off-to-on* switching quantum yields (Table 1). Note that absolute values of *off-to-on* switching quantum yields are notoriously difficult to determine, as evidenced by the spread in values determined in different laboratories (e.g. for rsEGFP2 in solution, values of $0.12^{[29]}$ and $0.34^{[26]}$ have been published). Yet, values determined under identical conditions in the same laboratory should be comparable. It is thus striking that similar *off-to-on*-switching quantum yields were measured here on rsEGFP2 (0.23) and rsEGFP2-V151A (0.25) embedded in polyacrylamide gels, but a two-fold increase of the quantum yields for the proteins in solution has been reported by us earlier (0.40 and 0.77 for rsEGFP2 and rsEGFP2-V151A, respectively^[25]). Unlike data in Table 1, the value for rsEGFP2-V151A in^[25] was determined from a single measurement and we suspect that an unidentified experimental flaw attributed to a laser power density calibration error lead to the erroneously high value (0.77) that should thus be discarded. Compared to rsEGFP2 and rsFolder2, the behavior of rsFolder is similar to that of the V151L variants. We note that the V151A variants are characterized by a lower fluorescence brightness than their parents (Table 1).

Overall, our results suggest that the higher and lower switching contrasts of the V151A and V151L variants relative to the parent proteins, respectively, are mainly due to lower absorptions of 488 nm light ($\epsilon_{488, \text{off}}$) by the *trans1* chromophore in V151A and to higher absorption of the *trans2* chromophore in V151L.

UV-Visible Absorption Spectroscopy on rsEGFP2, rsFolder2 and Their Variants in Solution

The differences in $\epsilon_{488, \text{off}}$ determined from fitting the experimental fluorescence switching curves (Table 1) can be rationalized by comparing UV-visible absorption spectra of rsEGFP2, rsFolder2 and their V151A and V151L variants in their *on*- and *off*-states, respectively (Figure 4). Indeed, we consistently observed that the maximum of the *off*-state spectra of the V151A variants are blue shifted, and the spectra of the V151L variants red shifted relative to those of the parent proteins (Table 1). In the V151A variants, the blue shifted *off*-state absorbance band leads to a lower residual extinction coefficient at 488 nm ($\epsilon_{488, \text{off}}$), resulting in less *on*-state contamination after *off*-switching (Figure 4) and thus to an increased switching contrast. In contrast, the red shifted *off*-state absorbance band in the V151L variants leads to a higher extinction coefficient at 488 nm, more *on*-state contamination and a lower contrast. Interestingly, a shoulder at 440 nm is visible in the *off*-state absorbance spectra of rsEGFP2-V151L, rsFolder2-V151L and rsFolder (Figure 4) that cannot be attributed to residual absorbance of the *on*-state. This shoulder is also visible in *off*-state absorption spectra of microcrystalline rsEGFP2-V151L (Supplementary Figure S4b).

We also recorded absorption spectra along *on-to-off* switching under alternating 488 nm illumination for all variants in the solution state. An isosbestic point (Supplementary Figure S7) was always observed, suggesting a homogenous *off*-state, not only for the V151A and V151L variants, but also for the parent proteins. Likewise, all our fluorescent switching curves (Supple-

Table 1. Photophysical parameters obtained *in vitro*.

	rsEGFP2	rsEGFP2-V151A	rsEGFP2-V151L	rsFolder2	rsFolder2-V151A	rsFolder2-V151L	rsFolder
Absorption max. anionic (on) [nm]	482	483	483	483	484	483	479
Absorption max. neutral (off) [nm]	403	397	405	397	397	400	402
Absorption max. switched (off) [nm]	409	406	417	413	410	418	413
on-to-off-switching brightness ^{a(b)} [M ⁻¹ cm ⁻¹]	563 ± 13	673 ± 9	415 ± 18	690 ± 28	827 ± 48	455 ± 15	441 ± 13
on-to-off-switching quantum yield, Q _{on-to-off}	9.3 × 10 ⁻³ ± 0.2 × 10 ⁻³	11.4 × 10 ⁻³ ± 0.2 × 10 ⁻³	6.5 × 10 ⁻³ ± 0.3 × 10 ⁻³	10.0 × 10 ⁻³ ± 0.4 × 10 ⁻³	14.1 × 10 ⁻³ ± 0.8 × 10 ⁻³	6.5 × 10 ⁻³ ± 0.2 × 10 ⁻³	7.3 × 10 ⁻³ ± 0.2 × 10 ⁻³
off-to-on-switching brightness ^(c) [M ⁻¹ cm ⁻¹]	5807 ± 233	6590 ± 134	8713 ± 193	6054 ± 173	6852 ± 198	8979 ± 210	7877 ± 125
off-to-on-switching brightness ^(d) [M ⁻¹ cm ⁻¹]	14.9 ± 0.9	6.8 ± 0.8	35.4 ± 1.2	16.9 ± 1.1	7.4 ± 0.5	39.3 ± 1.7	26.0 ± 0.8
off-to-on-switching quantum yield, Q _{off-to-on}	2.3 × 10 ⁻¹ ± 0.09 × 10 ⁻¹	2.5 × 10 ⁻¹ ± 0.05 × 10 ⁻¹	2.9 × 10 ⁻¹ ± 0.06 × 10 ⁻¹	1.5 × 10 ⁻¹ ± 0.04 × 10 ⁻¹	2.2 × 10 ⁻¹ ± 0.06 × 10 ⁻¹	2.7 × 10 ⁻¹ ± 0.06 × 10 ⁻¹	2.4 × 10 ⁻¹ ± 0.04 × 10 ⁻¹
ε _{max,on} [M ⁻¹ cm ⁻¹]	65474	62284	68295	72675	61091	74470	71871
ε _{488,on} [M ⁻¹ cm ⁻¹]	60807	59090	63851	69124	58798	70254	59509
ε _{488,off} [M ⁻¹ cm ⁻¹]	65 ± 3	27 ± 3	122 ± 3	111 ± 6	34 ± 2	145 ± 5	110 ± 3
ε _{max,off} [M ⁻¹ cm ⁻¹]	25758	26694	33333	42434	32267	37079	38518
ε _{405,off} [M ⁻¹ cm ⁻¹]	25349	26670	29987	39841	31473	33061	36137
off-to-on thermal recovery time [hours]	4.5	65	10	25	75	13	69
Switching contrast [fold-change] ^(e)	43 ± 5	119 ± 21	15 ± 1	46 ± 3	125 ± 11	15 ± 1	20 ± 1
Fluorescence brightness	20952	16194	19123	24709	12829	33511	21561
Fluorescence quantum yield	0.32 ± 0.02	0.26 ± 0.01	0.28 ± 0.01	0.34 ± 0.01	0.21 ± 0.01	0.45 ± 0.04	0.30 ± 0.01
Maturation time [min]	39.1 ± 4.2	116.7 ± 3.3	90.8 ± 7.7	70.8 ± 6.6	157.7 ± 2.3	119.7 ± 60.3	77.2 ± 5.3
pKa	5.9	6.4	5.7	5.8	6.4	5.9	5.5

[a] Switching brightness refers to the product (switching quantum yield × extinction coefficient). [b] Off switching brightness at 488 nm [c] On switching brightness at 405 nm. [d] On switching brightness at 488 nm. [e] Experimentally measured switching contrast, i.e. ratio of the measured fluorescence at the beginning and at the end of the 488 nm illumination period. This experimental switching contrast is always higher than the ratio of on-off and off-on switching brightnesses. This stems from the fact that the reported minor dark state harbors a population of nonfluorescent molecules and therefore provides additional contrast (supplementary Figure S8). All parameters were determined by measurements on protein in solution at pH 7.5 except switching brightness, switching quantum yield and switching contrast values that were extracted from measurements on protein in polyacrylamide gel at pH 8.0. Values obtained from at least three independent measurements for each variant. ND: Not Determined

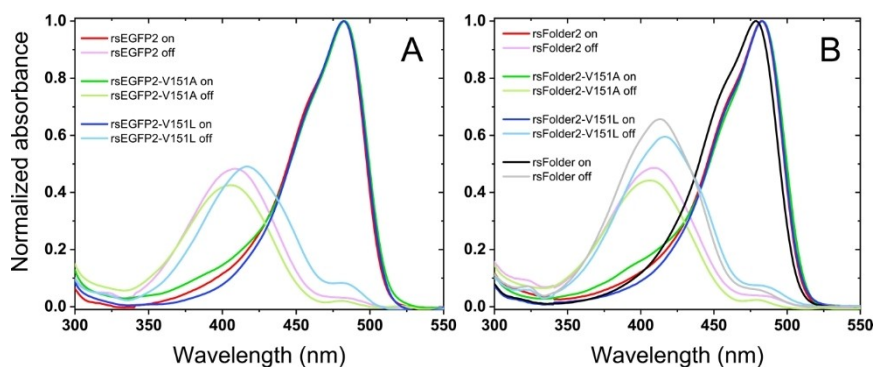


Figure 4. Absorption spectra of fluorescent proteins presented in this study in their fluorescent *on*-state (dark colors) and non-fluorescent *off*-state (dim colors) in solution. (a) rsEGFP2 and its variants rsEGFP2-V151A and rsEGFP2-V151L, (b) rsFolder2 and its variants rsFolder2-V151A and rsFolder2-V151L and rsFolder. Spectra are normalized relatively to the respective *on* state spectra and are measured in HEPES buffer at pH 7.5.

mentary Figure S8) displayed a similar trend, with no sign of more complex kinetics in the parent proteins compared to the V151A and V151L variants.

Quantum Chemical Calculation Analysis of Chromophore Conformations in Parental rsEGFP2

So far, we implicitly assumed that the *trans1* and *trans2* conformations observed in the crystal structures occur in the proteins in solution, and hence, the blue- and red-shifted absorption could be attributed to *trans1* and *trans2* chromophores, respectively. To test this assumption, the absorption spectra of the *trans1* and *trans2* conformers were characterized by quantum chemistry calculations. Starting from the SFX structure of parental rsEGFP2 (PDB entry 6T39^[23]), the geometries of models featuring *trans1* and *trans2* chromophore conformations in their respective protein environment (*i.e.* *trans1* being H-bonded to a water molecule and *trans2* to His149; Figure 5a) were optimized. The planarity of the chromophore remained similar to the experimentally derived one (Supplementary table S3) with *trans1* being rather distorted from the planar configuration in contrast to *trans2* (Figure 5a). The two configurations also differ in the length of the phenolic OH bond and bonds of the conjugated system indicating a

stronger binding of the phenolic proton concomitant with a reduced π -conjugation in *trans1* as compared to *trans2*. The energy cross sections computed for the phenolic OH bond stretching (Figure 5b) demonstrate a shape typical for the protonated *p*-hydroxybenzylidene imidazolinone chromophore interacting with a proton acceptor^[30] and confirm a stronger proton binding in *trans1*. Consistent with reduced π -conjugation, the S_0 - S_1 energy is higher for *trans1* than for *trans2* (Figure 5b, Supplementary table S4), suggesting a blue-shifted absorption maximum for the former. The enhanced proton binding in *trans1* could be linked to a substantial electronic coupling of 15 meV between *trans1* chromophore and electron donor Tyr146. The coupling is facilitated by a H-bond between His149 and Tyr146. The *trans2* chromophore is H-bonded with His149 itself, and its electronic coupling with Tyr146 is reduced to 0.5 meV. The absorption band shapes obtained with a quantum-mechanical model considering the one-dimensional OH-stretching potential (Supplementary Figure S9 and Supplementary table S5) also suggest a blue shifted absorption band of *trans1* compared to *trans2*.

Geometry optimization and excitation energy calculations were performed for the *trans1* and *trans2* models with alanine and leucine, respectively, at position 151. Similar distorted and planar geometries of *trans1* and *trans2*, respectively, were found in these models (Supplementary Figure S10 and Supplementary

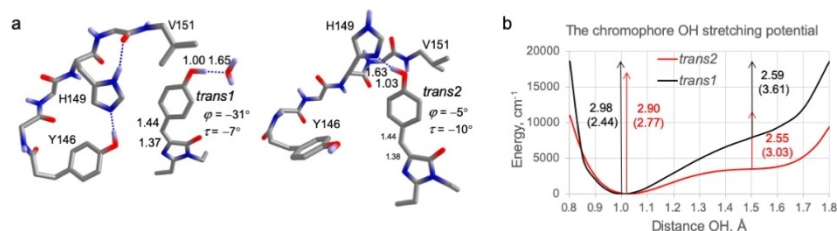


Figure 5. Quantum chemical calculations of *trans1* and *trans2* within parental rsEGFP2. (a) Fragments of the chromophore models and selected distances (Å) and angles in the optimized geometries. (b) The OH stretching energies. Vertical arrows indicate the S_0 - S_1 excitation energies (eV) and transition dipole moments (in brackets; Hartree/Bohr). The decrease of the S_0 - S_1 energy along the OH stretching coordinate is demonstrated. The effect of the OH-stretching potentials, showing strong anharmonicity, on the S_0 - S_1 vibronic band structure potentially explaining the observed spectral shift is demonstrated in Supplementary Figure S9.

table S3). Further, the calculations confirmed that the S_0 - S_1 excitation energy is higher for *trans1* compared to *trans2* independent of the residue at position 151 (Supplementary table S4). Hence, our calculations suggest an increase of the excitation energy for *trans1* in comparison to *trans2*, consistent with the blue-shifted absorption band assigned to *trans1*, which we correlate with the increased out of plane distortion and increased proton binding of *trans1*. The calculations thus corroborate our assumption that the *trans1* and *trans2* conformers are adopted both *in crystallo* and in solution.

Determination of *in Vivo* Switching Contrasts of rsEGFP2, rsFolder2 and Their Variants and RESOLFT Experiments on rsFolder2-V151A

To investigate the *in vivo* switching properties of rsEGFP2, rsFolder2 and their variants at light intensities similar to those typically utilized in RESOLFT nanoscopy, we recorded switching curves on *E. coli* colonies expressing the respective proteins using high light intensities (Figure 6a, b). The determined contrasts of rsEGFP2-V151A (109) and rsFolder2-V151A (119) increased and that of rsEGFP2-V151L (6) decreased with respect

to parental rsEGFP2 (28) and rsFolder2 (22), in line with the results obtained with low light intensities *in vitro* (Table 1). We also compared the switching fatigue of parental rsEGFP2 and rsFolder2 and their variants. To this end, the fluorescence of *E. coli* colonies was switched *on* and *off* 4000 times and the maximal fluorescence of the *on*-state was recorded for every switching cycle (Figure 6c). While rsEGFP2 and rsFolder2 could be switched more than 2000 times before their fluorescence was reduced to 50% of the initial brightness, the V151A variants could be switched \sim 1500 times. Based on *in vivo* switching properties, both V151A variants appeared to be suitable for RESOLFT nanoscopy.

For investigating the usefulness for RESOLFT imaging, we decided to concentrate on rsFolder2-V151A, as this variant showed the highest photoswitching contrast *in vitro* (Table 1) and *in vivo*, and could be particularly useful because of its superfolding properties. A fusion protein of the cytoskeletal protein Keratin with rsFolder2-V151A was expressed in cultured human HeLa cells and imaged on the RESOLFT microscope. While the resulting image shows the expected clear improvement in resolution compared to the confocal counterpart (Figure 7), its resolution of \sim 60 nm is comparable to the one of previous RESOLFT recordings on the same microscope using

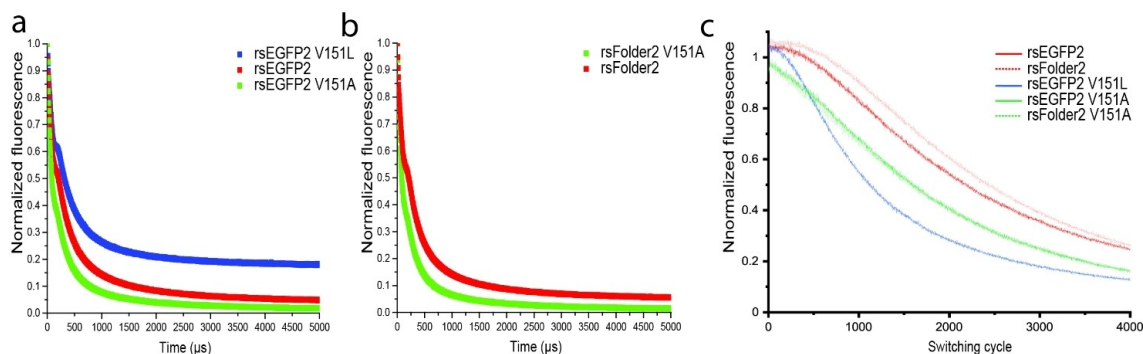


Figure 6. Switching kinetics and switching fatigue of rsEGFP2, rsEGFP2 V151A, rsEGFP2 V151L, rsFolder2 and rsFolder2 V151A. Comparison of the *off* switching curve of rsEGFP2, rsEGFP2-V151A and rsEGFP2-V151L (a), as well as rsFolder2 and rsFolder2-V151A (b). Switching fatigue measurements of the five proteins (c). All graphs were recorded on living *E. coli* colonies using high light intensities.

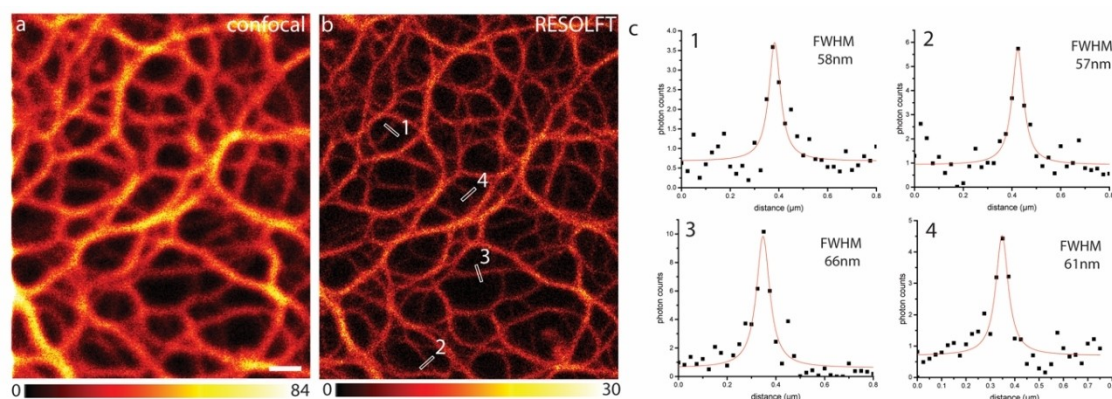


Figure 7. RESOLFT imaging using rsFolder2-V151A. Comparison of a confocal (a) and RESOLFT (b) recording of a HeLa cell expressing Keratin-rsFolder2-V151A. Line profiles were taken at the indicated positions and the FWHM was determined on the fitted functions (c). Scale bar: 1 μ m. The color maps indicate the actual photon counts.

parental rsEGFP2,^[31] as judged by the full width at half maximum (FWHM) of line profiles across small Keratin-rsFolder2-V151A filaments. Hence, despite the increased switching contrast of the V151A variant, evidenced *in vitro* (Table 1) and *in vivo* (Figure 6), the recorded images do not show a significant increase in resolution compared to the parent protein. We mainly attribute this result to the lower molecular and cellular brightnesses of these variants compared to the parents (Table 1).

Discussion

Correlation between Off-State Conformations, Switching Contrast and Absorbance Spectra

We establish a link between the switching contrast and *off*-state occupancy of the *trans1* or *trans2* chromophore conformations in rsEGFP2 and rsFolder2 variants by combining our structural and photophysical results. For the *trans1* conformer (V151A variants), the switching contrast is high, whereas the *trans2* conformer (V151L variants) leads to a lower contrast. Parental rsEGFP2 and rsFolder2, exhibiting *trans1/trans2* *off*-state heterogeneity (see Supplementary text S4), display an intermediate contrast (Table 1). The quantitative evaluation of fluorescence switching kinetics and the *off*-state absorbance spectra of the investigated variants strongly suggest that the main contribution to modulation of the switching contrast arises from red- and blue-shifted absorption maxima of the *off*-state in the V151L and V151A variants, respectively. This observation correlates with the differences in twist and tilt dihedral angles of the chromophore in *trans1* and *trans2*, as well as in its local environment, that tune the energy gap between the S_0 and S_1 electronic states as shown by our high-level quantum chemistry calculations. The red-shift of the experimental absorption maximum of the rsEGFP2-V151L *off*-state was reproduced computationally (Figure 5b) and is consistent with the more extended electron delocalization in the near-planar chromophore of its *trans2* conformation compared to *trans1* (Figure 5a). The less planar *trans1* chromophore conformation might result from stabilization of the protonated form by charge transfer (CT) from Tyr146, activated by H-bonding to His149, that is absent for *trans2*. Of note, based on the calculation of ratiometric absorption spectra between the *on* and *off* states for the three rsEGFP2 variants, we do not expect an increase in switching contrast by employing illumination at red-shifted wavelengths (Supplementary Figure S11).

When linking structural and spectroscopic results, we rely on the assumption that the *off*-state heterogeneity observed in crystals of parental rsEGFP2 and rsFolder2 is maintained in solution. Our high-level quantum chemistry calculations justify this assumption. Yet, the presence of isobestic points in the absorbance spectra along *off*-switching (Supplementary Figure S7) and detection of a single long-lived *off*-state in our fluorescence-based switching curves (Supplementary Figure S12) indicate a homogeneous *off*-state in solution. These findings are consistent if we postulate a fast exchange between

trans1 and *trans2* in parental rsEGFP2 and rsFolder2 in solution, occurring on timescales faster than detectable (~ 0.1 s) in our absorbance and switching kinetics measurements. Our measurements in solution thus capture the average photophysical behavior between those of *trans1* and *trans2*, giving rise to an apparently homogeneous *off*-state. The postulated fast exchange contrasts the assumption by Chang et al that *trans* conformations are locked on the second time scale (see Supplementary information S3 in^[24]).

Photoswitching Fragility in Parental rsEGFP2 and rsFolder2

The differential *trans2* occupancies found in *off*-state structures of rsEGFP2 determined by RT SFX under identical buffer conditions on microcrystals of the same batch but of different age and with varying illumination conditions (Supplementary text S1), as well as the absence of *trans2* in flash-cooled parental rsEGFP2 microcrystals (Supplementary Figure S13) and its presence in rsFolder2 (Supplementary text S2, Supplementary Figure S6), suggest that experimental and environmental parameters determine to which extent *trans2* gets populated in parental rsEGFP2 and rsFolder2. We suggest that this is the result of a low, environmentally dependent, barrier in the protein conformational energy landscape^[32] separating access to, or exchange between, *trans1* and *trans2*, a notion that we refer to as “switching fragility”. Yet, the experimental conditions that would reproducibly control heterogeneity in the *off*-states of rsEGFP2 and rsFolder2 have not been identified. Alternatively, or additionally, conformational heterogeneity of the *cis* chromophore in the *on*-state could be at the origin of the observed *off*-state heterogeneity.

Photoswitching fragility in parental rsEGFP2 or rsFolder2 may have consequences for imaging applications, when labels are addressed to various cellular locations with potentially different physicochemical environments. These different environments (e.g. viscosity, ionic strength, or nature of a fusion protein) could lead to different levels of heterogeneity and variability in switching contrast (beyond that expected from pH induced effects^[15]). Such variability is expected to be alleviated in rsFolder2, the V151L variants, and the high switching contrast V151A variants so that they may be considered as more “robust” than their parents.

In conclusion, this work establishes a causal relationship between the occupancy of two *off* conformations in rsEGFP2 and rsFolder2 and the achievable switching contrast, essentially through absorbance shifts of the *off*-switched chromophore. A point mutation is sufficient to enforce single *trans* conformations in the *off*-state. These had also been observed in more or less densely packed crystals of *off*-state variants containing a monochlorinated chromophore.^[24] *Trans1* seems to be favoured in a more spacious chromophore pocket (V151A variant (this work) and in crystals with a less contracted unit cell^[24]) and *trans2* in a more constricted pocket (V151L variant (this work) and in crystals with a contracted unit cell^[24]). The rsEGFP2- and rsFolder2-V151A variants, containing only the *trans1* conformer, exhibit greatly enhanced switching contrasts as compared to

their parents, both *in vitro* and *in vivo*. Due to a loss in fluorescence brightness of these variants, however, the optical resolution obtained by RESOLFT nanoscopy on Keratin-rsFolder2-V151A filaments did not significantly increase compared to previous studies using either parental rsFolder2 or rsEGFP2. In the future, it would be interesting to investigate whether an optimum illumination wavelength exist, possibly deviating from the employed 488 nm light, that would further enhance the switching contrast to a point overcompensating the observed loss in brightness of the *on* form. Our rsEGFP2-V151A and rsFolder2-V151A variants constitute promising leads for the next-generation RSFPs, for which the fluorescence brightness has to be increased while maintaining the enhanced switching contrast described here.

Acknowledgments

We thank Elke de Zitter for critically commenting on the manuscript. The XFEL experiments were carried out at BL2-EH3 of SACLA with the approval of the Japan Synchrotron Radiation Research Institute (JASRI; Proposal No. 2018 A8026; 27–29 July 2018) and at the CXI beamline at the LCLS (Proposal No. LM47 (23–27 June 2016) and LR38 (22–26 February 2018)). We warmly thank the SACLA and LCLS staff for assistance. Use of the LCLS, SLAC National Accelerator Laboratory, is supported by the U.S. Department of Energy, Office of Science, Office of Basic Energy Sciences under Contract no. DE-AC02-76SF00515. Part of the sample injector used at LCLS for this research was funded by the National Institutes of Health, P41 GM103393, formerly P41RR001209. We acknowledge support from the Max Planck Society. The study was supported by travel grants from the CNRS (GoToXFEL) to MW, an ANR grant to MW, MC, MSI (BioXFEL), an ANR grant to DB (grant no. ANR-17-CE11-0047-01), a PhD fellowship from Lille University to LMU and an MENESR – Univ. Grenoble Alpes fellowship to KH. This work was partially carried out at the platforms of the Grenoble Instruct-ERIC center (IBS and ISBG; UMS 3518 CNRS-CEA-UGA-EMBL) within the Grenoble Partnership for Structural Biology (PSB). Platform access was supported by FRISBI (ANR-10-INBS-05-02) and GRAL, a project of the University Grenoble Alpes graduate school (Ecoles Universitaires de Recherche) CBH-EUR-GS (ANR-17-EURE-0003). The IBS acknowledges integration into the Interdisciplinary Research Institute of Grenoble (IRIG, CEA).

Conflict of Interest

The authors declare no conflict of interest.

Data Availability Statement

The data that support the findings of this study are openly available in pdb at pdb, reference number 1111.

Keywords: nanoscopy · photoswitchable fluorescent proteins · serial femtosecond crystallography · switching contrast · quantum chemistry

- [1] D. Bourgeois, V. Adam, *IUBMB Life*. **2012**, *64*, 482–491.
- [2] K. Nienhaus, G. U. Nienhaus, *ACS Nano* **2016**.
- [3] M. Hofmann, C. Eggeling, S. Jakobs, S. W. Hell, *Proc. Natl. Acad. Sci. USA* **2005**, *102*, 17565–17569.
- [4] T. Grotjohann, I. Testa, M. Leutenegger, H. Bock, N. T. Urban, F. Lavoie-Cardinal, K. I. Willig, C. Eggeling, S. Jakobs, S. W. Hell, *Nature* **2011**, *478*, 204–208.
- [5] T. Brakemann, A. C. Stiel, G. Weber, M. Andresen, I. Testa, T. Grotjohann, M. Leutenegger, U. Plessmann, H. Urlaub, C. Eggeling, M. C. Wahl, S. W. Hell, S. Jakobs, *Nat. Biotechnol.* **2011**, *29*, 942–947.
- [6] M. G. L. Gustafsson, *Proc. Natl. Acad. Sci. USA* **2005**, *102*, 13081–13086.
- [7] T. Dertinger, R. Colyer, G. Iyer, S. Weiss, J. Enderlein, *Proc. Nat. Acad. Sci.* **2009**, *106*, 22287.
- [8] H. Shroff, C. G. Galbraith, J. A. Galbraith, H. White, J. Gillette, S. Olenych, M. W. Davidson, E. Betzig, *Proc. Nat. Acad. Sci.* **2007**, *104*, 20308.
- [9] G. Marriott, S. Mao, T. Sakata, J. Ran, D. K. Jackson, C. Petchprayoon, T. J. Gomez, E. Warp, O. Tulyathan, H. L. Aaron, E. Y. Isacoff, Y. Yan, *Proc. Natl. Acad. Sci. USA* **2008**, *105*, 17789–17794.
- [10] J. Quéraud, R. Zhang, Z. Kelemen, M.-A. Plamont, X. Xie, R. Chouket, I. Roemgens, Y. Korepina, S. Albright, E. Ipendey, M. Volovitch, H. L. Sladitschek, P. Neveu, L. Gissot, A. Gautier, J.-D. Faure, V. Croquette, T. Le Saux, L. Jullien, *Nat. Commun.* **2017**, *8*, 969.
- [11] Y. Arai, H. Takauchi, Y. Ogami, S. Fujiwara, M. Nakano, T. Matsuda, T. Nagai, *ACS Chem. Biol.* **2018**, *13*, 1938–1943.
- [12] M. Andresen, M. C. Wahl, A. C. Stiel, F. Grater, L. V. Schafer, S. Trowitzsch, G. Weber, C. Eggeling, H. Grubmuller, S. W. Hell, S. Jakobs, *Proc. Natl. Acad. Sci. USA* **2005**, *102*, 13070–13074.
- [13] M. Andresen, A. C. Stiel, S. Trowitzsch, G. Weber, C. Eggeling, M. C. Wahl, S. W. Hell, S. Jakobs, *Proc. Natl. Acad. Sci. USA* **2007**, *104*, 13005–13009.
- [14] N. A. Jensen, I. Jansen, M. Kamper, S. Jakobs in *Reversibly Switchable Fluorescent Proteins for RESOLFT Nanoscopy*, Vol. (Eds.: T. Salditt, A. Egner, D. R. Luke), Springer International Publishing, Cham, **2020**, pp.241–261.
- [15] H. Shinoda, K. Lu, R. Nakashima, T. Wazawa, K. Noguchi, T. Matsuda, T. Nagai, *Cell Chem. Biol.* **2019**, *26*, 1469–1479 e1466.
- [16] D. Ruhlandt, M. Andresen, N. Jensen, I. Gregor, S. Jakobs, J. Enderlein, A. I. Chizhik, *Commun. Biol.* **2020**, *3*, 627.
- [17] X. Zhang, M. Zhang, D. Li, W. He, J. Peng, E. Betzig, P. Xu, *Proc. Natl. Acad. Sci. USA* **2016**, *113*, 10364–10369.
- [18] N. E. Christou, K. Giandoreggio-Barranco, I. Ayala, O. Glushonkov, V. Adam, D. Bourgeois, B. Brutscher, *J. Am. Chem. Soc.* **2021**, *143*, 7521–7530.
- [19] E. De Zitter, D. Thédié, V. Mönkemöller, S. Hugelier, J. Beaudouin, V. Adam, M. Byrdin, L. Van Meervelt, P. Dedecker, D. Bourgeois, *Nat. Methods* **2019**, *16*, 707–710.
- [20] E. De Zitter, J. Ridard, D. Thédié, V. Adam, B. Lévy, M. Byrdin, G. Gotthard, L. Van Meervelt, P. Dedecker, I. Demachy, D. Bourgeois, *J. Am. Chem. Soc.* **2020**, *142*, 10978–10988.
- [21] D. Morozov, G. Groenhof, *Angew. Chem. Int. Ed.* **2016**, *55*, 576–578; *Angew. Chem.* **2016**, *128*, 586–588.
- [22] T. Grotjohann, I. Testa, M. Reuss, T. Brakemann, C. Eggeling, S. W. Hell, S. Jakobs, *eLife* **2012**, *1*, e00248.
- [23] J. Woodhouse, G. Nass Kovacs, N. Coquelle, L. M. Uriarte, V. Adam, T. R. M. Barends, M. Byrdin, E. de la Mora, R. Bruce Doak, M. Feliks, M. Field, F. Fieschi, V. Guillon, S. Jakobs, Y. Joti, P. Macheboeuf, K. Motomura, K. Nass, S. Owada, C. M. Roome, C. Ruckebusch, G. Schirò, R. L. Shoeman, M. Thepaut, T. Togashi, K. Tono, M. Yabashi, M. Cammarata, L. Foucar, D. Bourgeois, M. Sliwa, J.-P. Colletier, I. Schlichting, M. Weik, *Nat. Commun.* **2020**, *11*, 741.
- [24] J. Chang, M. G. Romei, S. G. Boxer, *J. Am. Chem. Soc.* **2019**, *141*, 15504–15508.
- [25] N. Coquelle, M. Sliwa, J. Woodhouse, G. Schirò, V. Adam, A. Aquila, T. R. M. Barends, S. Boutet, M. Byrdin, S. Carbajo, E. De la Mora, R. B. Doak, M. Feliks, F. Fieschi, L. Foucar, V. Guillon, M. Hilpert, M. S. Hunter, S. Jakobs, J. E. Koglin, G. Kovacsova, T. J. Lane, B. Lévy, M. Liang, K. Nass, J. Ridard, J. S. Robinson, C. M. Roome, C. Ruckebusch, M. Seaberg, M. Thepaut, M. Cammarata, I. Demachy, M. Field, R. L. Shoeman, D. Bourgeois, J.-P. Colletier, I. Schlichting, M. Weik, *Nat. Chem.* **2018**, *10*, 31–37.

- [26] M. El Khatib, A. Martins, D. Bourgeois, J. P. Colletier, V. Adam, *Sci. Rep.* **2016**, *6*, 18459.
- [27] G. Schiro, J. Woodhouse, M. Weik, I. Schlichting, R. L. Shoeman, *J. Appl. Crystallogr.* **2017**, *50*, 932–939.
- [28] W. W. Ward in *Properties of the coelenterate green-fluorescent proteins. Bioluminescence and chemiluminescence: basic chemistry and analytical applications.*, Vol. xxviii (Ed. M. A. D. a. W. D. McElroy), New York, Academic Press, **1981**, pp. 782.
- [29] S. Duwé, E. De Zitter, V. Gielen, B. Moeyaert, W. Vandenberg, T. Grotjohann, K. Clays, S. Jakobs, L. Van Meervelt, P. Dedecker, *ACS Nano* **2015**, *9*, 9528–9541.
- [30] J. Langeland, N. W. Persen, E. Gruber, H. V. Kiefer, A. M. Kabylda, A. V. Bochenkova, L. H. Andersen, *ChemPhysChem* **2021**, *22*, 833–841.
- [31] S. Schnorrenberg, T. Grotjohann, G. Vorbrüggen, A. Herzig, S. W. Hell, S. Jakobs, *eLife* **2016**, *5*, e15567.
- [32] H. Frauenfelder, S. G. Sligar, P. G. Wolynes, *Science* **1991**, *254*, 1598–1603.

Manuscript received: March 22, 2022

Revised manuscript received: June 25, 2022

Version of record online: ■■■, ■■■■

6.3 Structural Information on the Trans-to-Cis Isomerisation Mechanism of the Photoswitchable Fluorescent Protein rsEGFP2 Revealed by Multiscale Infrared Transient Absorption

Structural Information about the *trans*-to-*cis* Isomerization Mechanism of the Photoswitchable Fluorescent Protein rsEGFP2 Revealed by Multiscale Infrared Transient Absorption

Lucas M. Uriarte,* Raffaele Vitale, Stanislaw Niziński, Kyprianos Hadjidemetriou, Ninon Zala, Andras Lukacs, Gregory M. Greetham, Igor V. Sazanovich, Martin Weik, Cyril Ruckebusch, Stephen R. Meech, and Michel Sliwa*



Cite This: *J. Phys. Chem. Lett.* 2022, 13, 1194–1202



Read Online

ACCESS |



Metrics & More

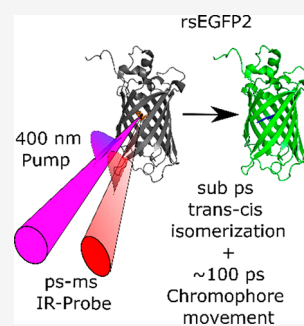


Article Recommendations



Supporting Information

ABSTRACT: RsEGFP2 is a reversibly photoswitchable fluorescent protein used in super-resolved optical microscopies, which can be toggled between a fluorescent On state and a nonfluorescent Off state. Previous time-resolved ultraviolet–visible spectroscopic studies have shown that the Off-to-On photoactivation extends over the femto- to millisecond time scale and involves two picosecond lifetime excited states and four ground state intermediates, reflecting a *trans*-to-*cis* excited state isomerization, a millisecond deprotonation, and protein structural reorganizations. Femto- to millisecond time-resolved multiple-probe infrared spectroscopy (TRMPS-IR) can reveal structural aspects of intermediate species. Here we apply TRMPS-IR to rsEGFP2 and implement a Savitzky–Golay derivative analysis to correct for baseline drift. The results reveal that a subpicosecond twisted excited state precursor controls the *trans*-to-*cis* isomerization and the chromophore reaches its final position in the protein pocket within 100 ps. A new step with a time constant of 42 ns is reported and assigned to structural relaxation of the protein that occurs prior to the deprotonation of the chromophore on the millisecond time scale.



The structure determination of intermediates involved in the early stages (femto- to picosecond time scales) of protein photoactivation mechanisms has recently become possible with the advent of X-ray free-electron lasers (XFELs), coupled to a femtosecond ultraviolet–visible (UV–vis) pump source [time-resolved serial femtosecond crystallography (TR-SFX)].^{1–4} Vibrational time-resolved (TR) spectroscopies such as Raman or infrared (IR) can disclose relevant structural information that complements the TR-SFX results. Importantly, they can uncover chromophore–protein interactions (which cannot be accessed by TRUV–vis, which is mainly sensitive to chromophore electronic transitions) and have been used to study complex photoactive biological systems such as fluorescent proteins^{5–8} and other photoactive biosystems.^{9–12} Moreover, when used in a multiscale approach [time-resolved multiple-probe spectroscopy (TRMPS)], the dynamics from a few hundreds of femtoseconds to the millisecond time range can be measured.¹³

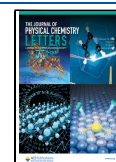
The photoswitching mechanism of reversible photoswitchable fluorescent proteins (RSFPs) involves in general a *trans*-to-*cis* isomerization, a proton transfer, and protein structural reorganizations.^{1,6,7,14} Recently, the Off-to-On photodynamics of isotopically labeled Dronpa2 were studied using TRMPS-IR.⁶ The formation of the first ground state photoproduct after a few picoseconds is followed by a protein reorganization in 596 ps and the formation of the final *cis* protonated chromophore (On like) state in 91 ns. A second protein

reorganization in 4.8 μ s takes place before the final microsecond deprotonation.⁶ On the contrary, recent studies from the femto- to picosecond¹ and pico- to millisecond¹⁴ time scales by TR-SFX and TRUV–vis spectroscopy on a similar RSFP,¹ rsEGFP2,¹⁵ proposed a different mechanism (Scheme 1a and Scheme S1). This protein has the same chromophore as Dronpa [*p*-hydroxybenzylidene-2,3-dimethylimidazolinone (HBDI)] but a different protein cage (Figure S6). The femto- to picosecond study by TRUV–vis revealed two excited state decays on the picosecond time scale involved in the *trans*-neutral (Off state) to *cis*-anionic (On state) photoswitching (Scheme 1a, Scheme S1, and Table S2), and the TR-SFX captured a twisted and a planar chromophore conformation at 1 ps and the formation of the *cis* On-like chromophore at 3 ps. The TRUV–vis pico- to millisecond study¹⁴ revealed the existence of four ground state intermediates in solution with lifetimes of 87 ps, 5.57 μ s, 36.1 μ s, and 825 μ s, where the last two were assigned to deprotonation steps (D₂O isotopic effect). The X-ray structure determined at 10 ns featured a *cis*-

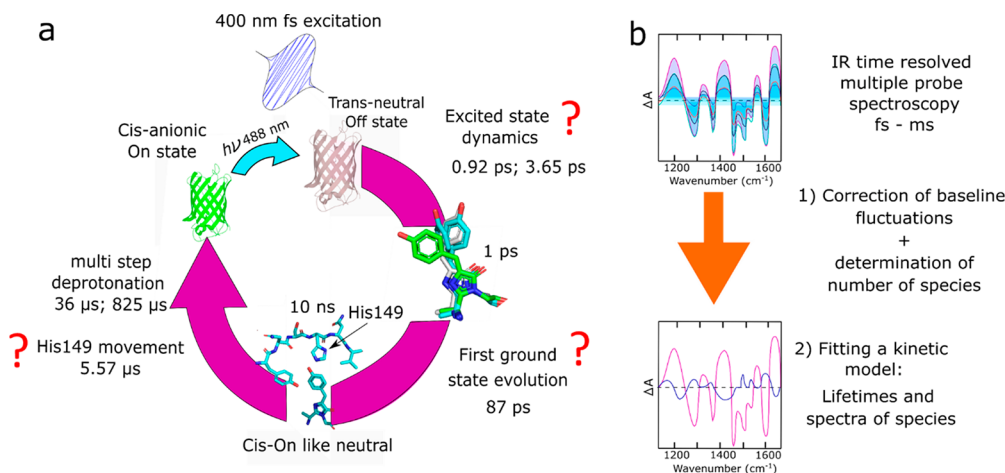
Received: September 4, 2021

Accepted: January 3, 2022

Published: January 27, 2022



Scheme 1. (a) Current rsEGFP2 Off-to-On Photoswitching Mechanisms Based on TRUV–Vis and TR-SFX Results^{1,14},^a and (b) General TRMPS-IR Data Analysis Scheme



^aThe first chromophore structures (1 ps) represented in the panel correspond to the Off state in light gray [reproduced from Protein Data Bank (PDB) entry 5DTY], the twisted and planar chromophore structures determined at 1 ps in cyan (reproduced from PDB entry 5O8B), and the On state in green (reproduced from PDB entry 5O89). The cyan protein chromophore with part of the protein cage (10 ns) corresponds to the structure determined at 10 ns (reproduced from PDB entry 6T3A).

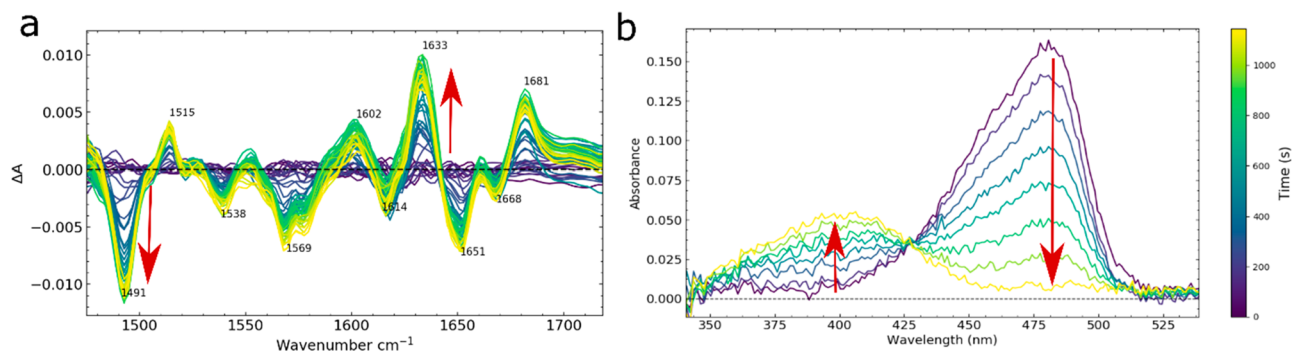


Figure 1. rsEGFP2 On-to-Off photoswitching reaction (480 nm irradiation) at pD 8 (50 mM NaCl and 50 mM HEPES) followed by (a) difference FTIR spectra in the range of 1475–1720 cm^{-1} (obtained by subtracting the non-irradiated On state spectrum) and (b) UV–vis steady state absorption spectra between 340 and 540 nm.

On-like chromophore geometry, where the main difference with the On state is found in the His149 side chain position.¹⁴ Therefore, the movement of the His149 side chain to the final On state was tentatively assigned to the 5.57 μs time constant; however, no structural data were available.¹⁴

Although the general Off-to-On photoswitching mechanism of rsEGFP2 is established, quantum chemical calculations predicted an almost zero transition dipole moment for the twisted model found in TR-SFX, which cannot correspond to either of the excited state species identified by TRUV–vis spectroscopy.¹ Thus, the precise geometries of the chromophore excited state species in solution and several of those in the ground state are still elusive (question marks in Scheme 1a). Here we use TRMPS-IR to gain structural information about the excited state dynamics and the different ground state intermediates in the solution phase switching of rsEGFP2.

The intrinsically low molar absorption coefficients in the IR spectral region and modest quantum yield of product formation make TRMPS-IR signals of RSFPs typically very weak compared to TRUV–vis signals. Consequently, despite advances in experimental methods,^{16–19} TRMPS-IR transient spectra of RSFPs are affected by intensity fluctuations.^{13,20} These fluctuations translate into baseline drifts and offsets,

making preprocessing and signal correction key steps before the analysis of TRMPS-IR data, which typically involve a multiexponential global fit of the time traces.^{21–24} The standard procedure for correcting the baseline drift (Scheme 1b) is to fit a polynomial baseline function to each individual spectrum and subtract it from the raw data.¹⁷ However, polynomial baseline correction methods commonly rely on parameters that are specified by the user (order of the polynomial and location of points for fitting). A major drawback of modeling the baseline shifts as a polynomial is, in some cases, the inability to select appropriate points that are both sufficiently well spread throughout spectral range and genuinely offset-free for the whole set of spectra. A common approach is to choose isosbestic points in the data, which are generally assumed to be crossing points (overlap between ground state depopulation and induced absorption) of modes that have shifted.¹⁷ Altogether, these aspects can hinder the determination of the number of species and time constants involved in the photodynamics. Here we applied Savitzky–Golay derivative filter,²⁵ a method used in different fields,^{26–29} to preprocess the TRMPS-IR data. The advantage of the Savitzky–Golay derivative approach rests on its non-arbitrary

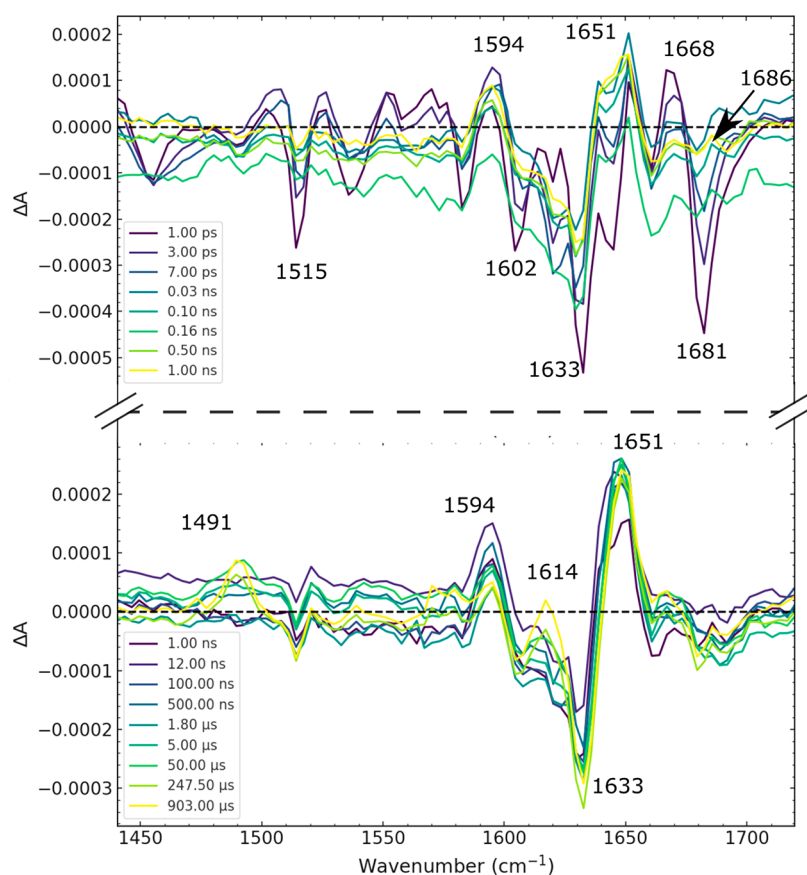


Figure 2. Transient IR absorption spectra of rsEGFP2 after 400 nm femtosecond laser excitation of the *trans*-neutral chromophore (Off state) at pD 8 (50 mM NaCl and 50 mM HEPES), recorded by TRMPS-IR from 1 ps to the millisecond range.

choice of support points and on the local nature of the derivative filter exploited to correct local drifts.

To characterize the On and Off forms, first the On-to-Off kinetics of rsEGFP2 were measured by FTIR (Figure 1a) and UV-vis spectroscopy (Figure 1b) under steady state 480 nm irradiation in deuterated water at pD 8. UV-vis absorbance spectra (Figure 1b) show an isosbestic point between the absorption bands of the chromophore in the Off state (*trans*-neutral conformation; 408 nm) and On state (*cis*-anionic conformation; 482 nm). Assuming that at pD 8 the thermodynamically stable state is the On state with the *cis*-anionic chromophore fully occupied, the photostationary Off state is calculated to be a mixture of 90% *trans*-protonated form and 10% *cis*-anionic form. The switching quantum yield was determined to be 1% and 18% for On-to-Off and Off-to-On transitions, respectively (Figure S2), and the thermal back recovery time was fitted with a single exponential decay of 1.81 h (Figure S3). These values are in agreement with those reported by Duwé et al.³⁰ Similar to UV-vis experiments, the FTIR difference absorbance spectra in Figure 1a (the resting On state spectrum is subtracted) are characterized by two species, the negative bands corresponding to the depopulation of the *cis*-anionic On state and the positive bands corresponding to the formation of the *trans*-neutral Off state. The assignment of the different vibrational bands can be made by comparison with Dronpa, which has the same chromophore^{6–8,31} and HBDI literature.³² The main On state bands are those at 1491, 1538, 1569, 1614, 1651, and 1668 cm⁻¹. The 1491 and 1569 cm⁻¹ bands are characteristic of phenolate vibrations. The 1668 cm⁻¹ band is assigned to the

imidazolinone C=O stretching mode,³² and the 1538 cm⁻¹ band to the C=N/C-C stretching mode.³³ The negative bands that cannot be assigned to the HBDI correspond to infrared active modes of protein residues that couple differently to the *cis*-anionic and *trans*-neutral chromophore; these are the 1614 and 1651 cm⁻¹ bands, respectively. The main *trans*-neutral chromophore vibrations are observed at 1681, 1633, 1602, and 1515 cm⁻¹. The 1681 cm⁻¹ band was assigned to the C=O stretching of the chromophore imidazolinone group,^{6–8,31} while the band at 1633 cm⁻¹ can be assigned to the delocalized C=C-N=C bond (which may have an underlying protein contribution and phenyl ring stretch vibration).⁸ The 1602 cm⁻¹ and 1515 cm⁻¹ bands are assigned to phenyl modes vibrations.^{6,7}

The TRMPS-IR spectra recorded after a 400 nm laser excitation of the rsEGFP2 Off state (1 ps to 900 μs) are displayed in Figure 2. The corresponding TRUV-vis data were published up to 40 ps¹ and are here extended until 2 ns in Figure S1. At 1 ps, the rsEGFP2 TRMPS-IR spectrum is characterized by several negative bands [ground state bleaching (GSB)], assigned to the depopulation of the *trans*-neutral Off form. Note that several of the negative bands in Figure 2 correspond to positive bands in the FTIR spectra in Figure 1a, while there are some new bands in Figure 2 that reflect prompt perturbations of the protein vibrational spectrum.

The ultrafast Off-to-On dynamics studied by TRUV-vis femtosecond spectroscopy (Figure S1) shows the formation of the transient signal in ~300 fs. At this time, several bands can be seen, two positive bands with maxima at 335 and 455 nm,

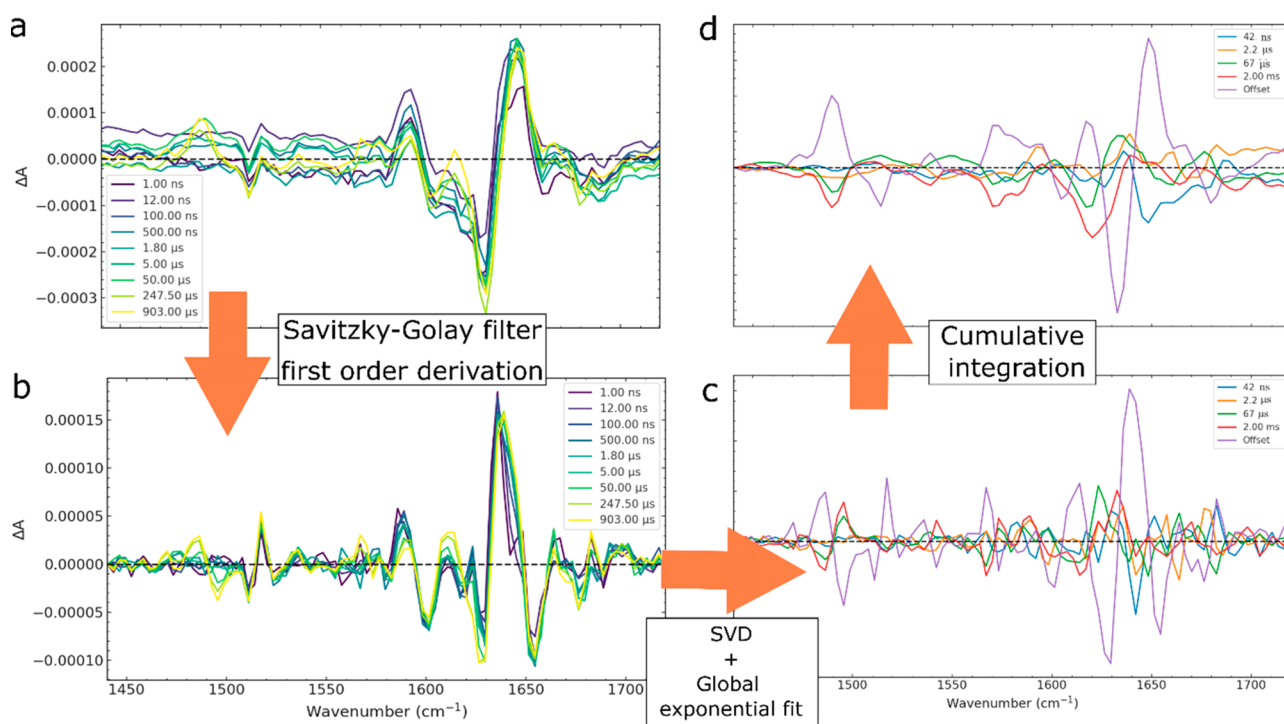


Figure 3. Methodology used to apply the Savitzky–Golay derivative filter to the TRMPS-IR data and obtain DADS and associated time constants. (a) IR transient absorption spectra of rsEGFP2 after 400 nm femtosecond laser excitation of the Off form. (b) Savitzky–Golay (five-point spectral window, third-order polynomial interpolation) first-order derivative of the time-resolved spectra. (c) Determination of the number of components by SVD followed by a global decay analysis to obtain the derivative DADS and time constants. (d) Cumulative integrated DADS.

which are attributed to excited state species absorption (ESA), and two negative bands. The first narrow negative band centered between 390 and 410 nm is attributed to GSB (depopulation of the *trans*-neutral form), and the second broadband negative band ranging from 490 to 700 nm is attributed to the stimulated emission (SE) of excited state species. The SE band is characterized by a large band (490–600 nm) with a minimum at 515 nm together with a red-shifted tail (600–720 nm). The growth of the latter occurs with a certain delay in comparison to the one centered at 515 nm (Figure S1a). A fast initial evolution around 1 ps can be seen in the ESA bands centered at 335 and 455 nm together with the GSB band and SE band centered at 515 nm; these bands decrease to around half of their intensities (Figure S1b). Importantly, within the same time, the red tail of the SE band decays completely. This evolution is followed by the decay of all of the transient absorption bands in ~ 10 ps to form at 40 ps a transient spectrum characterized by a positive band at 375 nm and a small negative band between 465 and 580 nm with a maximum at 502 nm. The absence of SE at 40 ps after this time indicates that processes in the ground state are being probed. These evolutions are followed by the formation of a new positive band at 390 nm (Figure S1c). The global analysis yielded three time constants, an ultrafast component of 0.2 ps assigned to decay of the Franck–Condon (FC) excited state followed by two excited state decays with lifetimes of 0.7 ± 0.1 and 4.8 ± 0.3 ps (Figure S1d), in agreement with previous results^{1,14} (Table S2).

Similar evolutions of species can be observed via TRMPS-IR. The relaxation of the first excited state is characterized in TRMPS-IR spectra by the recovery of the GSB bands ($\sim 30\%$ decrease of the 1681 cm^{-1} band at 3 ps) and a decrease and growth of positive bands at 1668 and 1651 cm^{-1} . This initial

evolution is followed by an incomplete recovery of the GSB bands during the relaxation of the second excited state. At 30 ps, both excited states have relaxed to the electronic ground state, and the formation of a band at 1686 cm^{-1} superimposed with a broad bleach band can be observed. The total recovery of the GSB bands is $\sim 80\%$, in agreement with the determined Off-to-On switching quantum yield of 18%. The growth of the band at 1686 cm^{-1} , slightly blue-shifted with respect to the *trans* C=O mode, is assigned to the formation of a *cis*-neutral photoproduct based on observations in Dronpa and the HBDI-associated DFT calculations⁶ (discussed below). The assignment of the other chromophore modes at lower wavenumbers is complex due to overlapping protein modes (e.g., at 1651 cm^{-1}). From 30 ps to 1 ns, further spectral evolutions are difficult to resolve due to baseline fluctuations (see 160, 500, and 1000 ps at 1600 cm^{-1}). The rsEGFP2 transient spectrum recorded at 1 ns (Figure 2) displays two main positive bands at 1594 and 1651 cm^{-1} and a ground state bleach at 1633 cm^{-1} . Strong baseline fluctuations hinder the observation of the photoproduct spectral evolution from 1 to 900 μs . Within the first 500 ns, there is an increase in the amplitude of the positive band at 1651 cm^{-1} and the GSB at 1633 cm^{-1} . Finally, the formation of two positive bands at 1491 and 1614 cm^{-1} , characteristic of the *cis*-anionic On state, can be seen in a few hundred microseconds (see the transient spectrum at 900 μs and FTIR spectra in Figure 1a).

As discussed above, baseline fluctuations need to be corrected when performing a global decay analysis to obtain intermediate species decay-associated difference spectra (DADS) and their lifetimes. Here we apply a Savitzky–Golay derivative filter, which to the best of our knowledge has not yet been applied to TRIR or TRMPS-IR data. The validation of the Savitzky–Golay derivative filter to correct

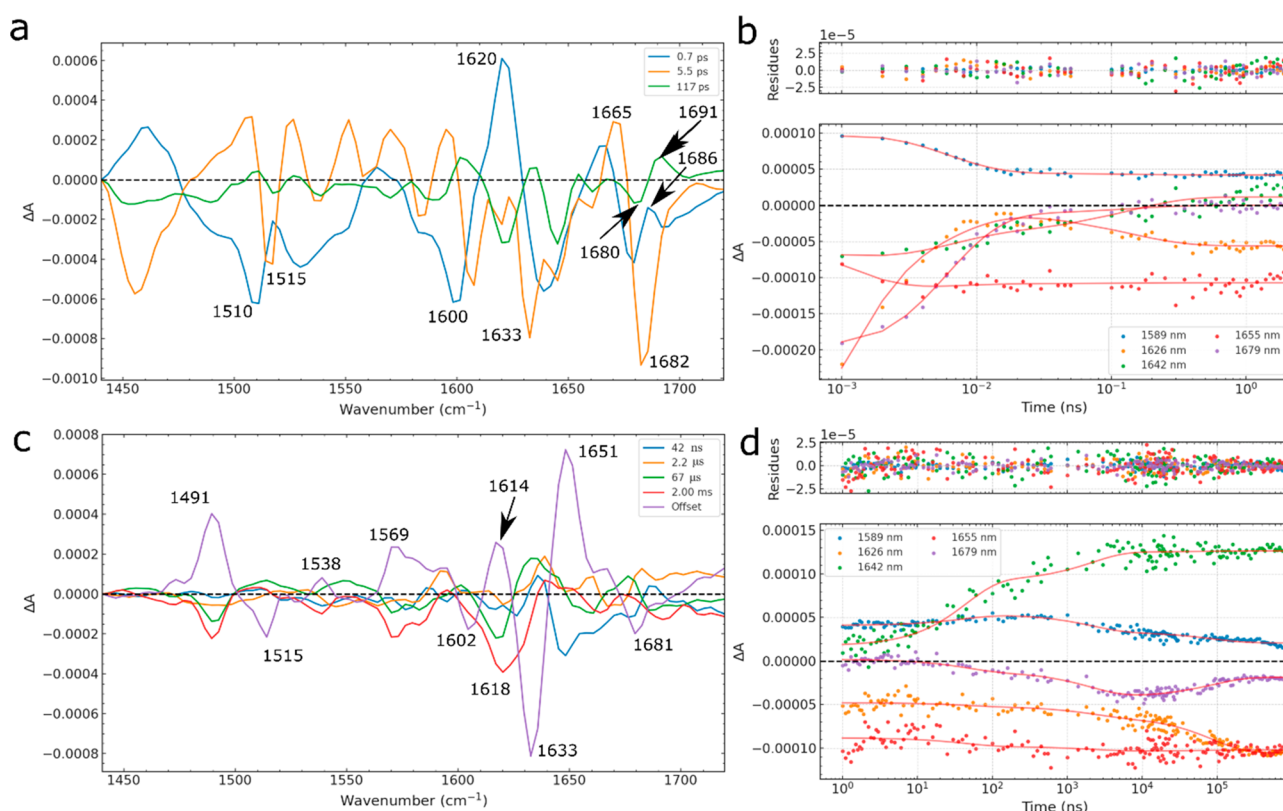


Figure 4. Results of global analysis of TRMPS-IR data. Left panels correspond to the cumulative integrated DADS reconstructed using the pre-exponential factors obtained from the global fit analysis of the preprocessed traces with a weighted sum of four exponential functions (note the DADS are already reintegrated). (a) Data from 1 ps to 2 ns. (b) Data from 1 ns to 900 μ s. In the right panels, a selection of traces is represented together with the corresponding fits and residuals. (c) Data from 1 ps to 2 ns. (d) Data from 1 ns to 900 μ s. Note that the time axes are set on a logarithmic scale.

baseline drifts was carried out on simulated data sets as described in the Supporting Information (Figures S7–S9) through a comparison with standard polynomial correction methods (see Figures S10–S14 and Table S3). Considering the simulations, after the baseline corrections, the most relevant feature of the Savitzky–Golay derivative filter compared with the polynomial correction is a much more accurate determination by singular-value decomposition (SVD) of the underlying number of components involved in the dynamics (see the outcomes with the simulated data in Figure S10). The analysis of TRMPS-IR data using the Savitzky–Golay derivative filter method is shown in Figure 3 (data from 1 ns to 900 μ s). The filter removes the baseline drift, revealing the spectral evolutions in the derivative spectra (Figure 3b). The associated time constants and (derivative) DADS obtained from the global analysis of the preprocessed derivative data can be seen in Figure 3c (bottom right panel). The final baseline drift-corrected DADS are obtained via a simple cumulative integration, to yield the DADS (Figure 3d).

After the application of the Savitzky–Golay filter, the global fit of the data has been performed in two steps, from 1 ps to 2 ns and then from 1 ns to 900 μ s; this prevents the high amplitudes of the initial evolution from biasing long time lower signal amplitude data. The SVD of the entire rEGFP2 TRMPS-IR derivative data set highlighted the presence of seven underlying components (three from 1 ps to 2 ns and four from 1 ns to 900 μ s). The results are displayed in Figure 4. Considering the higher signal-to-noise ratio of the TRUV-

vis data and the number of time points collected between 0 and 1 ps (the first time point recorded in TRMPS-IR is 1 ps), we fixed the first time constant to 0.7 ps and left the other two free for the TRMPS-IR data,³⁴ obtaining values of 5.5 ± 0.1 and 117 ± 7 ps. The DADS of the first component (0.7 ps) is characterized by a positive contribution of the excited state at 1620 cm^{-1} and a negative one at 1686 cm^{-1} [a negative DADS for a positive signal in the transient spectra implies the formation of this signal (Figure 4a, blue curve)], consistent with the appearance of the positive band at 1686 cm^{-1} in the original data [discussed above (Figure 2), 30 ps]. The 1620 cm^{-1} band can be assigned to the chromophore C=C vibration by comparison with the attributions by Warren et al.⁷ in Dronpa, although there may be contributions from protein modes according to Laptенок et al.⁶ The 1686 cm^{-1} band is assigned to the C=O stretching of a *cis* chromophore and is located near the C=O stretching band of the *trans* chromophore peaking at 1681 cm^{-1} (positive band in Figure 1). This red-shift of the C=O stretching peak between a *cis* chromophore and a *trans* chromophore has been observed and considered the primary *trans*-to-*cis* isomerization signature for Dronpa and Dronpa2 and the *o*-HBDI analogue.³⁵ Concomitantly with the decay of the 0.7 ps excited state, a partial recovery of the GSB is observed. The partial recovery of the GSB signals indicates that the ultrafast isomerization occurs through a conical intersection in which part of the chromophore population evolves back to the original *trans*-neutral conformer and the remainder forward to a *cis*-neutral chromophore.

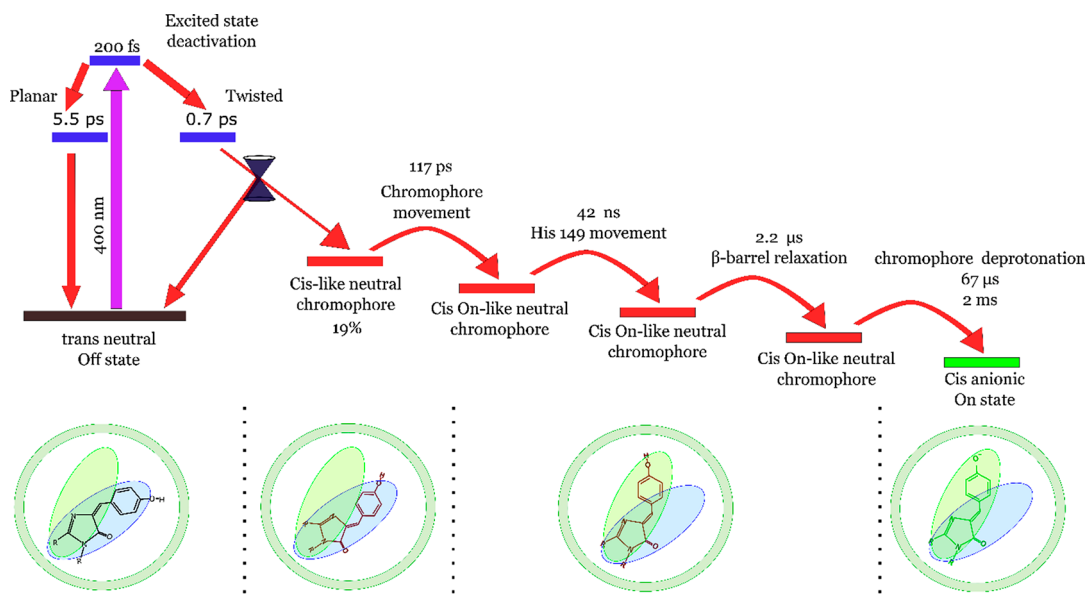
Contrary to the 0.7 ps component, the 5.5 ps (4.8 ps in TRUV–Vis) DADS (Figure 4a, orange curve) is mainly characterized by GSB recovery and ESA decay. The existence of an SE band for the 4.8 ps DADS indicates the presence of an ESA. The presence of a positive band that is red-shifted in comparison to the maximum of the GSB band can also be assigned to the presence of a hot ground state. This hot ground state population is attributed to the relaxation of part of the excited state species that, after the decay through a conical intersection in 0.7 ps, relaxes back to the original *trans* form. Such vibrational relaxation could explain the longer time component found for the second ESA by TRMPS-IR (5.5 ps vs 4.8 ps) because IR signals are more affected by vibrational cooling processes. Within the 5.5 ps component in TRMPS-IR, essentially, the recovery of the main characteristic bands of the *trans*-neutral chromophore peaking at 1515, 1602, and 1682 cm^{-1} is observed. The first two bands correspond to the phenyl vibrations, and the last one corresponds to the C=O stretching of the imidazolinone group. Therefore, the 5.5 ps component is attributed to a conformation that does not lead to isomerization, while the 0.7 ps excited state corresponds to the *cis* photoproduct precursor. Because the DADS of the TRUV–vis data short component [0.7 ps (Figure S1f)] has a red-shifted stimulated emission, it is assigned to a twisted chromophore in the excited state while the 5.5 ps feature is assigned to a planar chromophore in the excited state, similarly to the case of fluorophores that show twisted intramolecular charge transfer, and the emission from the TICT is red-shifted in comparison to that from the localized excited state that presents no change in geometry.³⁶ Moreover, twisted HBDI chromophores have lifetimes that are much shorter than those of planar HBDI.^{37,38} The twisted geometry of the chromophore in the excited state suggested by UV–vis and IR probably differs from that captured by TR-SFX at 1 ps considering that quantum mechanical calculations predicted a zero transition dipole moment for the latter.¹ On the contrary, the same calculations predicted that the formation of the twisted chromophore in the excited state is completed in <0.5 ps via a Hula–Twist mechanism. For the S_1 state, they yielded a major twisted chromophore conformation ($\tau = -73^\circ$, and $\Phi = 11^\circ$) and an additional minor planar conformation ($\tau = -30^\circ$, and $\Phi = -11^\circ$).¹ The two excited state species (0.7 and 5.5 ps) may arise from a bifurcation of the FC state in 200 fs, populating two distinct excited states. Alternatively, two distinct chromophore ground state conformations may lead to two excited states with different decay times; note that the presence of two different coexisting *trans* forms was recently reported for crystalline rsEGFP2.^{14,39,40} After the decay of the 5.5 ps component, the GSB bands recover to ~80%. Because no extra recovery of the main GSB band can be observed at longer delay times, we consider that there is no thermal back reaction from the intermediate photoproducts back to the Off state. To support the proposed mechanism, we performed a target fit analysis (Figure S5e) assuming that the population of each excited state to be 50%. As described previously, the decay time of the first component is fixed to 0.7 ps. All other rate constants are fitted, and the results are shown in Figure S5. The species associated difference spectra (SADS) and their lifetimes are similar to those obtained from the exponential global fit [DADS (Figure S5a) and SADS (Figure S5c)]. Finally, the Off-to-On photoswitching quantum yield calculated from the rate constants is 19% (Figure S5e), in

agreement with that measured with steady state irradiation (Figure S2).

After the decay to the ground state, a species with a time constant of 117 ± 7 ps was observed (Figure 4a, green curve), in agreement with the 98 ± 16 ps time constant retrieved from the UV–vis data (Figure S1). The corresponding species is characterized by negative and positive bands at 1680 and 1691 cm^{-1} assigned to a shift of the C=O stretching. Similarly, negative signals at 1650 and 1620 cm^{-1} assigned to a protein residues and phenyl ring stretches are also observed. The shift of the C=O stretching after the decay of the excited state suggests the relaxation of the *cis*-neutral chromophore to its final *cis* On-like neutral position [TR-SFX structure captured at 10 ns (Scheme 1)] and not solely to a protein rearrangement as previously reported.¹⁴ The appearance of the *cis* isomer (1691 cm^{-1} band) for rsEGFP2 in a few picoseconds following an excited state isomerization reaction is different from observations on the related Dronpa2 protein,⁶ where the *cis* isomer (1702 cm^{-1} band) appears in 91 ns, after a protein ground state reorganization of the picosecond formed metastable intermediate. In Dronpa2, the assignment of the 1702 cm^{-1} band to the *cis* isomer was confirmed by ¹³C isotope labeling.⁶ In rsEGFP2, the isomerization precedes the change in protein structure. The difference is ascribed to a significant difference in the structure between the two proteins (see the X-ray structures of Dronpa and rsEGFP2 in Figure S6), which include both On and Off structures of the chromophore ground state and the H-bonding environment of the C=O imidazolinone group with the surrounding residues.

Four time constants were needed to fit the signal evolutions after 1 ns [DADS (Figure 4c,d) and SADS (Figure S5d)]. Note that the 2 ms time constant reported elsewhere (in D_2O)¹⁴ cannot be obtained precisely as the longest time delay probed by TRMPS-IR is 900 μs , and thus a 2 ms time constant was used as fixed value in the fit. If it is omitted, the quality of the fit is unaffected but the final state (offset) then fails to reproduce the FTIR data, as required at long times (Figure S4b). The other three time constants found are 42 ± 2 ns, 2.2 ± 0.1 μs , and 67 ± 3 μs . In addition to the 2 ms time constant, our previous UV–vis study¹⁴ reported two time constants of 5.16 and 88.4 μs (no evolution in the nanosecond range was reported). The 10 ns intermediate state structure obtained by TR-SFX features His149 in an Off-like position.¹⁴ Thus, the first UV–vis time (5.16 μs) constant was attributed to the structural evolution of His149 prior to the multistep chromophore deprotonation (88.4 μs and 2 ms; time constants both show significant deuterium isotope effects).¹⁴ The 67 μs and 2 ms species IR DADS (Figure 4c; the two DADS are represented solely in Figure S4a for the sake of clarity; SADS in Figure S5d) revealed the formation of the phenolate vibration band at 1491 cm^{-1} , and this finding agrees with the D_2O isotope effect and multistep deprotonation observed by Woodhouse et al.¹⁴ The movement of the His149 side chain was expected to occur before the deprotonation steps¹⁴ and, thus, can be attributed to the 42 ns or 2.2 μs constants found in TRMPS-IR. The δ nitrogen atom (ND1) of His149 is hydrogen-bonded to the chromophore phenolate in the On state. The 42 ns evolution has important contributions in the 1651 cm^{-1} positive band (assigned to the amide mode of residues interacting with the chromophore) and in the 1633 cm^{-1} GSB representative of the *trans* form [FTIR (Figure 1a)] and thus agrees with the movement of an amino acid side

Scheme 2. Proposed Off-to-On Photoswitching Mechanism for rsEGFP2



chain interacting with the chromophore. The fact that the 2.2 μ s DADS [SADS (Figure S5d)] shows only small variations in the band intensities suggests rearrangements that provoke small or no changes in the chromophore environment. Therefore, we tentatively attribute the 2.2 μ s evolution to the β -barrel relaxation, involving particularly the seventh, eighth, and tenth β -strands, which, as shown by rsFolder NMR studies⁴¹ or Dronpa,⁴² are the strands undergoing major distortions during the photoswitching process. Moreover, NMR studies of GFP have shown that the β -barrel is rigid on the pico- to nanosecond time scale, while significant flexibility on the micro- to millisecond time scale has been observed in β -strands 3, 7, 8, and 10 and in the α -helix carrying the chromophore.⁴³ This time scale agrees with the time constant of 2.2 μ s being attributed to β -barrel relaxation.

In summary, we hypothesize that once the *cis*-neutral chromophore (117 ps) and the surrounding amino acids (42 ns) adopt their final position, a general relaxation of the protein occurs (2.2 μ s), which provokes changes in the pK_a that in turn triggers the chromophore deprotonation in the micro- to millisecond time range (Scheme 2). The offset obtained from the fit (Figure 4c) is in agreement with the FTIR spectra and confirms both the deprotonation step occurring in the millisecond range and the formation of the final *cis*-anionic On state.¹⁴ The two-deprotonation processes can be due to either a multistep deprotonation via Thr204 and His149 to the solvent outside the protein as suggested for GFP,⁴⁴ which is triggered by a change in the pK_a once all protein rearrangements have taken place, or an average signal of several protonation/deprotonation events between the chromophore and His149 on a submillisecond time scale, as suggested by recent studies on rsFolder,⁴⁵ that finally connects the water molecule that is hydrogen bonded to the chromophore with the solvent via His149 and a chain of three water molecules.¹⁴

Altogether, the UV-vis, TR-SFX, and TRMPS-IR results allow us to suggest the following modified Off-to-On photodynamical scheme for rsEGFP2 in solution (Scheme 2; time constants are those obtained by exponential global analysis).

The proposed scheme could be obtained because of the TRMPS-IR study of rsEGFP2 photodynamics combined with the Savitzky-Golay derivative filter (only one *trans* Off state is considered).¹ We revealed a previously unreported decay time in the nanosecond range, which has been tentatively attributed to the movement of the His149 side chain, and the few-microsecond evolution reassigned to the relaxation of the β -barrel (Scheme 2 and Table S2). More importantly, the appearance of a *cis*-like chromophore band in a few picoseconds is evidence of a subpicosecond twisted excited state precursor that controls the *trans*-to-*cis* isomerization followed by a hundred-picosecond relaxation in the ground state to the protonated *cis*-On like chromophore. Ongoing theoretical calculations of IR vibrations that take into account the different bands observed to unveil the different chromophore-protein interactions. Future studies of rsEGFP2 variants mutating the His149 could verify the hypothesis that the nanosecond time constant is assigned to histidine movement.

■ ASSOCIATED CONTENT

Supporting Information

The Supporting Information is available free of charge at <https://pubs.acs.org/doi/10.1021/acs.jpcllett.1c02920>.

Materials and methods (sample preparation, acquisition of TR data, photoswitching quantum yields, generation of simulated data sets, and the fitting procedure), HBDI On and Off state formulas (Scheme S1), nature of the different vibration bands for HBDI in the literature (Table S1), TRUV-vis data of rsEGFP2 in D₂O (Figure S1), comparison of decay times obtained with published results (Table S2), UV-vis photoswitching spectra (Figure S2), thermal back reaction (Figure S3), TRMPS-IR exponential global analysis and global target fit analysis (Figures S4 and S5), X-ray structures of rsEGFP2 and Dronpa (Figure S6), validation of the Savitzky-Golay derivative filter on simulated TR data sets and application of the Savitzky-Golay derivative filter to simulated data sets (Figure S7), first-order

Savitzky–Golay derivative filter (Figure S8), integration of derivative DADS (Figure S9), influence of the baseline contribution on SVD (Figure S10), decay times obtained after the correction of the baseline drifts with a polynomial fit or via derivatives (Table S3), decay traces with fits and residues (Figure S11), reconstructed DADS (Figure S12), difference between the DADS from fits and simulated data (Figure S13), and DADS with the wrong selection of points for polynomial correction (Figure S14) (PDF)

AUTHOR INFORMATION

Corresponding Authors

Lucas M. Uriarte – Univ. Lille, CNRS, UMR 8516, LASIRE, Laboratoire de Spectroscopie pour les Interactions, la Réactivité et l'Environnement, Lille S9000, France; Email: lucasmuriarte@gmail.com

Michel Sliwa – Univ. Lille, CNRS, UMR 8516, LASIRE, Laboratoire de Spectroscopie pour les Interactions, la Réactivité et l'Environnement, Lille S9000, France; orcid.org/0000-0002-5073-8180; Email: michel.sliwa@univ-lille.fr

Authors

Raffaele Vitale – Univ. Lille, CNRS, UMR 8516, LASIRE, Laboratoire de Spectroscopie pour les Interactions, la Réactivité et l'Environnement, Lille S9000, France; orcid.org/0000-0002-7497-1673

Stanisław Niziński – Univ. Lille, CNRS, UMR 8516, LASIRE, Laboratoire de Spectroscopie pour les Interactions, la Réactivité et l'Environnement, Lille S9000, France; Quantum Electronics Laboratory, Faculty of Physics, Adam Mickiewicz University, Poznan 61-614, Poland

Kyprianos Hadjidemetriou – Univ. Grenoble Alpes, CEA, CNRS, Institut de Biologie Structurale, 38000 Grenoble, France

Ninon Zala – Univ. Grenoble Alpes, CEA, CNRS, Institut de Biologie Structurale, 38000 Grenoble, France

Andras Lukacs – Department of Biophysics, Medical School, University of Pecs, 7624 Pecs, Hungary; orcid.org/0000-0001-8841-9823

Gregory M. Greetham – Central Laser Facility, Research Complex at Harwell, Harwell Science and Innovation Campus, Didcot, Oxon OX11 0QX, U.K.

Igor V. Sazanovich – Central Laser Facility, Research Complex at Harwell, Harwell Science and Innovation Campus, Didcot, Oxon OX11 0QX, U.K.

Martin Weik – Univ. Grenoble Alpes, CEA, CNRS, Institut de Biologie Structurale, 38000 Grenoble, France

Cyril Ruckebusch – Univ. Lille, CNRS, UMR 8516, LASIRE, Laboratoire de Spectroscopie pour les Interactions, la Réactivité et l'Environnement, Lille S9000, France; orcid.org/0000-0001-8120-4133

Stephen R. Meech – School of Chemistry, University of East Anglia, Norwich NR4 7TJ, U.K.; orcid.org/0000-0001-5561-2782

Complete contact information is available at:

<https://pubs.acs.org/10.1021/acs.jpcllett.1c02920>

Notes

The authors declare no competing financial interest.

ACKNOWLEDGMENTS

L.M.U. thanks the Lille University for the Ph.D. fellowship and Jean-Julien Dubois for technical support with time-resolved spectroscopy experiments. MENESR-Univ. Grenoble Alpes Ph.D. fellowship to K.H. The Chevreul Institute (FR 2638), the Ministère de l'Enseignement Supérieur et de la Recherche, the Région Hauts de France, and FEDER are acknowledged for financial support. ANR grant to M.W. and M.S. (BioXFEL). S.R.M. acknowledges EPSRC for financial support (EP/N033647/1 and EP/M001997/1). A.L. acknowledges funding from EFOP-3.6.2-16-2017-00005. The authors acknowledge UKRI (STFC) for access to the Central Laser Facility.

REFERENCES

- (1) Coquelle, N.; Sliwa, M.; Woodhouse, J.; Schirò, G.; Adam, V.; Aquila, A.; Barends, T. R. M.; Boutet, S.; Byrdin, M.; Carbajo, S.; et al. Chromophore twisting in the excited state of a photoswitchable fluorescent protein captured by time-resolved serial femtosecond crystallography. *Nat. Chem.* **2018**, *10*, 31–37.
- (2) Nass Kovacs, G.; Colletier, J.-P.; Grünbein, M. L.; Yang, Y.; Stensitzki, T.; Batyuk, A.; Carbajo, S.; Doak, R. B.; Ehrenberg, D.; Foucar, L.; et al. Three-dimensional view of ultrafast dynamics in photoexcited bacteriorhodopsin. *Nat. Commun.* **2019**, *10*, 3177.
- (3) Pande, K.; Hutchison, C. D. M.; Groenhof, G.; Aquila, A.; Robinson, J. S.; Tenboer, J.; Basu, S.; Boutet, S.; DePonte, D. P.; Liang, M.; et al. Femtosecond structural dynamics drives the trans/cis isomerization in photoactive yellow protein. *Science (New York, N.Y.)* **2016**, *352*, 725–729.
- (4) Barends, T. R. M.; Foucar, L.; Ardevol, A.; Nass, K.; Aquila, A.; Botha, S.; Doak, R. B.; Falahati, K.; Hartmann, E.; Hilpert, M.; et al. Direct observation of ultrafast collective motions in CO myoglobin upon ligand dissociation. *Science (New York, N.Y.)* **2015**, *350*, 445–450.
- (5) Laptanok, S. P.; Lukacs, A.; Gil, A.; Brust, R.; Sazanovich, I. V.; Greetham, G. M.; Tonge, P. J.; Meech, S. R. Complete Proton Transfer Cycle in GFP and Its T203V and S205V Mutants. *Angew. Chem., Int. Ed. Engl.* **2015**, *54*, 9303–9307.
- (6) Laptanok, S. P.; Gil, A. A.; Hall, C. R.; Lukacs, A.; Iuliano, J. N.; Jones, G. A.; Greetham, G. M.; Donaldson, P.; Miyawaki, A.; Tonge, P. J.; et al. Infrared spectroscopy reveals multi-step multi-timescale photoactivation in the photoconvertible protein archetypal dronpa. *Nat. Chem.* **2018**, *10*, 845–852.
- (7) Warren, M. M.; Kaucikas, M.; Fitzpatrick, A.; Champion, P.; Sage, J. T.; van Thor, J. J. Ground-state proton transfer in the photoswitching reactions of the fluorescent protein Dronpa. *Nat. Commun.* **2013**, *4*, 1461.
- (8) Lukacs, A.; Haigney, A.; Brust, R.; Addison, K.; Towrie, M.; Greetham, G. M.; Jones, G. A.; Miyawaki, A.; Tonge, P. J.; Meech, S. R. Protein photochromism observed by ultrafast vibrational spectroscopy. *J. Phys. Chem. B* **2013**, *117*, 11954–11959.
- (9) Iuliano, J. N.; Hall, C. R.; Green, D.; Jones, G. A.; Lukacs, A.; Illarionov, B.; Bacher, A.; Fischer, M.; French, J. B.; Tonge, P. J.; et al. Excited State Vibrations of Isotopically Labeled FMN Free and Bound to a Light-Oxygen-Voltage (LOV) Protein. *J. Phys. Chem. B* **2020**, *124*, 7152–7165.
- (10) Pirisi, K.; Nag, L.; Fekete, Z.; Iuliano, J. N.; Tolentino Collado, J.; Clark, I. P.; Pécsi, I.; Sournia, P.; Liebl, U.; Greetham, G. M.; et al. Identification of the vibrational marker of tyrosine cation radical using ultrafast transient infrared spectroscopy of flavoprotein systems. *Photochem. Photobiol. Sci.* **2021**, *20*, 369–378.
- (11) Kübel, J.; Chenchiliyan, M.; Ooi, S. A.; Gustavsson, E.; Isaksson, L.; Kuznetsova, V.; Ihalainen, J. A.; Westenhoff, S.; Maj, M. Transient IR spectroscopy identifies key interactions and unravels new intermediates in the photocycle of a bacterial phytochrome. *Phys. Chem. Chem. Phys.* **2020**, *22*, 9195–9203.

- (12) Fang, C.; Tang, L. Mapping Structural Dynamics of Proteins with Femtosecond Stimulated Raman Spectroscopy. *Annu. Rev. Phys. Chem.* **2020**, *71*, 239–265.
- (13) Greetham, G. M.; Sole, D.; Clark, I. P.; Parker, A. W.; Pollard, M. R.; Towrie, M. Time-resolved multiple probe spectroscopy. *Rev. Sci. Instrum.* **2012**, *83*, 103107.
- (14) Woodhouse, J.; Nass Kovacs, G.; Coquelle, N.; Uriarte, L. M.; Adam, V.; Barends, T. R. M.; Byrdin, M.; de la Mora, E.; Bruce Doak, R.; Feliks, M.; et al. Photoswitching mechanism of a fluorescent protein revealed by time-resolved crystallography and transient absorption spectroscopy. *Nat. Commun.* **2020**, *11*, 741.
- (15) Grotjohann, T.; Testa, I.; Reuss, M.; Brakemann, T.; Eggeling, C.; Hell, S. W.; Jakobs, S. rsEGFP2 enables fast RESOLFT nanoscopy of living cells. *eLife* **2012**, *1*, e00248.
- (16) Towrie, M.; Grills, D. C.; Dyer, J.; Weinstein, J. A.; Matousek, P.; Barton, R.; Bailey, P. D.; Subramaniam, N.; Kwok, W. M.; Ma, C.; et al. Development of a broadband picosecond infrared spectrometer and its incorporation into an existing ultrafast time-resolved resonance Raman, UV/visible, and fluorescence spectroscopic apparatus. *Appl. Spectrosc.* **2003**, *57*, 367–380.
- (17) Greetham, G. M.; Burgos, P.; Cao, Q.; Clark, I. P.; Codd, P. S.; Farrow, R. C.; George, M. W.; Kogimtzis, M.; Matousek, P.; Parker, A. W.; et al. ULTRA: A Unique Instrument for Time-Resolved Spectroscopy. *Appl. Spectrosc.* **2010**, *64*, 1311–1319.
- (18) Matousek, P.; Towrie, M.; Stanley, A.; Parker, A. W. Efficient Rejection of Fluorescence from Raman Spectra Using Picosecond Kerr Gating. *Appl. Spectrosc.* **1999**, *53*, 1485–1489.
- (19) Ghosh, A.; Smits, M.; Bredenbeck, J.; Dijkhuizen, N.; Bonn, M. Femtosecond time-resolved and two-dimensional vibrational sum frequency spectroscopic instrumentation to study structural dynamics at interfaces. *Rev. Sci. Instrum.* **2008**, *79*, 093907.
- (20) Feng, Y.; Vinogradov, I.; Ge, N.-H. Optimized noise reduction scheme for heterodyne spectroscopy using array detectors. *Opt. Express* **2019**, *27*, 20323–20346.
- (21) Beechem, J. M.; Ameloot, M.; Brand, L. Global and Target Analysis of Complex Decay Phenomena. *Instrum. Sci. Technol.* **1985**, *14*, 379–402.
- (22) Meuwis, K.; Depuydt, G.; Boens, N.; C. De Schryver, F. Comparison of simultaneous biexponential and compartmental analyses of fluorescence decay surfaces of intermolecular two-state excited-state processes. *Chem. Phys. Lett.* **1995**, *246*, 641–648.
- (23) van Stokkum, I. H. M.; Larsen, D. S.; van Grondelle, R. Global and target analysis of time-resolved spectra. *Biochim. Biophys. Acta* **2004**, *1657*, 82–104.
- (24) Ruckebusch, C.; Sliwa, M.; Pernot, P.; de Juan, A.; Tauler, R. Comprehensive data analysis of femtosecond transient absorption spectra: A review. *J. Photochem. Photobiol., C* **2012**, *13*, 1–27.
- (25) Savitzky, A.; Golay, M. J. E. Smoothing and Differentiation of Data by Simplified Least Squares Procedures. *Anal. Chem.* **1964**, *36*, 1627–1639.
- (26) Zimmermann, B.; Kohler, A. Optimizing Savitzky-Golay parameters for improving spectral resolution and quantification in infrared spectroscopy. *Appl. Spectrosc.* **2013**, *67*, 892–902.
- (27) Carlos Cobas, J.; Bernstein, M. A.; Martín-Pastor, M.; Tahoces, P. G. A new general-purpose fully automatic baseline-correction procedure for 1D and 2D NMR data. *J. Magn. Reson.* **2006**, *183*, 145–151.
- (28) Rinnan, Å.; van den Berg, F.; Engelsen, S. B. Review of the most common pre-processing techniques for near-infrared spectra. *TrAC, Trends Anal. Chem.* **2009**, *28*, 1201–1222.
- (29) Vitale, R.; Bevilacqua, M.; Bucci, R.; Magri, A. D.; Magri, A. L.; Marini, F. A rapid and non-invasive method for authenticating the origin of pistachio samples by NIR spectroscopy and chemometrics. *Chemom. Intell. Lab. Syst.* **2013**, *121*, 90–99.
- (30) Duwé, S.; De Zitter, E.; Gielen, V.; Moeyaert, B.; Vandenberg, W.; Grotjohann, T.; Clays, K.; Jakobs, S.; van Meervelt, L.; Dedeker, P. Expression-Enhanced Fluorescent Proteins Based on Enhanced Green Fluorescent Protein for Super-resolution Microscopy. *ACS Nano* **2015**, *9*, 9528–9541.
- (31) Kaucikas, M.; Tros, M.; van Thor, J. J. Photoisomerization and proton transfer in the forward and reverse photoswitching of the fast-switching M159T mutant of the Dronpa fluorescent protein. *J. Phys. Chem. B* **2015**, *119*, 2350–2362.
- (32) He, X.; Bell, A. F.; Tonge, P. J. Isotopic Labeling and Normal-Mode Analysis of a Model Green Fluorescent Protein Chromophore. *J. Phys. Chem. B* **2002**, *106*, 6056–6066.
- (33) van Thor, J. J.; Ronayne, K. L.; Towrie, M.; Sage, J. T. Balance between ultrafast parallel reactions in the green fluorescent protein has a structural origin. *Biophys. J.* **2008**, *95*, 1902–1912.
- (34) Debus, B.; Orio, M.; Rehault, J.; Burdzinski, G.; Ruckebusch, C.; Sliwa, M. Fusion of Ultraviolet-Visible and Infrared Transient Absorption Spectroscopy Data to Model Ultrafast Photoisomerization. *J. Phys. Chem. Lett.* **2017**, *8*, 3530–3535.
- (35) Hsieh, C.-C.; Chou, P.-T.; Shih, C.-W.; Chuang, W.-T.; Chung, M.-W.; Lee, J.; Joo, T. Comprehensive Studies on an Overall Proton Transfer Cycle of the ortho-Green Fluorescent Protein Chromophore. *J. Am. Chem. Soc.* **2011**, *133* (9), 2932–2943.
- (36) Kumpulainen, T.; Lang, B.; Rosspeintner, A.; Vauthey, E. Ultrafast Elementary Photochemical Processes of Organic Molecules in Liquid Solution. *Chem. Rev.* **2017**, *117*, 10826–10939.
- (37) Conyard, J.; Heisler, I. A.; Chan, Y.; Bulman Page, P. C.; Meech, S. R.; Blancafort, L. A new twist in the photophysics of the GFP chromophore: a volume-conserving molecular torsion couple. *Chem. Sci.* **2018**, *9*, 1803–1812.
- (38) Conyard, J.; Kondo, M.; Heisler, I. A.; Jones, G.; Baldrige, A.; Tolbert, L. M.; Solntsev, K. M.; Meech, S. R. Chemically modulating the photophysics of the GFP chromophore. *J. Phys. Chem. B* **2011**, *115*, 1571–1577.
- (39) Chang, J.; Romei, M. G.; Boxer, S. G. Structural Evidence of Photoisomerization Pathways in Fluorescent Proteins. *J. Am. Chem. Soc.* **2019**, *141*, 15504–15508.
- (40) Adam, V.; Hadjidemetriou, K.; Jensen, N.; Shoeman, R. L.; Woodhouse, J.; Aquila, A.; Banneville, A.-S.; Barends, T. R. M.; Bezchastnov, V.; Boutet, S.; et al. Rational control of structural off-state heterogeneity in a photoswitchable fluorescent protein provides switching contrast enhancement. *bioRxiv* **2021**, DOI: 10.1101/2021.11.05.462999.
- (41) Christou, N.-E.; Ayala, I.; Giandoreggio-Barranco, K.; Byrdin, M.; Adam, V.; Bourgeois, D.; Brutscher, B. NMR Reveals Light-Induced Changes in the Dynamics of a Photoswitchable Fluorescent Protein. *Biophys. J.* **2019**, *117*, 2087–2100.
- (42) Mizuno, H.; Mal, T. K.; Wälchli, M.; Kikuchi, A.; Fukano, T.; Ando, R.; Jeyakanthan, J.; Taka, J.; Shiro, Y.; Ikura, M.; et al. Light-dependent regulation of structural flexibility in a photochromic fluorescent protein. *Proc. Natl. Acad. Sci. U. S. A.* **2008**, *105*, 9227–9232.
- (43) Seifert, M. H. J.; Georgescu, J.; Ksiazek, D.; Smialowski, P.; Rehm, T.; Steipe, B.; Holak, T. A. Backbone dynamics of green fluorescent protein and the effect of histidine 148 substitution. *Biochemistry* **2003**, *42*, 2500–2512.
- (44) Agmon, N. Proton pathways in green fluorescence protein. *Biophys. J.* **2005**, *88*, 2452–2461.
- (45) Christou, N. E.; Giandoreggio-Barranco, K.; Ayala, I.; Glushonkov, O.; Adam, V.; Bourgeois, D.; Brutscher, B. Disentangling Chromophore States in a Reversibly Switchable Green Fluorescent Protein: Mechanistic Insights from NMR Spectroscopy. *J. Am. Chem. Soc.* **2021**, *143*, 7521–7530.

